

**A SYSTEMS FRAMEWORK AND ANALYSIS TOOL FOR
RAPID CONCEPTUAL DESIGN OF AEROCAPTURE
MISSIONS**

by

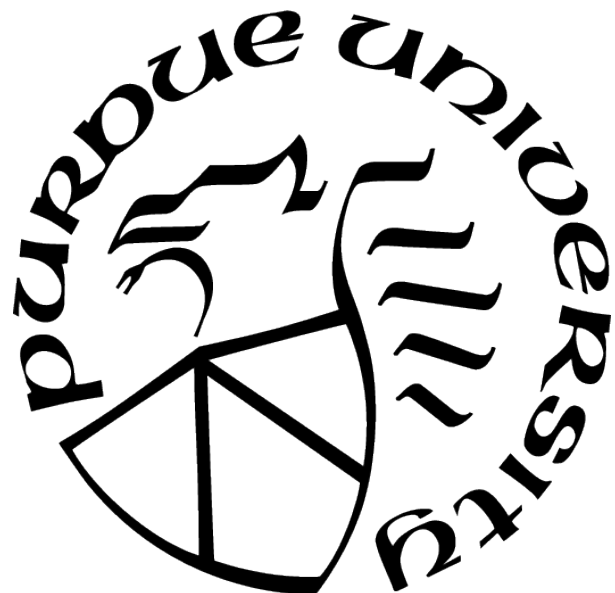
Athul Pradeepkumar Girija

A Dissertation

Submitted to the Faculty of Purdue University

In Partial Fulfillment of the Requirements for the degree of

Doctor of Philosophy



School of Aeronautics and Astronautics

West Lafayette, Indiana

August 2021

THE PURDUE UNIVERSITY GRADUATE SCHOOL
STATEMENT OF COMMITTEE APPROVAL

Dr. Sarag J. Saikia, Co-chair

School of Aeronautics and Astronautics

Dr. James M. Longuski, Co-chair

School of Aeronautics and Astronautics

Dr. David A. Spencer, Member

School of Aeronautics and Astronautics

Dr. Carolin Frueh, Member

School of Aeronautics and Astronautics

Dr. James A. Cutts, Member

NASA Jet Propulsion Laboratory

Approved by:

Dr. Gregory A. Blaisdell

Dedicated to

My parents, Pradeepkumar D. and Girija S. for their extraordinary support

Sarag Saikia for his inspiration, resolve, and steadfast commitment

ACKNOWLEDGMENTS

I would like to express my sincere gratitude to my advisors Dr. Sarag J. Saikia and Dr. James M. Longuski for introducing me to the exciting field of planetary exploration. Throughout my Ph.D., I had the opportunity to work on mission studies for nearly every target across the Solar System, which helped me learn a great deal about planetary missions from both scientific and engineering perspectives. I am grateful to them for the many opportunities I had during my doctoral study such as attending the Venus Exploration and Assessment Group (VEXAG) meetings, the Outer Planets Assessment Group (OPAG) meetings, and the International Planetary Probe Workshops (IPPW). These meetings allowed me to meet with and learn from some of the finest scientists, engineers, and students working in planetary exploration from across the globe. I would also like to thank my committee members, Dr. David Spencer and Dr. Carolin Frueh for their time and support of this work. I would like to thank Dr. James A. Cutts at the NASA Jet Propulsion Laboratory for his continued support of my work and its presentation at numerous meetings and conferences. I would like to thank my colleagues Ye Lu, Rachana Agrawal, Archit Arora, Paul Witsberger, Jeffrey Pekosh, Alec Mudek, and Robert Potter for many interesting conversations and enriching my graduate school experience. I would like to thank Morgan Delaney and Xiaomin Qian from the School of Aeronautics and Astronautics for their administrative help throughout my Ph.D. program. Special thanks are due to April Valentine from the Office of International Students and Scholars for her help during my Ph.D. studies.

I would like to acknowledge the financial support provided by the NASA Jet Propulsion Laboratory which partially supported my doctoral work. In addition, I want to acknowledge the School of Aeronautics and Astronautics and Purdue College of Engineering for providing financial support during my study. I am also grateful to the International Planetary Probe Workshop community, the Venus Exploration and Analysis Group, the Outer Planets Assessment Group, NASA Planetary Science Division, and the School of Aeronautics and Astronautics for various travel grants which I received during my graduate studies.

TABLE OF CONTENTS

LIST OF TABLES	14
LIST OF FIGURES	16
LIST OF SYMBOLS	22
ABBREVIATIONS	25
ABSTRACT	27
1 INTRODUCTION	28
1.1 The Aerocapture Mission Concept	30
1.2 Planetary Atmospheres and Models	32
1.3 A Systems View of Aerocapture	35
1.4 Dissertation Overview	38
1.5 Dissertation Contributions	39
2 LITERATURE SURVEY	40
2.1 Evolution of the Aerocapture Concept	40
2.1.1 1960s and 1970s	40
2.1.2 1980s and 1990s	41
2.1.3 2000s	44
2.1.4 2010s	46
2.2 Bibliometric Study	48
2.3 Summary	50
3 FEASIBILITY AND MASS-BENEFIT ANALYSIS OF AEROCAPTURE FOR MISSIONS TO VENUS	54
3.1 A Brief History of Venus Exploration	55
3.1.1 Science Goals and Objectives	55
3.1.2 Missions to Venus: Past, Present, and Future	55

3.2	Study Objective	62
3.3	Methodology	63
3.3.1	Atmospheric Flight Mechanics	63
3.3.2	Atmosphere Model	65
3.3.3	Arrival Conditions and Post-capture Orbit	65
3.3.4	Aerocapture Vehicles	66
3.3.5	Aerodynamic Heating and Thermal Protection System	69
3.4	Aerocapture Feasibility	73
3.4.1	Theoretical Corridor Width	73
3.4.2	Peak Deceleration	80
3.4.3	Peak Heat Rate and Total Heat Load	82
3.4.4	Aerocapture Feasibility Chart	86
3.5	Mass-Benefit Analysis	92
3.5.1	Interplanetary Trajectory	92
3.5.2	Entry System Payload Mass Fraction	93
3.5.3	Mass-Benefit Analysis	95
Dedicated Mission to Venus	96	
SmallSat Rideshare on Venus Mission	97	
SmallSat Rideshare on a Lunar Mission	98	
3.5.4	Mass-Benefit of Aerocapture	98
3.6	Conclusion	101
4	QUANTITATIVE ASSESSMENT OF AEROCAPTURE AND APPLICATIONS TO FUTURE MISSIONS	104
4.1	Methodology	104
4.1.1	Theoretical Corridor Width	105
4.1.2	Peak Deceleration	105
4.1.3	Peak Heat Rate	106
4.1.4	Total Heat Load	107
4.1.5	Vehicle Design	108

4.1.6	Atmosphere Models	110
4.1.7	Interplanetary Arrival Conditions and Target Capture Orbit	111
4.2	Interplanetary Trajectory Trade Space	112
4.2.1	Venus	113
4.2.2	Uranus and Neptune	113
4.3	Aerocapture Feasibility Charts	115
4.3.1	Venus	115
4.3.2	Earth	117
4.3.3	Mars	118
4.3.4	Jupiter	120
4.3.5	Saturn	121
4.3.6	Titan	121
4.3.7	Uranus	123
4.3.8	Neptune	125
4.4	Mass-Benefit Analysis	126
4.4.1	Methodology	126
4.4.2	Venus	128
4.4.3	Earth	130
4.4.4	Mars	130
4.4.5	Titan	132
4.4.6	Uranus	132
4.4.7	Neptune	134
4.5	Comparative Studies	136
4.6	Technology Readiness and Recommendations	139
4.7	Summary	141
4.8	Conclusions	142
5	SYSTEMS FRAMEWORK FOR RAPID CONCEPTUAL MISSION DESIGN . .	144
5.1	Mission Objective	144
5.2	Requirements Definition	145

5.2.1	Launch Vehicle	146
5.2.2	Interplanetary Trajectory and Aerocapture Vehicle Design	149
5.2.3	Science Orbit	153
5.2.4	Probe Delivery	153
5.2.5	Disposal	154
5.2.6	Summary of Requirements Definition	154
5.3	Trade Space Exploration	155
5.3.1	Launch Vehicle	155
5.3.2	Interplanetary Trajectory and Vehicle Design	157
5.3.3	Science Orbit	158
5.3.4	Probe Delivery	158
5.3.5	Disposal	159
5.4	Reference Baseline Mission Design	159
5.5	Performance Analysis	160
5.5.1	Navigation Uncertainty	162
5.5.2	Atmospheric Uncertainty	163
5.5.3	Aerodynamics Uncertainty	163
5.5.4	Guidance Algorithm	164
5.5.5	Monte Carlo Simulation Set Up	165
5.5.6	Interpretation of Results	165
5.5.7	Summary	167
5.6	Conclusions	167
6	ASSESSMENT OF SMALLSAT DRAG MODULATION AEROCAPTURE AT VENUS	169
6.1	Introduction	169
6.2	Study Objective	169
6.3	Aerocapture Trade Space and Feasibility Analysis	170
6.4	Mission Design	170
6.5	Guidance Scheme	172

6.6	Performance Analysis	174
6.6.1	Case I: Large delivery error (± 0.2 deg, 3σ)	175
6.6.2	Case II: Small delivery error (± 0.1 deg, 3σ)	175
6.7	Conclusion	177
7	ASSESSMENT OF AEROCAPTURE AT NEPTUNE USING HERITAGE BLUNT-BODY AEROSHELLS	180
7.1	A Brief History of Ice Giant Exploration	180
7.1.1	The Voyager Encounter at the Ice Giants	181
7.1.2	Objectives of the Study	184
7.2	Aerocapture Trade Space and Feasibility Analysis	186
7.3	Aerocapture Mission Design	190
7.3.1	Selection of Target Capture Orbit	192
7.4	Uncertainty Quantification	193
7.4.1	Navigation Uncertainty	193
7.4.2	Atmospheric Uncertainty	198
7.4.3	Aerodynamics Uncertainty	200
7.5	Guidance Scheme	201
7.6	Hybrid Propulsive-Aerocapture Concept	205
7.7	Pathfinder Probe Concept	208
7.8	Performance Analysis	213
7.8.1	Maximum Range of Fminmax	214
	Retrograde Entry	215
	Prograde Entry	217
7.8.2	Reduced Atmospheric Uncertainty	219
	Retrograde Entry	219
	Prograde Entry	221
7.8.3	Very Low Atmospheric Uncertainty	223
7.8.4	Sensitivity to Lift-to-Drag Ratio	225
7.9	Summary	227

7.10 Conclusion	230
8 AEROCAPTURE MISSION ANALYSIS TOOL (AMAT)	231
8.1 History	231
8.2 Previously Developed Aerocapture Tools	232
8.2.1 ACAPS	232
8.2.2 HyperPASS	232
8.3 Software Description	233
8.3.1 Choice of Programming Language	233
8.3.2 Source Code	233
8.3.3 Documentation	234
8.3.4 Installation and Example Jupyter Notebooks	234
8.4 Workflow	234
8.5 Examples	235
8.5.1 Venus SmallSat Aerocapture	235
8.5.2 Neptune Aerocapture Using Blunt-Body Aeroshells	236
8.6 Future Work	236
8.7 Summary	237
9 MAGNETIC SAILS FOR SPACECRAFT DEORBIT	238
9.1 Introduction to Magnetic Sails	239
9.2 Analytic Model for MagSail Drag in LEO	239
9.2.1 Magnetosphere Boundary for Plasma Flow Past a Dipole	240
9.2.2 Analytic Model for Magsail Performance in LEO	241
9.3 Computational MHD	245
9.3.1 Ideal MHD	246
9.3.2 BATS-R-US MHD Code	248
9.3.3 Test Cases: Earth and Ganymede	251
9.3.4 Computational MHD Model of Magsail in Plasma Wind without Ambient Field	254
9.4 MagSail Deployer Studies	256

9.5	CubeSat Flight Experiment Concept	262
9.5.1	Mission Requirements and Constraints	263
9.5.2	Key System Trades	264
	Orbit Selection	264
	Satellite Form Factor	265
	Number of Satellites	265
	Attitude Control	266
	Telemetry and Command	267
	Tracking	267
	Power System and Batteries	268
	On Board Data Handling	268
	Deployment System	269
9.5.3	Baseline Mission Concept	270
9.5.4	Flight System Design	272
	Mass Budget	272
	Power Budget	273
	Link Budget	275
9.5.5	Configuration Drawings	277
9.5.6	Mission Analysis	277
9.6	Magnetoshell Aerocapture	282
9.7	Conclusion	282
10	TECHNOLOGY RECOMMENDATIONS	284
10.1	Mission Design Tools	284
10.2	Navigation and Guidance	285
10.3	Aerocapture Vehicle Design	286
10.4	Thermal Protection Systems	287
10.5	Spacecraft and Probe Design	288
10.6	Atmosphere Models	289
10.7	Satellite Tour Design	290

10.8	Programmatic, Cost, and Risk Considerations	291
10.9	Small Satellite Constellations	294
10.10	Design Reference Missions	295
10.11	Conclusions	296
11	SUMMARY	297
	REFERENCES	300
A	ENTRY SYSTEM MASS BREAKDOWN	326
A.1	MSL Mass Breakdown	326
A.2	ADEPT Mass Breakdown	326
B	ADDITIONAL FEASIBILITY CHARTS	327
B.1	Venus	327
B.2	Earth	329
B.3	Mars	331
B.4	Jupiter	333
B.5	Saturn	335
B.6	Titan	337
B.7	Uranus	339
B.8	Neptune	341
C	NEPTUNE AEROCAPTURE GUIDANCE PARAMETERS	343
D	AMAT INSTALLATION INSTRUCTIONS	345
E	AMAT: EXAMPLE JUPYTER NOTEBOOKS	349
F	AMAT EXAMPLE: VENUS SMALLSAT AEROCAPTURE: PART 1	368
G	AMAT EXAMPLE: VENUS SMALLSAT AEROCAPTURE: PART 2	377
H	AMAT EXAMPLE: NEPTUNE AEROCAPTURE: PART 1	382

I AMAT EXAMPLE: NEPTUNE AEROCAPTURE: PART 2	391
VITA	403
PUBLICATIONS	404

LIST OF TABLES

1.1	Key advantages and disadvantages of using aerocapture.	30
3.1	Comparison of planetary parameters of Venus and Earth	65
3.2	L/D and TRL of some selected entry vehicles	68
3.3	TPS materials used in past entry missions	72
3.4	Mass fractions for past entry missions/concepts and estimated payload mass fraction at Venus	95
4.1	Aerodynamic heating correlations	107
4.2	Atmospheric models and entry interface definition	111
4.3	Target capture orbits	112
4.4	Initial capture orbits for aerobraking	128
4.5	Aerocapture recommendations for future missions	141
5.1	Nominal aeroshell mass fractions	148
5.2	Sample of feasible interplanetary trajectory options for a Neptune mission . . .	152
5.3	Potential aeroshell designs for a Neptune mission	152
5.4	Summary of requirements	155
5.5	Launch vehicle trade study	156
5.6	Interplanetary trajectory and vehicle design study	157
5.7	Reference baseline design	161
5.8	Nominal 3σ EFPA errors	163
6.1	Monte Carlo uncertainties	175
6.2	Statistics from Monte Carlo simulations	178
6.3	Summary of vehicle performance parameters	179
7.1	Camera specifications	194
7.2	Data tracking schedules and assumed noise	194
7.3	Estimated navigation filter parameters and uncertainties	196
7.4	1σ EFPA uncertainty using current Neptune ephemeris	197
7.5	Minimum required L/D and deterministic propulsive ΔV cost for hybrid aerocapture-propulsive approach using small initial capture orbits	206
7.6	Minimum L/D for hybrid approach with a propulsive ΔV at exit.	209

7.7	Monte Carlo uncertainties	214
7.8	Statistics from Monte Carlo simulation with full range of Fminmax	220
7.9	Statistics from Monte Carlo simulation with reduced atmospheric uncertainty .	222
7.10	Statistics from Monte Carlo simulation with very low atmospheric uncertainty .	226
7.11	Statistics from Monte Carlo simulation with $L/D = 0.35$	228
7.12	Statistics from Monte Carlo simulation with $L/D = 0.30$	229
7.13	Summary of results from L/D trade study.	230
9.1	Comparison of magsail and aerodynamic drag sail drag-to-mass ratio.	245
9.2	CubeSat mass budget	273
9.3	CubeSat power budget for option #1 (powered only during sunlight)	274
9.4	CubeSat power budget for option #2 (constant power the entire time).	275
9.5	CubeSat link budget	276
A.1	Mass breakdown for MSL entry system	326
A.2	Mass breakdown for ADEPT entry system	326

LIST OF FIGURES

1.1	Schematic showing various aeroassist techniques.	29
1.2	Schematic showing the various phases of the aerocapture maneuver.	31
1.3	Schematic showing the variety of planetary atmospheres in the Solar System.	33
1.4	Illustration of various density models for planetary atmospheres.	35
1.5	Key elements of the aerocapture mission concept.	36
1.6	A systems view of the aerocapture mission concept.	37
2.1	Schematic of the aerocapture mission concept.	42
2.2	Schematic of the proposed AFE entry vehicle.	43
2.3	Schematic of the proposed AFTE entry vehicle for aerocapture technology demonstration.	45
2.4	Schematic of the proposed mid- <i>L/D</i> vehicle for aerocapture at Neptune.	47
2.5	Histogram showing the number of publications since 1960	50
2.6	Histogram showing the number of publications, classified by target planet	51
2.7	Pie chart showing the target break-up from the publications. Mars is the most well-studied destination, while Uranus is the least studied destination for aerocapture.	52
2.8	Pie chart showing the sources of aerocapture related publications.	52
2.9	Pie chart showing the institutional affiliations of first authors.	53
2.10	Number of publications every year, classified by country of origin.	53
3.1	Artist's illustration of an ancient water ocean on Venus.	54
3.2	180 degree panorama of Venus surface from the Venera-9 lander.	56
3.3	Color panorama of Venus surface from the Venera-13 lander (Camera 1).	57
3.4	Color panorama of Venus surface from the Venera-13 lander (Camera 2).	57
3.5	Color panorama of Venus surface from the Venera-14 lander (Camera 1).	58
3.6	Color panorama from the Venera-14 lander (Camera 2).	58
3.7	Radar map of Venus from Magellan.	59
3.8	False color image of Venus in ultraviolet light.	60
3.9	Artist's concept of the future Venera-D mission approaching Venus.	61
3.10	Lift and drag modulation aerodynamic control approaches.	67

3.11	Illustration of Theoretical Corridor Width (TCW) and other aerocapture vehicle design considerations.	73
3.12	Overshoot and undershoot boundaries for lift modulation aerocapture	74
3.13	TCW contours for lift modulation aerocapture.	77
3.14	TCW contours for drag modulation aerocapture.	78
3.15	Loss of corridor for single-event drag modulation aerocapture at Venus.	79
3.16	Contours of peak deceleration (Earth g) for lift modulation aerocapture.	81
3.17	Contours of peak deceleration (Earth g) for drag modulation aerocapture.	82
3.18	Contours of peak heat rate (W/cm^2) for lift modulation aerocapture	83
3.19	Contours of peak heat rate (W/cm^2) for drag modulation aerocapture	84
3.20	Contours of total heat load (kJ/cm^2) for lift modulation aerocapture	84
3.21	Contours of total heat load (kJ/cm^2) drag modulation aerocapture	85
3.22	Feasible design space for lift modulation aerocapture with $\beta = 50 \text{ kg}/\text{m}^2$	88
3.23	Feasible design space for lift modulation aerocapture with $\beta = 500 \text{ kg}/\text{m}^2$	88
3.24	Lift modulation aerocapture feasibility chart for $\beta = 50 \text{ kg}/\text{m}^2$	89
3.25	Lift modulation aerocapture feasibility chart for $\beta = 500 \text{ kg}/\text{m}^2$	90
3.26	Feasible design space for drag modulation aerocapture with $\beta_1 = 5 \text{ kg}/\text{m}^2$	91
3.27	Feasible design space for drag modulation aerocapture with $\beta_1 = 50 \text{ kg}/\text{m}^2$	91
3.28	Drag modulation aerocapture feasibility chart for $\beta_1 = 5 \text{ kg}/\text{m}^2$	92
3.29	Drag modulation aerocapture feasibility chart for $\beta_1 = 50 \text{ kg}/\text{m}^2$	93
3.30	Earth-Venus interplanetary trajectory trade space.	94
3.31	Propulsive payload mass fraction to $400 \times 60,000 \text{ km}$ Venus orbit.	99
3.32	Comparison of different orbit insertion techniques for Venus missions.	100
3.33	Effect of arrival V_∞ on different orbit insertion techniques at Venus.	102
4.1	L/D of various existing and conceptual entry vehicles.	109
4.2	A drag modulation vehicle concept with detachable drag-skirt	110
4.3	Trade space for Venus interplanetary trajectories.	113
4.4	Trade space for Uranus interplanetary trajectories.	114
4.5	Trade space for Neptune interplanetary trajectories.	115
4.6	Aerocapture feasibility charts for Venus.	116

4.7	Aerocapture feasibility charts for Earth.	117
4.8	Aerocapture feasibility charts for Mars.	119
4.9	Aerocapture feasibility charts for Jupiter.	120
4.10	Aerocapture feasibility charts for Saturn.	121
4.11	Aerocapture feasibility charts for Titan.	122
4.12	Aerocapture feasibility charts for Uranus.	124
4.13	Aerocapture feasibility charts for Neptune.	126
4.14	Comparison of payload mass fractions to a 400×400 km Venus orbit	129
4.15	Comparison of payload mass fractions to a 400×400 km Earth orbit using various techniques.	131
4.16	Comparison of payload mass fractions to a 400×400 km Mars orbit using various techniques.	131
4.17	Comparison of payload mass fractions to a 1700×1700 km Titan orbit using various techniques.	133
4.18	Comparison of payload mass fractions to a 10-day Uranus orbit using various techniques.	134
4.19	Comparison of payload mass fractions to a $4000 \times 400,000$ km Neptune orbit using various techniques.	135
4.20	Comparison of entry speed and entry corridor for aerocapture at various destinations.	136
4.21	Comparison of theoretical corridor width for aerocapture at various destinations.	137
4.22	Comparison of peak deceleration load for aerocapture at various destinations.	138
4.23	Comparison of stagnation-point heat rate and total heat load for aerocapture at various destinations.	138
4.24	Peak heat rate and stagnation pressure curves for lift modulation aerocapture at various targets.	139
5.1	Escape performance of various launch vehicles.	147
5.2	Interplanetary trajectory trade space for missions to Neptune.	150
5.3	Neptune aerocapture feasibility chart.	151
5.4	Density variations in Titan's atmosphere.	164
5.5	Sample result from a Monte Carlo simulation	166
5.6	Flowchart showing the systems framework for rapid aerocapture mission design.	168
6.1	Drag modulation aerocapture feasibility chart for Venus (SmallSat).	171

6.2	Drag modulation guidance schematic.	173
6.3	On-board density estimation during drag modulation aerocapture at Venus.	174
6.4	Apoapsis distribution for ± 0.2 deg, 3σ EFPA error.	176
6.5	Peak deceleration and stagnation-point heat rate for ± 0.2 deg, 3σ EFPA error.	176
6.6	Apoapsis distribution for ± 0.1 deg, 3σ EFPA error.	177
6.7	Peak deceleration and stagnation-point heat rate for ± 0.1 deg, 3σ EFPA error.	179
7.1	Uranus and Neptune as seen by the Voyager 2 spacecraft.	180
7.2	Artist's illustration of a blunt-body aerocapture vehicle approaching the Neptune-Triton system.	186
7.3	Neptune aerocapture feasibility chart.	188
7.4	Contribution of various uncertainties for required TCW.	189
7.5	Mean density profile variations from Neptune-GRAM.	199
7.6	Random perturbed density profiles from Neptune-GRAM.	199
7.7	Altitude history of the aerocapture maneuver showing the equilibrium glide phase and exit phase of the guidance algorithm.	202
7.8	Comparison of an actual perturbed random profile from Neptune-GRAM and estimated density profile from measured drag deceleration.	203
7.9	Percentage error in on-board density estimation	204
7.10	Effect of initial capture orbit period on vehicle L/D requirement.	206
7.11	Second hybrid propulsive-aerocapture technique.	207
7.12	Effect of allowable propulsive ΔV at exit on vehicle L/D requirement.	208
7.13	Effect of mean density variation on the theoretical aerocapture corridor.	210
7.14	Effect of reduced atmospheric uncertainty on EFPA selection.	212
7.15	Apoapsis histogram for maximum range of Fminmax (retrograde).	216
7.16	Apoapsis dispersion for maximum range of Fminmax (retrograde).	216
7.17	Peak deceleration and stagnation-point heat rate for maximum range of Fminmax (retrograde).	217
7.18	Apoapsis vs periapsis altitude for maximum range of Fminmax (prograde).	218
7.19	Peak deceleration vs. stagnation-point heat rate for maximum range of Fminmax (prograde).	218
7.20	Apoapsis distribution for reduced atmospheric uncertainty (retrograde).	221
7.21	Apoapsis distribution for reduced atmospheric uncertainty (prograde).	223

7.22	Apoapsis distribution for very low atmospheric uncertainty (retrograde).	224
7.23	Apoapsis distribution for very low atmospheric uncertainty (prograde).	224
8.1	AMAT rapid mission design workflow.	235
9.1	Analytic solution of the magnetopause for a dipole in a plasma flow.	241
9.2	Comparison of a 10 m radius magsail and aerodynamic sail drag-to-mass ratio as a function of altitude.	246
9.3	Magnetosphere cavity created by the Earth’s magnetic field.	253
9.4	Alfven wings created by Ganymede in Jupiter’s magnetosphere.	254
9.5	Magsail-plasma interaction in LEO.	255
9.6	Composite bistable tape spring in its coiled configuration.	257
9.7	Composite bistable tape spring in its deployed configuration.	257
9.8	InflateSail mission with its drag sail deployed using bistable tape springs.	258
9.9	View of the inside of the prototype magsail deployer.	258
9.10	Stowed configuration of the deployer with the magsail wire.	259
9.11	Uncontrolled deployment of the tape spring magsail.	260
9.12	Controlled deployment of the tape spring magsail.	261
9.13	InflateSail mission with its drag sail in its deployed configuration in orbit.	269
9.14	InflateSail mission with its sail deployed during ground testing.	270
9.15	Artist’s concept of the magsail deorbit CubeSat flight experiment.	271
9.16	Battery charge time history for option #1.	274
9.17	Battery charge time history for option #2.	276
9.18	Exploded view of the 1U CubeSat.	277
9.19	Orbit evolution of the two 1U CubeSats over the first 100 days.	278
9.20	Relative separation between the two 1U CubeSats over the first 100 days.	279
9.21	Deorbit predictions for the CubeSat flight experiment.	280
9.22	Orbit decay predictions for a 100 kg satellite from various circular orbits.	281
9.23	Plasma aerocapture with a trailing magnetoshell configuration.	283
B.1	Lift modulation aerocapture feasibility chart for Venus.	327
B.2	Drag modulation aerocapture feasibility chart for Venus.	328
B.3	Lift modulation aerocapture feasibility chart for Earth.	329

B.4	Drag modulation aerocapture feasibility chart for Earth.	330
B.5	Lift modulation aerocapture feasibility chart for Mars.	331
B.6	Drag modulation aerocapture feasibility chart for Mars.	332
B.7	Lift modulation aerocapture feasibility chart for Jupiter.	333
B.8	Drag modulation aerocapture feasibility chart for Jupiter.	334
B.9	Lift modulation aerocapture feasibility chart for Mars.	335
B.10	Drag modulation aerocapture feasibility chart for Saturn.	336
B.11	Lift modulation aerocapture feasibility chart for Titan.	337
B.12	Drag modulation aerocapture feasibility chart for Titan.	338
B.13	Lift modulation aerocapture feasibility chart for Uranus.	339
B.14	Drag modulation aerocapture feasibility chart for Uranus.	340
B.15	Lift modulation aerocapture feasibility chart for Neptune.	341
B.16	Drag modulation aerocapture feasibility chart for Neptune.	342
C.1	Actual dynamic pressure profile and linear approximation used to calculate guidance gain parameters.	344

LIST OF SYMBOLS

a_{drag}	measured drag acceleration
A, S	aerodynamic reference area, m ²
C_L	coefficient of lift
C_D	coefficient of drag
C_3	characteristic energy, km ² /s ²
D	aerodynamic drag force, N
f_P	overall payload mass fraction for mission architecture
f_{ESS}	entry support system mass fraction
f_{TPS}	thermal protection system mass fraction
$f_{P, \text{entry}}$	entry system useful payload mass fraction
$f_{\text{TPS, Venus entry}}$	thermal protection system mass fraction for Venus entry
$f_{P, \text{Venus entry}}$	entry useful payload mass fraction for Venus entry
g, g_0	standard acceleration due to gravity, m/s ²
g_r	radial component of gravitational acceleration, m/s ²
g_θ	longitudinal component of gravitational acceleration, m/s ²
g_ϕ	latitudinal component of gravitational acceleration, m/s ²
G	peak deceleration load, Earth g
$G_h, G_{\bar{q}}$	guidance gain parameters
I_{sp}	propulsion system specific impulse, s
J_2, J_3, J_4	zonal harmonic terms
K	constant in Sutton-Graves empirical relation
K_1, K_2, K_3	constants in radiative heating correlation
L	aerodynamic lift force, N
L/D	lift-to-drag ratio
$(L/D)_{\text{trim}}$	hypersonic trim lift-to-drag ratio
m	vehicle mass, kg
q	dynamic pressure, N/m ²
\dot{q}	total stagnation-point heat rate, W/cm ²

\dot{q}_c	stagnation-point convective heat rate, W/cm ²
\dot{q}_r	stagnation-point radiative heat rate, W/cm ²
Q	integrated heat load, J/cm ²
r	radial distance from the center of the planet, m
r_p	mean equatorial radius of the planet, m
r_{pe}	periapsis radius of the capture orbit, m
RCW	required corridor width, degrees
TCW	theoretical corridor width, degrees
ToF	time of flight, days
U	gravitational potential
V	planet-relative velocity, m/s
V_∞	hyperbolic excess speed, m/s
$V_{e,i}$	inertial entry velocity at atmospheric entry interface, m/s
V_e	planet-relative entry velocity at atmospheric entry interface, m/s
V_{pe}	orbital speed of the capture orbit at periapsis, m/s
β	ballistic coefficient, kg/m ²
β_1	ballistic coefficient before drag skirt separation, kg/m ²
β_2	ballistic coefficient after drag skirt separation, kg/m ²
β_2/β_1	ballistic coefficient ratio
γ	planet-relative flight-path angle; angle between the local horizontal plane and the velocity vector, rad
ΔV	velocity increment or decrement, m/s
ϵ	additional margin over RCW, degrees
θ	longitude, rad
μ_p	standard gravitational parameter of the planet, m ³ /s ²
ρ	atmospheric density, kg/m ³
ρ_∞	freestream atmospheric density, kg/m ³
ρ_{est}	estimated density from drag deceleration
σ	bank angle, rad
δ_{CMD}	bank angle command, rad

$\delta_{\text{eq. gl.}}$ equilibrium glide bank angle, rad

ϕ latitude, rad

ψ planet-relative heading angle, rad

Ω planet rotation rate, rad/s

Subscripts

ac aerocapture insertion

e value at atmospheric entry interface

DSM deep space maneuver

max maximum value

min minimum value

OI orbit insertion

prop propulsive insertion

ABBREVIATIONS

ADEPT	Adaptive, Deployable, Entry and Placement Technology
AFE	Aerossist Flight Experiment
AFTE	Aerocapture Flight Test Experiment
AIAA	American Institute of Aeronautics and Astronautics
AMAT	Aerocapture Mission Analysis Tool
ASAT	Aerocapture Systems Analysis Team
ASI	Atmospheric Structure Instrument
AU	Astronomical Unit
CP	Carbon Phenolic
DCO	Data Cut Off
EFPA	Entry Flight Path Angle
ESA	European Space Agency
GCM	Global Circulation Model
GE	General Electric (company)
GRAM	Global Reference Atmospheric Model
GTO	Geosynchronous Transfer Orbit
HEEET	Heatshield for Extreme Entry Environment Technology
IFOV	Instantaneous Field-of-View
IRI	International Reference Ionosphere
ISP	In Space Propulsion (NASA program)
ISRO	Indian Space Research Organization
JAXA	Japanese Aerospace Exploration Agency
JPL	Jet Propulsion Laboratory
LEO	Low Earth Orbit
LORRI	Long Range Reconnaissance Imager Camera
MHD	Magneto-hydrodynamics
MSR	Mars Sample Return
MSL	Mars Science Laboratory

NASA	National Aeronautics and Space Administration
NIAC	NASA Innovative Advanced Concepts
OPAG	Outer Planets Assessment Group
RMA	Rapid Mission Architecture
RPS	Radioisotope Power System
PV	Pioneer Venus
PICA	Phenolic Impregnated Carbon Ablator
SAR	Synthetic Aperture Radar
SLS	Space Launch System
STOUR	Satellite Tour Design Program
TCM	Trajectory Correction Maneuver
TCW	Theoretical Corridor Width
TPS	Thermal Protection System
VAV	Venus Ascent Vehicle
VIRA	Venus International Reference Atmosphere
VITaL	Venus Intrepid Tessera Lander

ABSTRACT

Aerocapture offers a near propellantless and quick method of orbit insertion at atmosphere bearing planetary destinations. Compared to conventional propulsive insertion, the primary advantage of using aerocapture is the savings in propellant mass which could be used to accommodate more useful payload. To protect the spacecraft from the aerodynamic heating during the maneuver, the spacecraft must be enclosed in a protective aeroshell or deployable drag device which also provides aerodynamic control authority to target the desired conditions at atmospheric exit. For inner planets such as Mars and Venus, aerocapture offers a very attractive option for inserting small satellites or constellations into very low circular orbits such as those used for imaging or radar observations. The large amount of propellant required for orbit insertion at outer planets such as Uranus and Neptune severely limits the useful payload mass that can delivered to orbit as well as the achievable flight time. For outer planet missions, aerocapture opens up an entirely new class of short time of flight trajectories which are infeasible with propulsive insertion. A systems framework for rapid conceptual design of aerocapture missions considering the interdependencies between various elements such as interplanetary trajectory and vehicle control performance for aerocapture is presented. The framework provides a step-by-step procedure to formulate an aerocapture mission starting from a set of mission objectives. At the core of the framework is the “aerocapture feasibility chart”, a graphical method to visualize the various constraints arising from control authority requirement, peak deceleration, stagnation-point peak heat rate, and total heat load as a function of vehicle aerodynamic performance and interplanetary arrival conditions. Aerocapture feasibility charts have been compiled for all atmosphere-bearing Solar System destinations for both lift and drag modulation control techniques. The framework is illustrated by its application to conceptual design of a Venus small satellite mission and a Flagship-class Neptune mission using heritage blunt-body aeroshells. The framework is implemented in the Aerocapture Mission Analysis Tool (AMAT), a free and open-source Python package, to enable scientists and mission designers perform rapid conceptual design of aerocapture missions. AMAT can also be used for rapid Entry, Descent, and Landing (EDL) studies for atmospheric probes and landers at any atmosphere-bearing destination.

1. INTRODUCTION

Aerocapture is an orbital transfer maneuver in which a spacecraft makes a *single* pass through a planetary atmosphere to decelerate and achieve orbit insertion. Aerocapture is a subset of the larger set of aeroassist maneuvers which include aerobraking, aero-gravity assist, and direct entry as shown in Fig. 1.1. Aeroassist technologies are applicable to Solar System destinations with significant atmospheres: Venus, Earth, Mars, Jupiter, Saturn, Titan, Uranus, and Neptune. It is important to distinguish aerocapture from aerobraking, as the terms are sometimes used interchangeably but are fundamentally different maneuvers. In aerobraking the spacecraft performs a propulsive burn on arrival to get captured into a highly elliptical orbit and subsequently uses *multiple* upper atmospheric passes to lower the apoapsis over the course of several weeks to a few months. The aerobraking maneuver typically requires no thermal protection system as the velocity decrements over any one upper atmospheric pass is only a few meters per second and hence the aerothermal stress encountered by the vehicle is low. In aerogravity assist the spacecraft performs a single atmospheric pass but is *not* captured and will fly an escape trajectory on atmospheric exit. The spacecraft uses aerodynamic forces to achieve a higher hyperbolic velocity deflection angle than is possible with gravity assist. In direct entry the spacecraft enters the atmosphere from hyperbolic or elliptic orbit, but will descend or land and *not* exit the atmosphere afterwards. Aerocapture, aerogravity assist, and direct entry involve large velocity changes (several km/s) over the course of only a few minutes and require a heat shield to protect the spacecraft during the maneuver. Aerobraking has been used on numerous missions to Venus and Mars, and direct entry has been performed at Venus, Earth, Mars, Jupiter, and Saturn's moon Titan. Aerocapture and aero-gravity assist have never been used on a planetary mission.

Aerocapture offers a near propellantless, and quick method of orbit insertion at atmosphere bearing planetary destinations. Compared to conventional propulsive insertion, the primary advantage of using aerocapture is the savings in propellant mass which could be used to accommodate more useful payload. In addition, for outer planet missions, aerocapture opens up an entirely new class of short time of flight trajectories which are infeasible with

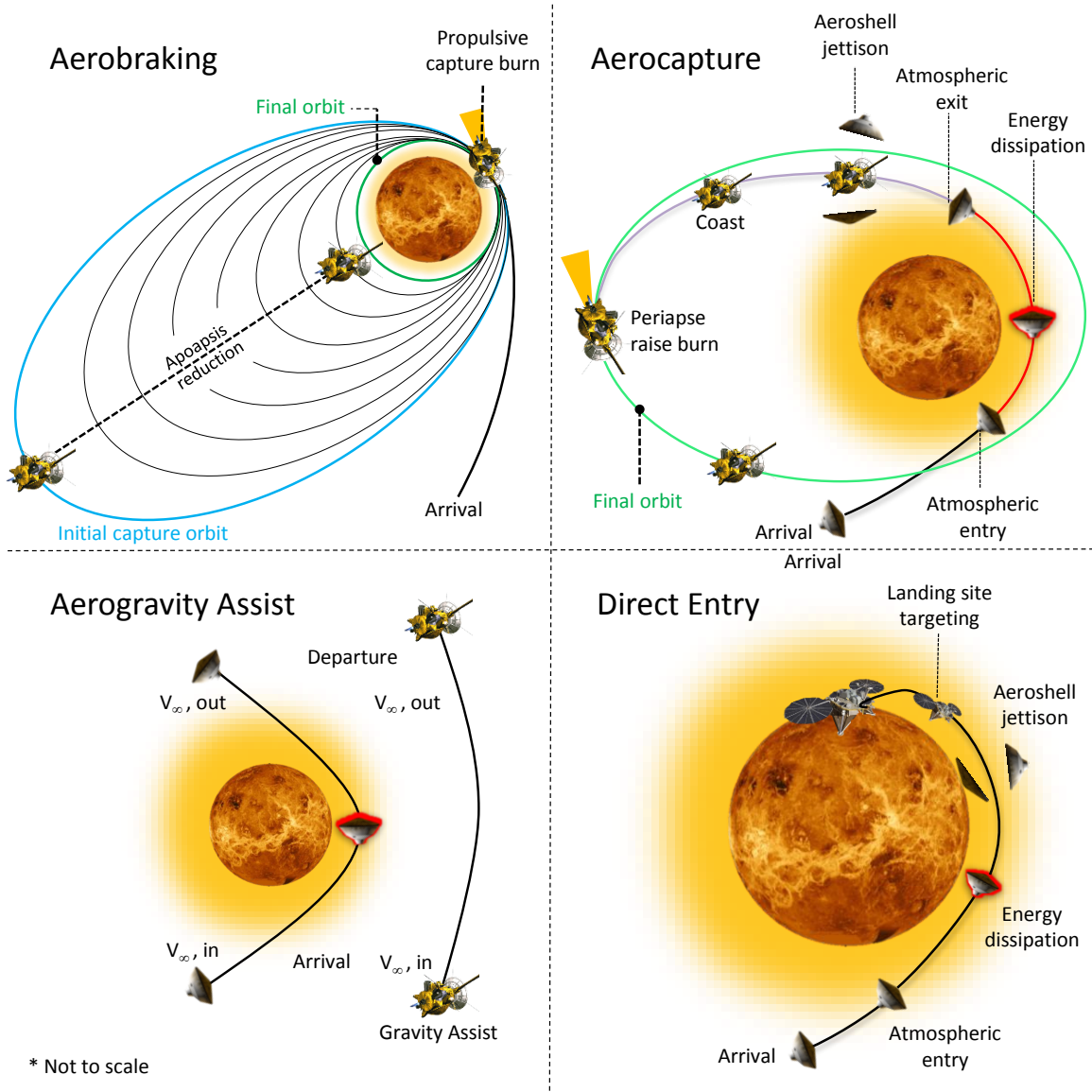


Figure 1.1. Schematic illustrating the various aeroassist techniques used in planetary exploration. The extent of the atmosphere is greatly exaggerated.

propulsive insertion. Another potential advantage of using aerocapture is that the propellant savings result in a smaller spacecraft which can be launched on a smaller launch vehicle.

Aerocapture also presents a number of challenges for spacecraft and mission design. The two most important challenges are: 1) ensuring the spacecraft has enough control authority to autonomously fly through a planetary atmosphere (sometimes not well-known) and exit the atmosphere with the correct set of conditions to achieve the target orbit; and 2) the addition of a thermal protection system (TPS) to protect the spacecraft from the aerothermal stresses

during the maneuver. The above two requirements are met by enclosing the spacecraft in an aeroshell with a heat shield, both of which add mass which is eventually not useful payload. The propellant mass savings from using aerocapture must be carefully weighed against the added mass penalty from the aeroshell structure and the TPS to quantify the performance benefit of aerocapture. Additional challenges include the higher cost and risk associated with aerocapture for an initial mission, qualification of TPS materials, relatively poor knowledge of the atmospheres for some destinations, and constraints arising from efficiently packaging the spacecraft inside an aeroshell. Table 1.1 summarizes the key advantages and disadvantages of using aerocapture for a planetary mission.

Table 1.1. Key advantages and disadvantages of using aerocapture.

Advantages	Disadvantages/risks
• Propellant mass savings	• Aeroshell and TPS mass penalty
• Shorter time of flight missions	• Poor knowledge of some atmospheres
• Smaller launch vehicle	• Spacecraft packaging constraints
• Increased science return per dollar*	• Lack of heritage missions • Higher cost and risk for initial missions

* Only few studies have estimated the costs of aerocapture mission concepts[1].

1.1 The Aerocapture Mission Concept

The aerocapture mission concept as we know it today was first articulated by Cruz [2] and is shown in Fig. 1.2. At the end of its interplanetary trajectory, the spacecraft arrives in the vicinity of the target planet. The navigation system uses trajectory correction maneuvers to target the required conditions at the atmospheric entry interface for the aerocapture maneuver. Accessories which are no longer required such as the cruise stage are now jettisoned in preparation for atmospheric entry. Once at the entry interface, the vehicle's on board autonomous guidance system is engaged. The guidance computer issues the required commands to steer the vehicle during the atmospheric flight so as to achieve a set of target conditions at atmospheric exit which will capture the spacecraft into a desired elliptical orbit.

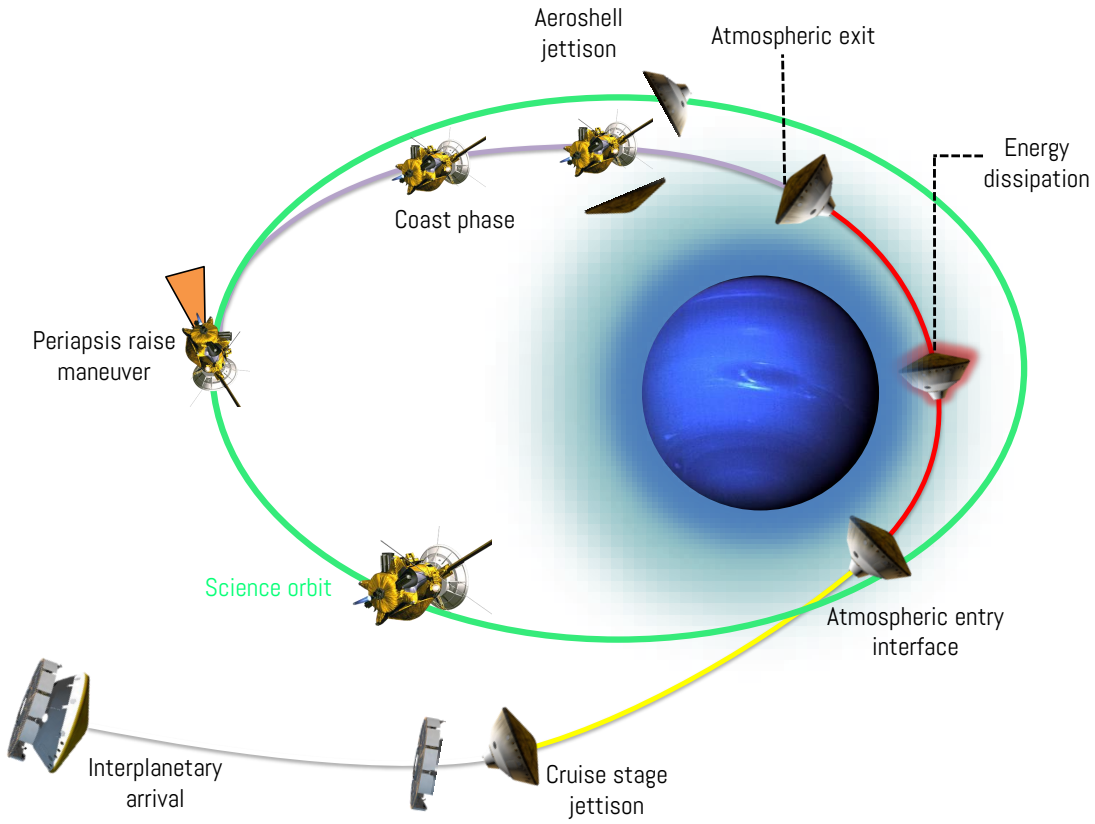


Figure 1.2. Various phases of the aerocapture maneuver from interplanetary arrival through atmospheric entry, energy dissipation, atmospheric exit, aeroshell jettison, periapsis raise, and achieving the science orbit. Both atmospheric height and the extent of the atmospheric flight in comparison to the radius of the planet are greatly exaggerated for clarity.

The entire duration of the atmospheric flight during which the energy dissipation occurs typically lasts only a few minutes after which the vehicle emerges out of the atmosphere. A small data relay satellite on a fly by trajectory may be used to capture real time vehicle telemetry data during the aerocapture maneuver. In the event of a catastrophic failure, this data will be crucial for the failure investigation if direct-to-Earth transmission is not possible. After atmospheric exit, the heat soaked shield must be jettisoned immediately, and the spacecraft antenna must be deployed along with other deployable elements such as the magnetometer boom and radioisotope power sources (RPS).

The spacecraft then coasts to the orbit apoapsis, at which a periapsis raise burn is performed to raise the periapsis outside the atmosphere. This is a critical step which will likely

be performed autonomously as a canned maneuver [3], as failure to do the burn will result in the spacecraft entering the atmosphere at the next periapsis leading to loss of mission. Other minor adjustments may be required to correct for apoapsis and inclination targeting errors from the aerocapture maneuver after which spacecraft enters its initial science orbit. The specific vehicle control requirements and the heating environments are strongly destination dependent and to some extent on the target capture orbit. Two critical failure modes for an aerocapture vehicle are: 1) penetrate too deep into the atmosphere and the vehicle will burn up or crash, and 2) exit the atmosphere without bleeding enough speed and the vehicle will continue on an escape trajectory without getting captured. The entry vehicle must have sufficient control authority to steer the vehicle away from both these scenarios in planetary atmospheres that have inherent variability, uncertainties, and density perturbations.

The schematic in Fig. 1.2 uses a blunt-body aeroshell which uses aerodynamic lift to provide control authority. The most common lift modulation technique is bank angle modulation which has been used on many entry vehicles. Alternatively, a non-lifting ballistic vehicle which can vary its drag area in a continuous or discrete manner can be used. The former control technique is called lift modulation, while the latter technique is called drag modulation and are the two most common control techniques used for aerocapture vehicles.

1.2 Planetary Atmospheres and Models

Atmospheric generation and loss processes over billions of years have resulted in a variety of planetary atmospheres across the Solar System as shown in Fig. 1.3. Apart from the scientific interest in why these worlds evolved so differently, a basic understanding of these atmospheres and their vertical structure is essential for aerocapture mission analysis.

The planet Mercury only has a very tenuous, transient atmosphere due to interaction of the solar wind with the surface, and is not of practical interest for aeroassist manuevers. The terrestrial planets Venus, Earth, and Mars have significant atmospheres that extend to about 120 km above their solid surfaces. Of course there is no distinct boundary where the atmosphere ends, but it is typical to define an atmospheric interface above which aerodynamic forces are negligible. For Venus, Earth, and Mars the atmospheric interface is typically defined at 150 km, 120 km, and 120 km respectively. Venus and Earth possess dense at-

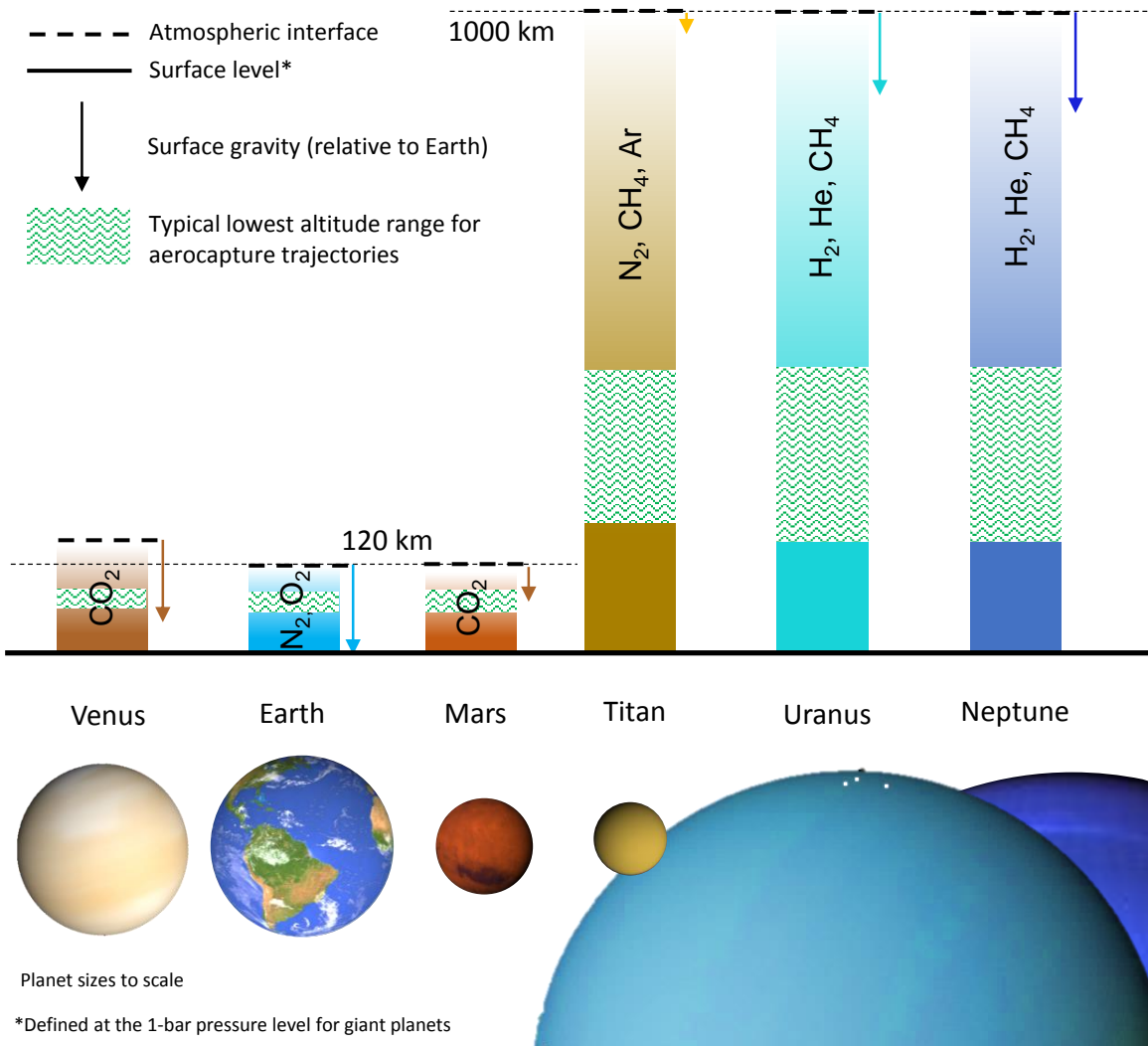


Figure 1.3. Schematic showing the variety of atmospheres with respect to their vertical extent, composition, and lowest altitude range attained by aerocapture vehicles.

mospheres, while that of Mars is relatively thin but still significant and useful for aeroassist manuevers. CO_2 is the dominant constituent in the atmospheres of Venus and Mars, while N_2 and O_2 make up most of Earth's atmosphere. The CO_2 atmosphere contributes to more convective heating at Venus compared to that of Earth as will be discussed further in Chapter 3. The basic atmospheric structure and chemistry of Venus, Earth, and Mars are fairly well known due to the abundance of both in-situ and remote sensing measurements.

In the outer Solar System, Saturn’s moon Titan is unique in that it is the only moon with a substantial atmosphere; one that may resemble that of the early Earth before life took hold. Titan’s low gravity results in a very extended atmosphere stretching out to nearly 1000 km, and is mainly comprised of N₂ and a small percentage of CH₄. The combination of small gravity well, extended atmosphere, and N₂ composition make Titan the most attractive destination for aerocapture in the Solar System as discussed further in Chapter 4. Uranus and Neptune also have thick extended atmospheres, mainly comprised of H₂, He, and traces of CH₄ which absorb in the red wavelengths and give them their characteristic blue green colors. Compared to the terrestrial planets, our knowledge of Uranus and Neptune atmospheres is relatively poor due to lack of measurements. H₂–He atmosphere chemistry is also not as well understood for prediction of aerothermal conditions encountered by the aerocapture vehicle. Jupiter and Saturn also have extended H₂–He atmospheres that may be used for aerocapture, but their enormous gravity wells result in such large entry speeds and aerothermal environments so harsh that existing thermal protection systems are infeasible.

Global Reference Atmosphere Models (GRAMs) provide engineering level estimates of the expected density profile and its uncertainty. Figure 1.4 illustrates the different models for the atmosphere of Neptune using Neptune-GRAM. The simplest possible model is an exponential profile with its scale height chosen to most closely resemble the actual density profile in the altitude range where most of the deceleration will occur. Despite its simplicity, substantial insight can be gained about aerocapture vehicle performance using just an exponential model. The next level of fidelity is look up table or piece-wise exponential model. Planetary atmospheres have spatial variations across latitude and longitude and temporal variations across time of day and seasons. GRAMs provide such latitudinal variations of the look up table where available. Monte Carlo simulations include the effects of variability, uncertainty, and random high frequency density perturbations. The most realistic, highest fidelity atmosphere models may be obtained from Global Circulation Model (GCM) simulations, which are developed for detailed studies by subject matter experts.

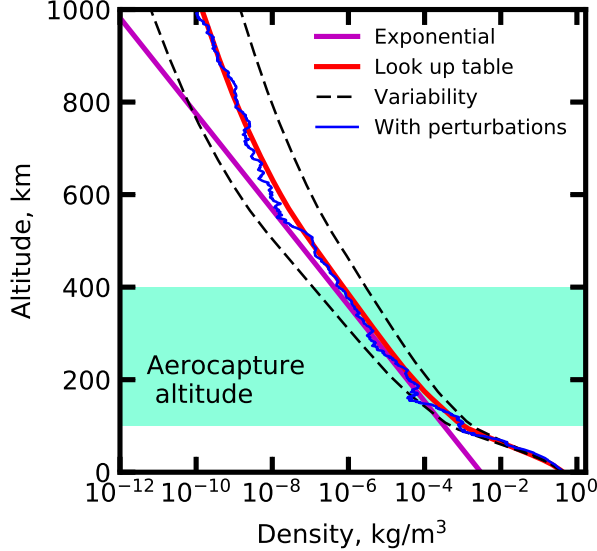


Figure 1.4. Illustration of various density models for a planetary atmosphere (Neptune). While simple exponential models are sufficient for preliminary analysis, higher fidelity calculations must use more complex models which include high frequency perturbations. Data generated using Neptune-GRAM.

1.3 A Systems View of Aerocapture

It is important to understand that the aerocapture maneuver itself is only a piece or an element within the broader set of systems that make up the mission concept as shown in Fig. 1.5. There is a launch vehicle which lofts the payload into an interplanetary trajectory which then delivers it to the destination planet’s atmospheric interface. Following the aerocapture maneuver, the spacecraft enters orbit and proceeds with the science mission and probe delivery operations. At the end of the mission, the spacecraft will be disposed of into the atmosphere or into a suitable orbit. Each of these elements are strongly interconnected with each other and the mission designer must select a synergistic combination of these elements to meet the mission objective most efficiently. This process leads to the systems engineering methodology for design of aerocapture missions, and is the primary subject of this thesis.

Figure 1.6 shows the systems engineering process flow down for aerocapture mission design. The process starts with the all important mission objective, which concisely summarizes the purpose of undertaking this endeavour. The mission objective could arise from science working groups, program managers, or study reports such as the Decadal Survey.

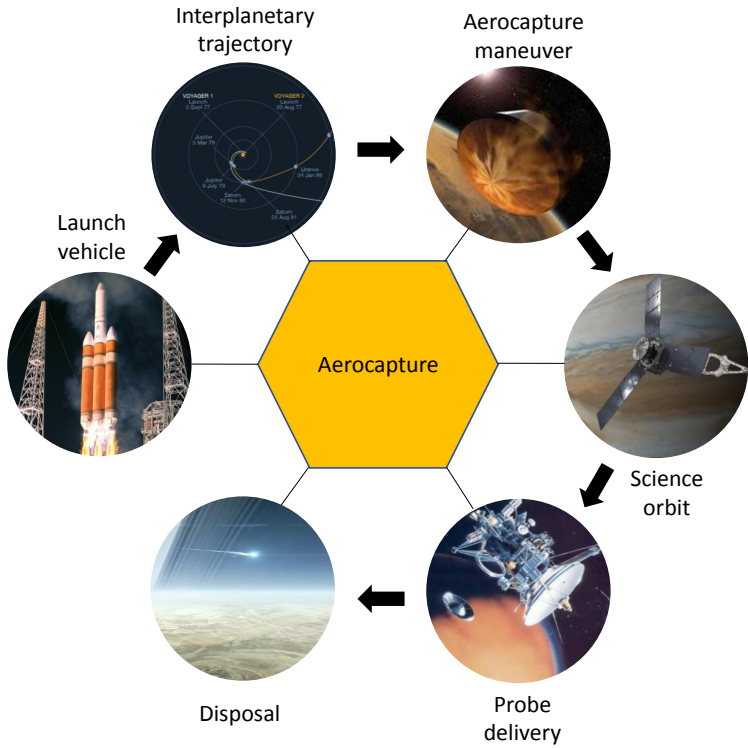


Figure 1.5. Key elements of the aerocapture mission concept. All images in the public domain. Credit: U.S. Air Force, NASA, JPL, and ESA.

An example of a high-level mission objective could be, “Deliver a spacecraft of at least 1000 kg into an orbit around Neptune which permits regular Triton flybys along with a 300 kg atmospheric probe within a \$2B cost cap and a launch date no later than June 31, 2032.” The mission designer’s first task is to define a set of functional requirements from the high-level mission objective, along with definition of study ground rules and constraints which could arise from technical, fiscal, programmatic or risk concerns. The design now enters the conceptual phase, where the objective is to seek a combination of launch vehicle, interplanetary trajectory, aerocapture vehicle, and capture orbit parameters which would meet the functional requirements and constraints identified earlier. Note the double sided arrows in this the conceptual design phase which indicates the interdependent nature of these systems. It is important to note that there is often no single solution that achieves the objectives. Multiple solutions will be possible and trade studies will be required to find an acceptable solution which minimizes or maximizes a performance index such as cost or delivered mass. A key

objective of the conceptual design phase is to perform rapid and comprehensive exploration of the trade space ideally with the capability to search through every possible point in the solution space in a reasonable timeframe and with the available mission analysis tools.

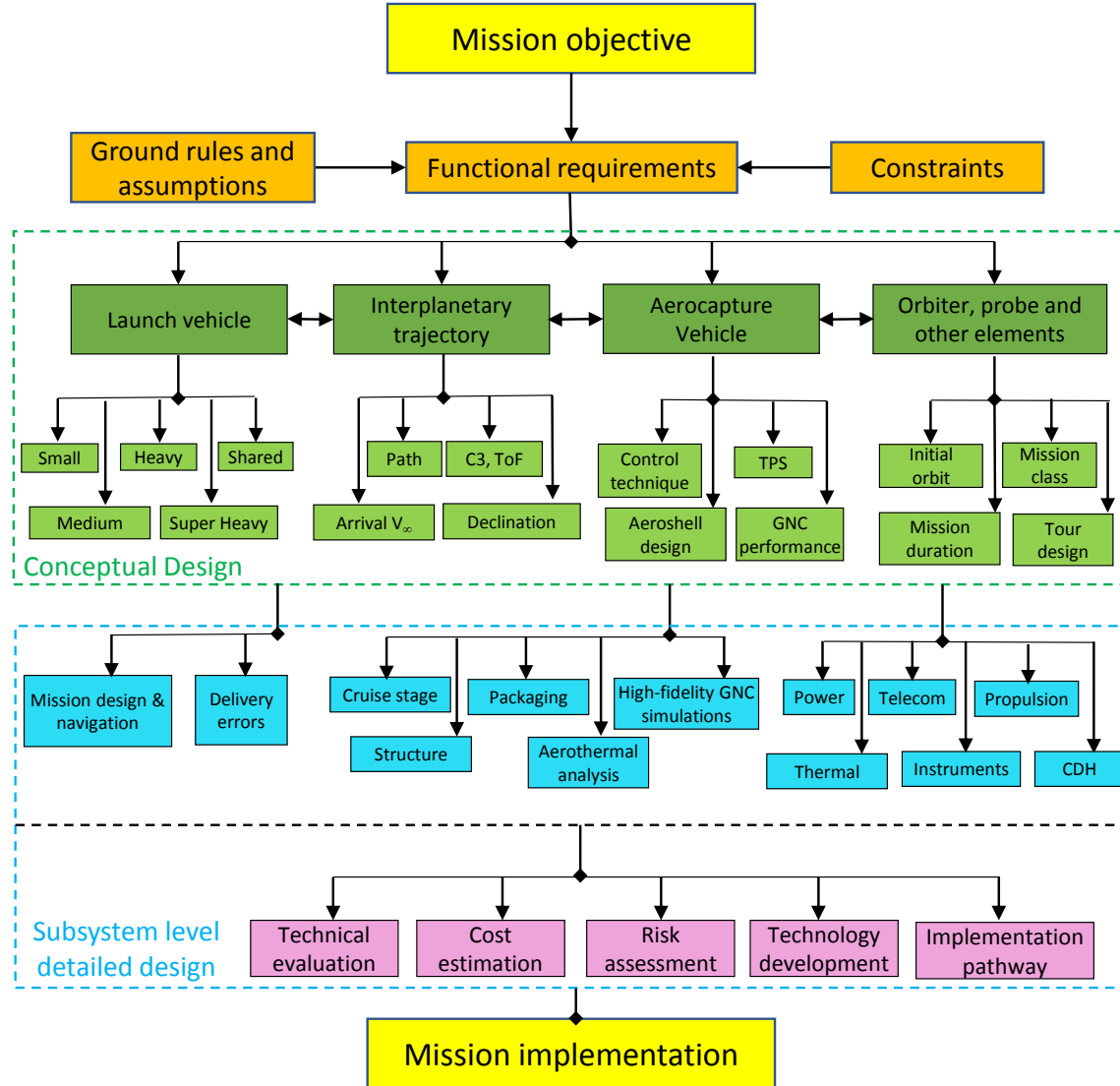


Figure 1.6. A systems view of the aerocapture concept showing the flow down from the high-level mission objective to conceptual and detailed design, and implementation.

Once an acceptable conceptual design is found and deemed worth further study, the concept proceeds to the subsystem level design which involves detailed mission design and analysis, aeroshell and TPS design, GNC simulations, orbiter and probe design etc. The

ability to perform trade studies is limited at this stage due to the much more involved and time-consuming nature of high-fidelity design calculations. The mission concept then undergoes a technical and cost evaluation (preferably independent, to remove any biases), and risk assessment. If found feasible, the study team will recommend any required developments and pathways which lead to mission implementation. It must be noted that though the process outlined in Fig. 1.6 involves aerocapture, alternative orbit insertion techniques such as aerobraking or purely propulsive insertion may be better suited to solve the problem and must be investigated in adequate detail by the mission designer.

1.4 Dissertation Overview

Chapter 1 introduces the concepts of aerocapture and aerobraking along with a brief overview of planetary atmospheres and aerocapture mission systems engineering concepts.

Chapter 2 presents an extensive review of the literature on aerocapture from the 1960s till early 2021. Results from a bibliometric study show the evolution of the concept, key events, contributors, and trends over a time span of six decades.

Chapter 3 presents a comprehensive feasibility and mass-benefit analysis of aerocapture for missions to Venus. The applicability of aerocapture is discussed for future Venus missions, and compared with alternative orbit insertion techniques such as aerobraking.

Chapter 4 extends the methodology developed in Chapter 3 for Venus to all atmosphere-bearing destinations in the Solar System including Jupiter and Saturn. Comparative studies are performed to illustrate the similarities and differences of aerocapture mission concepts across planetary targets from Venus to Neptune.

Chapter 5 describes the systems engineering framework for rapid aerocapture mission design developed in this work. This chapter provides mission designers a step-by-step procedure to formulate an aerocapture mission starting from a set of mission objectives.

Chapters 6 and 7 illustrate the application of the systems framework to perform rapid conceptual design of a Venus SmallSat mission and a Flagship-class Neptune mission respectively which are of current interest to the planetary science community.

Chapter 8 describes the Aerocapture Mission Analysis Tool (AMAT), an open-source Python package which implements the framework described in the study to enable mission designers perform rapid conceptual design of aerocapture missions.

Chapter 9 explores the concept of magnetic sails for aerobraking in a planet's ionosphere. The magnetic sail create drag forces by deflecting charged particles in the upper atmosphere. A proposed CubeSat mission concept to demonstrate the technology in LEO is described along with advanced techniques such as magnetoshell aerocapture for planetary missions.

Chapter 10 presents recommendations for aerocapture technology developments and Chapter 11 presents a summary along with directions for future work.

1.5 Dissertation Contributions

1. A comprehensive systems engineering framework has been developed for rapid conceptual design of aerocapture missions at any planetary destination taking into account the interconnected nature of various mission elements such as the launch vehicle, interplanetary trajectory, vehicle design, control techniques, and target capture orbit.
2. Aerocapture feasibility charts have been compiled for every atmosphere-bearing planetary destination, and a comprehensive, quantitative, and comparative study of aerocapture at the various Solar System destinations has been completed.
3. The framework is used to show that aerocapture is a viable and efficient method of inserting small satellites into low circular orbits at Venus and Mars.
4. The framework is used to show that a new class of trajectories enable the use of flight-heritage low- L/D vehicles to perform aerocapture at Neptune.
5. The framework is implemented in a free and open-source software, the Aerocapture Mission Analysis Tool (AMAT). AMAT enables scientists and mission designers to perform rapid aerocapture mission analysis and atmospheric probe Entry, Descent, and Landing (EDL) trade studies at any atmosphere-bearing planetary destination.

2. LITERATURE SURVEY

2.1 Evolution of the Aerocapture Concept

The use of aerodynamic forces to achieve orbit insertion as an alternative to propulsive braking has been the subject of study for nearly six decades. As part of this dissertation work, an extensive literature survey was conducted to trace the origin and evolution of the aerocapture concept over the decades. This chapter will present a comprehensive review of the existing literature, and the key milestones that occurred during each decade.

2.1.1 1960s and 1970s

The aerocapture concept or the word itself is not yet visible in the literature. London [4] in 1962, published an article which is regarded as the earliest precursor which may be related to the concept of aerocapture. London investigated the possibility of using aerodynamic maneuvering to change the plane of a satellite in Earth orbit, instead of using a propulsive maneuver. The study showed that a vehicle with lift-to-drag ratio L/D greater than 1.0 could offer significant savings for plane change maneuvers for Earth-orbiting satellites¹. London also pointed out the need for having a thermal protection system for such a vehicle, and the constraints arising from entry angles, aerodynamic deceleration, peak heat rate and total heat load to successfully perform the plane change maneuver as proposed. Finch [6] in 1965, published an article in the Journal of Spacecraft and Rockets on the use of aerodynamic braking trajectories for Mars orbit attainment. Finch's study may be considered the earliest article which proposed to use "aerodynamic braking" as an alternative to propulsive braking for the orbit insertion maneuver. Finch examined the entry corridor for such trajectories at Mars as a function of vehicle L/D and ballistic coefficient, and highlighted the sensitivity of some trajectories near the corridor bounds which made them susceptible to accidental escape. In the same year, Lichtenstein [7] published a report investigating the use of an Apollo entry vehicle to perform atmospheric braking into Martian orbit. The study concluded that aerodynamic braking can be used to reduce the spacecraft speed from interplanetary

¹There is speculation that the secretive USAF X-37B space plane with a L/D ratio of 1.0, may be leveraging this capability to achieve rapid orbital plane changes using aerodynamic forces. Performing this maneuver while on the far-side of Earth from an adversary makes it difficult for adversaries to predict its orbit [5].

approach to orbital speed, without exceeding a peak deceleration of $10\ g$. Lichtenstein also concluded that though an ablative heat shield such as the one used on Apollo was required, its mass was considerably less compared to the fuel required for propulsive braking. In 1968, Repic [8] studied the use of “aerobraking” as a potential planetary capture mode for Mars and Venus missions. This appears to be the first mention of the word aerobraking in the literature, though we now use the term to refer to a related but different maneuver than aerocapture. There appears to be a hiatus in aerocapture publications in the 1970s, this may be because the Apollo program was underway and the focus was on manned lunar exploration. In 1979, Cruz [9] at the Jet Propulsion Laboratory published a conference paper titled the “The Aerocapture Vehicle Mission Design Concept”. This appears to be the first time the word “aerocapture” is used in the literature, and articulated the mission concept as shown in Fig. 2.1. The study focused on the application of aerocapture for a Mars Sample Return mission, a problem of great scientific interest back then (and even today!). Cruz’s study was not only important due to the fact that it coined the term aerocapture, but it sparked a series of further studies in the early 1980s to refine and further develop the mission concept for both human and robotic Mars missions. The concept of aerocapture is now well established and will see remarkable developments by numerous researchers over the next several decades, even though it will not be flown and remains a “concept” to this day.

2.1.2 1980s and 1990s

Hassett [10] in 1980, studied the design integration of an aerocapture vehicle for a Mars sample return mission building on Cruz’s earlier work. The system design would enable for a Viking-type lander and an orbiter to be delivered to Mars using a single aeroshell. The orbiter would separate from the aeroshell after the aerocapture maneuver and before the periapse raise maneuver. The aeroshell with the lander would re-enter Mars at the next periapse and deliver the lander to the surface. In 1980, the General Electric (GE) Company was contracted by the Jet Propulsion Laboratory to establish the feasibility of aerocapture for missions to Mars, Saturn, and Uranus and develop conceptual designs for entry vehicles [11]. For the Saturn mission, the aerocapture maneuver will be performed at Titan which offers a benign aerothermal environment for the entry vehicle. The GE study was the first

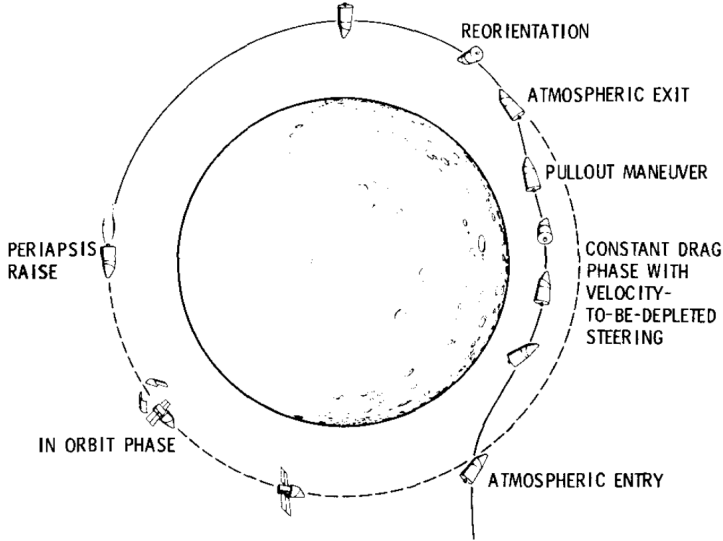


Figure 2.1. Schematic of the aerocapture mission concept by Cruz, 1979 [9]. Original work by M. I. Cruz.

study to propose the use of Titan's atmosphere to achieve orbit insertion at Saturn. Cruz [2], [12] studied the spacecraft integration, navigation, communications, and thermal protection system for Mars Sample Return (MSR) and Saturn Orbiter Dual Probe (SO2P) missions.

Tiwari et al. [13] was the first to analyze the aerothermodynamic heating environment for an aerocapture vehicle at Titan, and showed that radiative heating contribution strongly depends on the atmospheric methane mass fraction, which at the time was poorly known. Mease et al. [14] was the first to perform detailed analysis of the approach navigation requirements, optical navigation aspects, and data compression for aerocapture missions to Venus, Mars, and Titan. Green et al. [15] performed a detailed study addressing the TPS system design for a Titan aerocapture vehicle, and showed the convective heating dominates the radiative heating by an order of magnitude.

In the mid-1980s, there is an increase in the number of publications which is attributed to the NASA Johnson Space Center led effort towards the Aeroassist Flight Experiment (AFE). AFE was scheduled to fly in the late 1980s, and would involve a Shuttle-launched entry vehicle shown in Fig. 2.2 that would demonstrate an aeroassist maneuver at Earth. Cerimele et al. [16] studied the effect of density shears, density pockets, and other atmospheric phenomena which may present a challenge to the AFE vehicle. Cermiele and Gamble

[17] developed an simple, yet effective analytical guidance algorithm for the AFE vehicle. Numerous other articles were published in relation to the AFE project, but they are omitted here for brevity. Unfortunately, the AFE project was canceled due to complexity and cost overruns and was never flown. Carpenter [18] gives an account of the scenario that led to the eventual cancellation of the project. Walberg [19] in 1985, wrote a survey article reviewing the current state of aeroassist technologies and its development over the past two decades. Walberg predicted that practical aeroassist vehicles would be operational within the decade.

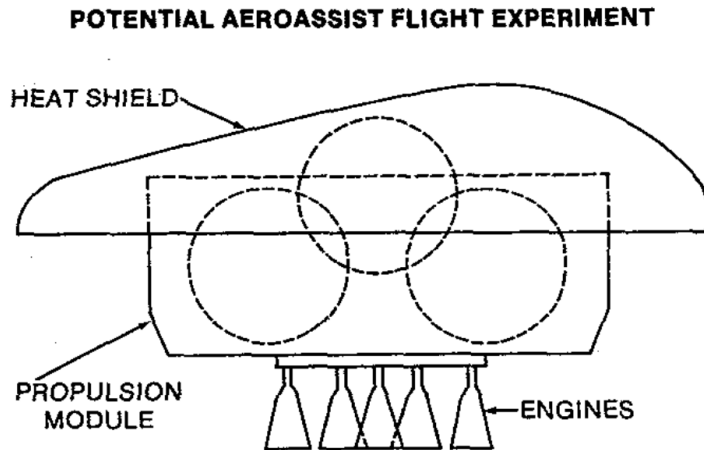


Figure 2.2. Schematic of the proposed AFE entry vehicle. Reproduced from work by Cerimele and Gamble [17].

In the early 1990s, Puig-Suari and Longuski [20] studied the use of flexible tethers for planetary aerocapture at atmosphere-bearing destinations. In 1992, Lyne et al. [21] studied the application of aerocapture at Earth and Mars for manned missions with a $5g$ peak deceleration constraint. Lyne [22] also studied the effect of parking orbit on aerocapture for manned Mars missions. In the late 1990s, aerocapture was considered for the Mars Odyssey mission (then referred to as Mars 2001 Surveyor), but was later dropped in favor of aerobraking due to cost reasons and heritage with other Mars missions [23]. Aerocapture was later also considered for the joint NASA/CNES Mars Sample Return Orbiter mission, but was canceled in the wake of the failure of the Mars Climate Orbiter and the Mars Polar Lander missions [24]. Tragesser and Longuski [25] studied the effect of errors in the knowledge of the atmosphere and initial conditions on an aerocapture tether and showed a

99% success probability at Mars. In 1998, Leszczynski [26] at the Naval Postgraduate School developed a MATLAB based tool for modeling, simulation, and visualization of aerocapture for JPL’s project design center and the concurrent engineering facility.

2.1.3 2000s

In the early 2000s, Vinh, Johnson, and Longuski [27] developed analytical solutions for Mars aerocapture using bank angle modulation and developed analytic control laws to guide the spacecraft to the desired exit state. Wercinski et al. [28] identified the aerocapture critical technology development needs for outer planet exploration in the coming decade and suggested strategies to close the gaps. In 2001, the Aerocapture Flight Test Experiment (AFTE) which proposed to demonstrate a low-cost demonstration of aerocapture at Earth using a sphere-cone aeroshell shown in Fig. 2.3. AFTE was one of the candidates in NASA’s New Millennium Program ST-7 competition [29]; and again in the ST-9 competition in 2006, though both were ultimately not selected [30]. Perot and Rousseau [31] highlighted the importance of on-board density estimation for aerocapture guidance algorithms, and showed that final orbit accuracy is significantly improved when on-board density estimation is used. Way et al. [32] studied the use of aerocapture for the Titan Explorer mission concept, a follow-on mission to the Cassini-Huygens mission. Olejniczak et al. [33] analyzed the radiative heating environment for a Titan aerocapture vehicle, and found that the radiative heating rates were five times the convective heating rates, in contrast to earlier studies by Tiwari et al. [13] who found radiative heating is not a significant contribution. McRonald, Gates, and Nock [34] at the Global Aerospace Corporation developed HyperPASS, an aerocapture simulation tool and used it to analyze manned missions at Earth and Mars as part of a NASA Innovative and Advanced Concepts (NIAC) funded study.

In 2003, aeroassist technology development was identified a vital part of the NASA In-Space Propulsion Program (ISP), which is managed by the NASA Headquarters and implemented by the NASA Marshall Space Flight Center. Within the ISP, aerocapture was identified as the focus of effort with the goal of advancing TRL 3-4 level technologies to TRL 6 for incorporation into mission planning in the immediate future [35]. A multi-center Aerocapture Systems Analysis Team (ASAT) was put together under this project to

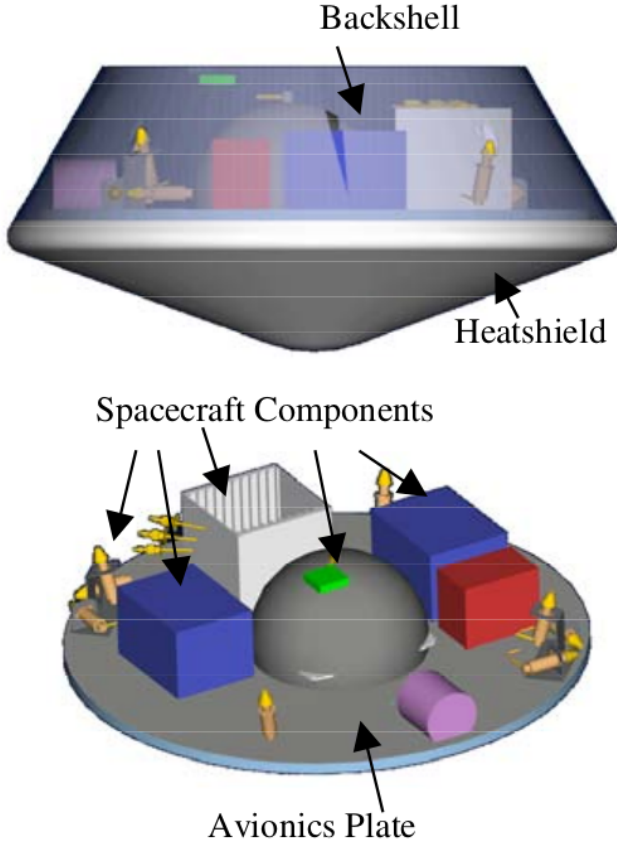


Figure 2.3. Schematic of the proposed AFTE entry vehicle for aerocapture technology demonstration. Reproduced from work by Hall [29].

define reference aerocapture missions at various Solar System destinations and identify any technology gaps to be closed before implementation on a flight project. The ASAT team led by Lockwood at the NASA Langley Research Center studied in great detail aerocapture mission concepts to Venus, Mars, Titan, and Neptune during the early 2000s, resulting in a large number of aerocapture related publications [36]–[39]. The studies concluded that using aerocapture at Titan can deliver twice as much payload to Titan orbit as compared to conventional propulsive insertion. Aerocapture at Venus can deliver twice the payload delivered with aerobraking, and over six times more mass compared to purely propulsive insertion. The benefits of aerocapture at Mars were small, but were significant for large and complex missions such as Sample Return (SR). The Neptune aerocapture studies show that

aerocapture opens up entirely new classes of missions at Neptune which are not feasible with propulsive insertion and could deliver a substantially larger spacecraft into orbit[40].

In 2008, Ingersoll and Spilker [41] highlighted the importance of aerocapture for a Cassini-style mission to Neptune with two atmospheric probes, to enable reasonable flight times and delivered mass to the distant reaches of the outer Solar System. In the late 2000s, the use of aerocapture with small satellites (SmallSat) gained attention. Fujita et al. [42] studied a drag modulation system for SmallSat orbit insertion at Venus, while Lemmerman [43] studied a small satellite mission to Neptune using aerocapture.

2.1.4 2010s

Gates and Longuski [44] compared the performance of aerocapture ballutes and tethers and found both systems offer advantages over aerocapture aeroshells and over propulsive capture. In the early 2010s, there are a number of studies from the Japanese Aerospace Exploration Agency (JAXA) investigating the aerothermal environments and mission concepts for a small-sized aerocapture demonstrator at Mars [45], [46]. Putnam and Braun [47] studied discrete-event and continuous drag modulation flight-control options for aerocapture at Venus, Mars, and Titan. Lu et al. [48] developed optimal guidance algorithms for lift modulation aerocapture and demonstrated its superior performance compared to existing numerical predictor-corrector algorithms. Nixon et al. [49] at NASA Goddard Spaceflight Center studied a Titan polar orbiter using aerocapture, though the near-ballistic non-lifting aeroshell used in the study does not provide any control authority. The first half of the 2010s appear to produce a relatively small number of publications which could be attributed to aerocapture being no longer supported by the ISPT program, and researchers who had been working on aerocapture changed their focus based on funding priorities.

The second half of the decade show a renewed interest in aerocapture primarily attributed to its applications for low-cost small satellite drag modulation system following the work of Putnam and Braun [47] at Georgia Institute of Technology, and for a Flagship-class Neptune mission in the next decade following the work of Saikia et al. [50] at Purdue University. In 2016, Saikia et al. [50] performed an assessment of aerocapture at Uranus and Neptune in support of the NASA Ice Giants Pre-Decadal Survey Mission Study [51]. The study

concluded that mid- L/D vehicles such as the one shown in Fig. 2.4 (L/D of 0.6–0.8) are required at Uranus and Neptune to accommodate the large uncertainties. Since development of new mid- L/D vehicles would be an expensive and time-consuming endeavour, the study recommended investigation of approaches to reduce the uncertainties and improve guidance algorithms to reduce the vehicle L/D requirement.

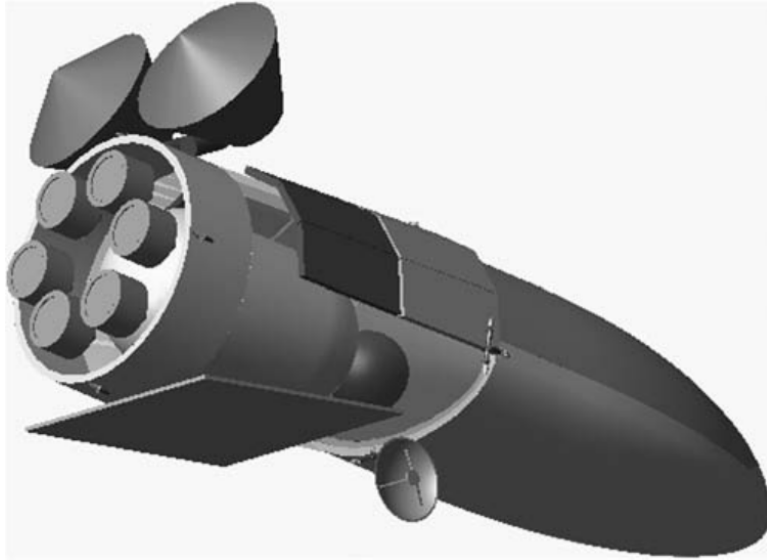


Figure 2.4. Schematic of the proposed mid- L/D vehicle for aerocapture at Neptune with two externally mounted atmospheric entry probes. Reproduced from work by Ingersoll and Spilker [41].

In 2016, Spilker et al. [3] performed a study initiated by the NASA Planetary Science Division (PSD) to assess the readiness of aerocapture at all planetary destinations. The study concluded that an aerocapture flight demonstration is not required prior to implementation on a NASA science mission, as many aerocapture system technologies have already been flown on different missions. The study recommended additional study of aerocapture at Uranus and Neptune to assess the need for mid- L/D vehicles.

In 2017, the Ice NASA Ice Giants Pre-Decadal Survey Mission Study [51] identified aerocapture as a potentially useful technology for ice giant missions. The study found pointed out the lack of architectural-level tool, models and sizing relations for rapid, high-level conceptual design of aerocapture missions. Aerocapture was not identified as an enabling technology for ice giant missions, but one that would significantly enhance the mission if it was available.

Beginning in 2018, drag modulation aerocapture has received considerable interest with its applications to small satellites for low-cost technology demonstration and rideshare planetary science missions. Werner and Braun [52] studied a SmallSat mission architecture to demonstrate aerocapture at Earth using a geosynchronous transfer orbit rideshare trajectory. Numerous recent studies have investigated the feasibility, mission and system design, and guidance performance for SmallSat mission concepts leveraging drag modulation aerocapture at Venus and Mars [53]–[56]. In 2019, the Outer Planets Analysis Group (OPAG) reiterated the potential and benefits offered by aerocapture for ice giant missions [57]. When combined with aerocapture, the Space Launch System (SLS) would enable trip times to Uranus and Neptune to be as short as 5 and 7 years respectively. Aerocapture offers substantial savings in flight time compared to a nominal 12 years to Uranus and more than 14 years to Neptune compared to propulsive insertion architectures.

Since 2016, researchers at Purdue University have been working on an integrated systems framework for comprehensive and rapid conceptual design of aerocapture missions [58]. Lu and Saikia [59] performed a comprehensive assessment of aerocapture for future Titan missions. Girija, Lu, and Saikia [60] performed a comprehensive feasibility and mass-benefit analysis of aerocapture for missions to Venus. Girija, Saikia et al. [61] used the integrated framework to show that high arrival V_∞ trajectories along with improvements in navigation and guidance algorithms can lower the L/D requirement from 0.6–0.8 to about 0.3–0.4 for aerocapture at Neptune. Aerocapture Mission Analysis Tool (AMAT) is a new software tool designed to provide rapid mission analysis capability for aerocapture concepts to the planetary science community. The lack of such a quick-look tool was identified by the NASA Ice-Giants Pre-Decadal Survey [51] and by Spilker et al. [3]. AMAT aims to fill this gap by enabling scientists and mission designers to perform rapid assessment aerocapture mission feasibility and vehicle performance at any atmosphere-bearing destination.

2.2 Bibliometric Study

The literature survey amassed over 300 publications which had aerocapture as their primary topic of discussion. The publications include journal articles, conference proceedings, book chapters, technical reports, oral presentations, and dissertations. The list of publica-

tions attempted to compile most of the available literature, but is not exhaustive. The data was compiled on Mar. 12, 2020. A few bibliometric charts are presented to illustrate some trends in aerocapture technology development over six decades, which may be of interest to some readers. The dataset is the most comprehensive collection of literature on aerocapture to the knowledge of the author and is available online as a Microsoft Excel sheet².

Figure 2.5 shows number of publications directly related to aerocapture in every year starting with London's article in 1962. Though the concept was established in the by the late 1960s, there is not much further development till the late 1970s. Cruz's paper in 1979 is the first to coin the term aerocapture, and resulted in a number of follow on studies focusing on Mars Sample Return (SR). Following a brief hiatus, the AFE project results in a number of publications in the late 1980s and early 1990s. In the late 1990s, aerocapture is considered for the Mars 2001 mission, but is eventually dropped in favor of aerobraking. The ISPT funded studies in the early 2000s, is the most prominent peak greatly adding to our knowledge of aerocapture mission concepts across the Solar System. Till the late 2010s, there is a downward trend in the number of publications. Beginning mid-2010s, there is renewed interest in aerocapture at Uranus and Neptune attributed to the NASA Ice Giants Pre-Decadal Mission Study and the use of drag modulation systems to insert small satellites into Venus orbit, to both of which this dissertation contributed data and analysis.

Figure 2.6 shows number of publications, classified by the target planet. Till the early 2000s, most studies have focused on Mars and Earth. The ISPT studies in the early 2000s are the first major studies to address aerocapture at Titan and Neptune. Beginning mid-2010s, there is an increase in the number of Neptune and Venus studies for reasons mentioned earlier. Figure 2.7 shows the percentage break-up of target planets. Mars is the most studied destination particularly for sample return missions in the 1990s, while Uranus is the least studied destination. This is likely due to the fact that there was no GRAM-model for Uranus until early 2018 [62], and this may have hampered systems analysis studies for which knowledge of the atmospheric variability and uncertainties are critical. In fact, there is no baseline reference mission concept for aerocapture at Uranus, and a future study is recommended to establish such a design reference mission. Figure 2.8 shows the sources of

²<https://github.com/athulpg007/AMAT/tree/master/bibliometric-data>

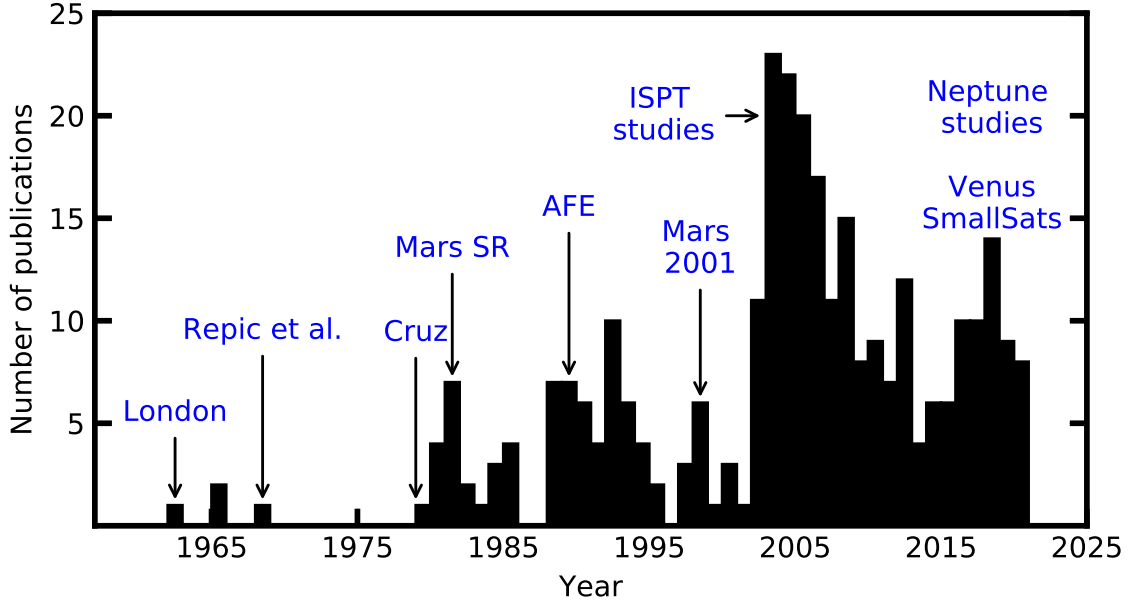


Figure 2.5. Number of publications directly related to aerocapture in every year since 1960. See text for a description of the highlighted events.

aerocapture related publications used in this study. American Institute of Aeronautics and Astronautics (AIAA) conferences and journals appear to be the leading source of information for aerocapture, with the Journal of Spacecraft and Rockets being the most prominent journal for aerocapture related publications. Figure 2.9 shows the institutional affiliations of first authors. NASA Langley Research Center, NASA Ames Research Center, and the Jet Propulsion Laboratory produced the most publications followed by Purdue University and Georgia Institute of Technology. Figure 2.10 shows the number of publications, by country of origin. The United States is the leading source, followed by Japan, Germany, and France. Beginning mid-2010s, there is considerable interest in aerocapture from Chinese researchers particularly related to drag modulation aerocapture at Mars [63], [64].

2.3 Summary

An extensive literature survey was performed to trace the origins and evolution of the aerocapture concept over the past six decades. The survey reveals several flight programs such as the AFE and the AFTE that could have demonstrated aerocapture technology and

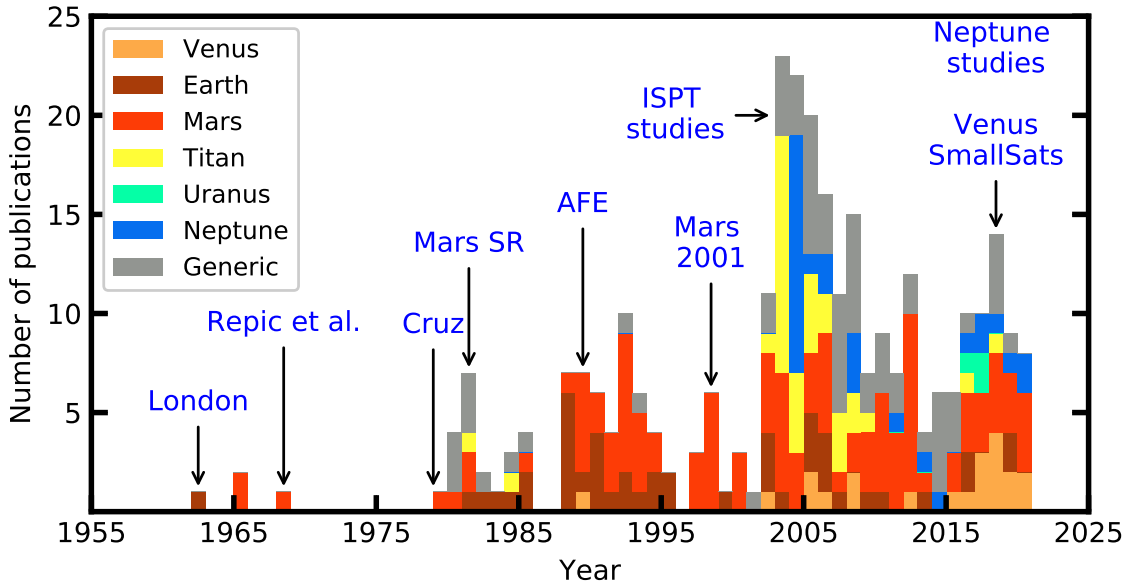


Figure 2.6. Number of publications in every year, classified by target planet. Most studies to date have been focused on Mars, followed by Earth, Venus, Titan and Neptune. Uranus is the least studied target.

may have led to its use on actual missions. Unfortunately, these experiments were not flown and hence aerocapture has never been demonstrated. Beginning late 2010s, there is renewed interest in aerocapture technology particularly for small satellite missions to Venus and Mars, and for future Flagship-class missions to Uranus and Neptune. Small satellites are of particular interest as they can accommodate higher risks without compromising large missions which are typically risk-averse. With the increasing capabilities of small satellites, it is likely that drag modulation aerocapture will be demonstrated at Mars or Venus within a decade. With advances in autonomous navigation, thermal protection system materials, improved guidance schemes and flight-control techniques, more ambitious Flagship-class missions using aerocapture at Uranus and Neptune are likely feasible within the next two decades.

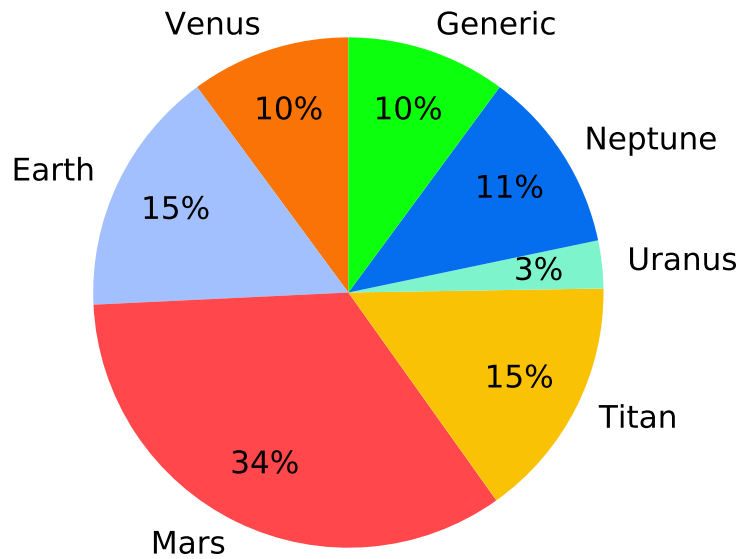


Figure 2.7. Pie chart showing the target break-up from the publications. Mars is the most well-studied destination, while Uranus is the least studied destination for aerocapture.

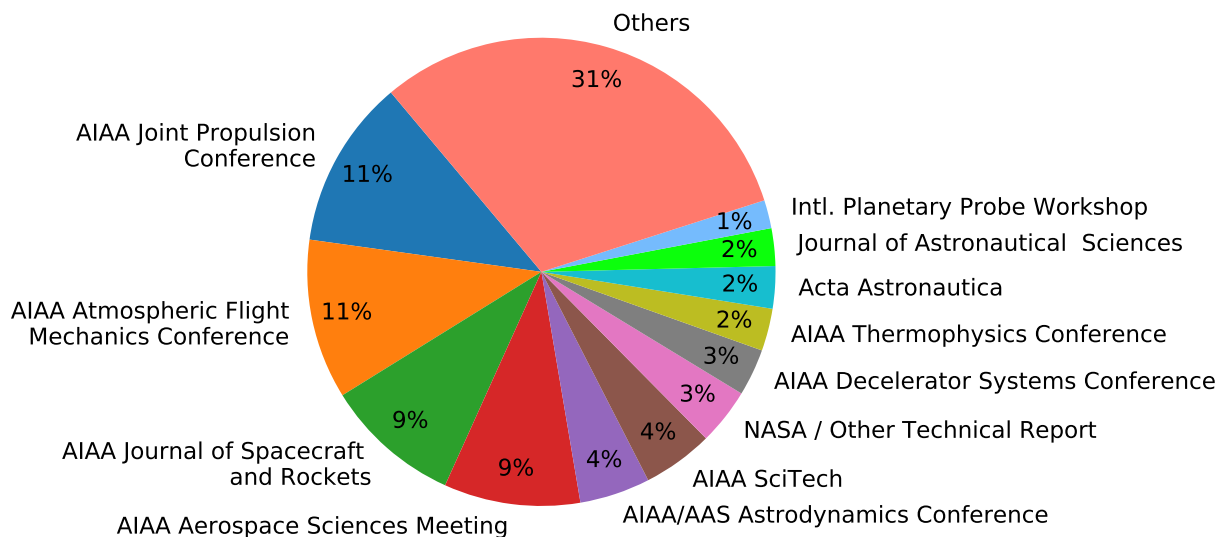


Figure 2.8. Pie chart showing the sources of aerocapture related publications.

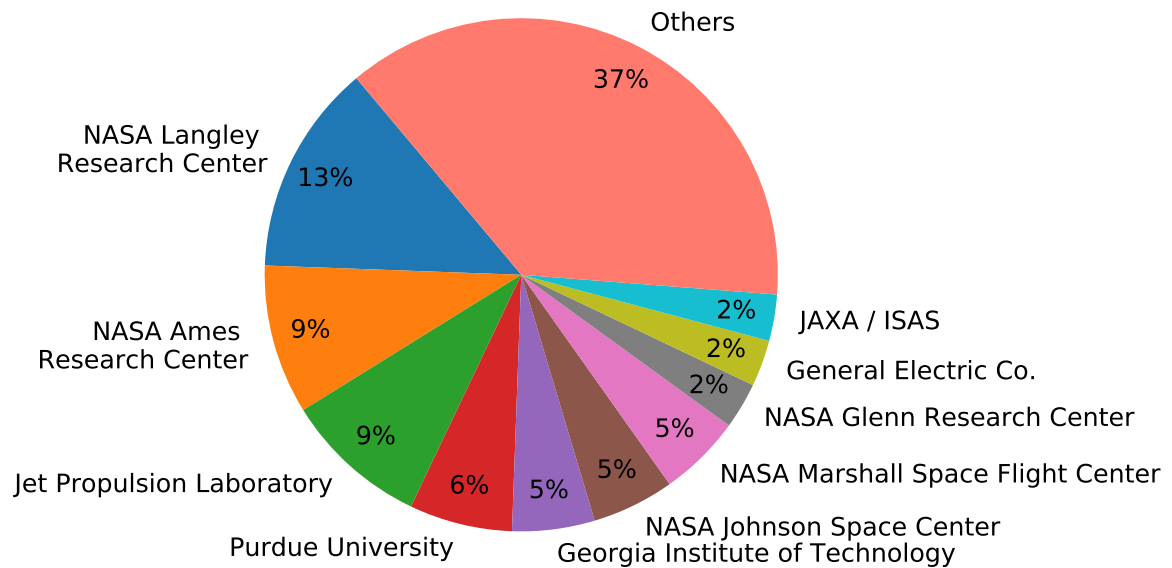


Figure 2.9. Pie chart showing the institutional affiliations of first authors.

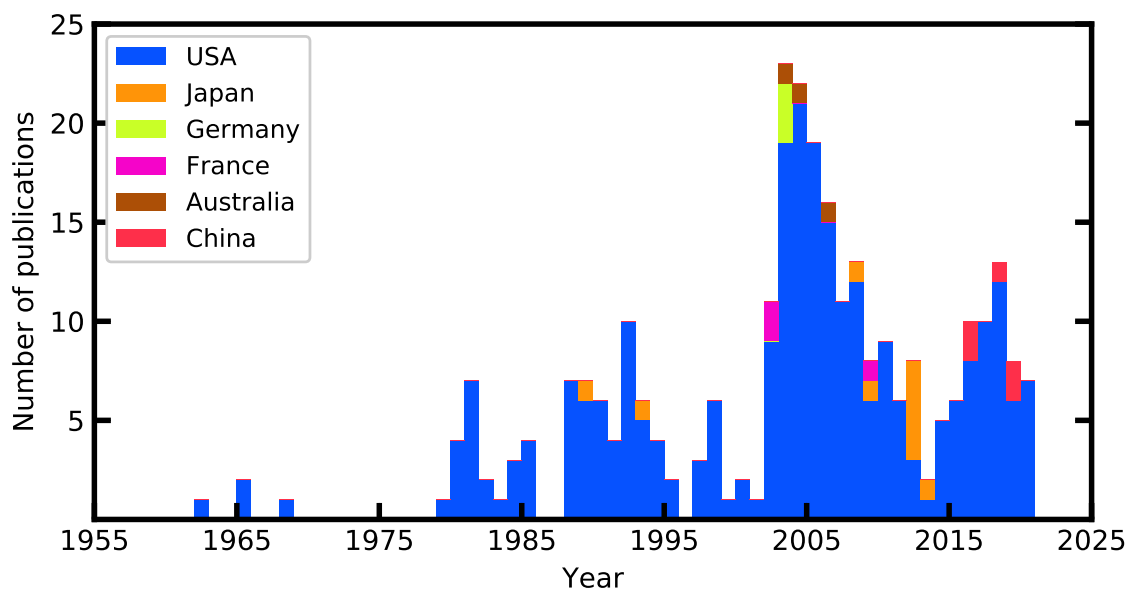


Figure 2.10. Number of publications every year, classified by country of origin.

3. FEASIBILITY AND MASS-BENEFIT ANALYSIS OF AEROCAPTURE FOR MISSIONS TO VENUS

Venus and Earth are considered planetary twins due to their nearly identical size, bulk densities, and location in the Solar System. Both likely shared similar initial conditions and early evolutionary processes such as delivery of water from comets. Despite these similarities, previous exploration missions have shown that Venus today is a hot, hellish world with no oceans and has a thick CO₂ atmosphere [65]. One of the most fundamental questions that drives Venus exploration is when, how, and why did the evolutionary paths of Earth and Venus diverge? Understanding the evolution of the Venus can shed light whether or not a planet evolves habitable environments and how long Earth-like planets elsewhere can sustain such environments [66]. With an increasing number of Earth-sized exoplanets being discovered, our understanding of Venus is critical in interpretation of exo-planetary data and to assess whether Earth-sized planets are Earth-like and their potential habitability [67].

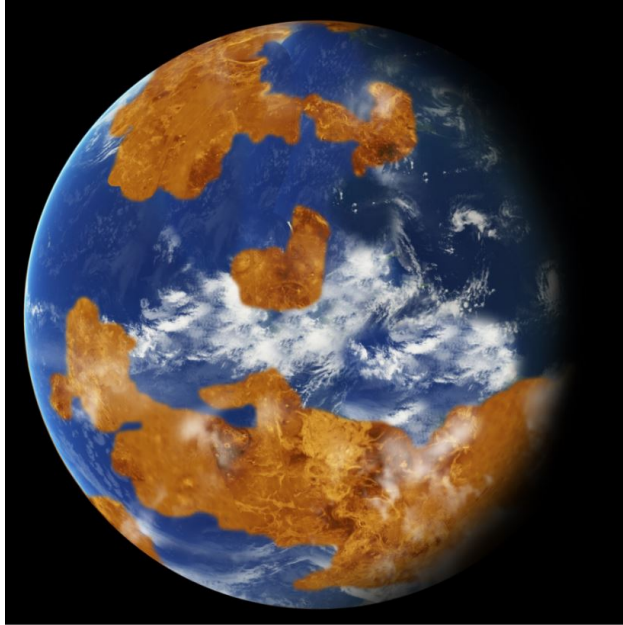


Figure 3.1. Artist's illustration of an ancient water ocean on Venus. Venus may have had liquid water oceans and a habitable environment for as much as 2 billion years of its early history. Image credit: NASA/Michael Way, NASA's Goddard Institute for Space Studies (GISS) [68].

3.1 A Brief History of Venus Exploration

Venus has been the target of over 40 spacecraft missions over the past five decades from NASA, space agency of the erstwhile USSR, ESA and JAXA, with nearly 20 achieving complete or partial successes. A brief overview of the current Venus science goals, lessons learned from past missions and future exploration plans is presented in this section.

3.1.1 Science Goals and Objectives

Science Goals: The 2013–2022 Planetary Science Decadal survey identifies understanding the origin of terrestrial planets, how the evolution of these planets enable or limit habitability and the origin of life, and the processes that control climate on Earth-like planets as high level goals for inner planets research [69]. The NASA Venus Exploration and Analysis Group (VEXAG) recommends that NASA’s future exploration of Venus should strive to accomplish the following non-prioritized goals [66].

1. Understand atmospheric formation, evolution, and climate history on Venus.
2. Determine the evolution of the surface and interior of Venus.
3. Understand the nature of interior-surface-atmosphere interactions over time.

The reader is referred to the VEXAG Goals, Objectives, and Investigations document [66] for further details on the nature of the investigations required to accomplish the above mentioned goals. More specific information on the measurement requirements of the relevant parameters such as noble gas isotopes for atmospheric evolution can be found in Chassefière et al. [70], Glaze et al. [71], and Ghail et al. [72]

3.1.2 Missions to Venus: Past, Present, and Future

Space exploration of the planets in the solar system with robotic spacecraft began with fly-by missions to Venus in the early 1960s by both the United States and the former USSR. Since then Venus has been studied using orbiters, entry probes, surface landers, and atmospheric

balloons which have provided measurements and images of critical importance in advancing our understanding of the mysterious planet permanently shrouded in thick clouds.

Past: The Mariner-2 flyby in 1962 provided the first confirmation of hot Venusian surface by observing conclusive evidence of limb darkening¹ [73]. Following the failures of Venera 1, 2, and 3, the Venera-4 descent vehicle obtained the first direct measurements of atmospheric structure, composition, and wind speed [74]. Venera-7 accomplished the first landing on Venus and provided in-situ measurements of the surface temperature. Venera-9 returned a panorama of Venus surface (Fig. 3.2) making it the first spacecraft to return images another planet [75], showing basaltic rocks and boulders strewn around the landing site.

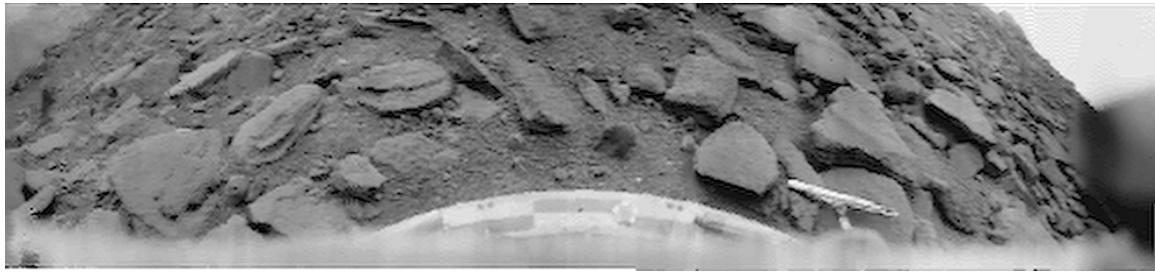


Figure 3.2. 180 degree panorama of Venus surface from the Venera-9 lander, showing a landscape filled with rocks about 30 cm across. The lander survived for 53 minutes. A camera cap on the second camera could not be released, and hence the other 180 degrees around the lander was not imaged. Image credit: NPO Lavochkin, NASA/GSFC. Processed by Don P. Mitchell.

Venera-9 performed measurement of the micro-physical properties of the clouds and emissions of the upper atmosphere [76]. In 1978, the Pioneer Venus orbiter released one large and three small probes into the atmosphere to measure the atmospheric structure, composition, and cloud properties at different locations [77]. In 1981, the Venera-13 lander returned the first color panorama and measured the elemental composition of surface rocks using an X-

¹↑The Mariner 2 mission is a hallmark example of how spacecraft measurements provide data unavailable otherwise to resolve competing hypotheses. At the time it was not clear if the observed radio brightness temperature originated at the hot surface or in the ionosphere. If a radiometer could resolve the Venus disk, it can then scan across the disk and measure how the emission changed. If the source is the surface, more of it would be absorbed by the overlying atmosphere and looking towards the limb, a darkening would be observed as there is more atmospheric column through which radiation has to pass through. If the source was the ionosphere, limb brightening would be observed as greater path length of the emitting ionosphere would be visible towards the limb. Earth-based telescopes at the time could not resolve the disk to make this measurement, and hence the Mariner 2 mission was conceived. Mariner 2 observed limb darkening, thus supporting the hot surface hypothesis, and would later be confirmed by in-situ measurements.

ray fluorescence spectrometer. Venera-13 also carried microphones and transmitted the first recordings of the sound of wind on another planet [78]. Venera-14 was identical to Venera-13 and successfully landed four days after Venera-13. Both landers carried two opposite facing cameras which scanned through 180 degrees, and returned the panoramas shown in Figs. 3.3, 3.4, 3.5, 3.6 showing a flat rock strewn surface with platy rocks and soil.



Figure 3.3. Color panorama of Venus surface from the Venera-13 lander (Camera 1). The lander survived for 2 hours and 7 minutes. Image credit: USSR, NPO Lavochkin, NASA/GSFC. Processed by Don P. Mitchell.



Figure 3.4. Color panorama of Venus surface from the Venera-13 lander (Camera 2). The lens cap is visible in the foreground. Image credit: USSR, NPO Lavochkin, NASA/GSFC. Processed by Don P. Mitchell.

In 1983, the Venera-15 and Venera-16 missions used radar to map the northern hemisphere (from the pole to about 30 deg N) with a resolution of about 1–2 km [79]. In 1984, the Vega 1 and 2 missions each released a balloon which drifted at an altitude of 53–54 km and measured the chemical composition as well as atmospheric dynamics making them the first balloons to fly on another planet. The Vega missions also each included a lander which touched down on the night-side, and performed atmospheric measurements but did not return any images. The Vega missions also marked the end of nearly three decades of Venus



Figure 3.5. Color panorama of Venus surface from the Venera-14 lander (Camera 1). The lander remained in contact with the relay spacecraft for 57 minutes. Image credit: Union of Soviet Socialist Republics, NPO Lavochkin, NASA/GSFC. Processed by Don P. Mitchell.



Figure 3.6. Color panorama of Venus surface from the Venera-14 lander (Camera 2). The color in these images is not true color due to limitations of the camera, and the exact color of the Venusian surface remains unknown. Image credit: Union of Soviet Socialist Republics, NPO Lavochkin, NASA/GSFC. Processed by Don P. Mitchell.

exploration by the Soviet Union, shortly after which the USSR dissolved. The panoramas returned by the Venera landers remain the first and only images of the Venusian surface.

The United States would now come to the forefront of Venus exploration with the ambitious Magellan mission. Launched in 1989 from the Space Shuttle, the Magellan orbiter used radar to map the entire surface at a resolution of 300 meters or better [76], [80]. Magellan would also become the first mission to demonstrate aerobraking at any planetary destination. Aerobraking would later be used extensively by future missions to both Mars and Venus to achieve low-circular orbits required for imaging and radar observations. The Magellan mission produced the most detailed radar map of the Venus surface to date, shown in Fig. 3.7. The Magellan mission would mark the end of the US Venus exploration programs as no new US missions to Venus would be flown in the next three decades.

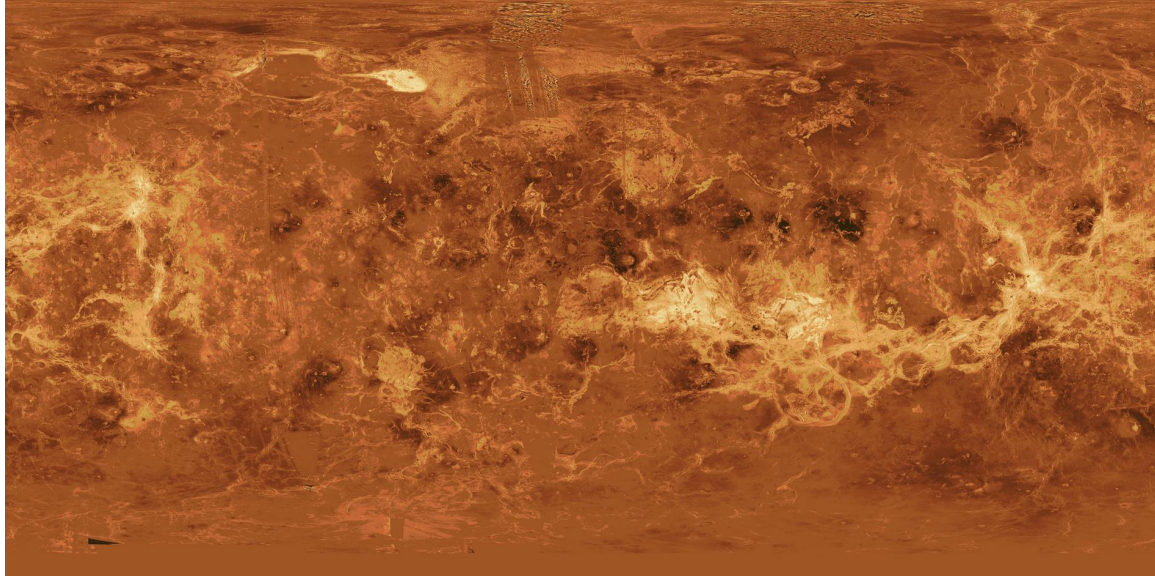


Figure 3.7. Radar map of Venus from images collected by the Magellan mission. Bright areas indicate higher elevation terrain. Darker areas correspond to young impact craters. Simulated color is used to enhance the image based on images returned by the Venera-13 and Venera-14 landers. Image and caption credit: NASA/JPL.

The European Space Agency’s Venus Express orbiter arrived at Venus in 2006 and performed successful aerobraking. Venus Express confirmed that a large quantity of water has been lost over billions of years and provided indirect evidence of potential volcanic activity today [81], [82]. The mission ended in 2014 when the spacecraft likely ran out of propellant and disintegrated into the atmosphere.

Present: The Japanese Space Exploration Agency JAXA’s Akatsuki orbiter is currently the only operational spacecraft at Venus [83]. Following the failure of the planned orbit insertion burn in December 2010, Akatsuki remained in heliocentric orbit for five years before the attitude control thrusters were used to insert the spacecraft into a highly eccentric orbit, and has remained operational since then. Akatsuki has reported evidence of a large stationary gravity wave generated in the lower atmosphere by mountain topography and propagated upwards, and the momentum transfer may have implications for the rotation rate and climatic evolution of Venus [84].

After more than four decades of vigorous exploration beginning in the 1960s, the number of Venus missions has been relatively low in the last two decades. Since the 1990s, more

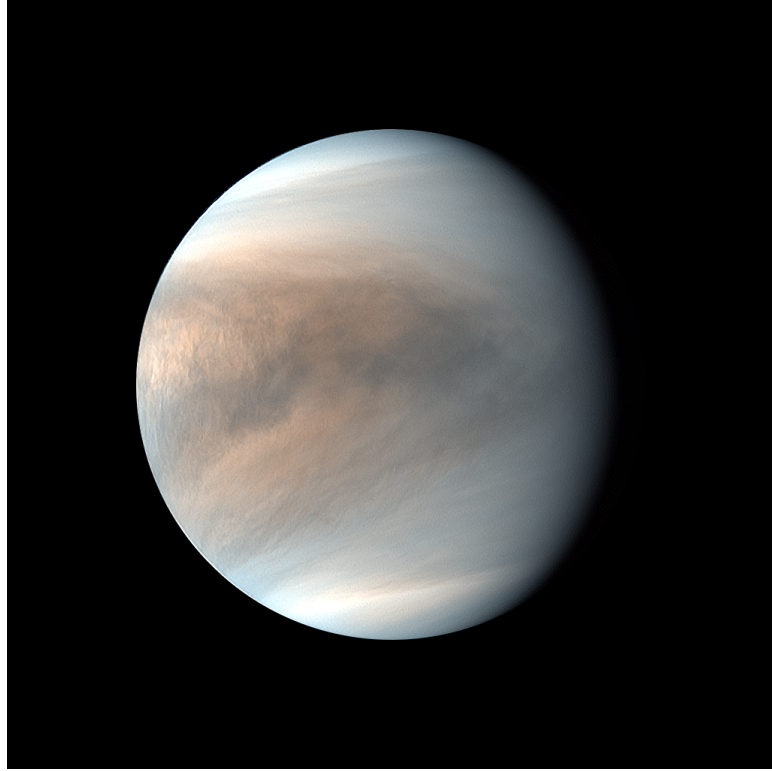


Figure 3.8. False color image of Venus in ultraviolet wavelength (283 and 365 nm) from Akatsuki. Venus appears almost featureless in the visible wavelength. Image and caption credit: JAXA/Planet-C Project Team.

than 30 mission concepts have been proposed in the NASA Discovery and New Frontiers programs, but none were selected for flight [85]. At the time of writing, two of the four Discovery program Phase A finalists in 2020 are missions to Venus raising hopes that the long hiatus in the US exploration of Venus may be coming to an end².

Future: Given the lack of US missions to Venus in the immediate future, NASA has turned attention to SmallSats for low cost Venus science missions. The Venus Bridge study investigated low-cost multi-element mission concepts under a cost cap of \$200 million has as a gap-filler between Magellan and a future Discovery or New Frontiers mission [86]. NASA's Planetary Science Deep Space SmallSat Studies (PSDS3) selected four Venus SmallSat mission concepts under \$100M for study in 2017 as potential secondary payloads [87]. Several

²[↑]In June 2021, NASA announced that two Discovery class missions, DAVINCI+ and VERITAS will be flown to Venus in the 2028–2030 timeframe. In the same month, ESA announced the M-class EnVision mission to Venus launching in the early 2030s. Both VERITAS and EnVision will use aerobraking to achieve their science orbit for radar observations. The next decade may very well be called the ‘decade of Venus’.

missions planned to launch before the end of the decade will use perform gravity assist flybys of Venus. These flybys provide opportunities to perform new scientific observations of Venus. Russian scientists have proposed the Venera-D mission to send an orbiter and lander to Venus in the 2020s and may include NASA participation [88]. The Chinese Space Agency has outlined plans for a Venus orbiter and a floating atmospheric probe, though no specific timeline is available [89]. The Indian Space Research Organization (ISRO) has announced plans for a Venus orbiter mission launching in 2024, and may include a balloon operating at 55 km altitude to study the cloud layers [90], [91].

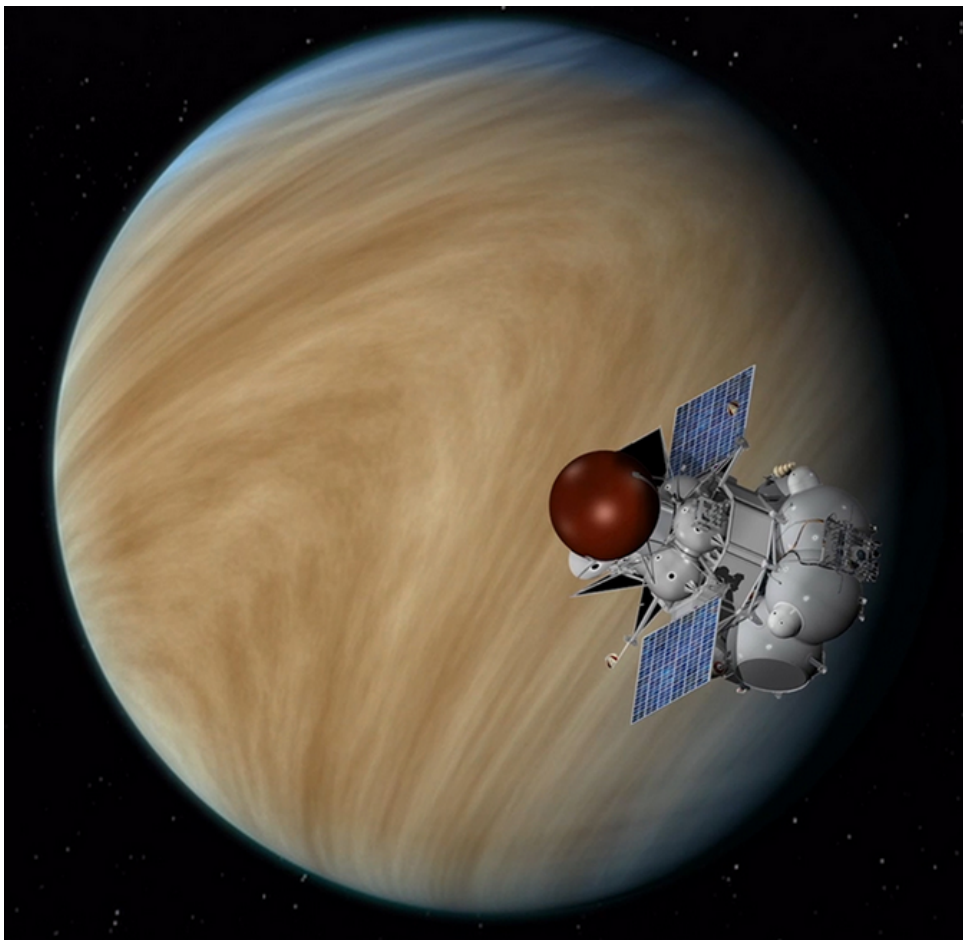


Figure 3.9. Artist's concept of the future Venera-D mission approaching Venus. Image credit: Russian Academy of Sciences Space Research Institute (IKI), NASA/JPL.

3.2 Study Objective

The high-level objective of this study is to assess the feasibility and technological readiness of aerocapture for future Venus missions. Aerocapture at Venus has been shown to be feasible using existing technology and allow significant increase in delivered mass compared to propulsive orbit insertion [1], [36]. However, these studies are almost always point-design studies, i.e. they investigate a single mission and vehicle design with limited trade space exploration and lack a systematic method for selecting the point-design [36], [40], [42], [53], [54], [92]. A comprehensive feasibility analysis of Venus aerocapture, applicability of different control methods and detailed mass-benefit analysis compared to purely propulsive capture and aerobraking is lacking in the literature. The study shows how constraints imposed by the allowable aerocapture entry corridor, deceleration loads, peak heat rates, total heat load constrain the feasible design space for Venus aerocapture using a graphical approach. Feasibility plots are presented for two vehicle control techniques - lift modulation and drag modulation aerocapture which is more applicable to SmallSats which may be secondary payloads on a carrier mission flying to/by Venus. Previous studies assessing the delivered mass benefit of aerocapture at Venus have used a constant aerocapture mass fraction, the ratio of aerocapture system mass to total entry vehicle mass based on historical data for entry vehicles and often a single interplanetary trajectory. This study performs a more comprehensive mass-benefit analysis by estimating the payload mass fraction using entry systems taking into account the mass of aeroshell structure, control systems, TPS and results from a broad search of several thousand interplanetary trajectories. The study quantifies the mass-benefit from using aerocapture in different mission architectures to Venus such as dedicated mission to Venus, or a rideshare with a carrier spacecraft which is flying to Venus or is using Venus for a gravity assist flyby. The aerocapture delivered mass fraction is also compared to purely propulsive insertion and aerobraking to allow mission designers to evaluate the different orbit insertion techniques during early mission concept studies.

3.3 Methodology

3.3.1 Atmospheric Flight Mechanics

The position of the vehicle flying in the vicinity of a planet in a planet-centered and planet-fixed coordinate system is specified by its radial distance from the center of the planet r , longitude θ , and latitude ϕ . The angle between the velocity vector \vec{V} and the local horizontal plane is the flight-path angle γ . The heading angle ψ is the angle between the projection of the velocity vector \vec{V} on the local horizontal plane and the local parallel of latitude [93]. Kinematic equations which govern the evolution of these variables are [93]:

$$\dot{r} = V \sin \gamma \quad (3.1a)$$

$$\dot{\theta} = \frac{V \cos \gamma \cos \psi}{r \cos \phi} \quad (3.1b)$$

$$\dot{\phi} = \frac{V \cos \gamma \sin \psi}{r} \quad (3.1c)$$

The dynamic equations of motion which govern the motion of the vehicle including the gravity, aerodynamic, Coriolis, and centrifugal forces are [26], [93], [94]:

$$\dot{V} = -\frac{q}{\beta} + g_r \sin \gamma + g_\theta \cos \gamma \cos \psi + g_\phi \cos \gamma \sin \psi \quad (3.2a)$$

$$+ \Omega^2 r \cos \phi (\sin \gamma \cos \phi - \cos \gamma \sin \phi \sin \psi) \\ \dot{\gamma} = \frac{q(L/D)}{V\beta} \cos \sigma + \frac{1}{V} (g_r \cos \gamma - g_\theta \sin \gamma \cos \psi - g_\phi \sin \gamma \sin \psi) + \frac{V \cos \gamma}{r} \quad (3.2b)$$

$$+ \frac{\Omega^2 r}{V} \cos \phi (\cos \gamma \cos \phi + \sin \gamma \sin \phi \sin \psi) + 2\Omega \cos \phi \cos \psi \\ \dot{\psi} = \frac{q(L/D) \sin \sigma}{V\beta} + \frac{1}{V \cos \gamma} (-g_\theta \sin \psi + g_\phi \cos \psi) - \frac{V}{r} \cos \gamma \cos \psi \tan \phi \quad (3.2c)$$

$$- \frac{\Omega^2 r}{V \cos \gamma} \sin \phi \cos \phi \cos \psi + 2\Omega (\tan \gamma \cos \phi \sin \psi - \sin \phi)$$

where σ is the bank angle, $\beta = m / (C_D A)$ is the vehicle ballistic coefficient, m is the vehicle mass, A is the aerodynamic reference area of the vehicle, $q = (1/2)\rho V^2$ is the dynamic pressure, $\rho = \rho(r, \theta, \phi)$ is the atmospheric density, Ω is the planet rotation rate about its

spin axis, V is the planet-relative vehicle speed; L is the lift force and D is the drag force, defined as

$$L = \frac{1}{2}\rho V^2 A C_L, \quad D = \frac{1}{2}\rho V^2 A C_D \quad (3.3)$$

assuming the atmosphere is rotating with the planet at the planet's rotation rate and the planet-relative and atmosphere-relative speeds are the same. C_L is the vehicle lift coefficient and C_D is the drag coefficient. g_r , g_θ , and g_ϕ are the radial, longitudinal, and latitudinal components of the gravitational acceleration respectively, defined as [26], [94]:

$$g_r = \frac{\partial U}{\partial r}, \quad g_\theta = \frac{1}{r \cos \phi} \frac{\partial U}{\partial \theta}, \quad g_\phi = \frac{1}{r} \frac{\partial U}{\partial \phi} \quad (3.4)$$

where U is the gravitational potential and is in general a function of r , θ , and ϕ . A simple representation of U can be expressed in terms of the zonal harmonic coefficients to fourth order expansion [95]:

$$U = \frac{\mu_p}{r} \left[1 + J_2 \left(\frac{r_p}{r} \right)^2 \left(\frac{1}{2} - \frac{3}{2} \sin^2 \phi \right) + J_3 \left(\frac{r_p}{r} \right)^3 \left(\frac{3}{2} \sin \phi - \frac{5}{2} \sin^3 \phi \right) + J_4 \left(\frac{r_p}{r} \right)^4 \left(-\frac{3}{8} + \frac{15}{4} \sin^2 \phi - \frac{35}{8} \sin^4 \phi \right) \right] \quad (3.5)$$

where μ_p is the the gravitational parameter of the planet, r_p is the mean equatorial radius of the planet, and J_2 , J_3 , and J_4 are the zonal harmonic terms. Venus has a slow rotation rate Ω , and very small J_2 value compared to other planets. For aerocapture at Venus, the duration of the atmospheric flight is typically only a few minutes, and the rotation terms and higher order gravity terms can be neglected in Eq. (3.2) without any significant loss of accuracy. However, these terms retained for the generality of formulation and may be required for analysis of aerocapture guidance algorithms, or for higher fidelity simulations. The values of standard gravitational parameter μ_p , planetary radius r_p , rotation rate Ω (-ve sign indicates retrograde) and zonal harmonic terms for Venus used in the simulations is listed in Table 3.1 and compared to Earth [96].

Given initial conditions for the state variables r_e , θ_e , ϕ_e , V_e , γ_e , ψ_e where the subscripts denote conditions at the atmospheric entry interface, Eqs. (3.1) and (3.2) can be used

Table 3.1. Comparison of planetary parameters of Venus and Earth

Planet	μ_p , m ³ /s ²	r_p , km	Ω , rad/s	$J_2(\times 10^{-6})$	$J_3(\times 10^{-6})$	$J_4(\times 10^{-6})$
Venus	3.24×10^{14}	6051.8	-2.99×10^{-7}	4.458	-1.93	-2.38
Earth	3.98×10^{14}	6378.1	7.27×10^{-5}	1082.6	-2.53	-1.62

to determine the vehicle state during the atmospheric phase of aerocapture maneuver. A non-dimensional form of the equations developed by Leszczynski [26] is used to avoid an ill-conditioned system during numerical integration.

3.3.2 Atmosphere Model

Propagation of Eq. (3.2) requires the atmospheric density profile of the planet. Venus Global Reference Atmospheric Model (Venus-GRAM) [97], [98], an engineering level atmosphere model developed by NASA is widely used for systems design and performance analysis of flight trajectories in the Venus atmosphere. Venus-GRAM outputs temperature, pressure, wind speed components, and chemical composition as a function of altitude, latitude, longitude, and local solar time. Venus-GRAM also provides dispersion for thermodynamic parameters, density, and winds. The atmosphere model implemented in Venus-GRAM is based on the Venus International Reference Atmosphere Model (VIRA) which incorporates data from the Pioneer Venus Orbiter and Multiprobes and the Venera entry probes [99]. The present work uses the mean density profile only as a function of altitude which is sufficient for preliminary aerocapture feasibility and performance-benefit analysis.

3.3.3 Arrival Conditions and Post-capture Orbit

The hyperbolic excess speed or arrival V_∞ and the declination δ with respect to the equatorial plane of the target planet are two important parameters which characterize the arrival conditions for an interplanetary transfer. The arrival V_∞ determines the inertial entry velocity $V_{e,i}$ at the atmospheric interface radius r_e :

$$V_{e,i}^2 = V_\infty^2 + \frac{2\mu_p}{r_e} \quad (3.6)$$

Venus rotation is neglected and inertial entry speed is assumed to be equal to the planet-relative entry speed V_e at atmospheric interface. However, the velocity due to rotating atmosphere cannot be neglected for entry at fast-rotating planets such as Saturn or Neptune and must be accounted for when computing V_e .

The desired orbit size and inclination depend on the science requirements and engineering constraints. Most previous orbiter missions to Venus used a near-polar high inclination orbit to get good latitudinal and longitudinal coverage as the planet rotates underneath. This study considers two target orbits—a low circular orbit of 400 km and an elliptical orbit of 400 km \times 60,000 km. The low circular orbit is representative of one used by a radar mapping mission [72], an orbiter to study the atmosphere above the cloud layers, or a sample return mission orbiter which requires low circular Venus orbit to minimize the mass of the Venus Ascent Vehicle (VAV) [100]. The elliptical orbit is representative of one used in several previous and proposed Venus orbiter missions [90], [101], as well as a communication relay orbiter for an aerial platform or lander [102]. To minimize ΔV requirement for propulsive orbit insertion, mission planners select a highly elliptical initial orbit, and then use aerobraking over several months to one or two years to lower the apoapsis and enter the desired science orbit. Aerocapture in contrast achieves the desired science orbit immediately upon arrival, allowing science operations to begin earlier. Some missions require low circular orbit for the science investigations and aerocapture is an enabling technology if the time penalty for aerobraking is prohibitive.

The arrival declination δ constrains the range of possible inclinations for the post-capture orbit with the arrival declination limiting the minimum inclination orbit. However, a high-inclination polar orbit is achievable from any arrival trajectory by appropriately selecting the aim point on the B-plane [103]. High-inclination orbits allow global coverage of the planet, thus are preferred for Venus orbiter missions. The B-plane targeting can also accommodate other missions requirements, such as delivering lander or balloon to a specific latitude.

3.3.4 Aerocapture Vehicles

The aerocapture vehicle serves two purposes: provide adequate aerodynamic control authority to compensate for navigation, atmospheric and vehicle aerodynamics uncertainties;

and protect the payload from the severe aerodynamic heating during the maneuver. Control authority allows the on-board guidance algorithm to guide the spacecraft from entry interface to the desired atmospheric exit state for the target capture orbit. This study considers two control approaches—lift modulation and drag modulation as shown in Fig. 3.10.

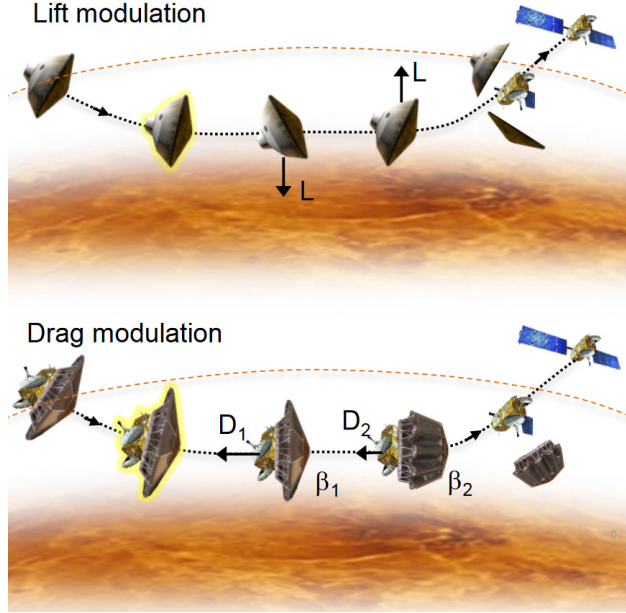


Figure 3.10. Two aerodynamic control approaches for an aerocapture vehicle—lift modulation and drag modulation. Dashed red line indicates the atmospheric interface.

Lift modulation uses an aeroshell which provides lift from offsetting the center of gravity with respect to the symmetry axis. Lift modulation control techniques include bank angle modulation, angle of attack, and sideslip angle control [104], [105], or a combination of these techniques. The present study considers only bank angle modulation in which the lift vector is rotated around the velocity vector by banking the vehicle and the bank angle is the sole control variable. The aerodynamic control authority from a lift-modulated vehicle is determined by the hypersonic trim lift-to-drag ratio $(L/D)_{\text{trim}}$ at a specified (trim) angle-of-attack. The term $(L/D) \cos \sigma$ in Eq. (3.2) can be modulated between $+(L/D)_{\text{trim}}$ and $-(L/D)_{\text{trim}}$ by varying the bank angle σ from 0° to $\pm 180^\circ$. A bank angle of zero indicates full lift up, while 180 degrees denotes full lift down. The guidance algorithm will continuously command the bank angle within this range during the atmospheric pass so that the vehicle achieves

the desired exit conditions. Bank angle modulation has been used on entry vehicles such as Apollo and the Mars Science Laboratory (MSL) [106], [107]. Aeroshells with $(L/D)_{\text{trim}}$ of up to 0.40 are low- L/D vehicles, 0.40 to 0.80 are mid- L/D aeroshells such as the ellipsled, and $(L/D)_{\text{trim}} \geq 0.8$ are high- L/D vehicles [39]. Low- L/D aeroshells have flight heritage on planetary entry missions and are considered a mature technology, while mid and high- L/D aeroshells need further development and testing [3]. Table 3.2 summarizes the achievable $(L/D)_{\text{trim}}$ for some past and proposed lifting aeroshells along with their notional Technology Readiness Levels (TRL). In addition to rigid aeroshells, lift modulation aerocapture can be performed using deployable entry systems such as lifting version of the Adaptive, Deployable Entry and Placement Technology (ADEPT) [108]. Deployable systems such as ADEPT offer two advantages: (1) small ballistic coefficient which results in lower peak heat rate, and (2) open back shell which relaxes spacecraft packaging constraints. Deployable platforms are particularly attractive for SmallSats because the restrictive mass and volume on SmallSats prevents the use of a traditional rigid aeroshell for aerocapture, especially when launched as a secondary payload [109].

Table 3.2. L/D and TRL of some selected entry vehicles

Vehicle design	Planet	Mission	$(L/D)_{\text{trim}}$	TRL	Ref.
70° sphere-cone	Mars	Viking	0.18	High	[107]
70° sphere-cone	Mars	MSL	0.24	High	[107]
Lifting ADEPT	Mars/Venus	—	0.25	Mid	[108]
Sphere section	Earth	Apollo	0.36	High	[106]
Ellipsled	Neptune	—	0.80	Low	[39]

Drag modulation uses a non-lifting ($L/D = 0$) entry system with aerodynamic drag as the sole control variable by changing the vehicle reference drag area ($C_D A$) during the atmospheric flight [110]. Two variants of this technique can be used: continuously variable and discrete-event drag modulation [47]. In continuously variable drag modulation, the drag area can be adjusted using deployable arms to expand or retract the drag skirt as commanded by the guidance algorithm. In discrete event drag modulation, the vehicle can only have certain configurations (i.e. certain allowable ballistic coefficients), and the drag skirt(s) are jettisoned when the on-board guidance predicts that the vehicle will achieve the

desired atmospheric exit conditions after drag skirt separation. The simplest variant is a single-event discrete drag modulation in which the vehicle can only have two possible values of the ballistic coefficient β —a small value β_1 with the drag skirt and a high value β_2 after the drag skirt is jettisoned. The vehicle enters the atmosphere with the drag skirt allowing a small β during entry. The small ballistic coefficient lowers aerodynamic heating rate as the vehicle decelerates at higher altitudes where the atmosphere is thinner [111]. The guidance algorithm predicts the target exit conditions if the drag skirt is jettisoned, and commands the drag skirt separation event when the predicted apoapsis is close to the target apoapsis [54]. The vehicle flies the remaining part of the trajectory with the high ballistic coefficient β_2 . The control authority for single-event discrete drag modulation is determined by the ballistic coefficient ratio before and after drag skirt separation β_2/β_1 [47] and is analogous to $(L/D)_{\text{trim}}$ for bank angle modulation.

3.3.5 Aerodynamic Heating and Thermal Protection System

Aerocapture vehicles encounter aerothermodynamic heating during the atmospheric pass at hypersonic speed resulting in significant convective and radiative heat rate. TPS materials protect the payload from the extreme heating and the TPS material is chosen based on the peak stagnation-point aerothermal conditions. Complex physics involved in hypersonic, chemically reacting, high temperature flows make accurate prediction of heating rates difficult [112]. Experimental testing often cannot fully recreate the severe conditions encountered during the flight and ground test is often limited by the conditions achievable at the testing facility. Mission concept studies often use engineering correlations based on empirical relations or previous computational work to estimate the stagnation-point convective and radiative heating rates. The stagnation-point convective heating rate is estimated using the Sutton-Graves empirical relation [113]:

$$\dot{q}_c = K \left(\frac{\rho_\infty}{R_N} \right)^{0.5} V^3 \quad (3.7)$$

where \dot{q}_c is the stagnation-point convective heat flux in watts per square centimeter, $K = 1.896 \times 10^{-8}$ [114] for Venus entry; ρ_∞ is the freestream atmospheric density in kilograms

per cubic meter, R_N is the vehicle nose radius in meters, and V is the freestream velocity in meters per second. The radiative heating is estimated using the following empirical relation [115], [116]:

$$\dot{q}_r = \begin{cases} K_1 \rho_\infty^{1.2} V^{10.0} R_N^{0.49} & \text{if } V \leq 8,000 \text{ meters per second} \\ K_2 \rho_\infty^{1.2} V^{5.5} R_N^{0.49} & \text{if } 8,000 \leq V \leq 10,000 \text{ meters per second} \\ K_3 \rho_\infty^{1.2} V^{13.4} R_N^{0.49} & \text{if } 10,000 \leq V \leq 12,000 \text{ meters per second} \end{cases} \quad (3.8)$$

where \dot{q}_r is the stagnation point radiative heat flux in watts per square centimeter, $K_1 = 3.33 \times 10^{-34}$, $K_2 = 1.22 \times 10^{-16}$ and $K_3 = 3.07 \times 10^{-48}$. The correlation for $10,000 \leq V \leq 12,000$ meters per second range is used for $V \geq 12,000$ meters per second in this study, and may provide at best only an order of magnitude estimate of the radiative heating rates.

TPS materials can be divided into two categories: insulative/reusable and ablative. Insulative TPS when exposed to atmospheric entry conditions rejects heat by re-radiation from the surface and internal storage. Insulative TPS is commonly used on reusable entry vehicles and can only withstand heat rates up to $\approx 100 \text{ W/cm}^2$. Examples of insulative TPS include Space Shuttle Tile and Toughened Unipiece Fibrous Reusable Oxidation Resistant Ceramic (TURFOC). Ablative TPS when exposed to entry conditions will pyrolyze, and reject heat by blowing of pyrolysis products into the boundary layer [117]. Ablative TPS is commonly used on planetary entry probes and can withstand much higher heat rates up to $\approx 30,000 \text{ W/cm}^2$ [118]. Examples of ablative TPS include Carbon Phenolic (CP) which was used on the Galileo and Pioneer Venus entry probes, and Phenolic Impregnated Carbon Ablator (PICA) which was used on Stardust and MSL entry vehicles [117], [119].

Despite the similar entry speeds on Earth and Venus, the thick CO_2 dominated Venusian atmosphere presents more demanding entry conditions than at Earth. Pioneer Venus entry probes used rigid aeroshells with high ballistic coefficient and sustained heat rates of up to $5,000 \text{ W/cm}^2$. CP was the only TPS material available that can withstand such heat rate. However, heritage CP is no longer available as the raw material Avtex rayon is not being produced since 1986. To close the technology gap, NASA has been investing in new ablative TPS material—Heatshield for Extreme Entry Environment Technology (HEEET). HEEET

is a 3-D woven resin infused material that has been tested for heat rates up to 8,000 W/cm² and allows 40% mass savings compared to CP [120].

The peak stagnation-point heat rate, stagnation pressure, and stagnation-point heat load are important parameters for aerothermal design. The peak heat rate and stagnation pressure determine the type of TPS material. The TPS material must be qualified for heat rates and stagnation pressure conditions greater than the vehicle's entry requirement. The TPS thickness required at any given point on the heat shield is determined by the integrated heat load at that location [119]. A higher heat load implies a higher TPS mass fraction and hence smaller payload mass fraction. The present study uses the stagnation-point heat load — the integral of the stagnation-point heat rate throughout the duration of the atmospheric flight to estimate the total TPS mass fraction. In certain situations, boundary layer transition can cause afterbody heating rates to approach values at the stagnation point and must be accounted for in TPS material selection and thickness. Data from previous entry missions (involving only low- L/D blunt-body aeroshells) have been used to obtain a regression formula between the stagnation-point heat load Q and TPS mass fraction f_{TPS} for rigid low- L/D aeroshells as follows [121]:

$$f_{\text{TPS}} = 0.091Q^{0.51575} \quad (3.9)$$

where Q has units of J/cm² and can be used to approximately estimate the TPS mass fraction for a blunt-body aeroshell. Table 3.3 summarizes some key aerothermodynamic parameters, TPS material used, and f_{TPS} for several past missions [122]–[124].

Low ballistic coefficient systems (~ 10 – 50 kg/m²) have been proposed as a potential solution to overcome the severe heating problems associated with conventional rigid high ballistic coefficient (~ 150 – 400 kg/m²) entry systems at Venus [111]. Low ballistic coefficient vehicles may reduce the peak heating rate by a factor of 10. Mechanically deployed entry platforms (e.g., ADEPT) can be stowed in the launch fairing and deployed just before atmospheric entry to achieve ballistic coefficients as low as 10 kg/m². Woven carbon cloth has been proposed as the TPS material for such deployable entry systems and has been arcjet tested

Table 3.3. Key aerothermodynamic parameters and TPS materials used in past entry missions.

Entry vehicle	Planet/ moon	β , kg/m ²	Peak heat rate, W/cm ²	Heat load, kJ/cm ²	TPS	f_{TPS}	Year (entry)
Apollo 17	Earth	396	392	33	AVCOAT	0.13	1972
PV Large probe	Venus	188	4,500	12.4	CP	0.10	1978
PV Small "North"	Venus	190	7,200	11.7	CP	0.13	1978
PV Small "Day"	Venus	"	3,900	14.0	"	"	"
PV Small "Night"	Venus	"	2,300	12.5	"	"	"
Galileo	Jupiter	256	17,000	200	CP	0.50	1995
Mars Exploration Rover-B	Mars	88	44	3.6	SLA561-V	0.04	2004
Huygens	Titan	38	50	40	AQ60	0.30	2005
Stardust	Earth	60	1,200	36	PICA	0.22	2006
Hayabusa	Earth	114	1,500	32	CP	0.43	2007
MSL	Mars	146	197	5.47	PICA	0.12	2011

to 246 W/cm^2 at 9.6 kPa [125]. A drag modulation system which uses a rigid drag skirt and PICA TPS has been studied for aerocapture at Venus [53].

3.4 Aerocapture Feasibility

3.4.1 Theoretical Corridor Width

To successfully perform aerocapture, an entry vehicle must target the entry flight-path angle within the aerocapture corridor bounded by the minimum and maximum acceptable entry flight-path angles. The minimum entry flight-path angle γ_{\min} or the undershoot boundary is the steepest at which the vehicle can enter and achieve the desired atmospheric exit conditions to achieve the target apoapsis. The maximum entry flight-path angle γ_{\max} or the overshoot boundary is the shallowest allowable for the vehicle to achieve the desired orbit upon atmospheric exit. The difference between the two limiting entry flight-path angles is the Theoretical Corridor Width (TCW) as shown in Fig. 3.11.

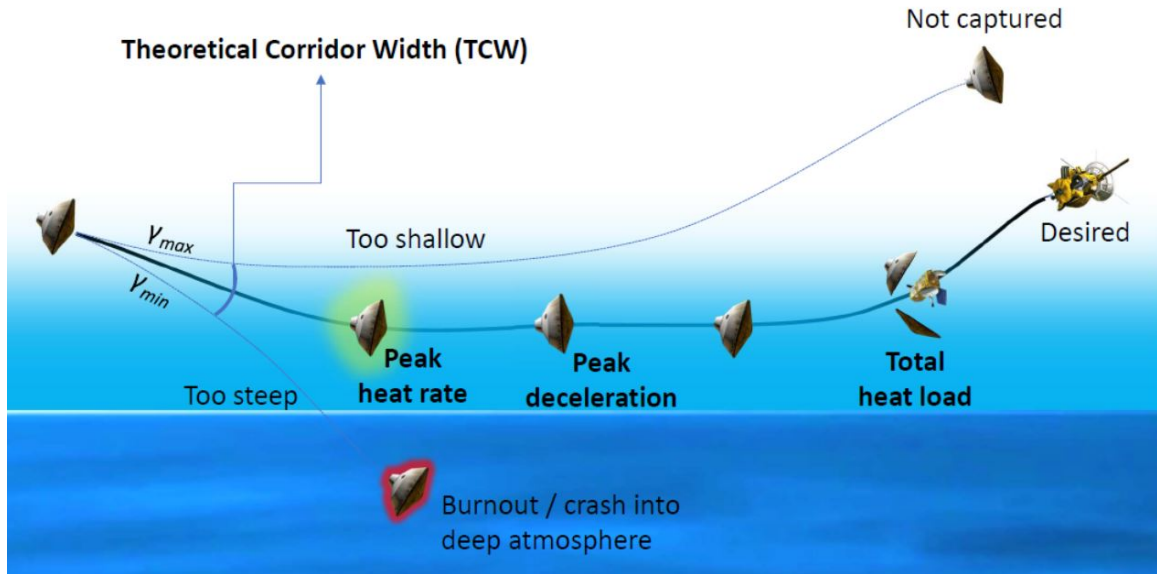


Figure 3.11. Illustration of Theoretical Corridor Width (TCW) and other aerocapture vehicle design considerations. To perform aerocapture, the vehicle must enter the atmosphere within the theoretical corridor. Entering too shallow will result in the spacecraft not bleeding enough speed to get captured, while entering too shallow will result in the spacecraft burning up or bleeding too much speed and getting trapped in the atmosphere.

The TCW is a measure of the control authority of the vehicle to compensate for uncertainties in navigation, atmospheric density, and vehicle aerodynamics.

$$TCW = |\gamma_{\max} - \gamma_{\min}| \quad (3.10)$$

If the vehicle enters steeper than γ_{\min} , then the vehicle will bleed more speed than required. This will result in undershoot of the target apoapsis, and may cause the vehicle to burn up in the deep atmosphere or crash on the surface. If the vehicle enters shallower than γ_{\max} , the vehicle will not have decelerated enough upon atmospheric exit resulting in overshoot of the target apoapsis, or not getting captured at all. If the vehicle enters at any flight-path angle within the corridor bounds, the aerocapture guidance algorithm will be able to successfully guide the vehicle to achieve the target orbit. When the vehicle is successfully captured, a small propulsive ΔV maneuver is performed at the apoapsis to raise the periapsis outside of the atmosphere. Additional propulsive maneuvers may be required to correct apoapsis errors before the initial science orbit is established.

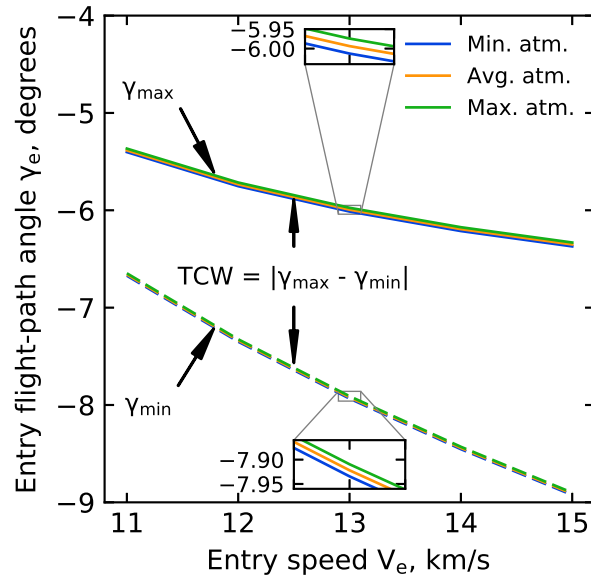


Figure 3.12. Overshoot (solid) and undershoot (dashed) boundaries for a lift modulation aerocapture vehicle with $L/D = 0.24$, $\beta = 200 \text{ kg/m}^2$ at Venus. Inset shows the variation of corridor bounds for minimum, average, and maximum mean density profiles from VenusGRAM.

For bank angle modulation, γ_{\min} is the steepest flight-path angle at which the vehicle can enter while pointing the lift vector fully upward ($\sigma = 0^\circ$) through the entire duration of the atmospheric flight. The shallowest allowable entry flight-path angle is γ_{\max} in which lift vector points fully downward ($\sigma = 180^\circ$) for the duration of the flight. TCW for bank angle modulation primarily depends on the vehicle lift-to-drag ratio L/D , arrival V_∞ , and to a lesser extent the ballistic coefficient β . Figure 3.12 shows the two limiting flight path angles for a lift modulation vehicle at Venus. In this study, entry flight-path angles are defined at an altitude of 150 km above Venus surface. The TCW varies slightly with target apoapsis altitude but its effect is small (< 10%) for capture orbits with apoapsis ranging from 400 km to 1000 km. The results are for reported for target apoapsis altitude of 400 km, and targeting capture orbits with apoapsis altitude greater than 1000 km will result in lower TCW than reported in the present work.

For drag modulation, γ_{\min} is the entry flight-path angle associated with the vehicle being successfully captured while flying with highest ballistic coefficient possible (β_2). The limiting entry flight-path angle associated with the vehicle flying with the lowest ballistic coefficient (β_1) for the entire atmospheric flight is γ_{\max} . The TCW for drag modulation aerocapture primarily depends on the ballistic coefficient ratio β_2/β_1 and arrival V_∞ and to a lesser extent on β_1 and the target apoapsis altitude.

The Required Corridor Width (RCW) is a measure of the uncertainty in approach navigation, uncertainty in atmospheric density profile, and uncertainty in vehicle aerodynamic properties [39]. Lockwood et al. estimated that the uncertainty in entry flight path angle ranges from ± 0.4 degrees to ± 0.2 degrees depending on whether the last update to the spacecraft inertial system is entry minus 48 hours or 5 hours [36]. Considering the short light-time of only a few minutes between Earth and Venus, it is reasonable to assume a navigation update can be made 5 hours before entry, and the contribution of navigation uncertainty to RCW is 0.4 degrees.

Contribution of the atmospheric and vehicle aerodynamics uncertainties to RCW has not been estimated for Venus in the literature. Simulations used in this study indicate that using the minimum and maximum mean density profiles from Venus-GRAM results in the corridor bounds changing by at most 0.05 degrees for vehicle $L/D = 0.24$ entering

at 13 km/s as shown in Fig. 3.12. High frequency density perturbations superposed on the mean variations not considered in this study will also contribute to the atmospheric uncertainty RCW component and will be investigated in future studies. Additional study is required to estimate the aerodynamic uncertainty component, and is outside the scope of the present work. Nominal aerodynamic uncertainties associated with a low- L/D vehicle performing aerocapture at Titan resulted in an RCW contribution of ≈ 1.0 deg [38], and could be a representative estimate for Venus aerocapture. The navigation, atmospheric, and aerodynamics uncertainties are root-sum-squared to compute the required RCW [39]. A larger TCW allows more safety margin over the computed RCW and enables the vehicle to compensate for larger uncertainties. Monte Carlo simulations can be used to estimate these uncertainties, but is outside the scope of the present work. For the vehicle to accomplish aerocapture

$$\text{TCW} \geq \text{RCW} + \epsilon \quad (3.11)$$

where ϵ is a small additional margin over the computed RCW to allow for guidance not being able to successfully capture the entire corridor and other unaccounted uncertainties.

Failure to satisfy this criteria implies that the vehicle risks crashing into the planet, or getting captured into a different orbit than desired, or not getting captured at all. Figure 3.13 shows contours of the TCW in degrees, for aerocapture at Venus with a lifting vehicle for two ballistic coefficients $\beta = 50 \text{ kg/m}^2$ and 500 kg/m^2 indicated by solid and dashed lines respectively. L/D from 0 to 0.4 is chosen, 0.4 being an upper limit for heritage, low- L/D entry vehicles as indicated in Table 3.2. A range of arrival V_∞ from 0 to 30 km/s is considered to represent a wide range of interplanetary trajectories. The upper limit of 30 km/s is chosen based on the Venus gravity assist flyby V_∞ for the Cassini-Huygens spacecraft en route to Saturn. For rigid aeroshells, $\beta = 50 \text{ kg/m}^2$ is an estimated lower limit of the ballistic coefficient possible, and $\beta = 500 \text{ kg/m}^2$ is used as an upper bound to illustrate the effect of ballistic coefficient variation. The two extremes of β are chosen so as to represent the range of ballistic coefficients expected for a bank angle modulation system.

Figure 3.13 shows that TCW increases with both increasing L/D and arrival V_∞ . Higher L/D implies that the vehicle has more aerodynamic control authority, and can achieve desired

atmospheric exit conditions from a wider range of entry flight-path angles than a lower L/D vehicle which increases the TCW. A higher arrival V_∞ allows the vehicle to enter at steeper angles to bleed more energy to get captured than a lower V_∞ . Thus a higher arrival V_∞ (or corresponding V_e) offers a higher TCW, as can be seen in Figs. 3.12 and 3.13. The filled circle in Fig. 3.13 indicates that a vehicle with $L/D = 0.2$ and $\beta = 50 \text{ kg/m}^2$ arriving at $V_\infty = 7.5 \text{ km/s}$ will achieve $\text{TCW} = 1.5 \text{ deg.}$. For arrival at $V_\infty = 7.5 \text{ km/s}$, to achieve a TCW of 1.5 deg., a minimum L/D of 0.20 is required. In other words, with a vehicle of $L/D = 0.20$, an arrival V_∞ of 7.5 km/s or greater is required to achieve a TCW of 1.5 deg.

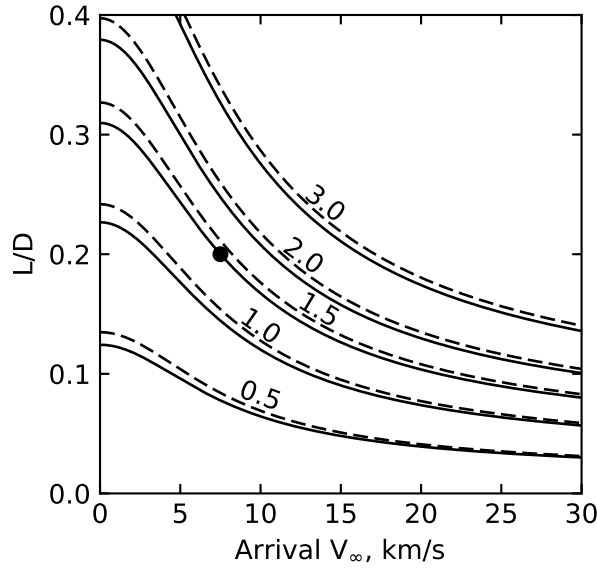


Figure 3.13. TCW contours (degrees) for lift modulation aerocapture with $\beta = 50 \text{ kg/m}^2$ (solid lines) and $\beta = 500 \text{ kg/m}^2$ (dashed lines).

Given an RCW, points on the specified TCW contour lines in Fig. 3.13 can be used to find pairs of L/D and V_∞ which represent the minimum L/D or V_∞ required for aerocapture to be feasible. Eq. (3.11) can be graphically interpreted as a constraint on the aerocapture design space in terms of L/D and V_∞ . For an RCW of 1.5 deg, the 1.5 deg contour bounds the feasible design space (i.e., L/D and V_∞ combination)—pairs of L/D and V_∞ lie on or above the contour of $\text{TCW} = 1.5^\circ$ satisfy Eq. (3.11), thus are feasible design points. Figure 3.13 shows that the effect of ballistic coefficient on TCW is small. For the same value of L/D and V_∞ , the vehicle has slightly higher TCW with lower ballistic coefficient.

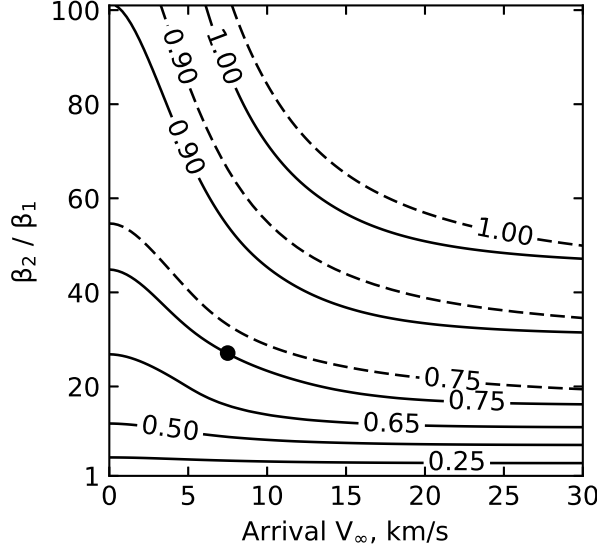


Figure 3.14. TCW contours (deg.) for drag modulation aerocapture with $\beta_1 = 5 \text{ kg/m}^2$ (solid lines) and $\beta_1 = 50 \text{ kg/m}^2$ (dashed lines).

Figure 3.14 shows TCW contours in degrees for single-event drag modulation for two initial low ballistic coefficients, $\beta_1 = 5 \text{ kg/m}^2$ and $\beta_1 = 50 \text{ kg/m}^2$ and ballistic coefficient ratio β_2/β_1 from 1 to 100. Note that if $\beta_2/\beta_1 = 1$, the vehicle has no control authority, (i.e., TCW = 0). For deployable entry systems, $\beta_2/\beta_1 = 100$ is a representative upper limit that can be achieved, and $\beta_1 = 5 \text{ kg/m}^2$ to 50 kg/m^2 is the range of ballistic coefficients expected for a drag modulation system.

In Fig. 3.14, TCW increases with increasing β_2/β_1 and arrival V_∞ . Higher β_2/β_1 implies that the vehicle has more control authority and can achieve desired atmospheric exit conditions from a wider range of entry flight-path angles than a vehicle with a smaller β_2/β_1 . The filled circle indicates a vehicle with $\beta_1 = 5 \text{ kg/m}^2$ and $\beta_2/\beta_1 = 27$ arriving at $V_\infty = 5 \text{ km/s}$ will achieve a TCW = 0.75 deg. Achieving a TCW of 0.75 deg at $V_\infty = 7.5 \text{ km/s}$ requires a minimum β_2/β_1 of 27.

Comparing Figs. 3.13 and 3.14, TCW for drag modulation is smaller than that for lift modulation. While a TCW of 1.5 degrees is available with a heritage low- L/D MSL-like aeroshell ($L/D = 0.24$) for arrival V_∞ of 5 km/s or greater, a drag modulation system with $\beta_2/\beta_1 = 20$ offers only 0.65 degrees for the same arrival V_∞ . For deployable entry

systems, $\beta_2/\beta_1 > 20$ may be difficult to implement due to the potential structural and packaging challenges of using a large drag area. The low TCW implies that drag modulation aerocapture will require navigation, atmospheric, and aerodynamics uncertainties to be lower than that required for lift modulation. Future studies will determine if entry flight path angle errors from navigation and other uncertainties could be sufficiently reduced, so that a drag modulation system with practical β_2/β_1 offers sufficient TCW to satisfy Eq. (3.11). Monte Carlo simulations which incorporate all relevant uncertainties and guidance algorithms are required to fully analyze drag modulation aerocapture performance at Venus, and is recommended for future work.

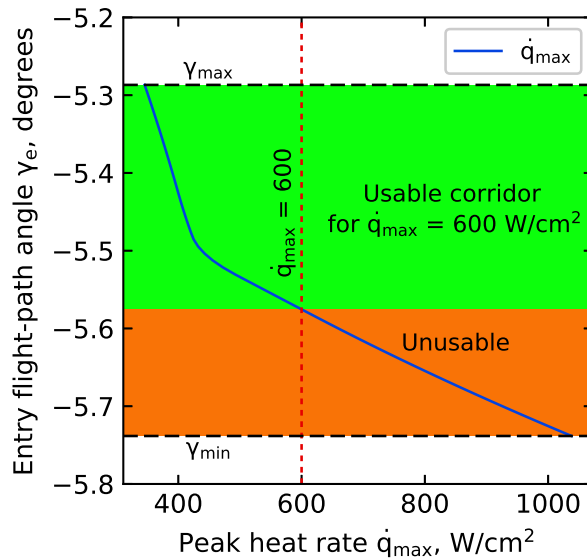


Figure 3.15. Loss of corridor for single-event drag modulation aerocapture at Venus due to peak heat rate constraint. Target apoapsis altitude = 400 km.

It is noted that the entire width of the corridor computed in Fig. 3.14 is not generally available for a single-event drag modulation aerocapture. This is due to the fact that entry at steep part of the corridor will require the large drag area to be jettisoned immediately after entry to hit the entry conditions for target apoapsis altitude. This will result in the vehicle encountering peak heat rate with the high ballistic coefficient and compromises the ability of the vehicle to keep the heating rates low. To keep the peak heat rate within the material TPS capability, a part of the steep end of the entry flight path angle corridor is

unusable. For a vehicle with $\beta_1 = 31.4 \text{ kg/m}^2$, $\beta_2/\beta_1 = 8.74$, $R_N = 0.1 \text{ m}$ [92] entering at 11 km/s, if \dot{q}_{\max} of 600 W/cm^2 is considered, the loss of corridor due to the peak heat rate constraint is shown in Fig. 3.15. If the allowable peak heat rate is lower than 600 W/cm^2 , the usable corridor is further reduced. This implies the TCW computed in Fig. 3.14 represents an upper bound for the usable corridor and the actual usable corridor is smaller. Delivery errors from approach navigation and other uncertainties should be low enough to fit within the usable aerocapture corridor. The fraction of the corridor rendered inaccessible due to the peak heat rate constraint depends on the specific vehicle design, nose radius, and entry conditions. Another important factor to be considered in single-event drag modulation aerocapture is the sensitivity of exit conditions to the drag skirt separation time. Retaining the drag skirt for just a few more seconds than the optimal separation time may result in the vehicle getting trapped in the atmosphere. Future studies will further investigate the above mentioned issues for a practical drag modulation system at Venus.

3.4.2 Peak Deceleration

The vehicle decelerates rapidly during the aerocapture maneuver with the trajectory changing from hyperbolic to elliptic in only a few minutes. The peak deceleration load G (measured in Earth g) to be sustained during the maneuver is an important design parameter. The aeroshell structure, orbiter payload, and on-board instruments are designed to withstand a maximum deceleration load G_{\max} and this limit must not be exceeded during the aerocapture maneuver.

$$G \leq G_{\max} \quad (3.12)$$

For lift modulation aerocapture, the peak g-load is the highest at the steep limit of the corridor which results in the vehicle flying lift up during the entire trajectory. The g-load for the steepest entry flight-path angle is the worst case, thus denoted as peak g-load and is used as a conservative estimate. Figure 3.16 shows contours of the peak deceleration load for lift modulation aerocapture for this worst-case scenario as a function of L/D and arrival V_∞ . The peak g-load encountered increases with increasing L/D and arrival V_∞ . Circle indicates that a vehicle with $L/D = 0.27$ with arrival $V_\infty = 5 \text{ km/s}$ will encounter a worst-case deceleration

of $20g$. Note that this deceleration rate is only the quasi-steady state component of the inertial loads. Turbulent buffeting not accounted for in the present analysis can significantly add to and increase the sensed deceleration. Scientific instruments are usually the most sensitive, and must be designed to withstand the g-loads during aerocapture. The small difference between the solid and dashed lines show that ballistic coefficient has a small effect on the peak deceleration. If $G_{max} = 30g$, the $30g$ contour line bounds the feasible design space. Combinations of L/D and V_∞ which lie to the left of the contour line are feasible design points, while those to the right are infeasible. Guidance algorithms can limit the peak g-load to a lower value than the worst-case scenario in the present study while still providing sufficient corridor if the L/D is sufficiently high [115].

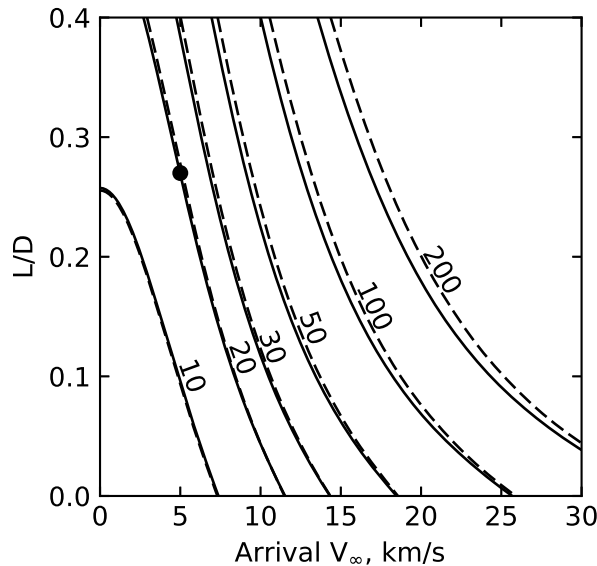


Figure 3.16. Contours of peak deceleration (Earth g) for lift modulation aerocapture with $\beta = 50 \text{ kg/m}^2$ (solid lines) and $\beta = 500 \text{ kg/m}^2$ (dashed lines) corresponding to full lift up undershoot trajectories.

For drag modulation aerocapture, the peak g-load is the highest for the shallowest entry flight path angle, which results in the vehicle flying with the smallest ballistic coefficient β_1 (largest drag area) during the entire trajectory. The peak g-load for the flight with β_1 , hence is a conservative estimate of the actual value encountered in flight. Figure 3.17 shows contours of the peak deceleration load for drag modulation aerocapture as a function of β_2/β_1 and arrival V_∞ . Figure 3.17 uses β_2/β_1 on the vertical axis for consistency with other

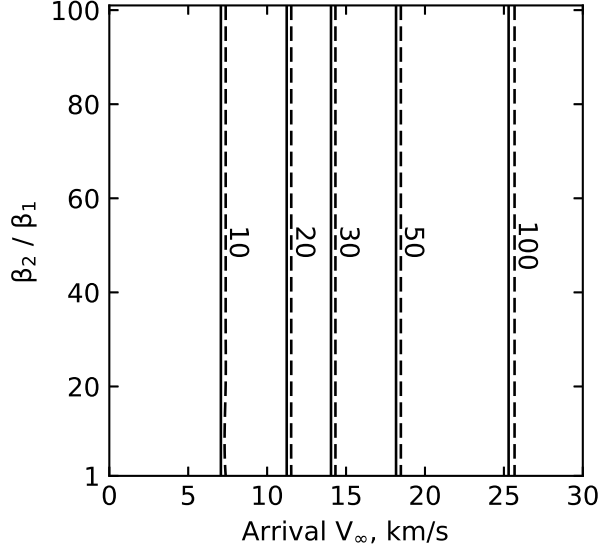


Figure 3.17. Contours of peak deceleration (Earth g) for drag modulation aerocapture with $\beta_1 = 5 \text{ kg/m}^2$ (solid lines) and $\beta_1 = 50 \text{ kg/m}^2$ (dashed lines).

figures, though the worst case g-load (as defined for the purpose of this study) is independent of the β_2/β_1 ratio and depends only on the arrival V_∞ and β_1 . The peak g-load increases with increasing arrival V_∞ and the effect of β_1 is small.

3.4.3 Peak Heat Rate and Total Heat Load

Figure 3.18 shows contours of stagnation-point peak heat rate for lift modulation aerocapture as a function of L/D and arrival V_∞ for $\beta = 50 \text{ kg/m}^2$ and $\beta = 500 \text{ kg/m}^2$. The results are reported for a vehicle with effective nose radius $R_N = 1$ meter which is representative of heritage blunt-body aeroshells. A smaller nose radius will increase the convective heating and decrease the radiative heating as indicated by Eqs. (3.7) and (3.8). The worst-case peak heat rate occurs at the steepest entry flight-path angle where the vehicle flies lift up ($\sigma = 0^\circ$) during the entire trajectory. The peak heat rate contours in Fig. 3.18 correspond to the worst case scenario. The peak heat rate is a strong function of the arrival V_∞ which in turn affects the entry speed V_e through Eq. (3.6) and the heating rates through Eq. (3.7) and Eq. (3.8).

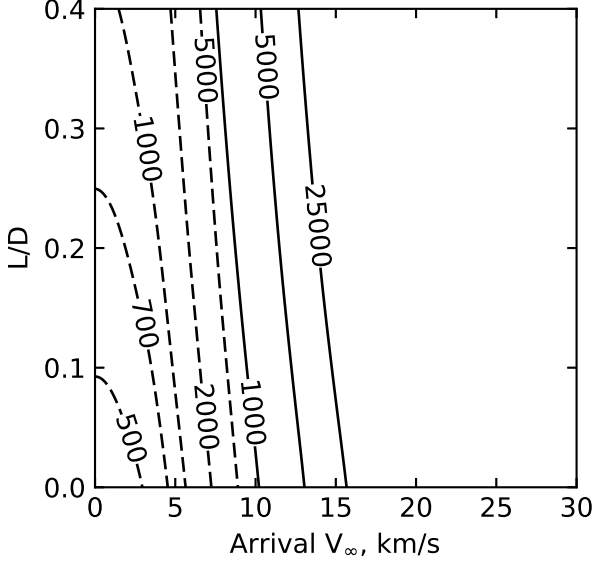


Figure 3.18. Contours of peak heat rate (W/cm^2) for lift modulation aerocapture with $\beta = 50 \text{ kg}/\text{m}^2$ (solid lines) and $\beta = 500 \text{ kg}/\text{m}^2$ (dashed lines) corresponding to full lift up undershoot trajectories.

TPS materials are qualified to withstand a maximum heat rate \dot{q}_{\max} along with maximum stagnation pressure and shear load. This study only considers the maximum heat rate limitation for the TPS material expressed as

$$\dot{q} \leq \dot{q}_{\max} \quad (3.13)$$

Currently, HEEET is the only available TPS material that can be used for lift modulation aerocapture at Venus. Other TPS materials such as PICA (used on MSL) are inadequate to handle the peak heat rate of Venus entry, and hence HEEET is an enabling technology for aerocapture at Venus. If \dot{q}_{\max} of $5,000 \text{ W}/\text{cm}^2$ is considered, then only the region to the left of the $5,000 \text{ W}/\text{cm}^2$ contour line is feasible. This constrains the maximum arrival V_∞ and hence imposes a constraint on the usable interplanetary trajectories.

The peak heat rate (shown in Fig. 3.18) has a strong correlation with ballistic coefficient as seen from the large difference in contours corresponding to $\beta = 50 \text{ kg}/\text{m}^2$ (solid lines) and $\beta = 500 \text{ kg}/\text{m}^2$ (dashed lines). A vehicle with a higher ballistic coefficient does not slow down as much as one with a lower ballistic coefficient before reaching the lower altitude, higher

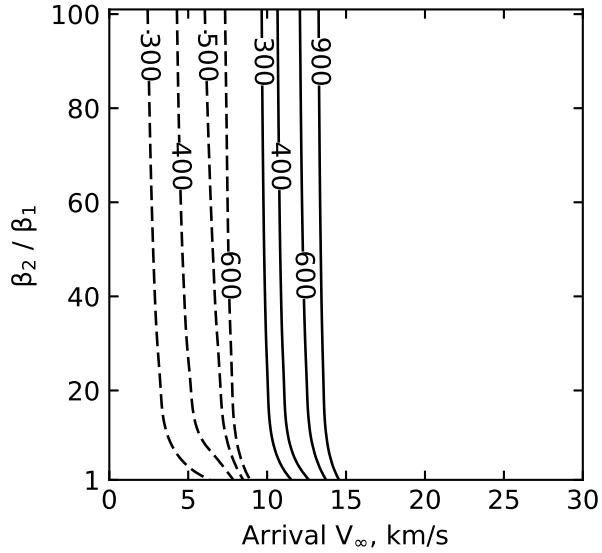


Figure 3.19. Contours of peak heat rate (W/cm^2) for drag modulation aero-capture with $\beta_1 = 5 \text{ kg}/\text{m}^2$ (solid lines) and $\beta_1 = 50 \text{ kg}/\text{m}^2$ (dashed lines).

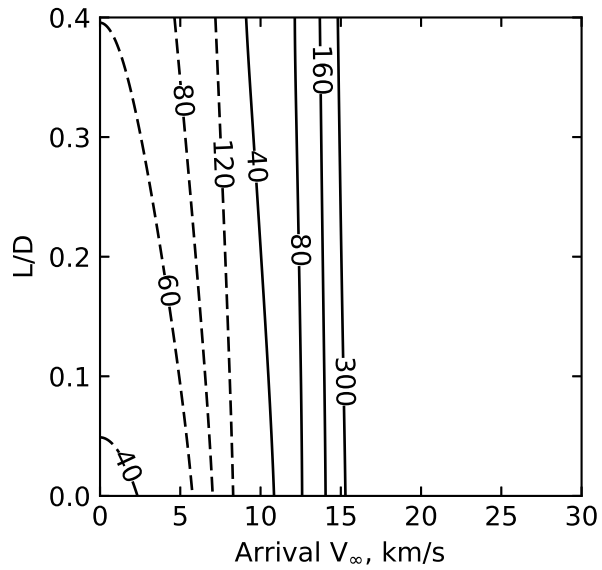


Figure 3.20. Contours of total heat load (kJ/cm^2) for lift modulation aero-capture with $\beta = 50 \text{ kg}/\text{m}^2$ (solid lines) and $\beta = 500 \text{ kg}/\text{m}^2$ (dashed lines) corresponding to full lift down overshoot trajectories.

density atmosphere, resulting in the higher β vehicle encountering a higher peak heating rate. The peak heat rate contours for the higher $\beta = 500 \text{ kg}/\text{m}^2$ is to the left of those for

$\beta = 50 \text{ kg/m}^2$ indicating that for higher ballistic coefficient, the same peak heat rate occurs at a lower V_∞ than the lower β .

Figure 3.19 shows contours of stagnation-point peak heat rate for drag modulation aerocapture as a function of β_2/β_1 and arrival V_∞ for $\beta_1 = 5 \text{ kg/m}^2$ and $\beta_1 = 50 \text{ kg/m}^2$. The results are reported for a vehicle with deployed base diameter of 2 meters and nose radius $R_N = 0.5 \text{ m}$ assuming a scaled version of the Nano-ADEPT concept [126]. Deployable entry system cannot use ablative TPS such as HEEET, but instead use foldable materials such as carbon cloth which can only accommodate significantly lower peak heat rates $\approx 400 \text{ W/cm}^2$. To keep the heat rates within the material limit, the large drag area (corresponding to β_1) must be retained till the vehicle passes through peak heating. The worst case peak heat rate in Fig. 3.19 is reported for the steepest entry flight-path angle and the vehicle flies with the large drag area. The large difference between the solid and dashed lines indicate that ballistic coefficient strongly affects the peak heat rate, and a smaller ballistic coefficient is desired to keep the heating rates low.

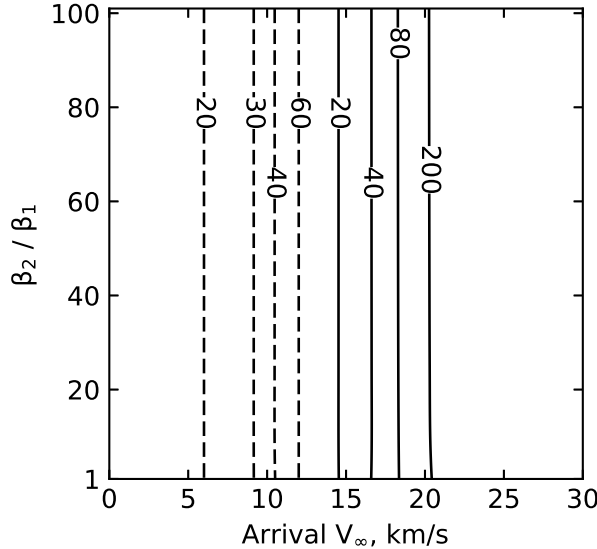


Figure 3.21. Contours of total heat load (kJ/cm^2) drag modulation aerocapture with $\beta_1 = 5 \text{ kg/m}^2$ (solid lines) and $\beta_1 = 50 \text{ kg/m}^2$ (dashed lines).

Figure 3.20 shows contours of stagnation-point total heat load Q for lift modulation aerocapture as a function of L/D and arrival V_∞ for $\beta = 50 \text{ kg/m}^2$ and $\beta = 500 \text{ kg/m}^2$.

The worst case total heat load occurs for the shallowest entry flight path angle where the vehicle flies lift-down ($\sigma = 180^\circ$) during the entire trajectory. Even though the shallow limit entry results in a lower peak heat rate than the steep limit entry, the shallow trajectory stays in the atmosphere for much longer and hence results in the larger total heat load than the steep limit trajectory. The heat load contours in Fig. 3.20 correspond to the worst case shallowest entry scenario. The total heat load is a strong function of the arrival V_∞ and a weaker function of the L/D for the higher ballistic coefficient. The total heat load can be correlated to the vehicle TPS mass fraction using Eq. (3.9). To keep the TPS mass fraction at a reasonable level, a maximum allowable heat load Q_{\max} can be specified and the heat load constraint on aerocapture can be expressed as

$$Q \leq Q_{\max} \quad (3.14)$$

Given a Q_{\max} , the contour line in Fig. 3.20 corresponding to Q_{\max} defines the feasible design space. This constraint limits the maximum acceptable V_∞ beyond which aerocapture is infeasible due to the excessive total heat load. As with the peak heat rate, ballistic coefficient strongly affects the total heat load shown by the large difference between the solid and the dashed lines. The larger ballistic coefficient results in more heating, while a smaller ballistic coefficient allows a larger arrival V_∞ for the same total heat load.

Figure 3.21 shows contours of stagnation-point total heat load Q for drag modulation aerocapture as a function of β_2/β_1 and arrival V_∞ for $\beta = 5 \text{ kg/m}^2$ and $\beta = 50 \text{ kg/m}^2$. The worst case total heat load in Fig. 3.21 corresponds to the steepest entry flight-path case and the vehicle flies with the large drag area. The heat load depends only on β_1 as the vehicle is forced to keep its lowest ballistic coefficient β_1 through the peak aerodynamic heating to keep the peak heat rate within the material capability.

3.4.4 Aerocapture Feasibility Chart

The constraints can be combined into a single chart to visualize the feasible aerocapture design space spanning interplanetary arrival V_∞ and vehicle performance determined by $(L/D)_{\text{trim}}$ or β_2/β_1 . Figure 3.22 shows the constraint lines corresponding to $\text{RCW} = [1.0,$

$1.5]$ deg., $G_{\max} = [30, 50]g$, $\dot{q}_{\max} = [7,000, 40,000]$ W/cm 2 and $Q_{\max} = [50, 100]$ kJ/cm 2 for lift modulation aerocapture with $\beta = 50$ kg/m 2 . The green shaded region indicates the feasible design space for TCW = 1.5 deg., $G_{\max} = 30g$, $\dot{q}_{\max} = 7,000$ W/cm 2 , and $Q_{\max} = 50$ kJ/cm 2 . The bottom right corner of the green region indicates that the lowest feasible vehicle L/D is 0.19 for an interplanetary trajectory with $V_{\infty} = 8.3$ km/s.

If the TCW requirement is lowered to 1.0 deg, then the yellow region becomes feasible in addition to the green region, and the vehicle L/D requirement can be lowered to 0.12 for $V_{\infty} = 9.8$ km/s. The lowest L/D occurs at the high end of arrival V_{∞} as described in Sec. 3.4.1. For a vehicle with a smaller arrival $V_{\infty} = 5$ km/s which is a nominal value for Earth-Venus chemical trajectories, the required L/D is 0.18. Relaxing the peak deceleration constraint to $50g$, in addition to the TCW constraint being relaxed to 1.0 deg. results in the cyan and magenta regions also becoming feasible. This allows the L/D requirement to be lowered further, and also allows a higher arrival V_{∞} .

Figure 3.23 shows the corresponding feasible design space for lift modulation aerocapture with $\beta = 500$ kg/m 2 . The high ballistic coefficient results in higher heat rates and heat loads compared to $\beta = 50$ kg/m 2 . For a maximum allowable heat load of 50 kJ/cm 2 there is no feasible design space as the TCW constraint cannot be satisfied. To obtain a feasible region, the heat load constraint is required to be relaxed to 100 kJ/cm 2 . The minimum required L/D as indicated by bottom right corner from the green (TCW = 1.5 deg.) and yellow (TCW = 1.0 deg.) regions is 0.22 and 0.16 respectively for the highest feasible V_{∞} .

Figures 3.24 and 3.25 show constraints from TCW, g-load, peak heat rate and total heat load in a single plot for lift modulation aerocapture with $\beta = 50$ kg/m 2 and $\beta = 500$ kg/m 2 . A mission designer can choose the values of acceptable TCW, g-load, peak heat rate, and total heat load to evaluate aerocapture feasibility at Venus. Given an interplanetary trajectory, its arrival V_{∞} can be used to calculate the minimum required L/D . Alternatively, given a vehicle L/D , the chart provides the range of feasible arrival V_{∞} . The constraints on the boundary of the feasible region indicates the limiting or driving constraints on aerocapture. From Fig. 3.22, it is apparent that for the particular constraint values considered, TCW and peak g-load are the limiting factors. The aerocapture feasibility charts show that the TCW constraint imposes a lower limit on the acceptable arrival V_{∞} , while the g-load and heating

constraints impose an upper limit on arrival V_∞ . The charts show the coupling between the interplanetary trajectory and aerocapture vehicle performance, through the dependence on arrival V_∞ . A high arrival V_∞ can lower the vehicle L/D requirement if it does not violate the heating or g-load constraints.

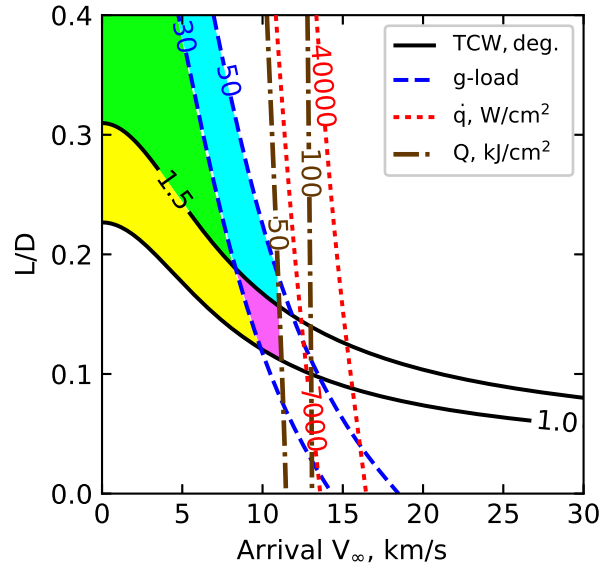


Figure 3.22. Feasible design space for lift modulation aerocapture with $\beta = 50 \text{ kg/m}^2$

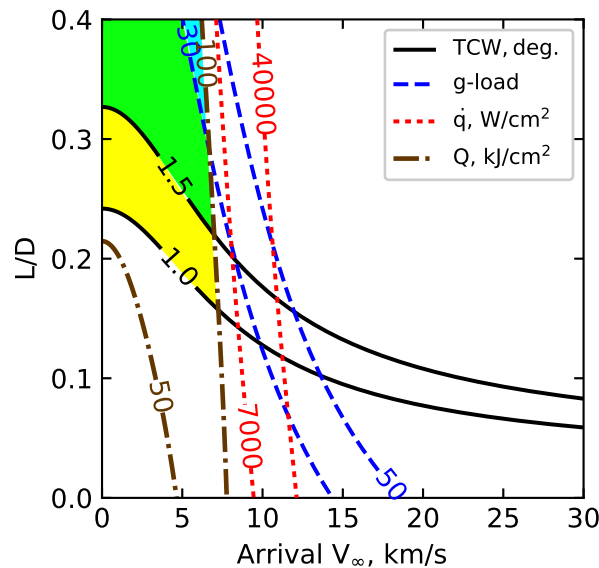


Figure 3.23. Feasible design space for lift modulation aerocapture with $\beta = 500 \text{ kg/m}^2$

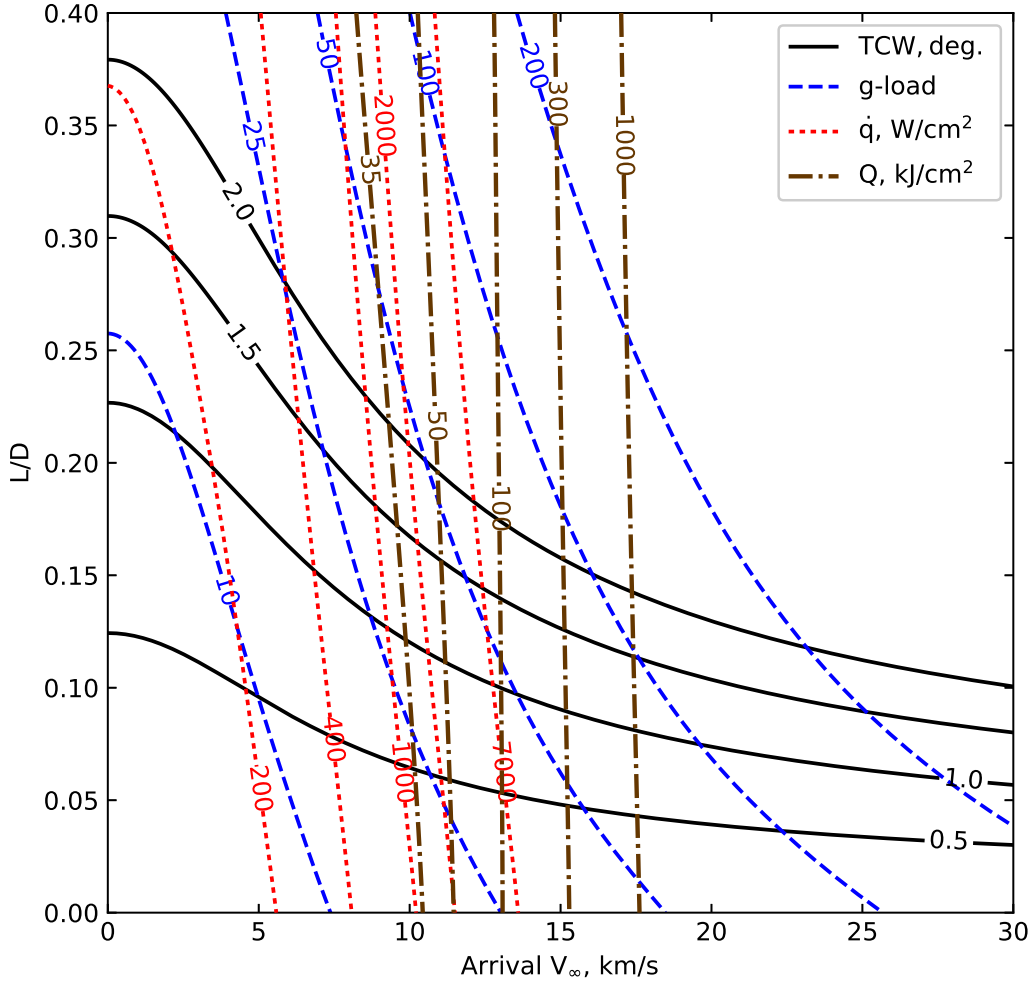


Figure 3.24. Lift modulation aerocapture feasibility chart for $\beta = 50 \text{ kg/m}^2$

For drag modulation aerocapture, it is desired to minimize the β_2/β_1 required, as high β_2/β_1 ratios present significant engineering challenges associated with very large deployable entry systems. Figure 3.26 shows the constraint lines corresponding to $\text{RCW} = [0.50, 0.75] \text{ deg.}$, $G_{\max} = 25g$, $\dot{q}_{\max} = [200, 400] \text{ W/cm}^2$ and $Q_{\max} = [20, 40] \text{ kJ/cm}^2$ for drag modulation aerocapture with $\beta_1 = 5 \text{ kg/m}^2$. The green shaded region indicates the feasible design space for $\text{RCW} = 0.75 \text{ deg.}$, $G_{\max} = 25g$, $\dot{q}_{\max} = 200 \text{ W/cm}^2$, and $Q_{\max} = 20 \text{ kJ/cm}^2$. The bottom right corner of the green region indicates that the lowest feasible β_2/β_1 is 25 for a vehicle arriving at $V_\infty = 8.4 \text{ km/s}$. If the TCW requirement is lowered to 0.5 deg, then the yellow region becomes feasible in addition to the green patch, and the β_2/β_1 requirement can be lowered to 8.9 for a vehicle arriving at $V_\infty = 8.9 \text{ km/s}$. For a vehicle with a smaller arrival

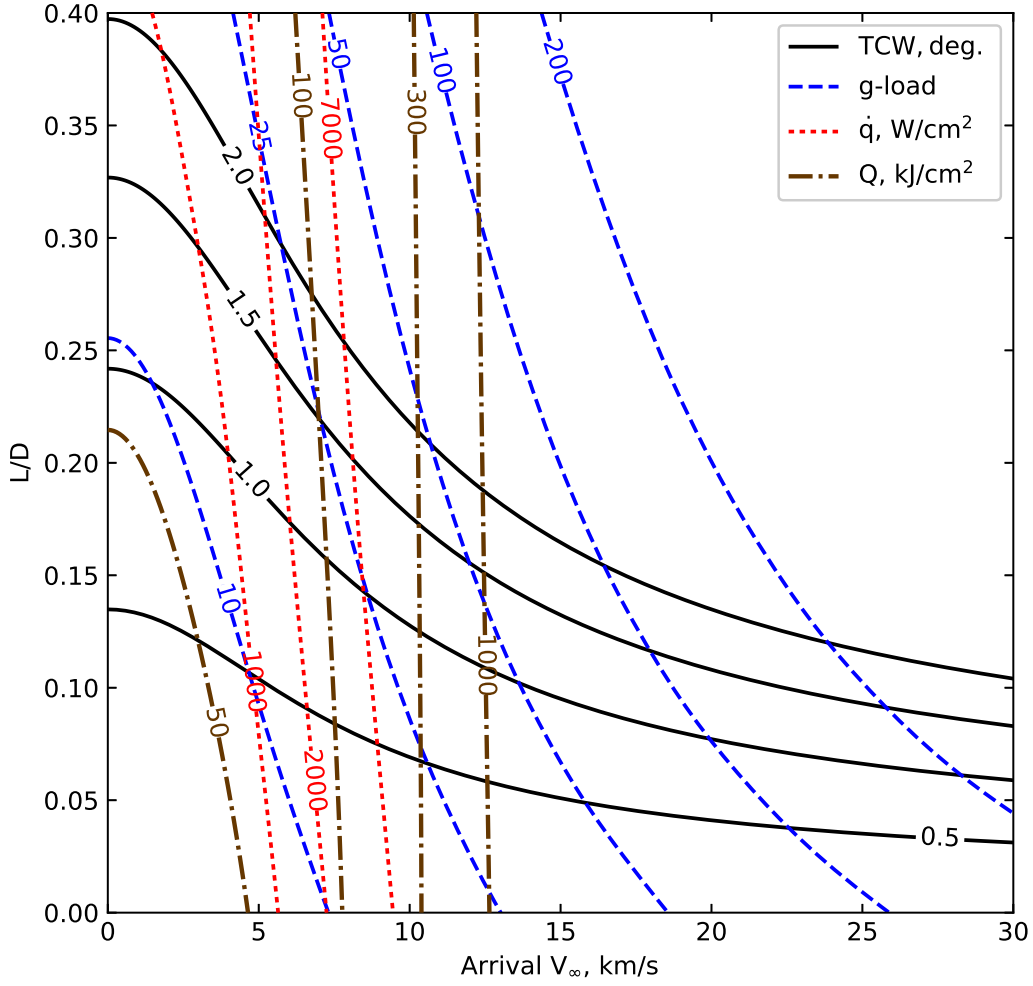


Figure 3.25. Lift modulation aerocapture feasibility chart for $\beta = 500 \text{ kg/m}^2$

$V_\infty = 5 \text{ km/s}$, the required β_2/β_1 is 10.3. Relaxing the peak heat rate constraint to 400 W/cm^2 , in addition to the TCW constraint being relaxed to 0.50 deg. results in the cyan and magenta regions also becoming feasible.

Figure 3.27 shows the corresponding feasible design space for drag modulation aerocapture with $\beta_1 = 50 \text{ kg/m}^2$. The high ballistic coefficient results in higher heat rates and heat loads compared to $\beta_1 = 5 \text{ kg/m}^2$. For a maximum allowable peak heat rate of 200 W/cm^2 there is no feasible design space as the TCW constraint cannot be satisfied. The heat rate constraint is required to be relaxed to 400 W/cm^2 to obtain a feasible region, and is the dominant constraint limiting the highest arrival V_∞ . The minimum required β_2/β_1 as indicated by bottom right corner from the green (TCW = 1.5 deg.) and yellow (TCW =

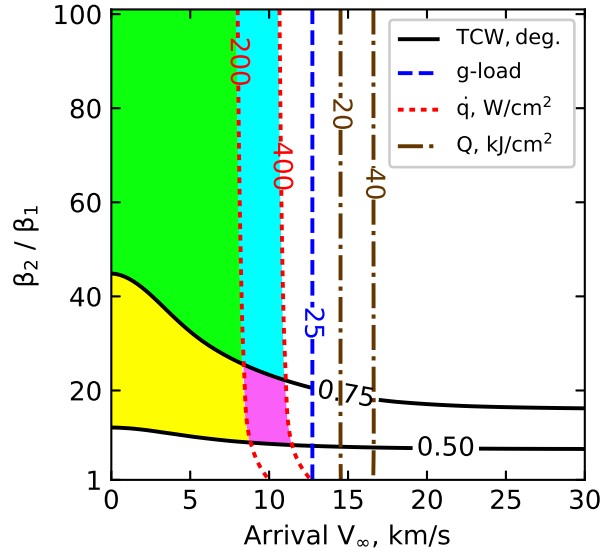


Figure 3.26. Feasible design space for drag modulation aerocapture with $\beta_1 = 5 \text{ kg/m}^2$

1.0 deg.) regions is 41 and 11 respectively for the highest feasible V_∞ . Figures 3.28 and 3.29 show the constraints from TCW, g-load, peak heat rate and total heat load in a single plot for drag modulation aerocapture with $\beta_1 = 5 \text{ kg/m}^2$ and $\beta_1 = 50 \text{ kg/m}^2$.

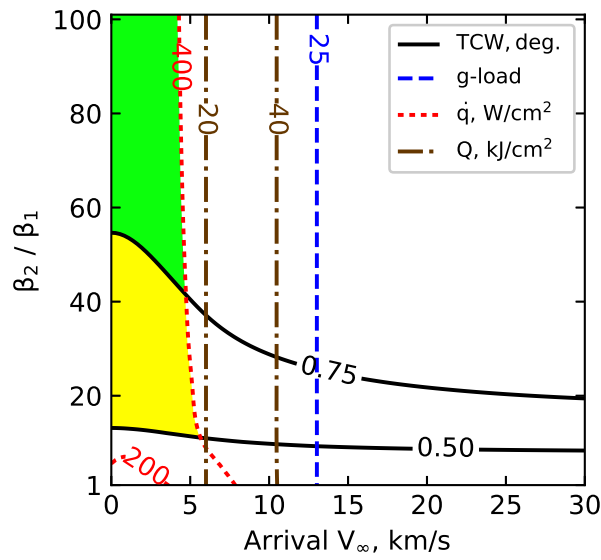


Figure 3.27. Feasible design space for drag modulation aerocapture with $\beta_1 = 50 \text{ kg/m}^2$

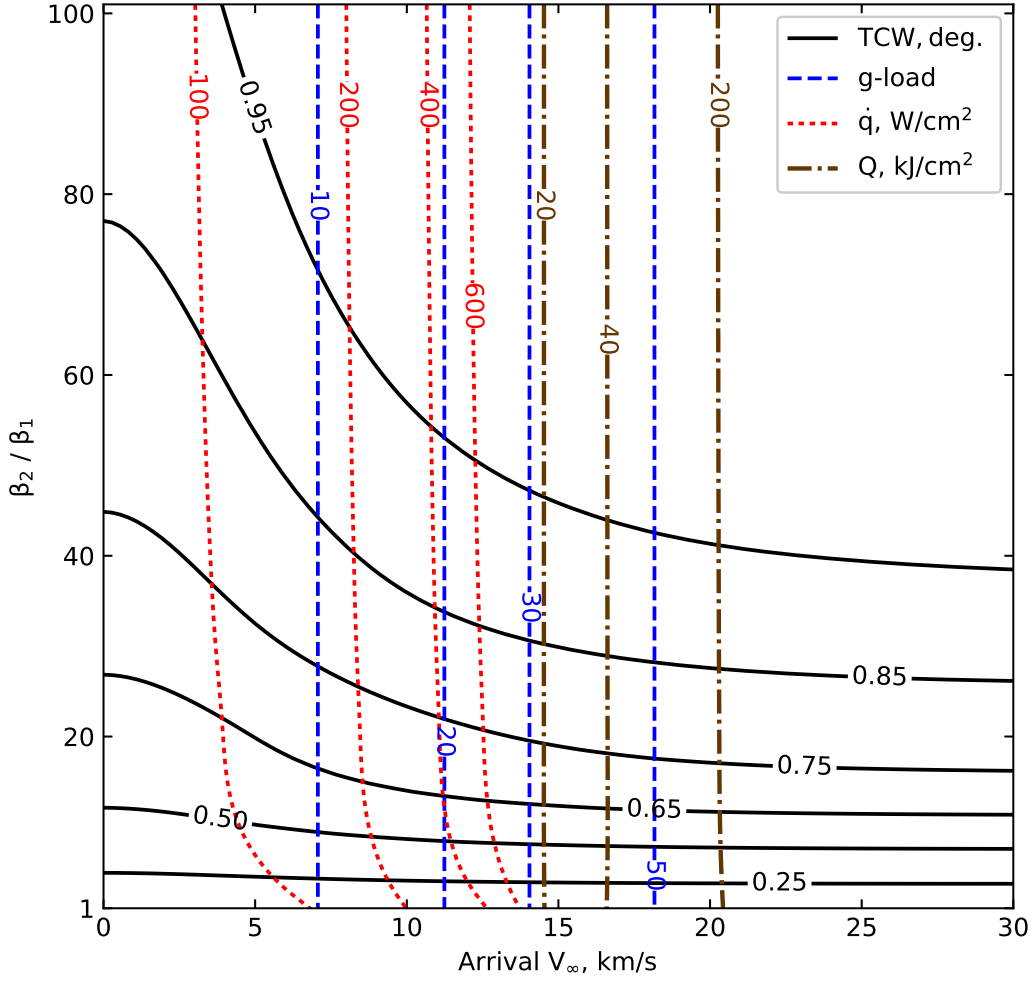


Figure 3.28. Drag modulation aerocapture feasibility chart for $\beta_1 = 5 \text{ kg/m}^2$

3.5 Mass-Benefit Analysis

3.5.1 Interplanetary Trajectory

Chemical interplanetary trajectories from Earth to Venus launching between 2018 and 2026 were generated using the STOUR software developed at JPL and upgraded at Purdue University for automated design of gravity assist trajectories [127], [128]. STOUR is a low-fidelity broad search trajectory tool which allows multiple body gravity assist sequences along with user-specified ΔV constraint, and has been used in mission concept studies [129], [130]. Launch dates spanning a period of 8 years is chosen, as the Earth-Venus orbital configuration approximately repeats every 8 Earth years and the trajectories are representative of the wide

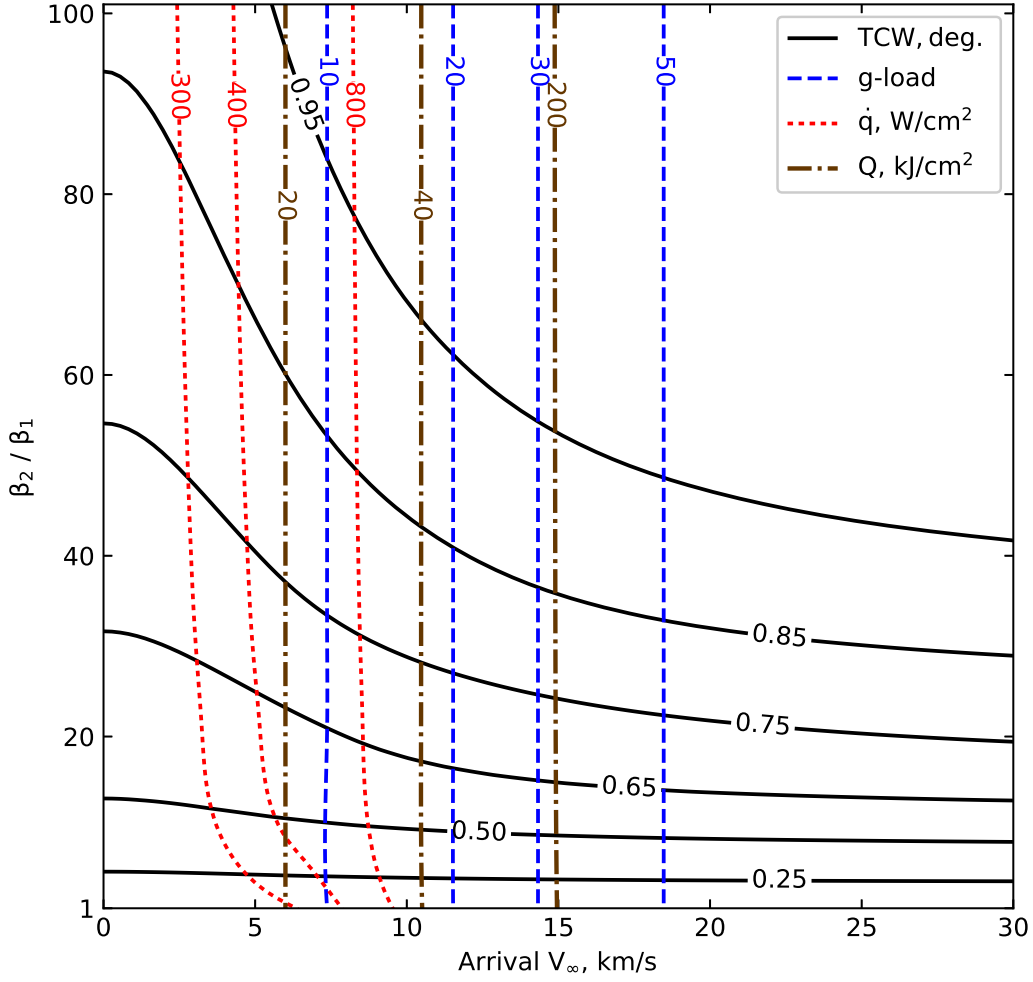


Figure 3.29. Drag modulation aerocapture feasibility chart for $\beta_1 = 50 \text{ kg/m}^2$

range of arrival conditions [131], [132]. The search includes results for ballistic transfer from Earth to Venus, and with up to one deep-space maneuver (DSM) and one Venus flyby. Figure 3.30 summarizes key parameters such as time-of-flight, arrival V_∞ , and launch C_3 for the Earth-Venus trajectories used in the study.

3.5.2 Entry System Payload Mass Fraction

In addition to TPS materials, the entry vehicle includes aeroshell structure, guidance systems, ballast masses, and other systems that are not useful payload. In the analysis, all systems (excluding the TPS materials) essential for aerocapture maneuver, but not usable

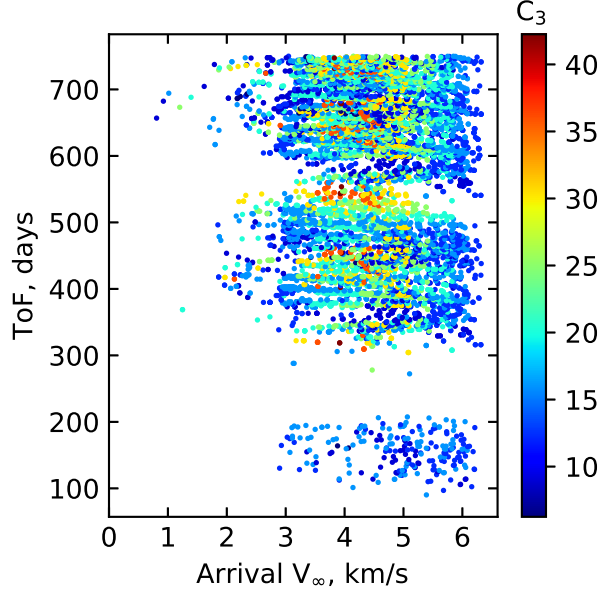


Figure 3.30. Arrival V_∞ , time-of-flight (ToF), and launch C_3 for Earth-Venus interplanetary trajectories launching between 2018 and 2026.

payload are lumped into a single parameter called entry support system mass M_{ESS} . Thus the total aerocapture vehicle entry mass can be broken down as:

$$M_{\text{Total}} = M_{\text{ESS}} + M_{\text{TPS}} + M_P \quad (3.15)$$

where M_{TPS} is the TPS mass, and M_P is the useful payload mass, i.e., delivered mass to orbit. The usable payload mass fraction for the entry system $f_{P, \text{entry}}$ is computed as

$$f_{P, \text{entry}} = 1 - f_{\text{ESS}} - f_{\text{TPS}} \quad (3.16)$$

where $f_{P, \text{entry}} = M_P/M_{\text{Total}}$, entry support systems mass fraction $f_{\text{ESS}} = M_{\text{ESS}}/M_{\text{Total}}$, and TPS mass fraction $f_{\text{TPS}} = M_{\text{TPS}}/M_{\text{Total}}$. The values of these mass fractions for aerocapture vehicle at Venus can only be computed accurately from detailed vehicle design which is outside the scope of the present study. There is a lack of architectural-level models of aerocapture systems for early mission concept studies in contrast to propulsive insertion where fairly accurate sizing relations are available [133]. To enable preliminary comparison

of aerocapture with propulsive insertion, available data for the existing entry vehicles is used to estimate the payload mass fraction for Venus entry. Table 3.4 lists the values of f_{ESS} and f_{TPS} for MSL and ADEPT Venus Intrepid Tessera Lander (ADEPT-VITaL) [134]. MSL is representative of low- L/D lifting aeroshell which could be used for Venus aerocapture with HEEET TPS replacing the original PICA heatshield. ADEPT-VITaL is a Venus entry mission concept that could be adapted for drag modulation aerocapture. The original MSL vehicle TPS is designed to accommodate a heat load of $\approx 5 \text{ kJ/cm}^2$, while $\approx 35 \text{ kJ/cm}^2$ is expected for aerocapture at Venus for a vehicle with $L/D = 0.24$ entering the atmosphere at $V_e = 12 \text{ km/s}$. To account for the higher heat load for Venus entry as compared to Mars entry, $f_{\text{TPS, Venus entry}}$ is revised to 0.19 based on Eq. (3.9). Assuming f_{ESS} is equal to the original vehicle, the usable payload mass fraction for Venus entry, $f_{\text{P, Venus entry}}$ is

$$f_{\text{P, Venus entry}} = 1 - f_{\text{ESS}} - f_{\text{TPS, Venus entry}} \quad (3.17)$$

Density differences in TPS materials and structural changes which may be required to adapt the entry vehicle into an aerocapture vehicle are not accounted for in $f_{\text{P, Venus entry}}$. Hence $f_{\text{P, Venus entry}}$ value must be regarded as nominal estimate in the absence of detailed Venus aerocapture vehicle design, and future studies will investigate its validity.

Table 3.4. Mass fractions for past entry missions/concepts and estimated payload mass fraction at Venus

Entry Vehicle	Planet	f_{ESS}	f_{TPS}	$f_{\text{TPS, Venus entry}}$	$f_{\text{P, Venus entry}}$	Details
MSL	Mars	0.23	0.12	0.19	0.58	App. A.1
ADEPT-VITaL	Venus	0.40	0.10	0.10	0.50	App. A.2

3.5.3 Mass-Benefit Analysis

The primary advantage of using aerocapture at Venus is the potential mass saving as compared to propulsive orbit insertion. Analysis of the mass-benefit of aerocapture using lift modulation and drag modulation systems has not been investigated comprehensively in the literature, which can be attributed to the difficulty in estimating the aerocapture delivered mass fraction without detailed vehicle design and the fact that previous studies often relied

on a single interplanetary trajectory to compare aerocapture and propulsive options. The present analysis uses mass numbers of the state-of-the-art entry systems to estimate the aerocapture payload mass fraction and uses a comprehensive set of interplanetary trajectories and different capture orbits to enable comparison of aerocapture with the propulsive option. This paper considers three Venus mission architectures to evaluate the potential mass-benefit of aerocapture compared to propulsive capture with and without aerobraking: a dedicated mission to Venus, a SmallSat riding along with a mission flying to or by Venus, and a SmallSat that rides along with a lunar mission and then transfers to Venus.

Dedicated Mission to Venus

This mission architecture requires a dedicated launch vehicle placing the spacecraft on an Earth-Venus trajectory. The orbit insertion ΔV_{OI} (for propulsive insertion) is then computed based on the arrival V_∞ and the target capture orbit assuming an impulsive burn at the periapsis.

$$\Delta V_{OI} = \sqrt{V_\infty^2 + \frac{2\mu_p}{r_{pe}}} - V_{pe} \quad (3.18)$$

where r_{pe} is the periapsis of the target capture orbit, V_{pe} is the orbital speed at periapsis of the target capture orbit. The useful payload mass fraction for purely propulsive insertion $f_{P, \text{prop}}$ for dedicated missions defined as the fraction of Earth escape mass that can be delivered into Venus orbit is:

$$f_{P, \text{prop}} = \exp \left[-\frac{\Delta V_{DSM}}{I_{sp}g_0} \right] \left(1 - 1.12 \left(1 - \exp \left[-\frac{\Delta V_{OI}}{I_{sp}g_0} \right] \right) \right) \quad (3.19)$$

where ΔV_{DSM} is the Deep Space Maneuver (DSM) ΔV , I_{sp} is the engine specific impulse in seconds, $g_0 = 9.80665 \text{ m/s}^2$ is the standard gravitational acceleration on Earth, and 1.12 represents a 12% tankage factor to account for the mass of the propulsion system. The above tankage factor is applicable for current large, space-storable, bipropellant propulsion systems. The useful payload mass fraction for aerocapture orbit insertion $f_{P, \text{ac}}$ for dedicated missions is:

$$f_{P, \text{ac}} = \exp \left[-\frac{\Delta V_{DSM}}{I_{sp}g_0} \right] f_{P, \text{Venus entry}} - f_{\text{Cruise stage}} \quad (3.20)$$

where, $f_{P, \text{Venus entry}}$ is the Venus entry system useful payload mass fraction calculated in Sec. 3.5.2. $f_{\text{Cruise stage}}$ accounts for an MSL-like cruise stage mass fraction (≈ 0.1) jettisoned prior to aerocapture.

SmallSat Rideshare on Venus Mission

The rideshare option involves a SmallSat riding along as a secondary payload with another mission flying to or by Venus, and is released a few weeks before the carrier spacecraft arrives at Venus. The SmallSat is assumed to be allotted a maximum allowable ridealong mass of 180 kg and enough volume to carry an ADEPT-like deployable entry system on the carrier spacecraft. Due to the mass and volume constraints for secondary payloads, it is not feasible for lifting rigid aeroshell like MSL to be used in the rideshare architecture. SmallSats typically do not have bi-prop engines used by large orbiters, but have mono-prop engines with a lower $I_{sp} = 230$ s. The useful payload mass fraction $f_{P, \text{prop}}$ for rideshare missions is defined as the fraction of allowable ridealong mass that can be delivered into Venus orbit using propulsive insertion. Equation (3.19) is used to compute $f_{P, \text{prop}}$ with $\Delta V_{\text{DSM}} = 0$, assuming any ΔV_{DSM} is performed by the carrier spacecraft. The fraction of allowable ridealong mass that can be delivered into Venus orbit using aerocapture denoted by $f_{P, \text{ac}}$, is equal to $f_{P, \text{Venus entry}}$ described in Sec. 3.5.2.

For a carrier spacecraft flying *to* Venus (i.e. The carrier spacecraft performs orbit insertion or probe entry at Venus.), V_∞ from the interplanetary trajectory dataset is used. For a spacecraft that is using Venus for a gravity assist and is flying *by* Venus on its way elsewhere in the inner solar System or the asteroid belt, a nominal $V_\infty = 10$ km/s is used. Missions flying by Venus and on to Jupiter and the outer solar system typically have $V_\infty \gg 10$ km/s. Such high flyby V_∞ trajectories cannot be used to get a secondary payload into orbit using propulsive technique because of the quasi-exponential increase of the propellant mass required for ΔV_{OI} , and heat rate limitation on TPS for aerocapture.

SmallSat Rideshare on a Lunar Mission

This option involves a SmallSat riding along as a secondary payload with a lunar mission, and subsequently uses Earth/Moon flybys and chemical or electric propulsion to transfer to Venus. The useful payload mass fraction $f_{P, \text{prop}}$ for lunar rideshare missions is defined as the fraction of mass delivered to the lunar vicinity that can be inserted into Venus orbit. The propulsive payload mass fraction $f_{P, \text{prop}}$ for this architecture is computed using Eq. (3.19) with ΔV_{DSM} replaced by ΔV_{escape} , where ΔV_{escape} is the propulsive ΔV required to escape the Earth's sphere of influence from the lunar vicinity. Mission design options presented in a recent Venus SmallSat study indicate that using ΔV_{escape} of ≈ 270 m/s along with Earth and Moon flybys can place the spacecraft on a transfer trajectory to Venus [135]. The trajectory had an arrival $V_\infty \approx 3.8$ km/s and is used to compute ΔV_{OI} . The useful payload mass that can be inserted into orbit using aerocapture $f_{P, \text{ac}}$, is computed using Eq. (3.20) with ΔV_{DSM} replaced by ΔV_{escape} , and $f_{\text{Cruise stage}} = 0$. A deployable SmallSat entry system with an open-backshell is assumed to not require a separate cruise stage.

3.5.4 Mass-Benefit of Aerocapture

Figure 3.31 shows the payload mass fraction for propulsive orbit insertion $f_{P, \text{prop}}$ for ballistic chemical trajectories to Venus launching between 2018 and 2027, capturing into a $400 \text{ km} \times 60,000 \text{ km}$ orbit. A standard bi-prop engine with I_{sp} of 323 s is assumed. The results are from a broad trajectory search (same as in Fig. 3.30) and indicate most favorable launch opportunities occur from 2023–2025. $f_{P, \text{prop}} \geq 0.70$ can be achieved in these years, and is taken as the nominal estimate for a spacecraft using a bi-prop engine. The corresponding nominal $f_{P, \text{prop}}$ to a 400×400 km orbit is 0.25.

Figure 3.32 compares the payload mass fraction that can be delivered to a 400 km circular Venus orbit with different orbit insertion techniques for the mission architectures described in Sec. 3.5.3. For aerobraking, the spacecraft first propulsively captures into an elliptical $400 \times 60,000 \text{ km}$ orbit and over the course of several months gradually lowers the orbit to $400 \times 400 \text{ km}$ using multiple upper atmospheric passes. The gradual apoapsis reduction using

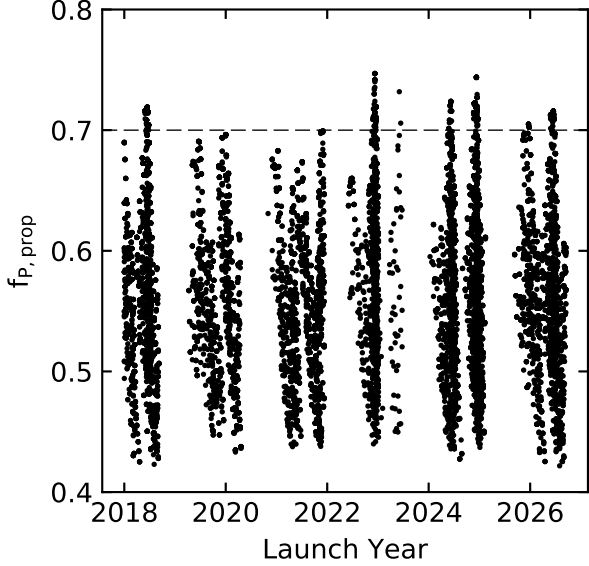


Figure 3.31. Propulsive insertion payload mass fraction ($f_{P, \text{prop}}$) to $400 \times 60,000$ km Venus orbit. During the most favorable launch opportunities from 2023–2025, $f_{P, \text{prop}} \geq 0.70$ can be achieved.

aerobraking is assumed to consume negligible propellant and hence entire delivered mass to the initial capture orbit is available in the low circular orbit.

Figure 3.32 shows that propulsive capture followed by aerobraking delivers the highest mass fraction to orbit for all mission architectures considered except for the rideshare with mission flying by Venus for a gravity assist. The elliptical initial capture orbit minimizes the orbit insertion ΔV_{OI} , and results in Eq. (3.19) delivering higher mass fraction compared to aerocapture which is limited by the entry system useful mass fraction. Entry system payload mass fraction is in the range of 0.5–0.6 for state-of-the-art entry systems considered in this study and this limits the maximum aerocapture payload mass fraction. While the entry system payload mass fraction is relatively insensitive to ΔV for the range of arrival $V_\infty < 6$ km/s, propulsive insertion mass with the lower ΔV offers a significant improvement. While propulsive insertion to the highly elliptical orbit is able to fully exploit this benefit, aerocapture is hampered by the entry support systems and significant TPS mass required for the demanding Venus entry. The study finds that entry system payload mass fraction needs to be improved to at least 0.7 for aerocapture to offer mass-benefit compared to propulsive

insertion into an elliptical orbit around Venus. For the case of a SmallSat riding along as a secondary payload on a mission flying *by* Venus for a gravity assist the high $V_\infty \approx 10$ km/s results in prohibitively high ΔV for propulsive technique to deliver reasonable payload mass even to a highly elliptical orbit. Aerocapture however can accommodate the higher heat rate (up to the TPS limit), and heat loads arising from this higher speed entry using higher TPS mass fraction, and still achieve a reasonable payload mass fraction.

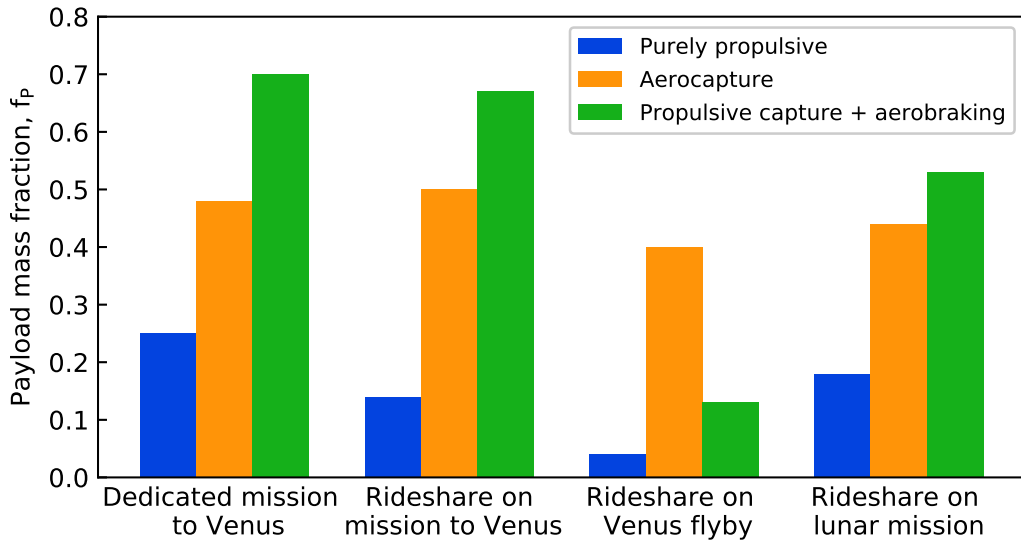


Figure 3.32. Comparison of payload mass fraction delivered to a 400 km circular Venus orbit with different orbit insertion techniques for various mission architectures.

Figure 3.32 shows that purely propulsive insertion results in the lowest payload mass fraction for all mission architectures, as the high ΔV_{OI} requires prohibitively high propellant mass to achieve the 400-km circular orbit. Though low circular orbits are preferred for radar mapping [136], data relay satellite for balloon missions [137], and sample return missions, such orbits cannot be achieved using propulsive insertion alone. Propulsive capture to highly elliptical orbit followed by aerobraking to the low circular orbit is the most mass-efficient option if the time of several months is acceptable. If low circular Venus orbit is critical for the mission science and time penalty is not acceptable as in the case of a SmallSat whose life may be only a few months, aerocapture allows the low circular orbit to be achieved immediately upon arrival.

Aerocapture offers an increase in delivered mass to a low circular Venus orbit compared to purely propulsive insertion. For dedicated missions to Venus, aerocapture using an MSL-derived aeroshell delivers 90% more mass into a 400 km orbit compared to propulsive insertion using a bi-prop engine. For a SmallSat rideshare with a mission flying *to* Venus, aerocapture using an ADEPT-derived entry system delivers 250% more mass to a 400 km circular orbit than propulsive insertion using a mono-prop engine. For a SmallSat as a secondary payload on a mission flying *by* Venus at high V_∞ for a gravity assist, aerocapture is an enabling option to perform orbit insertion. For a SmallSat rideshare with a lunar mission, aerocapture delivers 140% more mass compared to propulsive insertion.

Figure 3.33 shows the comparison of payload mass fractions to a 400×400 as a function of arrival V_∞ . For V_∞ in the range of 2–6 km/s, aerobraking delivers the most mass and is the preferred orbit insertion technique. A scenario of interest is the possibility of delivering small satellites to Venus orbit from a spacecraft which uses Venus as a gravity assist body on its way elsewhere in the Solar System. Typically such flyby trajectories have much higher V_∞ compared to direct Earth-Venus transfers. Aerocapture outperforms aerobraking for V_∞ in the range of 6–10 km/s which is typical for spacecraft using Venus as a gravity assist flyby body, and may be used to insert a secondary payload into Venus orbit. For a flyby V_∞ of 8 km/s, aerocapture delivers 83% more mass; and for V_∞ of 10 km/s, 194% more mass compared to aerobraking. For missions which flyby Venus with V_∞ greater than 10 km/s, the peak heat rates exceed that of existing TPS materials and aerocapture is likely infeasible.

3.6 Conclusion

The study indicates that aerocapture is a feasible orbit insertion technique at Venus and allows increased delivered mass to a low Venus orbit compared to propulsive insertion. Both lift and drag modulation have been studied with respect to their TCW, peak deceleration, peak heat rate, and total heat load. Lift modulation aerocapture at Venus is feasible with existing MSL-like low- L/D aeroshells and HEEET TPS. Drag modulation aerocapture is an attractive option for SmallSats as secondary payloads given its small mass and volume footprint on a carrier spacecraft. A future study to further investigate the constraints arising

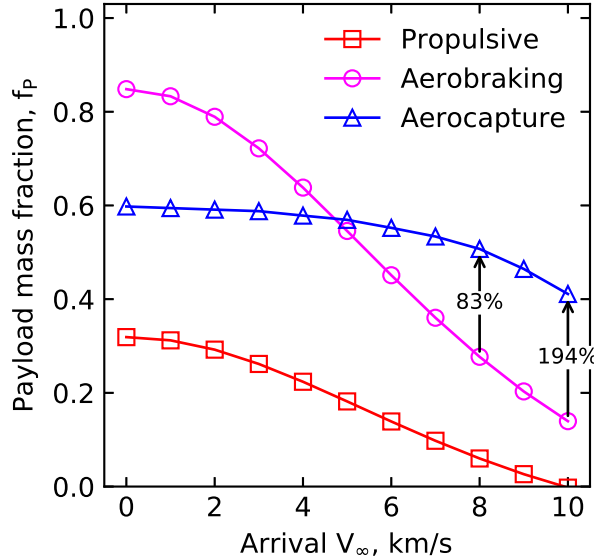


Figure 3.33. Comparison of payload mass fractions to a 400×400 km Venus orbit using various techniques.

from small corridor width and heating rate is recommended for drag modulation at Venus. The constraints have been combined into a single plot to visualize the Venus aerocapture feasible design space for both lift and drag modulation techniques. The aerocapture feasibility charts allow a mission designer to rapidly assess aerocapture feasibility for selected constraint values, and determine the vehicle L/D or β_2/β_1 required along with the range of acceptable arrival V_∞ . Detailed analysis of Earth-Venus trajectories, and useful mass fraction delivered by entry systems is used to assess the mass-benefit of aerocapture at Venus. Aerocapture offers significant mass-benefit to future radar mapping missions, sample return missions, and other missions for which a low circular Venus orbit is highly desirable. Propulsive capture to highly elliptical orbit followed by aerobraking to low circular orbit is the most attractive option for orbit insertion at Venus, if the time penalty of several months to a few years for aerobraking is acceptable. If low Venus orbit is desired immediately upon arrival, aerocapture allows for 90–250% increase in delivered mass to a 400 km circular orbit compared to propulsive insertion depending on the mission architecture.

Acknowledgments

Portions of this work were presented at the NASA Venus Exploration Analysis Group (VEXAG) meetings held in 2017 and 2018 at the Johns Hopkins University Applied Physics Lab. VEXAG student travel support for the author to attend these meetings is gratefully acknowledged. Feedback provided by scientists, engineers, and program managers at the VEXAG meetings helped in the completion of this study and is gratefully acknowledged.

4. QUANTITATIVE ASSESSMENT OF AEROCAPTURE AND APPLICATIONS TO FUTURE MISSIONS

The study by Hall et al. [1] in 2005 remains the only study to quantitatively assess and compare aerocapture performance across the entire range of planetary destinations. One limitation of the study is that it assumed both aerocapture and propulsive insertion architectures use the same interplanetary trajectory, which is not necessarily optimized for a particular architecture. Also, since 2005, many technology developments have occurred in the field of TPS, guidance techniques, and interplanetary SmallSats. Spilker et al. [3] performed a comprehensive review of the aerocapture technology readiness for future missions, but it remains largely qualitative. The present study aims to perform a quantitative and comparative assessment of aerocapture across the full set of Solar System targets with applications to future missions. Aerocapture feasibility charts are used to concisely present the various constraints arising from corridor width, deceleration, and heating requirements for both lift and drag modulation control techniques. Mission designers can quickly assess the feasibility of aerocapture for a mission concept to any atmosphere-bearing destination using a limited number of design parameters. The mass-benefit analysis enables comparison of the delivered mass with alternative orbit insertion techniques such as aerobraking and purely propulsive insertion for a range of interplanetary arrival conditions.

4.1 Methodology

Aerocapture feasibility charts use a graphical approach to visualize the various constraints arising from control authority requirement, peak deceleration, stagnation-point peak heat rate, and total heat load as a function of vehicle aerodynamic performance and interplanetary arrival conditions. The mission designer can select acceptable values of the constraint values in the feasibility charts and define the feasible set of key vehicle performance parameters such as lift-to-drag ratio L/D (for lift modulation aerocapture) or the ballistic coefficient ratio β_2/β_1 (for drag modulation aerocapture) and the range of feasible interplanetary arrival V_∞ .

4.1.1 Theoretical Corridor Width

To perform aerocapture, the aerocapture vehicle must enter the atmosphere within the aerocapture corridor bounded by the minimum and maximum acceptable entry flight-path angles γ_{\min} and γ_{\max} . The difference between the two bounding entry flight-path angles is termed the Theoretical Corridor Width (TCW), and is a measure of the vehicle's aerodynamic control authority during atmospheric flight.

$$TCW = |\gamma_{\max} - \gamma_{\min}| \quad (4.1)$$

The Required Corridor Width (RCW) is a measure of the combined uncertainties in approach navigation, atmospheric density, and other uncertainties [39]. For the vehicle to perform the aerocapture maneuver without risking crashing into the planet or flyaway without getting captured, the available TCW must exceed the RCW.

$$TCW \geq RCW + \epsilon \quad (4.2)$$

where ϵ is a small additional margin above the computed RCW. Typical values of RCW are expected to be in the range of 0.5–1.0 deg for Venus, Earth, Mars, and Titan whose atmospheres are fairly well known. For Uranus and Neptune whose atmospheres are not well-known and have large uncertainties, typical values are in the range of 1.0–2.0 deg [61].

4.1.2 Peak Deceleration

The peak deceleration load G (in Earth g) to be withstood by the aeroshell structure, orbiter payload, and on-board instruments is a critical design parameter for aerocapture missions. The peak deceleration must be less than maximum allowable deceleration G_{\max} set by the mission designer based on the structural and instrument sensitivity considerations.

$$G \leq G_{\max} \quad (4.3)$$

4.1.3 Peak Heat Rate

The aerocapture vehicle needs to withstand aerothermodynamic heating during the atmospheric pass at hypersonic speed. TPS materials protect the orbiter inside the aeroshell from the heating and the TPS material is chosen based on the peak stagnation-point aerothermal conditions. The convective heating rate \dot{q}_c is estimated using the Sutton-Graves empirical relation [113]:

$$\dot{q}_c = K \left(\frac{\rho_\infty}{R_N} \right)^{0.5} V^3 \quad (4.4)$$

where K is a constant determined by the planet's mean atmospheric composition, ρ_∞ is the freestream atmospheric density in kilograms per cubic meter, R_N is the vehicle's effective nose radius in meters, and V is the freestream velocity in meters per second. The values of the constant K for the various planets are listed in Table 4.1. Note that \dot{q}_c has units of watts per square centimeter. The radiative heating rate \dot{q}_r is computed using the correlations from sources listed in Table 4.1 [114]. The total stagnation-point heat rate \dot{q} is the sum of the convective and radiative heating rates. Typical values of peak heat rate for lift modulation aerocapture vehicles are in the range of 50–400 W/cm² at Mars and Titan [59], [138], 500–2000 W/cm² at Venus and Earth [60], [115], and 1000–8000 W/cm² at Uranus and Neptune [39], [61]. Reusable TPS materials such as Space Shuttle tiles can withstand about 100 W/cm² [117], while ablative TPS such as PICA can accommodate up to about 1200 W/cm² [139]. Heatshield for Extreme Entry Environment Technology (HEEET) is a novel 3D woven TPS material and has been tested to about 8000 W/cm² under certain conditions [140].

Drag modulation systems use a low-ballistic coefficient configuration which allows the vehicle to decelerate in the thinner upper regions of the atmosphere and thus keep the heating rates low [47], [111]. Drag modulation vehicles can use a jettisonable rigid drag skirt with reusable tiles or PICA TPS, or a deployable system such as ADEPT with woven carbon cloth as the TPS. Carbon cloth has been tested to about 250 W/cm² [125]. The TPS used for drag modulation vehicles is expected to be able to sustain peak heat rates in the range of

Table 4.1. Aerodynamic heating correlations

Planet or moon	Convective heating (value of K) [114]	Radiative heating correlation (Source)
Venus	1.8960E-8	Ref. [115]
Earth	1.7623E-8	Ref. [141]
Mars	1.8980E-8	Assumed negligible*
Jupiter	0.6556E-8	Ref. [142]
Saturn	0.6356E-8	Ref. [142]
Titan	1.7407E-8	Assumed negligible*
Uranus	0.6645E-8	Ref. [143]
Neptune	0.6719E-8	Ref. [143]

* No empirical relations were available.

50–1000 W/cm². The available TPS material and testing limitations imposes the constraint that the peak heat rate is less than the maximum allowable value.

$$\dot{q} \leq \dot{q}_{\max} \quad (4.5)$$

4.1.4 Total Heat Load

The stagnation-point heat load Q — the integral of the stagnation-point heat rate for the duration of atmospheric flight is an important parameter which determines the TPS mass fraction. A higher heat load implies that more TPS thickness is required, hence a higher TPS mass fraction and a lower overall useful payload mass fraction. Using data from flown entry vehicle designs, Laub and Venkatapathy [\[121\]](#) has reported a correlation between the stagnation-point heat load Q and TPS mass fraction f_{TPS} for heritage blunt-body aeroshells as follows:

$$f_{\text{TPS}}(\%) = 0.091Q^{0.51575} \quad (4.6)$$

in which Q has units of J/cm². Equation 4.6 can be used to approximately estimate the TPS mass fraction, though it is a preliminary estimate and is valid only for initial trade studies. Higher fidelity studies can use CFD simulations and other thermal analysis packages to refine the TPS distribution and the TPS mass fraction. For initial concept studies, to keep the

TPS mass fraction within a reasonable value, the mission designer can specify a maximum allowable heat load:

$$Q \leq Q_{\max} \quad (4.7)$$

Typical values of the total heat load for lift modulation aerocapture range from about 5–25 kJ/cm² at Mars [107], [138], 10–50 kJ/cm² at Earth, Venus and Titan [60], and 100–600 kJ/cm² at Uranus and Neptune [39], [61]. These heat loads roughly correspond to TPS mass fractions of about 10% at Mars, 10–25% at Earth, Venus, and Titan, and 35–60% at Uranus and Neptune. The validity of the relationship at very high heat loads such as those expected at Uranus and Neptune is not clear, and additional studies are required to estimate the TPS mass fraction for aerocapture at these destinations. The total heat load attempts to quantify the mass penalty from having to carry a TPS for aerocapture as opposed to conventional propulsive insertion or aerobraking where no TPS is required. This allows a mission designer to compare the delivered mass using different orbit insertion options (purely propulsive insertion, aerobraking, aerocapture) during the early stages of a mission study when a detailed vehicle design is likely not available.

4.1.5 Vehicle Design

For the lift modulation technique, the critical vehicle design parameter which dictates control authority is the vehicle lift-to-drag ratio L/D . Most planetary entry vehicles flown to date have L/D in the range of 0–0.40, and are classified low- L/D vehicles as shown in Fig. 4.1. Another important vehicle design parameter is the vehicle ballistic coefficient β . A vehicle with a lower ballistic coefficient will slow down higher up in the atmosphere where it is thinner, and encounters lower peak heat rates as compared to a high ballistic coefficient vehicle. Typical values of β for rigid blunt-body aeroshells fall in the range of 150 (MSL)–400 (Apollo) kg/m² [106], [107]. The present work assumes a nominal value of $\beta = 200$ kg/m² for all the lift modulation results, which is representative of an MSL-derived aeroshell.

For drag modulation, the vehicle control authority is determined by the ballistic coefficient ratio after and before drag skirt separation β_2/β_1 . In a simple discrete event drag

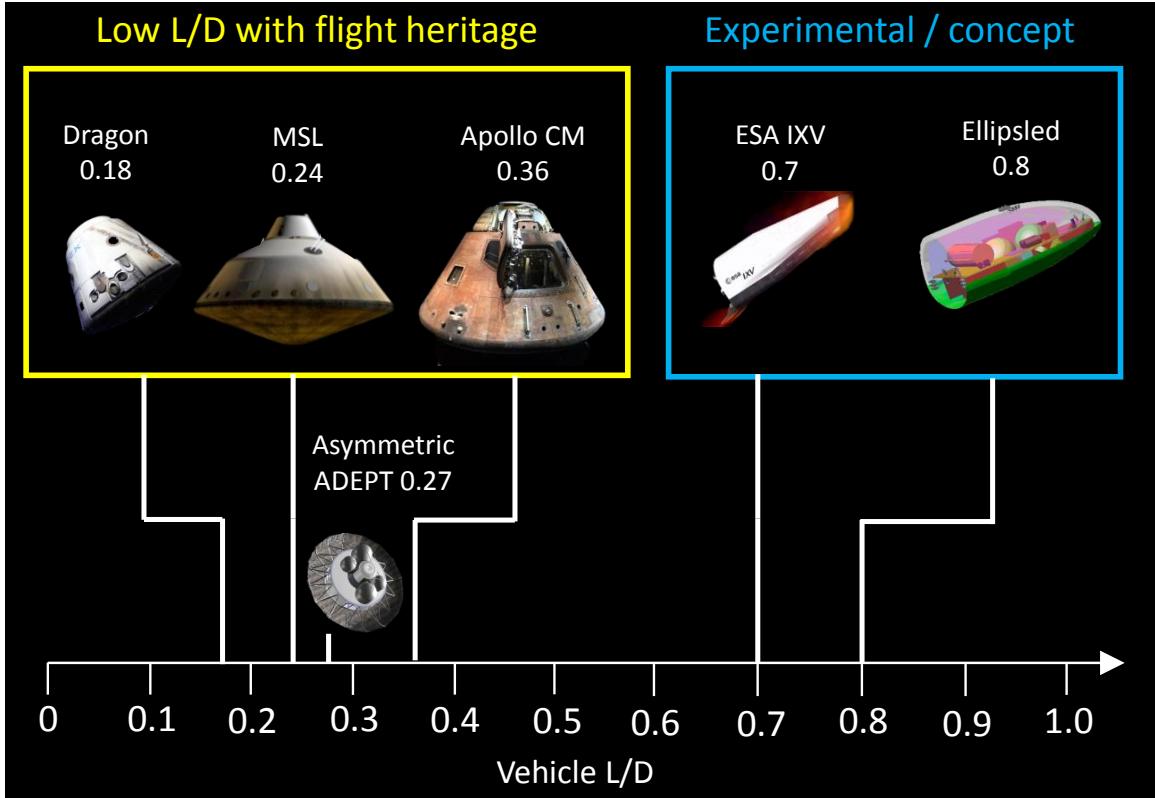


Figure 4.1. L/D of various existing and conceptual vehicles. Image credits: SpaceX, NASA/JPL, NASA/LaRC, ESA, Lockwood et al. [39], Venkatapathy et al. [108]

modulation vehicle, the ballistic coefficient is allowed to take two values, a small value β_1 with the drag skirt on and a high value β_2 after the drag skirt is jettisoned [47]. The present study assumes that the drag modulation technique is used to insert a small satellite (less than 200 kg) into orbit such as the one studied by Austin et al. [56], and uses a nominal value of $\beta_1 = 20 \text{ kg/m}^2$.

Another important vehicle design parameter is the effective nose radius R_N which strongly affects the stagnation point heat rate as seen in Eq. 4.4. The present study assumes $R_N = 1.0 \text{ m}$ which is comparable to the MSL geometry for all the lift modulation results, and $R_N = 0.1 \text{ m}$ (based on Austin et al. [56]) drag modulation results.

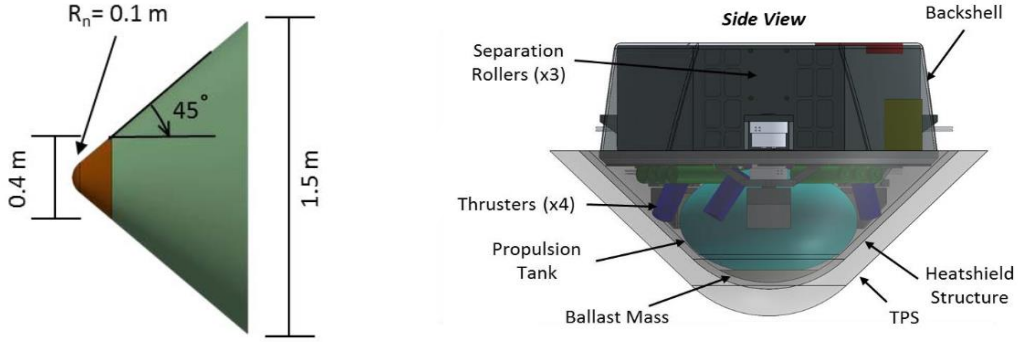


Figure 4.2. A drag modulation vehicle concept for Venus by Austin et al. [56]. Left figure shows the vehicle (brown) with the detachable drag-skirt (green). The vehicle control authority parameter is the ballistic coefficient ratio after and before drag-skirt jettison, which for this particular design concept is 7.5. Similar concepts have been proposed for Mars and technology demonstration flights at Earth [52]. Right figure shows the internal layout of the aerocapture vehicle without the drag-skirt. The TPS material is PICA. Original work by Austin et al. [56]

4.1.6 Atmosphere Models

The present study uses mean density profiles from the Global Reference Atmospheric Models (GRAMs) for Venus, Earth, Mars, Titan, and Neptune. GRAMs are engineering level atmosphere models developed by NASA Marshall Spaceflight Center and are widely used for analysis of flight trajectories in planetary atmospheres [97], [98], [144], [145]. For Jupiter, data from the Galileo entry probe Atmospheric Structure Instrument (ASI) is used [146]. For Saturn, a nominal atmospheric profile from Voyager radio occultation measurements is used [147]. For Uranus, a nominal atmospheric profile developed by NASA Ames Research Center for entry probe studies and made available to the authors is used [148]. All the atmosphere models used in this study are available at the AMAT project website¹.

For preliminary mission studies, it is sufficient to use a nominal mean density profile for aerocapture trajectory analysis as done in the present work. Higher fidelity studies to quantify guidance performance will need to include the effect of mean density variations, uncertainty in mean profiles, and high frequency density perturbations in the atmosphere

¹<https://github.com/athulpg007/AMAT/tree/master/atmdata>

model [61]. Table 4.2 lists the atmospheric models used in the study and the height of the atmospheric interface at which the Theoretical Corridor Width (TCW) values are reported in the paper in Sec. 4.3.

Table 4.2. Atmospheric models and entry interface definition

Planet or moon	Atmosphere model	Entry interface (height above surface, km)
Venus	Venus-GRAM	150
Earth	Earth-GRAM	140
Mars	Mars-GRAM	120
Jupiter	Galileo ASI data	1000*
Saturn	Voyager radio occultation data	1000*
Titan	Titan-GRAM	1000
Uranus	Ames model	1500*
Neptune	Neptune-GRAM	1000*

* Surface defined at the 1 bar pressure level.

4.1.7 Interplanetary Arrival Conditions and Target Capture Orbit

The arrival V_∞ is an important parameter which characterizes the interplanetary trajectory. The arrival V_∞ determines the planet-relative entry speed at the atmospheric entry interface, which in turn determines the available TCW, deceleration, and heating encountered by the aerocapture vehicle. Typical arrival V_∞ values are less than 6 km/s for targets such as Venus and Mars [60], and less than about 12 km/s in the outer solar system for propulsive insertion architectures [51], [61]. The present study considers a wide range of arrival V_∞ for every planetary destination. The wide range is chosen to accommodate scenarios such as a small satellite being delivered to Venus by a mother spacecraft which is using Venus as a gravity-assist body on its way to the outer solar system. Another scenario would be a very short time-of-flight (< 6 years), high energy trajectory to Neptune which arrives with a V_∞ of 25 km/s or more, though such trajectories may be infeasible from an aerothermal perspective. Table 4.3 lists the target capture orbits for the various destinations considered in the study and are based on previous aerocapture or other mission concept studies.

Table 4.3. Target capture orbits

Planet or moon	Target orbit periapsis × apoapsis, km	
	Lift modulation	Drag modulation
Venus	400 × 400	400 × 400
Earth	400 × 400	400 × 400
Mars	400 × 400	400 × 400
Jupiter	4000 × 430,000	4000 × 430,000
Saturn	4000 × 265,000	4000 × 265,000
Titan	1700 × 1700	1700 × 1700
Uranus	4000 × 903,323 ^a	4000 × 50,000 ^b
Neptune	4000 × 400,000 ^c	4000 × 50,000 ^b

^a Based on an assumed 10-day science orbit.

^b Based on an assumed close-in orbit for a small spacecraft.

^c Based on an orbit which permits Triton flybys [39], [61].

4.2 Interplanetary Trajectory Trade Space

A database of interplanetary trajectories to Venus, Uranus, and Neptune was compiled to assess the range of arrival V_∞ values for each destination, and provide a catalog of trajectories for rapid mission studies. The interplanetary trajectory study was limited to these destinations because of the time constraints of this study, and these destinations are representative of an inner planet and an outer planet mission using aerocapture. The interplanetary trajectories from Earth to Venus were generated using the STOUR software developed at JPL and upgraded at Purdue University for automated design of gravity assist trajectories [128]. STOUR is a broad search tool which allows multiple body gravity assist sequences along with user-specified ΔV constraints and has widely been used in preliminary mission studies [130], [149], [150]. Trajectories data for Uranus and Neptune come from two sources: the NASA Ice Giants Pre-Decadal Mission Study [51], and a set of high V_∞ trajectories computed at the Jet Propulsion Laboratory and made available to the author during the same study. In addition to the arrival V_∞ , two other important parameters for an interplanetary trajectory are the launch C_3 which dictates the launch mass capability for a given launch vehicle, and the time of flight which is of utmost importance for outer planet missions. Trade-offs between the launch C_3 , time of flight, and arrival V_∞ and their implications for aerocapture mission design is discussed for the various destinations considered in the study.

4.2.1 Venus

Figure 4.3 shows the interplanetary trajectory trade space for Earth-Venus transfers. Launch dates spanning a period of 8 years (2018–2026) is chosen, as the Earth-Venus orbital configuration approximately repeats every 8 Earth years and the results are representative of the wide range of launch and arrival conditions [131], [132].

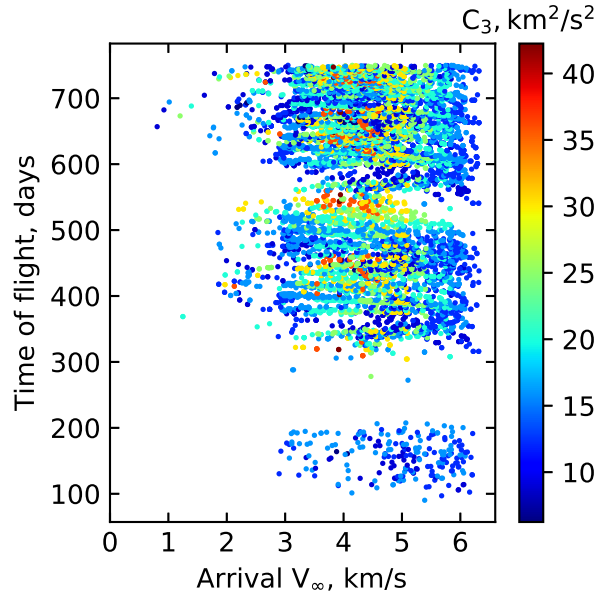


Figure 4.3. Trade space for Venus interplanetary trajectories.

The results are for ballistic transfers from Earth to Venus, and with up to one deep-space maneuver (DSM) and one Venus flyby. The set of trajectories with time of flights between 100 and 200 days are the direct Earth-Venus transfers, while those in the range of 300 to 700 days correspond to trajectories with a Venus flyby and a deep space maneuver before arrival at Venus. The range of arrival V_∞ is from 2–6 km/s for Earth-Venus trajectories as seen in Fig. 4.3.

4.2.2 Uranus and Neptune

Figures 4.4 and 4.5 shows the trajectory trade space for Uranus and Neptune respectively. The trajectories can be divided into two classes: 1) a set of low C_3 , low arrival V_∞ , ballistic

and Solar Electric Propulsion trajectories shown in blue; and 2) a set of high C_3 , high arrival V_∞ (12–25 km/s) ballistic trajectories shown in the color range from green to red. The first class is well suited for propulsive insertion architectures as the low arrival V_∞ keeps the orbit insertion ΔV as small as possible and hence the propellant mass low. The first class of trajectories have C_3 in the range of 10–75 km²/s² and are suitable when the largest launch vehicles available are Atlas V551 or similar.

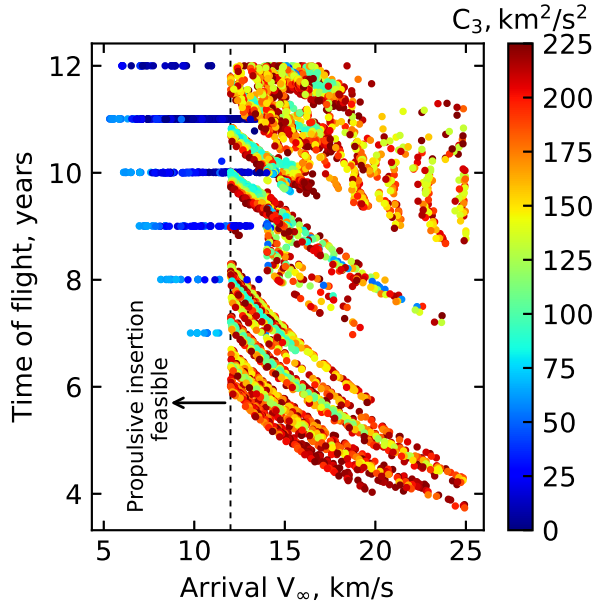


Figure 4.4. Trade space for Uranus interplanetary trajectories.

The second class of trajectories become feasible only if aerocapture is considered, as propulsive insertion becomes infeasible for arrival V_∞ of 12 km/s or higher as will be shown in Sec. 4.4.6. The second class is characterized by high C_3 in the range of 75–200 km²/s² and requires the use of launch vehicles such as the Delta IVH, Falcon Heavy or the SLS. For a launch C_3 of 100 km²/s², the second class of trajectories can enable flight times as low as 6 years to Uranus, and as low as 8 years to Neptune. The high arrival V_∞ reduces the vehicle L/D requirement as will be shown in Sec. 4.3.7, though the high entry speeds also result in substantial aerothermal loads. Preliminary calculations indicate existing TPS materials such as HEEET can accommodate arrival V_∞ up to about 20 km/s at Uranus and Neptune.

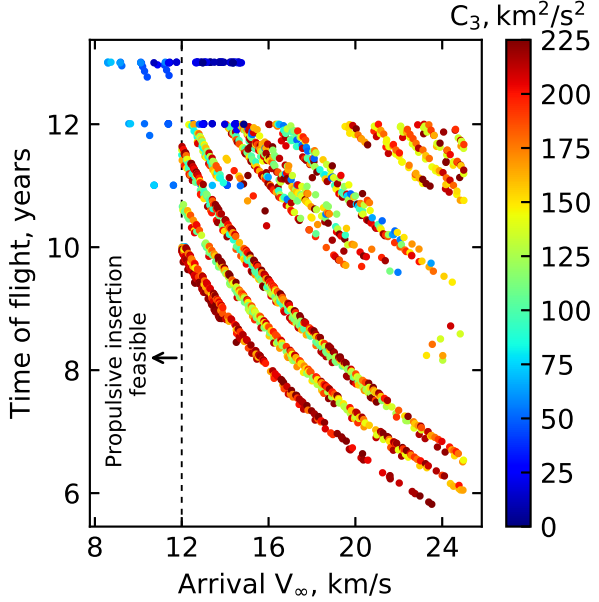


Figure 4.5. Trade space for Neptune interplanetary trajectories.

4.3 Aerocapture Feasibility Charts

Aerocapture feasibility charts for lift and drag modulation aerocapture at Venus, Earth, Mars, Jupiter, Saturn, Titan, Uranus, and Neptune are presented in this section. The vehicle control authority and heating environments are strongly destination dependent and these charts enable a quantitative comparison of the feasibility of aerocapture across the Solar System. Additional charts with more contour levels are included in Appendix B.

4.3.1 Venus

Figure 4.6a shows the lift modulation aerocapture feasibility chart for Venus with a selected set of constraint values. The green shaded region indicates the feasible set of L/D and arrival V_∞ for TCW requirement of 1.0 deg. If only 0.5 deg of TCW is required, the feasible space expands to include the yellow shaded region. Typical values of arrival V_∞ fall in the range of 2–6 km/s for Earth-Venus transfers [60], though gravity assist flybys of Venus could have much higher V_∞ . Figure 4.6a shows that heritage-blunt body aeroshells with L/D in the range 0.1–0.4 offer sufficient control authority for aerocapture at Venus,

which imply that heritage aeroshell designs such as Apollo and MSL can be leveraged for future Venus missions [106], [107], [151], [152]. Figure 4.6a allows the mission designer to quantitatively estimate the required vehicle L/D based on the required TCW and arrival V_∞ , while staying within the deceleration and heating constraints. The peak heat rates at Venus are higher compared to Earth because of the different atmospheric characteristics, but is within the capability of PICA for V_∞ of up to about 5 km/s, and within the capability of HEEET for V_∞ of up to about 10 km/s. For the shaded region, the total heat load does not exceed 50 kJ/cm² and expected TPS mass fraction is less than 24% based on Eq. 3.9.

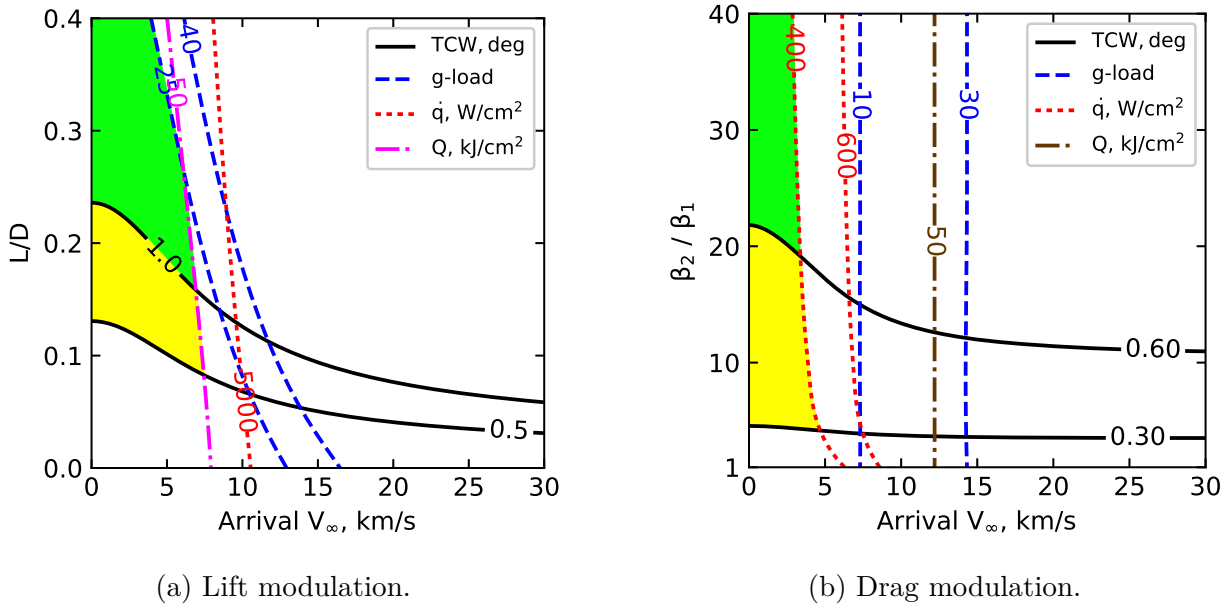


Figure 4.6. Aerocapture feasibility charts for Venus.

Figure 4.6b shows the drag modulation aerocapture feasibility chart for Venus. The available TCW for drag modulation technique is generally smaller than that for lift modulation. If the TCW requirement is 0.60 deg, the required vehicle β_2/β_1 is about 20. If the TCW requirement is lowered to 0.30 deg, a vehicle with β_2/β_1 of approximately four can provide the required control authority. For comparison, the Venus drag modulation concept studied by Austin et al. [56] used a β_2/β_1 of 9.2 to accommodate a ± 0.2 deg EFPA uncertainty at the entry interface. If the EFPA uncertainty is larger, the required TCW will be larger, and the required vehicle β_2/β_1 can be computed from Fig. 4.6b. The selected peak heat rate constraint of 400 W/cm², limits the arrival V_∞ to about 5 km/s, though materials such

as PICA can handle higher heat rates and hence accommodate V_∞ of up to about 10 km/s. Drag modulation technique is an attractive option to insert small rideshare satellites into Venus orbit from a larger mission which uses Venus as a gravity assist body [56].

4.3.2 Earth

Figure 4.7a shows the lift modulation chart for Earth and is similar to Venus (Fig. 4.6a) except for the less demanding heating environment. The shaded feasible region indicates that heritage low- L/D vehicles (L/D of 0.1–0.4) offer sufficient control authority at Earth for the aerocapture maneuver. For the selected heat rate constraint of 1000 W/cm² which can be accommodated by PICA the arrival V_∞ is limited to about 8 km/s. For a potential sample return mission from the outer Solar System which has a higher V_∞ of about 12 km/s and peak heat rate of about 5000 W/cm², HEEET TPS can be used. Aerocapture at Earth is of particular interest for two mission categories: an aerocapture demonstration at Earth as proposed by Hall [29] and Keys [30]; and a sample return from a Solar System target that is desired to be captured into Earth orbit instead of bringing the samples to the surface for planetary protection reasons.

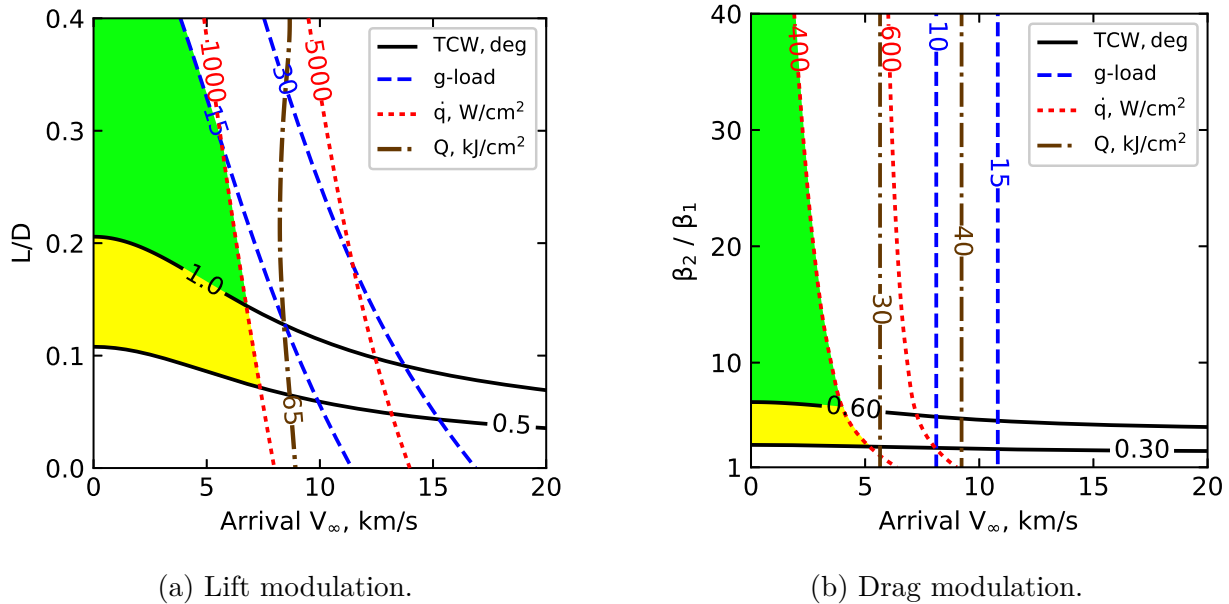


Figure 4.7. Aerocapture feasibility charts for Earth.

Figure 4.7b shows the drag modulation chart for Earth. Earth's well known atmosphere and small EFPA uncertainties compared to planetary destinations make the vehicle control authority requirements the least demanding. As seen from the shaded region in Fig. 4.7b, ballistic coefficient β_2/β_1 ratios as small as five offers sufficient control authority if the TCW requirement is 0.6 deg. For TCW requirement of 0.3 deg the β_2/β_1 ratio can be reduced to two. The peak heat rates are well within the capability of PICA for V_∞ less than 10 km/s, and for smaller values of V_∞ , carbon cloth may be sufficient enabling a deployable system such as Adaptable, Deployable, Entry, and Placement Technology (ADEPT) to be used.

Drag modulation at Earth is particularly attractive as an option to demonstrate a low cost end-to-end aerocapture mission using a SmallSat. Werner and Braun [52] studied such a SmallSat mission concept with a β_2/β_1 ratio of 4.5 and a jettisonable drag skirt with PICA TPS. The SmallSat would fly as a secondary payload on a Geosynchronous Transfer Orbit (GTO) launch and demonstrate aerocapture, greatly reducing the cost of such a mission.

4.3.3 Mars

Figure 4.8a shows the lift modulation chart for Mars, and is similar to that for Venus and Earth, but with a significantly less demanding aerothermal loads. Low- L/D vehicles once again offer sufficient control authority as seen from the shaded feasible regions, and the peak heat rates are well within the capability of PICA. The MSL aeroshell design ($L/D = 0.24$, PICA TPS) may be readily adapted to a future Mars aerocapture vehicle. Spilker et al. [3] point out that the hypersonic maneuvering capabilities for precision landing demonstrated by MSL at Mars are more challenging than that required for aerocapture. The relatively benign peak heat rates and experience with entry systems make Mars another attractive destination for future technology demonstration missions after Earth. Fujita and Narita [46] have studied a small-sized Mars aerocapture demonstrator concept with $L/D = 0.2$ and a non-ablative lightweight TPS (NALT) which could sustain the expected peak heat rate of 50 W/cm². In future, more ambitious missions using aerocapture at Mars may be able to deliver a lander or rover and an orbiter using a single aeroshell similar to the concept studied by Hassett [10] in the 1980s. Numerous studies have analyzed the application of aerocapture at Mars for Sample Return (SR) missions [12], [24], [153], [154]. The propellant savings

offered by aerocapture compared for such large and complex missions such as SR, and future manned missions make it an attractive option to be considered in future studies [21], [40].

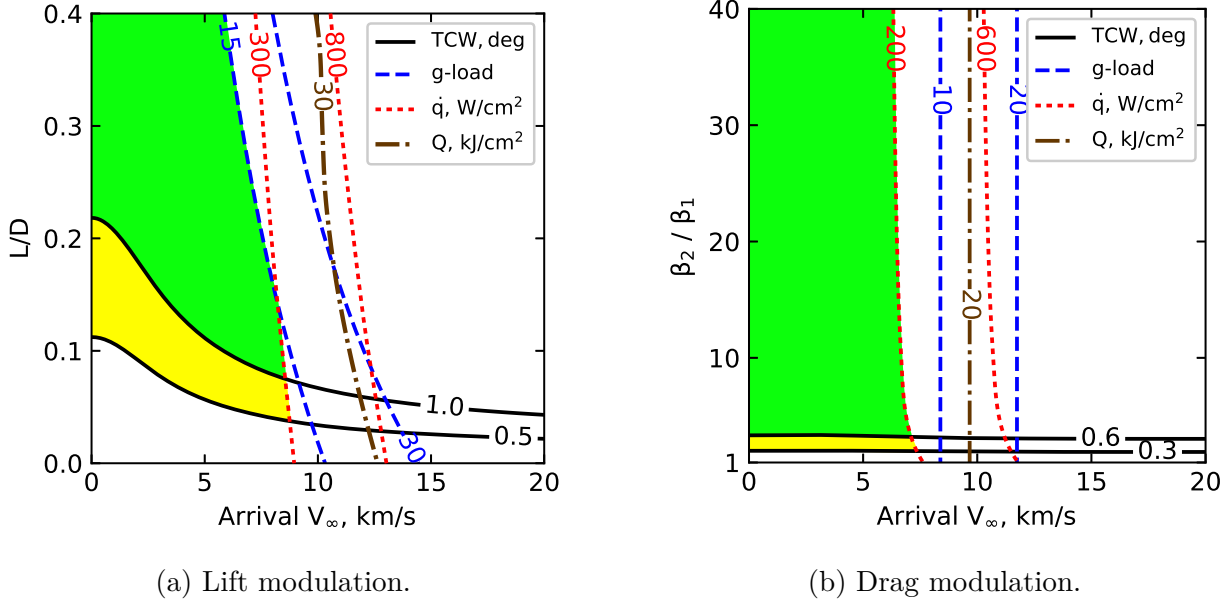


Figure 4.8. Aerocapture feasibility charts for Mars.

Figure 4.8b shows the drag modulation chart for Mars, which is similar to that for Earth (Fig. 4.7b), but with a much more benign heating environment. The shaded region indicates that ballistic coefficient ratios as small as three may be sufficient to provide the required control authority at Mars while keeping the peak heat rate below 200 W/cm². Putnam and Braun [47] have extensively analyzed drag modulation flight performance for Mars missions. Werner and Braun [52] analyzed the performance of drag modulation system with $\beta_2/\beta_1 = 4.5$ designed for Earth demonstration, and found comparable performance for the system at Mars. With its relatively benign heating environment and excellent control authority provided by low β_2/β_1 vehicles, Mars presents an attractive opportunity for a low-cost aerocapture demonstration at a planetary target. Falcone, Williams, and Putnam [55] analyzed a low-cost SmallSat mission concept using drag modulation at Mars with a β_2/β_1 ratio of 9, and expected peak heat rates less than 100 W/cm².

4.3.4 Jupiter

Figure 4.9a shows the lift modulation aerocapture feasibility chart for Jupiter. Jupiter's large gravity well results in planet-relative entry speeds in excess of 50 km/s and presents extremely high heat rates and heat loads on the entry vehicle. The harsh aerothermal environment for aerocapture at Jupiter makes it challenging to perform aerocapture, and propulsive insertion is the preferred orbit insertion method for the foreseeable future. The available corridor width is much smaller compared to that of Earth or Mars, and low- L/D blunt-body aeroshells do not offer sufficient control authority at Jupiter. For these reasons, aerocapture is considered by experts as long-term goal when there are significant advances in thermal protection systems capable of handling such extreme entry conditions [3].

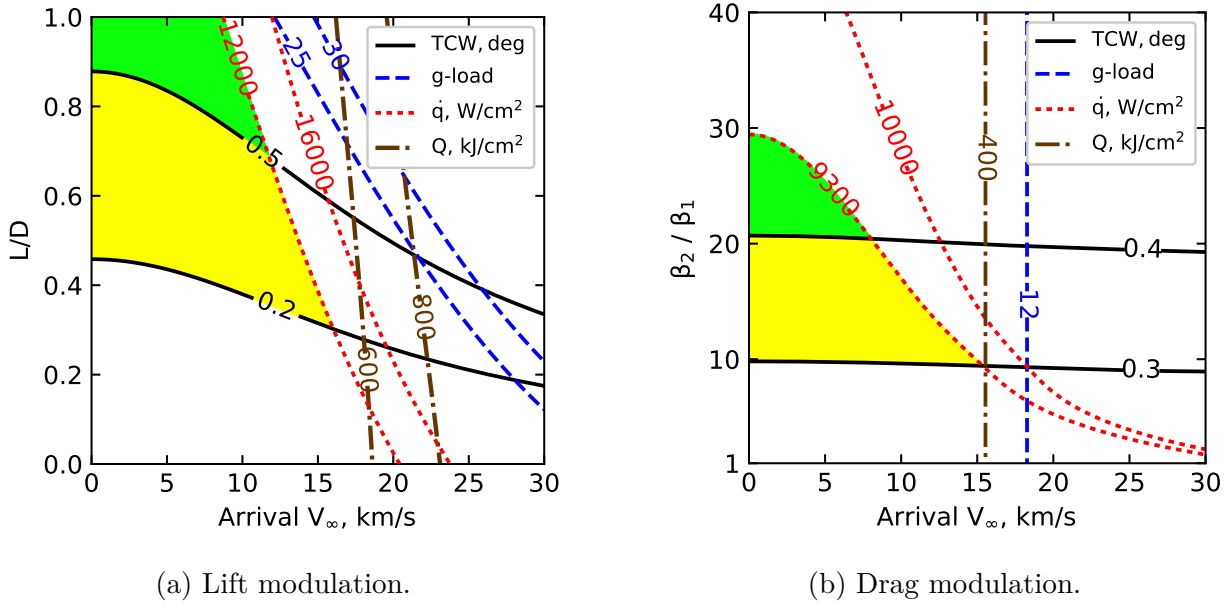


Figure 4.9. Aerocapture feasibility charts for Jupiter.

Figure 4.9b shows the drag modulation chart for Jupiter. Once again, the extremely high peak heat rates in the range of 1000s of W/cm² is considered well beyond the capability of any existing thermal protection systems used on drag modulation systems. The available corridor width is also quite small. A ballistic coefficient ratio of 20 is required even for a very low TCW of 0.4 degrees. These factors make drag modulation aerocapture at Jupiter infeasible in the near-term, and is not of practical interest for missions to Jupiter.

4.3.5 Saturn

Figure 4.10a shows the lift modulation aerocapture feasibility chart for Saturn which is quite similar to that of Jupiter (Fig. 4.9a), but with less severe aerothermal conditions. For a TCW requirement of 1 degree, mid- L/D vehicles are required to provide sufficient control authority except at high arrival V_∞ (> 15 km/s) where blunt-body aeroshells might be sufficient. The peak heat rate is within the capability of HEEET. While aerocapture at Saturn appears feasible, it is well known that performing aerocapture or aerogravity assist at Titan is a much more attractive option [155].

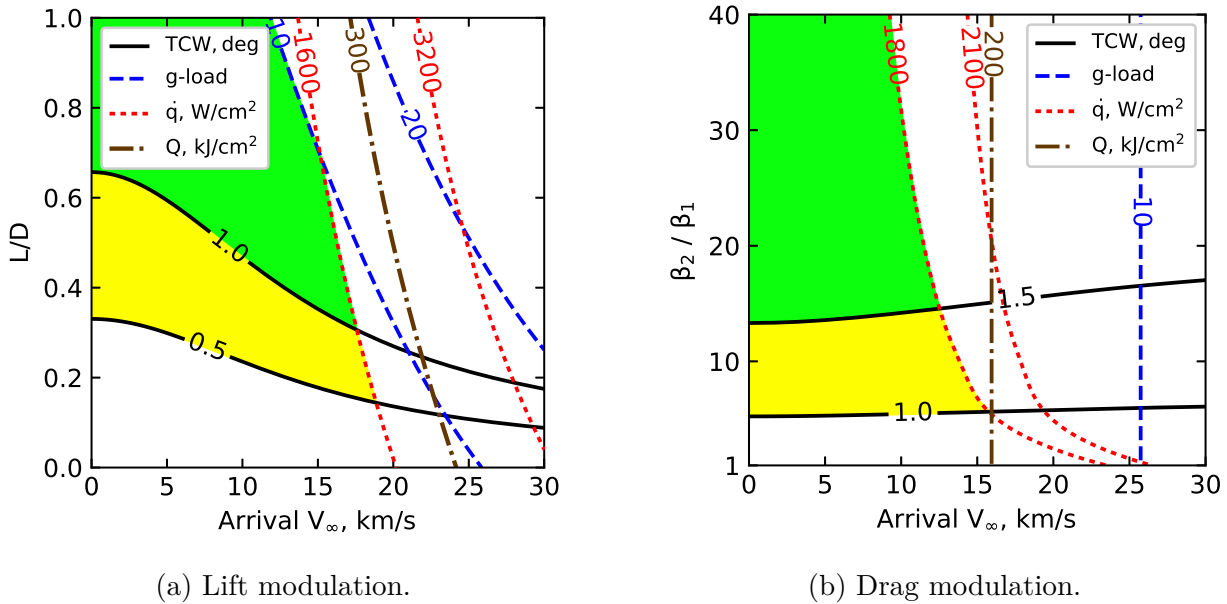


Figure 4.10. Aerocapture feasibility charts for Saturn.

Figure 4.10b shows the drag modulation chart for Saturn. The peak heat rates are not as high as that at Jupiter, but still are quite high values for drag modulation systems making them an infeasible option for aerocapture at Saturn. As explained in Sec. 4.3.6, it is desirable to use Titan’s atmosphere to achieve orbit insertion at Saturn.

4.3.6 Titan

Figure 4.11a shows the lift modulation aerocapture feasibility chart for Titan, and is similar to that for Mars (Fig. 4.8a). Titan’s low-gravity and the extended dense atmosphere

result in large scale heights, which enable vehicles with L/D as small as 0.1 to provide excellent control authority. The low-gravity also implies the planet-relative entry speeds are low, resulting in benign heating rates even less than that for Mars. The large available TCW and very low peak heat rates make Titan the least demanding destination for aerocapture in our Solar System [3]. Lu and Saikia [59] have extensively studied the feasibility of lift modulation aerocapture for future Titan missions. Spilker et al. [3] concluded that aerocapture at Titan can be accomplished using existing aeroshells and TPS, and no new technology development efforts would be required other than engineering developments common to any mission.

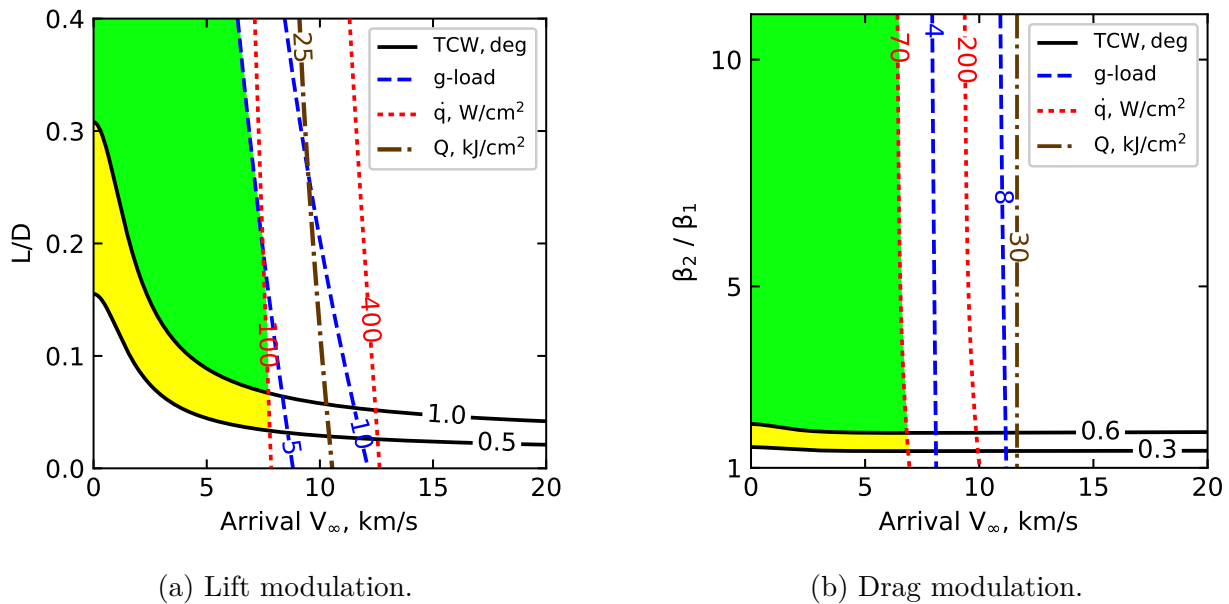


Figure 4.11. Aerocapture feasibility charts for Titan.

Figure 4.11b shows the drag modulation chart for Titan, which is similar to that for Mars (Fig. 4.8b). For a TCW requirement of 0.6 deg, vehicles with β_2/β_1 as low as two provide sufficient control authority. The heat rates are much lower than that for Mars, making Titan an attractive destination for drag modulation aerocapture. Putnam and Braun [47] have extensively analyzed the aerothermal environment and flight performance for drag modulation aerocapture vehicles at Titan. Future missions may use drag modulation aerocapture to insert multiple small satellites into appropriate Titan orbits such as those for low-altitude global mapping constellations or communication relays for surface missions [55].

4.3.7 Uranus

Figure 4.12a shows the lift modulation aerocapture feasibility chart for Uranus. The green shaded region indicates that for TCW requirement of 2 deg, vehicles with L/D in the range of 0.6–0.8 are required to provide sufficient control authority. Such mid- L/D vehicles have not yet been flown on planetary missions and will require significant development and testing. The lack of a flown mid- L/D vehicle presents a major hurdle for aerocapture at Uranus (and Neptune). Heritage blunt-body aeroshells such as Apollo entry vehicle have L/D values less than 0.40. If the TCW requirement is lowered to 1 deg, the yellow region becomes feasible lowering the L/D requirement, and vehicles with $L/D = 0.40$ offer sufficient control authority for high values of arrival V_∞ . It is worth noting interplanetary trajectories with V_∞ less than a critical value (defined for a given TCW requirement and L/D) are infeasible for aerocapture missions due to lack of control authority. For example, for TCW = 1 deg and $L/D = 0.4$, the minimum required arrival V_∞ is about 17 km/s as seen in Fig. 4.12a. For a trajectory with arrival V_∞ of about 10 km/s (which is typical for architectures with propulsive insertion [51]), aerocapture is infeasible even with a mid- L/D vehicle.

The expected peak heat rates are in the range of a few to several thousand W/cm², and HEEET is the likely TPS material to be used. PICA may be sufficient in certain situations with less demanding entry conditions such as at the low end of feasible arrival V_∞ , and near-equatorial prograde entry. Selecting a high arrival V_∞ to lower the vehicle L/D requirement must be carefully balanced against the proximity to the peak heat-rate constraint boundaries. Figure 4.12a neglects the effects of planetary rotation for simplicity, but the entry latitude and orientation are known to affect heat-rates substantially for Uranus and Neptune when planetary rotation is included [61]. Higher fidelity studies must account for these effects when selecting TPS materials for aerocapture at the ice giants.

Figure 4.12b shows the drag modulation chart for Uranus. As seen with other destinations, the available TCW for drag modulation is smaller compared to lift modulation. TCW values of 1.0–2.0 deg are not achievable even with very large ballistic coefficient ratios. Fig. 4.12b shows the feasible values of β_2/β_1 and arrival V_∞ if the TCW requirement is lowered to 0.6 and 0.3 deg. The peak heat constraint of 700 W/cm² limits the maximum arrival

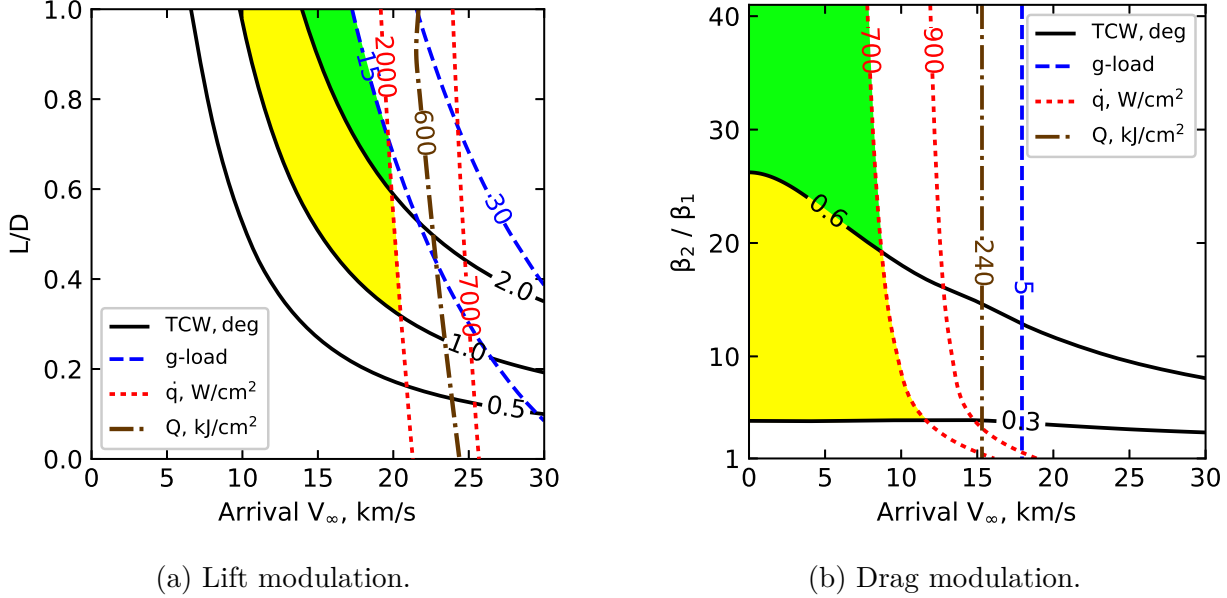


Figure 4.12. Aerocapture feasibility charts for Uranus.

V_∞ to about 10 km/s, though it is only applicable to the specific vehicle design being considered. Given the large atmospheric uncertainties to be expected at Uranus, the delivery EFPA errors would have to be driven down to an order of magnitude lower than likely possible with existing navigation technologies [61], if drag modulation aerocapture is to become feasible. Autonomous navigation (AutoNAV) technology which removes the requirement for ground in the loop in tracking and trajectory correction maneuvers (TCMs) may allow such tight tolerances on EFPA to be achieved [156]. Similar studies addressing the EFPA errors have been performed for drag modulation aerocapture at Venus by Austin et al. [56], and extension of these results to Uranus and Neptune is recommended for future studies.

The study also notes that the stated TCW requirement assumes that achieving the specified target orbit (in Table 4.3) is a strict requirement. Instead, if the requirement is relaxed to just achieve one within a wide range of specified capture orbits, the drag modulation technique may offer sufficient control authority. Another possibility is to use drag modulation to deliver small spacecraft into different orbits from a mother spacecraft which has already been inserted into orbit using propulsive insertion or lift modulation aerocapture. In that case, the EFPA errors may be much smaller given accurate tracking of

the mother spacecraft over an extended period of time and improved atmospheric knowledge from a probe which has entered prior to the drag modulation vehicle entering the atmosphere.

4.3.8 Neptune

Figure 4.13a shows the lift modulation feasibility chart for Neptune, and is similar to that for Uranus (Fig. 4.12a). The green shaded region indicated that vehicle L/D in the range of 0.6–0.8 is required for TCW requirement of 2 deg as concluded by Lockwood et al. [39] in 2006. For TCW requirement of 1 deg, the feasible region expands to include the yellow shaded area. Recent work has indicated that using a trajectory with arrival V_∞ of 20 km/s coupled with improvements in navigation and guidance can reduce the L/D requirement to 0.3–0.4, enabling heritage blunt-body aeroshells such as Apollo to perform aerocapture at Neptune [61]. Additional study is recommended to investigate if the TCW requirement can be further reduced to about 0.5 deg, which will allow MSL-derived aeroshells ($L/D = 0.24$) to be used for aerocapture at Neptune. The expected peak heat rates for Neptune aerocapture fall in the range of 1000–8000 W/cm² which requires the use of HEEET TPS, or PICA in some conditions at the lower end of the range. Neptune’s large gravity well results in planet-relative entry speeds in the range of 27–33 km/s and heat loads in the range of few to several hundred kJ/cm². Additional study is required to ascertain if the TPS mass fraction can be kept within an acceptable level for such large total heat loads.

Aerocapture was considered a potentially enhancing new technology by the Ice Giants Pre-Decadal Mission Study which investigated both Uranus and Neptune mission concepts [51]. Missions to Uranus and Neptune stand to benefit the most from aerocapture owing to their large heliocentric distances. In addition to delivering substantially more mass than propulsive architectures, aerocapture can enable a new class of short time of flight, fast arrival V_∞ trajectories which are infeasible with propulsive orbit insertion. When combined with aerocapture, the Space Launch System (SLS) would enable trip times to Uranus and Neptune to be as short as 5 and 7 years respectively [57].

Figure 4.13b shows the drag modulation chart for Neptune. Vehicles with β_2/β_1 of 10 or provide sufficient control authority for TCW requirement of 1.0 deg or less. Additional study is required to ascertain if a small satellite using drag modulation can achieve the

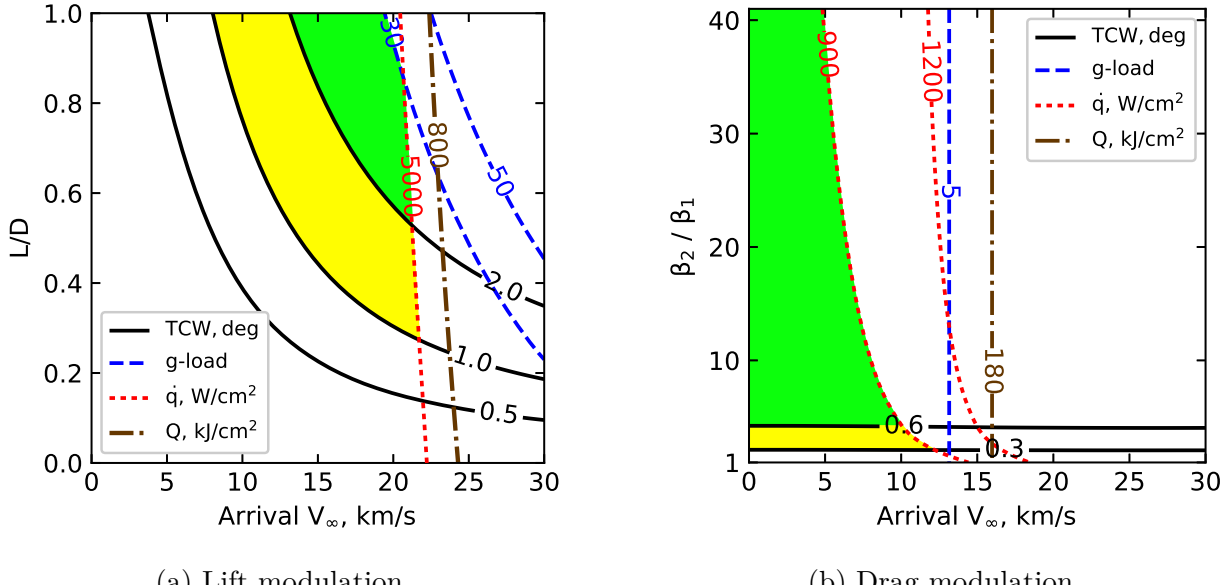


Figure 4.13. Aerocapture feasibility charts for Neptune.

tight EFPA error requirements required to meet this TCW requirement. As is the case with Uranus, deployment of small satellites into different orbits from a mother spacecraft on arrival or after orbit insertion using drag modulation may be possible and is worth future investigation. The considered peak heat rate constraint of 900 W/cm^2 though a high value for drag modulation systems can only accommodate arrival V_∞ up to about 10 km/s.

4.4 Mass-Benefit Analysis

The mass-benefit offered by aerocapture is strongly destination dependent, and on the interplanetary trajectory arrival V_∞ . Though aerocapture offers savings in terms of propellant mass, the aeroshell structure which encloses the payload and the heat-shield impose a mass penalty and must be considered in mission concept studies.

4.4.1 Methodology

This section compares the delivered mass to orbit for the atmosphere-bearing destinations using three orbit insertion techniques: 1) purely propulsive orbit insertion to the target orbit, 2) propulsive insertion to a large elliptical orbit followed by aerobraking to the target orbit,

and 3) aerocapture into the target orbit. For purely propulsive insertion and propulsive insertion followed by aerobraking, the useful payload mass fraction $f_{P, \text{prop}}$ defined as the fraction of arrival mass (before orbit insertion) that is inserted into orbit is [60]

$$f_{P, \text{prop}} = 1 - 1.12 \left(1 - \exp \left[-\frac{\Delta V_{\text{OI}}}{I_{\text{sp}} g_0} \right] \right) \quad (4.8)$$

where, 1.12 is a 12% tankage factor to account for the mass of the propulsion system, ΔV_{OI} is the orbit insertion ΔV , I_{sp} is the propulsion system specific impulse, and $g_0 = 9.80665 \text{ m/s}^2$ is the standard gravitational acceleration on Earth. The orbit insertion ΔV is computed as

$$\Delta V_{\text{OI}} = \sqrt{V_{\infty}^2 + \frac{2\mu_p}{r_{\text{pe}}} - V_{\text{pe}}} \quad (4.9)$$

where, μ_p is the standard gravitational parameter of the planet, r_{pe} is the periapsis radius of the target capture orbit, V_{pe} is the orbital speed at periapsis of the target capture orbit. The study uses an $I_{\text{sp}} = 320$ seconds assuming a conventional bi-propellant engine. For purely propulsive insertion, V_{pe} is the periapsis speed of the target capture orbits defined in Table 4.3 under the lift modulation heading. For aerobraking, V_{pe} is the periapsis speed of an intermediate capture orbit defined in Table 4.4. The spacecraft will over the course of several weeks or months, make multiple aerobraking passes in the upper atmosphere during each periapsis pass to gradually reduce the apoapsis to that of the target capture orbits defined in Table 4.3. For aerobraking, the entire mass delivered to the initial large orbit is assumed delivered to the smaller target orbit after the aerobraking period. Jupiter and Saturn are not included in the mass-benefit analysis, as the correlation used to estimate the TPS mass fraction (Eq. 3.6) is not likely valid at such high heat loads at these destinations.

In addition to TPS materials, the entry vehicle for aerocapture includes aeroshell structure, guidance and navigation systems, and other supporting equipment that is not considered useful payload delivered to orbit. All such systems (excluding the TPS materials) essential for entry vehicle function, but not usable payload are lumped into a single parameter called entry support system mass M_{ESS} . The total aerocapture vehicle entry mass is

$$M_{\text{Total}} = M_{\text{ESS}} + M_{\text{TPS}} + M_P \quad (4.10)$$

Table 4.4. Initial capture orbits for aerobraking

Planet or moon	Periapsis × apoapsis altitude, km
Venus	400 × 60,000
Earth	400 × 60,000
Mars	400 × 60,000
Titan	1700 × 300,000
Uranus	4000 × 4,962,409 ^a
Neptune	4000 × 5,248,815 ^a

^a Based on an assumed 120-day initial orbit.

where M_{TPS} is the TPS mass, and M_P is the useful payload mass. The usable payload mass fraction for the aerocapture vehicle $f_{P, \text{ac}}$ defined as the fraction of arrival mass (before aerocapture) that is delivered to orbit is [60]

$$f_{P, \text{ac}} = 1 - f_{\text{ESS}} - f_{\text{TPS}} \quad (4.11)$$

where $f_{P, \text{ac}} = M_P/M_{\text{Total}}$, entry support systems mass fraction $f_{\text{ESS}} = M_{\text{ESS}}/M_{\text{Total}}$, and TPS mass fraction $f_{\text{TPS}} = M_{\text{TPS}}/M_{\text{Total}}$. The aerocapture payload mass fraction reported in this study assumes an MSL-derived aeroshell with $f_{\text{ESS}} = 0.23$ [60], and is only applicable to lift modulation. Drag modulation is not considered in the mass-benefit analysis in this study. The TPS mass fraction is computed using Eq. 3.6, based on the average heat load as a function of the arrival V_∞ from the lift modulation aerocapture feasibility charts presented in Appendix A. For very high heat loads in the range of 200–400 kJ/cm² expected at Uranus and Neptune, the TPS mass fraction from Eq. 3.6 is multiplied by a scale factor of 0.60 to keep the TPS mass fraction at 60% or lower. Additional studies are required to accurately compute the TPS mass fraction for such high heat load scenarios for aerocapture at Uranus and Neptune.

4.4.2 Venus

Figure 4.14 shows the comparison of payload mass fractions to a 400 × 400 km Venus orbit using the various orbit insertion techniques. For V_∞ in the range of 2–6 km/s, aerobraking delivers the most mass and is the preferred orbit insertion technique. Purely propulsive

insertion to a 400 km circular orbit is prohibitive as seen from the very low payload mass fractions. The harsh thermal environment for Venus entry and the large heat loads penalize the aerocapture mass fraction, while aerobraking keeps the orbit insertion ΔV the required propellant mass low. Aerobraking has been demonstrated at Venus by the Magellan and Venus Express missions; and is planned for the proposed ESA EnVision orbiter and the Venus orbiter mission proposed by ISRO [72], [90]. Aerobraking is the most mass efficient orbit insertion method at Venus for large missions in the near future. For small short-lived missions (less than a year) whose science requirements demand a low-circular orbit, aerobraking may be infeasible because of the associated time penalty to reach the circular orbit. In this case, aerocapture offers a 100–200% increase in delivered mass compared to purely propulsive insertion (for V_∞ in the range of 2–6 km/s) as seen in Fig. 4.14.

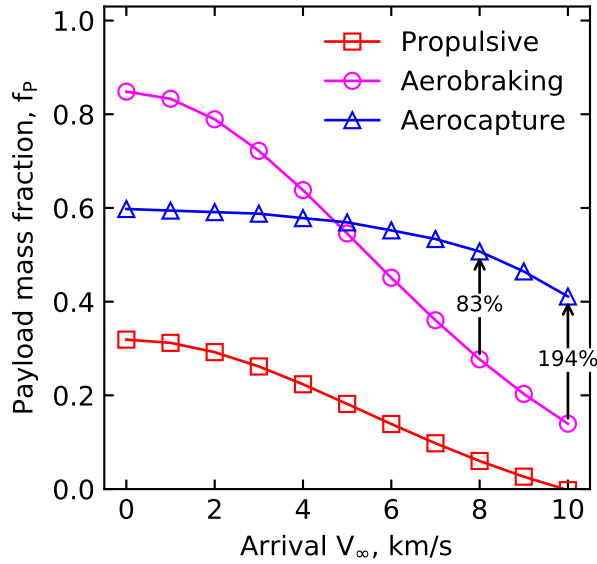


Figure 4.14. Comparison of payload mass fractions to a 400×400 km Venus orbit using various techniques.

Another scenario of interest is the possibility of delivering small satellites to Venus orbit from a spacecraft which uses Venus as a gravity assist body on its way elsewhere in the Solar System. Typically such flyby trajectories have much higher V_∞ compared to direct Earth-Venus transfers. Aerocapture outperforms aerobraking for V_∞ in the range of 6–10 km/s which is typical for spacecraft using Venus as a gravity assist flyby body, and may be

used to insert a secondary payload into Venus orbit. For a flyby V_∞ of 8 km/s, aerocapture delivers 83% more mass; and for V_∞ of 10 km/s, 194% more mass compared to aerobraking. For missions which flyby Venus with V_∞ greater than 10 km/s, the peak heat rates exceed that of existing TPS materials and aerocapture is likely infeasible as seen in Fig. 4.6a.

4.4.3 Earth

Figure 4.15 shows the performance of the different techniques for orbit insertion at Earth, and is very similar to that for Venus (Fig. 4.14). Aerobraking outperforms aerocapture for arrival V_∞ in the range of 0–5 km/s, which is the expected range for return trajectories from the Moon and Mars. However, the repeated passage of the spacecraft through the Van Allen radiation belts is a concern during aerobraking and may place additional demands on the spacecraft in terms of shielding [1]. For crewed missions, both the time penalty and the radiation dose make aerobraking infeasible, and aerocapture is the preferred orbit insertion technique. In the range of V_∞ from 0–5 km/s, aerocapture delivers 100–200% more mass to a 400 km circular orbit compared to purely propulsive insertion. For sample return missions from the asteroid belt or elsewhere in the Solar System with much higher arrival V_∞ , aerocapture clearly outperforms aerobraking. For a mission with arrival V_∞ of 8 km/s, aerocapture delivers 73% more mass, and for an arrival V_∞ of 10 km/s, 195% more mass to a 400 km circular orbit compared to aerobraking.

4.4.4 Mars

Figure 4.16 compares the delivered mass using the different techniques for Mars missions. For low arrival V_∞ in the range of 0–3 km/s, aerobraking is the preferred orbit insertion technique. As is the case with Venus, the lack of a magnetic field and hence radiation belts make aerobraking a feasible technique at Mars. Aerobraking has been demonstrated at Mars by mission such as Mars Odyssey and the ExoMars Trace Gas Orbiter. The significant heritage associated with aerobraking makes it the likely orbit insertion technique at Mars for missions in the near future.

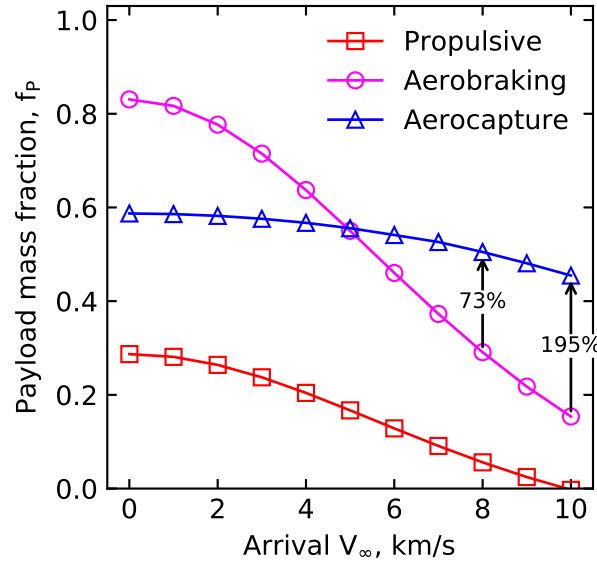


Figure 4.15. Comparison of payload mass fractions to a 400×400 km Earth orbit using various techniques.

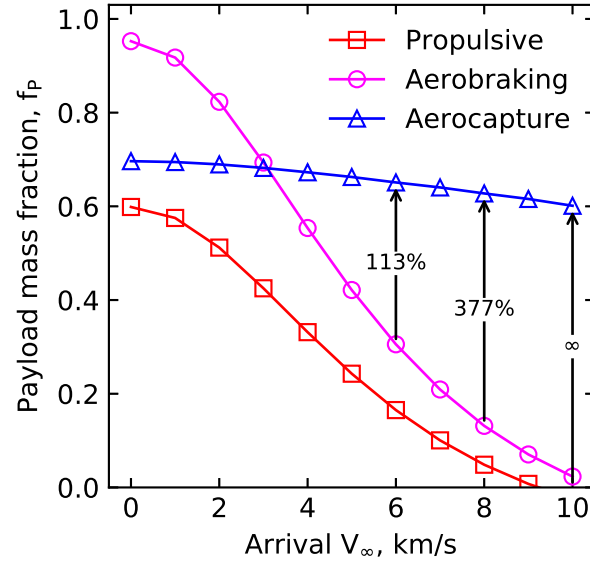


Figure 4.16. Comparison of payload mass fractions to a 400×400 km Mars orbit using various techniques.

For missions with arrival V_∞ in the range of 6–10 km/s, aerocapture outperforms aerobraking. Aerocapture delivers 113% more mass to a 400 km circular orbit compared to aerobraking for V_∞ of 6 km/s. Such high arrival V_∞ trajectories may be of interest to crewed

missions which seek to reduce the Earth-Mars transfer time to a few months, or crewed missions which use cycler trajectories. For trajectories with arrival V_∞ of 7 km/s or more, aerocapture is an enabling option as both aerobraking and purely propulsive insertion deliver little useful payload at such high arrival speeds.

4.4.5 Titan

Figure 4.17 compares the delivered mass using the different techniques to 1700×1700 km Titan orbit. For V_∞ in the range of 0–2 km/s aerobraking outperforms aerocapture, but this is not of practical interest as such low arrival speeds at Titan result in unacceptably large flight times. When interplanetary trajectories with reasonable flight times are considered, the arrival V_∞ falls in the range of 5–10 km/s. Aerocapture outperforms aerobraking for all speeds in this range, and is the preferred orbit insertion method both due to the significant mass-benefit and the particularly less demanding requirements on the vehicle as mentioned in Sec. 4.3.6. For V_∞ of 6 km/s, aerocapture delivers 300% more mass compared to aerobraking, and for V_∞ of 8 km/s the percentage increase is nearly 1700%. For trajectories with arrival V_∞ of 10 km/s or more, aerocapture is an enabling option for future Titan missions.

The flexibility in the range of arrival V_∞ offered by aerocapture opens up entirely new class of missions to Titan with flight times as short as three years. Titan’s benign aerothermal environment keeps the TPS mass fraction low, and delivers substantially more payload to orbit compared to aerobraking or propulsive insertion. The increased payload mass capacity could be leveraged to accommodate multiple elements such as orbiter, a lander, and one or more aerial platforms in a single launch vehicle, thus enabling an entirely new class of missions for future Titan exploration.

4.4.6 Uranus

Figure 4.18 compares the delivered mass using the different techniques to a 10-day Uranus orbit. For arrival V_∞ up to about 10 km/s, both propulsive insertion and aerobraking deliver a reasonable payload to orbit. For arrival V_∞ below 10 km/s, aerocapture is infeasible due to insufficient TCW as shown in Fig. 4.12a. Note that the above conclusion is valid only

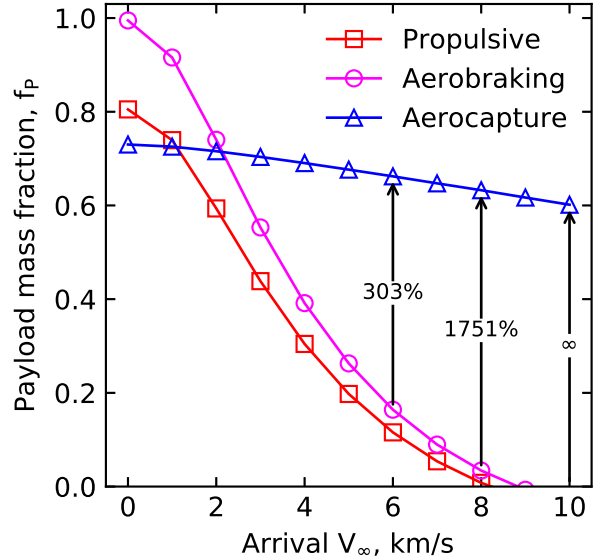


Figure 4.17. Comparison of payload mass fractions to a 1700×1700 km Titan orbit using various techniques.

for lift modulation, and does not apply to drag modulation aerocapture. For trajectories with arrival V_∞ greater than 10 km/s, aerocapture clearly outperforms aerobraking as the aerobraking delivered mass fraction falls off sharply with increasing V_∞ . For an arrival V_∞ of 12 km/s, aerocapture delivers nearly 100% more mass compared to aerobraking. A caveat in this conclusion for V_∞ of 12 km/s is that as seen in Fig. 4.12a, the required L/D is in the range of 0.6–1.0, for which the structural and TPS mass fractions used in the study do not apply to. Hence the mass-benefit for V_∞ of 12 km/s must be used with caution. For V_∞ of 16 km/s, aerocapture delivers 646% more mass compared to aerobraking and may be considered a strongly enhancing to enabling technology since the aerobraking payload mass fraction is prohibitively low. For V_∞ of 20 km/s or higher, both propulsive insertion and aerobraking are infeasible, and aerocapture is an enabling technology for orbit insertion from such fast arrival trajectories for missions to Uranus.

As is the case with Titan, aerocapture opens up a class of high arrival V_∞ fast interplanetary trajectories for Uranus missions with flight times as low as five years. Trajectories with V_∞ of 20 km/s may enable an Apollo-derived aeroshell with $L/D = 0.40$ to be used for aerocapture at Uranus, and V_∞ of 25 km/s may enable MSL-derived aeroshells with $L/D =$

0.24 to be used as seen from Fig. 4.12a. The mass savings offered by aerocapture can enable a more capable spacecraft to be inserted into orbit within a substantially shorter flight time than possible with propulsive insertion architectures, along with additional elements such as entry probes and small satellites for a future Uranus mission.

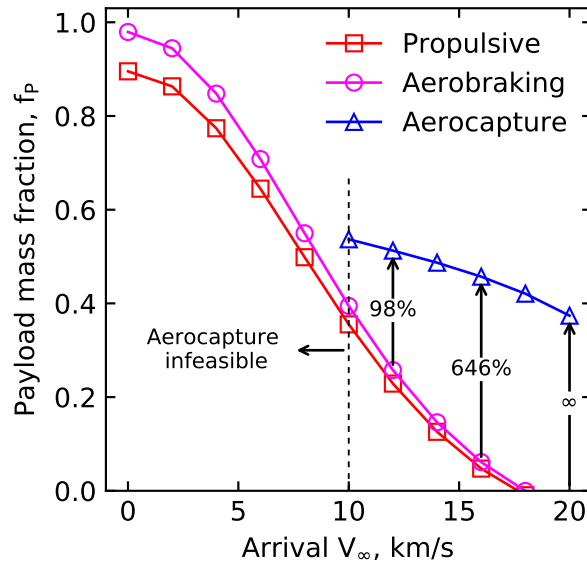


Figure 4.18. Comparison of payload mass fractions to a 10-day Uranus orbit using various techniques.

4.4.7 Neptune

Figure 4.19 compares the delivered mass using the different techniques to a 4000 x 400,000 km Neptune orbit, and is similar to that for Uranus (Fig. 4.18). Both purely propulsive insertion and aerocapture offer reasonable payload mass fractions for arrival V_∞ up to about 10 km/s. Aerocapture is infeasible for trajectories with V_∞ up to about 10 km/s due to lack of sufficient TCW as shown in Fig. 4.13a. As the V_∞ increases beyond 10 km/s, the aerobraking mass fraction falls off sharply and becomes prohibitively small beyond 12 km/s. Aerocapture, on the other hand becomes feasible for V_∞ of 12 km/s or more, does reduce with increasing V_∞ but much less sharply than that for aerobraking. For V_∞ of 12 km/s, aerocapture delivers 79% more mass compared to aerobraking. The caveat mentioned in the case of Uranus, for the L/D requirement of 0.6–0.8 with the V_∞ of 12 km/s and

the entry vehicle mass fractions used not being applicable also applies here. For V_∞ of 16 km/s, aerocapture delivers 424% more mass compared to aerobraking, and is an enabling technology for Neptune mission as the propulsive and aerobraking payload mass fractions are unacceptably low. For V_∞ of 20 km/s or higher, aerocapture is the only feasible orbit insertion technique for missions to Neptune.

As seen in the case of Titan and Uranus, high V_∞ trajectories using aerocapture can enable flight times to be as short as seven years for missions to Neptune. In addition, the high V_∞ trajectories (15–20 km/s) can lower the vehicle L/D requirement to about 0.3–0.4 which is within the capability of blunt-body aeroshells. Additional study is recommended to characterize the aerothermodynamic environment encountered by aerocapture vehicles at such high entry speeds, and to validate the TPS mass fraction estimates used in this study. In addition the savings in flight time compared to propulsive architectures, the substantial mass-benefit offered by aerocapture will enable a well instrumented spacecraft with additional elements such as a Triton lander to be accommodated in a future mission to Neptune.

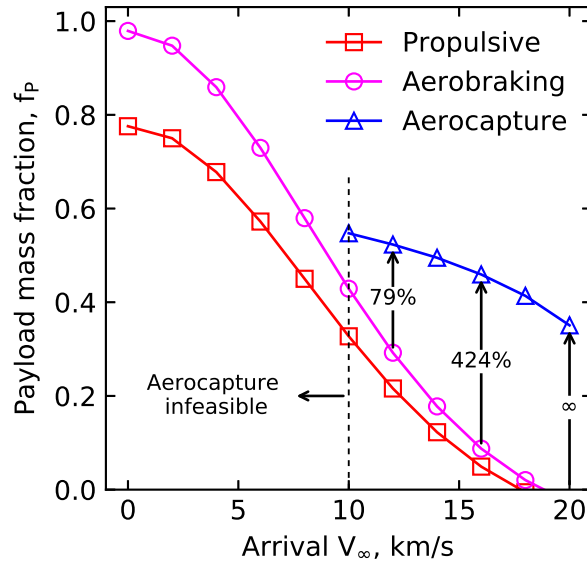


Figure 4.19. Comparison of payload mass fractions to a $4000 \times 400,000$ km Neptune orbit using various techniques.

4.5 Comparative Studies

Figure 4.20 shows the range of typical entry speeds and the aerocapture corridor for lift and drag modulation control techniques at various destinations. Venus and Earth show relatively similar entry conditions due to their similarity in size and gravity. At Mars, the entry speeds are smaller than that at Earth or Venus. Titan with its extremely low gravity and extended atmosphere result in the steepest entry of any planetary destination for aerocapture. Aerocapture vehicles at Uranus and Neptune encounter planet relative entry speeds in the range of 20–30 km/s.

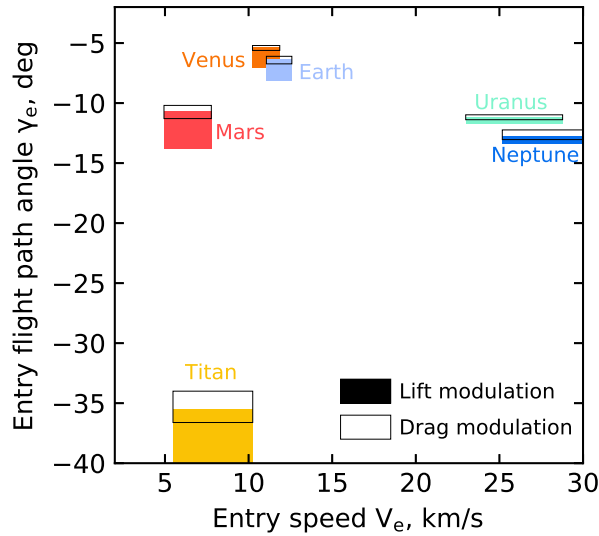


Figure 4.20. Comparison of entry speed and entry corridor for aerocapture at various targets for a vehicle with $L/D = 0.30$ for lift modulation and $\beta_2/\beta_1 = 7$ for drag modulation.

Jupiter and Saturn are not included in Fig. 4.20 because the entry speeds are much higher than encountered at the other planets. Figure 4.21 shows the aerocapture theoretical corridor width at various destinations. For the inner planets and Titan, TCW for lift modulation aerocapture is in general larger than that for drag modulation. This implies that drag modulation entry vehicles must be delivered with much smaller delivery errors compared to lifting vehicles to ensure they enter within the corridor. For the giant planets, the trend is reversed i.e. drag modulation corridor width is larger than that for lift modulation. It is not immediately clear why this is the case, and additional studies are required. The

corridor width is largest at Titan, and smallest at Jupiter. Uranus and Neptune also have substantially smaller corridor widths than at the inner planets, thus imposing stringent constraints on delivery errors for aerocapture vehicles.

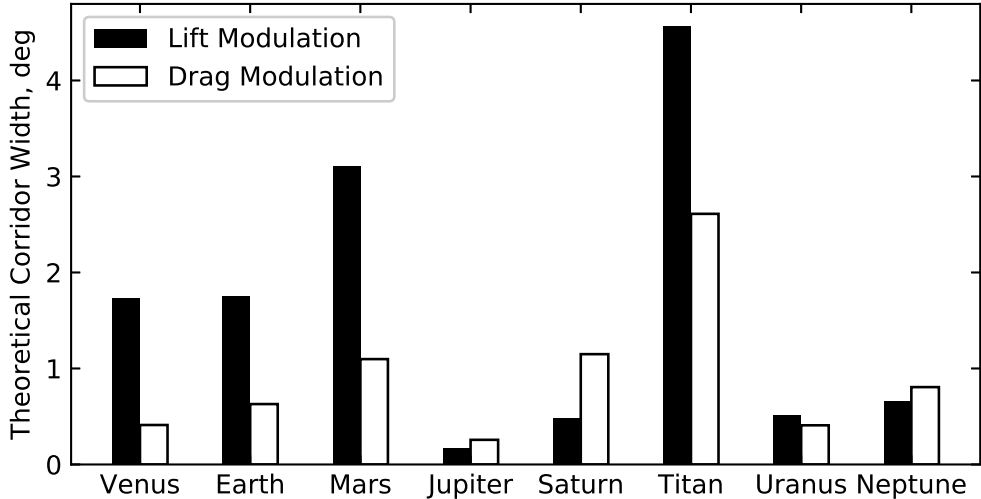


Figure 4.21. Comparison of theoretical corridor width for aerocapture at various targets. $L/D = 0.30$ for lift modulation and $\beta_2/\beta_1 = 7$ for drag modulation.

Figure 4.22 shows the peak deceleration during the maneuver at various targets for typical entry conditions. For most destinations, the peak g-load is below $6g$ for lift modulation and below $4g$ for drag modulation. The peak deceleration does not show a strong dependence on the destination, and the values for drag modulation is roughly half of that for lift modulation aerocapture. Figure 4.23 shows a relative comparison of the stagnation point heat rate and total heat load at the various targets and shows a clear destination dependence. Mars and Titan present the most benign targets with peak heat rates less than 200 W/cm^2 and heat load less than 50 kJ/cm^2 making them ideal targets for an initial aerocapture mission with minimal requirements on the thermal protection systems. Aerocapture at Venus and Earth present heat rates in the range of several hundred W/cm^2 , while Uranus and Neptune result in heat rates in the range of several thousand W/cm^2 and heat loads in the range of hundreds of kJ/cm^2 . While the peak heat rate at Uranus and Neptune is within the capability of TPS materials such as HEEET, the large heat loads may result in substantial TPS mass fraction and needs additional study. Jupiter presents an extreme case with heat rates in the range

of tens of thousands of W/cm^2 and thousands of kJ/cm^2 total heat load well beyond the capability of any existing TPS materials.

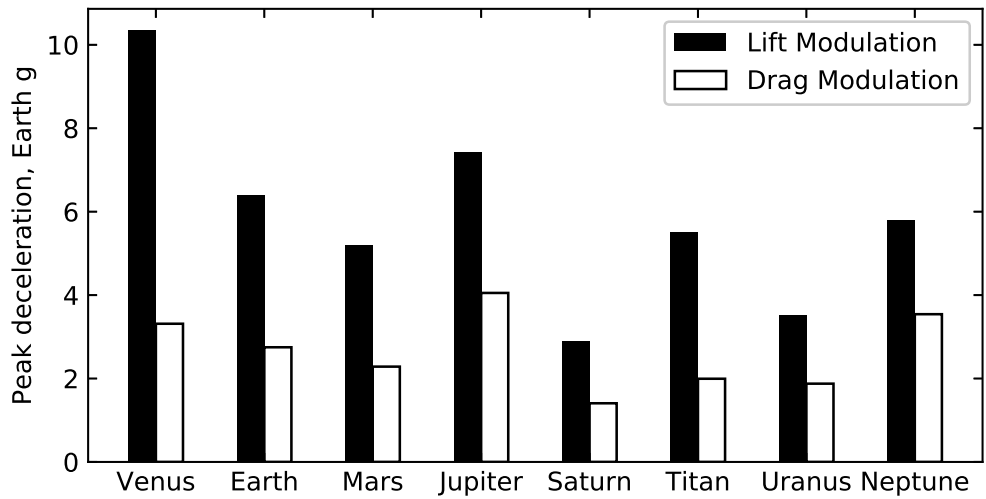


Figure 4.22. Comparison of peak deceleration load for aerocapture at various targets. $L/D = 0.30$ for lift modulation and $\beta_2/\beta_1 = 7$ for drag modulation.

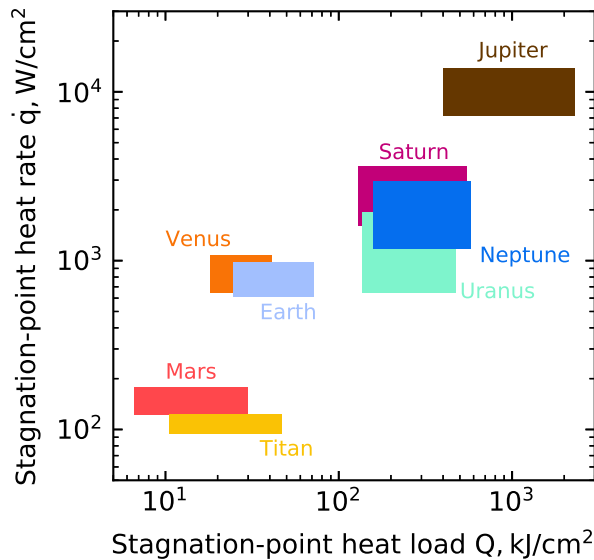


Figure 4.23. Comparison of stagnation-point heat rate and total heat load for aerocapture at various targets. Results for a lift modulation vehicle with $L/D = 0.30$.

Stagnation-point heat rate and stagnation pressure important parameters for TPS material qualification as test facility constraints often limit the combination of the two parameters which can be achieved. Figure 4.24 shows the variation of stagnation-point heat rate and stagnation pressure for lift modulation aerocapture trajectories at various targets. Once again, Titan and Mars offer the most benign aerothermal conditions for aerocapture. Aerocapture at Venus require the TPS material to accommodate several hundred W/cm^2 at about 0.35 atm stagnation pressure. Aerocapture at Uranus and Neptune require TPS materials to be qualified at a few thousand W/cm^2 and about 0.1 atm.

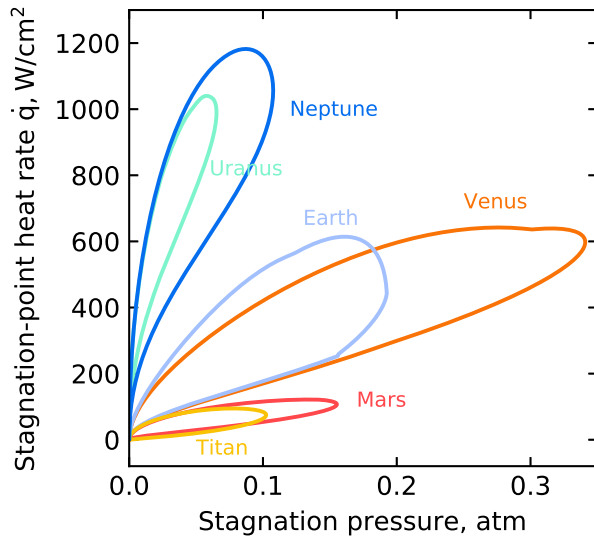


Figure 4.24. Peak heat rate and stagnation pressure curves for lift modulation aerocapture at various targets.

4.6 Technology Readiness and Recommendations

Existing blunt-body aeroshells ($L/D < 0.35$) and TPS materials such as PICA are sufficient for aerocapture at Mars and Titan. In fact, a MSL-derived aeroshell ($L/D = 0.24$) could perform aerocapture at Mars and Titan with no new technology developments other than that related to spacecraft packaging, deployable antennae, and aeroshell jettison after the aerocapture maneuver. Such a system could also potentially be used at Venus, with some modifications to accommodate the slightly higher heat rates and heat loads. Drag modula-

tion aerocapture is also viable at Mars, Venus, and Titan with modest ballistic coefficient ratios ($\beta_2/\beta_1 < 7$), and proven carbon cloth or PICA TPS. Drag modulation aerocapture has the potential to enable a new paradigm in the exploration of Mars and Venus through small satellite constellations at these destinations within the next decade. Aerocapture at Earth is viable using existing aeroshells such as Orion, and is a viable option for sample return and crewed missions returning from the Moon or Mars. Aerocapture at Uranus and Neptune has been shown to be possible using blunt-body aeroshells with L/D of 0.30–0.40 with improvements in interplanetary navigation and vehicle guidance techniques. HEEET has already been tested under conditions relevant for aerocapture. More detailed flight-system studies are likely required to establish a baseline design reference mission, and estimate with better accuracy some factors the TPS mass fraction which is currently not well known for Uranus and Neptune. With some additional studies to quantify the aerothermal environment and modest technological developments such as tailoring HEEET for a particular mission profile, aerocapture at Uranus and Neptune is viable for a Flagship class mission in the next decade. Aerocapture at Jupiter and Saturn are not viable using blunt-body aeroshells, well beyond the capability of existing TPS materials and is considered a long-term goal.

The present study recommends NASA support efforts to demonstrate drag modulation aerocapture at Earth using the small satellite mission concept proposed by Werner and Braun [52] leveraging a low-cost launch as secondary payload on a GTO mission. Dynamics of drag skirt separation and the risk of re-contact of the skirt has been studied using CFD and ballistic range tests by Rollock et al. [157] and by McClary and Putnam [158]. Austin et al. [56] has developed a reference drag modulation aerocapture flight system design using the drag skirt for use at Mars and Venus. The study recommends continued NASA support of these efforts to realize small, low-cost aerocapture missions potentially as secondary payloads on future Mars and Venus science missions. A low cost demonstration mission at Earth or Mars will establish flight-heritage for aerocapture and lower the risk for larger science missions. Table 4.5 lists some recommendations for future missions leveraging aerocapture.

The study recommends continued development of the HEEET thermal protection system particularly tailoring the material layup for the aerothermal conditions encountered at Uranus and Neptune, and more detailed aerothermodynamic studies to estimate the TPS

Table 4.5. Aerocapture recommendations for future missions

Planet	Lift Modulation	Drag Modulation
Venus	Not recommended ^a	Useful for inserting SmallSats into low-circular orbits
Earth	Lunar/Mars sample return	Low-cost technology demonstration
Mars	Not recommended ^a	Useful for inserting SmallSats into low-circular orbits
Jupiter	Not recommended ^b	Not recommended ^b
Saturn	Not recommended ^c	Not recommended ^c
Titan	Recommended ^d	Recommended ^e
Uranus	Recommended ^f	Requires additional study ^g
Neptune	Recommended ^f	Requires additional study ^g

^a Aerobraking is recommended for large orbiter missions at Venus and Mars

^b Extreme aerothermal environment for aerocapture, propulsive insertion is recommended

^c Propulsive insertion is recommended, or using Titan's atmosphere for aerocapture

^d Ideal for multi-element missions involving orbiters, landers, and/or rovers

^e Recommended for small satellite constellation mission at Titan

^f Recommended for large Flagship-class missions

^g Limited control authority against large navigation and atmospheric uncertainties

mass fraction for aerocapture at the outer planets. Probe delivery along with aerocapture at the outer planets is a topic of current research [159], and additional studies are required to establish a baseline aerocapture mission architecture with a probe delivery at Uranus and Neptune for a future Flagship class mission. Other technologies relevant to outer planet aerocapture include autonomous spacecraft navigation, improved flight control techniques and guidance schemes, spacecraft autonomy (automatically determine orbit and perform corrective maneuvers after aerocapture without ground intervention) and spacecraft packaging inside the aeroshell. The study recommends NASA's continued support of the GRAM model development especially for Uranus and Neptune for which our knowledge is most lacking and leverage opportunistic stellar occultations to and ground based observations to improve our understanding of their atmospheres [3], [62].

4.7 Summary

The present study performed a comprehensive quantitative and comparative assessment of the feasibility of aerocapture at all atmosphere-bearing solar system destinations. Aerocapture feasibility charts are used to concisely present the various constraints arising from

corridor width, deceleration, and heating constraints for both lift and drag modulation control techniques. Results indicate that existing heritage blunt-body aeroshells ($L/D < 0.30$) and flight proven TPS materials are sufficient for lift modulation aerocapture at Venus, Earth, Mars, and Titan. Drag modulation aerocapture at these destinations is also viable using modest ballistic coefficient ratios ($\beta_2/\beta_1 < 7$), making them an attractive choice for inserting small satellites into orbit. Aerocapture at Uranus and Neptune is viable with blunt-body aeroshells (L/D of 0.30–0.40) with certain high arrival V_∞ interplanetary trajectories and improved guidance schemes. For Venus and Mars, aerobraking outperforms aerocapture for low arrival V_∞ (< 5 km/s) and is the preferred orbit insertion method. For interplanetary trajectories with higher arrival V_∞ aerocapture delivers 100–200% more mass to Venus, and 100–400% more mass to Mars. For Titan, aerocapture can deliver more than 300% more mass along with lower interplanetary flight times. At Uranus and Neptune, aerocapture can deliver as much as 600% and 400% more mass respectively and shorten flight times by five and seven years respectively. Comparing the aerothermal conditions encountered during aerocapture, Mars and Titan offer the most benign entry environments while Jupiter and Saturn present the most extreme conditions. Aerocapture at Saturn and Jupiter is not viable in the near term due to the extreme aerothermal entry conditions at these planets. A new open-source software, the Aerocapture Mission Analysis Tool has been developed to aid rapid conceptual design of aerocapture missions considering both interplanetary trajectory and vehicle design aspects. The study reviewed the technology readiness of aerocapture for various destinations and provides recommendations for flight experiments, technology developments, and its applicability for future planetary missions across the Solar System.

4.8 Conclusions

Aerocapture has been shown to be feasible at Mars, Titan, and Venus with existing vehicle designs for both lift modulation and drag modulation control techniques and flight-proven TPS materials. Aerocapture at Uranus and Neptune is shown to be viable with lifting vehicles with L/D of 0.30–0.40 with the use of high arrival V_∞ interplanetary trajectories, improvements in interplanetary navigation, and vehicle guidance schemes. While the aerothermal loads at Uranus and Neptune are substantially larger than that at Mars or Titan, it is within

the limits of HEEET TPS which has been laboratory tested under comparable conditions. Additional studies are required to evaluate the feasibility of drag modulation systems at Uranus and Neptune considering the more demanding aerothermal conditions at these destinations. Aerocapture at Jupiter and Saturn is not feasible using existing vehicle designs and will require significant advances over existing thermal protection systems. Aerocapture is shown to provide enhancing capability for missions to Venus (100%–200% more delivered mass) and Mars (100%–400%) with high arrival V_∞ interplanetary trajectories. For missions to Titan, aerocapture is strongly enhancing (300%–1700% more mass) for interplanetary trajectories with arrival V_∞ from 6–8 km/s, and an enabling technology for higher arrival V_∞ trajectories. For missions to Uranus, aerocapture is strongly enhancing (100%–600%) for V_∞ from 12–16 km/s and enabling for arrival V_∞ beyond 16 km/s. For missions to Neptune, aerocapture delivers 80%–400% more mass for interplanetary trajectories with V_∞ from 12–16 km/s and is an enabling technology for higher arrival V_∞ . High arrival V_∞ trajectories ($V_\infty > 16$ km/s) can potentially allow interplanetary flight times to be as low as 6 and 8 years to Uranus and Neptune respectively. A low cost technology demonstration mission at Earth or Mars can establish flight-heritage for aerocapture and lower the risk for larger science missions. As pointed out by Spilker et al. [3], the benefits offered by aerocapture for future could be compared to the vastly increased capability for exploration offered by the gravity-assist technique in the early days of interplanetary flight. Once proven, aerocapture will be a key strategy enabling large constellations of small satellites around Mars and Venus and delivering sizeable orbiters within reasonable flight times to the outer Solar System.

5. SYSTEMS FRAMEWORK FOR RAPID CONCEPTUAL MISSION DESIGN

The basic purpose of this thesis is to provide a systems engineering framework for rapid aerocapture mission formulation, starting from a high-level mission objective to a viable mission concept¹. As mentioned in Sec. 1.3, the job of the mission designer is to select a mutually compatible, harmonious set of systems that when tied together, will accomplish the stated objective(s) within the technical, cost, schedule, and risk constraints. A key element in the system engineering process is the ability of the mission designer to perform trade space exploration, and trade studies to understand the extent of the design space and to understand what combination of systems work together (or not). During the concept exploration phase, it is important to retain as wide a selection of options as possible for each of the system variables. Once the feasibility assessment phase is complete, a baseline reference design is selected from the trade space, as analyzing every possible design combination in further detail is in most cases not possible. The next step is performance evaluation, where more detailed calculations are performed to assess the viability and performance metrics of the reference design. If the performance is satisfactory with respect to the mission objectives set out initially, and is feasible from other perspectives (technical, risk etc.) the reference design can be used as a starting point for higher-fidelity studies leading to mission implementation. If the performance metrics are not satisfactory, a different baseline design may be selected, or the mission objective may need to be revised. This chapter describes the systems framework developed in this study, and is illustrated further with its application to two future mission concepts of current interest in Chapters 6 and 7.

5.1 Mission Objective

The primary mission objective is the starting point for the design process, and must preferably be concisely stated in no more than a couple of sentences. There may be secondary objectives in addition, and may vary in priority or may augment the primary mission in

¹↑Some of the concepts and terminology used in this chapter are derived from the book *Space Mission Engineering*, Chapters 3–5 by Wertz, Everett, and Puschell. [160]

some sense. Following are few examples of how primary mission objectives may be stated for aerocapture mission concepts.

1. Assess the feasibility and mass-benefit of aerocapture for SmallSat (< 180 kg) missions to Venus using rideshare or secondary payload launch opportunities.
2. Assess the feasibility of aerocapture at Neptune using an aeroshell with L/D of 0.4 or less to deliver a 1000 kg orbiter which permits regular Triton flybys.
3. Assess the feasibility of aerocapture at Titan to deliver a 1000 kg orbiter and a 400 kg lander using a single launch vehicle of Atlas V551 or smaller.

In addition to the mission objective, constraints, ground rules, and assumptions provide additional information and helps bound the scope and extent of the mission study. Constraints could arise from the availability and readiness of technology, cost caps, programmatic and schedule concerns, what is considered acceptable risk, etc. In the case of objective #1 above, such constraints could be to use existing a drag modulation system which can be easily accommodated as a secondary payload as opposed to a rigid aeroshell. Schedule constraints could be for example to use launch opportunities available in the next decade. Ground rules and assumptions could be of the following form: 1) The host spacecraft performs any required manuevers and deliver the SmallSat to the atmospheric entry interface. 2) The spacecraft must be less than 1 m in diameter when attached on the host spacecraft. 3) The aerocapture system must use existing TPS materials such as those used on the MSL entry vehicle. 4) The system should demonstrate the capability to achieve a $2,000 \times 400$ km orbit with less than 50 m/s of allowable deterministic propulsive ΔV .

5.2 Requirements Definition

The mission designer must derive a set of quantitative requirements from the mission objective, constraints and ground rules. During the initial stages of the study, many important parameters are not known and reasonable assumptions must be made to allow the progress of the study. Despite the complex nature of the mission architecture with many

interconnected elements, a small set of parameters characterizing the key aspects of these systems is sufficient for conceptual design.

5.2.1 Launch Vehicle

As with the actual mission which begins with lift-off, the first element in the framework is the launch vehicle. Usually, the ground rules of the mission study will specify the highest performance launcher available. The decision of the launcher is often dictated by top-level cost constraints, as the launch vehicle is a significant contributor to the total mission cost. For interplanetary missions, the defining parameter for launch vehicle performance is the trajectory C_3 , which is the square of the departure V_∞ . Larger the C_3 , lesser is the payload that can be launched on that trajectory. Figure 5.1 shows the launch capability of various launch vehicles that are commonly used (or considered) for interplanetary missions. The vehicles range from the relatively cheap and modestly performing Atlas V401, to the intermediate and heavy launchers such as Atlas V551 and Delta IVH, to the highest performing (and expensive) SLS Block 1B launchers. A mission in the Discovery class ($< \$500M$) will generally be limited to launcher such as the Atlas V401 or recoverable Falcon Heavy. Missions in the New Frontiers class ($< \$1B$) are expected to use the Atlas V551 or smaller, and Flagship class missions ($< \$2\text{--}4B$) will likely use Delta IVH or the expendable Falcon Heavy. Super heavy lift launch vehicles such as the SLS offer excellent launch performance for high-energy launches but are also very expensive and may preclude their use on near-term planetary missions. However, the continued development and use of such heavy lift vehicles for commercial ventures may reduce their cost in the long run.

The mission designer generally is given the spacecraft mass that needs to be inserted into orbit and needs to calculate the launch mass. For example, if the objective is to insert a 1000 kg orbiter into orbit around Neptune with a Delta IVH and kick stage, the first step is to estimate the spacecraft launch mass. For preliminary design, the launch mass M_L is estimated as the sum of the cruise stage M_{cs} , deep space maneuver propellant M_{DSM} ,

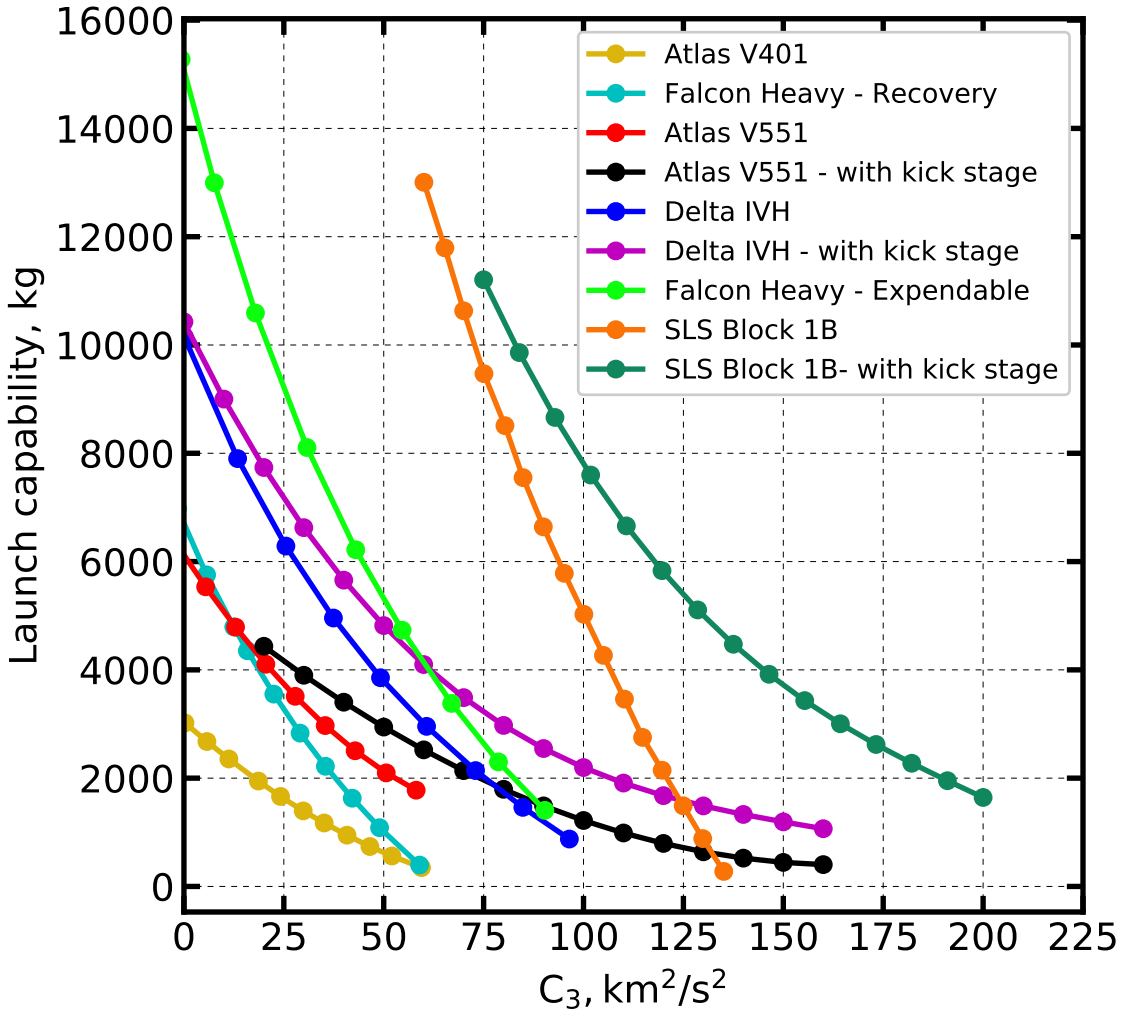


Figure 5.1. Escape performance of various launch vehicles. Data from NASA Kennedy Space Center Launch Services and NASA Ice Giant Pre-Decadal Studies [51].

aeroshell structure and TPS M_{as} , the orbiter mass M_{orb} , and mass of any additional elements such as probes $M_{\text{add.}}$.

$$M_L = M_{\text{cs}} + M_{\text{DSM}} + M_{\text{as}} + M_{\text{orb}} + M_{\text{add.}} \quad (5.1)$$

The aeroshell mass fraction can be estimated as a fraction χ of total entry vehicle mass ($M_o rb + M_{as}$). The nominal values of χ (applicable only for rigid blunt-body aeroshells) for different destinations is listed in Table 5.1².

Table 5.1. Nominal aeroshell mass fractions

Planet or moon	χ
Venus	0.25
Earth	0.25
Mars	0.10
Titan	0.05
Uranus	0.40–0.60 ^a
Neptune	0.40–0.60 ^a

^a Depending on prograde or retrograde entry.

The cruise stage mass is estimated to be fraction κ of the the orbiter mass. Typical values of κ fall in the range of 0.20 to 0.40 based on past experience with Mars entry missions such as MSL and the InSight lander. Hence the estimate for the launch mass is

$$M_L = \kappa M_{orb} + M_{DSM} + \frac{\chi}{1 - \chi} M_{orb} + M_{orb} + M_{add}. \quad (5.2)$$

$$M_L = \left(1 + \kappa + \frac{\chi}{1 - \chi}\right) M_{orb} + M_{DSM} + M_{add}. \quad (5.3)$$

Assuming there is no deep space maneuver and no additional elements, for $M_{orb} = 1000$ kg, assuming $\chi = 0.5$, $\kappa = 0.3$ the launch mass is estimated to be

$$M_L = (1 + 0.3 + 1.0) M_{orb} = 2.3 M_{orb} = 2300 \text{ kg} \quad (5.4)$$

It is customary to add a 30% mass margin during the initial phase of the design, hence the estimated launch mass with margin is about 3000 kg. As the design progresses, this estimate will be revised as necessary as more information becomes available and the mass breakdown is understood better. Based on the C_3 curve for Delta IVH with kick stage

²Based on the author's experience. As the design progresses, these values are refined as more information about the vehicle and mission design becomes available.

in Fig. 5.1, maximum allowable C_3 is about $75 \text{ km}^2/\text{s}^2$. Fig. 5.1 also allows the mission designer to consider trade-offs with other launch vehicles. For example, with an cheaper Atlas V551 with kick stage, the maximum C_3 is about $50 \text{ km}^2/\text{s}^2$; and with a recoverable Falcon Heavy it is about $25 \text{ km}^2/\text{s}^2$. The maximum allowable C_3 has important implications for interplanetary trajectory selection described in Sec. 5.2.2. In addition to the C_3 , another important parameter for the launch vehicle is the declination of the departure asymptote and imposes constraints on the feasible departure declinations from the launch site.

5.2.2 Interplanetary Trajectory and Aerocapture Vehicle Design

The launch vehicle injects the spacecraft into the interplanetary trajectory from Earth to its target destination which might be a direct transfer in the case of Mars or Venus, or a complex gravity-assist path to the outer solar system. Three critical parameters characterize the interplanetary trajectory: C_3 , time of flight, and the arrival V_∞ . For missions to Neptune, achieving reasonable time of flight is of great importance as missions owing to its great heliocentric distance. The challenge is to find the right balance of these parameters which deliver sufficient useful mass to orbit in a reasonable time, and with the available launch vehicles. Traditionally, the interplanetary trajectory selection and the aerocapture maneuver analysis is performed independently. A key feature of the framework presented here is the unification of interplanetary trajectory and aerocapture vehicle design, to account for the implications of their interconnected nature in the mission architecture.

Figure 5.2 shows the interplanetary trajectory options for Neptune missions. The high level objective did not specify a limit for the time of flight, so a range from about 6 to 13 years is available for the mission designer to choose from. From the analysis presented in Sec. 5.2.1, the maximum allowable C_3 is $75 \text{ km}^2/\text{s}^2$. This constraint renders most of the high C_3 options (shown in red, yellow, and green) infeasible.

The remaining variable is the arrival V_∞ which ranges from about 8 to 24 km/s as seen from Fig. 5.2. The mission objective requires that a vehicle with L/D of 0.4 or lower must be used. As shown in the Fig. 5.3, the required L/D is strongly dependent on the TCW requirement and the arrival V_∞ . If TCW requirement of 1 deg is considered, along with L/D

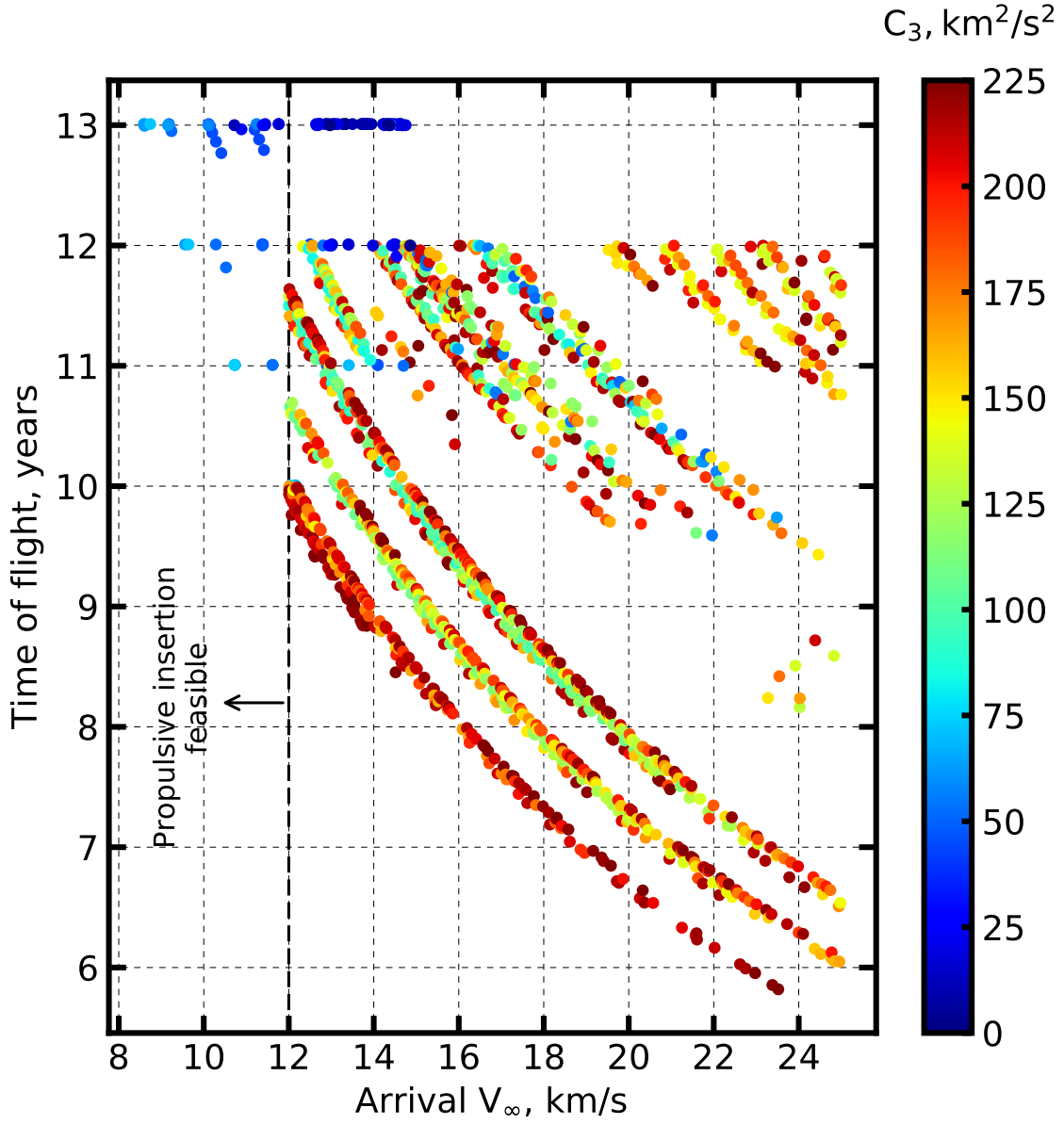


Figure 5.2. Interplanetary trajectory trade space for missions to Neptune.

constraint of 0.4, the minimum required V_∞ is 16 km/s. For V_∞ below this critical value, the L/D constraint cannot be met.

Thus, the high-level L/D constraint dictates a TCW requirement of approximately 1 deg, along with arrival V_∞ of 16 km/s or higher. Constraints on the g-load, peak heating and total heat load are not specified in the mission objective. Nominal values of $30g$, 5000 W/cm², and 800 kJ/cm² are used to identify initial upper bounds for the arrival V_∞ . As seen

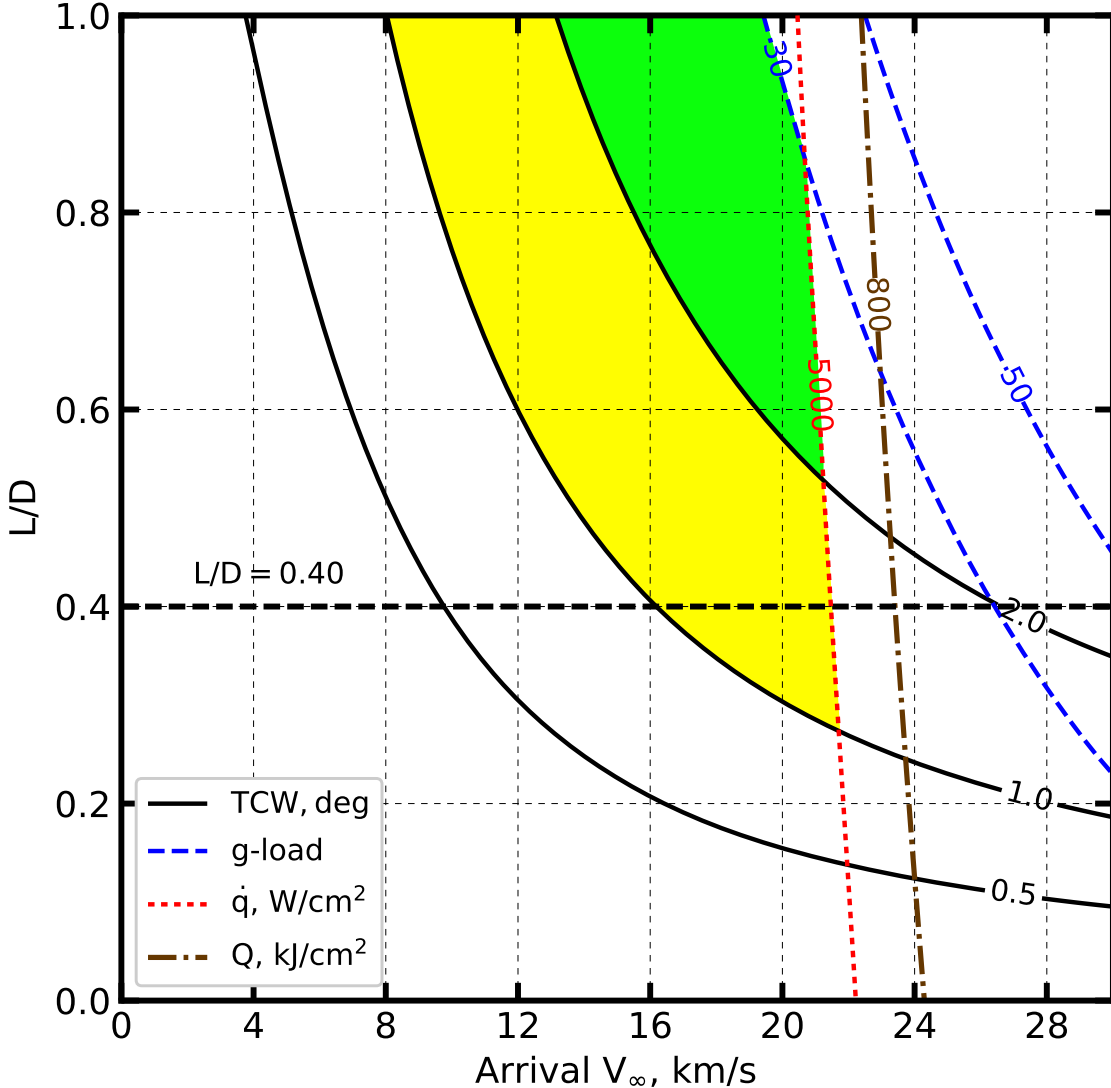


Figure 5.3. Neptune aerocapture feasibility chart. Green and yellow regions indicate feasible regions for TCW requirement of 2.0 deg and 1.0 deg respectively.

in Fig. 5.3, the peak heat rate is the limiting constraint and limits the arrival V_∞ to about 22 km/s. Thus considering the vehicle control authority and TPS material constraints, the arrival V_∞ should fall in the range of 16 to 22 km/s. This constraint on V_∞ along with the C_3 constraint from Sec. 5.2.1 is used to shortlist the feasible trajectories from nearly 10,000 trajectories shown in Fig. 5.2. Only about 150 trajectories satisfied the shortlisting criteria, and additional filters such as launch dates can be used to narrow down the list. A

few sample trajectories and their characteristics along with their delivered mass to orbit are listed in Table 5.2. Trajectory #1 is the one which maximizes delivered mass, nearly twice the desired value thus providing substantial mass margins. Trajectory #3 offers a slightly lower time of flight and higher arrival V_∞ and delivers 1547 kg to orbit. Trajectory # 5 is the lowest time of flight option (9.6 years), with a high arrival V_∞ of 22 km/s and also the lowest delivered mass among the feasible trajectories.

Table 5.2. Sample of feasible interplanetary trajectory options for a Neptune mission

No.	Launch date	Path	C_3	Launch mass, kg ^a	ToF, years	DSM ΔV , km/s	V_∞ , km/s	Delivered mass, kg ^b
1	2028-03-28	EEJN	48.4	4915	11.23	0.44	18.6	1986
2	2028-04-05	EEJN	54.7	4460	10.73	0.64	20.0	1668
3	2028-03-16	EEJN	51.6	4727	10.59	1.04	20.6	1547
4	2029-05-11	EEJN	55.4	4414	10.51	1.24	18.7	1336
5	2028-05-11	EEJN	55.4	4414	9.59	2.04	22.0	1002

^a Assuming Delta IVH with kick stage.

^b Assuming $I_{sp} = 320$ seconds for the DSM maneuver, $\kappa = 0.3$, $\chi = 0.5$.

Based on Fig. 5.3, the required L/D range from 0.4 for V_∞ of 16 km/s to 0.25 for V_∞ of 22 km/s. A rigid blunt-body aeroshell such as Apollo or MSL entry vehicle is expected to provide this range of L/D , and thus offer sufficient control authority. In addition to the L/D , the vehicle ballistic coefficient β is a key parameter for entry vehicle design. As a preliminary estimate $\beta = 200 \text{ kg/m}^2$ is used. As the entry vehicle shape and mass characteristics are better understood, the ballistic coefficient is revised accordingly. Table 5.3 lists two potential aeroshell designs with flight heritage which with more capable TPS materials can be used for aerocapture at Neptune. For outer planet missions, HEEET TPS is expected to be the nominal heat-shield material whose tested limit imposes the 5,000 W/cm² heat rate constraint. The 800 kJ/cm² total heat load constraint is used to limit the TPS mass fraction.

Table 5.3. Potential aeroshell designs for a Neptune mission

Entry vehicle	L/D	$\beta, \text{kg/m}^2$
Apollo	0.36	400
MSL	0.24	150

5.2.3 Science Orbit

The choice of the initial capture orbit and the subsequent science orbits has substantial impact on the overall mission architecture. For example, if the objective is to perform regular close flybys of Neptune's moon Triton, the orbit size and inclination should be such that frequent moon encounters are possible. Detailed design of satellite tours is beyond the scope of conceptual design studies, but it is important to have a basic understanding of the initial orbits required to start such tours. Previous studies have indicated that an orbit with an apoapsis close to Triton's circular orbital radius is required to achieve this objective. Radar and mapping missions to Venus and Mars typically use a low-circular orbit to view the surface up close for high resolution observations.

5.2.4 Probe Delivery

In-situ measurements that can only be made from atmospheric probes make them a critical component of many mission architectures, especially outer planet missions. Probe (or aerial robot, lander etc.) delivery with aerocapture presents its own unique set of challenges which have not been investigated in the literature. Probes may be delivered before the aerocapture maneuver, or after the maneuver from orbit. Both scenarios and their impact on the aerocapture mission architecture is described below.

The first option is to release the entry probe several weeks ahead of the main orbiter performing aerocapture reaching the target planet. In this case the probe(s) will be mounted external to the aeroshell, and jettisoned at the appropriate time. The probe trajectory will be timed to enter the atmosphere a few hours before the aerocapture maneuver. This allows the aerocapture vehicle to be in relatively close proximity to relay the probe data back to Earth. Once the probe mission is complete, the aerocapture vehicle enters the atmosphere and completes its orbit insertion. Alternatively, the orbiter can perform a speed-up burn to allow it to reach the planet faster than the probe so that the orbiter is already in orbit by the time the probe enters the atmosphere and can then relay the data back to Earth.

The second option is to carry the probes inside the aerocapture vehicle aeroshell, and deploy the probes after the aerocapture maneuver. This option allows more flexibility in

the timing and targeting of where the probe enters the atmosphere, but brings with it the challenge of accommodating the entry probe inside the main aeroshell. The flexibility in probe release timing is important, as it allows the orbiter to perform close-range reconnaissance of the planet before committing the probe entry location. Multiple probes can easily be delivered from orbit (for example one day-side and one night-side), however once again present the challenge of packaging them within the main aerocapture vehicle.

At the conceptual study level, it is important to understand if there are requirements for probe delivery and incorporate them into preliminary mass and volume budgets. If the design proceeds to the next level of detailed design, additional analysis will be required to investigate probe release options with aerocapture along with the required maneuvers.

5.2.5 Disposal

Following the completion of the operational phase of the science orbit, the spacecraft is typically disposed of so as to conform to planetary protection requirements. At the conceptual study level, it is sufficient to allocate a small propulsive ΔV budget (50–100 m/s based on experience) to perform the de-orbit maneuver. In more detailed phases of the design, alternative strategies may be investigated such as escaping the planetary system or using a gravity assist flyby of a moon to dispose of the spacecraft.

5.2.6 Summary of Requirements Definition

Table 5.4 summarizes the requirements definition for the mission objective #2 stated in Sec. 5.1, which is to “assess the feasibility of aerocapture at Neptune using an aeroshell with L/D of 0.4 or less to deliver a 1000 kg orbiter which permits regular Triton flybys.” The purpose of the requirement definition is to translate the high-level mission objective into quantifiable ranges of design parameters and allow trade space exploration. It is noted that these are “initial” values, and as more information becomes available, some of these requirements will need to be revised.

Table 5.4. Summary of requirements

Element	Parameter	Constraint / value	Remark
Launch vehicle	Class	\leq Heavy lift	Programmatic
	C_3	$\leq 75 \text{ km}^2/\text{s}^2$	Ensure sufficient launch mass
Interplanetary trajectory	Arr. V_∞	$\geq 16 \text{ km/s}$	To allow $L/D \leq 0.4$
	Arr. V_∞	$\leq 22 \text{ km/s}$	To constrain heat rate
	ToF	free	—
Vehicle design	L/D	≤ 0.40	Programmatic
	L/D	≥ 0.25	For control authority
	β	$= 200 \text{ kg/m}^2$	Based on heritage
	TCW	$\geq 1.0 \text{ deg}$	Assume $\pm 0.5 \text{ deg}$ EFPA error
	G-load	$\leq 30g$	Assumption
	Heat rate	$\leq 5000 \text{ W/cm}^2$	Based on HEEET TPS
	Heat load	$\leq 800 \text{ kJ/cm}^2$	Galileo probe heritage
Science orbit	Size	$4,000 \times 400,000 \text{ km}$	Allow Triton flybys
	Inclination ^a	157 deg or 23 deg	Triton's orbital plane
Probe	Mass	0 kg	Not considered
Disposal	ΔV	$\geq 50 \text{ m/s}$	Assumption

^a With respect to Neptune's equatorial plane

5.3 Trade Space Exploration

With preliminary bounds established on key design variables that characterize each of the systems, it is now possible to explore in more detail these systems. Trade studies are an essential part of conceptual mission studies. The ability to perform such exercises become more limited and expensive as the study advances to the more detailed stages. The objective of these trade studies to identify combinations of elements which work well together and thus identify a baseline reference design for more detailed analysis. This section considers a few possible trade options and their implications for each of various mission elements such as launch vehicle, interplanetary trajectory, and vehicle design within the constraints established in Table 5.4.

5.3.1 Launch Vehicle

In this subsection, a launch vehicle trade study is performed among the three launch vehicles: the Delta IVH, Atlas V551, and the Falcon Heavy (recoverable). Such trades are

of interest to cost constrained missions as smaller launch vehicles can significantly reduce mission cost. For example the cost per launch for an Atlas V551 is about \$153 M compared to \$350 M³ for a Delta IVH. The recoverable Falcon Heavy is an even cheaper option at about \$90 M⁴. The delivered mass to orbit with different launchers for the five sample trajectories listed in Table 5.2 is shown in Table 5.5.

Table 5.5. Launch vehicle trade study

Trajectory #	Delivered mass to orbit, kg				
	Delta IVH	Delta IVH ^a	Atlas V551	Atlas V551 ^a	Falcon Heavy ^b
1	1536	1986	801	1153	332
2	1233	1668	629	966	125
3	1170	1547	593	888	184
4	976	1336	484	762	62
5	722	1002	341	557	0

^a With kick stage.

^b In recovery mode.

Table 5.5 shows that the recoverable Falcon Heavy, though a substantially cheaper option is infeasible, as it fails to deliver sufficient mass to orbit. With trajectory #1, Atlas V551 is a feasible option should it be desired to reduce launch costs. If the initial requirement of 1000 kg is relaxed to 700 kg, then trajectory options 2, 3, and 4 also become feasible with the Atlas V551. With the Delta IVH, trajectories 1 through 3 deliver sufficient mass to achieve the objective even without the kick stage, allowing for the option of cost reduction if required. Alternatively, the increased mass budget with a kick stage may be used to increase the delivered mass beyond 1000 kg, or add other mission elements such as an atmospheric probe. With trajectory 1, both variants of the Delta IVH allow for the addition of a 300 kg atmospheric probe as a mission enhancing option while still providing reasonable mass margins. Such trade studies allow the mission designer to provide feedback to the stakeholders on the the mission requirements before selecting a baseline launch vehicle.

³↑United Launch Alliance, public domain.

⁴↑<https://www.spacex.com/about/capabilities>

5.3.2 Interplanetary Trajectory and Vehicle Design

This subsection deals with a trade study among the five sample interplanetary trajectories listed in Table 5.2, and the two vehicle designs listed in Table 5.3. Trajectory 1 is the highest performing option in terms of delivered mass with and the lowest arrival V_∞ of 18.6 km/s. Trajectory 5 delivers the lowest mass to orbit, and has the highest arrival V_∞ of 22 km/s. The arrival V_∞ as seen from Fig. 5.3 affects the required vehicle L/D , and the heating environment the vehicle will encounter. Trajectory 1 with V_∞ of 18.6 km/s requires the use of a vehicle with L/D of at least 0.32 as seen from Fig. 5.3, whereas Trajectory 5 with V_∞ of 22 km/s requires an L/D of only about 0.25. This implies that an Apollo-derived aeroshell is required for use with Trajectory 1, while a MSL-derived aeroshell is sufficient for Trajectory 5. While the faster arrival V_∞ offers the use of a lower L/D , the resulting higher entry speeds imply the vehicle will encounter higher aerodynamic heating compared to trajectory with a smaller V_∞ . Table 5.6 lists the required vehicle L/D and the expected peak heat rates and total heat loads for each of the five sample trajectories.

Table 5.6. Interplanetary trajectory and vehicle design study

Trajectory #	Delivered mass, kg ^a	Arrival V_∞ , km/s	$(L/D)_{\min}^{\text{b}}$	\dot{q} , W/cm ² , ^b	Q , kJ/cm ² , ^b
1	1986	18.6	0.32	2000	250
2	1668	20.0	0.30	3500	400
3	1547	20.6	0.29	4000	450
4	1336	18.7	0.32	2000	450
5	1002	22.0	0.25	5000	600

^a Assuming Delta IVH with kick stage ^b Approximate values based on Fig. B.15, not accounting for effect of planetary rotation on the entry speed

As seen from Table 5.6, while Trajectory 5 enables the use of vehicle with $L/D = 0.25$ the peak heat rate and heat load is more than twice that for Trajectory 1. The mission designer must select an interplanetary trajectory and L/D such that the aerodynamic heating environment is within the limits of the available TPS materials.

5.3.3 Science Orbit

Both the size and inclination of the target orbit are of interest for conceptual design studies, as they serve as initial conditions for the subsequent tour design if the concept advances to the detailed design phase. In general, most planetary missions seek to use either a low circular orbit or a highly elliptical orbit. Low circular orbits are commonly used for Mars and Venus missions, while highly elliptical orbits are typically used for outer planet missions for both scientific and engineering reasons⁵.

In the case of the Neptune orbiter with Triton flybys as a top-level requirement, the nominal requirement is a $4,000 \times 400,000$ km orbit. Attempting to capture into a large elliptical orbit such as this one brings with it the risk of accidental escape for aerocapture for low- L/D vehicles. An even larger capture orbit will further exacerbate the problem. When vehicle performance is assessed in the presence of navigation and atmospheric uncertainties, it may be necessary to use a smaller capture orbit to ensure the vehicle is captured. A possible work-around is to then use propulsive manuevers and gravity assists to boost the orbit after the aerocapture maneuver.

For fast-rotating planets such as Neptune, the choice of retrograde vs prograde orbits has a substantial impact on the aerocapture mission architecture. A retrograde orbit is preferred to keep the Triton flyby speeds low. However, the atmosphere relative entry speeds for a retrograde entry could be as much as 5 km/s higher compared to a prograde entry resulting in a much more severe aerothermal environment.

5.3.4 Probe Delivery

Though the requirement of delivering a probe was not a requirement, it is clear from Table 5.5 that a vehicle such as the Delta IVH would allow for the option of an atmospheric probe along with a 1000 kg orbiter. Trade options for such a probe would include the size and

⁵Almost all spacecraft to date haven been inserted into elliptical orbits first using propulsive insertion. For Mars and Venus missions which desire a low circular orbit for scientific reasons, aerobraking is used to gradually transition to a low circular orbit. For outer planet missions (continued on the next page), highly elliptical orbits are typically used to achieve magnetosphere science, allow time for data download after the periapse pass. The giant planets' radiation belts likely preclude an aerobraking campaign to lower the orbit, though this problem has not been investigated in the literature.

number of probes (for example, one large probe vs. two small probes), method of delivery (before or after the aerocapture maneuver), timing of probe release, prograde vs. retrograde entry and orbiter deflection maneuver ΔV . Of course the addition of a probe would impose additional constraints on the main orbiter spacecraft trajectory to ensure radio link during probe descent, and require the addition of separation mechanisms which would add cost and complexity to an architecture without a probe. The mission designer must balance the added costs of such a probe vs. the science benefits gained for the overall mission architecture.

In addition to probes, the additional mass margins may be used to carry secondary payloads such as CubeSats or SmallSats which flyby or perform orbit insertion independently. Such CubeSats could perform the role of a real-time data relay while the main orbiter performs aerocapture (potentially without line-of-sight communication with Earth). In the event of a loss of the aerocapture vehicle, telemetry from the CubeSats would be of vital importance in the failure investigation. SmallSats could independently perform orbit insertion using deployable drag modulation systems into different orbits; offering the possibility of multiple platforms for some investigations.

5.3.5 Disposal

The primary driver for spacecraft disposal is often planetary protection requirements for destinations which may harbor habitable environments. Trade options for end of mission include crashing into the planet’s atmosphere, impact with a moon for which planetary protection requirements allow so, escape from the planetary system, or the Solar System itself. Typical values of budgeted ΔV fall in the range of 25–100 m/s based on past missions, and require only a small fraction of the propellant mass.

5.4 Reference Baseline Mission Design

Having explored the some of the trade options for each of the elements listed in Table 5.4, it is now possible to select a baseline design for further study. It is noted that the baseline design is not intended to be an “optimal” solution, but simply a combination of systems that work to achieve the stated objective within the imposed constraints. The purpose of

the trade studies is to allow the mission designer to explore the several combinations of the component systems and their interdependencies before selecting a promising combination for more detailed analysis.

Table 5.7 lists the parameters for the selected baseline design to insert a 1000 kg spacecraft into a Neptune orbit that allows Triton flybys. The largest allowable launch vehicle, Delta IVH with kick stage is used along with the lowest C_3 interplanetary trajectory (from the sample feasible set listed in Table 5.2) to maximize the delivered mass to orbit. The estimated delivered mass to orbit is 1686 kg, with the addition of a 300 kg probe. The arrival V_∞ and the time of flight are defined by the selected trajectory. Based on Table 5.6, the selected vehicle L/D is 0.32, with $\beta = 200 \text{ kg/m}^2$ assuming an Apollo-type vehicle. A required corridor width of at least 1 deg is imposed, assuming delivery errors result in 3σ EFPA uncertainty of less than ± 0.3 deg. The additional margin over the delivery errors is to accommodate atmospheric and aerodynamic uncertainties. Based on the aerocapture feasibility chart (Fig. B.15), the nominal deceleration, heat-rate and heat load values are $10g$, 2000 W/cm^2 , and 250 kJ/cm^2 respectively. The expected heat rate is chosen to be within the performance envelope of state-of-the-art HEEET TPS material, and the total heat load is expected to result in about 50% TPS mass fraction. The initial capture orbit size is $4,000 \times 400,000 \text{ km}$, selected to allow regular Triton flybys. A 23 deg prograde orbit is selected to minimize the aerothermal loads during the aerocapture maneuver, though this will result in higher Triton encounter speeds. With the additional mass available over the required 1000 kg, a 300 kg atmospheric probe is included as an optional add-on element. A nominal 50 m/s propulsive ΔV is budgeted for disposal of the orbiter into Neptune's atmosphere following the end of the mission. Based on the information in Table 5.7, it is now possible for the designer revise the estimates for the cruise stage mass (κM_{orb}) and the aeroshell mass fraction (χ), and thus allow more accurate estimation of the system mass breakdown.

5.5 Performance Analysis

One of the most commonly raised (and relevant) question concerning an aerocapture mission concept is the effect of uncertainties (eg: atmospheric density profile) on the vehicle performance. What if the atmosphere is much denser or thinner than expected? Will

Table 5.7. Reference baseline design

Element	Value	Remark
Launch vehicle	= Delta IVH	Largest vehicle allowed
C_3	= 48.4 km ² /s ²	Lowest C_3 trajectory from Table 5.2
Arr. V_∞	= 18.6 km/s	Satisfy $L/D \leq 0.40$ from Fig. 5.3
ToF	= 11.23 yr	From selected trajectory
L/D	= 0.32	From Fig. 5.3
β	= 200 kg/m ²	Based on heritage
RCW	= 1.0 deg	Assume ± 0.3 deg 3- σ EFPA error ^a
G-load	= 10g	Based on Fig. B.15
Heat rate	= 2000 W/cm ²	Based on Table 5.6
Heat load	= 250 kJ/cm ²	Based on Table 5.6
Orbit size	= 4,000 x 400,000 km	Based on previous studies [39]
Inclination	= 23 deg	Prograde to reduce entry aerothermal loads
Probe mass	= 300 kg	Optional add-on element
Disposal ΔV	= 50 m/s	Assumption

^a Detailed navigation study is required to investigate the achievable EFPA accuracy using the reference interplanetary trajectory and definition of the spacecraft navigation systems. Such calculations can be performed using the MONTE software toolkit developed by JPL [161]. Some margin is provided to accommodate atmospheric uncertainties and other factors which are described in Sec. 7.7.

the vehicle crash into the planet, or fly away into space without getting captured? The concern is especially relevant for aerocapture at Uranus and Neptune, whose atmospheres are relatively poorly understood and carry large uncertainties. The goal of this section is to answer the above questions and provide quantitative estimates of vehicle performance for the reference baseline design identified in Sec. 5.4. Estimation of the input parameters required to perform performance analysis typically requires a reference interplanetary trajectory and vehicle design in place. The time-consuming nature of the estimation of these input parameters generally imply that a single promising reference trajectory is used, as performing the analysis for more than a few baseline designs is often not possible. This is the rationale for comprehensive design space exploration and trade studies performed in Sec. 5.2 and Sec. 5.3 respectively, before selecting a baseline design. The uncertainties relevant for aerocapture fall into three categories: 1) navigation, 2) atmospheric, and 3) vehicle aerodynamics. Because these uncertainties can never be practically driven to zero, a real-time on

board guidance system is required to command the vehicle control authority to adjust the trajectory based on accelerometer and other measurements. Once the relevant uncertainties are quantified and a guidance algorithm is selected, Monte Carlo simulations are used to propagate a large number of guided aerocapture trajectories within the atmosphere. Statistical parameters such as orbit targeting accuracy and peak heat rate can then be deduced from the simulation results to quantify vehicle performance in the presence of the modeled uncertainties. This section describes the process by which uncertainties are quantified, along with a brief description of aerocapture guidance algorithms, Monte Carlo simulation set up, and the interpretation of the statistical results for vehicle performance analysis.

5.5.1 Navigation Uncertainty

Starting several months ahead of reaching the planet, a series of interplanetary trajectory correction manuevers (TCM) will be performed by the mission operations team to target the desired EFPA for aerocapture. The EFPA error bar (typically defined at $\pm 3\sigma$) is of critical importance for aerocapture missions as it must fall within the theoretical corridor. The EFPA accuracy is a strong function of the destination, the spacecraft navigation equipment (resolution of optical telescope), the accuracy with which corrective maneuvers can be executed, and the data cut off (DCO) time prior to entry. Radiometric and optical navigation is typically used to estimate the spacecraft state, with optical navigation imposing the requirement of data download to the ground. The corrective manuevers are then computed by the ground operations, and the commands uploaded to the spacecraft. In the future as autonomous navigation (AutoNav) technologies become more mature, it may be possible to remove the ground-in-the-loop and let the spacecraft perform autonomous TCMs to substantially reduce EFPA errors. Navigation uncertainty data is available in the literature only for flown missions and few advanced concept studies. Table 5.8 shows the typical 3σ EFPA errors for various Solar System destinations.

Table 5.8. Nominal 3σ EFPA errors

Destination	Mission or study	Error, deg	Reference	Year
Venus	Venus aerocapture	± 0.20	Lockwood et al. [36]	2006
Venus	Venus aerocapture	± 0.10	Austin et al. [56]	2019
Earth	Hayabusa	± 0.01	Haw et al. [162]	2011
Mars	MSL	± 0.01	Martin et al. [163]	2012
Titan	Titan Explorer	± 0.93	Way et al. [32]	2003
Neptune	Neptune aerocapture	± 0.51	Starr et al.. [164]	2004
Neptune	Neptune aerocapture	± 0.33	Girija et al.. [61]	2020

5.5.2 Atmospheric Uncertainty

Planetary atmospheres have seasonal, latitudinal, and diurnal variations in density profiles along with measurement and other uncertainties from instrument data gathered by spacecraft. The aerocapture performance analysis must incorporate such atmospheric variability data provided by the GRAM models. A common question that is asked is how good are the models for atmospheres with no prior in-situ measurements. Fig. 5.4 shows the predicted bounds of the density profile for Titan using pre-Cassini data, and the actual density profile measured by the Huygens probe on its descent. It is clear that the actual density profile is well within the bounds from TitanGRAM, thus illustrating the accuracy and usefulness of GRAM models. Venus, Earth, Mars, and Titan have well understood atmospheres with very low uncertainties, while Uranus and Neptune atmospheres have large uncertainties.

5.5.3 Aerodynamics Uncertainty

Aerodynamic uncertainties estimates are required to account for factors such as mass uncertainties, shape change due to ablation, uncertainty in the location of center of mass and CFD limitations in predicting aerodynamic coefficients. For lifting vehicles, the most dominant effect is from the uncertainty in L/D about the nominal trim value. For drag modulation vehicles, the corresponding uncertainty is that for the ballistic coefficient ratio β_2/β_1 . Accurate estimation of these uncertainties is often not possible at the level of conceptual studies, as it requires detailed vehicle layouts, CFD analysis, and sometimes even wind tunnel testing. However, the aerodynamics uncertainties are generally small, and nominal

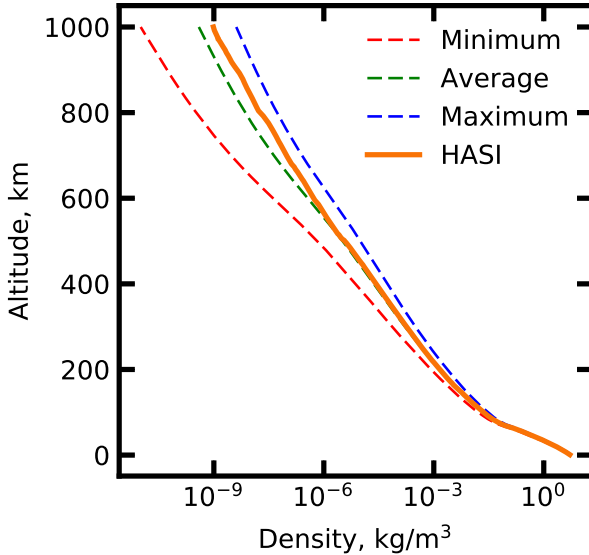


Figure 5.4. Density variations in Titan’s atmosphere. The dashed lines indicate the minimum, average, and maximum predicted density profiles from TitanGRAM. The solid line indicates the reconstructed density profile (based on in-situ temperature and pressure measurements) by the Huygens Atmospheric Structure Instrument (HASI).

values such as 10–20% uncertainty may be used based on MSL flight reconstruction data [165], [166].

5.5.4 Guidance Algorithm

The purpose of the guidance algorithm is to command the vehicle control authority during the atmospheric flight so as to achieve the desired conditions at atmospheric exit. For lift modulation aerocapture, the guidance algorithm output is the commanded bank angle. For drag single event modulation, the only control variable is the drag skirt jettison time. Entry vehicles typically have a maximum roll rate and acceleration, and hence there is a delay between the commanded bank angle and the actual bank angle profiles which must be accounted for in aerocapture simulations. Guidance schemes work by predicting the exit state using current state and control input information, along with an on-board atmospheric density model. A key feature of aerocapture guidance algorithms is that during the descending leg of the maneuver, accelerometer measurements can be used to construct

an in-situ density model on board the vehicle prior to initiation of apoapsis prediction. Using the measured density profile has been shown to provide significantly better performance in apoapsis targeting compared to using a preset density profile prior to entry, especially for targets such as Neptune with large atmospheric uncertainties [61].

5.5.5 Monte Carlo Simulation Set Up

With the relevant uncertainties quantified, a Monte Carlo simulation is set up to analyze the aerocapture vehicle trajectories in the planetary atmosphere for the baseline design. An example of the uncertainty distribution for Monte Carlo simulation set up is shown in Table 7.7. For each run, a random perturbed atmospheric profile is used along with the specified uncertainty distributions for EFPA and aerodynamics. The guidance scheme attempts to steer the vehicle to the target exit conditions subject to imposed constraint such as the maximum roll rates. The terminal conditions (achieved apoapsis altitude) and a host of other parameters (such as deceleration, heat rate etc.) are recorded during every run. In some combinations such as very shallow EFPA and rarefied atmosphere, the control variable may become saturated and could result in the vehicle not getting captured. The simulations must be designed to handle such off-nominal cases without “crashing” the program and record all relevant parameters, as such cases are of special interest during post-processing. Typically, several thousand trajectories are simulated to provide reliable estimates of the performance metrics in the presence of atmospheric and other uncertainties.

5.5.6 Interpretation of Results

Monte Carlo simulations are widely used in the analysis of entry vehicle to provide 3σ landing footprints and other performance parameters. For aerocapture trajectories, the equivalent of landing footprint is the target orbit dimensions achieved after atmospheric exit. Fig. 5.5 shows a sample result from a Monte Carlo simulation for aerocapture at Neptune. The effect of navigation, atmospheric, and aerodynamic uncertainties result in the dispersion in post-aerocapture orbit. In this particular case, no trajectories resulted in escape or crashing into the planet. Statistically, the mission designer can state with 95%

confidence that the vehicle will achieve apoapsis altitude within an arbitrary 50,000 km of the target value. If the results indicate that the orbit dispersion is unacceptably large, or significant fraction of cases resulting in escape or crashing, the performance may not be satisfactory and a revision of the baseline design is required. Similar results can be deduced for other parameters of interest such as 3σ (99.87 percentile) peak deceleration, peak heat rate, total heat load and periapsis raise ΔV . The 99.87 percentile values of peak deceleration for example is of particular interest for aeroshell structural design if the concept proceeds to the next design phase. Similarly, the 99.87 percentile periapsis raise ΔV is used to estimate the required propellant mass on-board the spacecraft.

It is important to note that the results from any simulation are only as good as the modelling assumptions used by the designer. Simulating a guided aerocapture trajectory requires several simplifying assumptions (such as perfect knowledge of the current state, neglecting the presence of localized density pockets etc.), and the mission designer must be aware of the effect of these limitations on the simulation results. More realistic Monte Carlo simulations can be performed using industry standard tools such as JPL DSENDS or POST, if such resources are available.

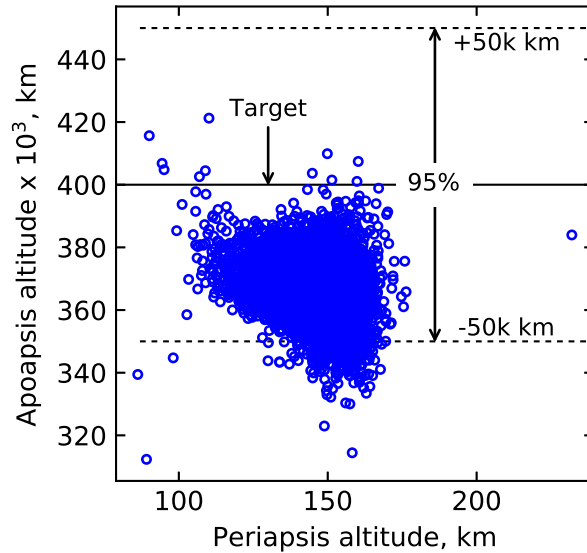


Figure 5.5. Sample result from a Monte Carlo simulation showing the achieved apoapsis vs. periapsis altitude for aerocapture at Neptune using a vehicle with $L/D = 0.40$. The target apoapsis altitude is 400,000 km. See Sec. 7.8.3 for more details.

5.5.7 Summary

Figure 5.6 shows a high-level flowchart summarizing the systems framework for rapid conceptual aerocapture mission design. In the early phases of conceptual mission studies, it is common for the baseline design to undergo several changes based on the feedback from performance analysis. For example, if the orbit targeting accuracy is not sufficient, the mission designer may increase the vehicle L/D to allow more aerodynamic control. Improvements in spacecraft navigation and atmospheric phase guidance can also improve the post-aerocapture orbit accuracy. If the aerodynamic heating is too high, the vehicle ballistic coefficient β may be reduced or the entry orientation may be changed from retrograde to prograde to reduce the aerothermal loads. Once all performance parameters are satisfactorily achieved, the conceptual design phase is complete and the results are documented for use by more advanced and detailed design studies.

5.6 Conclusions

This chapter presented a systems engineering framework for rapid conceptual design of aerocapture missions. The framework highlights the various interdependencies between aerocapture mission elements such as interplanetary trajectory and vehicle design, and provides a step-by-step methodology to formulate an aerocapture mission architecture starting from a set of high-level objectives. Based on the mission requirements drawn from the objective, constraints are imposed on a set of key design parameters which characterize the various systems. Trade studies are performed to identify combination of systems which fit together well to achieve the objective within the imposed constraints. A reference baseline design is selected based on the trade study results and subject to performance analysis using Monte Carlo simulations. Key aerocapture performance parameters such as orbit targeting accuracy, peak heat rate, and periapse raise ΔV are estimated from the Monte Carlo simulations, and is used to assess if the performance is satisfactory for the mission architecture to proceed to the next design phase. The step-by-step framework is illustrated with its application to two aerocapture mission concepts in Chapters 6 and 7.

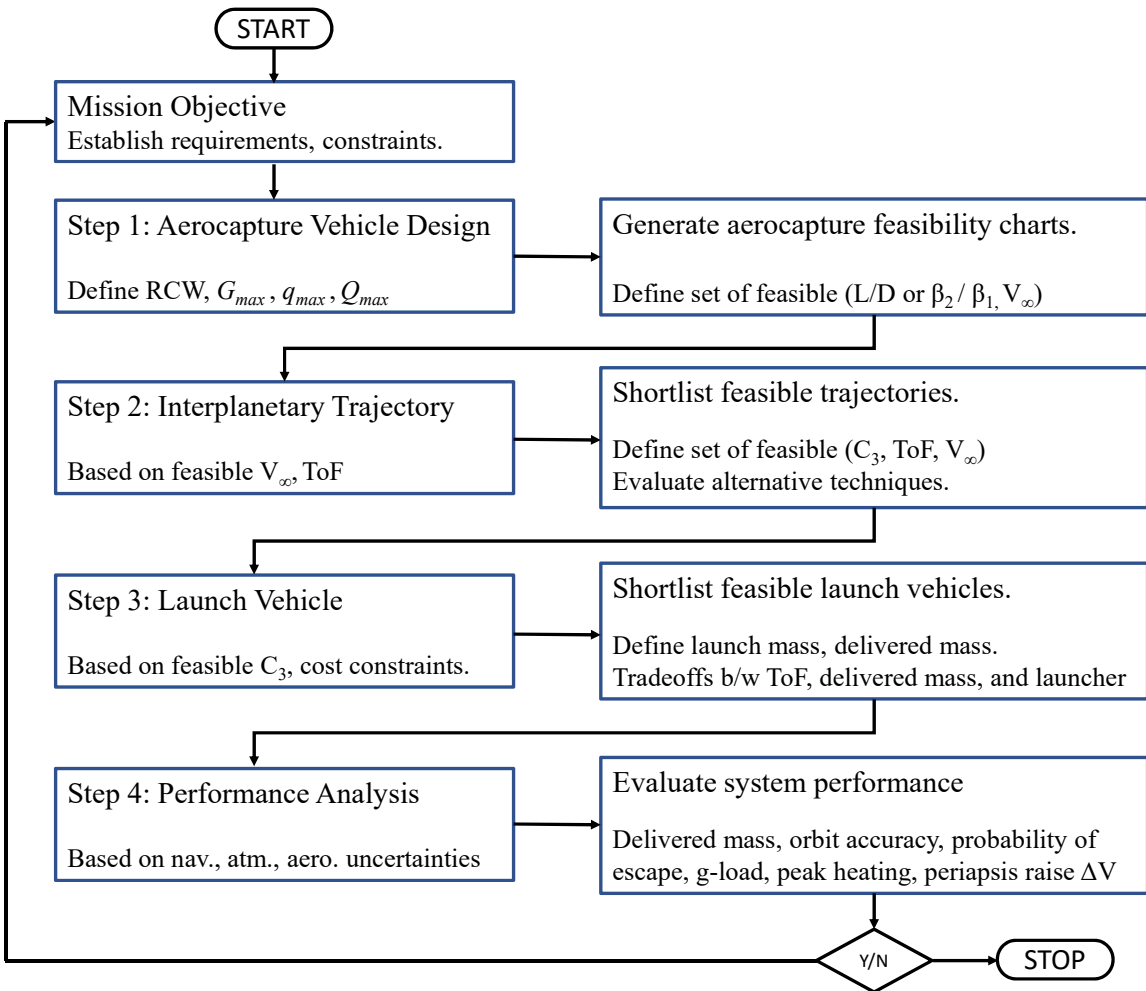


Figure 5.6. Flowchart showing the systems framework for rapid conceptual design of aerocapture missions.

6. ASSESSMENT OF SMALLSAT DRAG MODULATION AEROCAPTURE AT VENUS

6.1 Introduction

Aerocapture is well-suited for inserting small satellites (SmallSats, weighing less than 180 kg) into orbit because of the inherent difficulty of accommodating a propulsion system that delivers several hundred to a few thousand meters per second of ΔV on board such small platforms [56]. Given the decline in the number of Venus missions in the last two decades, there is significant interest in the scientific community to investigate low-cost SmallSat concepts which could be inserted into orbit [86]. Such missions would leverage rideshare along with other missions which fly to or by Venus, or to GTO or lunar vicinity to keep the launch costs low. Low-thrust or other propulsive insertion techniques may be sufficient for highly elliptical orbits (period exceeding 10-days or so), but would still carry significant mass penalty for the propulsion system. Aerocapture offers a quick mass-efficient orbit insertion technique for such mission architectures. Lift modulation aerocapture using a conventional blunt-body aeroshell is likely infeasible for small cost-constrained missions due to the difficulty of having to include auxiliary systems such as reaction control thrusters and aeroshell jettison mechanisms. Drag modulation offers a much simpler, and cost-effective method of aerocapture for such SmallSat missions to Venus and Mars. In the single-event drag modulation architecture, the only action required (and possible) is to jettison the drag skirt at the correct time when the spacecraft has depleted enough energy to insert itself into the desired orbit. A disadvantage of this method of aerocapture is that there is no control authority after the drag-skirt jettison, and hence orbit targeting accuracy is expected to be less than that for lift modulation aerocapture, though it may be acceptable for SmallSat missions which are less risk-averse.

6.2 Study Objective

The objective of the study are as follows; 1) Assess the feasibility of drag modulation aerocapture at Venus. 2) Define a reference mission concept and vehicle design based on top-level constraints such as TCW requirement and peak heating constraints. 3) Use Monte

Carlo simulations to provide statistical performance metrics such as orbit targeting accuracy and periapse raise ΔV .

6.3 Aerocapture Trade Space and Feasibility Analysis

Figure 6.1 shows the drag modulation feasibility chart for Venus. Ballistic coefficient ratio of 1 to 20 is considered, along with arrival V_∞ in the range of 0 to 16 km/s. Based on MSL EFPA delivery error of ± 0.1 deg, and including a factor of two safety a TCW constraint of at least 0.4 deg is imposed. Based on TPS peak heat constraint for material such as carbon cloth or PICA, a heat rate constraint of 300 W/cm^2 is considered. The green shaded region indicates the feasible set of $(\beta_2/\beta_1, V_\infty)$ for drag modulation aerocapture at Venus. Based on Fig. 3.30, the range of arrival V_∞ for Earth-Venus transfers fall in the range of 2-6 km/s. Considering an average value of 4 km/s for the arrival V_∞ , a vehicle with β_2/β_1 of at least 7.5 provides sufficient control authority for aerocapture. The combination of $\beta_2/\beta_1 = 7.5$ and $V_\infty = 4 \text{ km/s}$ is the selected reference design.¹ If the navigation errors can be significantly reduced below that of MSL levels, the ballistic coefficient ratio can be further reduced. Note that the selected arrival V_∞ is representative of missions that fly to Venus. Missions that use Venus as a gravity assist fly by target, typically have arrival V_∞ of 10 km/s or greater. The selected β_2/β_1 does offer sufficient control authority for such trajectories and remains feasible for fly by mission architectures within about 10 km/s. However, the aerocapture vehicle will incur higher peak deceleration, heat rates and heat loads as seen in Fig. 6.1 due to the increased entry speeds.

6.4 Mission Design

For the purpose of this study, a specific interplanetary trajectory is not selected as the spacecraft is assumed to be delivered to the vicinity of Venus with an arrival V_∞ in the range of 2–6 km/s by a host spacecraft on its way to Venus. On approach to Venus, the host spacecraft will release the SmallSat on its trajectory to enter the atmosphere within the aerocapture corridor. A detailed navigation study was not performed to quantify the

¹↑This reference design was also selected (independently) by Austin et al. [56] for a JPL-led SmallSat aerocapture mission concept to Venus at about the same time this work was performed.

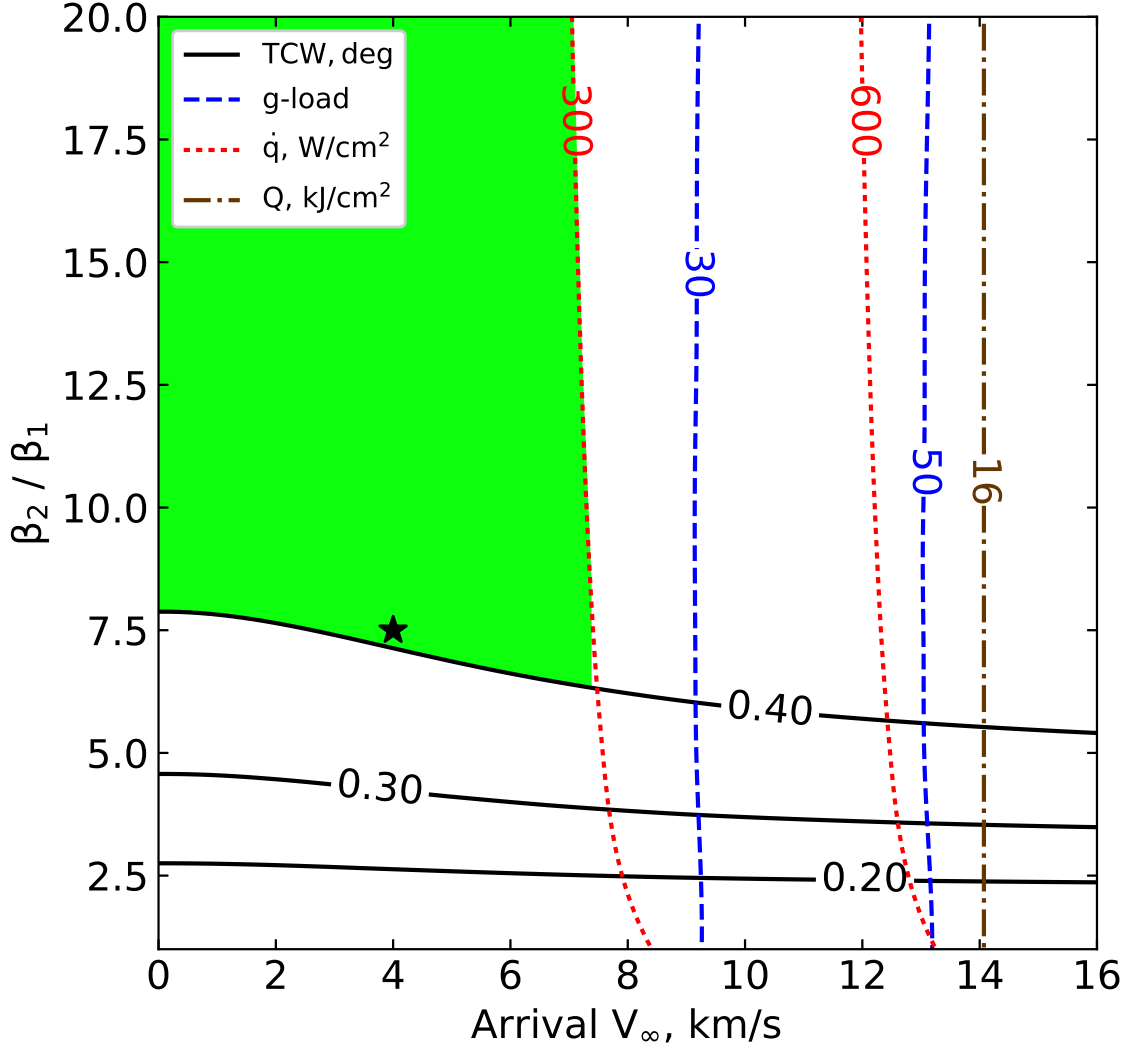


Figure 6.1. Drag modulation aerocapture feasibility chart for Venus; $\beta_1 = 50 \text{ kg/m}^2$, $R_N = 0.1 \text{ m}$, Target apoapsis altitude = 2000 km. The green region indicates the feasible space for TCW requirement of 0.4 deg, and peak heat rate constraint of 300 W/cm². Typical values of arrival V_∞ for Earth-Venus transfers fall in the range of 2–6 km/s. The black star indicates the selected reference design of $(\beta_2/\beta_1, V_\infty = 7.5, 4 \text{ km/s})$ which is used for further analysis and aerocapture performance evaluation. If the TCW requirement is reduced further, the required β_2/β_1 will be correspondingly reduced as shown by the TCW contour lines for 0.30 deg and 0.20 deg.

EFPA errors for the aerocapture vehicle, however such calculations have been performed by Austin et al. [56]. Representative values of ± 0.2 deg and ± 0.1 deg ($3-\sigma$) errors are used for further analysis. Following the release of the SmallSat, the host spacecraft will make

corrective manuevers as dictated by the mission requirements for its own orbit insertion. The target orbit for the SmallSat is chosen to be $400\text{ km} \times 2000\text{ km}$ following the definition by Austin et al. [56]. The SmallSat enters the atmosphere with its drag-skirt deployed. The on-board guidance algorithm continuously predicts the apoapsis altitude at atmospheric exit if the drag-skirt is jettisoned and triggers the jettison event at the commanded time. The timing of the jettison event is critical for drag modulation aerocapture. Jettisoning too early will result in overshoot or failure to capture, while jettisoning too late will result in the spacecraft failing to leave the atmosphere. Simulations indicate the margin between achieving the correct apoapsis and getting trapped in the atmosphere is of the order of a few seconds or smaller. Following the jettison, the vehicle is in its high ballistic coefficient configuration and has no further control authority. Following atmospheric exit, the spacecraft coasts to its apoapsis where it performs a propulsive burn to raise the periapsis out of the atmosphere and subsequently enters the desired orbit. The exact purpose of the SmallSat is not defined for this study. The satellite could perform scientific observations, act as a data relay for descent probes or landers, or could simply serve as a technology demonstration for aerocapture. The mission architecture may be easily adapted to insert a constellation of SmallSats into different inclination orbits for global coverage or mapping of the planet.

6.5 Guidance Scheme

Having selected a baseline reference design in Sec. 6.3, the next objective is to assess vehicle performance in the presence of navigation, atmospheric, and aerodynamic uncertainties. For drag modulation aerocapture, the purpose of the guidance scheme is to issue the drag-skirt jettison command at the correct time to achieve the desired exit conditions. Various guidance schemes for drag modulation aerocapture have been reported in the existing literature and with applications to Venus, Earth, Mars and Titan [47], [52], [54], [56]. A simple easy-to-implement guidance scheme with on-board density estimation is developed in this section as illustrated in Fig. 6.2.

The guidance scheme uses the current navigated vehicle state information along with an atmospheric model to predict the vehicle state at exit. The basic guidance logic is to jettison the drag-skirt at the appropriate time. The atmospheric model may be a preset look up table

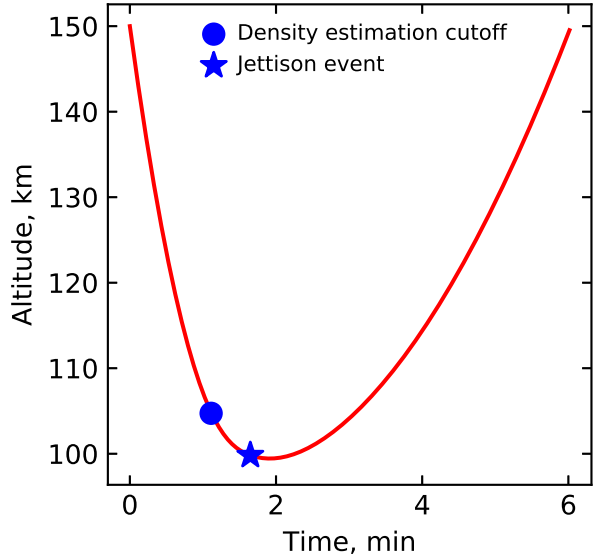


Figure 6.2. Schematic showing the altitude history of a drag modulation aerocapture maneuver at Venus. Starting at the entry interface, the accelerometer measurement is used to build an on-board density model till a predetermined altitude rate \dot{h} threshold (set to -300 m/s for this simulation) is reached. The blue circle indicates the altitude at which density estimation is cut-off and apoapsis prediction is initiated. Below the altitude where a density measurement is available, an exponential extrapolation is used to evaluate the density. The star indicates the when the jettison event was commanded by the algorithm to achieve the desired apoapsis altitude (2000 km).

loaded on to the flight computer prior to entry. Alternatively, during the descending leg of the maneuver, on-board accelerometer readings can be used to construct a density model which can then be used to predict the exit conditions. The on-board density estimation method is more robust to atmospheric density variations that the vehicle will encounter, and is the one chosen for the guidance method described here. Beginning at the entry interface, the accelerometer measurement is used to compute the vehicle drag and estimate the atmospheric density as the vehicle descends into the lower atmosphere as shown in Fig. 6.3. The density estimation phase is terminated when the vehicle crosses a predetermined altitude rate threshold, following which apoapsis prediction is initiated. When the predicted apoapsis is sufficiently close to the target, the jettison event is triggered.

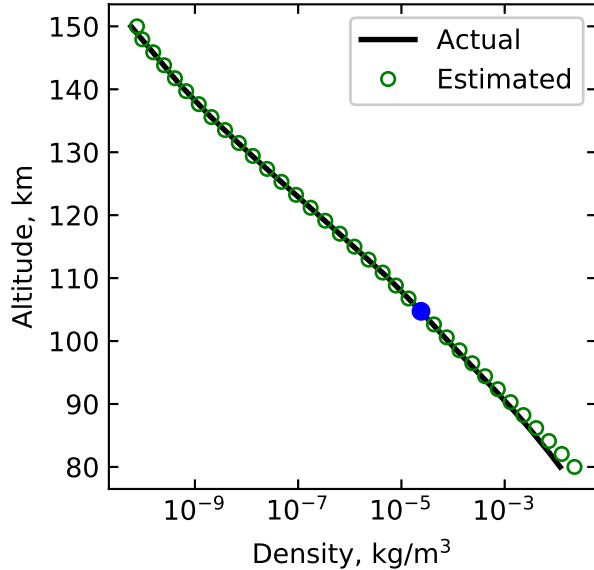


Figure 6.3. On-board density estimation during drag modulation aerocapture at Venus. The blue circle indicates the minimum altitude at which density measurement was available, beyond which values are extrapolated.

6.6 Performance Analysis

Monte Carlo simulation is used to assess aerocapture performance for the selected reference mission and vehicle design in the presence of navigation, atmospheric, and other uncertainties. The simulations are performed for two values of navigation uncertainties (± 0.2 deg and ± 0.1 deg, 3σ EFPA error). The full range of atmospheric uncertainties from Venus-GRAM including random high frequency perturbations are used in the simulations. Aerodynamics uncertainties are expected to be small as the vehicle mass and shape are expected to be known fairly accurately for SmallSats that will be weighed prior to launch. For simplicity, aerodynamic uncertainties are neglected in this study, but must be included in higher fidelity studies in terms of uncertainty in vehicle L/D , β_1 , and β_2/β_1 . The guidance cycle frequency during the density estimation phase is 1 Hz. During the apoapsis prediction, a higher frequency of 10 Hz is used as precise timing of the jettison event is critical. Following the jettison, the vehicle has no control authority and guidance commands are no longer required. Table 6.1 lists the Monte Carlo simulation parameters used in the study. The simulations assume perfect knowledge of the vehicle state vector and aerodynamic parameters.

One thousand trajectories are simulated for each of the two navigation uncertainties listed and the results are used to assess vehicle performance in terms of orbit targeting accuracy, deceleration, heating, and periapse raise ΔV .

Table 6.1. Monte Carlo uncertainties

Category	Variable	Nominal	$\pm 3\sigma$ or [min,max]	Distribution or other
Navigation	EFPA	-5.40 deg	[± 0.20 , ± 0.10] deg	Normal
Atmosphere	Latitude	-	[-80, +80] deg	Uniform
	Mean density	-	3σ	Normal
	High frequency perturbation	-	rpscale = 1	Uniform

6.6.1 Case I: Large delivery error (± 0.2 deg, 3σ)

For the purpose of the analysis in this subsection, the criteria for mission success is arbitrarily defined as achieving an apoapsis altitude within 1000 km and 18,000 km. Of the 1000 trajectories simulated, 99.2% of the cases satisfied the success criteria. 0.3% of the cases achieved apoapsis altitude less than 1000 km. These trajectories did not crash into the planet but achieved apoapsis altitude in the range of 500–700 km. 0.5% of the cases resulted in apoapsis altitudes greater than 18,000 km. Figure 6.4 shows the achieved apoapsis distribution for the simulations with ± 0.2 deg, 3σ EFPA error. 72% of the cases achieved apoapsis within 1000 km of the target value. The cases which did not meet the success criteria defined above are omitted from Fig. 6.4. Figure 6.5 shows the peak deceleration and stagnation-point heat rate distribution. The 99.87 percentile values are 11g and 394 W/cm². Table 6.2 lists the statistics from Monte Carlo simulations for ± 0.2 deg, 3σ EFPA error.

6.6.2 Case II: Small delivery error (± 0.1 deg, 3σ)

For the purpose of the analysis in this subsection with the reduced delivery uncertainty, the criteria for mission success is arbitrarily defined as achieving an apoapsis altitude within 800 km and 6,000 km. 99.7% of the cases achieved the defined success criteria. No cases resulted in apoapsis altitudes below 800 km or crashing into the planet. 0.03% of the cases

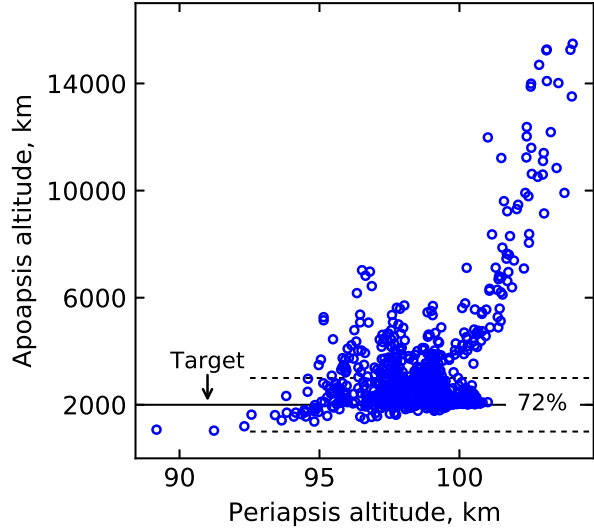


Figure 6.4. Apoapsis distribution for ± 0.2 deg, 3σ EFPA error. 72% of the cases achieved apoapsis within 1000 km of the target value. No case crashed into the planet, but a significant number resulted in overshooting the target apoapsis.

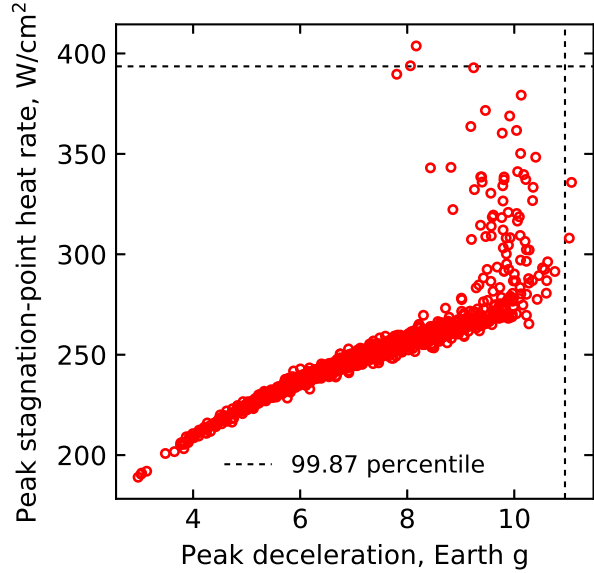


Figure 6.5. Peak deceleration and stagnation-point heat rate for ± 0.2 deg, 3σ EFPA error. The 99.87 percentile values are $11g$ and 394 W/cm^2 .

resulted in apoapsis altitude exceeding 6,000 km. The improvement in apoapsis targeting accuracy compared to Case I with the larger delivery error is significant. Figure 6.5 shows the

peak deceleration and stagnation-point heat rate distribution. The 99.87 percentile values are $10g$ and 292 W/cm^2 . The 99.87 percentile periapsis raise ΔV is 30 m/s . Table 6.2 lists the statistics from Monte Carlo simulations for $\pm 0.1 \text{ deg}$, 3σ EFPA error.

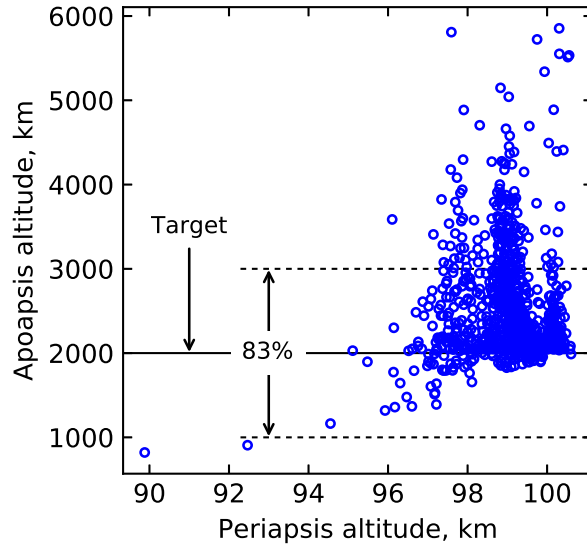


Figure 6.6. Apoapsis distribution for $\pm 0.1 \text{ deg}$, 3σ EFPA error. 83% of the cases achieved apoapsis within 1000 km of the target value. Note the effect of reducing EFPA error on apoapsis targeting accuracy compared to Fig. 6.4.

6.7 Conclusion

The study assessed the feasibility of drag modulation aerocapture to insert small satellites into orbit around Venus. The aerocapture feasibility chart is used to identify the feasible region in the aerocapture vehicle and mission design space. A reference mission concept ($\beta_2/\beta_1 = 7.5$, $V_\infty = 4 \text{ km/s}$) is selected as the baseline for more detailed analysis. Monte Carlo simulation is used to assess vehicle performance in the presence of expected navigation and atmospheric uncertainties. The reference mission and vehicle design is shown to provide acceptable orbit targeting accuracy, peak deceleration, stagnation-point heat rate, and periapse raise ΔV for both cases of EFPA errors considered in the study as shown in Table 6.3.

Table 6.2. Statistics from Monte Carlo simulations

± 0.2 deg, 3σ EFPA error						
Percentage captured	100%					
Percentage within $\pm 1,000$ km of target	72%					
Statistics for the 100% cases captured						
Parameter	Minimum	0.13 percentile	Median	99.87 percentile	Maximum	
Apoapsis altitude, km	518	627	2,335	31,123	31,699	
Peak deceleration, Earth g	2.97	3.03	7.15	10.95	11.07	
Peak heat rate, W/cm ²	189	191	249	394	404	
Periapsis raise ΔV , m/s	10.3	10.4	26.8	33.1	35.4	
± 0.1 deg, 3σ EFPA error						
Percentage captured	100%					
Percentage within $\pm 1,000$ km of target	83%					
Statistics for the 100% cases captured						
Parameter	Minimum	0.13 percentile	Median	99.87 percentile	Maximum	
Apoapsis altitude, km	820	983	2,261	7,209	8,497	
Peak deceleration, Earth g	4.15	4.57	7.21	10.31	10.40	
Peak heat rate, W/cm ²	210	216	249	292	296	
Periapsis raise ΔV , m/s	20.4	21.5	26.8	30.1	31.3	

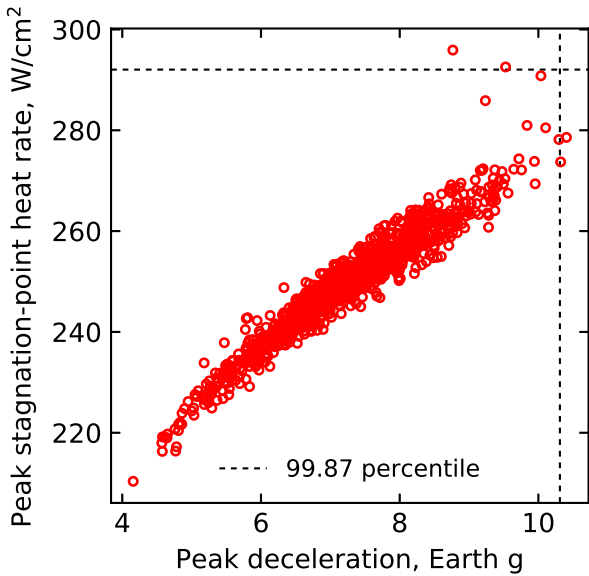


Figure 6.7. Peak deceleration and stagnation-point heat rate for ± 0.1 deg, 3σ EFPA error. The 99.87 percentile values are $10g$ and 292 W/cm^2 .

Table 6.3. Summary of vehicle performance parameters

Parameter (99.87 percentile)	3- σ EFPA error	
	± 0.2 deg	± 0.1 deg
Apoapsis altitude, km	31,123	7,209
Peak deceleration, g	10.9	10.3
Peak heat-rate, W/cm^2	394	292
Periapsis raise ΔV , m/s	33	30

7. ASSESSMENT OF AEROCAPTURE AT NEPTUNE USING HERITAGE BLUNT-BODY AEROSHELLS¹

7.1 A Brief History of Ice Giant Exploration

The ice giants Uranus and Neptune represent a distinct class of planets that is fundamentally different from the rocky planets and the gas giants Jupiter and Saturn. The inner rocky planets are composed almost entirely of metal and rock and the gas giants are predominantly H₂ and He. The ice giants are believed to be mostly composed of planetary “ices”, which include water, ammonia, and methane and make up 70–80% of the mass, while H₂ and He make up only about 20%.

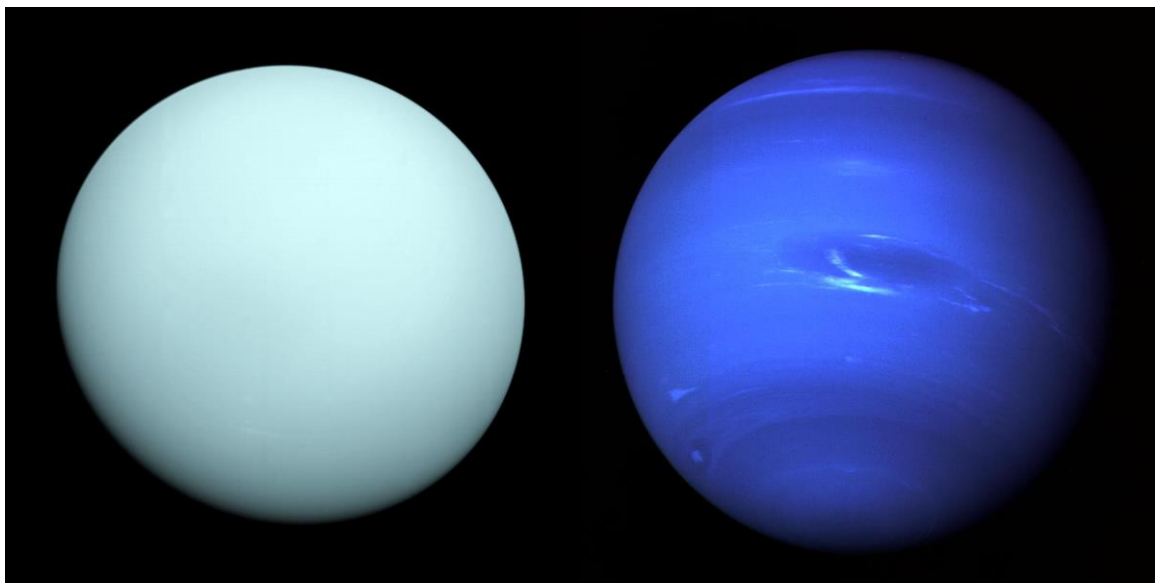


Figure 7.1. Uranus and Neptune as seen by the Voyager 2 spacecraft (color enhanced for clarity). Uranus’ southern hemisphere is seen as a near-featureless disk possibly because it was southern summer solstice at that time. The blue-green color is attributed to methane in the atmosphere absorbing in the red wavelengths. Not to scale with each other. Credit: NASA/JPL.

Contrary to the name “ice”” giants, most of these ices exist as supercritical fluids at extremely high temperatures and pressures deep inside the planet. The rocky planets have been studied in great detail by numerous orbiters and lander missions. The gas giants

¹↑The research described in this chapter was carried out at Purdue University and was supported in part by the Jet Propulsion Laboratory, California Institute of Technology, under subcontract #1578703. U.S. government sponsorship is acknowledged.

Jupiter and Saturn have been studied by well-instrumented spacecraft such as Galileo, Juno, and Cassini-Huygens. The ice giants remain the last class of planets to be explored with a dedicated mission. Our limited knowledge is mostly attributed to the Voyager 2 flybys which provided a tantalizing glimpse of these exciting planetary systems.

The story of the formation and evolution of the giant planets is the story of the Solar System. The 2013-2022 Planetary Science Decadal survey underscores the importance of giant planets in understanding our planetary system and those beyond [69]. The Decadal survey recommends a Uranus orbiter and probe as the third-highest priority flagship mission for this decade. Exoplanet statistics indicate that ice-giant sized planets may be the most abundant in our galaxy, much more abundant than Jupiter-sized planets [167]. In-situ exploration of at least one of the ice giants is critical to advancing our understanding of exoplanetary systems and planetary formation, evolution, migration, volatile delivery to the inner planets and ultimately their role in the formation of a biosphere sustaining world [168], [169].

Both Uranus and Neptune are equally compelling science targets, though there are significant differences as well. Triton believed to be a captured Kuiper Belt Object (KBO) is thought to have ejected the major satellites of Neptune, while the Uranian satellite system may be more representative of an ice giant satellite system. Programmatic, cost, and flight time concerns favor a Uranus mission over Neptune [69], though recent Ice Giant Mission studies have investigated both Uranus and Neptune mission concepts [51]. Aerocapture is a technology which holds great promise in enabling short time of flight missions to the ice giants in the coming decades, and is the subject of this chapter, with a specific focus on performing the maneuver at Neptune with existing blunt-body aeroshells.

7.1.1 The Voyager Encounter at the Ice Giants

Brief History of the Voyager Missions: Exploration of the planets in the solar system with robotic spacecraft began with fly-by missions to Venus in the early 1960s by both the United States and the former USSR. While the inner planets were reachable using existing launch vehicles at the time, getting spacecraft to the outer solar system required the gravity

assist technique. Even with gravity assist, missions to Uranus and Neptune at 19 AU and 30 AU respectively would still take multiple decades.

Fortuitously, it was discovered in the 1960s that a rare planetary alignment that occurs only once every 176 years would allow a single spacecraft to visit the four giant planets if it launched in the late 1970s [170]. Leveraging gravity assists at Jupiter, Saturn and Uranus would enable the spacecraft to reach Neptune in just 12 years. NASA decided to exploit this rare opportunity and decided to launch two spacecraft, giving birth to the Voyager missions. The mission as originally conceived was to visit Jupiter and Saturn using a Mariner derived spacecraft and was called the Mariner Jupiter Saturn (MJS) mission [171]. At the time, there was considerable scientific interest in Saturn's moon Titan and was a high priority target for the mission [172].

However, a Titan encounter would bend the trajectory out of the plane of the solar system and preclude encounters at Uranus and Neptune. Voyager 1 which would arrive at the Saturnian system first would attempt a Titan flyby, thus ending its planetary tour and if successful would allow Voyager 2 to forego its Titan encounter and continue on Uranus and Neptune. Voyager 1 had a close call at launch due to hardware problem choking some propellant and resulting in the Titan final stage shutting down too soon. Fortunately, the Centaur upper stage flight computers recognized the problem, and burned longer to make up for underperfomance of the lower stage². If Voyager 1 failed to accomplish the Titan flyby, Voyager 2 would make another attempt at Titan and would end its planetary tour as well. Fortunately, Voyager 1 succeeded at Titan and Voyager 2 was free to continue on its Uranus trajectory. After 11 years of cruising and gravity assists at Jupiter and Saturn, Voyager 2 became the first spacecraft to ever reach the Uranian system in 1986.

Voyager 2 Encounter with the Uranian System: Voyager 2 flew by Uranus at a closest approach distance of 107,000 km from the center of the planet on 24 January 1986. The gravity assist aim point for the Uranus encounter was chosen so as to send the spacecraft

²When the Centaur engine finally cut-off, it had only 3.4 seconds of fuel left to spare [173], a remarkably close call for the spacecraft which would go on to flyby Jupiter, Saturn, Titan, and one day become the most distant man-made object from Earth. If the problem had occurred on the Voyager 2 launch which had a more demanding launch trajectory, the Centaur upper stage would not have been able to make up for the underperforming lower stage and the mission would have been lost. Had Voyager 1 failed at launch, Voyager 2 would have been redirected to flyby Titan and forego the Uranus and Neptune flybys.

on to Neptune. The arrival time in the Uranus system was chosen to allow a close approach to Miranda and based on ground tracking station geometry constraints for radio science experiments [174]. At the time of the encounter, Uranus was near its southern summer solstice with its southern hemisphere bathed in continuous daylight as the south pole points towards the sun for nearly two decades.

Measurement of the helium abundance of 0.262 ± 0.048 in the atmosphere was consistent with the solar abundance of 0.274 indicating that He has not differentiated to the planet's core [175]. The estimated methane abundance in the deep atmosphere is about 2% and is 20 times solar as expected from ice abundant material which formed Uranus. Two new ring systems 1986U1R and 1986U2R were discovered using Voyager images. The observations suggest that Uranus' rings are dynamic and potentially young, rather than having formed along with Uranus [174].

Voyager images revealed ten new satellites within the orbit of Miranda, and provided the first disk resolved images of these moons. The five major satellites are in synchronous rotation with one side always facing Uranus. Much of Miranda's surface was imaged at resolutions of less than a kilometer and showed evidence of tectonic activity. Given its small size and low temperature, some additional heat source and some means to let the icy material flow is likely. The darkness of the rings and small moons could be indicative of carbonaceous material, or from bombardment of methane trapped in ice by high energy particles [174]. Voyager revealed a magnetic field with its dipole axis tilted by 60° from the planet's rotation axis, and offset from the planet's center by 0.3 Uranus radii. This came as a big surprise as all the known planetary magnetic fields of the terrestrial and giant planets had their dipole axis nearly aligned with the rotation axis. The unusual tilt, offset, and existence of significant quadrupole and octupole components to the field suggest a fundamentally different dynamo mechanism as compared to gas giants or terrestrial planets [174].

Voyager 2 Encounter with the Neptunian System: Voyager 2 flew by Neptune at a closest approach distance of 29,240 km from the center of the planet on 25 August 1989. Because there were no other planetary targets after the Neptune encounter, the mission designers had the flexibility to allow a close encounter with Triton at a distance of 39,800 km from the center of the satellite and occultation to maximize science return during the encounter. As

with Uranus, measurements of the helium and methane abundance were performed. Methane was found to be more abundant in the upper atmosphere than at Uranus, and absorption of red light by methane gives Neptune its distinctive blue color. Unlike Uranus which did not display much atmospheric activity presumably due the encounter happening during a solstice, Neptune was an active world with several cloud features and storms, The most prominent was the Great Dark Spot (GDS) which was flanked by cirrus-like cloud features which are thought to be optically thick extensions of the methane cloud deck [176].

Voyager images revealed six new satellites on approach. Triton was found to be have the coldest surface temperature in the solar system at 38 ± 4 K, and a tenuous atmosphere (surface pressure $16 \pm 3 \mu\text{ bar}$) predominantly nitrogen, and some CH₄ in the lower atmosphere. The polar regions are covered in nitrogen ice with a reddish tint, possibly due to organic compounds produced from CH₄ and N₂ through photochemistry and particle bombardment. A number of wind streaks with albedos lower than the ices, and overlying deeper ice deposits have been identified. These have been attributed to active geyser-like plumes potentially from explosive release of N₂ gas with entrained dark material. Similar to Uranus, Neptune's magnetic field has its dipole axis tilted by 47° from the planet's rotation axis, and offset from the planet's center by 0.55 planet radii. The field is poorly represented by an offset tilted dipole (OTD) model, and has significant higher order contributions. This confirmed that Uranus was not a one off case of such planetary magnetic fields could be indicative of the dynamo action in a “shallow” ionic ocean at about 0.7 R_N or a “deep” dipole field modified by overlying conducting and convecting fluid layers [176].

7.1.2 Objectives of the Study

In 2016, Saikia et al. [50] performed an assessment of aerocapture at Uranus and Neptune in support of the NASA Ice Giants Pre-Decadal Survey Mission Study [51]. Saikia et al. demonstrated the importance of coupling between interplanetary arrival conditions and aerocapture feasibility at Uranus and Neptune. The study concluded that mid-*L/D* vehicles (*L/D* of 0.6–0.8) are required at Uranus and Neptune to accommodate the uncertainties, using uncertainty estimates available from Lockwood et al. [39]. Development and testing of a new mid-*L/D* vehicle requires substantial funding commitment and at least a decade’s

time. This merits investigation of approaches which obviate the need for mid- L/D vehicles. The study recommended several directions of future work: 1) investigate the feasibility of high-energy fast arrival interplanetary trajectories which allow for more control authority compared to conventional trajectories used for propulsive insertion architectures, 2) perform studies to better quantify the relevant uncertainties such as delivery errors from approach navigation and atmospheric uncertainties, and 3) investigate approaches such as guidance schemes with onboard density estimation, hybrid aerocapture-propulsive techniques, and a pathfinder entry probe.

One or a combination of these techniques may allow the use of a heritage low- L/D vehicle for Neptune aerocapture thus obviating the need for a new mid- L/D vehicle, and leads to the objectives of the study: 1) Assess the feasibility of Neptune aerocapture using heritage blunt-body aeroshells with L/D of 0.4 or less. 2) Provide statistical performance metrics of the aerocapture performance incorporating the state-of-the-art knowledge in navigation, atmospheric, and aerodynamic uncertainties. In 2019, the Outer Planets Analysis Group (OPAG) reiterated the potential and benefits offered by aerocapture for ice giant missions [57]. When combined with aerocapture, the Space Launch System (SLS) would enable trip times to Uranus and Neptune to be as short as 5 and 7 years respectively.

Aerocapture offers substantial savings in flight time compared to a nominal 12 years to Uranus and more than 14 years to Neptune compared to propulsive insertion architectures [133]. The Planetary Science Decadal survey recommends a Uranus orbiter with probe as the third-highest priority Flagship-class mission in the next decade, after Mars Sample Return and Europa orbiter [69]. The more difficult requirements of achieving orbit at Neptune appear to be the reason for Uranus being preferred over Neptune [69]. There is significant scientific interest in Neptune and Triton, as evident in the evaluation of mission concepts for both Uranus and Neptune in the NASA Ice Giants Pre-Decadal Mission Study [51] and the ESA Study [177]. Aerocapture strongly enhances and in some cases enables missions to either of the ice giants without being constrained by a large propulsive insertion mass penalty due to the high orbit insertion ΔV [3], [41], [178]. The present study aims to consolidate the state-of-the-art knowledge of aerocapture mission design to allow scientists, mission designers, and program managers to assess its readiness for a future ice giant mission.



Figure 7.2. Artist’s illustration of a blunt-body aerocapture vehicle approaching the Neptune-Triton system. The atmospheric extent is greatly exaggerated. Original work by the author, created using the Blender open-source software.

7.2 Aerocapture Trade Space and Feasibility Analysis

Multiple aerocapture studies have used a limited number of candidate interplanetary trajectories and vehicle designs to perform aerocapture systems analysis, and quantify the performance benefits compared to propulsive insertion [1], [36], [38], [39], [179]. The interplanetary trajectories are often optimized for propulsive insertion, and do not take into account the often differing requirements for aerocapture. In addition to the mass benefit, aerocapture can allow significantly shorter time of flights for outer solar system missions compared to propulsive insertion. Recent work by Hughes [150] compiled a catalog of short time of flight, high arrival V_∞ trajectories to Uranus and Neptune though its applicability to aerocapture has not been investigated in further detail. Such high V_∞ trajectories greatly widen the interplanetary trajectory options for missions to Uranus and Neptune, especially when combined with heavy lift launchers such as the Falcon Heavy and the SLS.

To accommodate for the large uncertainties at Uranus and Neptune the aerocapture vehicle must have sufficiently large L/D . All interplanetary entry missions flown to date

have used ballistic or low- L/D vehicles ($L/D \leq 0.4$) and are considered high heritage entry systems. Studies investigating aerocapture at Neptune have used a mid- L/D vehicle (L/D of 0.6–0.8), assuming such a vehicle would be available. The non-availability of a mid- L/D vehicle presents a major hurdle for aerocapture at the ice giants. This study uses the interplanetary trajectory data set and feasibility charts presented in Chapter 4 for Neptune to formulate and analyze an aerocapture mission concept using blunt body aeroshells.

Figure 7.3 shows the aerocapture feasibility chart for Neptune. The left chart shows the arrival V_∞ , time of flight, and launch C_3 for a comprehensive set of interplanetary trajectories from Earth to Neptune and shows the trade-off between these parameters for Neptune mission design. The trajectory data comes from two sources: the NASA Ice Giants Pre-Decadal Mission Study [51], and a set of high V_∞ trajectories computed at the Jet Propulsion Laboratory and made available to the authors during the same study. The trajectories include both slow arrival ($V_\infty \leq 15$ km/s) trajectories conventionally used for propulsive insertion and fast arrival ($15 < V_\infty \leq 25$ km/s) trajectories which are feasible only with aerocapture orbit insertion. To perform aerocapture the vehicle must enter the atmosphere within a narrow range of entry flight-path angles called the “theoretical corridor.” Entering too steep results in the vehicle undershooting the target apoapsis and possibly encountering aerodynamic heating beyond the TPS limits. Entering too shallow results in the vehicle not getting captured. The right chart in Fig. 7.3 shows contours of the theoretical corridor width (TCW), peak deceleration, peak stagnation-point heat rate \dot{q} , and total heat load as a function of the arrival V_∞ and vehicle L/D . A nominal deceleration limit of $30g$ is imposed. For the peak heat rate constraint, 8000 W/cm 2 is used based on Heatshield for Extreme Entry Environment Technology (HEEET) test results [140]; and a total heat load constraint of 600 kJ/cm 2 is used which is about twice the nominal stagnation point heat load for the Galileo entry probe [180].

The green shaded area shows the feasible combinations of ($L/D, V_\infty$) for a TCW requirement of 2.0 deg [39], and deceleration and heating constraints bounding the feasible region. The bottom corner of the green shaded region indicates the smallest L/D for which aerocapture is feasible if the required TCW = 2.0 deg. To minimize the required L/D , high arrival V_∞ trajectories are desired as the higher entry speed allows a larger theoretical corridor

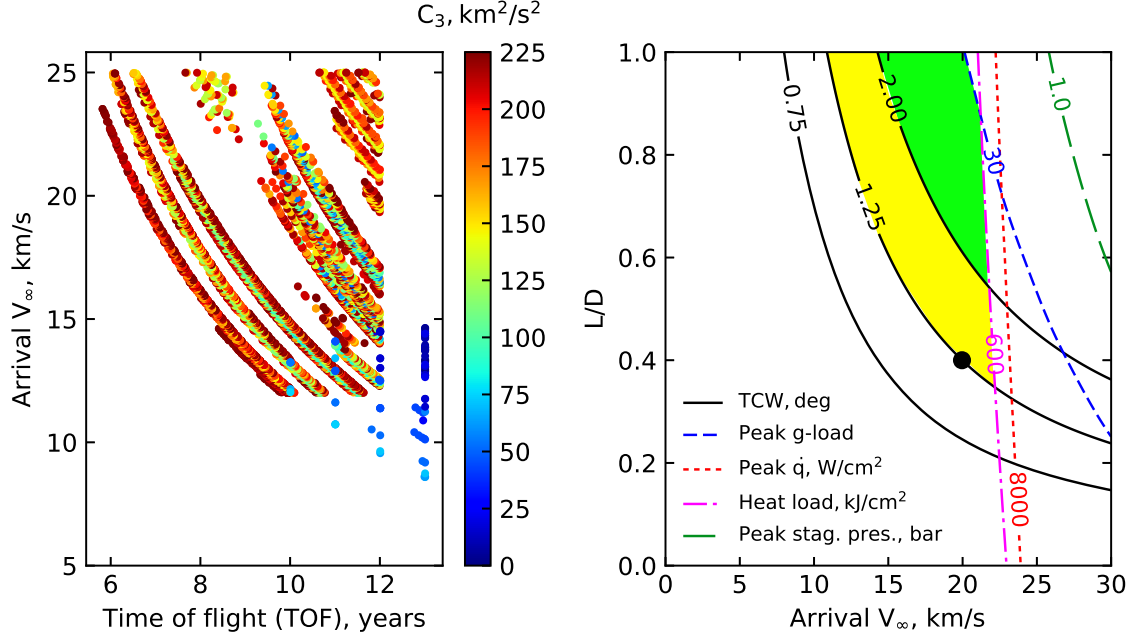


Figure 7.3. Neptune aerocapture feasibility chart. The green region indicates the feasible space for TCW requirement of 2.0 deg, for which the required L/D is 0.6–1.0 [39]. The yellow region becomes feasible if TCW requirement is lowered to 1.0 deg.

compared to slow arrival trajectories. The fast arrival trajectories using aerocapture also allow significantly shorter time of flight to Neptune (< 8 years) as compared to the conventional slow arrival trajectories using propulsive insertion (≈ 13 years). Figure 7.3 shows that propulsive insertion and aerocapture require a different class of interplanetary trajectories. Propulsive insertion requires arrival V_∞ to be small enough that the propulsion system can handle the capture burn. Short time of flight trajectories typically have high arrival V_∞ , and results in large propellant mass requirement which in turn severely limits the useful delivered mass. On the other hand, aerocapture requires a high arrival V_∞ to minimize the L/D requirement; trajectories with arrival V_∞ less than a critical value (defined by vehicle L/D and the TCW requirement in Fig. 7.3) are in fact infeasible for aerocapture. The range of feasible arrival V_∞ for aerocapture is bounded on the upper end by peak deceleration and TPS material constraints.

The TCW requirement is computed based on the navigation, atmospheric, and aerodynamic uncertainties to be accommodated by the aerocapture vehicle and it dictates the

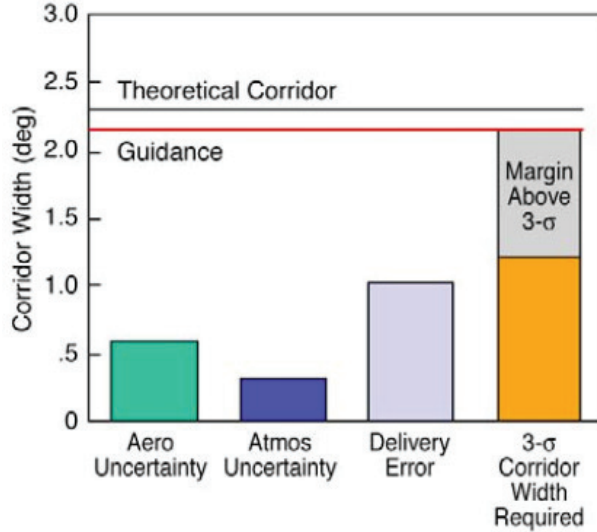


Figure 7.4. Contribution of various uncertainties and root-sum-squared required corridor width for Neptune aerocapture as estimated by Lockwood et al. [39].

required L/D . The contributions of various uncertainties as quantified by Lockwood et al. [39] and the root-sum-squared required corridor width (RCW) are shown in Fig. 7.4. To ensure the aerocapture vehicle achieves the desired atmospheric exit conditions, the TCW should be greater than the estimated RCW with adequate safety margin. Failure to satisfy this criteria implies the vehicle risks crashing into the planet or not getting captured. Based on the estimated RCW in Fig. 7.4, a TCW of at least 2.0 deg is required and the required L/D falls in the range of 0.6–1.0 as seen in Fig. 7.3. If the uncertainties are reduced (for example by reducing the delivery error) such that the TCW requirement is reduced to 1.25 deg, then the yellow shaded region in Fig. 7.3 becomes feasible in addition to the green region. The reduced TCW requirement lowers the L/D requirement. Figure 7.3 shows that if the TCW requirement is lowered to 1.25 deg, fast arrival trajectories with $V_\infty \geq 20$ km/s allow the vehicle L/D requirement to be lowered to 0.4. The selected baseline design ($L/D = 0.4$, $V_\infty = 20$ km/s) is indicated by the black circle. Further reduction in L/D is possible if the uncertainties are reduced even further, and TCW requirement is reduced to 0.75 deg, which may allow an MSL-derived aeroshell with $L/D = 0.24$ to be used.

7.3 Aerocapture Mission Design

A reference interplanetary trajectory is selected to allow a future Cassini-style exploration of the Neptune system. A comprehensive set of trajectories considering a wide range of arrival V_∞ at Neptune is used to assess the broad interplanetary trajectory trade space. For the purpose of this study, a maximum allowable time of flight of 8 years is considered. The minimum delivered mass requirement is 2000 kg to Neptune orbit, and SLS Block 1B is the baseline launch vehicle. Based on the allowable time of flight, delivered mass requirement at Neptune, and the available launch vehicle performance, a set of feasible candidate trajectories is considered. The study assumes the use of an Apollo-like aerocapture vehicle with a total mass of approximately 5000 kg; with an additional 1000 kg allotment for a cruise stage jettisoned before the maneuver. The study assumes that 40% of the arrival mass (i.e. before aerocapture, which includes aeroshell structure, TPS, etc.) is delivered to orbit [1]. This results in about 2000 kg being delivered to Neptune orbit, comparable to the dry mass of Cassini spacecraft at Saturn. Trajectories with C_3 low enough to satisfy the delivered mass requirement and also meet the flight time constraint are selected. For the feasible set of interplanetary trajectories the minimum required vehicle L/D can be computed from the right chart in Fig. 7.3 based on their arrival V_∞ . If heritage blunt-body aeroshells are used, the L/D requirement should not exceed 0.4. The chart also demarcates constraints arising from deceleration loads, heat rate, and total heat load. Interplanetary trajectories that provide sufficient TCW, and do not violate the peak deceleration, and aerodynamic heating constraints are feasible options. From the set of feasible trajectories, one that maximizes delivered mass is a desired candidate. Alternatively, a performance index based on a combination of time of flight and delivered mass may be minimized.

Preliminary results indicate that a trajectory launching in February 2031, with a Jupiter flyby in June 2032, and arriving at Neptune in January 2039 is a promising candidate. The flight time is 7.87 years and the launch C_3 is $111 \text{ km}^2/\text{s}^2$. The launch capability of SLS Block 1B with kick stage is 6250 kg at the desired C_3 [51]. Trajectories to Neptune with flight times less than 13 years are infeasible with propulsive insertion [51], [181]; and hence the use of aerocapture with SLS allows a 5 year reduction in flight time. The high energy

trajectory with a fast arrival V_∞ of 20 km/s allows the use of a heritage blunt-body aeroshell with $L/D = 0.4$ if the Theoretical Corridor Width (TCW) requirement can be lowered to about 1.25 degrees as seen in Fig. 7.3. The expected peak heat rate is within the current tested capability of HEEET TPS [140]. The study emphasizes that these are preliminary estimates using engineering correlations for the convective and radiative heating rates [143]. The selected reference trajectory is used for analysis of the approach navigation errors and aerocapture performance analysis.

Upon arrival near the Neptune sphere of influence, the spacecraft targets the aim point on the B-plane to achieve the desired entry flight-path angle (EFPA) at atmospheric interface and the target orbit inclination [103]. Radiometric and optical navigation is used to guide the spacecraft to achieve the desired trajectory. Trajectory correction maneuvers (TCMs) are performed to reduce targeting errors as the spacecraft approaches the Neptune system. On exit from the atmosphere after aerocapture, the spacecraft coasts to an apoapsis of 400,000 km and following a propulsive periapsis raise maneuver—establishes the science orbit of 4,000 km \times 400,000 km. The target apoapsis altitude is chosen to be close to Triton’s circular orbital altitude. Two candidate inclinations for the science orbit to allow Triton flybys are: 1) 157 deg retrograde with respect to Neptune, and 2) 23 deg prograde with respect to Neptune which results in higher Triton encounter speeds compared to the prograde case. The retrograde entry results in higher planet-relative entry speeds and hence higher peak heat rate and heat load compared to the prograde entry.

Errors in the B-plane targeting translate to errors in EFPA at the atmospheric entry interface. Knowledge of the B-plane targeting uncertainty is critical to assessing aerocapture mission feasibility using low- L/D aeroshells. If the delivery error is beyond what the vehicle control authority can accommodate, the vehicle guidance control variable is saturated and the guidance algorithm is unable to achieve the desired capture orbit. Low- L/D blunt body aeroshells offer less control authority than mid- L/D aeroshells, and can only accommodate smaller EFPA uncertainties compared to mid- L/D aeroshells. Accurate estimation of the navigation uncertainties along with atmospheric and other uncertainties are key to determining if blunt-body aeroshells offer sufficient control authority for Neptune aerocapture.

Delivery navigation error from spacecraft approach at Neptune were last quantified in 2004 by Lockwood et al.[39], and is the dominant uncertainty component as seen in Fig. 7.4. Improvements in navigation techniques (higher performance camera, refined ephemerides etc.) could reduce the navigation uncertainty component and hence lower the vehicle L/D requirement. Atmospheric uncertainties at Neptune have been modeled in the Neptune Global Reference Atmospheric Model (Neptune-GRAM), but no improvements are available over the data used by Lockwood et al. [39]. Spilker et al. [3] recommends performing opportunistic stellar occultations of Uranus and Neptune to improve the atmospheric models, but also notes that the technique may only provide information at high altitudes and extrapolating to altitudes relevant to aerocapture carries greater uncertainties. A dedicated research effort using Voyager data combined with new ground-based observations and modeling efforts may reduce the atmospheric uncertainties at altitudes relevant to aerocapture. Aerodynamic uncertainties have been quantified for a mid- L/D vehicle at Neptune during the 2004 systems analysis study [39], but no estimates are available for a low- L/D vehicle. A refined estimate of the delivery error is presented, along with a discussion of the current state of atmospheric and aerodynamic uncertainties.

7.3.1 Selection of Target Capture Orbit

The target orbit size and inclination are important parameters for both aerocapture and the subsequent tour of the Neptune system. The present study assumes a target capture orbit in Triton's orbital plane with apoapsis altitude nearly equal to Triton's orbital radius (400,000 km) and periapsis altitude around 4,000 km. The basis of the assumption is that the ability to perform close targeted flybys of Triton will be a driver for a future Neptune mission. However, both larger and smaller capture orbits and other inclinations may be considered. For example, a highly elliptical orbit (apoapsis greater than about 1 million km) may be suitable for certain observations while close-in circular orbits may be ideal for magnetic field or gravity science. Because highly elliptical orbits are prone to escape, the recommended option is to first aerocapture to a 400,000 km or lower apoapsis altitude orbit and then transfer to a higher orbit. Previous studies using propulsive insertion have considered a retrograde target orbit to achieve low flyby speeds at Triton [51]. However,

for aerocapture the retrograde entry heating rates are about five times greater compared to prograde entry as will be shown later in Sec. 7.8. Hence from an aerothermal perspective a prograde capture orbit is favorable if the the high flyby speeds does not compromise Triton science objectives. The mission designer must take into account all of the above trade-offs and their implications of the target orbit on aerocapture feasibility, performance, and overall mission cost and complexity.

7.4 Uncertainty Quantification

The aerocapture vehicle should have sufficient control authority to compensate for delivery error from approach navigation, atmospheric density uncertainties, and aerodynamic uncertainties. Quantification of these uncertainties is essential to evaluate the required vehicle L/D and is discussed in more detail in the following subsections.

7.4.1 Navigation Uncertainty³

For the reference interplanetary trajectory, standard navigation covariance analysis is used to quantify the entry flight-path angle uncertainty at atmospheric entry interface (defined at 1000 km above the 1 bar pressure level). In this process, tracking data measurements are simulated along the reference trajectory and input into a linearized least-squares filter to estimate the spacecraft orbit and other parameters; the filter also produces a covariance matrix containing the uncertainties of the estimated parameters. Details of the navigation covariance analysis process is beyond the scope of this paper; a description of the data, methodology, and current state-of-the-art is available in the study by D'Amario and Watkins [182]. A high level description and details relevant to the approach of Neptune are as follows.

For deep space missions, the tracking data includes Doppler and Range (which measures the line-of-sight velocity and distance of the spacecraft relative to a tracking station, respectively), and Delta Differential One-Way Ranging (Δ DOR), an interferometric data type in which the time delay of a radio signal from a spacecraft received at two tracking stations

³This subsection is co-authored by the author, Dr. Shyam Bhaskaran, and Matthew Smith at the Jet Propulsion Laboratory (JPL). The author provided the reference trajectories and other parameters to estimate the delivery errors presented in this section.

is used to compute an angular location of the spacecraft in the plane-of-sky. In addition, images of natural bodies taken by an onboard optical navigation (OpNav) camera provides a target-relative data type, especially important for approaching bodies whose orbit is not well known, such as Triton. The observable for OpNav data is the center of the observed body in the camera field-of-view (FOV) relative to the inertial pointing direction of the camera, computed through various centroiding techniques [183]. Since this is fundamentally an angular measure, the higher the angular resolution of the camera, the higher the accuracy of the OpNav data. The angular resolution is specified in terms of the angle extended by a single camera pixel, the instantaneous field-of-view (IFOV). For this study, two candidate optical navigation cameras are considered: 1) a generic medium resolution camera (Mid-Res) with a relatively wide IFOV, and 2) a high resolution camera (Hi-Res) with physical characteristics similar to the Long Range Reconnaissance Imager Camera (LORRI) flown on the New Horizons spacecraft. The camera specifications are shown in Table 7.1. Table 7.2 lists the 1σ noise on all the data types assumed in the analysis, and the tracking schedule for the radio and OpNav data.

Table 7.1. Camera specifications

Camera	Specifications
Mid-Res	<ul style="list-style-type: none"> • IFOV: $60 \mu\text{rad}$ • FoV: 122 mrad • focal length: 500 mm
Hi-Res	<ul style="list-style-type: none"> • IFOV: $5 \mu\text{rad}$ • FoV: 5 mrad • focal length: $2,619 \text{ mm}$

Table 7.2. Data tracking schedules and assumed noise

Data type	Tracking schedule	1σ noise
Doppler	$3 \times 8 \text{ hrs/week}$	0.1 mm/s
Range	$3 \times 8 \text{ hrs/week}$	3m
ΔDOR	2 pairs/week	0.06 ns
OpNav	3 pictures/day (Triton OpNav begins at E-60 days)	1 pixel

The reference trajectory is obtained via numerical integration, with the force model including gravitational attraction from 8 planets, the Neptunian moons Triton and Nereid, and the spherical harmonic gravity terms J_2 , J_4 for Neptune. Four impulsive burns are also modeled, at Entry (E) - 30, 7, 5, and 2 days, and finally, small impulsive burns every 3 days are also included to account for minor spacecraft attitude adjustments. The nominal value for all burns in the reference trajectory is 0, but they are included in the filter so that their error is included in the estimated covariance. Of special note is the Neptune ephemeris; since errors in Neptune's position at arrival is a major driver of the navigation dispersion at entry, two cases were examined. The first case uses the current level of uncertainty in Neptune's orbit. The second case assumes the uncertainty in Neptune ephemeris could be reduced by a factor of 100. The latter is a hypothetical improvement based on assumptions of future Neptune observations⁴.

The integration of the reference trajectory, data simulation, and the estimation process is accomplished using the MONTE software set [161]. Typically, for deep space missions the estimated parameters include, in addition to the spacecraft state (position and velocity), dynamic parameters which affect the spacecraft orbit (such as ephemerides and gravity fields of nearby natural bodies), non-gravitational forces acting on the spacecraft (such as solar radiation pressure and thrusting events), and parameters which affect the data (such as range biases). Also, some parameters are included in the filter as so-called "considered" parameters. These are bias parameters which contribute to the overall error covariance but are not estimated by the filter. They are typically used to account for parameters which are difficult to model or are poorly observed but are included in the covariance to prevent overly optimistic uncertainties. Examples of these are media propagation effects on the radio signal, and motion of the Earth's crust which affect the location of the tracking stations. A complete list of standard filter parameters can be found in the article by D'Amario and Watkins [182]; for the analysis performed in this study, Table 7.3 lists all the relevant ones, along with their *a priori* 1σ uncertainty.

The standard coordinate frame for the integration and estimation is the International Celestial Reference Frame (ICRF), centered at Neptune, and the estimated state is provided

⁴↑William Folkner, Private communication

Table 7.3. Estimated navigation filter parameters and uncertainties

Parameter	<i>a priori</i> 1σ uncertainty
• Spacecraft state at epoch (Cartesian)	5E4 x 5E4 x 5E4 (km)
	5E-1 x 5E-1 x 5E-1 (km/s)
• Neptune barycenter state (Cartesian)	2328 x 790 x 434 (km)
	3.2E-6 x 4.2E-7 x 1.3E-7 (km/s)
• Triton state (Cartesian)	5.8 x 11.6 x 8.4 (km)
	9.4E-5 x 6.8E-5 x 4.2E-5 (km/s)
• Nereid state (Cartesian)	180 x 111 x 108 (km)
	1.6E-5 x 6.7E-6 x 1.2E-5 (km/s)
• Impulsive maneuvers (E-30, E-7, E-5, E-2)	5 cm/s per axis
• Small burns for repointing (every 3 days)	0.2 mm/s per axis
• Neptune pole	Right Ascension: 4.6E-2 deg Declination: 9.1E-3 deg
• Neptune barycenter GM	4.845 km ³ /s ²
• Neptune J ₂ , J ₄	1.5E-6, 9.6E-7
• Triton GM	6.3E-1 km ³ /s ²
• Stochastic range biases at stations	2 m

in Cartesian coordinates at the beginning of the integration arc. For analyzing entry performance, however, the covariance estimate can be mapped forward in time and rotated into more suitable coordinates. One of these is the B-plane, which is a plane centered at the target body (Neptune in this case), and perpendicular to the incoming asymptote of the trajectory [184]. The mapped covariance is projected onto the B-plane as an ellipse, with the uncertainties represented by the major and minor axis of the ellipse (SMAA, SMIA). The covariance can also be mapped to the EFPA, and the EFPA error is proportional to the magnitude of the B-vector in the B-plane.

The 1σ entry flight path angle uncertainty with current level of Neptune ephemeris is shown in Table 7.4. For the selected interplanetary trajectory with arrival $V_\infty = 20$ km/s, a vehicle with $L/D = 0.4$ entering prograde near the equator results in $\text{TCW} \approx 1.25$ deg. If the $\pm 3\sigma$ navigation uncertainty alone exceeds the TCW, atmospheric and aerodynamic uncertainties cannot be accommodated. Preliminary simulations indicated the 1σ delivery error cannot exceed 0.2 deg if a blunt body aeroshell with $L/D = 0.40$ is used for the reference interplanetary arrival conditions. Table 7.4 shows that radiometric tracking alone (i.e. without OpNav) cannot achieve the desired delivery accuracy. Optical navigation using

a Mid-Res camera with specifications listed in Table 7.1, along with radiometric navigation is also unable to achieve the desired targeting accuracy. The Hi-Res camera significantly lowers the delivery error, and Data Cut Off (DCO) at E-07 meets the preliminary requirement and DCO at E-04 days exceeds it. The delivery error for the E-04 DCO with current ephemeris uncertainty is considered baseline for the remainder of the study. The EFPA errors for the scenario with 100x improvement in Neptune ephemeris were similar to that obtained with the current Neptune ephemeris for E-07 and E-04 DCO. The calculations with the improved ephemeris did not produce a significantly different result and hence are not reported.

Table 7.4. 1σ EFPA uncertainty using current Neptune ephemeris

Only radiometric tracking, no OpNav			
DCO, days	B-plane ellipse SMAA \times SMIA, km	$1\sigma B $ error, km	1σ EFPA error, deg
E - 09	328.8×255.3	272.9	1.78
E - 07	327.5×254.2	271.3	1.77
E - 04	325.1×253.3	270.3	1.76
With radiometric tracking and OpNav (Mid-Res)			
E - 09	170.3×160.3	162.9	1.06
E - 07	151.5×144.1	146.3	0.95
E - 04	116.5×113.5	114.4	0.74
With radiometric tracking and OpNav (Hi-Res)			
E - 09	39.8×35.4	39.2	0.26
E - 07	30.5×26.9	30.1	0.20
E - 04	17.6×14.6	17.1	0.11

Results using current Neptune ephemeris and the Hi-Res camera is an improvement over the previous estimate in literature which was ± 0.17 deg (1σ) [39]. The smaller delivery error lowers the TCW requirement and hence the required L/D as shown in Fig. 7.3. The results represent a preliminary assessment of the delivery uncertainties. Sources of error not considered in the study may inflate these uncertainties to some degree. The primary concern would be non-gravitational effects on the spacecraft from mis-modeled thrusting events, such as outgassing or momentum wheel desaturations. Other non-gravitational effects [185] that were not considered in the study include solar radiation pressure, but at Neptune distances, this should be a small effect. Finally, systematic errors in OpNav centerfinding of extended

bodies, such as Triton, may also degrade the results. Future studies with improved spacecraft system definition can refine the estimation of delivery uncertainties.

7.4.2 Atmospheric Uncertainty

The large heliocentric distance presents a challenge to accurate measurement of Neptune's atmospheric characteristics. The Voyager 2 spacecraft remains the only spacecraft to provide a glimpse of the Neptune atmospheric profile during its flyby in 1989 [3], [176]. Despite the limited data and the uncertainties in measurements, Neptune-GRAM is the state-of-the-art atmospheric model for aerocapture trajectory analysis. GRAMs are engineering level models for planetary atmospheres, and are widely used for systems design and performance analysis of flight trajectories [39], [97], [98]. The atmosphere model implemented in Neptune-GRAM is based on the data from Voyager 2 radio science experiment, infrared interferometer-spectrometer (IRIS), and ultraviolet spectrometer (UVS) instrument [145]. Neptune-GRAM provides the density, temperature, pressure, winds and chemical composition as a function of altitude, latitude, longitude, season, and local time. The model accounts for: 1) uncertainty in analysis of Voyager data, 2) latitudinal variations in the atmospheric structure, and 3) temporal changes due to seasonal and diurnal variations [144].

Neptune-GRAM uses a single input parameter “Fminmax” to account for uncertainty and variability of the mean density profile. $F_{\text{minmax}} = -1$ corresponds to the minimum mean density and $F_{\text{minmax}} = +1$ corresponds to the maximum mean density as shown in Fig. 7.5. Neptune-GRAM recommends using F_{minmax} near 0 for near-equatorial entry at equinox, negative F_{minmax} for polar entry during winter, and positive F_{minmax} for polar entry during the summer. Neptune-GRAM also provides the expected $\pm 3\sigma$ variation of the mean profile about the selected F_{minmax} value as shown in Fig. 7.5. The full range of F_{minmax} along with the 3σ dispersion is expected to cover the worst-case uncertainty in mean density profile. For aerocapture at Neptune, knowledge of the density profile uncertainty is most important in the altitude range 100 km to 400 km which is referred to as the aerocapture altitude range. Neptune-GRAM also provides high frequency density perturbations superimposed on the mean profiles to account for random variations expected in the atmosphere as seen in Fig. 7.6. The parameter “rpscale” controls the high frequency variability of the atmospheric

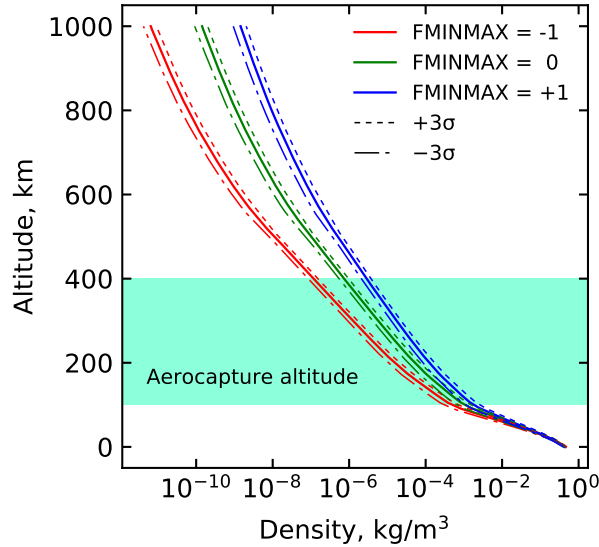


Figure 7.5. Mean density profile variations from Neptune-GRAM by varying F_{minmax} from -1 to $+1$ and $\pm 3\sigma$ uncertainties about the mean profiles.

density and ranges from 0 to 2, with 0 indicating no perturbations and 2 indicating the highest perturbation amplitude.

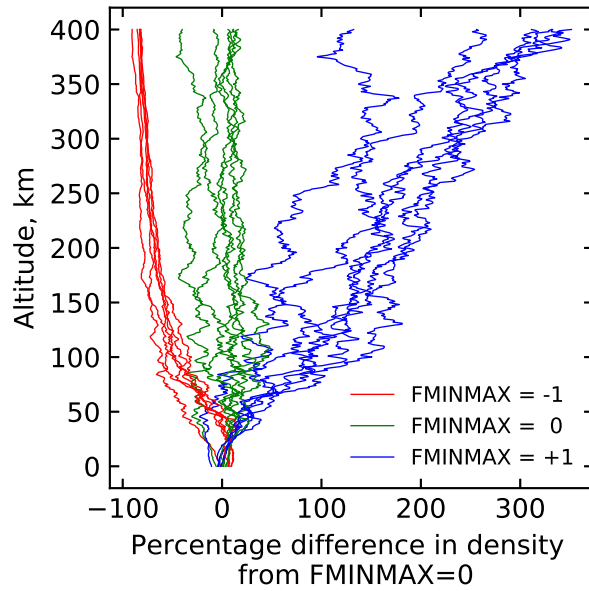


Figure 7.6. Random perturbed density profiles from Neptune-GRAM [39].

Previous studies have recommended using a smaller range of $F_{\min\max}$ depending on the arrival season and entry latitude instead of the full range. Lockwood et al. [39] used $0.60 \leq F_{\min\max} \leq 0.93$ for an aerocapture vehicle flying in low latitudes in the season corresponding to the arrival time. The present study uses the full range of $F_{\min\max}$ from -1 to +1 as a worst-case estimate of the atmospheric uncertainties. Better knowledge of the atmosphere from ground based observations and modeling may reduce the atmospheric variability both in terms of mean profile and high frequency content. It is possible that existing observations when combined with global circulation models could constrain the range of $F_{\min\max}$ depending on the arrival season, and is worth further investigation. The present study investigates a novel approach called a pathfinder probe recommended by Spilker et al [3]. An entry probe enters the atmosphere several weeks ahead of the main aerocapture vehicle and relays the in-situ atmospheric density data. The aerocapture vehicle performs a trajectory correction maneuver to adjust the target EFPA, and is discussed in Section 7.7.

7.4.3 Aerodynamics Uncertainty

The vehicle aerodynamic control authority for bank angle modulation is quantified by the hypersonic trim lift-to-drag ratio $(L/D)_{\text{trim}}$. Uncertainties in the mass distribution, ablation of the TPS material during aerocapture, shape changes, and mass imbalances translate into uncertainty in the vehicle $(L/D)_{\text{trim}}$. Quantification of aerodynamics uncertainties is important for entry vehicle performance analysis [165], [166], but is outside the scope of the present work. The present study uses a 10% 3σ dispersion about the nominal $(L/D)_{\text{trim}}$ as a representative estimate based on MSL entry vehicle aerodynamics reconstruction data [186]. Entry at Neptune presents a different and significantly more severe aerothermal environment than at Mars or Titan due to the higher entry speed and the H₂-He atmosphere. Additional study is required to quantify the aerodynamics uncertainties for a Neptune aerocapture vehicle using CFD and other numerical models for prediction of TPS ablation during the maneuver.

7.5 Guidance Scheme

The aerocapture guidance algorithm guides the vehicle from the entry interface through atmospheric flight such that a desired set of terminal conditions are achieved when the vehicle exits the atmosphere. The desired terminal conditions at atmospheric exit allows the spacecraft to achieve the target capture orbit apoapsis and inclination. The present work uses bank angle modulation as the control method. Bank angle modulation uses an aeroshell which provides lift from offsetting the center of gravity with respect to the symmetry axis. The lift vector is rotated around the velocity vector by banking the vehicle and the bank angle is the sole control variable. Bank angle modulation has been successfully used on entry vehicles such as Apollo and the Mars Science Laboratory (MSL) and is considered a high-heritage flight control technique for low- L/D blunt body aeroshells [106], [107]. The guidance scheme used in the present work is a derivative of the Analytical Predictor-Corrector developed by Cerimele and Gamble [17]. The guidance consists of two phases: 1) the equilibrium glide phase, and 2) the exit phase as shown in Fig. 7.7. In the equilibrium glide phase, the vehicle attempts to maintain equilibrium glide condition i.e. altitude acceleration $\ddot{h} = 0$. The bank angle command δ_{CMD} during the equilibrium glide phase is computed as [17]

$$\cos \delta_{\text{CMD}} = \cos \delta_{\text{eq. gl.}} - G_h \dot{h} + G_{\bar{q}} \left(\frac{\bar{q} - \bar{q}_{\text{ref}}}{\bar{q}} \right) \quad (7.1)$$

where $\cos \delta_{\text{eq. gl.}}$ is the calculated equilibrium glide bank angle to which increments are added, and is given by [17]

$$\cos \delta_{\text{eq. gl.}} = \frac{mg}{C_L \bar{q} S} \left(1 - \frac{v^2}{gr} \right) \quad (7.2)$$

where, m is the vehicle mass, g is the local gravitational acceleration, C_L is the vehicle lift coefficient, \bar{q} is the dynamic pressure, S is the aerodynamic reference area, v is the atmosphere relative speed, and r is the radial distance from the center of the planet. G_h and $G_{\bar{q}}$ refer to the gain parameters and are chosen based on the method developed by Cerimele and Gamble [17] described in Appendix C. The reference dynamic pressure \bar{q}_{ref} is computed as [17]

$$\bar{q}_{\text{ref}} = -\frac{mg}{0.75 C_L S} \left(1 - \frac{v^2}{gr} \right) \quad (7.3)$$

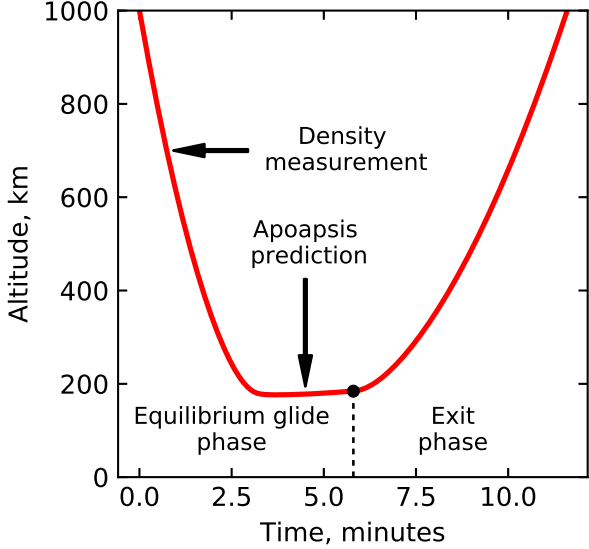


Figure 7.7. Altitude history of the aerocapture maneuver showing the equilibrium glide phase and exit phase of the guidance algorithm.

A key feature of the guidance algorithm proposed in the present work is the onboard density estimation during the descending leg of the aerocapture maneuver. The vehicle uses the accelerometer measurements to estimate the atmospheric density during the equilibrium glide phase until a predetermined altitude rate \dot{h} is exceeded.

$$\rho_{\text{est}} = \frac{2ma_{\text{drag}}}{SC_D v^2} \quad (7.4)$$

where, ρ_{est} is the estimated density, a_{drag} is the measured drag acceleration, and C_D is the drag coefficient. The present study assumes the drag deceleration can be accurately estimated from onboard accelerometer readings [187], [188]. Figure 7.8 shows the comparison of actual and estimated density profiles for a vehicle with $L/D = 0.4$ entering Neptune retrograde equatorial at 33 km/s (planet-relative speed) and accelerometer measurement frequency of 2 Hz. For altitudes below the minimum altitude at which density measurements are available, the algorithm extrapolates the density using an exponential model. The extrapolation uses the density estimate and computed scale height at the minimum altitude at which a measurement is available. The blue circle in Fig. 7.8 indicates the minimum altitude at which measurement was available, beyond which the profile is extrapolated. Figure 7.9 shows the percentage error in density estimation as a function of altitude. Potential sources

of error in the density measurement such as data noise, uncertainty in vehicle mass and speed are not considered in the present study. The effect of turbulent buffeting, data noise and filtering, sensor response time, and computational cost of constructing a reliable density function using onboard computing resources are beyond the scope of the present work.

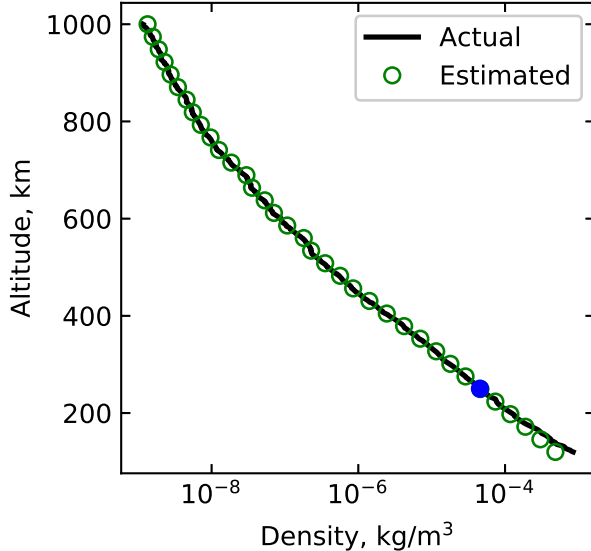


Figure 7.8. Comparison of an actual perturbed random profile from Neptune-GRAM and estimated density profile from measured drag deceleration.

While onboard density estimation is proposed by many studies addressing aerocapture at Mars [31], [188], [189], its application to Neptune aerocapture has not been studied. Onboard density estimation significantly improves the guidance performance compared to using a preset density profile, and is of critical importance to aerocapture at Neptune due to low theoretical corridor width compared to Mars or Titan. Encountering a higher than expected density atmosphere could result in failure due to undershooting of the target apoapsis; a less dense atmosphere can result in apoapsis overshoot. Worst case scenarios involving low density atmosphere can result in the spacecraft leaving the atmosphere without getting captured. The proposed guidance scheme is shown to be able to achieve satisfactory performance even with large atmospheric uncertainties as shown in Section 7.8.

Once a predetermined altitude rate \dot{h} threshold is exceeded, the vehicle starts predicting its apoapsis altitude at exit using full lift up for the remainder of the atmospheric flight.

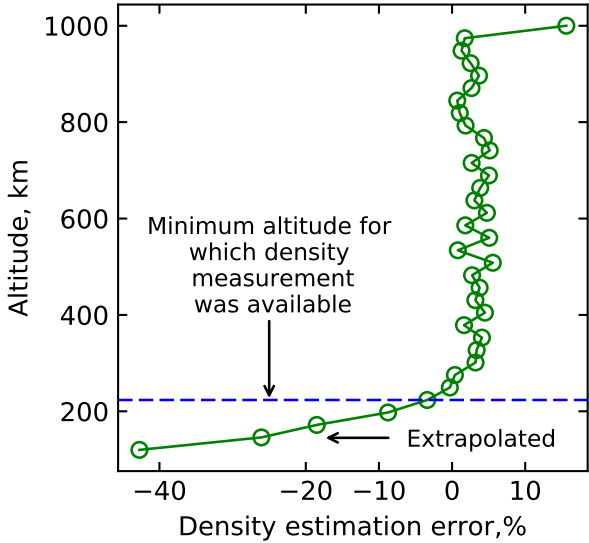


Figure 7.9. Density estimation error. Below the minimum altitude for which on-board measurements are available, an exponential extrapolation is used.

The prediction is done by numerically integrating the equations of motion using the density profile measured during the descending leg of the aerocapture maneuver as shown in Fig. 7.7. When the predicted apoapsis altitude at exit is sufficiently close to the desired value, the exit phase is initiated and the vehicle pulls out of the atmosphere with full lift up for the remainder of the atmospheric flight. Density pockets and density shears are not modeled in Neptune-GRAM and may be a concern for aerocapture vehicles [190]. A case for concern would be if the density pockets are localized, and not encountered by the vehicle during the descending leg but only during the ascending leg resulting in erroneous apoapsis prediction. Further study is required to investigate the magnitude and spatial extent of density pockets in ice giant atmospheres and its effect of aerocapture performance.

The bank angle commanded to target the desired apoapsis will result in an out-of-plane force component for bank angles other than 0 deg (lift up) or 180 deg (lift down). The out-of-plane force component will cause the inclination to change as the vehicle flies through the atmosphere. Since bank angle is the only control available to target both the apoapsis at exit and the inclination, the strategy adopted is to perform bank angle reversals when the inclination exceeds prescribed bounds [17]. Because the maximum roll rate is limited, the

vehicle will take a few seconds to complete the roll reversal and lead to some error in apoapsis targeting. The present study focuses only on the apoapsis targeting and leaves the inclination unconstrained for simplicity. Inclination errors from the atmospheric pass are expected to be small and can be corrected along with the periapsis raise maneuver. Additional study is required to include inclination targeting in the proposed guidance scheme, and analyze its effect on apoapsis targeting accuracy for aerocapture at Neptune.

7.6 Hybrid Propulsive-Aerocapture Concept

The hybrid propulsive-aerocapture concept refers to a technique where rocket propulsion provides a component of the deterministic ΔV for orbit insertion along with aerocapture. Using a combination of aerocapture and propulsion has been suggested as a method to reduce the vehicle L/D requirement for ice giant missions by Spilker et al. [3]. The present work considers two hybrid approaches which show potential in preliminary calculations to enable use of low- L/D blunt body aeroshells.

The first approach involves aerocapture into an initial orbit with apoapsis lower than the planned science orbit, and then propulsively boosting the apoapsis to the desired orbit. The small initial capture orbit widens the theoretical corridor (TCW) and hence lowers the required vehicle L/D . An additional advantage of a small initial orbit is that it reduces the risk of accidental escape following aerocapture. The primary performance penalty for this hybrid approach is the propulsive ΔV cost for the apoapsis raise maneuver, as a high propulsive ΔV implies significant mass penalty. Additional risks from a small capture orbit include: 1) increased ring plane crossing hazard (particularly if the initial apoapsis is close to or inside the rings) and 2) less available time for orbit determination and corrective maneuvers compared to large orbits which have a several day coast period to the first apoapsis. Figure 7.10 shows the effect of initial capture orbit period on vehicle L/D requirement. The TCW constraint lines show the 2.0 deg contours for a range of initial capture orbits. The analysis assumes the desired science orbit has a 20-day period with periapsis radius of 1.1 Neptune radius. The green shaded patch shows the feasible set of $(L/D, V_\infty)$ if the initial capture orbit is 20 days. If a smaller one-day capture orbit is used, the blue patch becomes

feasible, lowering the L/D requirement. After the periapsis raise maneuver, an apoapsis raise maneuver is performed at the periapsis.

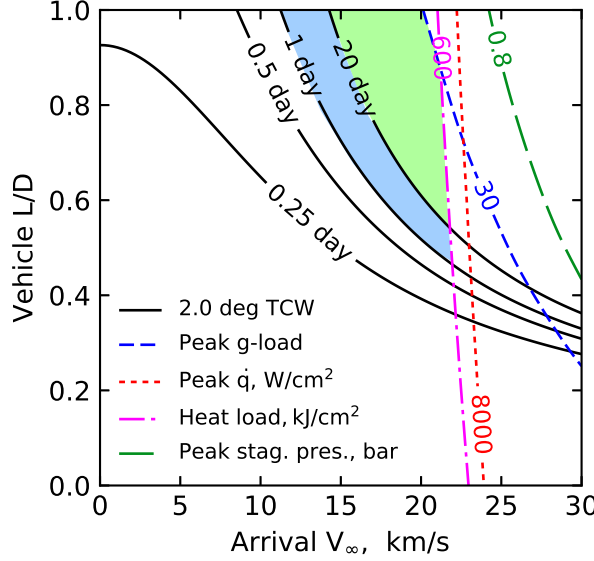


Figure 7.10. Effect of initial capture orbit period on vehicle L/D requirement. Shaded regions show the feasible set of $(L/D, V_\infty)$ for 20-day and 1-day orbits.

Table 7.5. Minimum required L/D and deterministic propulsive ΔV cost for hybrid aerocapture-propulsive approach using small initial capture orbits, $V_\infty = 20$ km/s, target science orbit period = 20 days

Initial capture orbit period, days	Initial apoapsis altitude, km	$(L/D)_{\min.}$	Apoapsis raise ΔV , m/s
20	1,553,575	0.61	0
1	166,163	0.51	1,252
0.5	85,543	0.45	2,148
0.25	34,755	0.38	3,658

Table 7.5 shows the minimum required L/D using different capture orbits for arrival at $V_\infty = 20$ km/s, and the apoapsis raise ΔV cost to achieve the 20-day science orbit. Using a small capture orbits does lower the L/D requirement (but not significantly to enable use of low- L/D aeroshells with reasonable ΔV penalty). Capture orbits less than one-day incur prohibitively high apoapsis raise ΔV and ring plane crossing hazard. ΔV of 2 km/s or

greater begin to approach the value for purely propulsive insertion, and accommodation of large propellant tanks inside an aeroshell presents another challenge.

The second hybrid approach involves aerocapture followed by a propulsive ΔV maneuver immediately after atmospheric exit as shown in Fig. 7.11. The propulsive ΔV capability allows a wider of range of entry flight path angles than conventional aerocapture and hence increases the TCW. $TCW_{\Delta V}$ indicates the modified theoretical corridor width with the additional ΔV , and is equal to the TCW for conventional aerocapture when $\Delta V = 0$. The ΔV corrects for the deficit in speed for a steeper entry than aerocapture, and corrects for excess speed in the case of a shallower entry than possible with aerocapture alone. The propulsive ΔV thus augments control authority and may allow reduction in vehicle L/D requirement. As with the first approach, the primary penalty for this approach is the propellant mass associated with the ΔV maneuver. In addition, the spacecraft has to autonomously determine its orbital state, compute the correction maneuvers, and execute the propulsive burn without any ground intervention immediately after atmospheric exit.

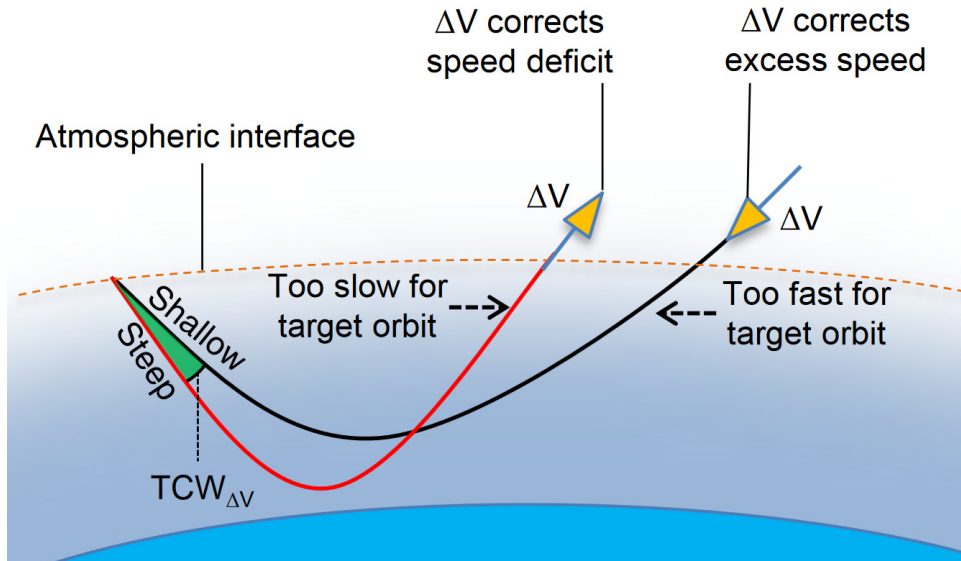


Figure 7.11. Second approach where a propulsive ΔV at atmospheric exit augments control authority.

Figure 7.12 shows the effect of additional propulsive ΔV on the required vehicle L/D . The TCW constraint lines show the 2.0 deg contours for a range of allowable propulsive ΔV .

The green shaded area shows the feasible set of $(L/D, V_\infty)$ for conventional aerocapture with no ΔV maneuver at exit. If a propulsive ΔV maneuver of 1 km/s is allowed, the blue patch becomes feasible, lowering the L/D requirement. After the ΔV maneuver is performed the vehicle has the correct speed to coast to the apoapsis and following a periapsis raise maneuver at the apoapsis enters the desired science orbit.

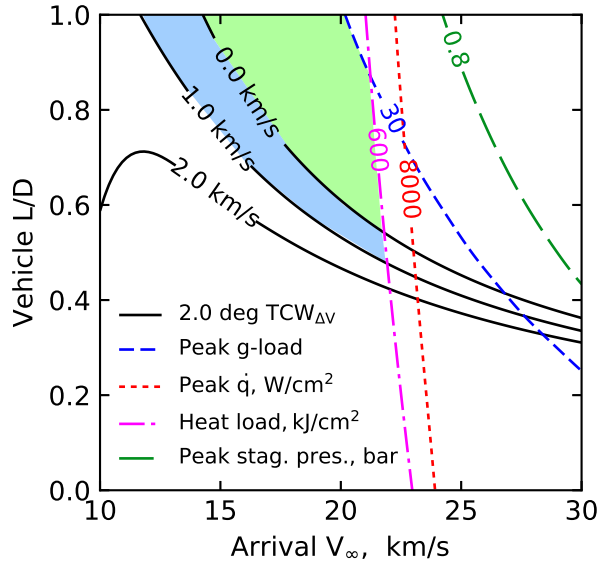


Figure 7.12. Effect of allowable propulsive ΔV at exit on vehicle L/D requirement.

Table 7.6 shows that the additional propulsive ΔV capability widens the theoretical corridor and thus lowers the L/D requirement. However, the reduction in required L/D is small and is not sufficient to enable the use of low- L/D aeroshells within reasonable ΔV of 1 km/s. The propulsive ΔV required to allow use of heritage aeroshells is prohibitively high and leads to unacceptable propellant mass penalty for this hybrid propulsive-aerocapture concept. The propellant mass penalties outweighs the performance benefits and likely introduces additional cost and complexity.

7.7 Pathfinder Probe Concept

The present study investigated the option of sending a pathfinder entry probe into Neptune's atmosphere several weeks ahead of the main aerocapture vehicle reaching the atmospheric entry interface. The objective of the pathfinder probe is to measure the in-situ

Table 7.6. Minimum required L/D for hybrid propulsive-aerocapture approach with a propulsive ΔV maneuver at exit, $V_\infty = 20$ km/s, target orbit = 20 day.

Allowable propulsive ΔV , km/s	$(L/D)_{\min.}$
0.0	0.61
1.0	0.54
2.0	0.47

atmospheric profile and thus reduce the uncertainty in atmospheric profile prior to the aerocapture vehicle arriving at Neptune. Before the discussion of the pathfinder probe concept, it is insightful to discuss the “targeting problem” for aerocapture to illustrate the combined effect of navigation and atmospheric uncertainties. The targeting problem refers to the selection of a nominal target entry flight-path angle (EFPA) for the aerocapture maneuver. Several weeks ahead of entering Neptune, the approach navigation maneuvers target the aim point on the B-plane to allow the spacecraft to reach the atmospheric interface at the selected nominal EFPA.

The TCW is bounded by the shallowest and steepest acceptable EFPA for aerocapture. Figure 7.13 shows the TCW for a vehicle with $L/D = 0.4$ entering Neptune’s atmosphere retrograde at the equator at a planet-relative speed of 33 km/s for $F_{\min\max} = -1, 0$, and $+1$. These values of $F_{\min\max}$ correspond to the minimum, average, and maximum mean density profiles from Neptune-GRAM. Theoretically, if the vehicle enters at any EFPA within the TCW the guidance algorithm can command the appropriate bank angle profile to achieve the desired exit conditions. However, simulations indicate that entry near the shallow limit of the corridor which requires almost full lift down for the entire trajectory are very sensitive to density perturbations. Such full lift down trajectories are not flyable in practice due to the risk of flyaway without getting captured. The hatched regions in Fig. 7.13 show the portion of the corridor rendered inaccessible due to the sensitivity of trajectories near the shallow limit using the guidance algorithm described in Section 7.5 and parameters listed in Appendix C. Thus the usable corridor for Neptune aerocapture is smaller than the theoretical corridor. Though the width of the corridor is not very sensitive to $F_{\min\max}$, the shallow and steep bounds of the usable corridor change significantly based on the mean density profile and

leads to the targeting problem. The selected nominal EFPA should be such that the $\pm 3\sigma$ navigation uncertainty falls within the usable corridor for the entire range of mean density profile uncertainties. Targeting the selected nominal EFPA allows the aerocapture vehicle to achieve the desired exit conditions for any mean atmospheric profile within the specified uncertainty.

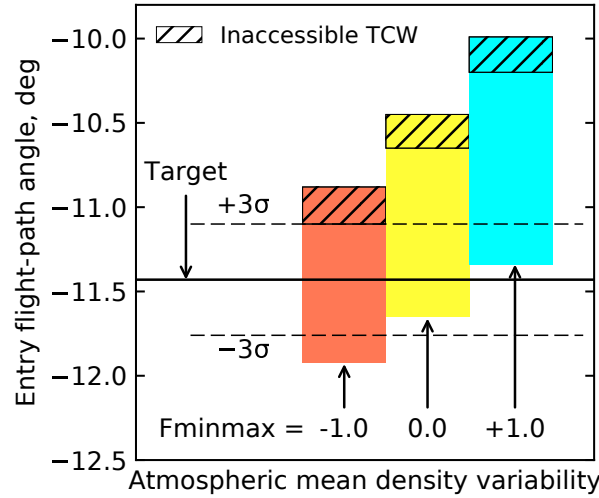


Figure 7.13. The colored blocks show the theoretical corridor for various mean density atmospheric profiles. The target EFPA is chosen to minimize the risk of escape.

In the present study, it is seen that a 3σ EFPA uncertainty of 0.33 deg (see Table 7.4) shown in Fig. 7.13 is not small enough to accommodate the entire range of mean density profiles from $F_{\text{minmax}} = -1$ to $+1$. There is no target EFPA that would allow both the $+3\sigma$ and -3σ delivery error to fall within the usable corridor for the range of atmospheric uncertainties considered. If the vehicle encounters the lowest density atmosphere (i.e. $F_{\text{minmax}} = -1$), and the EFPA falls outside $+3\sigma$, then the vehicle risks not getting captured. To minimize the risk of escape, the target EFPA is chosen such that the $+3\sigma$ delivery error falls just within the usable corridor for the minimum density atmosphere. For the case with the maximum density atmosphere (i.e. $F_{\text{minmax}} = +1$), the target EFPA itself and the -3σ delivery error fall below the theoretical corridor, which implies that the vehicle will undershoot the apoapsis altitude in such a scenario.

Simulations indicate that off-nominal EFPA outside $+3\sigma$ are very likely to flyaway without getting captured, while off-nominal EFPA outside -3σ will only likely result in undershoot of apoapsis but certainly not crash into the planet. The flyway case will almost certainly lead to loss of mission, while the apoapsis undershoot can be corrected using propulsive maneuvers and Triton gravity assists during the course of the mission. It is recommended to bias the target EFPA towards the steep side of the usable corridor to provide sufficient safety margin against the flyaway scenario for minimum density atmosphere, even if the -3σ EFPA bound falls outside the usable corridor for the maximum density atmosphere. Two possible options to increase the safety margin are: 1) decrease the navigation uncertainties further, and 2) reduce the atmospheric uncertainties. The pathfinder probe concept aims to use the second option of reducing atmospheric uncertainties to improve the safety margin against accidental escape.

The concept of operations for the pathfinder probe is as follows. Ahead of the main aerocapture vehicle reaching Neptune, an atmospheric entry probe is released from the main spacecraft. The carrier spacecraft also releases one or more SmallSats on a flyby trajectory with their arrival timed so as to act as a data relay from the probe during entry. The probe coasts to Neptune, while the main spacecraft performs a small propulsive burn such that it arrives at entry interface for aerocapture a few weeks after the probe entry. The probe measures the density in-situ (from accelerometer measurements), along with atmospheric structure and composition. The data is relayed to the main spacecraft via the SmallSats, which in turn relay the data back to Earth. The present study hypothesizes that the in-situ data when coupled with improved atmospheric models and ground based observation campaigns can reduce the uncertainty in the mean density profile to be encountered by the main aerocapture vehicle. The aerocapture vehicle then performs a small TCM to target the optimal EFPA based on the improved atmospheric profile knowledge.

Quantification of the atmospheric uncertainty reduction from a pathfinder entry probe is not possible at the level of the study. For illustration, the present study assumes that the pathfinder probe data is able to constrain the atmospheric uncertainties such that $0.6 \leq F_{\min\max} \leq 0.8$ instead of the full range of $F_{\min\max}$ from -1 to +1. With the reduced uncertainty in $F_{\min\max}$, the target EFPA can be chosen so as to provide sufficient margin

against escape above 3σ in the case of low density atmosphere, and against undershoot in the case of high density atmosphere as shown in Fig. 7.14. The pathfinder probe allows optimal selection of the target EFPA to minimize the risk of accidental escape or apoapsis undershoot. The pathfinder probe can improve the safety margin for aerocapture against escape and undershoot scenarios. Constraints on the timing of probe and SmallSat release, data transmission from the probe to the SmallSats, propulsive ΔV associated with deflection maneuvers, the time available for data analysis and command upload to spacecraft for targeting the optimal EFPA are recommended for further study. It may be possible to let the relay SmallSat carry the pathfinder probe, and the SmallSat separate several months ahead of the main spacecraft reaching Neptune to keep the deflection maneuver ΔV reasonably low. If the two spacecraft can separate before the Jupiter gravity assist, it may be possible to further reduce the required deflection ΔV to achieve the few weeks separation between the pathfinder probe and the main spacecraft reaching Neptune; though this will add significant complexity to the mission architecture.

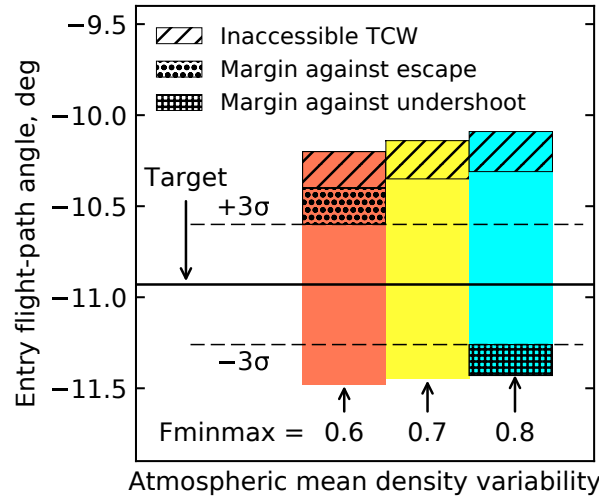


Figure 7.14. Reduced atmospheric uncertainty from a pathfinder probe allows target EFPA selection such that both $+3\sigma$ and -3σ delivery errors fall within the usable corridor. The hatched regions indicate additional margin against escape and undershoot if the EFPA lies beyond the $+3\sigma$ and -3σ respectively.

Inclusion of a pathfinder probe (in addition to a main entry probe) will add cost and complexity to the mission architecture. The design of the pathfinder probe is not part of the

study, and assumes that the primary mission can accommodate the additional mass. The possibility of the pathfinder probe failing to accomplish its mission should be considered, due to entry probe failure, loss of data etc. Loss of the pathfinder probe cannot be a single point failure for the main aerocapture vehicle and should be capable of performing the maneuver with sufficient safety margin even if the data from the pathfinder probe is lost.

In the following section on performance analysis, the hybrid aerocapture approaches in Sec. 7.6 are not considered further. The improved navigation uncertainty estimates from Sec. 7.4, the guidance scheme with onboard density estimation from Sec. 7.5, and the use of a pathfinder probe from Sec. 7.7 are considered for aerocapture performance analysis using a blunt-body aeroshell.

7.8 Performance Analysis

Monte Carlo analysis is used to quantify the vehicle performance in the presence of combined navigation, atmospheric, and aerodynamic uncertainties. Nominal values of the parameters used and the associated uncertainties are listed in Table 7.7. The target entry flight-path angle is chosen based on the discussion presented in Section 7.7. For arrival $V_\infty = 20$ km/s of the reference interplanetary trajectory, the planet/atmosphere relative entry speed can range from 28 km/s for prograde entry to 33 km/s for retrograde entry. The location and width of the entry corridor changes as a function of the planet-relative entry speed and must be accounted for in aerocapture guidance analysis. The arrival declination is 8.8 deg, the entry latitude and heading angles can be computed based on the target orbit inclination [103]. The heading angle is defined as the angle between the velocity vector and the local parallel of latitude following the definition by Vinh et al. [93]. To simplify the trajectory analysis, the aerocapture simulations in this study use equatorial retrograde (180 deg heading angle) and prograde (0 deg heading angle) entry. The apoapsis altitude is computed using the trajectory state at atmospheric exit, defined at the same altitude as the entry interface (1000 km above the 1 bar pressure level). Atmospheric mean density uncertainties and random high frequency perturbations are used from Neptune-GRAM. Three sets of simulations were performed: 1) maximum range of Fminmax, 2) reduced atmospheric uncertainty, and 3) very low atmospheric uncertainty.

7.8.1 Maximum Range of Fminmax

The maximum atmospheric uncertainty case assumes that no improvement is available over data available from Neptune-GRAM and the aerocapture vehicle must accommodate the full range of Fminmax from -1 to +1.

Table 7.7. Monte Carlo uncertainties

Category	Variable	Nominal	$\pm 3\sigma$ or [min,max]	Distribution or other
Navigation	EFPA	-11.43 deg (retrograde)	± 0.33 deg	Normal
		-13.85 deg (prograde)	± 0.33 deg	Normal
Atmosphere	Fminmax	-	[−1, +1]	Uniform
	Mean density	0	3σ (from GRAM)	Normal
	High frequency perturbation	-	rpscale = 1	Uniform
Aerodynamics	L/D	0.40	± 0.04	Uniform

Vehicle parameters used for the simulation are ballistic coefficient $\beta = 200 \text{ kg/m}^2$, drag coefficient $C_D = 1.59$, and nose radius $R_N = 1.0 \text{ m}$. The target apoapsis altitude is 400,000 km, and the apoapsis error tolerance used by the guidance algorithm is 10,000 km. The apoapsis prediction is initiated when the altitude rate exceeds -500 m/s and a guidance frequency of 2 Hz is used for the equilibrium glide phase. The onboard density estimation assumes perfect knowledge of the total measured acceleration and other vehicle parameters and computes the density once during every guidance cycle. Guidance gain parameters used in the simulation are described in Appendix C. If the guidance algorithm predicts an apoapsis altitude lower than the target value, the equilibrium glide phase is terminated immediately and the vehicle flies full lift up. Higher guidance frequency can improve the apoapsis targeting, albeit at the cost of greater onboard computing requirements. Vehicle position and velocity states used by the guidance scheme will have uncertainties associated with inertial sensors but are assumed to be known perfectly. The maximum roll rate is constrained to 30 deg/s. Inclination targeting during the aerocapture maneuver is not considered.

A high-fidelity 3-DoF simulation including gravity zonal harmonics up to J_4 , aerodynamic forces, Coriolis, and centrifugal forces is used to simulate the trajectory of a spacecraft flying in the vicinity of an oblate, rotating planet. The initial state for the entry simulation is the terminal state of the interplanetary approach trajectory using the B-plane targeting method [103]. The aerocapture trajectory is propagated from atmospheric entry to the atmospheric exit interface. The simulation uses an outer loop to propagate the actual vehicle trajectory, and an inner loop to simulate the guidance scheme. Five thousand aerocapture trajectories were simulated for both prograde and retrograde entry for different atmospheric uncertainty levels, and the results are used to assess guidance performance at Neptune using a blunt-body aeroshell.

Retrograde Entry

For the purpose of comparing the targeting accuracy for different cases evaluated, an arbitrary $\pm 50,000$ km bound about the target apoapsis is defined in this study. For the retrograde entry, all but one of the 5000 cases captured successfully with 75% of the cases achieving apoapsis within $\pm 50,000$ km of the target apoapsis (400,000 km). Figure 7.15 shows the histogram of the achieved apoapsis altitude. Figure 7.16 shows the dispersion in apoapsis and periapsis altitude. One trajectory failed to capture and is omitted from Figs. 7.15 and 7.16. The failure is attributed to low mean density (i.e. $F_{\text{minmax}} = -1.0$), -0.4σ variation about the mean profile, and shallow EFPA = -11.02 deg ($+3.7\sigma$) along with the effect of high frequency perturbations.

Figure 7.17 shows the dispersion in peak deceleration and peak stagnation-point heat rate. The stagnation point heat rate is the sum of convective and radiative heating rates computed using engineering correlations [143]. The 99.87 percentile peak deceleration load is $14.32g$, an important parameter for aeroshell structural design and instrument qualification. The 99.87 percentile peak stagnation-point heat rate is $8,152 \text{ W/cm}^2$, an important parameter for TPS material selection and qualification. The heat rate is significantly higher compared to entry at Mars or Titan, but is expected to be within the performance envelope of the HEEET thermal protection system [140]. The 99.87 percentile propulsive ΔV requirement for the periapsis raise and the apoapsis correction maneuver are 315 m/s and 1,841 m/s respectively.

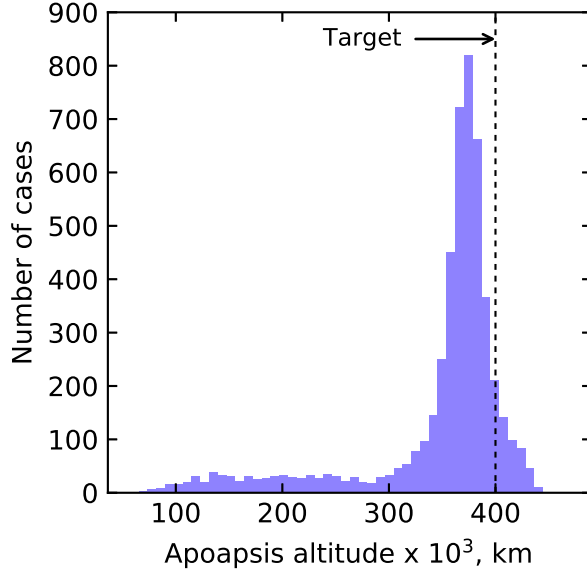


Figure 7.15. Histogram of achieved apoapsis altitude for maximum range of Fminmax. Some cases resulted in significant undershoot (below 300,000 km).

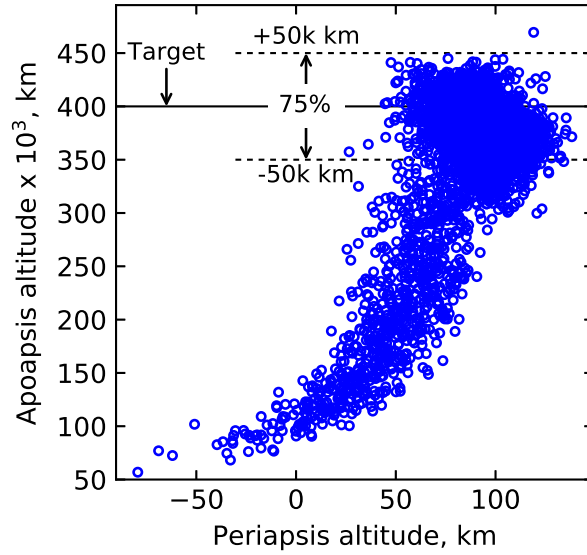


Figure 7.16. Apoapsis dispersion for maximum range of Fminmax (retrograde). 75% of the cases achieved apoapsis within 50,000 km of the target.

The high apoapsis correction ΔV is due to a significant fraction of the cases undershooting the target apoapsis. The apoapsis undershoot in turn is attributed to selection of the target EFPA so as to minimize the risk of escape in the event of minimum density atmosphere

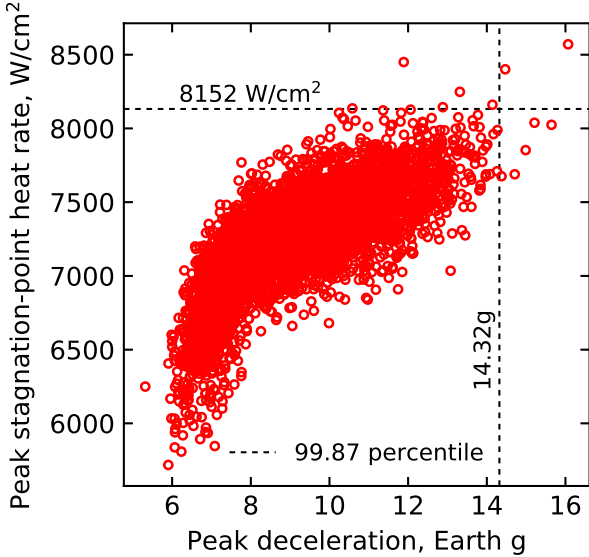


Figure 7.17. Peak deceleration and peak stagnation-point heat rate for maximum range of Fminmax (retrograde). The 99.87 percentile values are 14.32g and 8152 W/cm².

as described in Section 7.7. In the event of high density atmosphere, the nominal target EFPA results in apoapsis undershoot. The study emphasizes that the reported apoapsis correction ΔV values are strongly dependent on the 400,000 km target apoapsis. This is based on the study ground rule that Triton is a high priority science target for a future Neptune mission, and the orbit should be large enough to permit close Triton flybys. If a future mission chooses to forego this requirement to use a much smaller target apoapsis, the apoapsis correction ΔV values will be much smaller. The apoapsis correction ΔV values are also reported to compare the cost of correcting targeting errors for the different atmospheric uncertainty levels and vehicle L/D values considered in this study.

Prograde Entry

For the prograde entry, 98.48% of the cases captured successfully; 0.70% of the cases captured but with apoapsis altitudes greater than 500,000 km; 96% of the cases achieved apoapsis within $\pm 50,000$ km of the target apoapsis ($= 400,000$ km). Figure 7.18 shows the dispersion in apoapsis vs periapsis altitude. The trajectories which failed to capture and

those which resulted in apoapsis altitude greater than 500,000 km are omitted from Fig. 7.18.

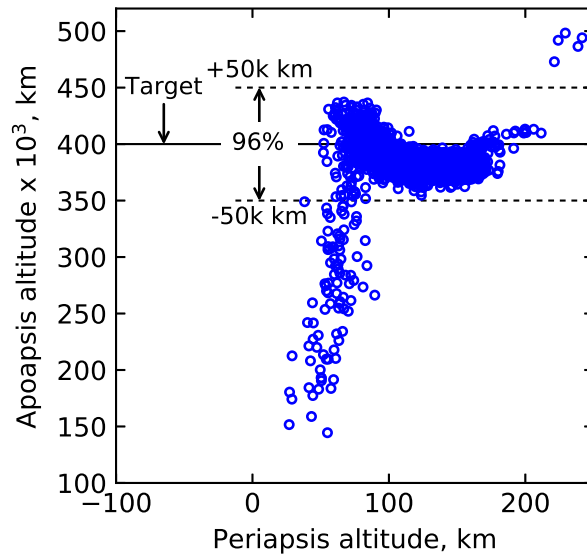


Figure 7.18. Apoapsis vs periapsis altitude for maximum range of Fminmax (prograde). 96% of the cases achieved apoapsis altitude within 50,000 km of the target.

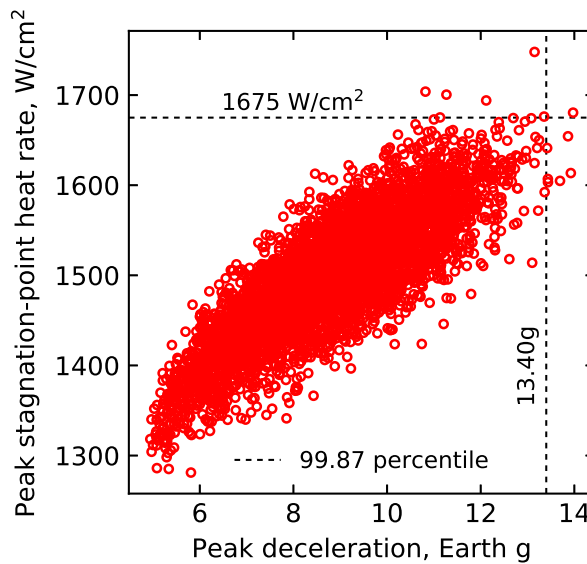


Figure 7.19. Peak deceleration vs peak stagnation-point heat rate for maximum range of Fminmax (prograde). Note the reduction in heat rate compared to retrograde entry (Fig. 7.17).

Figure 7.19 shows the dispersion in peak deceleration and peak stagnation-point heat rate. The 99.87 percentile peak deceleration load and stagnation-point heat rate is $13.40g$ and $1,675 \text{ W/cm}^2$ respectively. The 99.87 percentile stagnation-point heat rate for prograde entry is substantially lower than the retrograde entry case due to the lower planet-relative entry speed for prograde entry. The 99.87 percentile propulsive ΔV requirement for the periapsis raise maneuver and apoapsis correction maneuver is 180 m/s and 664 m/s respectively. Compared to the retrograde entry case where only 0.02% of the cases failed to capture, 1.5% of the cases failed to capture in the prograde case. Despite the lower capture probability, the fraction of cases which achieved apoapsis within $\pm 50,000 \text{ km}$ for the prograde case is 96% compared to 75% for the retrograde case. The cases which failed to capture or resulted in large orbits are attributed to combinations of shallow entry flight-path angles and low density atmosphere. Table 7.8 summarizes the percentiles for various parameters from Monte Carlo simulations with the full range of Fminmax.

7.8.2 Reduced Atmospheric Uncertainty

To investigate the effect of reduced atmospheric uncertainty from potential ground based observations and modelling efforts, the simulation is run with $-0.5 \leq \text{Fminmax} \leq +0.5$, and $\text{rpscale} = 0.5$. Other simulation parameters are the same as listed in Table 7.7. The results are reported for retrograde and prograde entry.

Retrograde Entry

One hundred percent of the cases captured successfully. The percentage of cases that achieved apoapsis within $\pm 50,000 \text{ km}$ of the target is 93% as shown in Fig. 7.20 compared to 75% for the simulations with maximum atmospheric uncertainty. The improved apoapsis targeting lowers the 99.87 percentile apoapsis correction ΔV from 1,840 m/s (Table 7.8) to 328 m/s. Table 7.9 summarizes the Monte Carlo simulation results for the retrograde entry.

Table 7.8. Statistics from Monte Carlo simulation with full range of Fminmax

Percentage captured		Retrograde entry				99.98%	
Percentage within $\pm 50,000$ km of target		Statistics for the 99.98% cases captured				74.94%	
Parameter		Minimum	0.13 percentile	Median	99.87 percentile	Maximum	
Apoapsis altitude, km	56,869	77,399	369,681	441,215	469,411		
Peak deceleration, Earth g	5.32	6.00	9.01	14.32	16.07		
Peak heat rate, W/cm ²	5,718	5,937	7,262	8,152	8,570		
Periapsis raise ΔV , m/s	82.22	87.95	101.67	315.46	372.18		
Apoapsis correction ΔV , m/s	0.04	0.18	51.43	1,840.71	2352.62		
Total propulsive ΔV , m/s	94.83	95.22	152.84	2,158.23	2,724.80		
Percentage captured		Prograde entry				98.48%	
Percentage within $\pm 50,000$ km of target		Statistics for the 98.48% cases captured				95.88%	
Parameter		Minimum	0.13 percentile	Median	99.87 percentile	Maximum	
Apoapsis altitude, km	144,476	183,243	382,066	3,222,790	46,519,543		
Peak deceleration, Earth g	4.75	4.95	8.87	13.40	13.97		
Peak heat rate, W/cm ²	1,264	1,287	1,502	1,675	1,747		
Periapsis raise ΔV , m/s	0.92	13.00	97.85	179.77	212.34		
Apoapsis correction ΔV , m/s	0.08	0.33	29.88	680.80	942.22		
Total propulsive ΔV , m/s	93.34	94.73	127.71	843.59	1154.76		

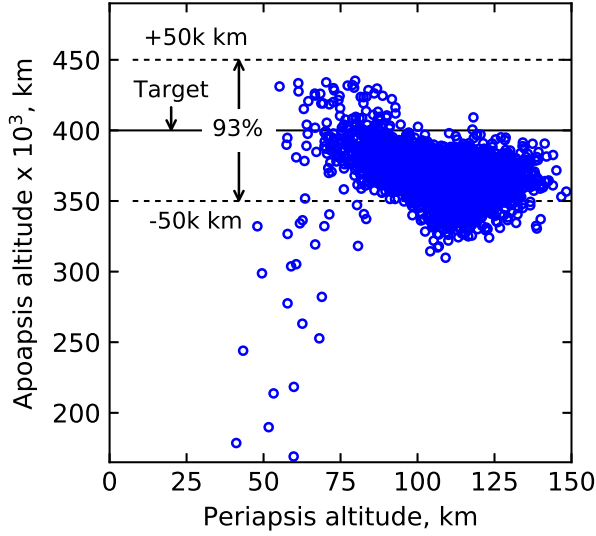


Figure 7.20. Apoapsis vs periapsis altitude for reduced atmospheric uncertainty (retrograde entry). Note the improvement compared to the full range of Fminmax (Fig. 7.16)

Prograde Entry

99.98% of the cases captured successfully. 99.9% of the cases achieved apoapsis within $\pm 50,000$ km of the target apoapsis. Two cases (0.04%) captured but with apoapsis altitudes of 1 million km and 2.8 million km as compared to the target 400,000 km. Compared to the retrograde entry results shown in Fig. 7.20, the improved apoapsis targeting accuracy for the prograde entry lowered the 99.87 percentile apoapsis correction ΔV from 328 m/s to 55 m/s. Table 7.9 summarizes the results for the prograde entry case with reduced atmospheric uncertainty.

The reduced atmospheric uncertainty is likely more realistic compared to the conservative full range of Fminmax [145]. In addition, the present study uses a uniform distribution for range of Fminmax considered to provide conservative estimates. For future studies with more information were available to reduce the atmospheric uncertainties, a more reasonable choice would be a normal distribution about the most likely value of Fminmax.

Table 7.9. Statistics from Monte Carlo simulation with reduced atmospheric uncertainty

	Retrograde entry					
Percentage captured	100%					
Percentage within $\pm 50,000$ km of target	92.60%					
Statistics for the 100% cases captured						
Parameter	Minimum	0.13 percentile	Median	99.87 percentile	Maximum	
Apoapsis altitude, km	169,065	257,918	368,495	430,094	435,187	
Peak deceleration, Earth g	4.94	5.92	7.52	11.82	12.26	
Peak heat rate, W/cm ²	5,701	5,881	6,921	7,631	7,703	
Periapsis raise ΔV , m/s	88.77	89.77	101.59	137.90	190.05	
Apoapsis correction ΔV , m/s	0.14	1.16	53.33	328.47	754.09	
Total propulsive ΔV , m/s	95.36	96.57	154.94	466.31	944.14	
Prograde entry						
Percentage captured	99.98%					
Percentage within $\pm 50,000$ km of target	99.90%					
Statistics for the 99.98% cases captured						
Parameter	Minimum	0.13 percentile	Median	99.87 percentile	Maximum	
Apoapsis altitude, km	263,169	368,826	381,941	425,621	2,778,000	
Peak deceleration, Earth g	4.84	5.31	8.78	12.45	12.78	
Peak heat rate, W/cm ²	1,280	1,317	1,489	1,645	1,681	
Periapsis raise ΔV , m/s	14.97	90.93	97.85	101.46	136.46	
Apoapsis correction ΔV , m/s	0.27	1.84	29.65	55.16	590.61	
Total propulsive ΔV , m/s	95.65	97.35	127.43	155.79	605.58	

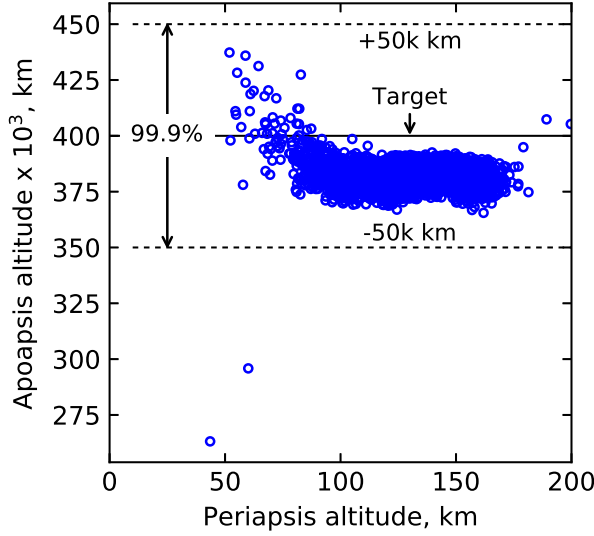


Figure 7.21. Apoapsis vs periapsis altitude for reduced atmospheric uncertainty (prograde entry). 99.9% of the cases achieved apoapsis within 50,000 km of the target.

7.8.3 Very Low Atmospheric Uncertainty

To illustrate the effect of very low atmospheric uncertainty as may be possible using data from a pathfinder probe, the simulation is run with $0.6 \leq F_{\min\max} \leq 0.8$, and $rpscale = 0.5$ as discussed in Sec. 7.7. Based on the discussion presented in Section 7.7 the target EFPA is adjusted to -11.00 deg for the retrograde entry to allow for sufficient margin against escape and undershoot as indicated in Fig. 7.14. The target EFPA for the prograde entry is adjusted to -13.71 deg. Other simulation parameters are the same as listed in Section 7.8.1. One hundred percent of the cases captured successfully for both retrograde and prograde entry scenarios. Figures 7.22 and 7.23 show the achieved apoapsis vs periapsis altitude for retrograde and prograde entry respectively.

The results illustrate the effect of significant reduction of atmospheric uncertainties on apoapsis targeting accuracy. Apoapsis targeting is significantly improved compared to the simulations with the full range of $F_{\min\max}$ but show only a marginal improvement compared to $-0.5 \leq F_{\min\max} \leq +0.5$. The results indicate that if $-0.5 \leq F_{\min\max} \leq +0.5$ is considered acceptable atmospheric uncertainty, a pathfinder probe is not required to provide satisfactory apoapsis targeting. However, if available a pathfinder probe will provide additional safety

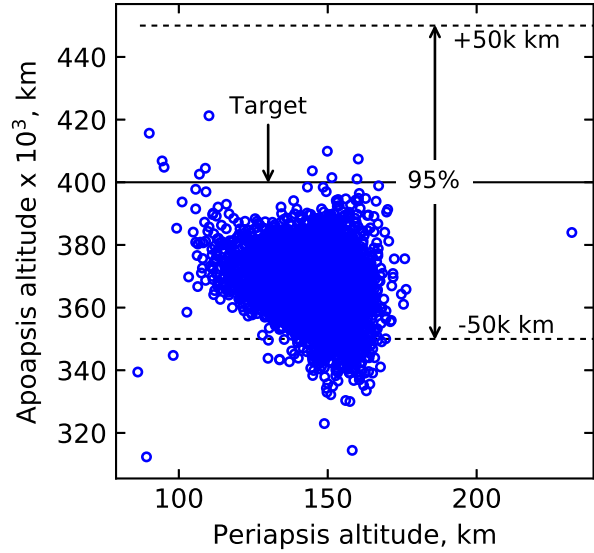


Figure 7.22. Apoapsis vs periapsis altitude for very low atmospheric uncertainty (retrograde entry). Note the significant improvement compared to Figs. 7.16 and 7.20.

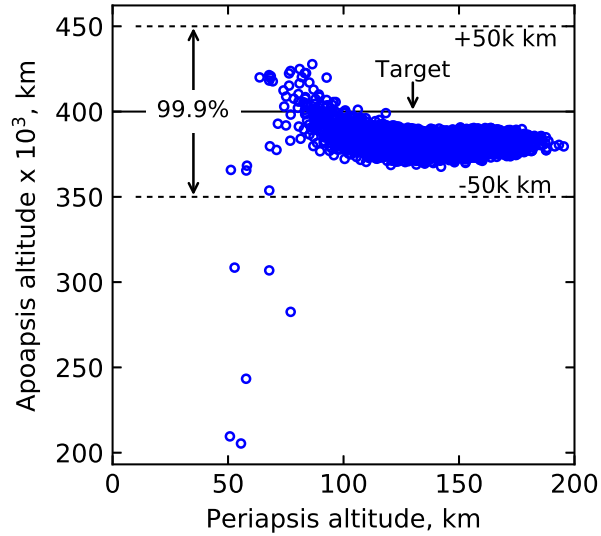


Figure 7.23. Apoapsis vs periapsis altitude for very low atmospheric uncertainty (prograde entry). The accuracy is significantly improved compared to Fig. 7.18, but is similar to Fig. 7.21.

margin against unknown atmospheric phenomena not accounted for in theoretical models. Table 7.10 summarizes the percentiles for various parameters for the very low atmospheric uncertainty scenario. In both Figs. 7.22 and 7.23, the mean apoapsis altitude falls slightly

short of the target 400,000 km. This undershoot is attributed to two reasons: 1) The guidance algorithm predicts exit conditions with full lift up. Once the full lift command is initiated, the vehicle takes a few seconds to roll from its current orientation to full lift up but the delay is not accounted for in the guidance scheme. 2) The estimated density model is not perfect and occasionally shows significant deviation below the minimum altitude at which a measurement was available. Further fine tuning of the guidance parameters may reduce the targeting errors.

7.8.4 Sensitivity to Lift-to-Drag Ratio

The aerodynamic lift-to-drag L/D is the most important vehicle control parameter for trajectory analysis [191], and the designer must account for the effect of variation in L/D on vehicle performance [192]. Even though the present study uses $L/D = 0.4$ as a nominal value for blunt-body aeroshells, the flight derived L/D values for the heritage Apollo entry vehicles range from 0.280 to 0.368 [191], [193]. For the purpose of the L/D sensitivity analysis, a capture probability of 98%, and 75% probability of achieving apoapsis within 50,000 km of the target are arbitrarily defined as the required criteria for mission success. A trade study is performed for $L/D = 0.35$ and 0.30 and various levels of atmospheric uncertainties. The results are for retrograde entry.

For simulations with $-1 \leq F_{\min\max} \leq +1$, $L/D = 0.35$ and 0.30 did not meet the success criteria. To ensure capture for these cases, the target EFPA is substantially biased towards the steep end of the corridor. This results in satisfactory capture rates, but also results in a large number of cases undershooting the target apoapsis as seen in the apoapsis altitude statistics in Tables 7.11 and 7.12. The study recommends a vehicle with L/D of at least 0.40 for such large atmospheric uncertainties if the target apoapsis of 400,000 km is desired. If the mission designer chooses to accept a wide apoapsis altitude distribution as listed in Tables 7.11 and 7.12, then $L/D = 0.35$ and 0.30 may be sufficient.

For $-0.5 \leq F_{\min\max} \leq +0.5$, $L/D = 0.35$ satisfied the success criteria, while $L/D = 0.30$ did not. For $L/D = 0.35$, only 83% achieved apoapsis within 50,000 km of the target compared to 93% for $L/D = 0.40$. For $L/D = 0.30$, EFPA biasing is able to once again provide satisfactory capture rates, but a significant fraction of the cases undershoot the

Table 7.10. Statistics from Monte Carlo simulation with very low atmospheric uncertainty

	Retrograde entry				
Parameter	Minimum	0.13 percentile	Median	99.87 percentile	Maximum
Percentage captured					
Percentage within $\pm 50,000$ km of target				100%	
				95.08%	
Statistics for the 100% cases captured					
Apoapsis altitude, km	312,349	333,208	367,388	404,061	421,240
Peak deceleration, Earth g	3.91	5.49	6.68	9.86	10.83
Peak heat rate, W/cm ²	5,535	5,833	6,553	7,226	7,366
Periapsis raise ΔV , m/s	90.58	93.43	100.93	100.95	117.30
Apoapsis correction ΔV , m/s	1.65	4.39	55.35	123.59	171.63
Total propulsive ΔV , m/s	94.89	98.81	156.27	232.77	288.94
Prograde entry					
Percentage captured				100%	
Percentage within $\pm 50,000$ km of target				99.88%	
Statistics for the 100% cases captured					
Parameter	Minimum	0.13 percentile	Median	99.87 percentile	Maximum
Apoapsis altitude, km	205,390	359,571	381,427	421,065	427,788
Peak deceleration, Earth g	6.00	6.40	8.87	11.80	13.16
Peak heat rate, W/cm ²	1,317	1,337	1,468	1,586	1,597
Periapsis raise ΔV , m/s	89.95	91.36	97.79	105.09	164.91
Apoapsis correction ΔV , m/s	0.28	0.75	30.51	70.10	543.47
Total propulsive ΔV , m/s	95.32	95.88	128.38	175.15	708.38

target apoapsis. L/D of at least 0.35 is recommended for atmospheric uncertainty of $-0.5 \leq F_{\min\max} \leq +0.5$.

For $+0.6 \leq F_{\min\max} \leq +0.8$, $L/D = 0.35$ offers sufficient control authority as seen in Table 7.11. One hundred percent of the cases captured, and the 99.87 percentile total propulsive ΔV required is 250 m/s. For $L/D = 0.30$, EFPA biasing is required to ensure vehicle capture, but 79% of the cases achieved apoapsis within 50k km of the target. The study recommends L/D of at least 0.30 for $+0.6 \leq F_{\min\max} \leq +0.8$. The results of the L/D trade study are summarized in Table 7.13 and the simulation statistics show the effect of L/D reduction in aerocapture performance.

7.9 Summary

The present study investigated the feasibility and guidance performance of using heritage low- L/D blunt-body aeroshells for aerocapture at Neptune. Previous studies addressing Neptune aerocapture have used a mid- L/D vehicle which requires significant development and testing before use in planetary missions. The lack of a mid- L/D vehicle motivated the investigation of techniques which may allow the use of low- L/D blunt-body aeroshells which have been extensively tested and flown. The aerocapture feasibility chart is used to concisely assess the coupling between interplanetary trajectory and vehicle performance trade space during preliminary mission design. Interplanetary trajectories with high arrival V_∞ allow the vehicle L/D requirement to be lowered while providing significantly shorter time of flight to Neptune. An Earth-Jupiter-Neptune trajectory launching in 2031 with a 7.87 year flight time is selected as the reference trajectory. Approach navigation analysis using state-of-the-art techniques have shown that delivery errors can be reduced compared to previous estimates. A new guidance algorithm with onboard density estimation is shown to be able to guide the spacecraft to the desired exit conditions even in worst case atmospheric uncertainties. The study concludes that the first hybrid aerocapture-propulsive approach does not allow the use low- L/D aeroshells for acceptable ΔV penalty, though this conclusion holds only for the 20-day science orbit considered. Smaller science orbits of the order of 1-day or smaller may use this approach without the prohibitively large ΔV associated with this approach. The second hybrid approach also does not allow the use of heritage blunt-body aeroshells. The

Table 7.11. Statistics from Monte Carlo simulation with $L/D = 0.35$

-1.0 ≤ Eminmax ≤ +1.0; Retrograde entry, EFPA = -11.58 deg (biased to the steep side to ensure capture)						
Parameter	Minimum	0.13 percentile	Median	99.87 percentile	Maximum	
Apoapsis altitude, km	26,799	28,526	293,630	441,328	448,812	
Periapsis raise ΔV , m/s	86.67	87.96	124.00	489.27	503.09	
Total propulsive ΔV , m/s	95.09	95.33	344.09	4,023	4,140	
-0.5 ≤ Eminmax ≤ +0.5; Retrograde entry, EFPA = -11.33 deg						
Percentage captured	100%	44.75%				
Percentage within ±50,000 km of target						
Parameter	Minimum	0.13 percentile	Median	99.87 percentile	Maximum	
Apoapsis altitude, km	73,049	92,774	368,664	436,622	442,759	
Periapsis raise ΔV , m/s	87.30	88.30	101.50	282.54	325.74	
Total propulsive ΔV , m/s	94.63	95.31	154.53	1,840	2,260	
+0.6 ≤ Eminmax ≤ +0.8; Retrograde entry, EFPA = -10.94 deg						
Percentage captured	100%	83.44%				
Percentage within ±50,000 km of target						
Parameter	Minimum	0.13 percentile	Median	99.87 percentile	Maximum	
Apoapsis altitude, km	287,017	326,223	364,423	407,931	430,583	
Periapsis raise ΔV , m/s	88.54	92.26	101.39	111.37	125.62	
Total propulsive ΔV , m/s	94.00	95.57	162.13	250.46	363.71	

Table 7.12. Statistics from Monte Carlo simulation with $L/D = 0.30$

-1.0 $\leq \bar{E}_{\text{minmax}} \leq +1.0$; Retrograde entry, EFPA = -11.61 deg (biased to the steep side to ensure capture)						
Parameter	Minimum	0.13 percentile	Median	99.87 percentile	Maximum	
Apoapsis altitude, km	5,811	8,815	93,028	441,715	446,133	
Periapsis raise ΔV , m/s	86.89	87.63	280.96	670.02	760.56	
Total propulsive ΔV , m/s	95.54	95.87	1,835	5,781	6,225	
-0.5 $\leq \bar{E}_{\text{minmax}} \leq +0.5$; Retrograde entry, EFPA = -11.33 deg (biased to the steep side to ensure capture)						
Parameter	Minimum	0.13 percentile	Median	99.87 percentile	Maximum	
Apoapsis altitude, km	54,508	55,198	361,561	426,603	430,035	
Periapsis raise ΔV , m/s	89.25	89.42	103.04	367.21	370.15	
Total propulsive ΔV , m/s	94.53	95.44	169.12	2,770	2,795	
+0.6 $\leq \bar{E}_{\text{minmax}} \leq +0.8$; Retrograde entry, EFPA = -10.93 deg (biased to the steep side to ensure capture)						
Parameter	Minimum	0.13 percentile	Median	99.87 percentile	Maximum	
Apoapsis altitude, km	77,679	124,057	363,001	408,606	419,946	
Periapsis raise ΔV , m/s	90.36	92.04	101.56	230.23	309.98	
Total propulsive ΔV , m/s	93.82	95.07	164.97	1,370	2,145	

Table 7.13. Percentage captured for various L/D and atmospheric uncertainty levels; values in parentheses indicate percentage which achieved apoapsis within 50k km of the target.

Fminmax range	Remark	L/D		
		0.4	0.35	0.30
-1.0 to +1.0	Maximum	99.9% (75%)	100% ^a (45%)	100% ^a (20%)
-0.5 to +0.5	Reduced	100% (93%)	100% (83%)	100% ^a (62%)
0.6 to 0.8	Very low	100% (98%)	100% (90%)	100% ^a (79%)

^a With EFPA biasing to the steep side to ensure capture, resulting in apoapsis undershoot. See Tables 7.11 and 7.12 for apoapsis distribution.

study finds that a pathfinder probe is not necessary for aerocapture at Neptune if the risk of apoapsis undershoot is within acceptable limits. The pathfinder probe is recommended to be used as an option to enhance the safety margins and probability of mission success, but not as an enabling option for ice giant missions. Monte Carlo simulation is used to test guidance performance with combined navigation, atmospheric, and aerodynamic uncertainties.

7.10 Conclusion

Results indicate that the reduced navigation uncertainty and the improved guidance scheme enable a heritage blunt-body aeroshell with $L/D = 0.30\text{--}0.40$ to perform aerocapture at Neptune. The expected peak heat-rate is in the range of 1600 to 8150 W/cm² and is within the capabilities of HEEET TPS material. For a vehicle with $L/D = 0.40$ entering retrograde and even with worst-case atmospheric uncertainty, 99.98% of the cases captured successfully and 75% of the cases achieved apoapsis altitude within 50,000 km of the target. For the lower atmospheric uncertainty levels considered, the L/D of 0.3–0.4 is shown to provide satisfactory performance. Additional study is required to estimate the TPS mass fraction of blunt-body vehicles entering Neptune at planet-relative speeds of 28–33 km/s.

8. AEROCAPTURE MISSION ANALYSIS TOOL (AMAT)

The tools for identification of trajectories and techniques that enhance or enable planetary missions or substantially reduce their cost is of utmost importance in realizing planetary exploration missions within budgetary and schedule constraints [69]. The history of planetary exploration provides numerous examples such as the Grand Tour trajectories identified by Flandro [170] at the Jet Propulsion Laboratory without which the Voyager missions may have never been flown. The Planetary Science Decadal Survey recommends a sustained investment in the development of new trajectories and techniques that would provide a rich set of options for future missions. Aerocapture has been the subject of study for nearly six decades as a key technology for future Solar System exploration. Generally, there are two types of studies to formulate new mission concepts: 1) rapid mission architecture (RMA) studies which investigate a very broad range of mission concepts to identify a promising approach, and 2) a point design study which subjects the most promising approach identified in the RMA to a full mission study [69]. Full mission studies typically involve multiple NASA centers and substantial labor, and hence it is of vital importance that extensive trade studies are performed before committing to a point design. The lack of architectural-level tools and methods and perform rapid high-level assessments of aerocapture at various destinations was identified by the Ice Giants Pre-Decadal Survey Mission Study in 2016 [133]. The Aerocapture Mission Analysis Tool (AMAT) is intended to fill this gap, by encapsulating the systems framework developed in this thesis in an interactive easy-to-use software package. AMAT may be used in real-time rapid aerocapture mission architecture studies such as those performed by the JPL A-Team, and for higher-fidelity point design mission studies by JPL Team X. AMAT is available for general public use under the CC-BY-SA-4.0 license.

8.1 History

Researchers at Purdue University led the aerocapture assessment studies in support of the Ice Giants Pre-Decadal Mission Study [133], and have since then been extending the methods and tools for other atmosphere-bearing Solar System destinations. The focus was on developing a systems engineering framework for rapid mission studies. Lu [59] and Girija

[60] conceptualized the aerocapture feasibility charts, a graphical method for aerocapture mission design and forms the core of the AMAT package. Much of the AMAT source code was originally written in support of Venus and Ice Giant mission studies performed as part of this dissertation. AMAT was first publicly released in October 2019, and has since then periodically maintained and updated by the author. In the spirit of open code for open science, AMAT is free and open-source to foster universal access to the knowledge, and allow reproducibility of results.

8.2 Previously Developed Aerocapture Tools

Two previously developed aerocapture mission analysis tools were identified in the literature survey (See Chapter 2), and are briefly described here for completeness.

8.2.1 ACAPS

The aerocapture simulation tool (ACAPS) is a MATLAB-based three-degrees-of-freedom point mass simulation model developed by Leszczynski [26] at the Naval Postgraduate School in 1998. ACAPS was designed to support the JPL Project Design Center toolkit as preliminary design software for the Mars 2005 Sample Return (MSR) Mission and other missions which proposed to use aerocapture at the time. The package and the source-code could not be located in the public domain at the time of writing.

8.2.2 HyperPASS

Hypersonic Planetary Aero-assist Simulation System (HyperPASS) is an aero-assist software tool developed by the Global Aerospace Corporation in 2003 [194]. HyperPASS features a MATLAB-based graphical user interface (GUI) which allows a user to set-up and run aerocapture simulations for both rigid aeroshells and ballute aerocapture. The package could not be located in the public domain at the time of writing.

8.3 Software Description

AMAT is an open source collection of Python subroutines designed to provide rapid mission analysis capability for aerocapture missions to the planetary science community. AMAT allows the user to perform low-fidelity broad sweep parametric studies; as well as high fidelity Monte Carlo simulations to quantify aerocapture performance. AMAT comes with a suite of tools to allow end-to-end conceptual design of aerocapture missions: launch vehicle performance calculator, extensive database of interplanetary trajectories, atmosphere models, guidance schemes, and aero-heating models. AMAT supports analysis for Venus, Earth, Mars, Titan, Uranus, and Neptune for both lift and drag modulation control techniques.

8.3.1 Choice of Programming Language

Python is a general purpose programming language with an extensive collection of free and open-source scientific computing libraries, and is well suited for interactive work and rapid prototyping. Alternative programming languages such as MATLAB[®], C++, and FORTRAN were considered in the early phase of the tool development. Since the tool was designed to be free and open-source, MATLAB[®] being a proprietary software was not a feasible option. Compared to C++ and FORTAN, Python is supported by a rich ecosystem of libraries for computing and data visualization and was the natural choice for an interactive analysis tool such as AMAT.

8.3.2 Source Code

The core AMAT package contains approximately 8,000 source lines of object oriented Python code providing functionalities for end-to-end conceptual design starting from launch vehicle performance to high-fidelity Monte Carlo simulations of aerocapture trajectories. The most up to date version of source code is available on GitHub¹. GitHub was the platform of choice to ensure long term archival, and facilitate contributions from future users who may add new functionalities to improve the package.

¹[↑https://github.com/athulpg007/AMAT](https://github.com/athulpg007/AMAT)

8.3.3 Documentation

AMAT features extensive documentation to help new users get started and use the package for their own conceptual design exercises in an interactive design environment. AMAT leverages the capability provided by the Sphinx software package to automatically generate documentation from the source code [195]. The most up to date AMAT documentation is available online², and is automatically updated if there are changes to the AMAT source code maintained on GitHub.

8.3.4 Installation and Example Jupyter Notebooks

AMAT can be easily installed on any Windows/Mac/Linux machine with a few simple steps. Three different installation methods are described in Appendix D. AMAT will automatically download any required libraries which are missing from the Python Package Index, and typically takes less than a minute to complete the installation. The user can now run the included interactive Jupyter Notebooks³. Jupyter Notebook is an open-source software that allows creation of documents with interactive live code, visualizations, and narrative text. Appendix E provides a sample set of example Jupyter Notebooks included with AMAT.

8.4 Workflow

The high-level workflow for using AMAT in rapid mission studies is shown in Fig. 8.1. The mission designer defines a set of key vehicle parameters such as the ballistic coefficient along with acceptable constraint values such as TCW and peak heat rate. Based on these vehicle parameters, AMAT creates aerocapture feasibility charts and determines if there is a feasible set of vehicle L/D (or β_2/β_1) and arrival V_∞ . The mission designer also defines a baseline launch vehicle and high-level constraints such as launch mass and time of flight for the interplanetary trajectory. If there is a feasible set of trajectories that satisfy both the vehicle design and interplanetary trajectory constraints, a baseline vehicle design and trajectory is selected. Monte Carlo analysis is used to quantify orbit targeting accuracy and

²<https://amat.readthedocs.io>

³<https://amat.readthedocs.io/en/master/jupyterlink.html>

other parameters such as the peak heat rate in the presence of navigation and atmospheric uncertainties. If the vehicle performance is acceptable, the selected baseline design may be used as a starting point for higher fidelity subsystem-level design and analysis.

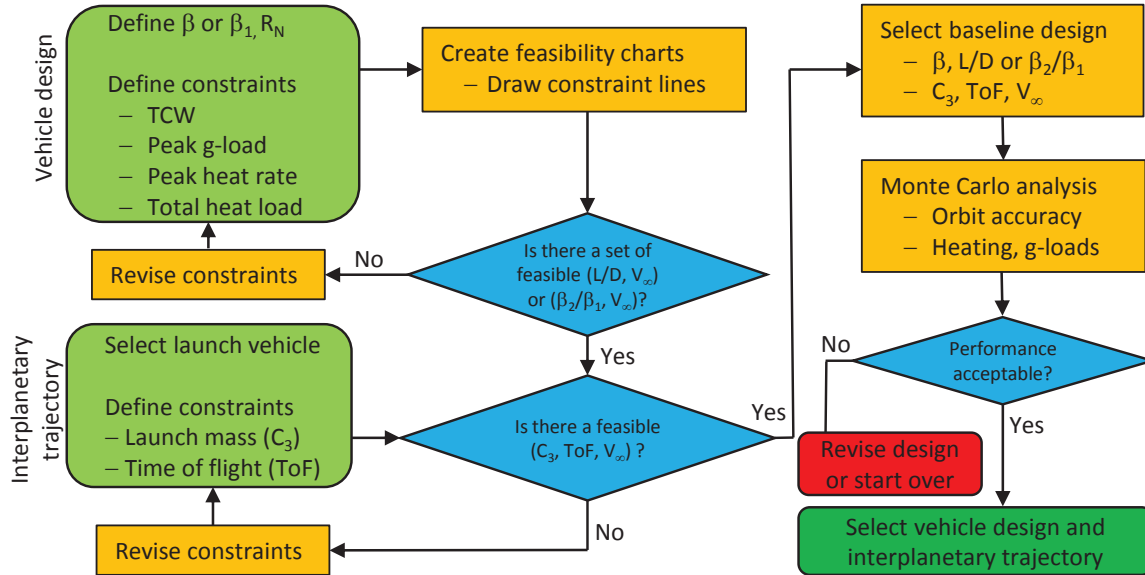


Figure 8.1. AMAT rapid mission design workflow.

8.5 Examples

In this section, the use of AMAT in rapid mission studies is illustrated with its application to two problems: Venus SmallSat aerocapture and Neptune aerocapture using blunt-body aeroshells. The above mentioned problems and potential solutions have been described extensively in Chapters 6 and 7 respectively and hence, are not repeated here. These examples illustrate the interactive rapid design capability offered by such AMAT in early concept exploration studies for aerocapture missions.

8.5.1 Venus SmallSat Aerocapture

The reader is referred to Appendix F for details on how AMAT is used to generate the feasibility charts for comprehensive trade space exploration. Appendix G illustrates the use of AMAT in performance assessment of the baseline design using Monte Carlo simulations.

AMAT enables the entire exercise can performed in a ‘real-time’ interactive mode, and can allows rapid trade studies and ‘what-if’ scenarios to allow the mission designers to select the most promising baseline candidate(s).

8.5.2 Neptune Aerocapture Using Blunt-Body Aeroshells

The reader is referred to Appendix H for details on how AMAT is used to explore the vehicle design and interplanetary trajectory trade space, and identity promising combinations for additional study. Appendix I illustrates the use of AMAT in performance assessment incorporating the effects of delivery, atmospheric, and aerodynamic uncertainties. For the case of Neptune where delivery and atmospheric uncertainties are rather large and not well known, AMAT offers the capability to perform parametric studies for a range of these uncertainties. Such studies allow mission designers to test extreme cases (eg: very large atmospheric uncertainty) and understand the limits of system performance in real-time trade studies.

8.6 Future Work

AMAT is a modular and extendable software tool designed to keeping in mind the evolving needs of future planetary exploration missions. The source-code is publicly available so as to allow future researchers to modify the core package, as well as add new functionality to AMAT and integrate it with other mission design tools. A few potential ideas for future investigation are listed below.

- Improved guidance schemes and estimation methods for lift and drag modulation aerocapture such as direct force control to improve orbit targeting accuracy.
- Add support for EDL and probe mission concepts in the areas of guidance for precision landing, probe-orbiter telecom link analysis, and real-time telemetry from aerocapture vehicles at deep space destinations.
- Add support for aero-gravity assist mission analysis, with potential applications to Titan and Enceladus mission concepts.

- Pairing AMAT with Blender⁴, an open-source 3D rendering software and NASA 3D models⁵ of planets and spacecraft to produce realistic high quality visualization of aerocapture mission concepts.

8.7 Summary

AMAT is an open-source Python package designed to provide rapid mission design and analysis capability for aerocapture mission concepts. The systems framework developed in this thesis forms the core of the AMAT package, and enables rapid end-to-end mission design in a concurrent engineering environment. The package comes with extensive documentation, numerous examples to help the user get started, and publicly available source code to ensure long-term accessibility of the code and facilitate potential contributions from future researchers and mission designers.

⁴↑<https://www.blender.org>

⁵↑<https://solarsystem.nasa.gov/resources>

9. [MAGNETIC SAILS FOR SPACECRAFT DEORBIT¹, ²

All atmosphere-bearing bodies in the Solar System also have an ionosphere which extends from their upper atmospheres to the edge of space. The ionosphere is ionized primarily by solar Extreme Ultraviolet (EUV) radiation and contains a significant concentration of ions and free electrons. The Earth's ionosphere extends from 100 km to about 2000 km and is mainly composed of O+, H+ ions and electrons. A magnetic sail is a concept which uses a magnetic field on board the spacecraft to deflect the oncoming charged particles, which in turn causes drag and allows the spacecraft to slow down and lower its orbit. This is the concept of ionospheric aerobraking or plasma aerobraking. A more ambitious and novel concept is magnetoshell aerocapture, where a powerful magnetic field on the spacecraft is used to create a plasma parachute which deflects both ions and neutral particles and decelerates the spacecraft in a single pass through a planetary ionosphere. Since the maneuver is performed much high up in the rarefied atmosphere, the spacecraft practically encounters no aerodynamic heating as compared to aerocapture and thus requires no special thermal protection systems much like present day aerobraking. Such devices are particularly attractive for outer planet missions such as those to Uranus and Neptune, where aerocapture often requires substantial thermal protection system mass. The drag produced by the magnetoshell can be modulated by controlling the power supplied to the plasma device, and hence allows continuous drag modulation control throughout the ionospheric maneuver. This chapter explores the possibility of using ionospheric braking to deorbit satellites in Low Earth Orbit (LEO) from altitudes of 800–2000 km, where conventional drag sail devices are no longer effective. A low-cost CubeSat mission is proposed to demonstrate the technology in LEO, and applications to future planetary missions as well as interstellar travel are briefly discussed.

¹↑This chapter describes advanced concepts such as plasma aerobraking and magnetoshell aerocapture. Readers who wish to focus on conventional aerocapture may skip this chapter without loss of continuity.

²↑The work described in this chapter was performed at Pioneer Astronautics, Lakewood, CO under contract with NASA (Contract #80NSSC20C0619). U.S. government sponsorship is acknowledged.

9.1 Introduction to Magnetic Sails

The magnetic sail was co-invented by Robert Zubrin and Dana Andrews in the early 1990s [196]. They showed how a magnetic sail making use of high temperature superconducting wire could utilize the dynamic pressure of the solar wind to generate sufficient force to enable a spacecraft to sail around the solar system, or alternatively, allow a relativistic interstellar spacecraft to generate sufficient drag against the interstellar medium to allow it to decelerate without the use of propellant.

Superconducting wire was necessary for interplanetary or interstellar applications because the low density of the plasmas present in such regions required very powerful magnetic fields to produce significant force. The unmet need for high temperature superconducting wire has put those applications on hold thus far. However in Earth orbit, the plasma density is five orders of magnitude greater than that in interplanetary space, and six orders greater than the interstellar medium. As a result, magsails using ordinary aluminum or copper wire can be highly effective drag devices in Earth orbit, particularly for deorbiting satellites from altitudes of 750–2000 km.

9.2 Analytic Model for MagSail Drag in LEO

The magsail creates drag against the ambient plasma wind by creating an artificial magnetosphere, similar to the one created by the Earth’s magnetic field in the solar wind. The magnetosphere is defined as the region surrounding an object within which the motion of charged particles is dominated by the magnetic field of that object. When a magnetic field is emplaced in a flow of charged particles, the object’s magnetic field deflects the particles around the object. The magnetosphere is a ‘hollow’ region from which the charged particles from the plasma flow are largely excluded, and the size and shape of the magnetosphere determines the drag produced by a magsail. This section reviews an analytic solution of the magnetosphere boundary (called the magnetopause) for plasma flow past a simple magnetic dipole, and is used to provide a preliminary estimate of the drag area produced by a magsail.

9.2.1 Magnetosphere Boundary for Plasma Flow Past a Dipole

An analytic solution for the magnetosphere boundary for a magnetic dipole immersed in a plasma flow was derived by Spreiter and Briggs in 1962 [197]. They applied the solution to compute the location of Earth's magnetopause, the boundary within which the Earth's magnetic field dominates the motion of charged particles, rather than the motion of the solar wind. McKinzie and Julius [198] extended the solution to compute the magnetopause and the drag force created by current loops in a plasma flow at various angles of flow incidence. A fundamental parameter in magnetosphere studies both in planetary magnetospheres and in artificial ones such as those created by magsails is the characteristic magnetosphere size L , which is defined (following Inamori et al. [199])

$$L = \left(\frac{\mu_0 M_d^2}{8\pi^2 n_0 m_i u^2} \right)^{\frac{1}{6}} \quad (9.1)$$

where μ_0 is the magnetic permeability of free space, M_d is the magnetic moment in Am^2 , n_0 is the plasma number density, m_i is the ion mass, and u is the plasma flow velocity. For the Earth in the solar wind, $M_d = 8 \times 10^{22} Am^2$, $n_0 = 5 \times 10^6 m^{-3}$, $m_i = 1$ amu (H+ ions), and $u = 400$ km/s, Eq. 9.1 yields $L \simeq 10 R_E$, where R_E is the radius of the Earth. This value is in good agreement with the observed magnetopause distance in the sunward direction under nominal solar wind conditions, although it changes substantially in response to the changing solar wind conditions. Nevertheless, it provides a good approximation for preliminary analysis of the magsail performance. It is noted that in LEO, the Earth's magnetic field is substantial ($\simeq 25,000$ nT) compared to that in interplanetary space which is only about 5 nT. Figure 1 shows the analytic solution for the magnetopause derived by Spreiter and Briggs [197]. The axes have been normalized by the characteristic length L . The dipole is located at the origin, and the plasma flow is from right to left.

The drag force due to charged particles being deflected is

$$F_D = \frac{1}{2} n_0 m_i C_D (\pi L^2) u^2 \quad (9.2)$$

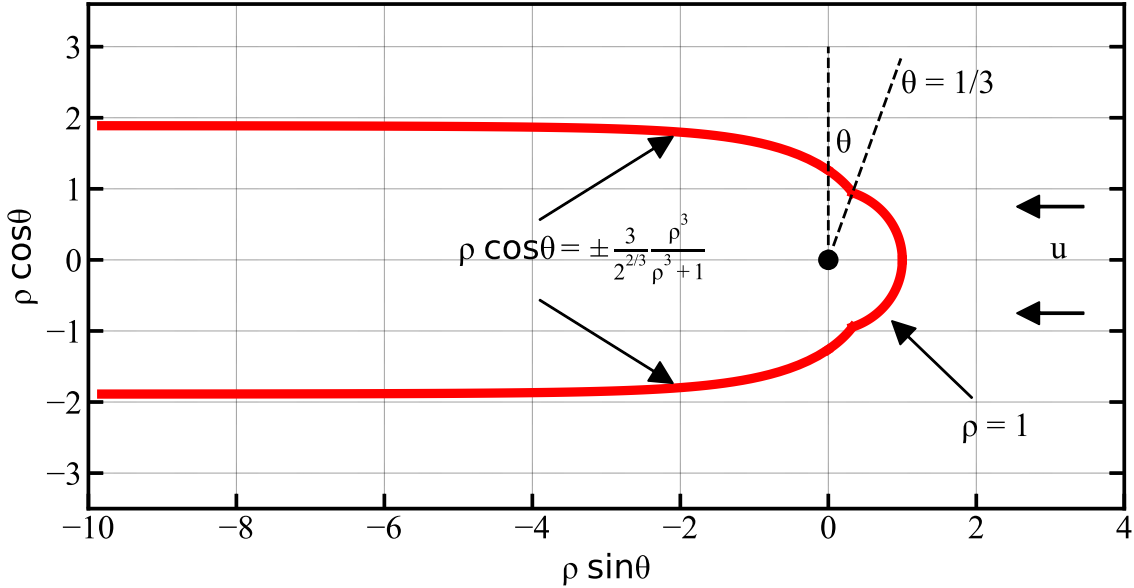


Figure 9.1. Analytic solution of the magnetopause for a dipole in a plasma flow derived by Spreiter and Briggs [197]. The axes have been normalized by L .

where, F_D is the drag force, C_D is the drag coefficient, and πL^2 is the reference area for drag calculation. McKinzie and Julius [198] reported an analytical value for the $CD = 4.10$, but more recent studies have corrected this to 3.60 based on more detailed MHD analysis [200]. The simple drag model enables an analytic treatment of magsail performance in the following subsection.

9.2.2 Analytic Model for Magsail Performance in LEO

Consider a magsail made of a circular wire loop of radius r_0 , with cross-sectional area a , wire length $2\pi r_0$, material density ρ , and electrical resistivity η . The mass M of the magsail (not including deployment and support structures) and the wire resistance R are

$$M = \rho a (2\pi r_0) \quad (9.3)$$

$$R = \frac{\eta (2\pi r_0)}{a} \quad (9.4)$$

The magnetic field at the center of the wire loop B_0 is

$$B_0 = \frac{\mu_0 I}{2r_0} \quad (9.5)$$

where I is the steady state DC current in the wire. To first approximation, the magnetic field strength falls off as $1/r^3$ with increasing distance from the center of the wire. Hence the magnetic field B at a distance r from the center of the loop is

$$B = B_0 \left(\frac{r_0}{r} \right)^3 \quad (9.6)$$

The characteristic length scale of the magnetosphere L is the distance at which the magnetic pressure is balanced by the plasma dynamic pressure.

$$\frac{B^2}{2\mu_0} = \frac{1}{2} n_0 m_i u^2 \quad (9.7)$$

Using Eqs. 9.5, 9.6 in Eq. 9.7 and simplifying,

$$\frac{1}{2\mu_0} \left(\frac{\mu_0 I}{2r_0} \right)^2 \left(\frac{r_0}{L} \right)^6 = \frac{1}{2} n_0 m_i u^2 \quad (9.8)$$

$$L = \left(\frac{\mu_0 I^2}{4r_0^2 n_0 m_i u^2} \right)^{\frac{1}{6}} r_0 \quad (9.9)$$

Using Eq. 9.2 the drag force on the magsail is

$$D = \frac{1}{2} n_0 m_i C_D \left[\pi \left(\frac{\mu_0 I^2}{4r_0^2 n_0 m_i u^2} \right)^{\frac{1}{3}} r_0^2 \right] u^2 \quad (9.10)$$

Typically, the available power on board a spacecraft is limited and a major design consideration, hence it is better to express the current I in terms of the available power P as

$$I^2 = \frac{P}{R} = \frac{Pa}{\eta(2\pi r_0)} \quad (9.11)$$

$$D = \frac{1}{2} n_0 m_i C_D \left[\pi \left(\frac{\mu_0 P a}{4r_0^2 n_0 m_i u^2 \eta (2\pi r_0)} \right)^{\frac{1}{3}} r_0^2 \right] u^2 \quad (9.12)$$

$$D = \frac{1}{2} n_0 m_i C_D \pi \left(\frac{\mu_0 P a}{4n_0 m_i u^2 \eta (2\pi)} \right)^{\frac{1}{3}} r_0 u^2 \quad (9.13)$$

For a fixed wire mass M ,

$$a = \frac{M}{2\pi r_0 \rho} \quad (9.14)$$

Using Eq. 9.14 in Eq. 9.13,

$$D = \frac{1}{2} n_0 m_i C_D \pi \left(\frac{\mu_0 P M}{4n_0 m_i (2\pi r_0 \rho) u^2 \eta (2\pi)} \right)^{\frac{1}{3}} r_0 u^2 \quad (9.15)$$

$$D = \frac{1}{2} n_0 m_i C_D \pi \left(\frac{\mu_0 P M}{16\pi^2 n_0 m_i \rho u^2 \eta} \right)^{\frac{1}{3}} r_0^{2/3} u^2 \quad (9.16)$$

The drag to mass ratio D/M (or the drag acceleration) for the magsail can thus be expressed as

$$\frac{D}{M} = \frac{1}{2} n_0^{2/3} m_i^{2/3} C_D \pi \left(\frac{\mu_0 P}{16\pi^2 \rho u^2 \eta} \right)^{\frac{1}{3}} \frac{r_0^{2/3} u^2}{M^{2/3}}$$

$$\boxed{\frac{D}{M} = \frac{1}{4} (n_0 m_i u^2)^{2/3} C_D \pi \left(\frac{\mu_0 P}{2\pi^2 \rho \eta} \right)^{\frac{1}{3}} \frac{r_0^{2/3}}{M^{2/3}}} \quad (9.17)$$

Eq. 9.17 implies that for a fixed power P , and wire mass M , the drag-to-mass ratio of the magsail goes as $r_0^{2/3}$. Hence the larger the loop radius, the better the magsail performance is in terms of the drag-to-mass ratio. This is an important conclusion from the analysis, as it is desirable to have as large a loop diameter as possible to maximize the magsail performance. Of course, a very large diameter loop will be difficult to deploy in practice and for a fixed mass, will result in very low wire cross sectional area which will overheat the wire. The magsail design must achieve as large a diameter as possible, while still being able to be deployed from a packaged configuration inside the spacecraft. Regarding the choice

of the material, it is desirable to have low mass density as well as low electrical resistivity. Aluminum is a desirable material for the wire as it offers a combination of low density and low electrical resistivity. Materials such as copper or silver provide lower electrical resistivity than aluminum, but are heavier.

It is illustrative to compare the D/M of a magsail to that of a solar sail (or drag sail) which uses a drag area to create aerodynamic drag for deorbiting satellites. The aerodynamic drag is

$$F_{D,aero} = \frac{1}{2}\rho_T u^2 S C_D \quad (9.18)$$

where ρ_T is the density of the atmosphere at the relevant altitude, S is the reference area which is typically the cross sectional area of the aerodynamic drag device and CD is the drag coefficient. Typical values of CD for a flat plate in LEO held normal to the wind range from 2.1 to 2.4 [201], a nominal value of 2.2 is used in this study. The mass of the drag sail is

$$M = \rho_{sail} S \quad (9.19)$$

where, ρ_{sail} is the mass of the sail material per square meter. Typical sail materials such as those used in balloons used for stratospheric research have a density of about 6 grams per square meter. The drag-to-mass ratio of the aerodynamic drag sail is thus

$$\left(\frac{D}{M}\right)_{aero} = \frac{\frac{1}{2}\rho_T u^2 S C_D}{\rho_{sail} S} = \frac{\frac{1}{2}\rho_T u^2 C_D}{\rho_{sail}} \quad (9.20)$$

It is interesting to note that the drag-to-mass ratio of the aerodynamic sail does not depend on the dimensions of the sail, but on the density and speed which in turn are only functions of altitude, and on the angle of attack of the aerodynamic sail with respect to the plasma. Table 9.1 shows a comparison of the magsail and aerodynamic drag sail drag-to-mass ratios as a function of altitude. The charged particle number density n_0 is computed using the International Reference Ionosphere model IRI 2016, and is assumed to be entirely O+. The atmospheric density ρ_T is computed using the MSISE00 model. Table 9.1 indicates that at altitudes below 700 km, the aerodynamic drag sail provides more drag per unit

mass than the magsail, provided that the aerodynamic sail can be held normal to the wind. Above 1000 km, the magsail provides nearly an order of magnitude advantage compared to the aerodynamic sail. The results are for a magsail power of 1000 W, which is likely a reasonable value for spacecraft at the end of life when power is not required for normal operations. Even with a power of only 100 W, the magsail drag-to-mass ratio only drops by a factor of $10^{1/3}$, as the D/M of a magsail is proportional to $P^{1/3}$.

Table 9.1. Comparison of magsail and aerodynamic drag sail drag-to-mass ratios as a function of altitude. Magsail parameters: radius $r_0 = 10$ m, power $P = 1000\text{W}$, cross-sectional area $a = 1.8 \text{ mm}^2$, material = aluminum, material density $\rho = 2700 \text{ kg/m}^3$, mass $M = 0.3 \text{ kg}$, electrical resistivity = $2.82\text{E-}8 \Omega\text{m}$. Aerodynamic sail parameters: $\rho_{\text{sail}} = 6$ grams per square meter (i.e. a balloon film 6 microns thick, with no allowance for supporting structure.)

Altitude, km	$n_0,$ m^{-3}	$\rho_T,$ kg/m^3	$(D/M)_{\text{magsail}}$ ms^{-2}	$(D/M)_{\text{aero.}}$ ms^{-2}
400	1.6×10^{12}	4.2×10^{-12}	5.0×10^{-3}	4.7×10^{-2}
700	1.9×10^{11}	5.4×10^{-14}	1.2×10^{-3}	5.9×10^{-4}
1000	4.3×10^{10}	3.8×10^{-15}	4.3×10^{-4}	4.0×10^{-5}
1300	1.5×10^{10}	1.2×10^{-15}	2.1×10^{-4}	1.2×10^{-5}
1600	4.7×10^9	5.5×10^{-16}	9.4×10^{-5}	5.2×10^{-6}

Figure 2 shows a comparison of magsail and aerodynamic sail drag-to-mass ratio as a function of orbital altitude. Results are shown for two magsail power levels of 100 W and 1000 W. Figure 2 demonstrates that the magsail outperforms the aerodynamic sail by an order of magnitude for altitudes above 1000 km.

9.3 Computational MHD

Magnetohydrodynamics (MHD) equations describe the large-scale behavior of conducting fluids such as plasma subject to electric and magnetic fields. One-fluid MHD is a subset of the larger class of methods used to analyze plasma behavior. These include multi-fluid MHD models, hybrid models typically use which treat electrons as fluids and ions as particles, and fully kinetic models such as the particle-in-cell (PIC) method. The type of model used depends on the plasma specifics of the problem, the level of detail required, and the available computational resources. MHD is the simplest and least computationally demand-

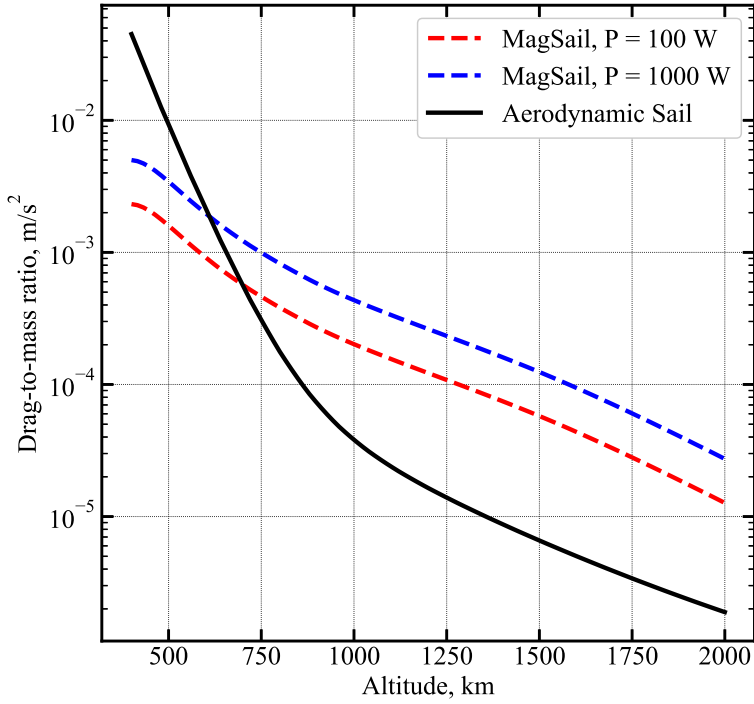


Figure 9.2. Comparison of a 10 m radius magsail and aerodynamic sail drag-to-mass ratio as a function of altitude. Design parameters are the same as listed in Table 9.1. The magsail, even with a power of 100 W, provides nearly an order of magnitude higher performance over an aerodynamic sail for altitudes above 1000 km. This implies that the magsail system can be one order of magnitude lighter compared to the aerodynamic drag sail, to achieve the same drag force at altitudes above 1000 km.

ing technique. MHD captures many important properties of plasma dynamics, and is often the first model used.

9.3.1 Ideal MHD

Plasma in general consists of multiple species of ions and electrons moving under the influence of electromagnetic fields, and changing the fields as the result of their motion. Under certain conditions it becomes possible to consider the plasma as a single fluid without differentiating between different species or electrons. This approach of plasma simulation is called single-fluid MHD or MHD in short. MHD is applicable when the characteristic length scale of interest is large compared to the Debye length, and the characteristic frequencies are small compared to the plasma frequency and the ion cyclotron frequency. The simplest

form of MHD is called the “ideal” MHD, which assumes the plasma has infinite conductivity (or zero resistivity). Ideal MHD requires that the 1) plasma is strongly collisional i.e. the collision time scale is shorter than other characteristic time scales in the system making particle distributions close to Maxwellian, 2) the characteristic length scale of interest is much larger than the ion Larmor radius, and 3) the resistivity due to collisions is small. These assumptions are mathematically expressed as follows in the order listed above as follows [202]:

$$\sqrt{\frac{m_i}{m_e}} \left(\frac{V_{Ti}\tau_{ii}}{a} \right) \ll 1 \quad (9.21)$$

$$\frac{r_{Li}}{a} \ll 1 \quad (9.22)$$

$$\left(\frac{r_{Li}}{a} \right)^2 \sqrt{\frac{m_e}{m_i}} \left(\frac{a}{V_{Ti}\tau_{ii}} \right) \ll 1 \quad (9.23)$$

where m_i is the ion mass, m_e is the electron mass, V_{Ti} is the thermal speed of the ions, τ_{ii} is the ion collision time scale, a is the characteristic length scale of interest and r_{Li} is the ion Larmor radius. Typically the length scale of interest in magnetospheres is the magnetosphere characteristic length L described earlier. The thermal speed, ion collision time scale, and the Larmor radius are given by

$$V_{Ti} = \sqrt{\frac{2kT_i}{m_i}} \quad (9.24)$$

$$\tau_{ii} = \sqrt{\frac{2m_i}{m_e}} \left(6.7 \times 10^{-6} \frac{T_{keV}}{n_{20}} \right) \quad (9.25)$$

$$r_{Li} = \frac{m_i V_{Ti}}{q_i B} \quad (9.26)$$

where k is the Boltzmann constant, T_i is the ion temperature, T_{keV} is the ion temperature in keV, n_{20} is ion number density in terms of $10^{20} m^{-3}$, q_i is the ion charge, and B is the magnetic field, evaluated at the characteristic length L .

Typically in most problems of interest such as tokamaks, planets in the solar wind etc., the strong collisional assumption is almost never satisfied while the remaining two assumptions are generally satisfied. Despite this limitation, ideal MHD provides a fairly accurate description of the large-scale plasma behavior in these problems as demonstrated by experimental and observational evidence.

9.3.2 BATS-R-US MHD Code

Despite the simplifying assumptions made, the resulting ideal MHD equations are non-trivial to solve even in simple geometries. Analytic solutions are available only for a handful of simple problems, and any detailed modeling of real-world geometries requires numerical simulations. The primary difficulty arises from the fact that MHD possesses families of solutions such as fast shocks, fast rarefactions, slow shocks, slow rarefactions, Alfvén waves, and compound waves of the fast or slow families. Capturing the wide range of such structures is a challenging task for numerical methods. Typically the maximum allowable time step for integration is set by the fast waves, and thus satisfying the Courant-Levy-Friedrich (CFL) condition requires a small time step to prevent numerical instability. Compared to numerical methods for solving hydrodynamics problems (CFD) which were well established for several decades, techniques for solving MHD equations were only developed starting in the 1990s. Much of the development in numerical schemes for MHD is attributed to space physics studies where MHD simulations are used extensively for space weather forecasting and modeling of in-situ observations by spacecraft instruments.

Designing, implementing, and validating an MHD code from scratch was not possible within the timeframe of this study. Hence, we use an established ideal MHD code BATS-R-US developed at the University of Michigan. BATS-R-US is a FORTRAN code which has been extensively used in the study of planetary magnetosphere-solar wind interactions over the past two decades [203]. BATS-R-US stands for Block Adaptive Tree Solar-wind Roe Upwind Scheme and solves the MHD equations using a finite volume upwind Roe-type scheme. BATS-R-US has been used to simulate the Earth’s magnetosphere, inner and outer heliosphere, the magnetosphere of most of the planets, several moons and various comets. The code can be used for any problem for which the MHD equations are a reasonable approx-

imation. BATS-R-US solves the following ideal MHD equations which represent continuity, momentum, magnetic flux and energy conservation.

$$\frac{\partial \rho}{\partial t} + \nabla \cdot (\rho \vec{u}) = 0 \quad (9.27)$$

$$\frac{\partial (\rho \vec{u})}{\partial t} + \nabla \cdot \left[\rho \vec{u} \vec{u} + I \left(p + \frac{1}{2} B^2 \right) - \vec{B} \vec{B} \right] = -\vec{B} \nabla \cdot \vec{B} \quad (9.28)$$

$$\frac{\partial \vec{B}}{\partial t} + \nabla \cdot \left[\vec{u} \vec{B} - \vec{B} \vec{u} \right] = -u \nabla \cdot \vec{B} \quad (9.29)$$

$$\frac{\partial e}{\partial t} + \nabla \cdot \left[\vec{u} \left(e + p + \frac{1}{2} B^2 \right) - \vec{u} \cdot \vec{B} \vec{B} \right] = -\vec{u} \cdot \vec{B} \nabla \cdot \vec{B} \quad (9.30)$$

$$e = \frac{p}{\gamma - 1} + \frac{\rho u^2}{2} + \frac{B^2}{2} \quad (9.31)$$

where ρ is the density, \vec{u} (vector) is the velocity, I is the identity matrix, \vec{B} (vector) is the magnetic field normalized by μ_0 , p is the pressure, e is the energy density, and $B^2 = \vec{B} \cdot \vec{B}$. Equations 9.27 through 9.30 represent eight scalar equations in eight scalar variables ρ , u_x , u_y , u_z , B_x , B_y , B_z , and e .

These equations along with boundary and initial conditions fully specify the MHD problem for analytical solutions. For numerical solution, the domain volume has to be discretized into finite cells. The computational domain is divided into blocks each consisting of $N_x \times N_y \times N_z$ cells, where N_x , N_y , N_z are the number of cells in each direction. Typically, blocks consisting of anywhere between $4 \times 4 \times 4 = 64$ and $12 \times 12 \times 12 = 1728$ cells are used. The memory requirement increase rapidly with increasing $N_x \times N_y \times N_z$ and care must be taken not to exceed the maximum available RAM memory. For example, with $N_x = N_y = N_z = 8$, and an initial division of the domain into $10 \times 10 \times 0$ blocks in the three directions results in 0.5 million cells. BATS-R-US requires 3.2 MB using 8 byte real numbers for each $8 \times 8 \times 8$ cell block. Hence, $10 \times 10 \times 10$ blocks require about 3.2 GB of RAM. It is easy to see how increasing the initial division of $20 \times 20 \times 20$ blocks will require about 26 GB of RAM.

BATS-R-US uses a block based, adaptive grid that allows the user to specify where he or she wants more resolution or to let the code determine where more resolution is needed. The code has Adaptive Mesh Refinement (AMR) capability which automatically subdivides a block into 8 smaller blocks, if additional resolution is required in certain parts of the domain. BATS-R-US provides a command to carve out a sphere inside the domain as an internal boundary which is useful for placing a body in the plasma flow. The inner sphere can be provided a dipole magnetic field strength and orientation to simulate a planet in the solar wind or in our case, a magsail in LEO. The diameter of the sphere is generally quite small compared to the domain size, and typically the field variables are not computed inside the domain. Generally a region slightly larger than the sphere itself is excluded from the computation zone as the magnetic field strength grows sharply near the dipole origin, and results in large wave speeds and consequently small allowable time steps. The inner boundary uses a ‘float’ boundary condition which means the values on either side of the boundary are the same. The sphere is enclosed by a cuboidal domain which results in six additional faces. One of these faces typically is used as an ‘inlet which has the plasma wind ambient conditions’ and the opposite face is an ‘outlet with the float boundary condition. Generally, the initial conditions are set to the plasma wind ambient conditions.

BATS-R-US can solve the MHD equations in time-accurate or steady state mode. Since we are not interested in time-varying phenomena, we use the steady-state mode which allows local time stepping. Each cell uses a maximum allowable time step based on the local numerical stability (CFL) condition, where C is a multiplier typically set to 0.8. The local time stepping allows the steady-state solution to be approached faster than the time accurate mode which requires the solver to take the most restrictive time step across the entire domain.

BATS-R-US provides several numerical schemes to compute the flux at the cell faces: Roe, Rusanov, Linde and Sokolov. The Roe flux scheme is the most accurate, most expensive, and least robust. The Rusanov scheme is efficient and robust, but is more diffusive which results in sharp discontinuities being smeared out.

The Linde scheme is more accurate and less robust than Rusanov, but less expensive and more robust than the Roe scheme. The most suited scheme is problem dependent, and is usually selected by experimentation.

This work uses the Linde scheme and the Sokolov schemes which were found to provide good balance between accuracy and cost.

$$\Delta t = C \times \max \left[\frac{c_x + |u_x|}{\Delta x}, \frac{c_y + |u_y|}{\Delta y}, \frac{c_z + |u_z|}{\Delta z} \right]^{-1} \quad (9.32)$$

9.3.3 Test Cases: Earth and Ganymede

Before analyzing the magsail-plasma interaction in LEO, two test cases are run to make sure the code is configured properly: the Earth in the solar wind, and Ganymede in Jupiter's magnetosphere.

The solar wind is a stream of charged particles primarily protons and electrons emitted from the Sun's corona and streams radially outward in all directions. The Earth's magnetic field deflects these charged particles and hollows out a cavity from where the solar wind is largely excluded, creating a magnetosphere. The Earth's magnetic field is modeled as an ideal dipole with an equatorial field strength of 31,000 nT and the dipole axis oriented perpendicular to the solar wind direction. At 1 AU, the upstream ambient solar wind parameters are: $n_0 = 5 \times 10^6 m^{-3}$, $m_i = 1$ amu (H+ ions), and $u \simeq 400$ km/s, $B_x = B_y = 0$ nT, and $B_z = -5$ nT.

The Earth is at the origin of the XYZ coordinate system, with the positive X axis pointing in the sunward direction and the Z axis pointing towards the ecliptic north pole. The Y axis completes the right handed system. The computational domain extends from $-120R_E$ to $20R_E$ in the X-direction, and from $-100R_E$ to $100R_E$ in the Y and Z directions. The grid uses a ‘spherical log’ geometry which uses logarithmic spacing in the radial direction, and uniform spacing in the longitudinal and latitudinal directions. Such a grid is more suited to planetary magnetosphere-solar wind interactions than a uniform Cartesian grid. The domain is divided into 20 blocks in the radial direction, 16 along the longitudinal coordinate, and 4 along the latitudinal coordinate. Each cell block has $8 \times 8 \times 8$ cells, resulting in 0.6 million cells. The solar wind conditions are applied at the inlet boundary at $X = 20R_E$ and flows in the -X direction. The float boundary condition is applied on the other five domain boundaries and the inner sphere. A second order scheme with Linde flux splitting and minmod type

limiter is used with local-time stepping to march towards a steady state solution. Message Passing Interface (MPI) is used to run BATS-R-US in parallel on 4 cores. A steady-state solution is achieved in 1000 iterations, which takes about 30 minutes to run on a standard workstation. Typical output from the simulation is a cut along the $Y=0$ plane, with all the eight data variables and is post-processed using a Python script.

Figure 9.3 shows the contours of ion number density (on a log scale) in the local noon-midnight meridional plane ($Y=0$) at steady state. The magnetopause boundary along the sunward direction is located at approximately $10R_E$ as predicted by Eq. 9.1. A bow shock is located just upstream of the magnetopause boundary indicated by the red region with high ion concentration. The dark blue region is the cavity carved out by the Earth's magnetic field from which solar wind particles are largely excluded. The dashed line shows the analytical solution for the magnetopause which is in good agreement with the MHD result.

Ganymede is a unique case in our solar system where a planetary body (in this case, a moon) with an intrinsic magnetic field is embedded in the magnetosphere of another body (Jupiter). Jupiter has the strongest and largest magnetosphere among all the planets, and because of its fast rotation, drags the field lines and the trapped plasma past the four large Galilean satellites. At Ganymede's orbit, the co-rotating plasma overtakes the moon at a relative speed of about 140 km/s. The ambient field due to Jupiter at Ganymede's orbit is about 85 nT, and has a particle number density of 4 cm^{-3} consisting of a mixture of O+ and H+ ions with a mean mass of 14 amu. For these parameters, the Alfvén wave speed and the thermal speed are

$$V_{\text{Alfvén}} = \frac{B}{\sqrt{\mu_0 \rho}} \simeq 248 \text{ km/s} \quad (9.33)$$

$$V_{\text{Ti}} = \sqrt{\frac{2kT_i}{m_i}} \simeq 62 \text{ km/s} \quad (9.34)$$

This implies that the plasma flow past Ganymede is subsonic and sub-Alfvenic which results in the formation of Alfvén wings at Ganymede and is analyzed using BATS-R-US. Ganymede is modeled as dipole with an equatorial field strength of 719 nT. The plasma flow

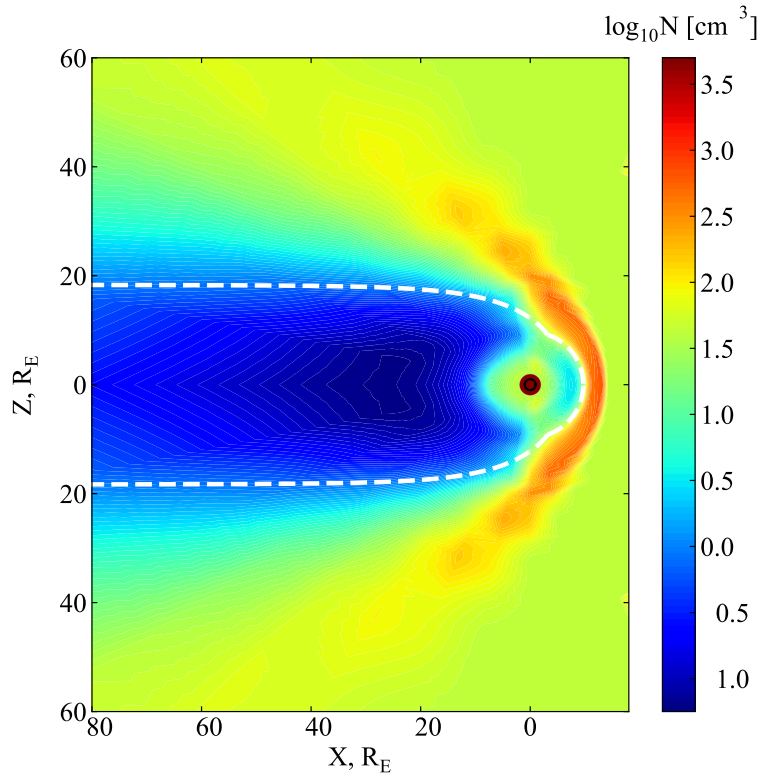


Figure 9.3. Magnetosphere cavity (blue) created by the Earth's magnetic field deflecting charged particles in the solar wind. The charged particles are largely excluded from the magnetosphere. The Earth is located at the origin, and the solar wind flows from right to left. The dashed line is the analytic solution for the magnetopause which is in good agreement with the MHD result.

parameters are $n_0 = 4 \times 10^6 m^{-3}$, mass = 14 amu, $u_x = 140$ km/s, $B_x = -10$ nT, $B_y = -6$ nT, $B_z = -86$ nT.

Ganymede is placed at the origin with the positive X axis pointing in the direction of the moon's orbital motion, and the Z axis pointing towards the orbit normal northwards. The computational domain extends from $-50R_G$ to $+50R_G$ in all three directions. A spherical log grid with 10 cell blocks in the radial direction and a uniform grid with 8 cell blocks each in the other two directions is used. The plasma wind conditions are applied at the $X = -50R_G$ boundary. The second order scheme is used with Sokolov flux splitting and monotonized central slope limiter. Figure 9.4 shows the contours of flow speed u_x in the plane containing the $Y=0$ plane. The region where the flow has been slowed down from the upstream speed resembles 'wings', and is a cylindrical structure that is tilted with respect to the background

field at an angle $\tan^{-1}(u/V_{Alfven})$. This structure is called “Alfvén wing” and in the case of Ganymede is tilted at around 30 degrees from the vertical and has a width of about $6R_G$ and extends to $\pm 30R_G$ along the Z axis.

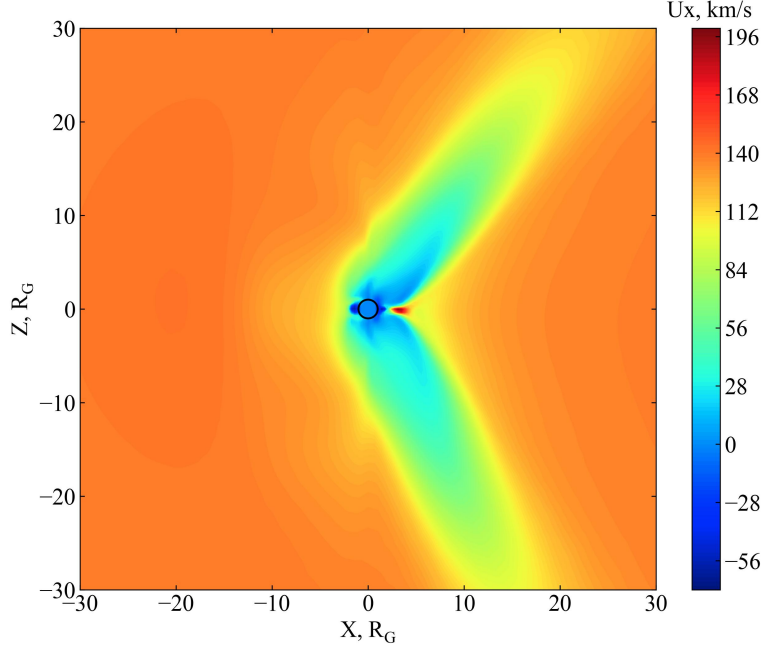


Figure 9.4. Alfvén wings created by Ganymede in Jupiter’s magnetosphere. Contours of flow speed u_x in the plane containing the $Y=0$ plane. Ganymede is located at the origin. The direction of Ganymede’s orbital motion is along the $+X$ direction. Plasma flow corotating with Jupiter flows along the $+X$ direction (from left to right) and overtakes Ganymede as it moves along its orbit.

The results for Earth in the solar wind and Ganymede in Jupiter’s magnetosphere help ensure that the BATS-R-US code is configured correctly, and can capture features such as bow shocks and Alfvén wings for plasma flows past a magnetic field. In the next subsection, we adapt these models to simulate the interaction of magnetic sail with the ambient plasma.

9.3.4 Computational MHD Model of Magsail in Plasma Wind without Ambient Field

In this section, we analyze the interaction between a magsail and the ambient plasma in LEO. The magsail has a radius of 1.0 m, with a current of 100 A. The plasma flow conditions are $n_0 = 5 \times 10^{11} m^{-3}$, $m_i = 16$ amu (O^+ ions), and $u = 7.6$ km/s. The ambient magnetic field

is neglected in this analysis. The magsail is located at the origin, with a magnetic moment of 314 Am^2 oriented perpendicular to the flow. The plasma flow is along the -X direction, and the magnetic moment is along the +Z direction. The computational domain extends from -50 m to +10 m along the X direction, and from -30 m to +30 m along the Y and Z directions. A spherical log grid spacing is used in the radial direction, and uniform spacing in the two angular directions with a cell block size of $20 \times 8 \times 8$.

Figure 9.5 shows the contours of O+ ion density (on a linear scale) in the Y=0 plane. The magnetopause boundary is located at $X = 3.6 \text{ m}$, upstream of which a bow shock is formed. The dashed line shows the analytic solution for the magnetopause. The magnetopause location upstream of the magsail is in good agreement with the analytic solution, but the magnetosphere cavity is somewhat larger than that predicted by the analytic solution.

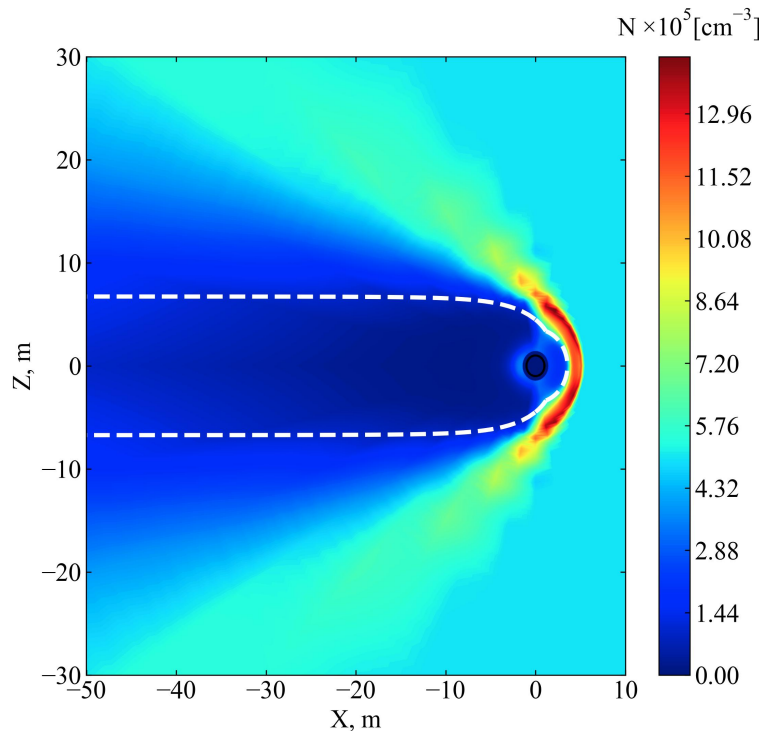


Figure 9.5. Magsail-plasma interaction in LEO. The magsail is located at the origin, and has a dipole moment equivalent to that of a 1 m radius coil with a current of 100 A oriented along +X. The plasma flow speed is 7.6 km/s from right to left. A bow shock is formed at $X = 3.6 \text{ m}$. The dashed line shows the analytic solution for the magnetosphere boundary.

9.4 MagSail Deployer Studies

A number of options were examined for methods of deploying the magsail. In theory it is possible to deploy a magsail using the hoop stress on the wire exerted by the magnetic field itself. However currents of the magnitude that would be involved in the magsail flight experiment would create insufficient force for effective deployment. Therefore a range of mechanical systems were considered.

Two modes of deployment were considered: 1) where the magsail wire loop will be deployed as a ‘free flyer’ tethered from the CubeSat and its self-acceleration from the drag would cause it to move in space, and 2) where the wire loop would be rigidly attached to the CubeSat and the entire CubeSat would experience the magsail drag. The wire based and inflatable deployment options below are designed to be used with the first ‘free flyer’ concept, whereas the bistable tape springs are intended for use with the second concept. The first mode deployment strategies were promising and the challenges discovered during testing could be solved. However, other alternatives, including inflatables and bistable tape springs appear to be more promising.

The bistable tape spring, which is a thin shell C-shaped structure. The rolled up and deployed states of the tape spring are shown in Figures 9.6 and 9.7, and the bistable tape spring is stable in both of these states. In contrast, ordinary tape springs are only stable in the deployed state. The composite tape spring is stable when completely rolled up, but will self-deploy if a small portion is left unrolled. The tape spring when deployed assumes a rigid boom structure and will be the primary structural element of the magsail, with electrically conducting wires stretched between the four booms. The bistable tape springs have been used on a number of CubeSat missions, most notably the InflateSail mission which deployed booms nearly 2 meters long to unfurl a drag sail as shown in Figure 9.8.

A proof-of-concept deployment system was developed and tested using ordinary tape springs. Ordinary tape springs were used because the composite bistable tape was not readily available for purchase within the time frame of the study. However, multiple vendors confirmed that they are capable of supplying the material for an actual flight experiment. Nevertheless, the deployer with ordinary tape spring demonstrates the ability to be able



Figure 9.6. Composite bistable tape spring in its coiled configuration [204].



Figure 9.7. Composite bistable tape spring in its deployed configuration. [204].

to pack four one meter long booms into a 10 cm x 10 cm x 4 cm volume, and self-deploy the magsail without requiring any motor. Designing the deployer also exposed some of the problems such as “blossoming” which is commonly encountered in tape spring deployers [206]. However, the problems was solved and a successful prototype deployer was realized.

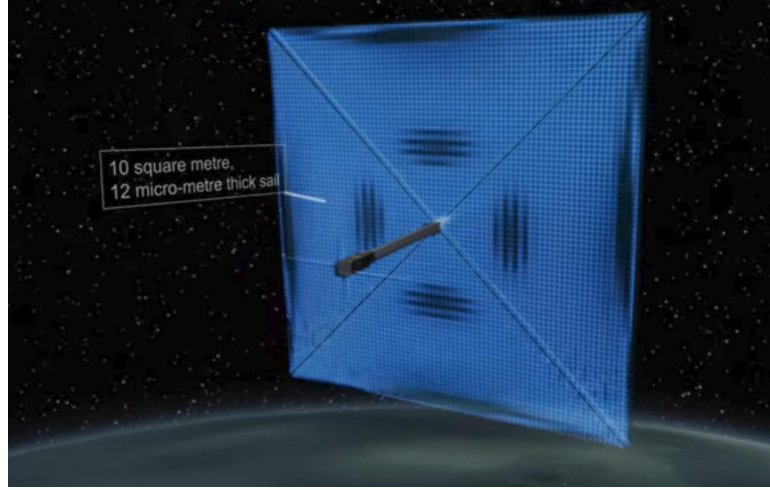


Figure 9.8. InflateSail mission with its drag sail deployed using bistable tape springs [205].

The deployer consists of the following parts as shown in Figure 9.9: a central spindle, a spool on which four 3/4 in wide tape springs are attached to, eight Teflon rollers arranged in a circular pattern, a base plate, and a top plate (not shown in this image). The Teflon rollers serve two purposes: act as a guide to deploy the tape radially outward, and to prevent blossoming in which the tape spring unfurls inside the deployer and hampers radial deployment outward because of friction against the side walls. The tape spring is wound using a custom-made handle. Figure 9.10 shows the “stowed” configuration of the magsail.

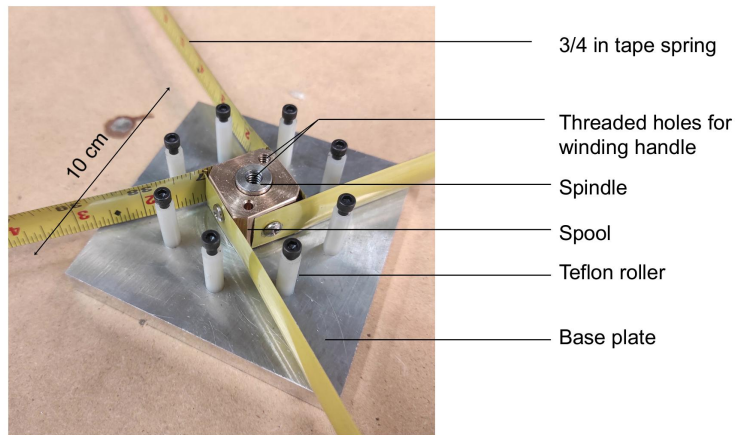


Figure 9.9. View of the inside of the prototype magsail deployer.

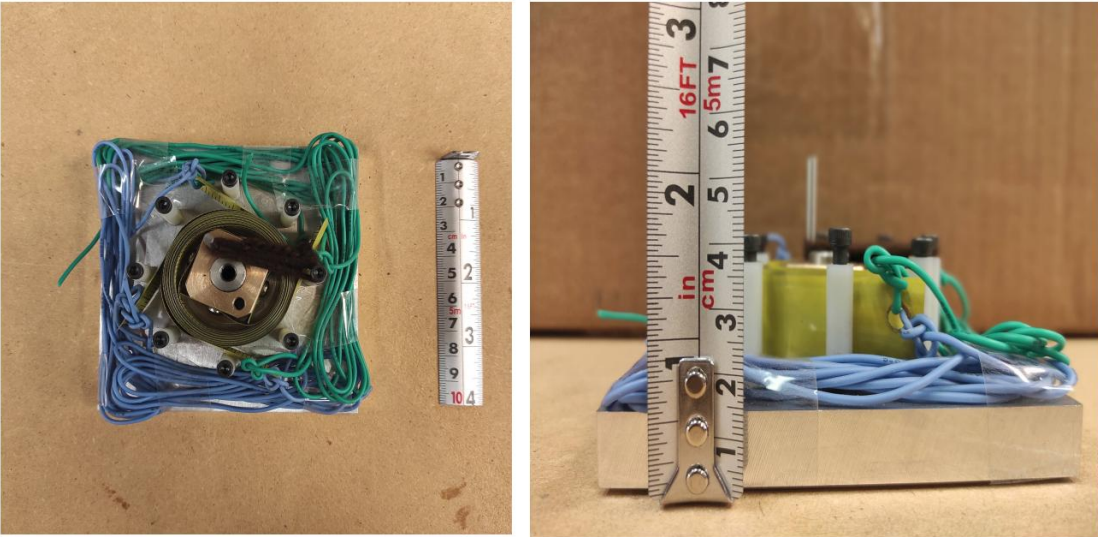


Figure 9.10. Stowed configuration of the deployer with the magsail wire. The baseplate is 0.5 in thick in this prototype, but the flight version will use 0.125 in or smaller thickness. The deployer fits within the allocated 10 cm × 10 cm × 4 cm volume.

Two modes of deployment were attempted: 1) an uncontrolled deployment where the restraints are released instantly, and 2) a controlled deployment where a small resistance torque is applied to control the deployment rate. Figure 9.11 shows a sequence of frames from an uncontrolled deployment which lasts less than a second. The sail successfully deployed to its final configuration, but some buckling is visible in frames 4 and 6. The buckling is attributed to 1) the low stiffness of the ordinary tape spring, and 2) the uncontrolled release of stored potential energy particularly towards the end of the deployment when the tapes have lot of kinetic energy but are restrained by the wires when they are fully deployed. The controlled deployment method solved these problems, and enables a much cleaner deployment.

Figure 9.12 shows a frame sequence from the controlled deployment where a small resistance torque is applied to control the deployment rate. The deployment takes several seconds, and avoids the problem of buckling toward the end of the deployment. The folding pattern used to package the wires could be somewhat improved to avoid undesired tangling

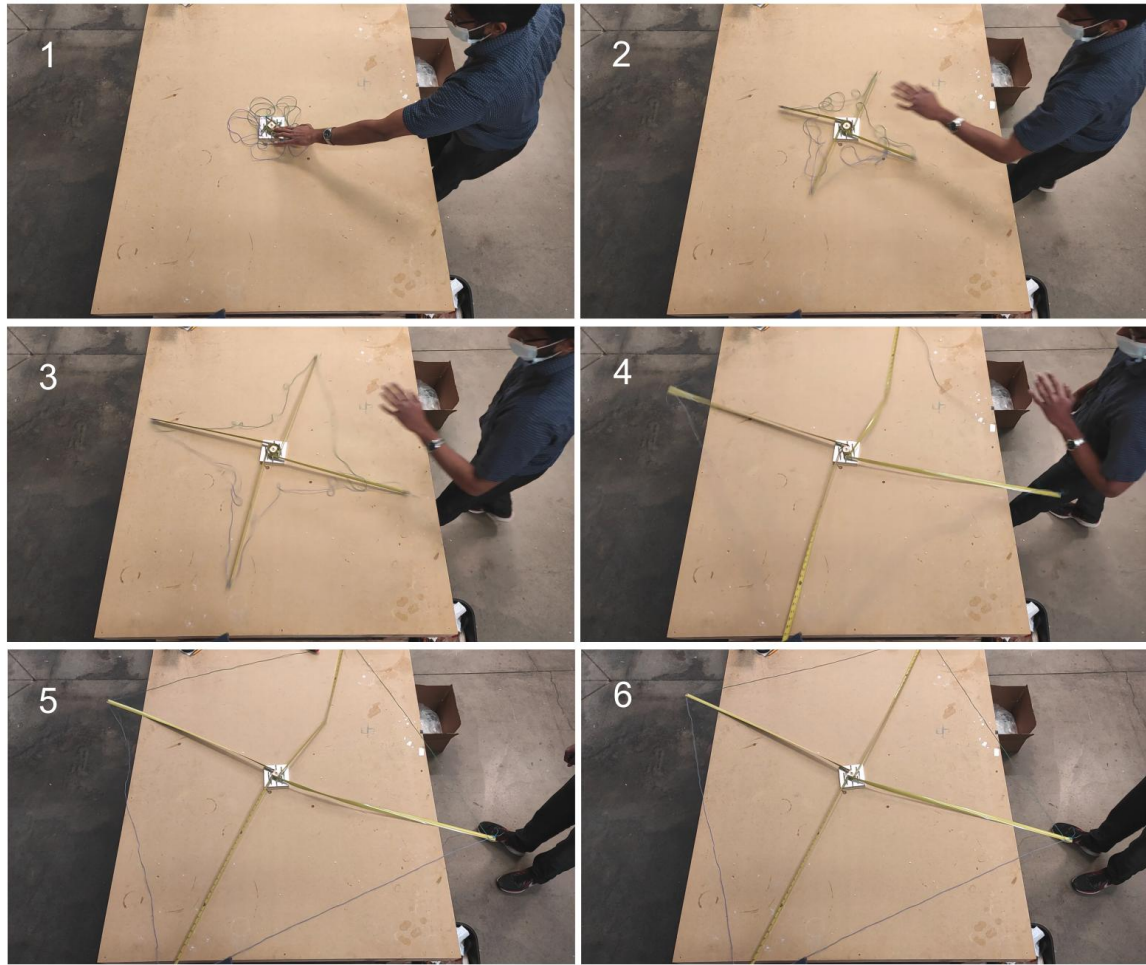


Figure 9.11. Uncontrolled deployment of the tape spring magsail. Some buckling is visible before the sail takes its final shape.

and produce better results, but overall the sail successfully deployed to its final configuration without any problems.

It is noted that the above experiments using ordinary tape springs are only used to show a proof-of-concept deployment system that will fit within a 0.4U volume and deploy four 1 meter booms for the magsail CubeSat experiment. The composite bistable tape springs which will actually fly on the experiment have much higher stiffness and can be tailored to the specific mission concept to avoid undesirable bending, buckling, and twisting motions which cannot be avoided with ordinary tape springs.

Bistable tape springs have seen significant developments in the last few years pioneered by the Air Force Research Laboratory for a CubeSat telescope concept, and by Roccor LLC,

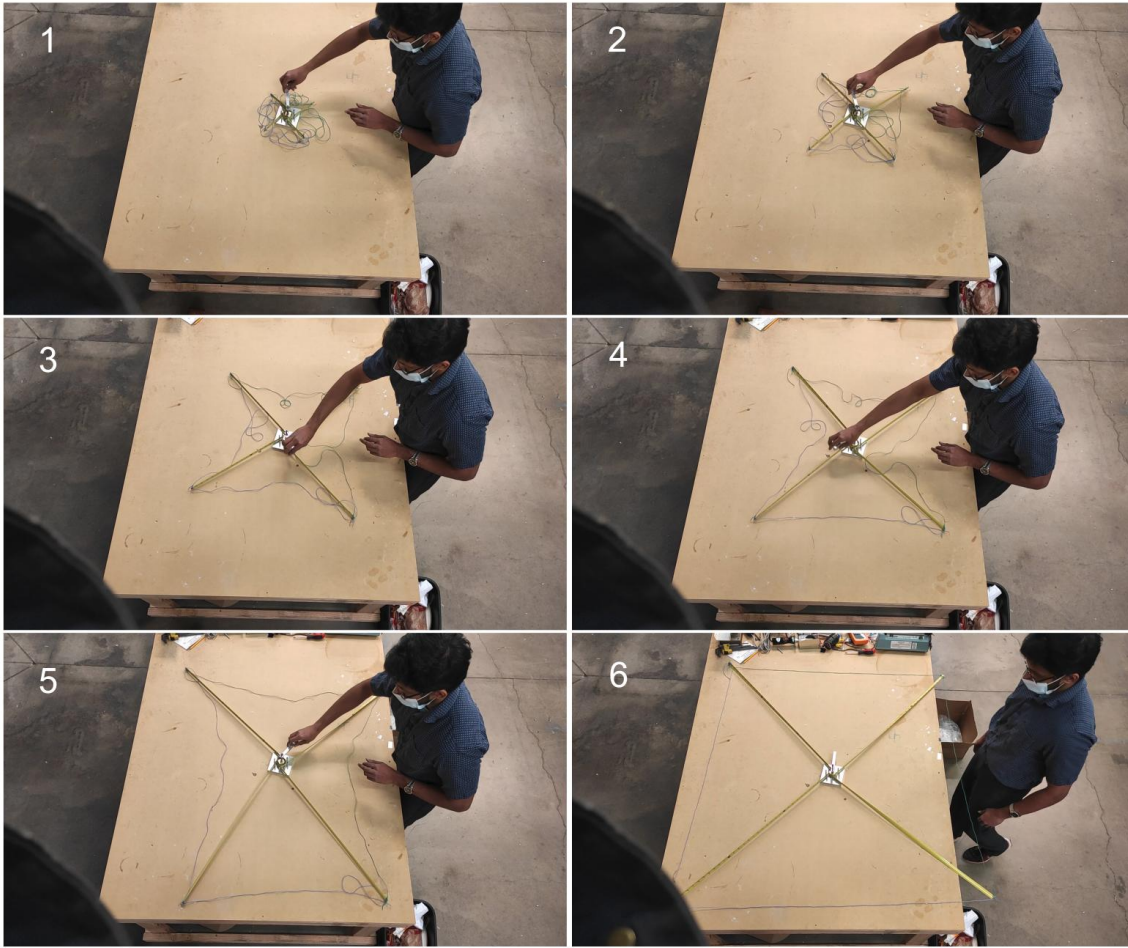


Figure 9.12. Controlled deployment of the tape spring magsail. The sail deploys to its final configuration without any buckling.

a Colorado based company which has developed flight-like engineering units for meter-sized booms to be used on CubeSats. In Europe, Oxford Space Systems has led the development of this technology and has supplied several flight units including those used on the Inflate-Sail and the AlSat-Nano CubeSat missions. Having successfully flown on several missions, bistable tape springs are now considered a mature technology and requires no additional technology developments. The bistable tape spring based deployment was selected for the CubeSat flight experiment because of its simplicity, reliability, and high packing efficiency. Bistable booms have been the choice of deployment for several recent CubeSats such as the InflateSail and SEAM missions [206], [207], and hence is a proven, flight-heritage technology which can be readily leveraged for the magsail mission.

9.5 CubeSat Flight Experiment Concept

The objective is to design a CubeSat flight experiment concept to test the hypothesis that magnetic sails can serve as a viable deorbit technique for satellites in Low Earth Orbit from altitudes of 700 to 1400 km.

The driving design considerations are as follows:

1. The experiment should strive to be low-mass and low-cost, a 1U CubeSat is the preferred choice.
2. The experiment should leverage orbits that allow frequent and flexible launch opportunities including deployment from the ISS.
3. The experiment should be able to conclusively and precisely detect the effect of the magsail drag, eliminating the effects of other drag forces such as aerodynamic drag and solar radiation pressure.
4. The CubeSat should use proven Commercial Off the Shelf (COTS) parts for flight systems (power, telecom etc.) with flight-heritage.
5. Multiple satellites if used should be completely identical to reduce qualification costs, and provide redundancy for complete failure of one CubeSat.
6. The magsail deployment system should be simple, reliable, and preferably with flight heritage.
7. The deployment system should be able to be amply tested on the ground. The system should preferably use stored energy such as a spring which when released by heating a nichrome wire would trigger the deployment of the magsail. The deployment system will include redundant nichrome wires for all boom deployments.
8. The design should strive to power the magsail wire whenever the CubeSat is in sunlight, and preferably during the entire orbit using energy stored in the battery.

9. The design shall incorporate an active tracking device such as GPS, and transmit a beacon with basic parameters and position information approximately once every minute.

9.5.1 Mission Requirements and Constraints

1. The CubeSat shall adhere to all the requirements and specifications listed in the CubeSat Design Specification document provided by California Polytechnic University. A few important ones for high level conceptual design are listed below.
 - The mass of a 1U, 2U, and 3U CubeSat shall not exceed 1.33 kg, 2.66 kg, and 4.00 kg respectively.
 - The CubeSat should adhere to the physical dimension constraints (10 cm x 10 cm x 10 cm for a 1U CubeSat).
 - All deployables shall be constrained by the CubeSat, and not the deployer.
 - The CubeSat will have an RF power of no greater than 1.5W at the transmitting antenna's output.
 - All deployables shall wait to deploy a minimum of 30 minutes after the CubeSat deployment switches are activated from the ejection by the deployer.
2. The CubeSat shall deploy a wire loop (a circle, square, or a polygon etc.) with a deployed radius of at least 0.5 m. The wire loop should maintain its shape after deployment, and the electrical wire should carry an effective current (i.e. current in all coils combined) of at least 10A.
3. The CubeSat should at minimum transmit a beacon to aid in its tracking by ground stations. The CubeSat may optionally carry a radio receiver, and a GPS receiver.
4. The CubeSat shall be in an orbit less than allows at least 30 days of operation before reentry.

5. The CubeSat should provide on board circuitry to power the magsail with at least 1.4 W of power when in sunlight, and a battery to power the satellite during eclipse.
6. The CubeSat should carry antenna that are omni directional, and can transmit signals irrespective of the satellite orientation and attitude rates.
7. The magsail should strive to keep the aerodynamic drag at a minimum level, so as to measure the isolate the effect of the magsail drag on the satellite orbit.
8. The mission concept should be able to observe and measure the effect of the magsail drag.

9.5.2 Key System Trades

Trade studies concerning the orbit selection, satellite form factor, number of satellites, attitude control, telemetry and command, tracking, power system and batteries, on board data handling, magsail deployment system are described below.

Orbit Selection

The operational orbit for the flight experiment is a compromise between two competing requirements. In order to isolate the magsail drag, the aerodynamic drag must be kept as low as possible. Ideally this would imply a high orbit with altitude greater than 700 km and preferably about 1000 km to keep the aerodynamic drag one order of magnitude smaller than the expected magsail drag. However, such high orbits are not available for CubeSats launched as secondary payloads. A GTO orbit was considered, but preliminary analysis indicated that the effect of the magsail drag on the orbit would not be observable within the 100 day time span of the mission. Launching from the ISS dictates a 420 km orbit. Preliminary analysis indicated that aerodynamic drag could be large, making it difficult to isolate the effect of the magsail on the orbit. However, if two identical CubeSats are used with the magsail turned on in only one of the satellites, the relative separation between the satellites would be readily observable from tracking data within a few weeks. Since both

satellites would have identical aerodynamic drag, any difference in their trajectories could only be from the magsail, making it possible to precisely assess magsail drag.

Based on the design driver that the mission concept should use an orbit that allows frequent and flexible launch opportunities including from the ISS, a 420 km orbit is selected as the baseline orbit. Analysis indicated the relative separation between two identical CubeSats with one magsail turned on will exceed 1000 km within the first two weeks, and the active magsail will reenter the atmosphere several weeks ahead of the dummy inactive magsail. Further details on the relative separation and deorbit calculations are provided in the mission analysis section. This mission architecture also provides redundancy, since if the active magsail failed for any reason, the other one could be made to assume the active role in its place.

Satellite Form Factor

The satellite form factor options include a 1U to a 3U CubeSat, with 1U being the preferred choice to keep the mass and cost as low as possible. The low mass of a 1U satellite also aids in faster orbit decay and eventual reentry as compared to a 2U or a 3U satellite. The limitations for a 1U CubeSat is the limited surface area for solar power generation, and the tight volume constraints (10 cm x 10 cm x 10 cm) to fit the magsail deployer into. Preliminary configuration studies indicated that the magsail deployer should fit within a 0.4U volume for a 1U CubeSat in order to accommodate other systems such as the flight computer, power system, and radio. The 1U form factor is selected for the baseline concept. Additional details on the mass and volume budget and the satellite configuration are provided in the flight system design section.

Number of Satellites

As mentioned in the orbit selection section, preliminary studies indicated that the contribution of aerodynamic drag could be comparable to the magsail drag for orbit altitudes less than 450 km. This implies that observing the effect of the magsail drag on the orbit within a 100 day time span would be difficult with a single satellite. Having two identical

satellites with the only difference between them being that one magsail is powered on, while the other serves as a dummy enables the isolation of the magsail drag from other forces. This provides a conclusive and precise estimate of the magsail drag. Since this is one of the mission's driving design requirements, two identical 1U CubeSats are selected for the baseline mission concept. This architecture also provides the redundancy by the fact that one CubeSat may fail after deployment and the other satellite can assume the active role without compromising the mission. Having identical satellites also reduces the testing effort, qualification costs, and total cost of the program.

Attitude Control

There are no pointing requirements for the satellite. The magsail orientation relative to the orbit velocity direction does not affect the drag significantly as seen in MHD simulations, and hence the satellite could be tumbling and the magsail would still be effective at producing drag. To save mass and power, the baseline concept does not include an attitude determination and control system. Omni directional antenna will be used for communication with the ground stations. Because the magsail itself creates a significant magnetic moment, it may provide the active CubeSat with passive stability by aligning itself with the Earth's magnetic field. However since neither drag nor communication depends upon attitude control, tumbling should not be an issue in any case.

The GPS antenna is the only on-board system that requires some pointing to ensure the GPS satellites are visible from the receiver. Kovar reported that for a 1U unstabilized CubeSat in a 520 km orbit, GPS position information was available approximately 80% of the time. Since the magsail CubeSat tracking requires GPS fixes only once every few hours to provide precise measurements of orbit decay, even having the position information only 5% of time would be acceptable. The baseline concept assumes no attitude control system to save mass. However, even if the GPS should fail, ground tracking of the satellites should provide adequate information to assess orbit decay, and thus measure magsail drag.

Telemetry and Command

The primary requirement for telemetry is to download GPS tracking information and spacecraft health parameters to ground stations. In the most basic form, the spacecraft will not carry a receiver, and will be commanded to automatically deploy the magsail and power it from the battery. The spacecraft will transmit a beacon (estimated to be about 5 kbit) every minute. The spacecraft may optionally carry a receiver which will allow the deployment and its operation to be commanded from a ground station. Most CubeSats typically use UHF/VHF amateur bands for communication for low data rate communication (few kbits/sec) due to their low cost, omni-directional pattern, and ease of use, and this is selected as the baseline communication system along with a standard transceiver circuit board. Other options include L-band communication with GlobalStar or Iridium satellites thus eliminating the need for a ground stations or S-band for higher data rates. The receiver antennae are not included in the baseline concept because there is no driving need to actively command the spacecraft. The CubeSat will be automated to power the magsail from the battery, and continuously transmit a beacon.

Not carrying a receiver however, implies that should the active CubeSat fail for any reason, there would be no way to command the dummy CubeSat to assume the active role from the ground. The workaround is to use a timer to automatically turn the dummy magsail on after 100 days. Since both CubeSats are expected to be in orbit for at least 250 days before re-entry, this will preserve the redundancy of the architecture to the failure of one CubeSat even without a receiver.

Tracking

Tracking the orbit of the two satellites as accurately as possible is desired to precisely estimate the magsail drag. The primary tracking method is an on-board GPS receiver which turns on and logs the position every few hours. The GPS position accuracy is estimated to be of the order of 10 m. The secondary tracking method uses the Two Line Elements (TLE) provided by NORAD and is expected to provide accuracy of about 1-2 km at the epoch. Other options include using commercial radar station networks such as those provided by

LeoLabs, or simply using information from the radio beacon (such as the Doppler shift) as the satellites pass over a ground station to get a coarse estimate of the orbit.

Power System and Batteries

Solar panels mounted on the body provide power to the CubeSat. A battery is used to store enough energy to power the satellite through the eclipse which is approximately 35 minutes of the 90 minute orbit and provide power to the magsail. A standard 1U side solar panel (such as the one shown in Figure 33) is estimated to produce 2.4 W of power when pointed directly at the Sun. Without attitude control, the satellite will be tumbling and exposing different faces to the Sun as it rotates. A rule of thumb used in the CubeSat community is that the Orbit Averaged Power (OAP) for a tumbling satellite with panels on all six faces is approximately 80% of the power from a single face facing the sun, which results in an OAP of about 1.9W for a 1U CubeSat. The solar panels will constantly be charging the battery, which will then provide power to the sail and other on-board systems.

The majority of CubeSats flown have used rechargeable Li-ion cells for energy storage. Standard 18650 cells have been extensively tested for terrestrial applications and is a commonly choice for CubeSat missions. A typical 18650 cell has a capacity of 12 Wh and weighs approximately 50g. Smaller Li-ion cells are available for lower capacity applications. Lithium-polymer (Li-Po) cells have also been used on CubeSat missions and come in a pouch format with lower weight than Li-ion cells, but are more prone to damage in vacuum. The baseline mission concept uses a small 3.7 Wh Li-ion battery as preliminary analysis showed this was sufficient to power the CubeSat through the eclipse with sufficient margin and acceptable depth of discharge. Additional information regarding the power budget and battery utilization is presented in the power subsystem design section.

On Board Data Handling

The on-board data handling (OBDH) system is the flight computer which consists of a microprocessor, a storage device, and interfaces to connect the various systems such as telemetry, power, and GPS. Several off the shelf, flight computers are available for CubeSats

and the 1U magsail CubeSat does not have any special requirements other than the fact that it should have sufficient clock speed, RAM, and storage to hold the GPS positions and satellite health data. In fact the magsail payload is quite simple to operate, and a simple microcontroller such as Raspberry Pi Zero is sufficient. Compared to the typical flight computers which weigh about 120g, the Pi weighs about 10g. From a cost perspective while the standard flight computers cost upward of several thousand dollars, the Pi costs only \$10. While the Pi is not space rated some aluminum shielding can be added, and two Pi units can fit within the PC104 standard, providing a cross strapped architecture for redundancy.

Deployment System

Based on the deployment studies, the mission concept uses four bistable tape springs to deploy the magsail wire. The bistable booms have been successfully deployed on the InflateSail mission shown in Figure 9.13, and hence has flight heritage. Figure 9.14 shows the InflateSail drag sail deployed during ground testing. The C-shaped bistable booms are fully deployed, and pull the sail into its final shape.



Figure 9.13. InflateSail mission with its drag sail in its deployed configuration in orbit.



Figure 9.14. InflateSail mission with its sail deployed during ground testing. The C-shaped bistable composite booms which pull out the sail from into its shape. Credit: Surrey Space Center.

9.5.3 Baseline Mission Concept

The baseline mission concept consists of two 1U CubeSats deployed from the ISS into a 420 km circular orbit. Both CubeSats are identical and deploy four 1 meter bistable tape spring booms which form a square loop as shown in Figure 9.15.

Only one of the CubeSat magsails is energized with DC current, while the other serves a ‘dummy’ or reference satellite. The magsail is constantly energized with a power of 1.2W drawing power from the battery, which is charged with 1.9 W whenever the CubeSat is in sunlight. The energized magsail encounters both aerodynamic and magsail drag while the dummy magsail only encounters aerodynamic drag. As the two satellites orbit the Earth, the relative separation between the two CubeSats increases because of the difference in drag and their orbit decays at different rates. Both CubeSats log their position using on board GPS receivers and transmit a beacon once every minute with the last several position fixes along with health data on a UHF/VHF frequency to a ground station. Tracking the relative separation accurately provides a precise estimate of the magsail drag against the ambient

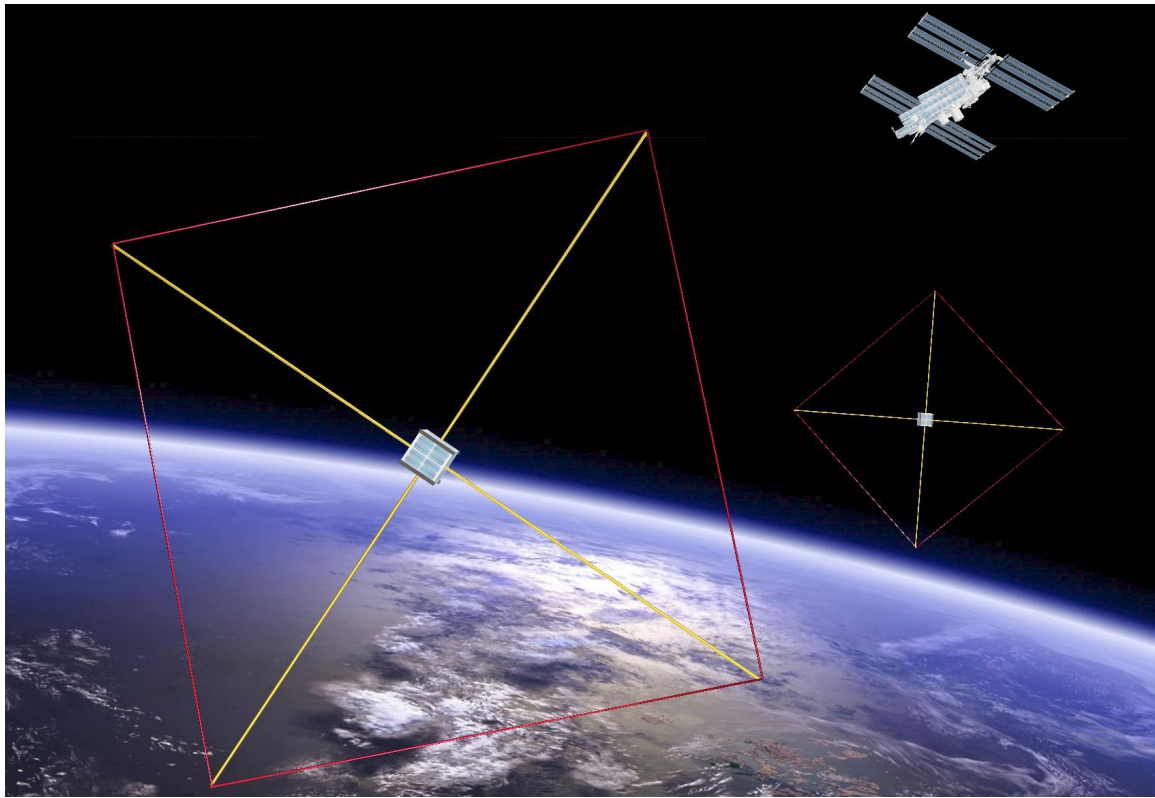


Figure 9.15. Artist's concept of the magsail deorbit CubeSat flight experiment. Two identical 1U CubeSats are launched from the ISS, which use 1 meter long bistable booms to deploy a current carrying wire loop. Only one magsail is energized with DC current, and tracking the relative separation between the two CubeSats provides a precise estimate the magsail drag.

ionospheric plasma, isolating the effects of aerodynamic drag and solar radiation pressure on the orbit. Having identical satellites provides redundancy should one of the CubeSats fail, as the other CubeSat will be programmed to automatically turn on at the end of about 100 days and become the active CubeSat.

The following sections describes the flight system design, mass, power, and volume budgets, and the flight system configuration for the experiment. The mission analysis section provides details of the orbit decay predictions for the two CubeSats, the relative separation and their eventual re-entry.

9.5.4 Flight System Design

The CubeSat uses a standard 1U frame such as the one available from ISIS. Solar panels mounted on all six faces provide an orbital average power (OAP) of 1.9 W. Standard solar panels such as that available from EnduroSat. Some modification or cut outs will be required to allow the magsail deployer to deploy the wire loop from its stowed configuration. The telecom system consists of a standard flight heritage UHF transmitter from ISIS. If it is desired at a later point in the design to include a receiver antenna to actively command the spacecraft, a typical deployable tape spring antenna can be used. Two Raspberry Pi Zero micro-controllers with aluminum shielding is used as the flight computer along with a micro-SD card for data storage. Alternatively, a more robust and space-rated flight computer may be used. To accommodate both options, an 80g mass allocation is provided in the mass budget. The selected battery is a 3.7 Wh Li-ion battery, along with a standard power management board. This battery has been found sufficient to power the magsail constantly at 0.8 W. Alternatively, if magsail operation is restricted to sunlit time only, it could be powered at 1.2 W. The selected EPS is a German Orbital Systems power conditioning and distribution board which is connected to the solar panels, the battery, and all other systems which require power supply including the magsail wire. A low-mass, low-power GPS tracking device from Hyperion Technologies designed for CubeSats is the primary tracking device and is estimated to provide on-orbit positioning accuracy of 10 meters. Should the GPS device fail to work, TLEs from NORAD will be used for tracking but with an accuracy of only 1-2 km. Even this, however, would be adequate, since calculations indicate that the two CubeSats are likely to separate by thousands of kilometers. The deployer consists of 4 tape springs wrapped around a spindle sandwiched between two 94 cm x 94 cm square plates 4 cm apart.

Mass Budget

Table 9.2 shows that the mass budget is within the 1.33 kg allowable for a 1U CubeSat with 250 g margin.

Table 9.2. CubeSat mass budget

Component	Mass, g
Structure	100
Solar panels	264
Transmitter module	75
On-board Computer	80
Li-ion battery	25
EPS	75
GPS Tracker	3
MagSail deployer	400
Connectors, harness	50
Margin	258
Total	1330 g

Power Budget

Two options of powering the magsail are presented below. In the first option, the magsail is powered on only when the CubeSat is in sunlight. This is the one selected for the baseline concept. The power budget for the first mode is shown in Table 9.3.

There are two main power options for the magsail CubeSat: 1) Alternating power, and 2) constant power. In the alternating power option, there are two modes: the sunlit mode during which the magsail is on, and eclipse mode when the magsail is off. The on-board computer, the electrical power system are powered on in both the modes during the entire time. The transmitter is turned on for 0.5 s every one minute during both the modes to transmit the beacon. The GPS is turned on for 3 minutes every one hour, to record a position fix. The power supplied to the magsail is 1.2 W (against the 1.4 W) requirement because the power budget could not be closed at 1.4 W. The selected battery capacity of 3.7 Wh offers nearly a factor of 4 margin against the required 1 Wh. Figure 9.16 shows the battery capacity as a function of time, with an initial charging time of about 10 hours after deployment to fully charge the battery for the first time. Once fully charged the battery discharges only about 0.25 Wh during the eclipse before charging back up fully when in sunlight.

The constant power option is considered to evaluate the possibility of powering the magsail during the entire duration of the orbit. In this option, the magsail is powered on both

Table 9.3. CubeSat power budget for option #1 (powered only during sunlight.)

		Sunlit	Eclipse	
Nominal time, hours		0.95	0.60	Total
System	Power, W	Energy use, Wh	Eclipse use, Wh	Wh
On-Board Computer	0.30	0.29	0.18	0.47
Telemetry, TX	0.20	0.0016	0.0010	0.0026
GPS	0.15	0.0070	0.0045	0.011
EPS	0.10	0.095	0.06	0.16
MagSail	1.20	1.14	0.00	1.14
Energy required, Wh		1.53	0.25	1.78
Energy generated, Wh		1.9 W, 0.95 h sunlight = 1.80 Wh		1.80
Energy margin		1.80 - 1.78		0.02
Energy req. (eclipse)		0.25 Wh		
Battery req.		For 25% DoD* = 1.00 Wh		
Battery capacity		Selcted = 3.70 Wh		

* DoD = Depth of Discharge

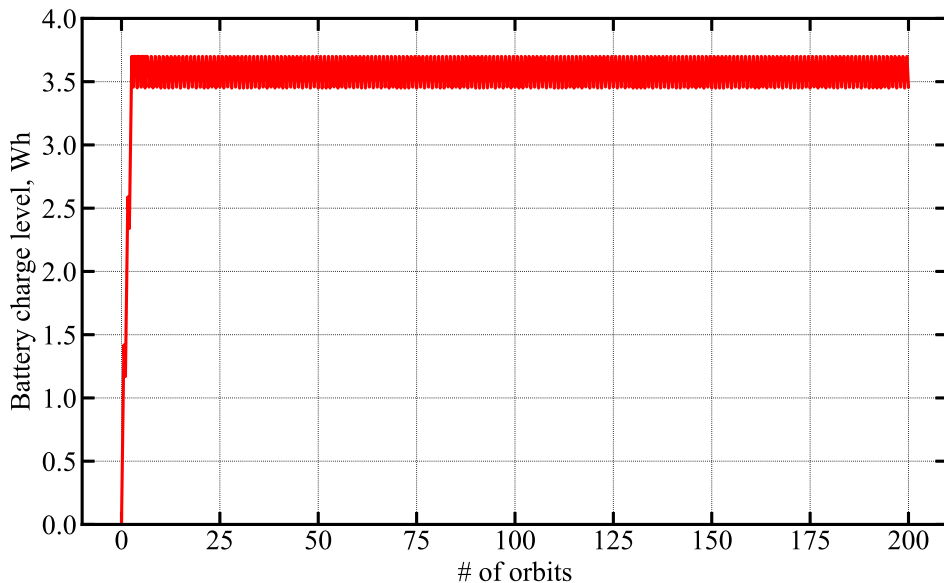


Figure 9.16. Battery charge time history for option #1.

during sunlight and eclipse with a power of 0.75 W. The power budget for the second option is shown in Table 9.4.

To compare the two options, we compare the total magsail drag force impulse in the two cases. From Eq. 9.17, D/M is proportional to $P^{1/3}$. The total impulse goes as $F \times t$. For

option #1 with the alternating power mode, the magsail is powered with 1.2 W for only 0.90 hours when the CubeSat is in sunlight. Hence, the total impulse per orbit goes as $1.2^{1/3} \times 0.95 = 1.08$. For option #2 where the magsail is powered on all the time with 0.75 W , the total impulse goes as $0.75^{1/3} \times 1.55 = 1.40$. Hence, it is desirable to operate the magsail all the time, even though at a lower power level to maximize the total impulse. Figure 9.17 shows the battery capacity utilization for option #2. The battery discharges 0.67 Wh during the eclipse before charging back to full capacity when in sunlight.

Table 9.4. CubeSat power budget for option #2 (constant power the entire time).

Nominal time, hours	Sunlit		Eclipse	Total
	Power, W	Energy use, Wh	Eclipse use, Wh	
On-Board Computer	0.30	0.29	0.18	0.47
Telemetry, TX	0.20	0.0016	0.0010	0.0026
GPS	0.15	0.0070	0.0045	0.011
EPS	0.10	0.095	0.06	0.16
MagSail	0.75	0.71	0.42	1.13
Energy required, Wh		1.10	0.67	1.77
Energy generated, Wh		1.9 W, 0.95 h sunlight = 1.80 Wh		1.80
Energy margin			1.80 - 1.77	0.03
Energy req. (eclipse)			0.67 Wh	
Battery req.			For 25% DoD* = 2.28 Wh	
Battery capacity			Selcted = 3.70 Wh	

* DoD = Depth of Discharge

Link Budget

Table 9.5 shows the link budget for the VHF uplink (CubeSat-to-ground) and the UHF downlink (ground-to-CubeSat, optional receiver). The calculations are adapted from the model by Popescu et al. [208].

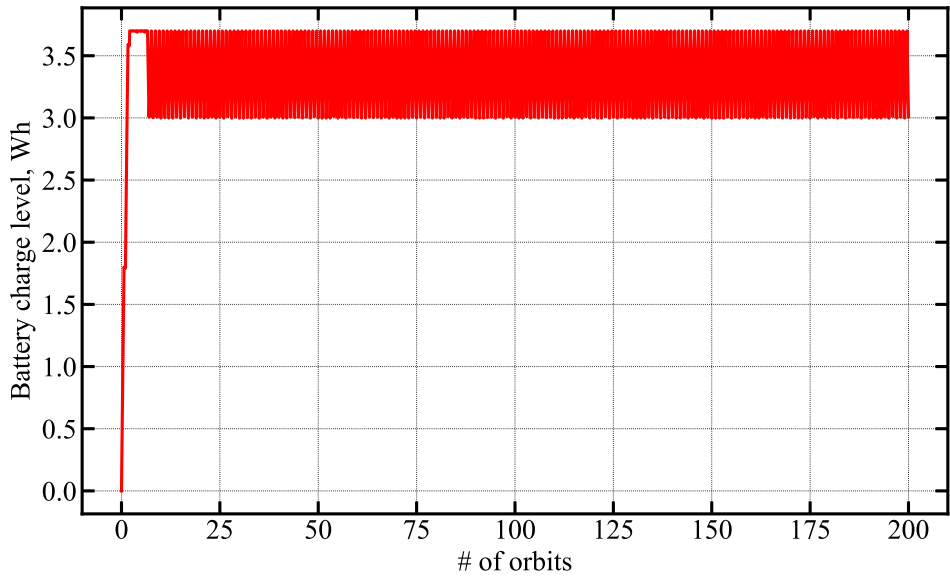


Figure 9.17. Battery charge time history for option #2.

Table 9.5. CubeSat link budget

	Uplink (to-ground)	Downlink (to-satellite)
Frequency, MHz	145	437
Range, km (slant @ 10 deg)	2500	2500
Transmit power, mW	200	100,000
Transmit power, dBm	23.01	50.00
Transmit loss, dB	0.2	3.1
Transmit gain, dBi	0	15.5
Path loss, W	2.31E14	2.09E15
Path loss, dB	143.63	153.21
Other prop. loss, dB	4.1	4.1
Receiver gain, dBi	12.34	0
Receiver noise temp, K	870	1228
Antenna noise temp, K	290	150
System noise temp Ts, K	1160	1378
10 log 10 (Ts), dBK	30.64	31.39
10 log 10(k) + 30	-198.6	-198.6
Data rate, bps	9600	1E6
10 log 10 (R), dBHz	39.8	60
Received SNR	15.76	15.40
SNR required for 1E-5 BER, dB	9.5	9.5
Link margin, dB	6.26	5.90

9.5.5 Configuration Drawings

Figure 9.18 shows configuration drawing of the proposed 1U CubeSat. The magsail deployer is a 0.4U assembly located at the center with slots in the side walls through which the booms are deployed.

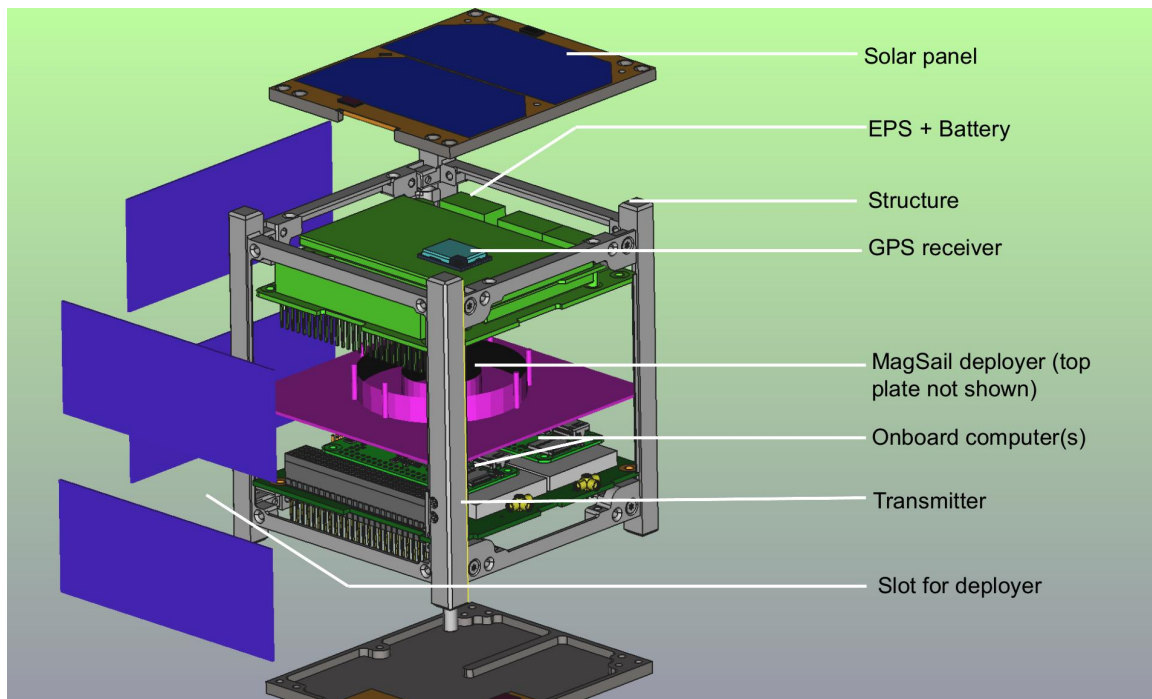


Figure 9.18. Exploded view of the 1U CubeSat.

9.5.6 Mission Analysis

Figure 9.19 shows the orbital decay of the two satellites, CubeSat A which is the dummy magsail and CubeSat B which is the energized magsail over the first 100 days after deployment. A simple RK4 integrator is used to propagate the satellite states forward in time starting from 420 km (ISS altitude). A nominal atmospheric profile is used from the MSISE-90 model for the aerodynamic drag prediction, while the IRI 2019 model is used for the ambient plasma density used in the magsail drag calculation. It is noted that both the neutral and ion density profiles exhibit significant variability with the solar activity, and hence the single profiles used here are only valid for preliminary conceptual design purposes.

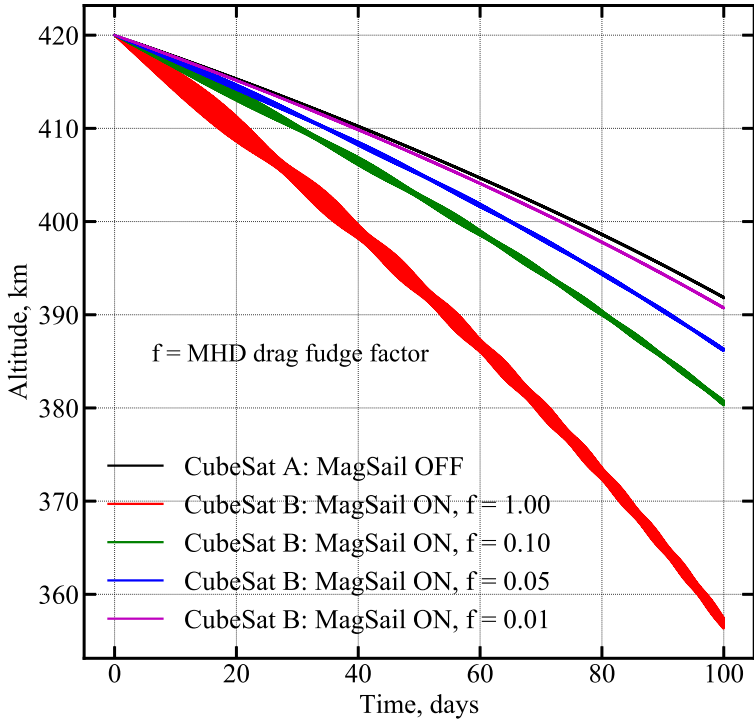


Figure 9.19. Orbit evolution of the two 1U CubeSats over the first 100 days. The black line is the CubeSat with the dummy magsail. The other curves show the orbit decay of the active magsail with various multipliers applied to the drag predicted by MHD.

The solid black line is the orbit decay of the dummy magsail, CubeSat A. The other curves represent the orbital decay of CubeSat B corresponding to various multipliers applied to the predicted MHD drag. For example, if the actual magsail drag is 10% of the MHD prediction ($f = 0.1$, green curve), the difference in orbit altitudes at the end of the 100 day period exceeds 10 km which would be readily observable in both GPS and TLE data. The relative separation between the two satellites is an even better observable parameter, as shown in Figure 9.20. The two satellites start out together as they are deployed simultaneously from the ISS deployer. Because CubeSat B experiences combined magsail drag and aerodynamic drag compared to CubeSat A which only experiences aerodynamic drag, the two satellites begin to drift away from each other and the relative separation grows with time. Eventually the two satellites will be on diametrically opposite sides of the planet, after which they come closer again to a minimum when the CubeSat B passes a few kilometers underneath CubeSat A. Simply observing the number of days it takes for the two CubeSats to achieve the first

maximum separation ($\simeq 2R_E \simeq 13,800$ km) will provide an estimate of the magsail drag, and subsequent orbits will provide even more accuracy. For example, with $f = 0.10$, maximum separation is achieved in about 50 days. The relative separation being a quadratic function of time is more easily observable than the orbital decay of the two CubeSats.

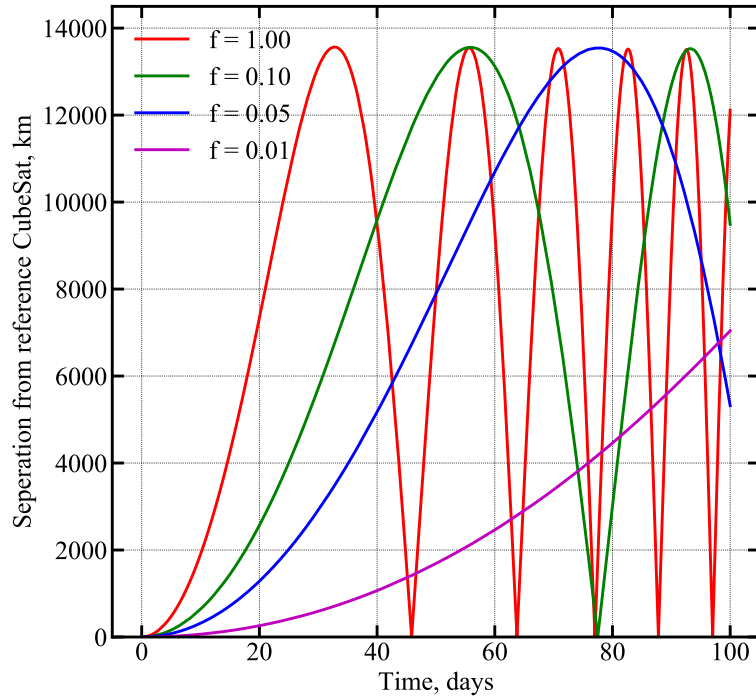


Figure 9.20. Relative separation between the two 1U CubeSats over the first 100 days for various MHD drag fudge factors. Even with $f=0.01$, the relative separation would be clearly observable. In fact simply observing how long the two satellites take to be on opposite sides of the planet (14000 km relative separation) will provide a precise estimate of the magsail drag.

Measuring the relative separation between the two CubeSats as a way of quantifying the magsail drag is one of the key strengths of this experiment. It is a simple, easily observable parameter which is very sensitive to the differential drag between the two satellites (in this case the magsail drag). Basically, simply plotting the observed relative separation on top of the curves in Figure 55 would immediately be able to discern the model which is closest to reality. Even with $f = 0.01$, the relative separation exceeds 1000 km within 40 days; which would be readily observable in tracking data.

Figure 9.21 shows the deorbit predictions until reentry for the two CubeSats. Once again, the number of days before which the active MagSail reenters the atmosphere compared to the dummy magsail can be correlated to the magsail drag. For $f = 0.1$, the active CubeSat will reenter nearly a month ahead of the dummy CubeSat. Even with $f = 0.01$, there will be several days between the reentry of the two CubeSats.

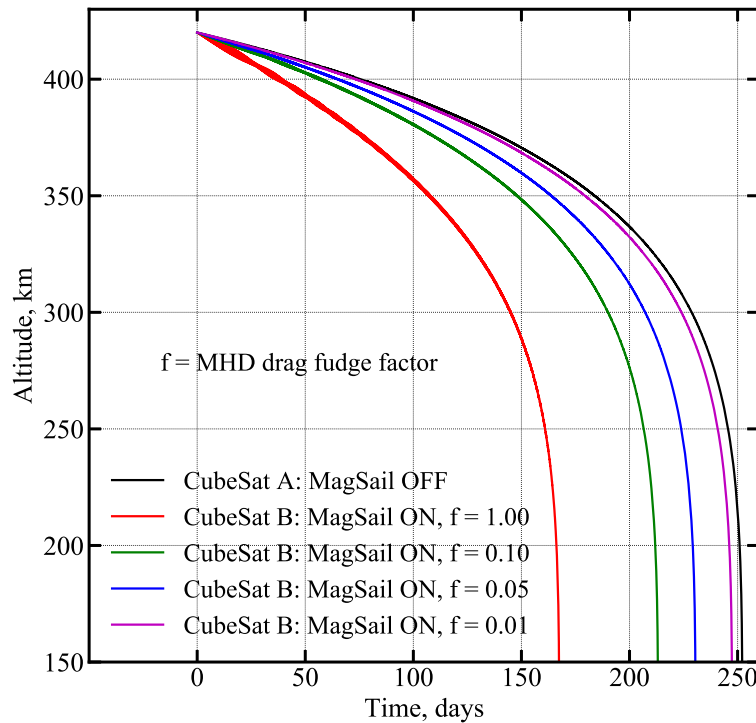


Figure 9.21. Deorbit predictions of the inactive magsail (CubeSat A) and the active magsail (CubeSat B) for various drag multipliers. Observing the time difference it takes for the two satellites to re-enter also provides an estimate of the magsail drag.

The CubeSat design presented here is for a low-cost technology demonstration, and hence operates at a low 400 km altitude. However, magsails are effective at much higher altitudes where aerodynamic drag sails are not effective. Figure 9.22 shows the orbit decay comparison for a 100 kg satellite from various circular orbits ranging from 800 km to 1400 km. The dash-dot black line indicates the orbit decay with no deorbit device. The dashed red line indicates the orbit decay with a 10 m diameter drag sail (such as the one deployed by the InflateSail mission), and the solid blue line indicates the orbit decay with a 10 m diameter magsail carrying 100 A of current.

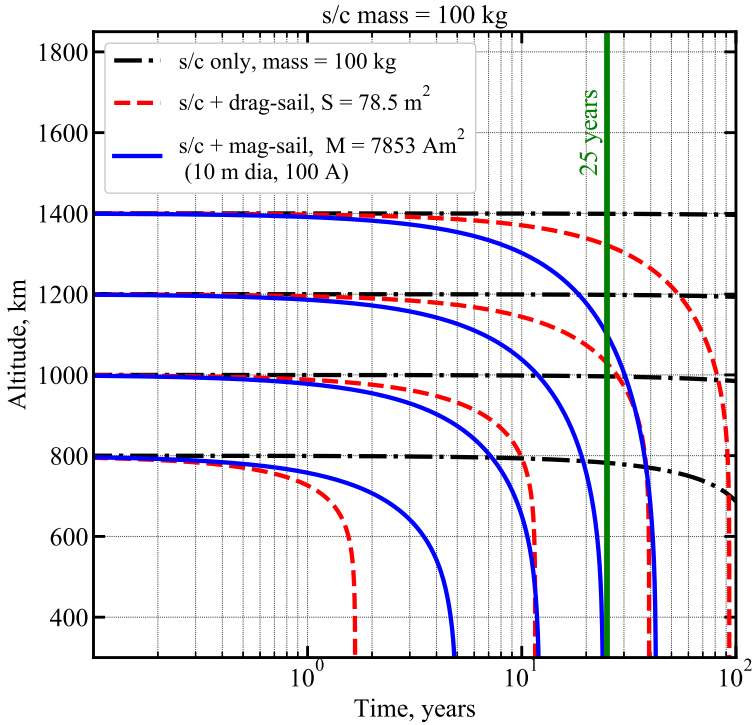


Figure 9.22. Orbit decay predictions for a 100 kg satellite from various circular orbits with no deorbit device (black lines), a 10 m diameter aerodynamic drag sail (red lines), and a 10 m diameter magsail with 100 A current (blue lines). At altitudes above 1000 km, the magsail deorbit offers shorter deorbit times as compared a similar sized aerodynamic sail.

Note that the aerodynamic sail deorbit predictions (red lines) assume the sail can be aligned in a perpendicular direction to the orbital velocity direction, which is likely not possible if the satellite has lost pointing capability. Hence the deorbit times for the drag sail reported in Fig. 9.22 a ‘best’ case scenario.

Even with this assumption, the effectiveness of the magsail as deorbit device above 1000 km is clear. For example, a 100 kg satellite in a 1200 km circular orbit will take at least 40 years to deorbit with the drag sail. With the magsail however, deorbit can be achieved in 25 years. For a 1400 km orbit, deorbit with a drag sail would require nearly a 100 years, whereas a magsail can achieve deorbit in about 35 years. Hence magsail technology offers an effective deorbit method for satellites in 1000-1400 km orbits where aerodynamic drag sails are not effective. In addition, the magsail does not require any pointing. The satellite could be tumbling, and still be able to produce drag using the magsail.

9.6 Magnetoshell Aerocapture

Magnetoshell aerocapture is an advanced concept which uses magnetized plasma in place of an aeroshell [209], [210]. The magnetized plasma generates drag by ionizing and magnetically deflecting the free stream flow using an electromagnet on-board the spacecraft along with some plasma injection [211]. The effective drag area created by the plasma interaction can be modulated by controlling the electromagnet current, and hence this technique offers continuous drag modulation control throughout the maneuver. Preliminary studies show that the effective drag diameter can be of the order of 10–40 m, much larger than that possible with state-of-the-art deployable entry systems such as ADEPT. In addition, the large drag area results in very low ballistic coefficients (as low as 4 kg/m^2) [211]. This allows the vehicle to decelerate in the thinner upper atmosphere and keep the heating rates low, which is of great interest for outer planet missions where planet-relative entry speeds can exceed 25 km/s. Figure 9.23 shows an example concept of operations using a trailing magnetoshell configuration. Additional studies are recommended to investigate the feasibility of accommodating a reliable high-discharge rate power system on-board the vehicle, validate numerical simulations using experimental data to the extent possible, and perform an end-to-end systems analysis study considering the effects of atmospheric and other uncertainties on system performance. Efforts are underway at the University of Washington to demonstrate the technology in a hypersonic rarefied neutral flow experiment [211].

9.7 Conclusion

The study concludes that the magnetic sail is a promising technology for deorbiting satellites. In orbits of 1000 km or higher, magsails with can exert equal drag to aerodynamic devices, with orders of magnitude lower mass requirements, and without any requirement for maintaining attitude control during the deorbiting process. A low cost can experiment can be flown to determine magsail performance, completely eliminating aerodynamic drag as a variable. The study recommends that such an experiment be flown so that magsail performance may be evaluated in space, significantly advancing this important technology towards operational status. Magnetoshell aerocapture, a more ambitious concept holds promise for

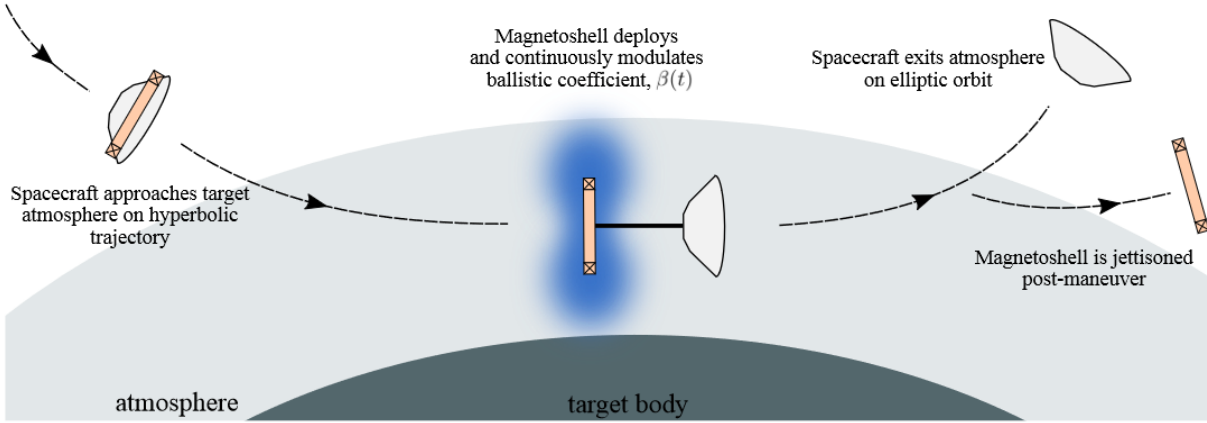


Figure 9.23. Plasma aerocapture with a trailing magnetoshell configuration. The electromagnet current can be modulated to control the effective drag area produced by the magnetoshell, and thus offering continuous drag modulation control without any mechanical parts. Preliminary studies at the University of Washington indicate that this technique may be able to generate an effective drag diameter on the order of 10–40 m, significantly larger than that achievable with current deployable entry systems such as ADEPT. Original work by Charles L. Kelly and Justin M. Little [211]. Used with permission.

future outer planet missions to perform drag modulated plasma aerocapture. The large drag area created by the magnetoshell keeps the heating rates low and perhaps will allow much higher entry speeds and lower interplanetary flight times. However, more experiments and detailed flight systems studies are required before they reach operational status.

Appendix

Software codes used in this work are available online at GitHub³.

³[↑https://github.com/athulpg007/magsail-deorbit](https://github.com/athulpg007/magsail-deorbit)

10. TECHNOLOGY RECOMMENDATIONS

As with any space mission and extensively discussed earlier in the thesis, aerocapture involves multiple disciplines and analyses: science, mission design, interplanetary and atmospheric navigation and control, vehicle and spacecraft design, thermal protection system design, atmospheric models, satellite tour design, programmatic, cost, and risk considerations. This chapter provides recommendations for developments in each of these disciplines and aims to inform NASA technologists in prioritizing aerocapture technology development investments.

10.1 Mission Design Tools

Aerocapture concepts utilize two main mission design tools: an interplanetary trajectory search software, and an atmospheric entry trajectory simulation software. The interplanetary search tool is often the starting point for any mission study. Such tools take in a set of constraints such as launch window, launch C_3 , maximum time of flight, minimum hyperbolic arrival mass, maximum arrival V_∞ etc. along with a list of planetary flyby sequences to be searched for and returns a set of trajectories which satisfy these constraints. Several interplanetary search tools exist such as the Satellite Tour Design Program (STOUR) [128], JPL-STAR [212], and the Evolutionary Mission Trajectory Generator (EMTG) [213] though these tools are generally not publicly available. PyGMO and PyKEP [214] are two open source projects developed at the ESA Advanced Concepts Team for preliminary interplanetary trajectory search. Atmospheric trajectory simulation software start with the initial vehicle state vector at entry interface and propagates the trajectory throughout the atmospheric phase of the flight. Examples include Program to Optimize Simulated Trajectories II (POST2) [215], JPL Dynamics, Simulator for Entry, Descent and Surface landing (DSEENDS) [216] software. The Aerocapture Mission Analysis Tool (AMAT) developed in this study is designed to act as a bridge between interplanetary and atmospheric trajectory codes to obtain better-optimized end-to-end trajectories for aerocapture. AMAT can inform initial constraint values for the interplanetary search tools such as STOUR, shortlist a set of feasible trajectories from the result catalog, perform preliminary aerocapture simulations to evaluate vehicle performance, and provide a reference initial state vector for higher-fidelity

tools such as POST2. The study recommends technology investments in the following areas with respect to preliminary mission design for aerocapture concepts:

- Compile an searchable online catalog of interplanetary trajectories to all Solar System destinations over the next several decades for a wide range of launch and arrival conditions. Hughes [150] has initiated efforts towards compiling such a trajectory catalog. An online trajectory database exists at the NASA Ames Trajectory Browser website¹, though the search query parameters are quite limited. The tool returns only a limited number of trajectories all of which are pre-computed. A more extensive trajectory catalog which permits more query parameters and can also search for new trajectories in addition to the pre-computed trajectories will aid rapid mission design studies. Such a catalog will when combined with tools such AMAT can help identify promising aerocapture trajectories, especially for outer planet missions.
- A full or limited release of at least one NASA developed tool for interplanetary trajectory search and support for aerocapture mission design tools such as AMAT to be incorporated with NASA interplanetary and atmospheric entry trajectory tools to generate end-to-end optimized mission concepts.
- Compile a list of promising design reference aerocapture missions to various Solar System destinations, and include aerocapture discipline experts in the early stage of mission studies to inform both the capabilities and risks of aerocapture.

10.2 Navigation and Guidance

Two areas of particular interest to aerocapture missions are interplanetary approach navigation near the target planet and the on-board guidance algorithm which steers the vehicle during the atmospheric flight. Currently, interplanetary approach navigation is done with the ground in the loop. The spacecraft state is determined using ranging, Doppler, and optical navigation images which are transmitted to Earth, using which ground controllers determine appropriate manuevers and then command the spacecraft to perform these manuevers.

¹[↑https://trajbrowser.arc.nasa.gov/](https://trajbrowser.arc.nasa.gov/)

For missions such as those to the outer planets, the one-way light time is substantial and hence it is not feasible to have the ground in the loop during the final days or hours of the planetary approach which are critical in determining the delivery error at atmospheric interface. NASA has been developing the AutoNav technology which automatically determines the spacecraft state (for example, using optical navigation images) and commands necessary maneuvers to achieve the desired entry conditions [217]. Spacecraft autonomy is also critical post-aerocapture, for the spacecraft to determine its capture orbit, perform propulsive burns to raise the periapsis outside the atmosphere and correct apoapsis targeting errors. The second area of interest is the development of advanced flight control methods and guidance schemes for atmospheric flight. Traditionally entry vehicles have only used bank angle modulation which gives limited aerodynamic control. In addition to the bank angle, the angle-of-attack, sideslip angle and trim tabs can be actively commanded to provide more aerodynamic control [218].

- The study recommends NASA support efforts to continue the development of AutoNav and related spacecraft autonomy technologies, particularly for outer planet missions where accurate delivery of the vehicle to the atmospheric interface and performing autonomous post-aerocapture propulsive burns are critical.
- The study recommends technology developments in the areas of advanced flight control methods for aerocapture vehicles, and robust and reliable guidance schemes which can steer entry vehicles in uncertain atmospheric environments.

10.3 Aerocapture Vehicle Design

Derivatives of lifting entry vehicles such as MSL, Apollo, and Orion can be readily used for aerocapture missions with some modifications such as the adapting the aeroshell jettison mechanism to work outside of an atmosphere. NASA has been supporting the development of a rigid drag skirt drag modulation aerocapture flight system which could be flown to Venus, Mars, and Titan in the near term. Of particular interest for drag modulation aerocapture is the drag skirt jettison event, during which a clean separation which minimizes any risk of re-contact is essential. While deployable systems such as ADEPT have been extensively studied

for entry missions, few studies have addressed its applicability for aerocapture. Compared to a rigid drag skirt, a deployable drag skirt can be stowed during launch and cruise and can be deployed just before aerocapture. This minimizes the volume footprint, particularly for rideshare satellites on the host spacecraft. Additional studies are required to understand the separation dynamics and recontact risk for deployable drag skirts. As shown in Chapters 6 and 7, using the accelerometer data to construct a real-time atmospheric density profile during the descending leg of aerocapture is of significant interest for aerocapture. Advanced and efficient on-board data processing algorithms are required to denoise the data and reconstruct a near real-time atmospheric profile during the maneuver for use by the guidance algorithm in apoapsis targeting.

- The study recommends continued NASA support for computational and experimental efforts to realize a feasible drag modulation aerocapture flight system which minimizes risk of recontact and ensure a clean separation.
- The study recommends support for efforts to realize a deployable drag skirt for drag modulation aerocapture which could enable CubeSat sized rideshare interplanetary spacecraft to achieve orbit insertion at Mars, Venus, and Titan.
- The study recommends the continued development of advanced on-board data processing algorithms to denoise the accelerometer data and construct a real-time atmospheric profile for accurate apoapsis targeting.

10.4 Thermal Protection Systems

Existing flight-proven thermal protection system materials such as PICA are sufficient for aerocapture at Mars, Titan, and possibly Venus. HEEET is the likely TPS for aerocapture at Uranus and Neptune, and has been tested under laboratory conditions for these entry environments. However due to facility limitations, often the combined effect of stagnation-point heat rate and stagnation pressure is somewhat difficult to replicate during testing. Computational models can complement such parameter regimes where experimental testing is difficult or prohibitive due to cost. Drag modulation aerocapture systems using PICA TPS are well understood and require no additional developments. However, deployable drag

skirts using materials such as carbon cloth can benefit from additional modeling and arc jet testing efforts. Aerothermodynamic environments at the ice giant planets are the most challenging due to the relatively high entry speeds (20–30 km/s). No accurate sizing relations are available to estimate the TPS mass fraction for aerocapture at these destinations, and presents a major challenge for conceptual studies. The study recommends NASA support the following efforts for advancing TPS technology for aerocapture missions:

- Perform computational studies to assess the aerothermodynamic environment for aerocapture at Uranus and Neptune, and refine empirical relations for computing heat rates, TPS material response, and TPS mass fraction.
- Expand HEEET arc-jet testing campaign results to the extent possible to simulate heat flux and stagnation pressure conditions at Uranus and Neptune, and complement experimental results with modeling studies to optimize the fabric layup for the aerocapture trajectory heating profiles at these destinations.
- Assess the performance of drag modulation system TPS materials for aerocapture at Uranus and Neptune with rigid and deployable drag skirts.
- Support development efforts to realize a deployable and jettisonable drag skirt which serves as both the structure and TPS for a drag modulation aerocapture.

10.5 Spacecraft and Probe Design

The fact that the spacecraft needs to be enclosed in an aeroshell for lift modulation aerocapture (and at least partially for drag modulation aerocapture) will be a design driver for the spacecraft. Prior to the aerocapture maneuver, an MSL-like cruise stage may provide communications and propulsion capability for the spacecraft which is inside the aeroshell. After the aerocapture maneuver, the heat soaked aeroshell must be jettisoned immediately and the spacecraft must activate its deployables such as antennae, instruments, and sensors so as to obtain attitude control and orbit determination. The spacecraft must also almost immediately prepare for the periapsis raise and apoapsis correction burns (likely autonomous). Four outer planet missions, the spacecraft almost certainly will carry an entry probe which

either needs to be accommodated inside the aeroshell and be released post aerocapture, or mounted externally and be released prior to the main spacecraft performing aerocapture. Probe accommodation inside the aeroshell presents packaging challenges, whereas externally mounted probes have to be deployed in such a way that the cruise stage can act as a relay while the probes enter the atmosphere. The study recommends the following technology developments for aerocapture spacecraft and probe design:

- Perform the design of an outer planet orbiter spacecraft which is designed to be packaged within an MSL or Apollo like aeroshell with a jettisonable heat shield and associated deployables such as antennae, RPS, and instrument booms.
- Perform studies to better understand the operational requirements for the spacecraft immediately after aerocapture such as the time constraints for heat shield and aeroshell jettison, antenna deployment, detumbling and attitude stabilization, orbit determination, preparation for propulsive burns to establish a stable initial capture orbit, and report critical telemetry to ground stations.
- Perform mission architecture studies for probe accommodation and deployment and data capture strategies for an outer planet aerocapture mission.

10.6 Atmosphere Models

To the extent required for aerocapture, the atmospheres of Venus, Mars, and Titan are fairly well constrained and require no significant advances over existing models such as GRAM. Our knowledge is most lacking for Uranus and Neptune whose atmospheres have large uncertainties due to the lack of any in situ measurements. Large atmospheric model uncertainties impose more aerodynamic control demands on the aerocapture vehicle to allow the vehicle to compensate for these uncertainties during the maneuver. If the control variable becomes saturated and the vehicle is not able to achieve the desired exit conditions, the spacecraft risks not getting captured and will lead to an almost certain loss of mission. The large atmospheric uncertainties remain one of the major hurdles for aerocapture at the ice giants, since sending a multi-billion dollar class spacecraft into a relatively unknown atmosphere presents an inherent and substantial risk for program managers. Since in-situ

measurements are not forthcoming until a probe enters their atmosphere, remote sensing observations using telescopes and opportunistic stellar occultation measurements for Uranus and Neptune, and development of global circulation models remain the only way to probe these atmospheres and provide bounds for engineering models. The study recommends the following technology efforts towards improving atmospheric models:

- Provide continued support for GRAM model development and upgrades, incorporating new datasets into models for Venus, Mars, and Titan from recent missions and development of GRAM models for Jupiter, Saturn, and Uranus.
- Study the possibility of using orbital and in-situ assets at Mars and Venus to create 'day-of-flight' density model which can be uploaded to a drag aerocapture vehicle just before entry so as to minimize orbit targeting errors.
- Support community efforts to use Earth and space-based telescopes for observations of the atmospheres of Uranus and Neptune including stellar occultations, development of global circulation models, and incorporating the data into engineering models such as GRAM to better constrain ice giant atmospheres.

10.7 Satellite Tour Design

Once captured into orbit, missions such as those to the Saturn-Titan system or the Neptune-Triton system will use planetary moon flybys to change the orbit without using propellant. Such targeted moon flybys will allow close observations of various latitudes and longitudes on both the moon and the planet as demonstrated by the Galileo and Cassini missions. Specialized tools such as Mystic Low-Thrust Trajectory Design and Visualization Software are available for designing and optimizing moon tours. The initial target orbit for aerocapture has to be selected considering the orbit requirements for such tours. The selection of a prograde vs. retrograde orbit at Neptune has important implications for the subsequent Triton tour and vehicle aerothermal loads. A retrograde orbit minimizes the Triton relative flyby speed, but results in much higher planet relative entry speed and aerothermal load compared to a prograde entry. Satellite tours are of particular interest for missions to the Saturn, Uranus, and Neptune systems where there is significant scientific

interest for the spacecraft to perform close targeted flybys of the satellites. The feasibility of performing such moon tours with an aerocapture mission architecture is not well understood, with the exception of Neptune-Triton system for which preliminary studies exist. The Saturn system offers a plethora of possibilities such as using aerocapture or aerogravity assist at Titan to place a spacecraft into orbit around Titan or Saturn and also flyby the various moons and ring systems. The study recommends the following technology efforts for moon tour design with aerocapture:

- Assess the viability of performing moon tours at Saturn, Uranus, and Neptune for aerocapture missions considering the constraints from interplanetary arrival trajectory, probe delivery, and post-aerocapture orbit targeting accuracy.
- Develop a design reference concept for a Flagship-class tour of the Neptune-Triton system considering the competing requirements of prograde vs. retrograde orbits for Triton flybys and aerocapture heating loads.

10.8 Programmatic, Cost, and Risk Considerations

Most of the work presented in this thesis concerns the ‘technical’ feasibility aspect of aerocapture missions. However, NASA program managers, in addition to the technical aspects are naturally concerned about the programmatic, cost, and risk considerations of using aerocapture. Very little literature exists about these aspects of aerocapture. For example, consider a hypothetical scenario² where the science community is planning to insert a Flagship-class orbiter into orbit around Neptune. The program manager is presented with two design alternatives: #1) a relatively modest science package inserted into orbit using conventional propulsive orbit insertion; and #2) a well-instrumented and fairly comprehensive science package inserted into orbit using aerocapture. Option #1 requires the use of a heavy-lift launch vehicle such as Delta-IVH, and the spacecraft takes 13 years to reach Neptune. Option #2 requires the use of a medium-lift launch vehicle such as Atlas V551, and

²Based on the example presented in NASA Risk Management Handbook [219]. The scenario and numbers used are hypothetical and for the purpose of discussion.

the spacecraft takes 10 years to reach Neptune. A Flagship-class mission can cost upwards of \$2B and the program manager must carefully take various factors into consideration.

Option #1 relies on a proven conventional orbit insertion technique which carries very low technical, cost, and schedule risk. Because the science package is modest, the returned total science data volume is low. However, there is a very high probability that certain key measurements can be performed within only few months of orbit insertion. Because the mission uses a heavy-lift launcher, the cost of this mission is higher than option #2. Also, the long transit time implies that the operational orbit duration is limited to 2 years as the Radioisotope Power Generators (RTGs) do not produce sufficient power beyond 15 years. This implies limited capability for follow up observations of new discoveries and an extended mission. The spacecraft bus design and instrument suite can be readily adapted from previously flown spacecraft and carries very little cost and schedule risk. Overall, this mission architecture allows the program manager to convince the stakeholders (eg: science community, NASA, Congress, public taxpayer) that the mission will achieve a modest set of science goals with a very high reliability and very low technical, cost, and risk posture.

Option #2 involves the hitherto untested aerocapture maneuver which carries at the very least moderate and worst case high technical, cost, and schedule risk. Because the science package is comprehensive, the returned total science data volume is much higher than option #1. However, if the aerocapture maneuver fails (eg: the spacecraft burns up or fails to capture into orbit) there is a risk of no data being returned at all. Because the mission uses a medium-lift launcher, the cost of this mission is lower than option #1. The shorter transit time allows a longer science orbit duration for an extended mission and follow up observations. Because the spacecraft must fit inside an aeroshell, a new spacecraft needs to be designed and incorporated with an entry vehicle which also needs modifications to an existing design. Designing a new spacecraft bus and aeroshell comes with a fair share of technical and cost risk, and schedule risk which may lead to the project not being able to meet the launch window. Overall, while this mission architecture promises a greater total science data volume and more science per dollar, there is risk of no science returned at all as well as cost and schedule risks from having to design, build, and test a new spacecraft design.

From the program manager's perspective, he or she has to choose between the low return, low risk option #1 and the high return, high risk option #2. Since NASA is accountable to Congress and the general public, a program manager will choose the low cost, low risk option as it offers the possibility of a near-certain success, however small it may be. It is general human nature to be risk-averse when offered the possibility of near certain gain (even though the reward is low as in the case of option #1) and risk-seeking when presented with a near certain loss [219]. For example, consider the scenario where a propulsion system has under-performed during orbit insertion leaving the spacecraft captured into an orbit from which its high priority science goals cannot be achieved within the time frame of the mission. Some data can be obtained, but it is likely not enough to answer the key science questions. It is proposed to use aerobraking to lower the orbit to one more suited for the mission, but the solar panels have not been designed for aerobraking loads and may disintegrate leading to loss of the spacecraft. If the aerobraking campaign is successful, the necessary data can be collected along with additional observations of the upper atmosphere. The mission manager is presented with near certain loss due to the initial orbit being sub-optimal, and will likely consider using aerobraking as the gains certainly outweigh the risk. The study recommends NASA support the following efforts to allow program managers to make risk informed decisions regarding future missions:

- Assess the technical, cost, and schedule risks associated with aerocapture missions for various destinations. For example technical risks include but are not limited to: the spacecraft burning up or skipping out due to higher than or lower than expected atmospheric density or navigation errors, the spacecraft being inserted into an unusable or sub-optimal orbit, the aeroshell fails to separate after aerocapture, the spacecraft failing to perform the periapse-raise propulsive burn resulting in re-entry at the first periapse pass. Cost risks include new spacecraft design and testing efforts overshooting the budget, also potentially affecting other missions. Schedule risks include not being able to meet the launch window, or increased costs associated with schedule slips.

- Perform independent cost and risk assessments of promising aerocapture mission concepts to avoid bias. Because of human nature, technologists trying to ‘push’ aerocapture as a technology for future missions will have a bias toward favoring the technology and portraying it as low cost and low risk; while mission managers will be biased toward the status-quo and proven low risk solutions.
- Identify areas where risk reduction activities could be performed such as observations of outer planet atmospheres, thermal protection system arc jet testing, spacecraft packaging issues, autonomous approach navigation and orbit determination post-aerocapture, and low-cost technology demonstration missions. Support development of parametric cost models for aerocapture missions which can be used with minimal set of inputs during conceptual design studies.

10.9 Small Satellite Constellations

Small satellite constellations such as those operated by Planet Labs, SpaceX (Starlink), OneWeb and ICEYE (SAR constellation) have demonstrated their cost-effectiveness and great utility in near real-time global imaging, communications, and radar observations over the past decade. Constellations of CubeSats and SmallSats (< 180 kg) can enable a new paradigm in planetary exploration by enabling global imaging and radar observations of Mars and Venus at a fraction of the cost and much less risk than that of a large mission. Such missions may also provide communication and internet services to future manned missions to Mars. Until now, orbit insertion has been a formidable challenge for small satellites due to their small form factor. However, with maturation of drag modulation technology over the last five years it is now possible to insert small satellites into very low circular orbits at Mars and Venus. Drag modulation technology is particularly attractive to small satellites as the deployable drag skirt can be stowed during launch and cruise, and can be deployed just prior to atmospheric entry eliminating the need for an aeroshell and RCS thrusters required for lift modulation aerocapture. Just as a single launch vehicle routinely launches several constellation satellites into Earth orbit, a single interplanetary cruise stage can deliver multiple small satellites into different orbits (for example, different inclinations) to form a

constellation. The study recommends the following to support small satellite constellations for future planetary science missions:

- Perform mission concept studies to assess the feasibility, cost, and technical challenges of inserting multiple imaging or SAR satellites from a single interplanetary cruise stage into different inclination orbits at Mars and Venus.
- Assess the feasibility of small satellite constellations for outer planet missions (Titan, Uranus, and Neptune) using drag modulation systems. While small satellites cannot be as well-instrumented or as long-lived as a large mission, small satellite constellations can enable multi-point observations particularly from close-in circular orbits which are not possible with a single spacecraft.

10.10 Design Reference Missions

Design reference missions are intended to provide science investigators and mission planners with an optimized baseline mission concept from the plethora of options available for a mission architecture. Such mission concept studies provide the high-level mission architecture (launch vehicle, interplanetary trajectory, arrival geometry etc.) along with the flight system design (spacecraft and aerocapture system), as well as cost and schedule estimates. The study recommends support for the following end-to-end design reference aerocapture mission concept studies:

- Demonstration of aerocapture at Earth using a low-cost drag modulation system launched as a secondary payload on a GTO mission.
- Inserting a small satellite (CubeSat or SmallSat) into a low circular orbit (400 km) at Mars or Venus using a drag modulation flight system.
- Inserting small satellite(s) into orbit around Venus which serve as a data relay for an aerial platform or a long-lived lander delivered on the same mission.
- Inserting multiple small satellite constellations into different inclination low circular orbits around Mars and Venus for optical imaging or SAR constellations from a single interplanetary cruise stage such as that flown on MSL.

- Delivering a lander, rover, or rotor-craft to Titan’s surface along with one or more small satellites into Titan orbit which serve as both science platforms and data relays for a Flagship-class mission following the Dragonfly mission.
- Delivering a Flagship-class orbiter and atmospheric probe to explore the Uranus system using a low- L/D blunt-body aeroshell within a \$2B cost-cap.
- Delivering a Flagship-class orbiter and probe to explore the Neptune system and perform multiple targeted Triton flybys using a low- L/D blunt-body aeroshell within a \$2B cost-cap, and a flight time not exceeding 10 years.

10.11 Conclusions

This chapter provided a list of recommended technology developments in the areas of mission design, navigation and guidance, aerocapture vehicle design, thermal protection systems, spacecraft and probe design, atmosphere models, and satellite tour design for future aerocapture missions. A brief discussion of the programmatic and risk considerations of aerocapture from a program management perspective is presented, along with recommendations for future studies. The importance of small satellite constellations using aerocapture enabling a new paradigm of planetary science mission is discussed, and a recommended list of design reference missions is provided for future aerocapture mission concept studies.

11. SUMMARY

Chapter 1 introduced the concepts of aerocapture and aerobraking along with a brief overview of planetary atmospheres and relevant systems engineering concepts. Key advantages and risks of aerocapture for future planetary missions were discussed, along with the need for a systems framework for rapid conceptual design of aerocapture missions.

Chapter 2 presented the results from an extensive literature survey tracing the origin and evolution of the aerocapture concept over the past six decades. The survey revealed that several flight programs such as the AFE that could have demonstrated aerocapture technology. Unfortunately, these experiments were not flown and hence aerocapture has never been demonstrated. Beginning late 2010s, there is renewed interest in aerocapture technology particularly for small satellite missions to Venus and Mars, and for future Flagship-class missions to Uranus and Neptune. Small satellites are of particular interest to untested technologies such as aerocapture, as they can accommodate higher risks without compromising large missions which are risk-averse. With increasing capability and applications of small satellites, it is likely that aerocapture will be demonstrated at Mars or Venus within a decade.

Chapter 3 presented a comprehensive feasibility and mass-benefit analysis of aerocapture for missions to Venus. The study indicated that aerocapture is a feasible orbit insertion technique at Venus and allows increased delivered mass to a low Venus orbit compared to propulsive insertion. Lift modulation aerocapture at Venus is feasible with existing MSL-like low- L/D aeroshells and HEEET TPS. Drag modulation aerocapture is an attractive option for SmallSats as secondary payloads given its small mass and volume footprint on a carrier spacecraft. Propulsive capture to highly elliptical orbit followed by aerobraking to low circular orbit is the most attractive option for orbit insertion at Venus. Aerocapture offers significant mass-benefit to future radar mapping missions, sample return missions, and other missions for which a low circular Venus orbit is highly desirable immediately upon arrival.

Chapter 4 applied the methodology developed in Chapter 3 for Venus to all atmosphere-bearing destinations in the Solar System including Jupiter and Saturn. Comparative studies are performed to illustrate the similarities and differences of aerocapture mission concepts across planetary targets from Venus to Neptune. Aerocapture is shown to provide enhanc-

ing capability for missions to Venus (100%–200% more delivered mass) and Mars (100%–400%) with high arrival V_∞ interplanetary trajectories. For missions to Titan, aerocapture is strongly enhancing (300%–1700% more mass) for trajectories with arrival V_∞ from 6–8 km/s, and an enabling technology for higher arrival V_∞ trajectories. For missions to Uranus, aerocapture is strongly enhancing (100%–600%) for V_∞ from 12–16 km/s and enabling for arrival V_∞ beyond 16 km/s. For missions to Neptune, aerocapture delivers 80%–400% more mass for trajectories with V_∞ from 12–16 km/s and is an enabling technology for higher arrival V_∞ . High arrival V_∞ trajectories ($V_\infty > 16$ km/s) can potentially allow interplanetary flight times to be as low as 6 and 8 years to Uranus and Neptune respectively.

Chapter 5 described the systems engineering framework for rapid aerocapture mission design developed in this work. This chapter provides a step-by-step procedure to formulate an aerocapture mission starting from a set of mission objectives. The framework highlights the various interdependencies between aerocapture mission elements such as interplanetary trajectory and vehicle design, and provides a step-by-step methodology to formulate an aerocapture mission architecture starting from a set of high-level objectives.

Chapter 6 illustrated the application of the systems framework to perform rapid conceptual design of a Venus SmallSat mission. The study assessed the feasibility of drag modulation aerocapture to insert small satellites into orbit around Venus. The aerocapture feasibility chart is used to identify the feasible region in the aerocapture vehicle and mission design space. A reference mission concept ($\beta_2/\beta_1 = 7.5$, $V_\infty = 4$ km/s) is selected as the baseline for more detailed analysis. Monte Carlo simulation is used to assess vehicle performance in the presence of expected navigation and atmospheric uncertainties. The reference mission and vehicle design is shown to provide acceptable orbit targeting accuracy, peak deceleration, stagnation-point heat rate, and periapse raise ΔV . Chapter 7 illustrated the application of the systems framework to a Flagship-class Neptune orbiter. Results indicate that the reduced navigation uncertainty and an improved guidance scheme enable a blunt-body aeroshell with L/D of 0.30–0.40 to perform aerocapture at Neptune.

Chapter 8 described the Aerocapture Mission Analysis Tool (AMAT). AMAT is an open-source Python package designed to provide rapid mission design and analysis capability for aerocapture mission concepts. The systems framework developed in this thesis forms the

core of the AMAT package, and enables rapid end-to-end mission design in a concurrent engineering environment. The package comes with extensive documentation, numerous examples to help the user get started, and publicly available source code to ensure long-term accessibility of the code and facilitate potential contributions from future researchers.

Chapter 9 explored the concept of magnetic sails for aerobraking in a planet's ionosphere. The magnetic sail create drag forces by deflecting charged particles in the upper atmosphere and is a promising technology for de-orbiting satellites from altitudes over 1,000 km. A low-cost Cube experiment is proposed to validate the concept in Low-Earth Orbit. More advanced versions of this technology such as magnetoshell aerocapture may one day be used for inserting large orbiters around Uranus and Neptune.

Chapter 10 presented recommendations for aerocapture technology developments. This chapter provided a list of recommended technology developments in the areas of mission design, navigation and guidance, aerocapture vehicle design, thermal protection systems, spacecraft and probe design, atmosphere models, and satellite tour design for future aerocapture missions. A brief discussion of the programmatic and risk considerations of aerocapture from a program management perspective is presented, along with recommendations for future studies. The importance of small satellite constellations using aerocapture enabling a new paradigm of planetary science mission is discussed, and a recommended list of design reference missions is provided for future aerocapture mission concept studies. A low cost technology demonstration mission at Earth or Mars can establish flight-heritage for aerocapture and lower the risk for larger NASA science missions.

As pointed out by Spilker et al. [3], the benefits offered by aerocapture for future missions could be compared to the vastly increased capability for exploration offered by the gravity-assist technique in the early days of interplanetary flight. Once proven, aerocapture will be a key strategy enabling large constellations of small satellites around Mars and Venus and delivering sizeable orbiters within reasonable flight times to the outer Solar System.

REFERENCES

- [1] J. L. Hall, M. A. Noca, and R. W. Bailey, “Cost-Benefit Analysis of the Aerocapture Mission Set,” *Journal of Spacecraft and Rockets*, vol. 42, no. 2, pp. 309–320, 2005, ISSN: 0022-4650. DOI: [10.2514/1.4118](https://doi.org/10.2514/1.4118).
- [2] M. Cruz, “Technology Requirements for a Generic Aerocapture System,” in *15th Thermophysics Conference*, Snowmass, CO, 1980, p. 1493. DOI: [10.2514/6.1980-1493](https://doi.org/10.2514/6.1980-1493).
- [3] T. R. Spilker, M. Adler, N. Arora, P. M. Beauchamp, J. A. Cutts, M. M. Munk, R. W. Powell, R. D. Braun, and P. F. Wercinski, “Qualitative Assessment of Aerocapture and Applications to Future Missions,” *Journal of Spacecraft and Rockets*, vol. 56, no. 2, pp. 536–545, 2018. DOI: [10.2514/1.A34056](https://doi.org/10.2514/1.A34056).
- [4] H. S. London, “Change of Satellite Orbit Plane by Aerodynamic Maneuvering,” *Journal of the Aerospace Sciences*, vol. 29, no. 3, pp. 323–332, 1962, ISSN: 1936-9999. DOI: [10.2514/8.9416](https://doi.org/10.2514/8.9416).
- [5] O. Pawlyk, “Former SecAF Explains How Secret X-37 Space Plane Throws Off Enemies,” *Military News*, vol. July, 2019. [Online]. Available: <https://www.military.com/daily-news/2019/07/23/former-secaf-explains-how-secret-x-37-space-plane-throws-enemies.html>.
- [6] T. W. Finch, “Aerodynamic Braking Trajectories for Mars Orbit Attainment,” *Journal of Spacecraft and Rockets*, vol. 2, no. 4, pp. 497–500, 1965. DOI: [10.2514/3.28218](https://doi.org/10.2514/3.28218).
- [7] J. H. Lichtenstein, “Some Considerations on the Use of Atmospheric Braking for a Transfer Into a Martian Orbit,” NASA Langley Research Center, Hampton, VA, Tech. Rep. NASA TN D-2837, 1965. [Online]. Available: <https://ntrs.nasa.gov/api/citations/19650016654/downloads/19650016654.pdf>.
- [8] E. M. Repic, Boobar, M. G., and F. G. Chapel, “Aerobraking as a Potential Planetary Capture Mode,” *Journal of Spacecraft and Rockets*, vol. 5, no. 8, pp. 921–926, 1968, ISSN: 0022-4650. DOI: [10.2514/3.29389](https://doi.org/10.2514/3.29389).

- [9] M. Cruz, “The Aerocapture Vehicle Mission Design Concept,” in *Conference on Advanced Technology for Future Space Systems*, Hampton, VA, 1979. DOI: [10.2514/6.1979-893](https://doi.org/10.2514/6.1979-893).
- [10] R. Hassett, “Design Integration of Aerocapture and Aeromaneuver Vehicles for a Mars Sample Return Mission,” in *21st Structures, Structural Dynamics, and Materials Conference*, Seattle, WA, 1980, p. 728. DOI: [10.2514/6.1980-728](https://doi.org/10.2514/6.1980-728).
- [11] Anonymous, “Generic Aerocapture Atmospheric Entry Study,” Philadelphia, PA, Tech. Rep. NASA-CR-164161, 1980. [Online]. Available: <https://ntrs.nasa.gov/api/citations/19810012569/downloads/19810012569.pdf>.
- [12] M. Cruz, “Aerodynamic Mission concepts for the Mars Sample Return Mission,” in *7th Atmospheric Flight Mechanics Conference*, Albuquerque, NM, 1981, p. 1859. DOI: [10.2514/6.1981-1859](https://doi.org/10.2514/6.1981-1859).
- [13] S. Tiwari, H. Chow, and J. Moss, “Analysis of Aerothermodynamic Environment of a Titan Aerocapture Vehicle,” in *16th Thermophysics Conference*, Palo Alto, CA, 1982, p. 1128. DOI: [10.2514/6.1981-1128](https://doi.org/10.2514/6.1981-1128).
- [14] K. Mease, J. Kechichian, L. Wood, M. Cruz, and R. Weidner, “Aerocapture - Guidance, Navigation, and Control,” in *9th Atmospheric Flight Mechanics Conference*, San Diego, CA, p. 1381. DOI: [10.2514/6.1982-1381](https://doi.org/10.2514/6.1982-1381).
- [15] M. Green, J. Moss, and J. Wilson, “Aerothermodynamic Environment and Thermal Protection for a Titan Aerocapture Vehicle,” in *19th Thermophysics Conference*, Snowmass, CO, 1984, p. 1714. DOI: [10.2514/6.1984-1714](https://doi.org/10.2514/6.1984-1714).
- [16] C. Cerimele, L. Skalecki, and J. Gamble, “Meteorological Accuracy Requirements for Aerobraking Orbital Transfer Vehicles,” in *22nd Aerospace Sciences Meeting*, Reno, NV: AIAA, 1984. DOI: [10.2514/6.1984-30](https://doi.org/10.2514/6.1984-30).
- [17] C. Cerimele and J. Gamble, “A Simplified Guidance Algorithm for Lifting Aeroassist Orbital Transfer Vehicles,” in *23rd Aerospace Sciences Meeting*, Houston, TX, 1985, p. 348. DOI: [10.2514/6.1985-348](https://doi.org/10.2514/6.1985-348).
- [18] R. Carpenter, “Aeroassist Flight Experiment: Mission Overview,” Texas Space Grant Consortium, Tech. Rep., 1992. [Online]. Available: <http://www.tsgc.utexas.edu/archive/PDF/AeroassistFlightExp.pdf>.

- [19] G. D. Walberg, “A Survey of Aeroassisted Orbit Transfer,” *Journal of Spacecraft and Rockets*, vol. 22, no. 1, pp. 3–18, 1985. DOI: [10.2514/3.25704](https://doi.org/10.2514/3.25704).
- [20] J. Puig-Suari, J. M. Logunski, and S. G. Tragesser, “Aerocapture with a Flexible Tether,” *Journal of Guidance, Control, and Dynamics*, vol. 18, no. 6, pp. 1305–1312, 1995. DOI: [10.2514/3.21546](https://doi.org/10.2514/3.21546).
- [21] J. E. Lyne, M. Taubert, and R. D. Braun, “Parametric Study of Manned Aerocapture Part I: Earth Return from Mars,” *Journal of Spacecraft and Rockets*, vol. 29, no. 6, pp. 808–813, 1992. DOI: [10.2514/3.25535](https://doi.org/10.2514/3.25535).
- [22] J. E. Lyne, “Effect of Parking Orbit Period on Aerocapture for Manned Mars Missions,” *Journal of Spacecraft and Rockets*, vol. 30, no. 4, pp. 484–487, 1993. DOI: [10.2514/3.25554](https://doi.org/10.2514/3.25554).
- [23] P. Papadopoulos, E. Venkatapathy, W. Henline, P. Wercinski, P. Papadopoulos, E. Venkatapathy, W. Henline, and P. Wercinski, “Aero-thermal Heating Simulations with Surface Catalysis for the Mars 2001 Aerocapture Mission,” in *35th Aerospace Sciences Meeting and Exhibit*, Reno, NV, 1997, p. 473. DOI: [10.2514/6.1997-473](https://doi.org/10.2514/6.1997-473).
- [24] C. Cazaux, F. Naderi, C. Whetsel, D. Beaty, B. Gershman, R. Kornfeld, B. Mitcheltree, and B. Sackheim, “The NASA/CNES Mars Sample Return — A status report,” *Acta Astronautica*, vol. 54, no. 8, pp. 601–617, 2004. DOI: [10.1016/j.actaastro.2003.07.001](https://doi.org/10.1016/j.actaastro.2003.07.001).
- [25] S. G. Tragesser and J. M. Longuski, “Analysis and Design of Aerocapture Tether with Accounting for Stochastic Errors,” *Journal of Spacecraft and Rockets*, vol. 35, no. 5, pp. 683–689, 1998. DOI: [10.2514/2.3385](https://doi.org/10.2514/2.3385).
- [26] Z. V. Leszczynski, “Modeling, Simulation and Visualization of Aerocapture,” Monterey, CA, Tech. Rep., 1998, pp. 9–17. [Online]. Available: <https://calhoun.nps.edu/handle/10945/32660>.
- [27] N. Vinh, W. Johnson, and J. Longuski, “Mars Aerocapture using Bank Modulation,” in *Astrodynamic Specialist Conference*, Denver, CO, 2000, p. 4424. DOI: [10.2514/6.2000-4424](https://doi.org/10.2514/6.2000-4424).

- [28] P. Wercinski, M. Munk, R. Powell, J. Hall, C. Graves, and H. Partridge, “Aerocapture Technology Development Needs for Outer Planet Exploration,” NASA Ames Research Center, Moffett Field, CA, Tech. Rep. NASA/TM-2002-211386, 2002. [Online]. Available: <https://ntrs.nasa.gov/archive/nasa/casi.ntrs.nasa.gov/20020077966.pdf>.
- [29] J. Hall, “An Overview of the ST-7 Aerocapture Flight Test Experiment,” in *AIAA Atmospheric Flight Mechanics Conference and Exhibit*, Monterey, CA, 2002, p. 4621. doi: [10.2514/6.2002-4621](https://doi.org/10.2514/6.2002-4621).
- [30] A. Keys, J. Hall, D. Oh, and M. Munk, “Overview of a Proposed Flight Validation of Aerocapture System Technology for Planetary Missions,” in *42nd AIAA Joint Propulsion Conference & Exhibit*, Sacramento, CA: AIAA, 2006, p. 4518. doi: [10.2514/6.2006-4518](https://doi.org/10.2514/6.2006-4518).
- [31] E. Perot and S. Rousseau, “Importance of an On-board Estimation of the Density Scale Height for Various Aerocapture Guidance Algorithms,” in *AIAA/AAS Astrodynamics Specialist Conference and Exhibit*, Monterey, CA, 2002, p. 4734. doi: [10.2514/6.2002-4734](https://doi.org/10.2514/6.2002-4734).
- [32] D. Way, R. Powell, J. Masciarelli, B. Starr, and K. Edquist, “Aerocapture Simulation and Performance for the Titan Explorer Mission,” in *39th AIAA/ASME/SAE/ASEE Joint Propulsion Conference and Exhibit*, Huntsville, Al, 2003, p. 4951. doi: [10.2514/6.2003-4951](https://doi.org/10.2514/6.2003-4951).
- [33] J. Olejniczak, D. Prabhu, M. Wright, N. Takashima, B. Hollis, K. Sutton, and E. Zoby, “An Analysis of the Radiative Heating Environment for Aerocapture at Titan,” in *39th AIAA/ASME/SAE/ASEE Joint Propulsion Conference and Exhibit*, Huntsville, AL, 2003, p. 4953. doi: [10.2514/6.2003-4953](https://doi.org/10.2514/6.2003-4953).
- [34] A. McDonald, K. Gates, and K. Nock, “Analysis of High-speed Aerocapture at Mars Using HyperPASS: A New Aeroassist Tool,” in *17th AIAA Aerodynamic Decelerator Systems Technology Conference and Seminar*, 2003, p. 2172. doi: [10.2514/6.2003-2172](https://doi.org/10.2514/6.2003-2172).
- [35] B. James and M. Munk, “Aerocapture Technology Development Within the NASA In-Space Propulsion Program,” in *39th AIAA Joint Propulsion Conference and Exhibit*, Monterey, CA, 2003, p. 4654. doi: [10.2514/6.2003-4654](https://doi.org/10.2514/6.2003-4654).

- [36] M. K. Lockwood, B. R. Starr, J. W. Paulson, D. A. Kontinos, Y. K. Chen, B. Laub, J. Olejniczak, M. J. Wright, N. Takashima, C. G. Justus, A. L. Duval, J. L. Hall, R. W. Bailey, R. J. Haw, M. A. Noca, T. R. Spilker, C. A. Graves, C. J. Cerimele, C. H. Westhelle, V. W. Keller, and K. Sutton, “Systems Analysis for a Venus Aerocapture Mission,” NASA Langley Research Center, Hampton, VA, Tech. Rep. NASA/TM-2006-214291, 2006. [Online]. Available: <https://ntrs.nasa.gov/api/citations/20060010899/downloads/20060010899.pdf>.
- [37] H. S. Wright, D. Y. Oh, C. H. Westhelle, J. L. Fisher, R. E. Dyke, K. T. Edquist, J. L. Brown, H. L. Justh, and M. M. Munk, “Mars Aerocapture Systems Study,” NASA Langley Research Center, Hampton, VA, Tech. Rep. NASA/TM-2006-214522, 2006. [Online]. Available: <https://ntrs.nasa.gov/api/citations/20060056070/downloads/20060056070.pdf>.
- [38] M. K. Lockwood, E. M. Queen, D. W. Way, R. W. Powell, K. Edquist, B. W. Starr, B. R. Hollis, E. V. Zoby, G. A. Hrinda, and R. W. Bailey, “Aerocapture Systems Analysis for a Titan Mission,” NASA Langley Research Center, Tech. Rep. NASA/TM-2006-214273, 2006. [Online]. Available: <https://ntrs.nasa.gov/archive/nasa/casi.ntrs.nasa.gov/20060007561.pdf>.
- [39] M. K. Lockwood, K. T. Edquist, B. R. Starr, B. R. Hollis, G. A. Hrinda, R. W. Bailey, J. L. Hall, T. R. Spilker, M. A. Noca, N. O’Kongo, *et al.*, “Aerocapture Systems Analysis for a Neptune Mission,” NASA Langley Research Center, Tech. Rep. NASA/TM-2006-214300, 2006. [Online]. Available: <https://ntrs.nasa.gov/api/citations/20060012088/downloads/20060012088.pdf>.
- [40] G. Artis and B. James, “Aerocapture Benefits to Future Science Missions,” in *Division for Planetary Sciences Meeting*, Pasadena, CA, October 08–13, 2006. [Online]. Available: <https://ntrs.nasa.gov/api/citations/20070002619/downloads/20070002619.pdf>.
- [41] A. P. Ingersoll and T. R. Spilker, “A Neptune Orbiter with Probes Mission with Aerocapture Orbit Insertion,” *Progress in Astronautics and Aeronautics: NASA Space Science Vision Missions*, vol. 224, pp. 81–113, 2008. DOI: 10.2514/5.9781600866920.0081.0114.

- [42] K. Fujita and T. Yamada, “Preliminary Study of Venus Exploration with Aerocapture System,” in *AIAA Atmospheric Flight Mechanics Conference and Exhibit*, Honolulu, HI, 2008, ISBN: 978-1-60086-998-3. DOI: [10.2514/6.2008-6392](https://doi.org/10.2514/6.2008-6392).
- [43] L. Lemmerman and P. Wercinski, “Small Neptune Orbiter Using Aerocapture,” in *AIP Conference Proceedings*, American Institute of Physics, vol. 387, 1997, pp. 101–110.
- [44] K. L. Gates and J. M. Longuski, “Aerocapture Ballutes versus Aerocapture Tethers for Exploration of the Solar System,” *Journal of Spacecraft and Rockets*, vol. 47, no. 4, pp. 590–596, 2010. DOI: [10.2514/1.46603](https://doi.org/10.2514/1.46603).
- [45] H. Takayanagi and K. Fujita, “Absolute Radiation Measurements Behind Strong Shock Wave in Carbon Dioxide Flow for Mars Aerocapture Missions,” in *43rd AIAA Thermophysics Conference*, New Orleans, LA, 2012, p. 2744. DOI: [10.2514/6.2012-2744](https://doi.org/10.2514/6.2012-2744).
- [46] K. Fujita and S. Narita, “Conceptual Study of a Small-Sized Mars Aerocapture Demonstrator,” in *51st AIAA Aerospace Sciences Meeting including the New Horizons Forum and Aerospace Exposition*, Grapevine ,TX, 2013, p. 729. DOI: [10.2514/6.2013-729](https://doi.org/10.2514/6.2013-729).
- [47] Z. R. Putnam and R. D. Braun, “Drag-modulation Flight-Control System Options for Planetary Aerocapture,” *Journal of Spacecraft and Rockets*, vol. 51, no. 1, pp. 139–150, 2013. DOI: [10.2514/1.A32589](https://doi.org/10.2514/1.A32589).
- [48] P. Lu, C. J. Cerimele, M. A. Tigges, and D. A. Matz, “Optimal Aerocapture Guidance,” *Journal of Guidance, Control, and Dynamics*, vol. 38, no. 4, pp. 553–565, 2015. DOI: [10.2514/1.G000713](https://doi.org/10.2514/1.G000713).
- [49] C. A. Nixon, F. Kirchman, J. Esper, D. Folta, and A. Mashiku, “Aerocapture Design Study for a Titan Polar Orbiter,” in *2016 IEEE Aerospace Conference*, IEEE, Big Sky, MT, 2016, pp. 1–16. DOI: [10.1109/AERO.2016.7500825](https://doi.org/10.1109/AERO.2016.7500825).
- [50] S. J. Saikia, J. Millane, Y. Lu, A. Mudek, A. Arora, P. Witsberge, K. Hughes, J. M. Longuski, T. Spilker, A. Petropoulos, *et al.*, “Aerocapture Assessment for NASA Ice Giants Pre-Decadal Survey Mission Study,” *Journal of Spacecraft and Rockets*, vol. 58, no. 2, pp. 505–515, 2021. DOI: [10.2514/1.A34703](https://doi.org/10.2514/1.A34703).

- [51] M. D. Hofstadter, A. Simon, K. Reh, and J. Elliot, “Ice Giants Pre-Decadal Study Final Report,” NASA, Tech. Rep. JPL D-100520, 2017, pp. 473–488. [Online]. Available: <https://www.lpi.usra.edu/icegiants/>.
- [52] M. S. Werner and R. D. Braun, “Mission Design and Performance Analysis of a Smallsat Aerocapture Flight Test,” *Journal of Spacecraft and Rockets*, vol. 56, no. 6, pp. 1704–1713, 2019. DOI: [10.2514/1.A33997](https://doi.org/10.2514/1.A33997).
- [53] A. Nelessen *et al.*, “Small satellite aerocapture for increased mass delivered to venus and beyond,” in *15th International Planetary Probe Workshop*, Boulder, CO: IPPW, Jun. 2018.
- [54] E. Roelke, M. Werner, and R. D. Braun, “Single-Stage Drag Modulation GNC Performance for Venus Aerocapture Demonstration,” in *AIAA Scitech 2019 Forum*, San Diego, CA, 2019, p. 0016. DOI: [10.2514/6.2019-0016](https://doi.org/10.2514/6.2019-0016).
- [55] G. Falcone, J. Williams, and Z. Putnam, “Assessment of Aerocapture for Orbit Insertion of Small Satellites at Mars,” *Journal of Spacecraft and Rockets*, vol. 56, no. 6, pp. 1689–1703, 2019. DOI: [10.2514/1.A34444](https://doi.org/10.2514/1.A34444).
- [56] A. Austin, A. Nelessen, B. Strauss, J. Ravich, M. Jesick, E. Venkatapathy, R. Beck, P. Wercinski, M. Aftosmis, M. Wilder, *et al.*, “SmallSat Aerocapture to Enable a New Paradigm of Planetary Missions,” in *2019 IEEE Aerospace Conference*, IEEE, Big Sky, MT, 2019, pp. 1–20. DOI: [10.1109/AERO.2019.8742220](https://doi.org/10.1109/AERO.2019.8742220).
- [57] J. Moore, “Scientific Goals for Exploration of the Outer Solar System,” Tech. Rep. OPAG-Report-Draft-Aug-2019, 2019. [Online]. Available: <https://www.lpi.usra.edu/opag/goals-08-28-19.pdf>.
- [58] A. P. Girija, S. J. Saikia, J. M. Longuski, and J. A. Cutts, “A Unified Framework for Aerocapture Systems Analysis,” in *2019 AAS/AIAA Astrodynamics Specialist Conference*, Portland, ME. [Online]. Available: <https://engrxiv.org/xtacw/>.
- [59] Y. Lu and S. J. Saikia, “Feasibility Assessment of Aerocapture for Future Titan Orbiter Missions,” *Journal of Spacecraft and Rockets*, vol. 55, no. 5, pp. 1125–1135, Sep. 2018, ISSN: 0022-4650. DOI: [10.2514/1.A34121](https://doi.org/10.2514/1.A34121).

- [60] A. P. Girija, Y. Lu, and S. J. Saikia, “Feasibility and Mass-Benefit Analysis of Aerocapture for Missions to Venus,” *Journal of Spacecraft and Rockets*, vol. 57, no. 1, pp. 58–73, 2020. doi: [10.2514/1.A34529](https://doi.org/10.2514/1.A34529).
- [61] A. P. Girija, S. J. Saikia, J. M. Longuski, S. Bhaskaran, M. S. Smith, and J. A. Cutts, “Feasibility and Performance Analysis of Neptune Aero-capture Using Heritage Blunt-Body Aeroshells,” *Journal of Spacecraft and Rockets*, vol. 57, no. 6, 2020.
- [62] H. L. Justh, “Overview of Global Reference Atmospheric Model (GRAM) Upgrades,” in *15th International Planetary Probe Workshop*, Boulder, Colorado, 2018.
- [63] Y.-m. Peng, B. Xu, B.-d. Fang, and H.-l. Lei, “Analytical Predictor-Corrector Guidance Algorithm Based on Drag Modulation Flight Control System for Mars Aerocapture,” *International Journal of Aerospace Engineering*, vol. 2018, 2018. doi: [10.1155/2018/5907981](https://doi.org/10.1155/2018/5907981).
- [64] Y.-m. Peng, B. Xu, X. Lu, B.-d. Fang, and H. Zhang, “Analytical Predictive Guidance Algorithm Based on Single Ballistic Coefficient Switching for Mars Aerocapture,” *International Journal of Aerospace Engineering*, vol. 2019, 2019. doi: [10.1155/2019/5765901](https://doi.org/10.1155/2019/5765901).
- [65] F. Taylor, “Venus: Not evil, just a bit unfortunate,” *Astronomy & Geophysics*, vol. 51, no. 1, pp. 1.26–1.31, 2010. doi: [10.1111/j.1468-4004.2010.51126.x](https://doi.org/10.1111/j.1468-4004.2010.51126.x).
- [66] Venus Exploration and Analysis Group (VEXAG), “Goals, Objectives, and Investigations for Venus Exploration,” Tech. Rep., 2016. [Online]. Available: <https://www.lpi.usra.edu/vexag/reports/GOI-Space-Physics-Update-0816.pdf>.
- [67] M. S. Gilmore and P. M. Beauchamp, “Venus Flagship Mission Planetary Decadal Survey Study,” in *AGU Fall Meeting Abstracts*, vol. 2020, Virtual Event, 2020, P077–0008.
- [68] M. J. Way, A. D. Del Genio, N. Y. Kiang, L. E. Sohl, D. H. Grinspoon, I. Aleinov, M. Kelley, and T. Clune, “Was Venus the First Habitable World of Our Solar System?” *Geophysical Research Letters*, vol. 43, no. 16, pp. 8376–8383, 2016. doi: [10.1002/2016GL069790](https://doi.org/10.1002/2016GL069790).

- [69] S. W. Squyres, “Vision and Voyages for Planetary Science in the Decade 2013–2022,” in. Washington D.C.: National Academies Press, 2011, ch. 5, ISBN: 9780309224642. [Online]. Available: <https://www.nap.edu/catalog/13117/vision-and-voyages-for-planetary-science-in-the-decade-2013-2022>.
- [70] E. Chassefière, R. Wieler, B. Marty, and F. Leblanc, “The Evolution of Venus: Present State of Knowledge and Future Exploration,” *Planetary and Space Science*, vol. 63, pp. 15–23, 2012. doi: [10.1016/j.pss.2011.04.007](https://doi.org/10.1016/j.pss.2011.04.007).
- [71] L. S. Glaze, C. F. Wilson, L. V. Zasova, M. Nakamura, and S. Limaye, “Future of Venus Research and Exploration,” *Space Science Reviews*, vol. 214, no. 5, p. 89, 2018. doi: [10.1007/s11214-018-0528-z](https://doi.org/10.1007/s11214-018-0528-z).
- [72] R. Ghail, C. Wilson, T. Widemann, L. Bruzzone, C. Dumoulin, J. Helbert, R. Herrick, E. Marcq, P. Mason, P. Rosenblatt, A. Carine Vandaele, and L.-J. Burtz, “EnVision: understanding why our most Earth-like neighbour is so different,” *ArXiv e-prints*, Mar. 2017. arXiv: [1703.09010](https://arxiv.org/abs/1703.09010) [[astro-ph.EP](#)].
- [73] S. Chase, L. Kaplan, and G. Neugebauer, “The Mariner 2 Infrared Radiometer Experiment,” *Journal of Geophysical Research*, vol. 68, no. 22, pp. 6157–6169, 1963. doi: [10.1029/JZ068i022p06157](https://doi.org/10.1029/JZ068i022p06157).
- [74] D. E. Reese and P. R. Swan, “Venera 4 Probes Atmosphere of Venus,” *Science*, pp. 1228–1230, 1968.
- [75] M. Keldysh, “Venus Exploration with the Venera 9 and Venera 10 Spacecraft,” *Icarus*, vol. 30, no. 4, pp. 605–625, 1977. doi: [10.1016/0019-1035\(77\)90085-9](https://doi.org/10.1016/0019-1035(77)90085-9).
- [76] M. Y. Marov and D. H. Grinspoon, “The Planet Venus,” in. New Haven, CT: Yale University Press, 1998, ch. 2.
- [77] L. Colin, “The Pioneer Venus Program,” *Journal of Geophysical Research: Space Physics*, vol. 85, no. A13, pp. 7575–7598, 1980. doi: [10.1029/JA085iA13p07575](https://doi.org/10.1029/JA085iA13p07575).

- [78] Y. A. Surkov, V. Barsukov, L. Moskalyeva, V. Kharyukova, and A. Kemurdzhian, “New Data on the Composition, Structure, and Properties of Venus Rock Obtained by Venera 13 and Venera 14,” *Journal of Geophysical Research: Solid Earth*, vol. 89, no. S02, B393–B402, 1984. DOI: [10.1029/JB089iS02p0B393](https://doi.org/10.1029/JB089iS02p0B393).
- [79] O. Rzhiga, “Venera-15 and-16 Spacecraft: Images and Maps of Venus,” *Advances in Space Research*, vol. 7, no. 12, pp. 269–278, 1987. DOI: [10.1016/0273-1177\(87\)90229-8](https://doi.org/10.1016/0273-1177(87)90229-8).
- [80] R. Saunders, G. Pettengill, R. Arvidson, W. Sjogren, W. Johnson, and L. Pieri, “The Magellan Venus Radar Mapping Mission,” *Journal of Geophysical Research: Solid Earth*, vol. 95, no. B6, pp. 8339–8355, 1990. DOI: [10.1029/JB095iB06p08339](https://doi.org/10.1029/JB095iB06p08339).
- [81] J. Luhmann, A. Fedorov, S. Barabash, E. Carlsson, Y. Futaana, T. Zhang, C. Russell, J. Lyon, S. Ledvina, and D. Brain, “Venus Express Observations of Atmospheric Oxygen Escape During the Passage of Several Coronal Mass Ejections,” *Journal of Geophysical Research: Planets*, vol. 113, no. E9, 2008. DOI: [10.1029/2008JE003092](https://doi.org/10.1029/2008JE003092).
- [82] E. V. Shalygin, W. J. Markiewicz, A. T. Basilevsky, D. V. Titov, N. I. Ignatiev, and J. W. Head, “Active Volcanism on Venus in the Ganiki Chasma Rift Zone,” *Geophysical Research Letters*, vol. 42, no. 12, pp. 4762–4769, 2015. DOI: [10.1002/2015GL064088](https://doi.org/10.1002/2015GL064088).
- [83] M. Nakamura, T. Imamura, N. Ishii, T. Abe, T. Satoh, M. Suzuki, M. Ueno, A. Yamazaki, N. Iwagami, S. Watanabe, *et al.*, “Overview of Venus Orbiter, Akatsuki,” *Earth, Planets and Space*, vol. 63, no. 5, pp. 443–457, 2011. DOI: [10.5047/eps.2011.02.009](https://doi.org/10.5047/eps.2011.02.009).
- [84] T. Fukuhara, M. Futaguchi, G. L. Hashimoto, T. Horinouchi, T. Imamura, N. Iwagami, T. Kouyama, S.-y. Murakami, M. Nakamura, K. Ogohara, *et al.*, “Large Stationary Gravity Wave in the Atmosphere of Venus,” *Nature Geoscience*, vol. 10, no. 2, pp. 85–88, 2017. DOI: [10.1038/NGEO2873](https://doi.org/10.1038/NGEO2873).
- [85] M. S. Gilmore and R. Grimm, “The Case for Venus,” in *Committee on Astrobiology and Planetary Sciences (CAPS) Meeting*, Washington D.C.: National Academies Press, Mar. 2018.

- [86] Venus Exploration and Analysis Group (VEXAG), “Venus Bridge Summary Report,” Tech. Rep., 2018.
- [87] C. Mercer, “Small Satellite Missions for Planetary Science,” in *15th NASA Venus Exploration and Analysis Group Meeting*, Laurel, MD: VEXAG, Mar. November 14–16, 2017.
- [88] D. Senske, L. Zasova, A. Burdanov, T. Economou, N. Eismont, M. Gerasimov, *et al.*, “Status Report of the Venera-D Joint Science Definition Team,” in *15th NASA Venus Exploration and Analysis Group Meeting*, Laurel, MD: VEXAG, 2017, pp. 1–23.
- [89] Y. Zou, W. Li, and Z. Ouyang, “China’s Deep-space Exploration to 2030,” *Chin. J. Space Sci.*, vol. 34, p. 516, 2014. DOI: [10.11728/cjss2014.05.516](https://doi.org/10.11728/cjss2014.05.516).
- [90] Indian Space Research Organization (ISRO), “Announcement of Opportunity (AO) to international science community for Space-Based Experiments to Study Venus,” Bangalore, Tech. Rep., 2018.
- [91] P. Bagla, “India Seeks Collaborators for a Mission to Venus,” 2018. DOI: [10.1126/science.aaw1484](https://doi.org/10.1126/science.aaw1484). [Online]. Available: <https://doi.org/10.1126/science.aaw1484>.
- [92] M. Werner, E. Roelke, and R. Braun, “Dynamic Propagation of Discrete-Event Drag Modulation for Venus Aerocapture,” in *15th International Planetary Probe Workshop*, Boulder, CO: IPPW, Jun. 2018.
- [93] N. X. Vinh, A. Busemann, and R. D. Culp, “Hypersonic and planetary entry flight mechanics.,” in. Ann Arbor, MI: University of Michigan Press, 1980, pp. 26–28. DOI: [10.1017/S0001924000031444](https://doi.org/10.1017/S0001924000031444).
- [94] M. Pontani and P. Teofilatto, “Post-Aerocapture orbit Selection and Maintenance for the Aerofast mission to Mars,” *Acta Astronautica*, vol. 79, pp. 168–178, 2012, ISSN: 00945765. DOI: [10.1016/j.actaastro.2012.04.020](https://doi.org/10.1016/j.actaastro.2012.04.020).
- [95] D. A. Vallado, “Fundamentals of astrodynamics and applications,” in. El Segundo, CA: Microcosm Press, 2001, vol. 12, p. 147.
- [96] I. de Pater, “Planetary Sciences,” in, 2nd ed. New York: Cambridge University Press, 2010, p. 250, ISBN: 0521853710.

- [97] C. Justus, A. Duvall, and V. Keller, “Atmospheric Models for Aerocapture,” in *40th AIAA/ASME/SAE/ASEE Joint Propulsion Conference and Exhibit*, Fort Lauderdale, FL, 2004, p. 3844, ISBN: 978-1-62410-037-6. DOI: [10.2514/6.2004-3844](https://doi.org/10.2514/6.2004-3844).
- [98] A. Duvall, C. Justus, and V. Keller, “Global Reference Atmospheric Model (GRAM) Series for Aeroassist Applications,” in *43rd AIAA Aerospace Sciences Meeting and Exhibit*, Reno, NV, 2005, p. 1239, ISBN: 978-1-62410-064-2. DOI: [10.2514/6.2005-1239](https://doi.org/10.2514/6.2005-1239).
- [99] L. Zasova, V. Moroz, V. Linkin, I. Khatuntsev, and B. Maiorov, “Structure of the Venusian Atmosphere from Surface up to 100 km,” *Cosmic Research*, vol. 44, no. 4, pp. 364–383, 2006. DOI: [10.1134/S0010952506040095](https://doi.org/10.1134/S0010952506040095).
- [100] J. A. Cutts, T. S. Balint, E. Chassefiere, and E. A. Kolawa, “Technology Perspectives in the Future Exploration of Venus,” *Geophysical Monograph Series*, vol. 176, p. 207, 2007. DOI: [10.1029/176GM13](https://doi.org/10.1029/176GM13).
- [101] H. Svedhem, D. Titov, F. Taylor, and O. Witasse, “Venus Express Mission,” *Journal of Geophysical Research: Planets*, vol. 114, no. E5, 2009. DOI: [10.1029/2008JE003290](https://doi.org/10.1029/2008JE003290).
- [102] A. Phipps, A. Woodroffe, D. Gibbon, A. Cropp, M. Joshi, P. Alcindor, N. Ghafoor, A. da Silva Curiel, J. Ward, M. Sweeting, *et al.*, “Venus Orbiter and Entry Probe: An ESA Technology Reference Study,” in *8th ESA Workshop on Advanced Space Technologies for Robotics and Automation 'ASTRA 2004'*, ESTEC, Noordwijk, The Netherlands: ESA, November 2–4, 2004.
- [103] A. B. Sergeyevsky, G. C. Snyder, and R. A. Cunniff, “Interplanetary Mission Design Handbook. Volume 1, Part 2: Earth to Mars Ballistic Mission Opportunities, 1990-2005,” Pasadena, CA, Tech. Rep. JPL-PUBL-82-43-VOL-1-PT-2, 1983, pp. 18–28. [Online]. Available: <https://ntrs.nasa.gov/api/citations/19840010158/downloads/19840010158.pdf>.
- [104] R. Y. Jits and G. D. Walberg, “Blended Control, Predictor–Corrector Guidance Algorithm, An Enabling Technology for Mars Aerocapture,” *Acta Astronautica*, vol. 54, no. 6, pp. 385–398, 2004. DOI: [10.1016/S0001-0590\(03\)00159-0](https://doi.org/10.1016/S0001-0590(03)00159-0).

- [105] J. Davis, A. Dwyer Cianciolo, R. Powell, J. Shidner, and E. Garcia-Llama, “Guidance and Control Algorithms for the Mars Entry, Descent and Landing Systems Analysis,” in *AIAA/AAS Astrodynamics Specialist Conference*, Toronto, ON, Canada, 2010, p. 7972. DOI: [10.2514/6.2010-7972](https://doi.org/10.2514/6.2010-7972).
- [106] E. R. Hillje, “Entry Flight Aerodynamics from Apollo Mission AS-202,” Washington D. C., Tech. Rep. NASA TN D-4185, October, 1967. [Online]. Available: <https://ntrs.nasa.gov/api/citations/19670027745/downloads/19670027745.pdf>.
- [107] D. W. Way, R. W. Powell, A. Chen, A. D. Steltzner, A. M. San Martin, P. D. Burkhardt, and G. F. Mendeck, “Mars Science Laboratory: Entry, Descent, and Landing System Performance,” in *Aerospace Conference, 2007 IEEE*, IEEE, Big Sky, MT, March 3–10, 2007, pp. 1–19. DOI: [10.1109/AERO.2007.352821](https://doi.org/10.1109/AERO.2007.352821).
- [108] R. Venkatapathy, “Ballistic and Lifting Nano ADEPT Flight Testing for Mission Infusion Opportunities,” in *NASA Outer Planets Assessment Group (OPAG) Meeting*, Johns Hopkins University, Applied Physics Lab, Laurel, MD: OPAG, August, 2016. [Online]. Available: <https://www.lpi.usra.edu/opag/meetings/aug2016/posters/Venkatapathy.pdf>.
- [109] A. Cassell, B. Smith, P. Wercinski, S. Ghassemieh, K. Hibbard, A. Nelessen, and J. Cutts, “ADEPT, A Mechanically Deployable Re-Entry Vehicle System, Enabling Interplanetary CubeSat and Small Satellite Missions,” in *32nd Annual AIAA/USU Conference on Small Satellites*, Logan, UT: AIAA/Utah State University, August 4–9, 2018.
- [110] Z. R. Putnam and R. D. Braun, “Analytical Assessment of Drag-Modulation Trajectory Control for Planetary Entry,” *The Journal of the Astronautical Sciences*, vol. 65, no. 4, pp. 470–489, 2018. DOI: [10.1007/s40295-018-0134-z](https://doi.org/10.1007/s40295-018-0134-z).
- [111] S. Dutta, B. Smith, D. Prabhu, and E. Venkatapathy, “Mission Sizing and Trade Studies for Low Ballistic Coefficient Entry Systems to Venus,” in *Aerospace Conference, 2012 IEEE*, IEEE, Big Sky, MT, 2012. DOI: [10.1109/AERO.2012.6187002](https://doi.org/10.1109/AERO.2012.6187002).

- [112] P. A. Gnoffo, K. J. Weilmuenster, H. H. Hamilton, D. R. Olynick, and E. Venkatapathy, “Computational Aerothermodynamic Design Issues for Hypersonic Vehicles,” *Journal of Spacecraft and Rockets*, vol. 36, no. 1, pp. 21–43, 1999. DOI: [10.2514/2.3430](https://doi.org/10.2514/2.3430).
- [113] K. Sutton and R. A. Graves Jr, “A General Stagnation-point Convective Heating Equation for Arbitrary Gas Mixtures,” NASA, Washington D. C., Tech. Rep. NASA-TR-R-376, 1971. [Online]. Available: <https://ntrs.nasa.gov/api/citations/19720003329/downloads/19720003329.pdf>.
- [114] J. A. Samareh, “A Multidisciplinary Tool for Systems Analysis of Planetary Entry, Descent, and Landing (SAPE),” NASA Langley Research Center, Hampton, VA, Tech. Rep. NASA/TM-2009-215950, 2009. [Online]. Available: <https://ntrs.nasa.gov/api/citations/20090041828/downloads/20090041828.pdf>.
- [115] S. Craig and J. E. Lyne, “Parametric Study of Aerocapture for Missions to Venus,” *Journal of Spacecraft and Rockets*, vol. 42, no. 6, pp. 1035–1038, 2005, ISSN: 0022-4650. DOI: [10.2514/1.2589](https://doi.org/10.2514/1.2589).
- [116] W. Page and H. Woodward, “Radiative and Convective Heating During Venus Entry,” *AIAA Journal*, vol. 10, no. 10, pp. 1379–1381, 1972. DOI: [10.2514/3.6632](https://doi.org/10.2514/3.6632).
- [117] S. M. Johnson, “Thermal Protection Materials and Systems: Past, Present, and Future,” NASA Ames Research Center, Tech. Rep. ARC-E-DAA-TN9472, 2013. [Online]. Available: <https://ntrs.nasa.gov/archive/nasa/casi.ntrs.nasa.gov/20130014035.pdf>.
- [118] B. Laub, M. J. Wright, and E. Venkatapathy, “Thermal Protection System Design and the Relationship to Atmospheric Entry Environments,” in *6th International Planetary Probe Workshop*, Atlanta, GA: IPPW, Jun. 2008. [Online]. Available: <https://pub-lib.jpl.nasa.gov/docushare/dsweb/Get/Document-4950/Day1Laub.ppt.pdf>.
- [119] M. Wright, “Aerothermodynamic and Thermal Protection System Aspects of Entry System Design Course,” in *Thermal and Fluids Analysis Workshop*, Pasadena, CA, August, 2012. [Online]. Available: <https://tfaws.nasa.gov/TFAWS12/Proceedings/Aerothermodynamics%20Course.pdf>.

- [120] E. Venkatapathy, D. Ellerby, P. Wercinski, and P. Gage, “Venus Entry Challenges and Solutions for Aerial Platform Deployment,” in *Venus Aerial Platform Workshop #2*, Pasadena, CA, December, 2017. [Online]. Available: <https://ntrs.nasa.gov/archive/nasa/casi.ntrs.nasa.gov/20180000811.pdf>.
- [121] Laub, B. and Venkatapathy, E., “Thermal Protection System Technology and Facility Needs for Demanding Future Planetary Missions,” in *Planetary Probe Atmospheric Entry and Descent Trajectory Analysis and Science*, ser. ESA Special Publication, vol. 544, Feb. 2004, pp. 239–247.
- [122] R. Orloff and S. Garber, “Apollo by the Numbers: A Statistical Reference,” NASA, Tech. Rep. NASA/SP-2000-4029, 2000. [Online]. Available: <https://ntrs.nasa.gov/archive/nasa/casi.ntrs.nasa.gov/20010008244.pdf>.
- [123] C. Davies and M. Arcadi, “Planetary Mission Entry Vehicles Quick Reference Guide. Version 3.0,” NASA Ames Research Center, Tech. Rep. NASA/SP-2006-3401, 2006. [Online]. Available: <https://ntrs.nasa.gov/archive/nasa/casi.ntrs.nasa.gov/20070022789.pdf>.
- [124] K. T. Edquist, B. R. Hollis, A. A. Dyakonov, B. Laub, M. J. Wright, T. P. Rivellini, E. M. Slimko, and W. H. Willcockson, “Mars Science laboratory Entry Capsule Aerothermodynamics and Thermal Protection System,” in *Aerospace Conference, 2007 IEEE*, IEEE, Big Sky, MT, March 3–10, 2007, pp. 1–13. DOI: [10.1109/AERO.2007.352823](https://doi.org/10.1109/AERO.2007.352823).
- [125] J. O. Arnold, Y.-K. Chen, D. K. Prabhu, M. Bittner, E. Venkatapathy, *et al.*, “Arcjet Testing of Woven Carbon Cloth for Use on Adaptive Deployable Entry Placement Technology,” NASA Ames Research Center, Tech. Rep. ARC-E-DAA-TN6341, 2013. [Online]. Available: <https://ntrs.nasa.gov/archive/nasa/casi.ntrs.nasa.gov/20130011056.pdf>.
- [126] B. Smith, A. Cassell, C. Kruger, E. Venkatapathy, C. Kazemba, and K. Simonis, “Nano-ADEPT: An Entry System for Secondary Payloads,” in *2015 IEEE Aerospace Conference*, IEEE, Big Sky, MT, 2015, pp. 1–11. DOI: [10.1109/AERO.2015.7119095](https://doi.org/10.1109/AERO.2015.7119095).
- [127] E. A. Rinderle, “Galileo Users Guide, Mission Design System, Satellite Tour Analysis and Design Subsystem,” NASA Jet Propulsion Lab, Pasadena, CA, Tech. Rep. JPL-D-263, 1986.

- [128] J. M. Longuski and S. N. Williams, “Automated Design of Gravity-Assist Trajectories to Mars and the Outer Planets,” *Celestial Mechanics and Dynamical Astronomy*, vol. 52, no. 3, pp. 207–220, 1991. DOI: [10.1007/BF00048484](https://doi.org/10.1007/BF00048484).
- [129] G. A. Henning, P. J. Edelman, and J. M. Longuski, “Design and Optimization of Interplanetary Aerogravity-assist Tours,” *Journal of Spacecraft and Rockets*, vol. 51, no. 6, pp. 1849–1856, 2014. DOI: [10.2514/1.A32881](https://doi.org/10.2514/1.A32881).
- [130] J. Mansell, N. Kolencherry, K. Hughes, A. Arora, H. Chye, K. Coleman, J. Elliott, S. Fulton, N. Hobart, B. Libben, *et al.*, “Oceanus: A Multi-Spacecraft Flagship Mission Concept to Explore Saturn and Uranus,” *Advances in Space Research*, vol. 59, no. 9, pp. 2407–2433, 2017. DOI: [10.1016/j.asr.2017.02.012](https://doi.org/10.1016/j.asr.2017.02.012).
- [131] D. M. F. Chapman, “Recurrent phenomena of Venus and the Venus/Earth Orbital Resonance,” *Journal of the Royal Astronomical Society of Canada*, vol. 80, pp. 336–343, Dec. 1986.
- [132] N. Scafetta, “The Complex Planetary Synchronization Structure of the Solar System,” *arXiv preprint arXiv:1405.0193*, 2014. [Online]. Available: <https://arxiv.org/abs/1405.0193>.
- [133] J. Elliot, K. Reh, M. D. Hofstadter, and A. Simon, “Ice Giants Pre-Decadal Study Final Report,” NASA, Tech. Rep. JPL D-100520, 2017, pp. 473–488.
- [134] B. Smith, E. Venkatapathy, P. Wercinski, B. Yount, D. Prabhu, P. Gage, L. Glaze, and C. Baker, “Venus In Situ Explorer Mission Design Using a Mechanically Deployed Aerodynamic Decelerator,” in *2013 IEEE Aerospace Conference*, IEEE, Big Sky, MT, March 2–10, 2013, pp. 1–18. DOI: [10.1109/AERO.2013.6497176](https://doi.org/10.1109/AERO.2013.6497176).
- [135] S. Oleson *et al.*, “V-BOSS: Venus Bridge Orbiter and Surface System Preliminary Report,” in *15th NASA Venus Exploration Analysis Group Meeting*, Laurel, MD: VEXAG, Jun. 2017.
- [136] M. R. de Oliveira, P. J. Gil, and R. Ghail, “A Novel Orbiter Mission Concept for Venus with the EnVision Proposal,” *Acta Astronautica*, vol. 148, pp. 260–267, 2018. DOI: [10.1016/j.actaastro.2018.05.012](https://doi.org/10.1016/j.actaastro.2018.05.012).

- [137] R. Grimm, “Venus Bridge: A Smallsat Program Through the Mid-2020s,” in *15th Venus Exploration and Analysis Group (VEXAG) Meeting*, Laurel, MD, Nov. 2018.
- [138] H. S. Wright, D. Y. Oh, C. H. Westhelle, J. L. Fisher, R. E. Dyke, K. T. Edquist, J. L. Brown, H. L. Justh, and M. M. Munk, “Mars Aerocapture Systems Study,” NASA Langley Research Center, Hampton, VA, Tech. Rep. NASA/TM-2006-214522, 2006. [Online]. Available: <https://ntrs.nasa.gov/archive/nasa/casi.ntrs.nasa.gov/20060056070.pdf>.
- [139] M. Covington, “Performance of a Light-weight Ablative Thermal Protection Material for the Stardust Mission Sample Return Capsule,” ELORET Corporation, Sunnyvale, CA, Tech. Rep. NASA/CP-2004-213456, 2005. [Online]. Available: <https://ntrs.nasa.gov/api/citations/20070014634/downloads/20070014634.pdf>.
- [140] D. Ellerby, D. Driver, M. Gasch, M. Mahzari, F. Milos, N. Owen, K. Peterson, M. Stackpoole, E. Venkatapathy, *et al.*, “Overview of Heatshield for Extreme Entry Environment Technology (HEEET) Project,” in *16th International Planetary Probe Workshop (IPPW)*, Boulder, CO, June, 2018.
- [141] A. M. Brandis and C. O. Johnston, “Characterization of Stagnation-point Heat Flux for Earth Entry,” in *45th AIAA Plasmadynamics and Lasers Conference*, Atlanta, GA, 2014, p. 2374. DOI: [10.2514/6.2014-2374](https://doi.org/10.2514/6.2014-2374).
- [142] H. Ritter, F. Mazoué, A. Santovincenzo, and A. Atzei, “Jupiter Entry Probe Feasibility Study from the ESTEC CDF Team: Heat Flux Evaluation and TPS Definition,” in *5th European Workshop on Thermal Protection Systems and Hot Structures*, Noordwijk, The Netherlands: ESA, 2006.
- [143] B. Bienstock, D. Atkinson, S. Atreya, P. Mahaffy, K. Baines, M. Wright, M. Wright, A. Stern, P. Steffes, D. Smith, R. Frampton, L. Peltz, S. Sichi, J. Masciarelli, J. Van Cleve, D. Murrow, and B. Landin, “NASA Vision Mission Neptune Orbiter with Probes,” NASA, Tech. Rep. Contract No. NNH04CC41C, 2005. [Online]. Available: <https://forum.nasaspacesflight.com/index.php?action=dlattach;topic=33971.0;attach=571182>.

- [144] C. Justus, A. Duvall, and D. Johnson, “Engineering-level Model Atmospheres for Titan and Neptune,” in *39th AIAA/ASME/SAE/ASEE Joint Propulsion Conference and Exhibit*, Huntsville, AL, 2003, p. 4803. DOI: [10.2514/6.2003-4803](https://doi.org/10.2514/6.2003-4803).
- [145] H. Justh, “Neptune-GRAM 2004 Documentation,” NASA Marshall Space Flight Center, Huntsville, AL, Tech. Rep. Neptune-GRAM 2004, 2004.
- [146] A. Seiff, D. B. Kirk, T. C. Knight, J. D. Mihalov, R. C. Blanchard, R. E. Young, G. Schubert, U. Von Zahn, G. Lehmacher, F. S. Milos, *et al.*, “Structure of the Atmosphere of Jupiter: Galileo Probe Measurements,” *Science*, vol. 272, no. 5263, pp. 844–845, 1996. DOI: [10.1126/science.272.5263.844](https://doi.org/10.1126/science.272.5263.844).
- [147] G. F. Lindal, D. Sweetnam, and V. Eshleman, “The Atmosphere of Saturn—an Analysis of the Voyager Radio Occultation Measurements,” *The Astronomical Journal*, vol. 90, pp. 1136–1146, 1985.
- [148] G. A. Allen Jr, M. S. Marley, and P. Agrawal, “Uranus Atmospheric Model for Engineering Application,” in *Workshop on the Study of the Ice Giant Planets*, vol. 1798, Laurel, MD, 2014, p. 2001.
- [149] C. H. Yam, D. C. Davis, J. M. Longuski, K. C. Howell, and B. Buffington, “Saturn Impact Trajectories for Cassini End-of-Mission,” *Journal of Spacecraft and Rockets*, vol. 46, no. 2, pp. 353–364, 2009. DOI: [10.2514/1.38760](https://doi.org/10.2514/1.38760).
- [150] K. M. Hughes, “Gravity-Assist Trajectories to Venus, Mars, and the Ice Giants: Mission Design with Human and Robotic Applications,” West Lafayette, IN: Ph.D. Thesis, Purdue University, 2016.
- [151] E. Harrison and E. Pritchard, “Lifting Entry Unmanned Viking Class Mars Landers,” NASA Langley Research Center, Hampton, VA, Tech. Rep. NASA TN D-5828, 1970. [Online]. Available: <https://ntrs.nasa.gov/api/citations/19700020498/downloads/19700020498.pdf>.
- [152] K. Murphy, G. Brauckmann, J. Bell, M. Rhode, D. B. Owens, T. Wilson, K. Bibb, D. Chan, and E. Walker, “Orion Crew Module Aerodynamic Testing,” in *29th AIAA Applied Aerodynamics Conference*, Honolulu, HI, 2011, p. 3502. DOI: [10.2514/6.2011-3502](https://doi.org/10.2514/6.2011-3502).

- [153] A. Cohen, “Mars Rover Sample Return Mission Delivery and Return Challenges,” in *1st International Symposium on Space Automation and Robotics*, Arlington, VA, 1988, p. 5007. DOI: [10.2514/6.1988-5007](https://doi.org/10.2514/6.1988-5007).
- [154] B. B. Donahue, S. E. Green, V. L. Coverstone, and B. Woo, “Chemical and Solar-Electric-Propulsion Systems Analyses for Mars Sample Return Missions,” *Journal of spacecraft and rockets*, vol. 43, no. 1, pp. 170–177, 2006. DOI: [10.2514/1.13958](https://doi.org/10.2514/1.13958).
- [155] P. Ramsey and J. E. Lyne, “Enceladus Mission Architecture Using Titan Aerogravity Assist for Orbital Capture About Saturn,” *Journal of Spacecraft and Rockets*, vol. 45, no. 3, pp. 635–638, 2008. DOI: [10.2514/1.31362](https://doi.org/10.2514/1.31362).
- [156] T. J. Martin-Mur, D. S. Abraham, D. Berry, S. Bhaskaran, R. J. Cesareone, and L. Wood, “The JPL Roadmap for Deep Space Navigation,” Pasadena, CA, Tech. Rep. JPL-TR-38710, 2006. [Online]. Available: <https://trs.jpl.nasa.gov/handle/2014/38710>.
- [157] A. E. Rollock and R. D. Braun, “Analysis of Hypersonic Tip-Off Rates for Venus Aerocapture,” in *AIAA Scitech 2020 Forum*, Orlando, FL, 2020, p. 1739. DOI: [10.2514/6.2020-1739](https://doi.org/10.2514/6.2020-1739).
- [158] M. McClary and Z. R. Putnam, “Assessment of Hypersonic Separation Dynamics For Drag Modulation Systems at Mars,” in *AIAA Scitech 2021 Forum*, Virtual Event, 2021, p. 1063. DOI: [10.2514/6.2021-1063](https://doi.org/10.2514/6.2021-1063).
- [159] S. W. Albert and R. D. Braun, “Conceptual Development of AeroDrop: Aerocapture and Direct Entry for Two Spacecraft on a Common Approach Trajectory,” in *AIAA Scitech 2020 Forum*, Orlando, FL, 2020, p. 1737. DOI: [10.2514/6.2020-1737](https://doi.org/10.2514/6.2020-1737).
- [160] J. R. Wertz, D. F. Everett, and J. J. Puschell, *Space Mission Engineering: The New SMAD*. Microcosm Press, 2011.
- [161] S. Evans, W. Taber, T. Drain, J. Smith, H.-C. Wu, M. Guevara, R. Sunseri, and J. Evans, “MONTE: The Next Generation of Mission Design and Navigation Software,” *CEAS Space Journal*, vol. 10, no. 1, pp. 79–86, 2018. DOI: [10.1007/s12567-017-0171-7](https://doi.org/10.1007/s12567-017-0171-7).

- [162] R. J. Haw, S. Bhaskaran, W. Strauss, E. Sklyanskiy, E. Graat, J. Smith, P. Menom, S. Ardalan, C. Ballard, P. Williams, *et al.*, “Hayabusa: Navigation Challenges for Earth Return,” Jet Propulsion Laboratory, Tech. Rep. JPL-TR-43827, 2011. [Online]. Available: <https://trs.jpl.nasa.gov/handle/2014/43827>.
- [163] T. Martin-Mur, G. Kruizinga, P. Burkhardt, F. Abilleira, M. Wong, and J. Kangas, “Mars Science Laboratory Interplanetary Navigation,” *Journal of spacecraft and rockets*, vol. 51, no. 4, pp. 1014–1028, 2014. DOI: [10.2514/1.A32631](https://doi.org/10.2514/1.A32631).
- [164] B. Starr, C. Westhelle, and J. Masciarelli, “Aerocapture Performance Analysis for a Neptune-Triton Exploration Mission,” in *AIAA Atmospheric Flight Mechanics Conference and Exhibit*, Providence, RI, 2004, p. 4955. DOI: [10.2514/6.2004-4955](https://doi.org/10.2514/6.2004-4955).
- [165] A. Dyakonov, M. Schoenenberger, and J. Van Norman, “Hypersonic and Supersonic Static Aerodynamics of Mars Science Laboratory Entry Vehicle,” in *43rd AIAA Thermophysics Conference*, New Orleans, LA, 2012, p. 2999. DOI: [10.2514/6.2012-2999](https://doi.org/10.2514/6.2012-2999).
- [166] S. Dutta and R. D. Braun, “Statistical Entry, Descent, and Landing Performance Reconstruction of the Mars Science Laboratory,” in *AIAA Atmospheric Flight Mechanics Conference*, National Harbor, MD, 2014, p. 0385. DOI: [10.2514/6.2014-0385](https://doi.org/10.2514/6.2014-0385).
- [167] S. B. Howell, C. Sobeck, M. Haas, M. Still, T. Barclay, F. Mullally, J. Troeltzsch, S. Aigrain, S. T. Bryson, D. Caldwell, *et al.*, “The K2 Mission: Characterization and Early Results,” *Publications of the Astronomical Society of the Pacific*, vol. 126, no. 938, p. 398, 2014. DOI: [10.1086/676406](https://doi.org/10.1086/676406).
- [168] O. Mousis, D. H. Atkinson, T. Cavalié, L. Fletcher, M. Amato, S. Aslam, F. Ferri, J.-B. Renard, T. Spilker, E. Venkatapathy, *et al.*, “Scientific Rationale for Uranus and Neptune In Situ Explorations,” *Planetary and Space Science*, vol. 155, pp. 12–40, 2018. DOI: [10.1016/j.pss.2017.10.005](https://doi.org/10.1016/j.pss.2017.10.005).
- [169] C. S. Arridge, N. Achilleos, J. Agarwal, C. Agnor, R. Ambrosi, N. André, S. V. Badman, K. Baines, D. Banfield, M. Barthélémy, *et al.*, “The Science Case for an Orbital Mission to Uranus: Exploring the Origins and Evolution of Ice Giant Planets,” *Planetary and Space Science*, vol. 104, pp. 122–140, 2014. DOI: [10.1016/j.pss.2014.08.009](https://doi.org/10.1016/j.pss.2014.08.009).

- [170] G. Flandro, “Fast Reconnaissance Missions to the Outer Solar System Utilizing Energy Derived from the Gravitational Field of Jupiter,” *Acta Astronautica*, vol. 12, no. 4, 1966.
- [171] E. McKinley and R. V. Allen, “Mariner Jupiter/Saturn 1977 Navigation Strategy,” *Journal of Spacecraft and Rockets*, vol. 13, no. 8, pp. 494–501, 1976. DOI: [10.2514/3.57113](https://doi.org/10.2514/3.57113).
- [172] C. Kohlhase, “Mariner Jupiter/Saturn 1977 Mission Design Tradeoffs,” in *13th Annual Meeting and Technical Display Incorporating the Forum on the Future of Air Transportation*, 1977, p. 281. DOI: [10.2514/6.1977-281](https://doi.org/10.2514/6.1977-281).
- [173] V. P. Dawson, “Taming Liquid Hydrogen: The Centaur Upper Stage Rocket, 1958–2002,” Washington, D.C., Tech. Rep. SP-4230, 2004. [Online]. Available: <https://history.nasa.gov/SP-4230.pdf>.
- [174] E. Stone and E. Miner, “The Voyager 2 Encounter with the Uranian System,” *Science*, vol. 233, no. 4759, pp. 39–43, 1986. DOI: [10.1126/science.233.4759.39](https://doi.org/10.1126/science.233.4759.39).
- [175] B. Conrath, D. Gautier, R. Hanel, G. Lindal, and A. Marten, “The Helium Abundance of Uranus from Voyager Measurements,” *Journal of Geophysical Research: Space Physics*, vol. 92, no. A13, pp. 15 003–15 010, 1987. DOI: [10.1029/JA092iA13p15003](https://doi.org/10.1029/JA092iA13p15003).
- [176] E. Stone and E. Miner, “The Voyager 2 Encounter with the Neptunian System,” *Science*, vol. 246, no. 4936, pp. 1417–1421, 1989. DOI: [10.1126/science.246.4936.1417](https://doi.org/10.1126/science.246.4936.1417).
- [177] S. Bayon, P. Falkner, and A. Pickering, “CDF Study Report: Ice Giants,” ESA, Noordwijk, The Netherlands, Tech. Rep. CDF-187(C), 2019. [Online]. Available: <https://sci.esa.int/s/8JgpdVA>.
- [178] T. R. Spilker, “Significant Science at Titan and Neptune from Aerocaptured Missions,” *Planetary and Space Science*, vol. 53, no. 5, pp. 606–616, 2005. DOI: [10.1016/j.pss.2004.12.003](https://doi.org/10.1016/j.pss.2004.12.003).
- [179] P. Agrawal, G. A. Allen, E. B. Sklyanskiy, H. H. Hwang, L. C. Huynh, K. McGuire, M. S. Marley, J. A. Garcia, J. F. Aliaga, and R. W. Moses, “Atmospheric Entry Studies for Uranus,” in *2014 IEEE Aerospace Conference*, IEEE, Big Sky, MT, 2014, pp. 1–19. DOI: [10.1109/AERO.2014.6836417](https://doi.org/10.1109/AERO.2014.6836417).

- [180] F. S. Milos, “Galileo Probe Heat Shield Ablation Experiment,” *Journal of Spacecraft and Rockets*, vol. 34, no. 6, pp. 705–713, 1997. DOI: [10.2514/2.3293](https://doi.org/10.2514/2.3293).
- [181] S. Campagnola, A. Boutonnet, W. Martens, and A. Masters, “Mission Design for the Exploration of Neptune and Triton,” *IEEE Aerospace and Electronic Systems Magazine*, vol. 30, no. 7, pp. 6–17, 2015. DOI: [10.1109/MAES.2015.140119](https://doi.org/10.1109/MAES.2015.140119).
- [182] L. D’Amario and M. Watkins, “Mars Exploration Rovers - A New Standard for Interplanetary Navigation,” in *55th International Astronautical Congress*, Vancouver, Canada, 2004. DOI: [10.2514/6.IAC-04-Q.3.A.04](https://doi.org/10.2514/6.IAC-04-Q.3.A.04).
- [183] W. M. Owen Jr., “Methods of Optical Navigation,” in *AAS Spaceflight Mechanics Conference*, New Orleans, LA, 2011.
- [184] W. Kizner, “A Method of Describing Miss Distances for Lunar and Interplanetary Trajectories,” *Planetary and Space Science*, vol. 7, pp. 125–131, 1961. DOI: [10.1016/0032-0633\(61\)90293-8](https://doi.org/10.1016/0032-0633(61)90293-8).
- [185] J. M. Longuski, R. E. Todd, and W. W. Koenig, “Survey of Nongravitational Forces and Space Environmental Torques - Applied to the Galileo,” *Journal of Guidance, Control, and Dynamics*, vol. 15, no. 3, pp. 545–553, 1992. DOI: [10.2514/3.20874](https://doi.org/10.2514/3.20874).
- [186] M. Schoenenberger, J. V. Norman, C. Karlgaard, P. Kutty, and D. Way, “Assessment of the Reconstructed Aerodynamics of the Mars Science Laboratory Entry Vehicle,” *Journal of Spacecraft and Rockets*, vol. 51, no. 4, pp. 1076–1093, 2014. DOI: [10.2514/1.A32794](https://doi.org/10.2514/1.A32794).
- [187] E. Roelke, P. D. Hattis, and R. Braun, “Improved Atmospheric Estimation for Aerocapture Guidance,” in *2019 AAS/AIAA Astrodynamics Specialist Conference*, Portland, ME, 2019.
- [188] J. F. Hamel and J. D. Lafontaine, “Improvement to the Analytical Predictor-Corrector Guidance Algorithm Applied to Mars Aerocapture,” *Journal of Guidance, Control, and Dynamics*, vol. 29, no. 4, pp. 1019–1022, 2006. DOI: [10.2514/1.20126](https://doi.org/10.2514/1.20126).

- [189] J. Wagner, A. Wilhite, D. Stanley, and R. Powell, “An Adaptive Real Time Atmospheric Prediction Algorithm for Entry Vehicles,” in *3rd AIAA Atmospheric Space Environments Conference*, Honolulu, HI, 2011, p. 3200. DOI: [10.2514/6.2011-3200](https://doi.org/10.2514/6.2011-3200).
- [190] L. Skalecki, C. Cerimele, and J. Gamble, “Meteorological Accuracy Requirements for Aerobraking Orbital Transfer Vehicles,” in *22nd Aerospace Sciences Meeting*, Houston, TX, 1984, p. 30. DOI: [10.2514/6.1984-30](https://doi.org/10.2514/6.1984-30).
- [191] E. R. Hillje, “Entry Aerodynamics at Lunar Return Conditions Obtained from the Flight of Apollo 4/AS-501,” NASA Johnson Space Center, Houston, TX, Tech. Rep. NASA/TN D-5399, 1969. [Online]. Available: <https://ntrs.nasa.gov/archive/nasa/casi.ntrs.nasa.gov/19690029435.pdf>.
- [192] C. A. Graves and J. C. Harpold, “Apollo Experience Report: Mission Planning for Apollo Entry,” NASA Johnson Space Center, Houston, TX, Tech. Rep. NASA/TN D-6725, 1972. [Online]. Available: <https://ntrs.nasa.gov/archive/nasa/casi.ntrs.nasa.gov/19720013191.pdf>.
- [193] R. Orloff and S. Garber, *Apollo by the Numbers: A Statistical Reference*. Washington, DC: NASA History Division, 2000, ISBN: 0-16-050631-X.
- [194] A. McDonald, K. Gates, and K. Nock, “Analysis of High-speed Aerocapture at Mars Using HyperPASS: A New Aeroassist Tool,” in *17th AIAA Aerodynamic Decelerator Systems Technology Conference and Seminar*, 2003, p. 2172. DOI: [10.2514/6.2003-2172](https://doi.org/10.2514/6.2003-2172).
- [195] G. Brandl *et al.*, *Sphinx: Python Documentation Generator*. [Online]. Available: <https://www.sphinx-doc.org/en/master/>.
- [196] R. M. Zubrin and D. G. Andrews, “Magnetic sails and interplanetary travel,” *Journal of Spacecraft and Rockets*, vol. 28, no. 2, pp. 197–203, 1991. DOI: [10.2514/3.26230](https://doi.org/10.2514/3.26230).
- [197] J. R. Spreiter and B. R. Briggs, “Theoretical Determination of the Form of the Boundary of the Solar Corpuscular Stream Produced by Interaction with the Magnetic Dipole Field of the Earth,” *Journal of Geophysical Research*, vol. 67, no. 1, pp. 37–51, 1962. DOI: [10.1029/JZ067i001p00037](https://doi.org/10.1029/JZ067i001p00037).

- [198] A. L. Julius Jr. and D. J. McKinzie Jr., “Calculations of the Interaction of the Solar Plasma with the Magnetic Field of a Current Loop and Two Parallel Infinite Lines of Current,” *Journal of Spacecraft and Rockets*, vol. 5, no. 1, pp. 3–8, 1968. DOI: [10.2514/3.29177](https://doi.org/10.2514/3.29177).
- [199] T. Inamori, R. Kawashima, P. Saisutjarit, N. Sako, and H. Ohsaki, “Magnetic Plasma Deorbit System for Nano and Micro-satellites Using Magnetic Torquer Interference with Space Plasma in Low Earth Orbit,” *Acta Astronautica*, vol. 112, pp. 192–199, 2015. DOI: [10.1016/j.actaastro.2015.02.025](https://doi.org/10.1016/j.actaastro.2015.02.025).
- [200] I. Funaki and H. Yamakawa, “Solar Wind Sails,” in *Exploring the Solar Wind*, IntechOpen, 2012. DOI: [10.5772/35673](https://doi.org/10.5772/35673).
- [201] M. M. Moe, S. D. Wallace, and K. Moe, “Recommended Drag Coefficients for Aeronomics Satellites,” *The Upper Mesosphere and Lower Thermosphere: A Review of Experiment and Theory, Geophys. Monogr. Ser.*, vol. 87, pp. 349–356, 1995. DOI: [10.1029/GM087p0349](https://doi.org/10.1029/GM087p0349).
- [202] J. P. Freidberg, *Ideal MHD*. Cambridge, United Kingdom: Cambridge University Press, 2014. DOI: [10.1017/CBO9780511795046](https://doi.org/10.1017/CBO9780511795046).
- [203] G. Tóth, B. Van der Holst, I. V. Sokolov, D. L. De Zeeuw, T. I. Gombosi, F. Fang, W. B. Manchester, X. Meng, D. Najib, K. G. Powell, *et al.*, “Adaptive Numerical Algorithms in Space Weather Modeling,” *Journal of Computational Physics*, vol. 231, no. 3, pp. 870–903, 2012. DOI: [10.1016/j.jcp.2011.02.006](https://doi.org/10.1016/j.jcp.2011.02.006).
- [204] J. Ekelöw, “Design and Manufacturing of Thin Composite Tape Springs,” Stockholm, Sweden: Master Thesis, KTH Royal Institute of Technology, 2014.
- [205] C. Underwood, A. Viquerat, B. Taylor, C. Massimiani, R. Duke, S. Fellowes, *et al.*, “The InflateSail CubeSat Mission—The First European Demonstration of Drag-Sail De-Orbiting,” *AAS Advances in the Astronautical Sciences Series*, vol. 163, 2018.
- [206] A. L. Hoskin, “Blossoming of Coiled Deployable Booms,” in *56th AIAA Structures, Structural Dynamics, and Materials Conference*, Kissimmee, FL, 2015, p. 0207. DOI: [10.2514/6.2015-0207](https://doi.org/10.2514/6.2015-0207).

- [207] P. Hyvönen, N. Ivchenko, and M. Tsamsakizoglou, “Small Explorer for Advanced Missions (SEAM), a CCSDS Compatible CubeSat Supported on a Global Commercial Ground Network,” in *14th International Conference on Space Operations*, Daejeon, Korea, 2016, p. 2626. DOI: [10.2514/6.2016-2626](https://doi.org/10.2514/6.2016-2626).
- [208] O. Popescu, “Power Budgets for Cubesat Radios to Support Ground Communications and Inter-Satellite Links,” *IEEE Access*, vol. 5, pp. 12 618–12 625, 2017. DOI: [10.1109/ACCESS.2017.2721948](https://doi.org/10.1109/ACCESS.2017.2721948).
- [209] J. Slough, D. Kirtley, and A. Pancotti, “Plasma Magnetoshell for Aero-braking and Aerocapture,” in *32nd International Electric Propulsion Conference*, Citeseer, Wiesbaden, Germany, 2011.
- [210] S. M. Hancock, R. W. Moses, and C. Goyne, “Magnetoshell Aerocapture Performance Opportunities at Mars,” in *2018 AIAA SPACE and Astrodynamics Forum and Exposition*, Orlando, FL, 2018, p. 5313. DOI: [10.2514/6.2018-5313](https://doi.org/10.2514/6.2018-5313).
- [211] C. L. Kelly and J. M. Little, “Performance and Design Scaling of Magnetoshells for Outer Planet Drag-Modulated Plasma Aerocapture,” in *2021 IEEE Aerospace Conference*, Virtual Event, 2021. DOI: [10.1109/AERO50100.2021.9438387](https://doi.org/10.1109/AERO50100.2021.9438387).
- [212] M. S. Net, E. Pellegrini, and J. Vander Hook, “Data Mules on Cycler Orbits for High-Latency, Planetary-Scale Data Transfers,” in *IEEE Aerospace Conference*, Big Sky, MT, 2020.
- [213] J. Englander *et al.*, “Evolutionary Mission Trajectory Generator (EMTG),” NASA Goddard Space Center, Tech. Rep. [Online]. Available: <https://ntrs.nasa.gov/api/citations/20200001624/downloads/20200001624.pdf>.
- [214] D. Izzo, “PYGMO and PYKEP: Open Source Tools for Massively Parallel Optimization in Astrodynamics (the case of Interplanetary Trajectory Optimization),” in *Proceedings of the Fifth International Conference on Astrodynamics Tools and Techniques, ICATT*, Noordwijk, The Netherlands, 2012.

- [215] R. A. Lugo, J. D. Shidner, R. W. Powell, S. M. Marsh, J. A. Hoffman, D. K. Litton, and T. L. Schmitt, “Launch Vehicle Ascent Trajectory Simulation using the Program to Optimize Simulated Trajectories II (POST2),” NASA Langley Research Center, Tech. Rep. AAS-17-274, 2017. [Online]. Available: <https://ntrs.nasa.gov/api/citations/20170001620/downloads/20170001620.pdf>.
- [216] J. Balaram, R. Austin, P. Banerjee, T. Bentley, D. Henriquez, B. Martin, E. McMahon, and G. Sohl, “DSENDS-A High-Fidelity Dynamics and Spacecraft Simulator for Entry, Descent and Surface Landing,” in *IEEE Aerospace Conference*, IEEE, vol. 7, Big Sky, MT, 2002, pp. 7–7. DOI: [10.1109/AERO.2002.1035313](https://doi.org/10.1109/AERO.2002.1035313).
- [217] S. Bhaskaran, “Autonomous Optical-Only Navigation for Deep Space Missions,” in *ASCEND 2020*, Virtual Event, 2020, p. 4139. DOI: [10.2514/6-2020-4139](https://doi.org/10.2514/6-2020-4139).
- [218] R. G. Deshmukh, D. A. Spencer, and S. Dutta, “Investigation of Direct Force Control for Aerocapture at Neptune,” *Acta Astronautica*, vol. 175, pp. 375–386, 2020. DOI: [10.1016/j.actaastro.2020.05.047](https://doi.org/10.1016/j.actaastro.2020.05.047).
- [219] H. Dezfuli, A. Benjamin, C. Everett, G. Maggio, M. Stamatelatos, R. Youngblood, S. Guarro, P. Rutledge, J. Sherrard, C. Smith, *et al.*, “NASA Risk Management Handbook. Version 1.0,” Tech. Rep. NASA/SP-2011-3422, 2011. [Online]. Available: <https://ntrs.nasa.gov/api/citations/20120000033/downloads/20120000033.pdf>.
- [220] P. F. Wercinski, E. Venkatapathy, P. J. Gage, B. C. Yount, D. K. Prabhu, B. Smith, J. O. Arnold, A. Makino, K. H. Peterson, and R. I. Chinnapongse, “Enabling Venus In-Situ Science - Deployable Entry System Technology, Adaptive Deployable Entry and Placement Technology,” in *10th Meeting of the Venus Exploration Analysis Group*, Washington, DC: NASA, 2012. [Online]. Available: <https://ntrs.nasa.gov/archive/nasa/casi.ntrs.nasa.gov/20130001711.pdf>.

A. ENTRY SYSTEM MASS BREAKDOWN

A.1 MSL Mass Breakdown

Table A.1. Mass breakdown for MSL entry system

System	Mass, kg*	Type
Backshell	450	ESS
Frontshell + Heatshield	385	TPS
Rover	899	P
Ballast (2 x 75 kg)	150	ESS
Ballast (6 x 25 kg)	150	ESS
Skycrane (dry)	829	P
Skycrane propellant	387	P
Parachute	50	P
Total	3300	

* <http://planet4589.org/space/jsr/back/news.664.txt>;
Retrieved 17 December 2019.

A.2 ADEPT Mass Breakdown

Table A.2. Mass breakdown for ADEPT entry system [220]

System	Mass, kg	Type
Structure	392	ESS
Mechanisms	205	ESS
Avionics & Power	17	ESS
Backshell	30	ESS
TPS (Carbon Cloth)	92	TPS
TPS (Rigid Nose)	71	TPS
Payload	813	P
Total	1620	

B. ADDITIONAL FEASIBILITY CHARTS

B.1 Venus

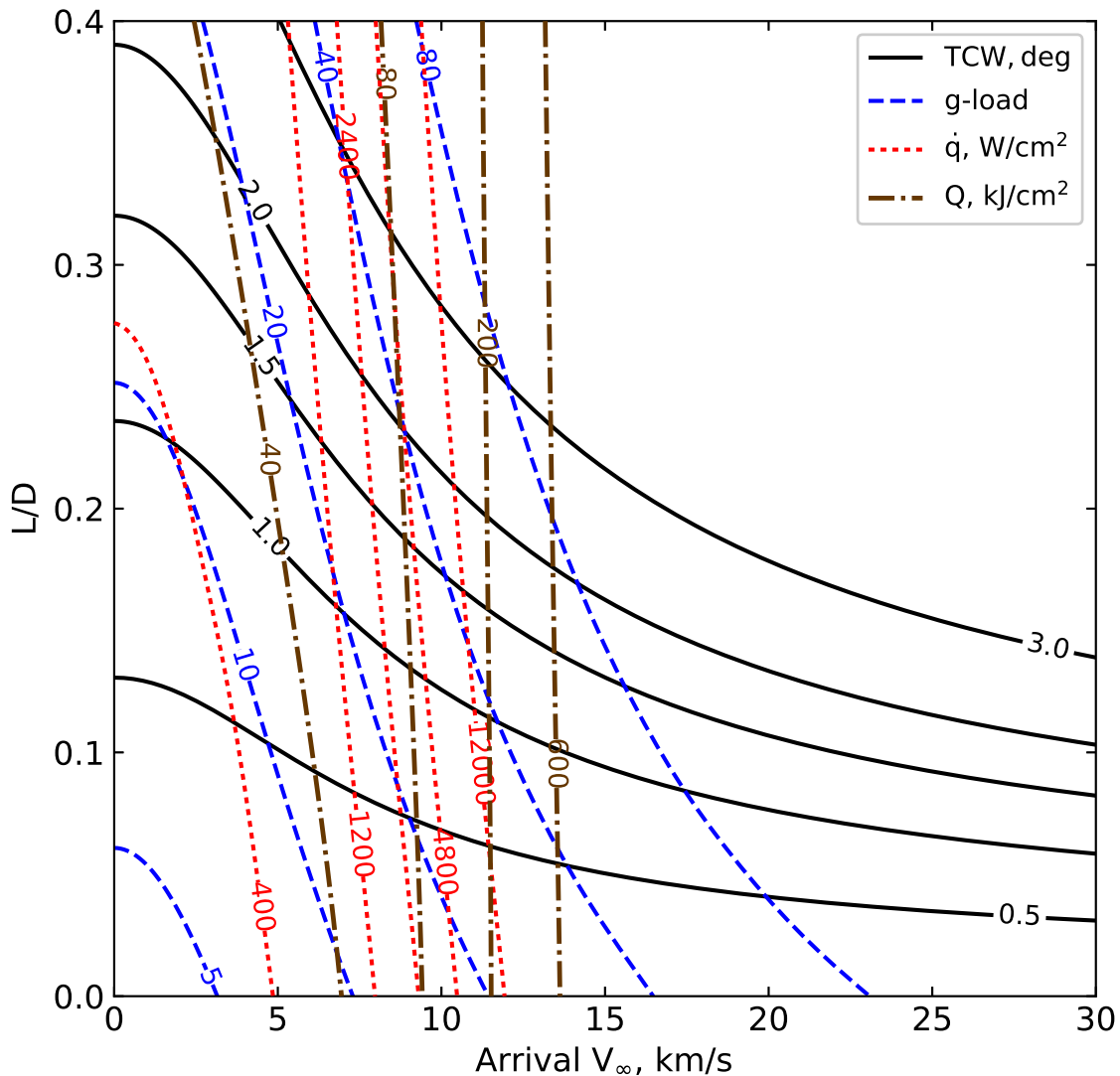


Figure B.1. Lift modulation aerocapture feasibility chart for Venus. $\beta = 200 \text{ kg/m}^2$, $R_N = 1.0 \text{ m}$.

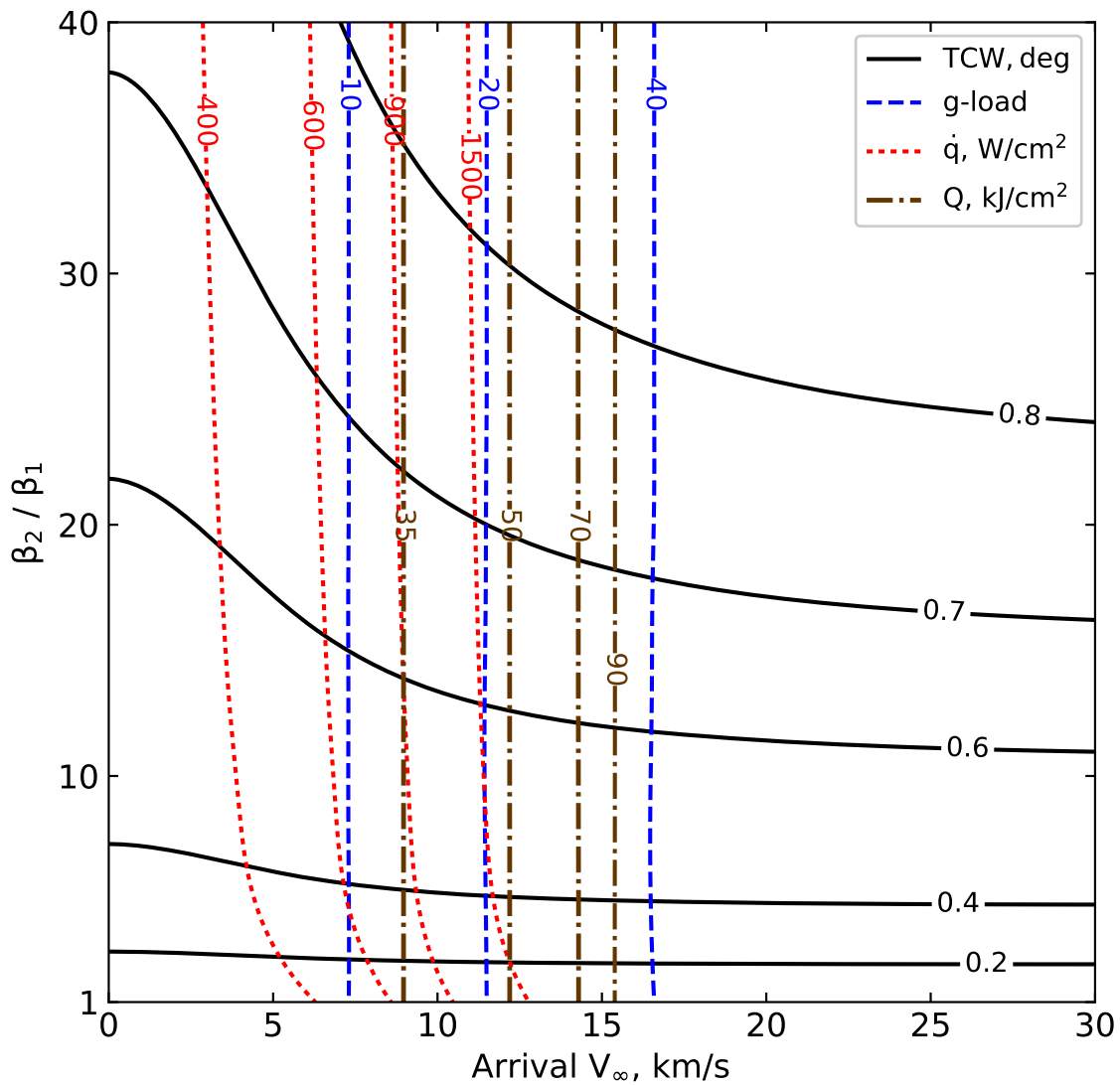


Figure B.2. Drag modulation aerocapture feasibility chart for Venus. $\beta_1 = 20 \text{ kg/m}^2$, $R_N = 0.1 \text{ m}$.

B.2 Earth

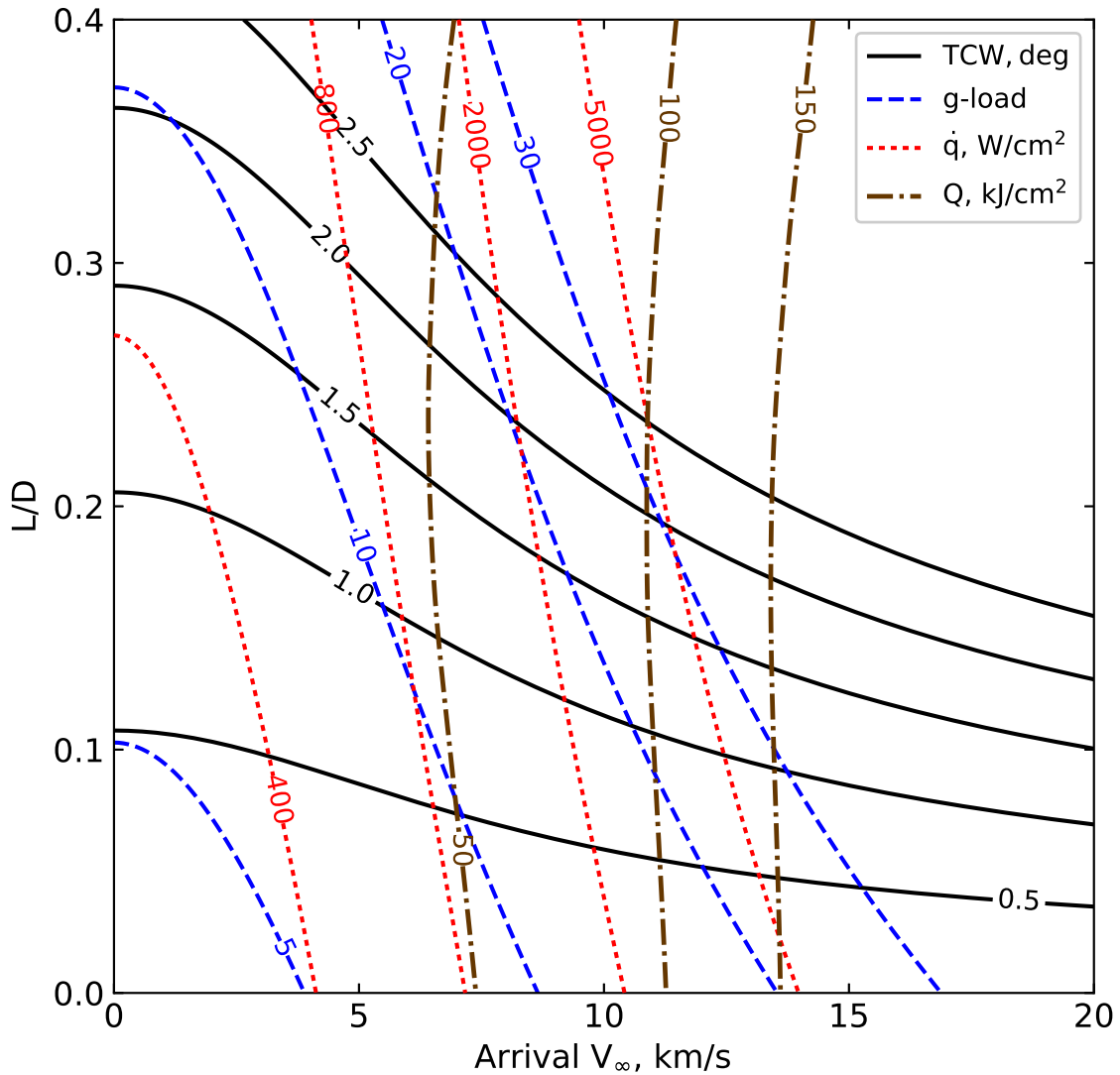


Figure B.3. Lift modulation aerocapture feasibility chart for Earth. $\beta = 200 \text{ kg/m}^2$, $R_N = 1.0 \text{ m}$.

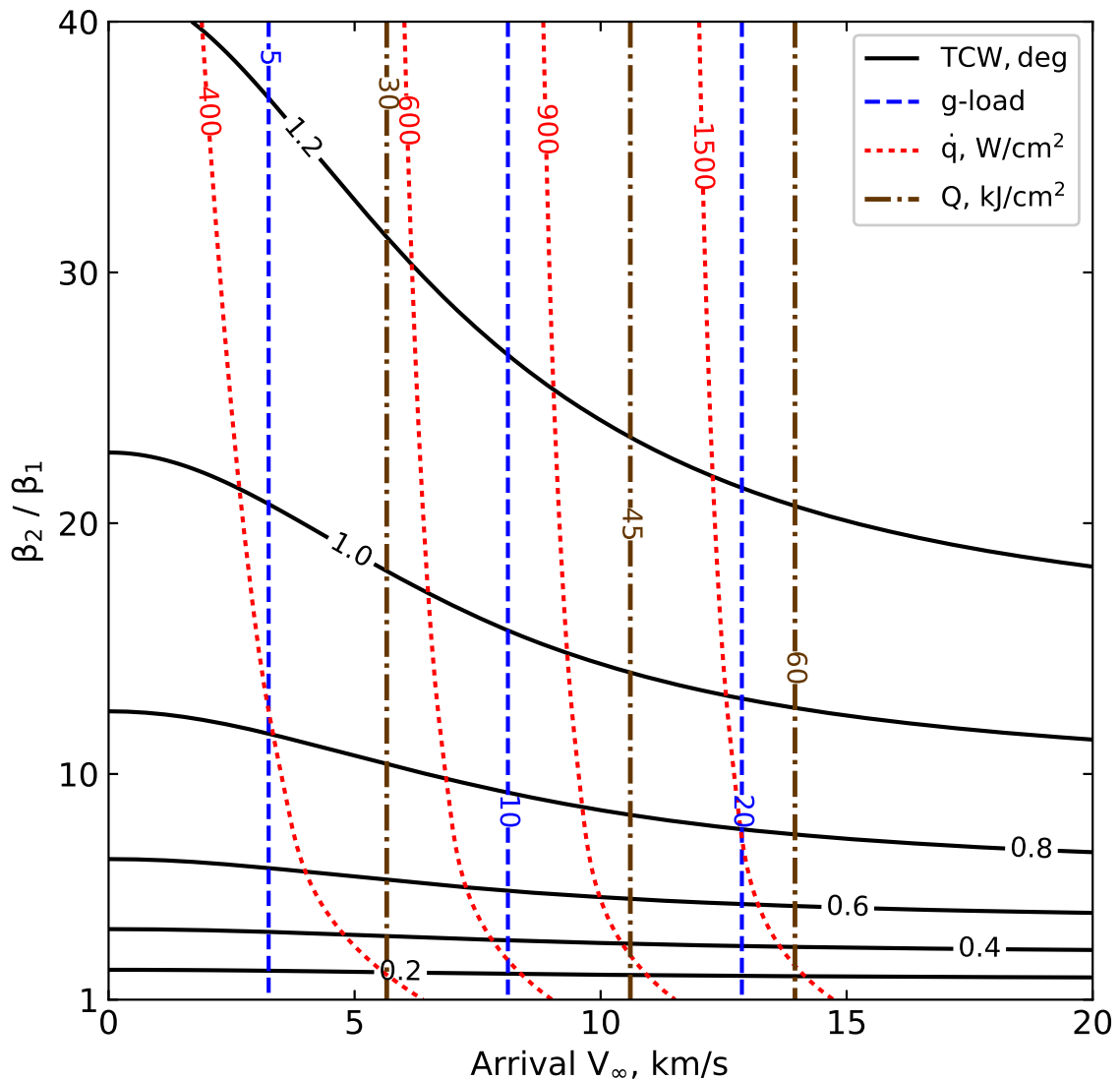


Figure B.4. Drag modulation aerocapture feasibility chart for Earth. $\beta_1 = 20 \text{ kg/m}^2$, $R_N = 0.1 \text{ m}$.

B.3 Mars

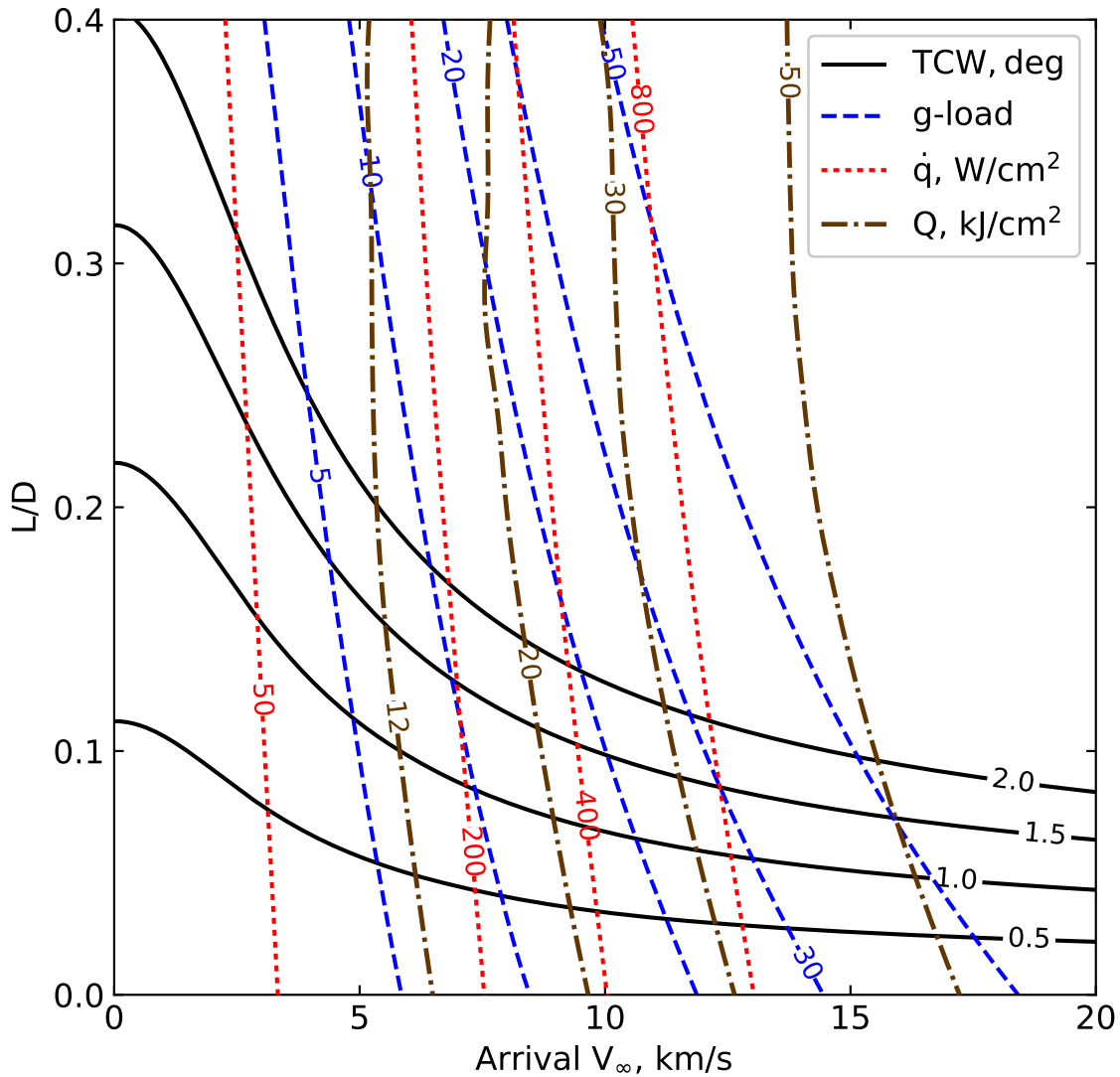


Figure B.5. Lift modulation aerocapture feasibility chart for Mars. $\beta = 200 \text{ kg/m}^2$, $R_N = 1.0 \text{ m}$.

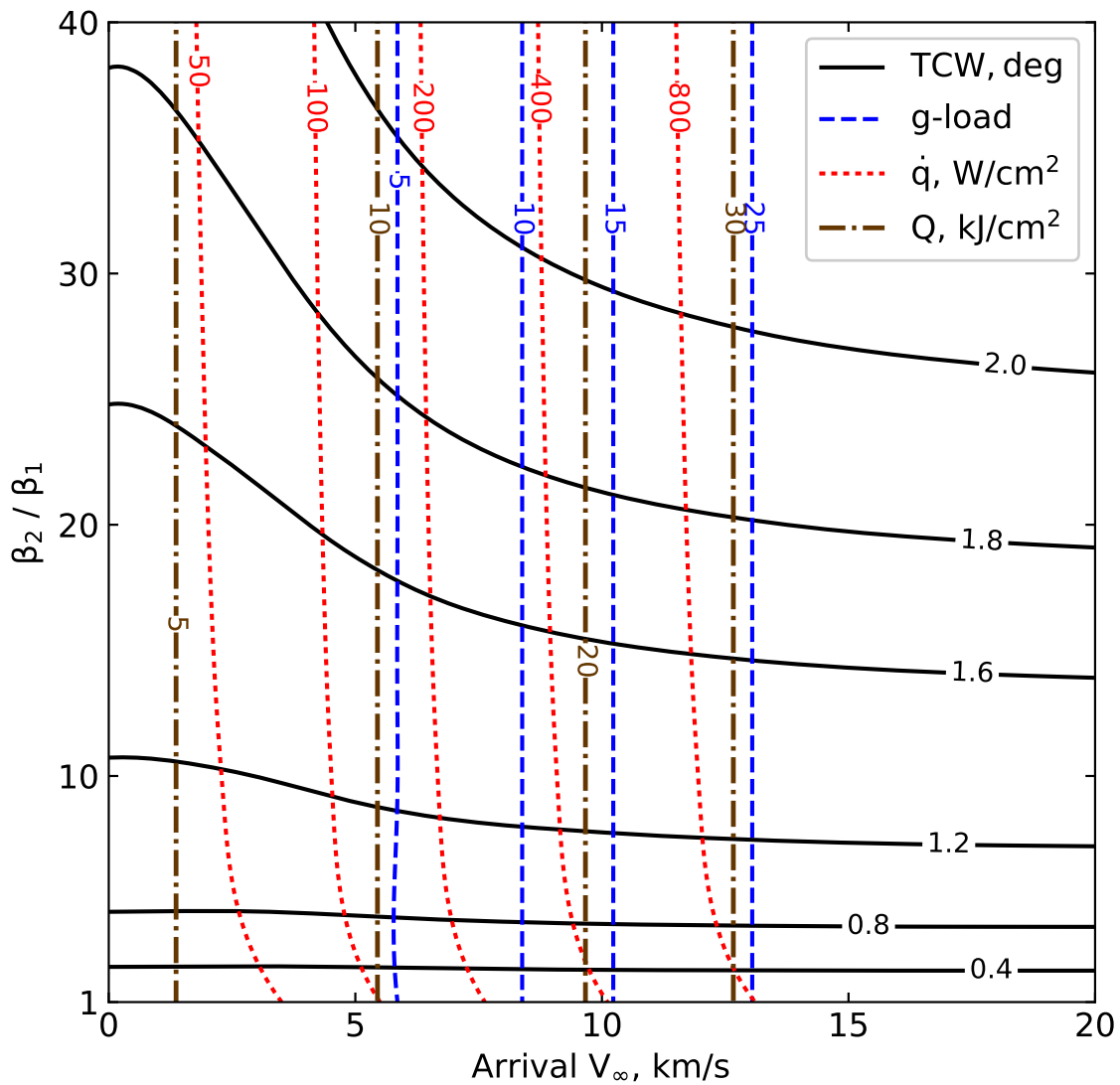


Figure B.6. Drag modulation aerocapture feasibility chart for Mars. $\beta_1 = 20 \text{ kg/m}^2$, $R_N = 0.1 \text{ m}$.

B.4 Jupiter

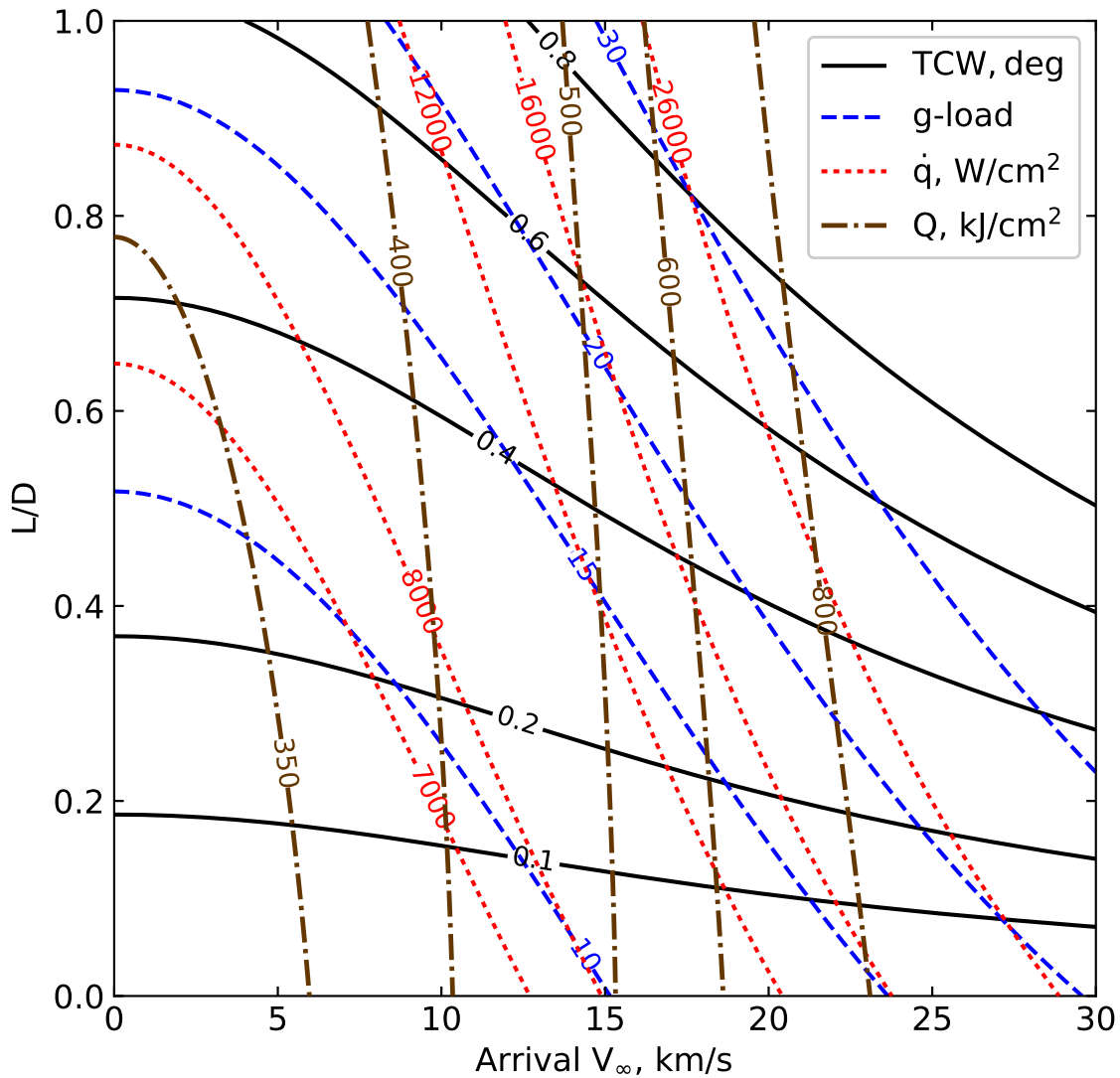


Figure B.7. Lift modulation aerocapture feasibility chart for Jupiter. $\beta = 200 \text{ kg/m}^2$, $R_N = 1.0 \text{ m}$.

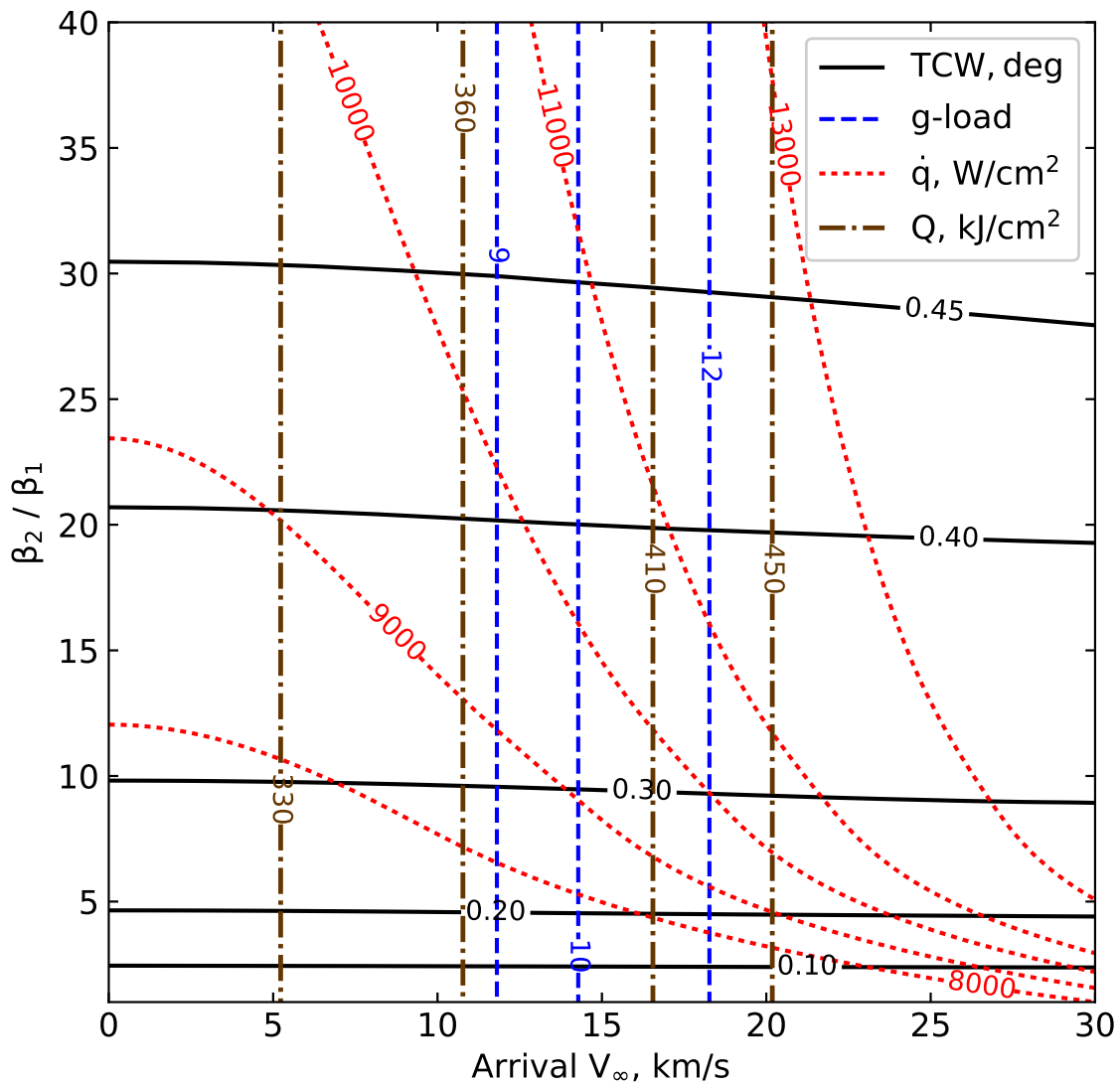


Figure B.8. Drag modulation aerocapture feasibility chart for Jupiter. $\beta_1 = 20 \text{ kg/m}^2$, $R_N = 0.1 \text{ m}$.

B.5 Saturn

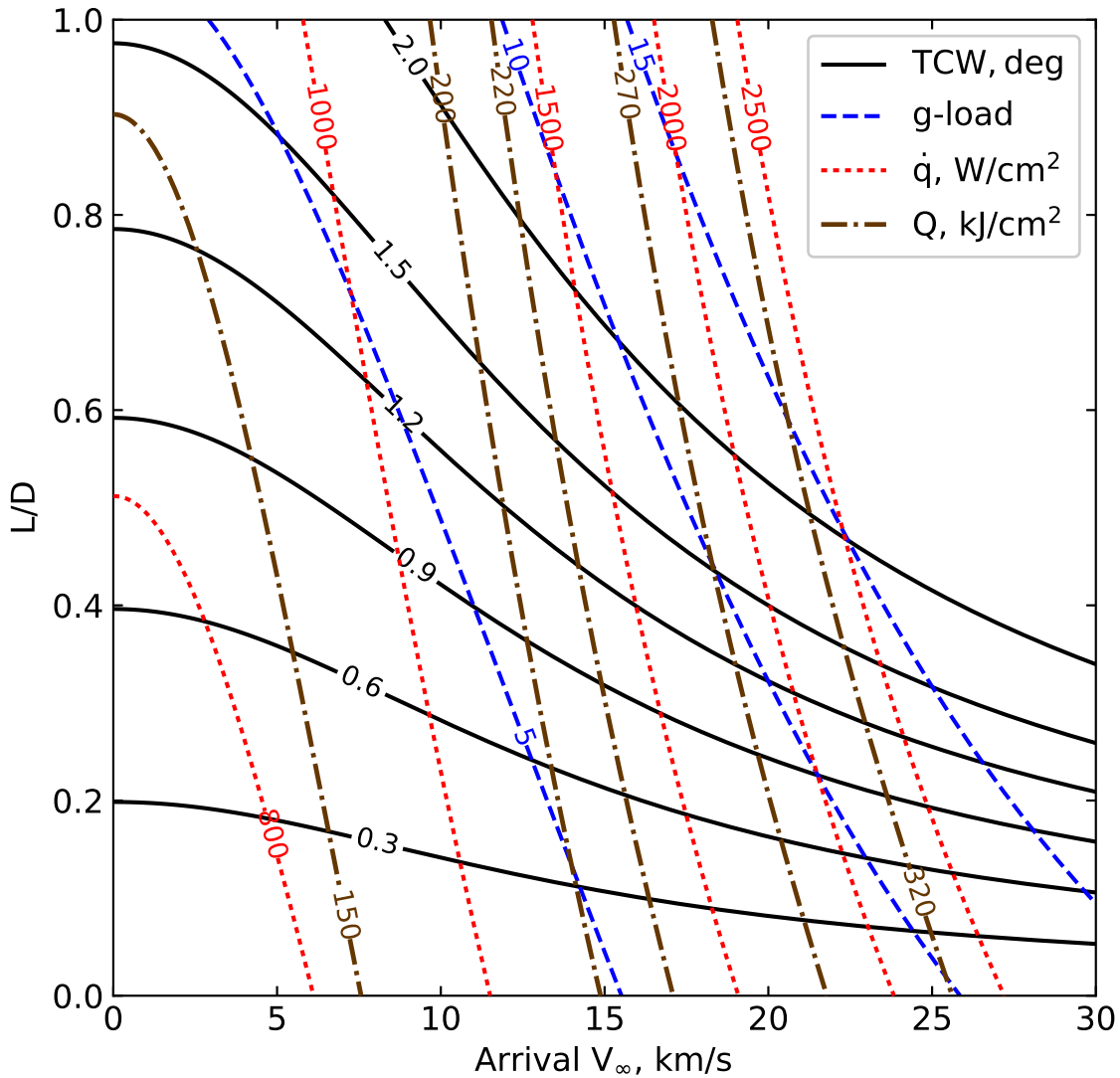


Figure B.9. Lift modulation aerocapture feasibility chart for Saturn. $\beta = 200 \text{ kg/m}^2$, $R_N = 1.0 \text{ m}$.

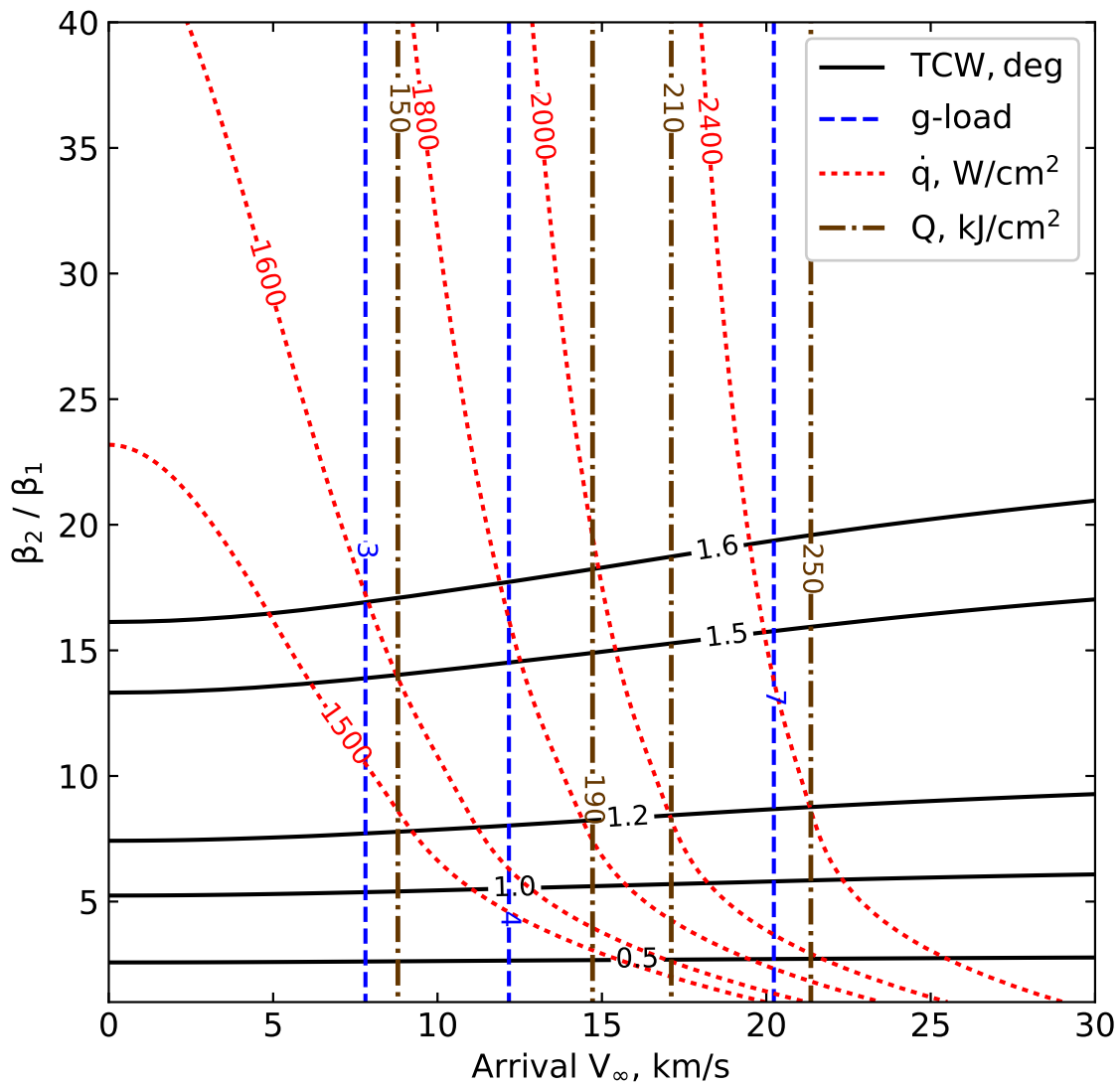


Figure B.10. Drag modulation aerocapture feasibility chart for Saturn. $\beta_1 = 20 \text{ kg/m}^2$, $R_N = 0.1 \text{ m}$.

B.6 Titan

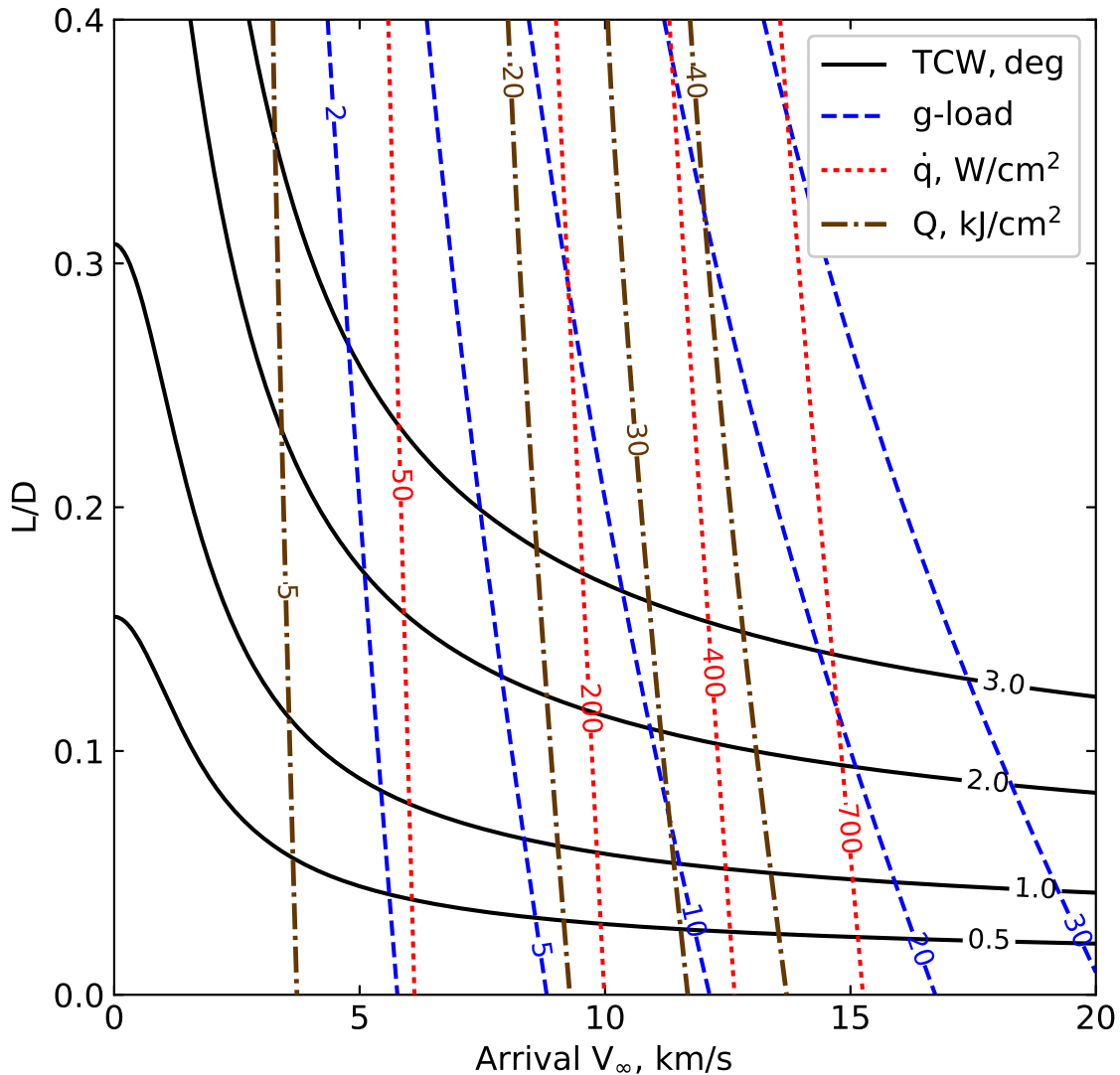


Figure B.11. Lift modulation aerocapture feasibility chart for Titan. $\beta = 200 \text{ kg/m}^2$, $R_N = 1.0 \text{ m}$.

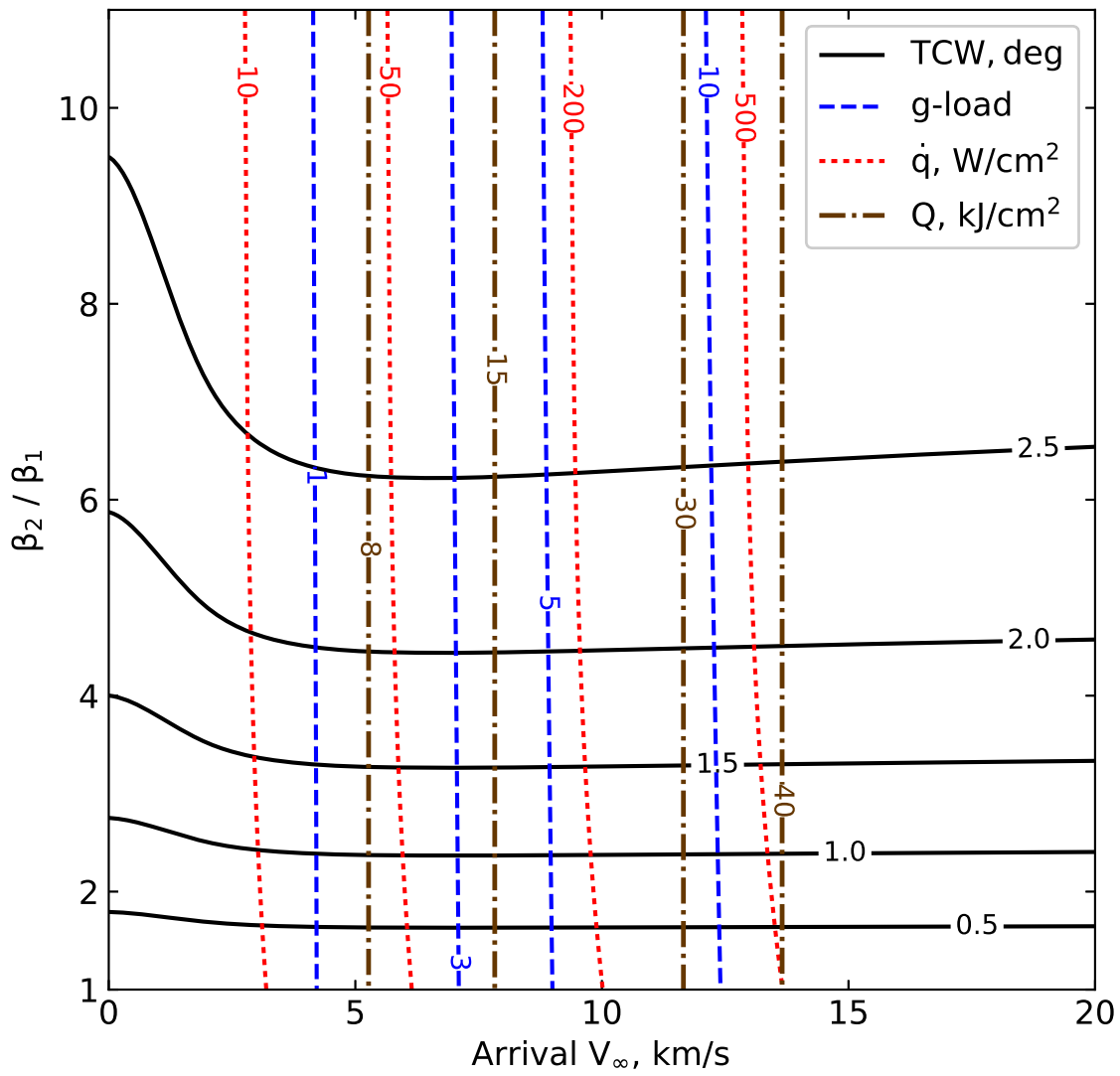


Figure B.12. Drag modulation aerocapture feasibility chart for Titan. $\beta_1 = 20 \text{ kg/m}^2$, $R_N = 0.1 \text{ m}$.

B.7 Uranus

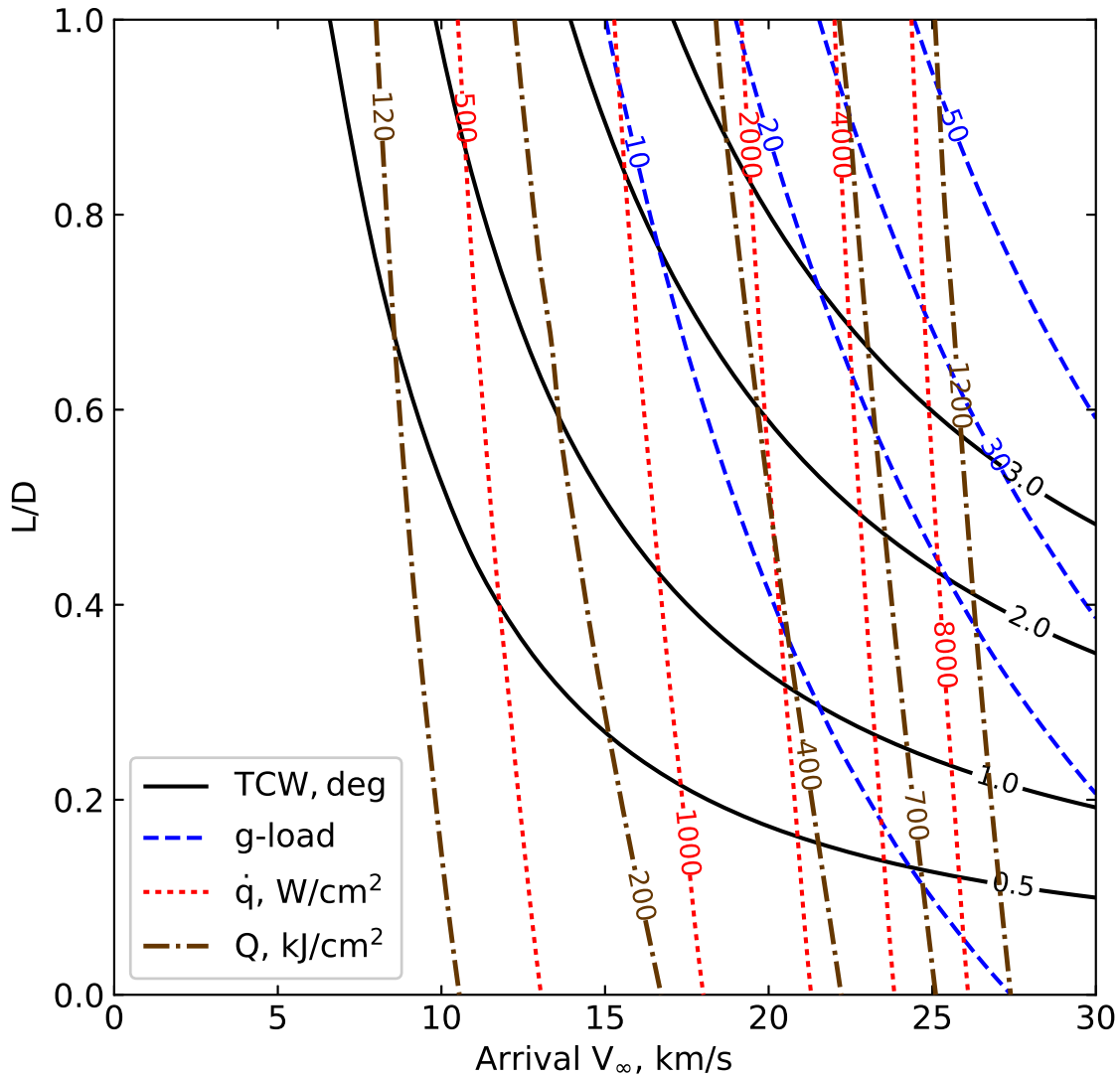


Figure B.13. Lift modulation aerocapture feasibility chart for Uranus. $\beta = 200 \text{ kg/m}^2$, $R_N = 1.0 \text{ m}$.

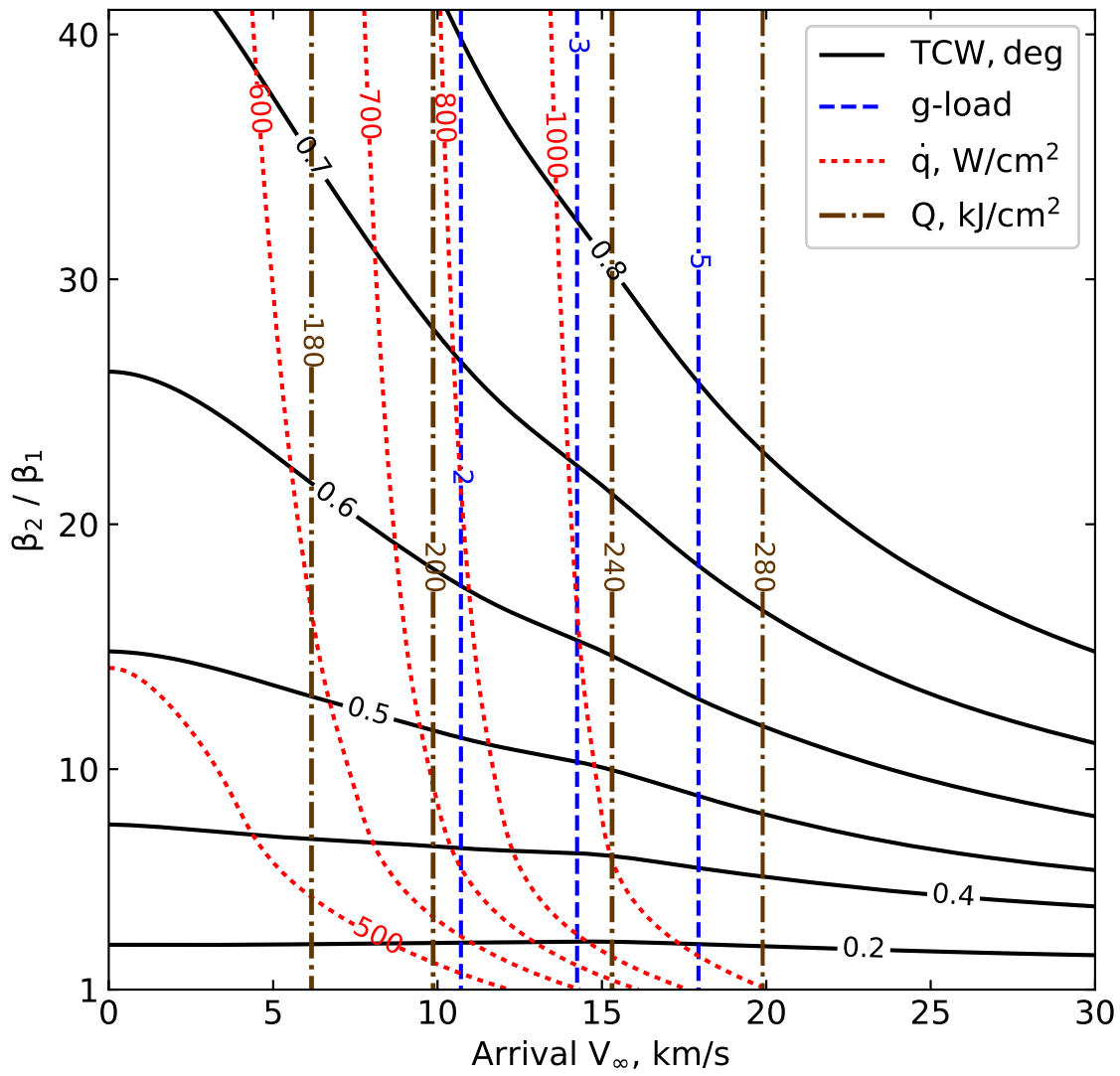


Figure B.14. Drag modulation aerocapture feasibility chart for Uranus. $\beta_1 = 20 \text{ kg/m}^2$, $R_N = 0.1 \text{ m}$.

B.8 Neptune

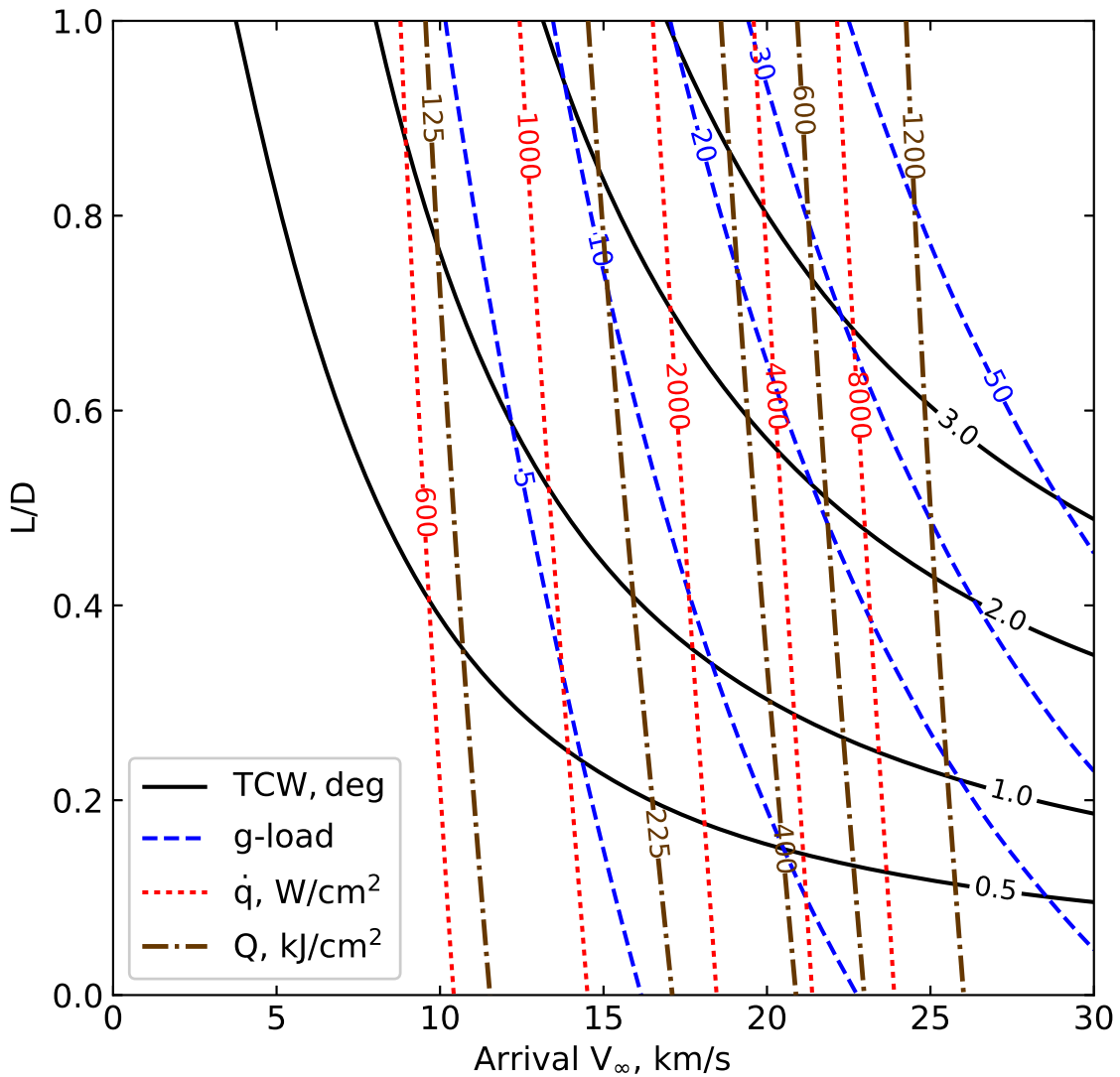


Figure B.15. Lift modulation aerocapture feasibility chart for Neptune. $\beta = 200 \text{ kg/m}^2$, $R_N = 1.0 \text{ m}$.

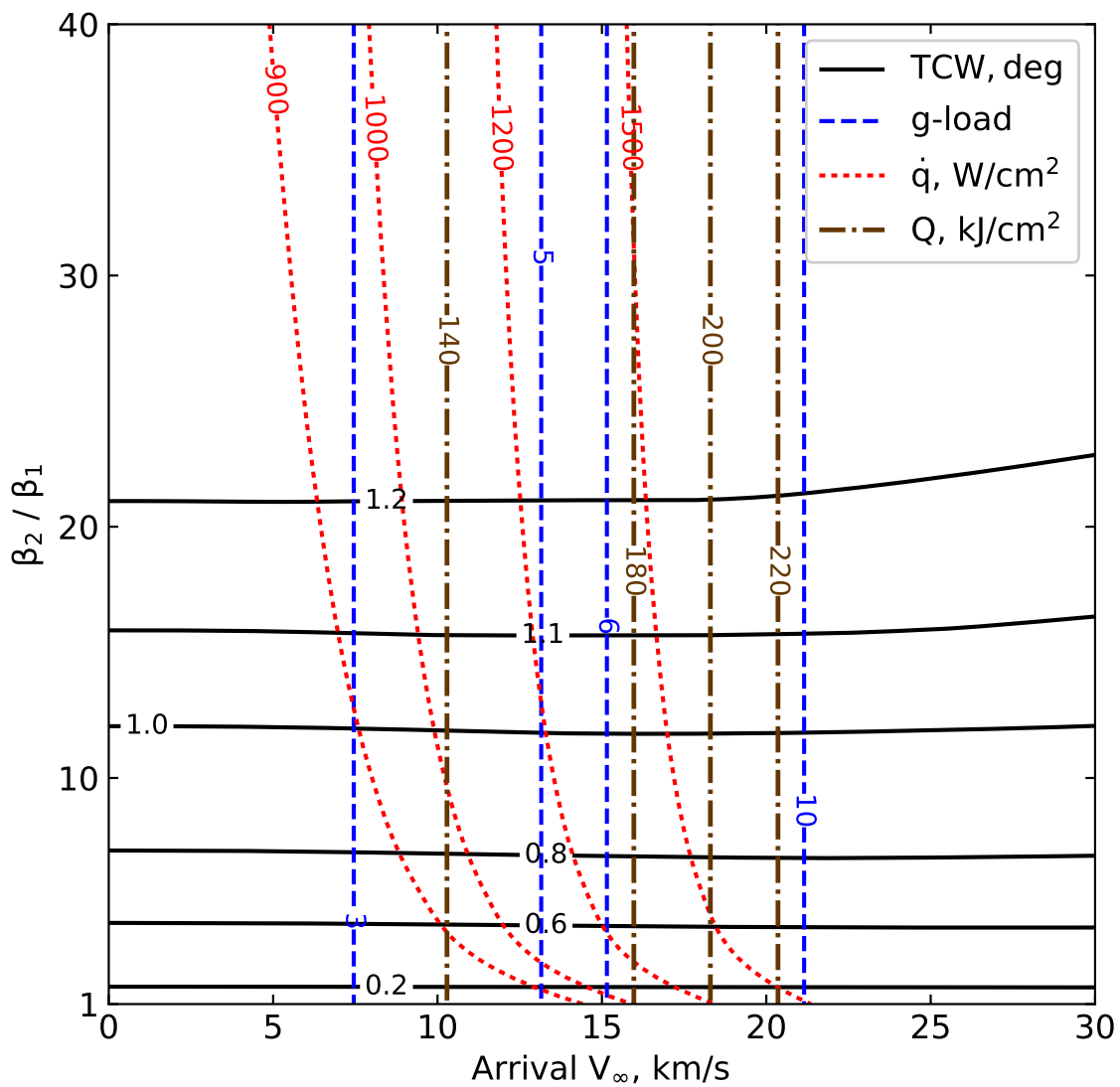


Figure B.16. Drag modulation aerocapture feasibility chart for Neptune. $\beta_1 = 20 \text{ kg/m}^2$, $R_N = 0.1 \text{ m}$.

C. NEPTUNE AEROCAPTURE GUIDANCE PARAMETERS

The gain parameters used in the equilibrium glide phase guidance is computed based on the procedure developed by Cerimele and Gamble [17]. The vehicle altitude dynamic response can be shown to be:

$$\ddot{h} + \frac{C_L S}{m} G_h \dot{h} - \frac{C_L S}{m} G_{\bar{q}} (\bar{q} - \bar{q}_{\text{ref}}) = 0 \quad (\text{C.1})$$

Equation C.1 can be approximated as a linear second order system by assuming $\bar{q} = ah + b$, and the system response is characterized by

$$\omega_n^2 = -\frac{C_L S}{m} G_{\bar{q}} a \quad (\text{C.2})$$

$$2\zeta\omega_n = \frac{C_L S}{m} G_h \quad (\text{C.3})$$

For a vehicle with $m/C_L S = 500 \text{ kg/m}^2$, $L/D = 0.4$ entering Neptune atmosphere retrograde with planet-relative speed $V = 33.0 \text{ km/s}$, EFPA = -11.30 deg and using full lift up, the dynamic pressure as a function of altitude is shown in Fig. C.1. A linear approximation can be made for the pressure profile as the vehicle descends below 300 km, and the aerodynamic forces become significant. Using $\omega_n = 0.05 \text{ rad/s}$ and $\zeta = 1.50$, the gain parameters can be calculated to be $G_h = 75.0$ and $G_{\bar{q}} = 7.41$. However, adjusting $G_{\bar{q}}$ to 3.0 was found to provide better performance and hence is the value used in the study. These values provided acceptable vehicle response, and were used for all simulations in the present study including the prograde cases for consistency. For a vehicle with different $m/C_L S$, or for different entry conditions, the above procedure can be used to recalculate the gain parameters.

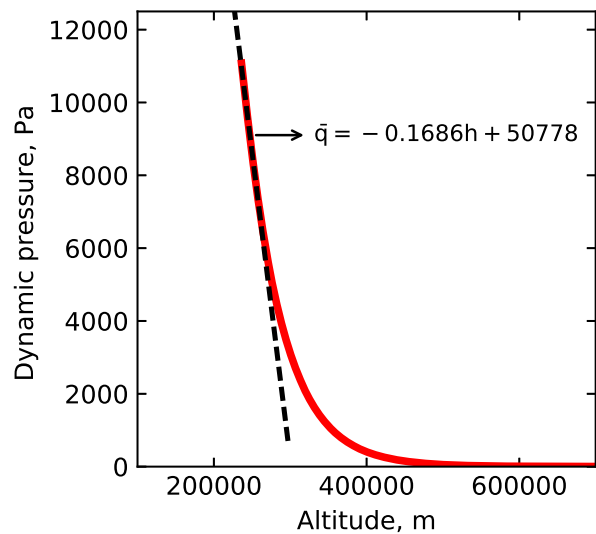


Figure C.1. Actual dynamic pressure profile (solid line) and linear approximation (dashed line) used to calculate guidance gain parameters. Based on the method developed by Cerimele and Gamble [17].

D. AMAT INSTALLATION INSTRUCTIONS

Refer to the next page for AMAT installation instructions. The document is an excerpt from the complete AMAT documentation available online¹.

¹↑<https://amat.readthedocs.io>

CHAPTER 2

Installation

Note: AMAT is designed to work with Python 3.0 or greater. You must have a Python 3 installation in your system.
There are three ways to install AMAT.

2.1 Option 1 : Install from source (recommended)

This allows you to download the “entire” package (with the required data files to run examples).

1. Make sure you have numpy, scipy, matplotlib and pandas installed. Most likely you already have these installed. If not, use the following commands to install these dependencies first. Open a terminal window (on Linux/Mac machines) and type the following commands. You must have pip installed.
 - \$ pip install numpy
 - \$ pip install scipy
 - \$ pip install matplotlib
 - \$ pip install pandas

It is recommended to have [Jupyter Notebook](#) installed to run the example notebooks.

- pip install jupyterlab

On Windows machines, the recommended option is to use [Anaconda](#) package manager to install these packages.

2. Navigate to the directory where you want AMAT to be installed. Open a terminal (or command window) and use the following command:
 - \$ cd home/path

where home/path is to be replaced with the path to the folder where AMAT will be installed.

3. Clone the github repository using the following command. You must have git installed.
 - \$ git clone https://github.com/athulpg007/AMAT.git

If you do not have git installed, you can download a .zip file from the github page and extract it. Copy the entire uncompressed folder into the directory where you want AMAT to be installed.

4. Change directory to AMAT and install package.

- \$ cd AMAT
- \$ python setup.py install

5. Check that you have the required data files. For example, in the root folder where AMAT is installed, you should see a folder names atmdata with data for various planets.

6. Run an example script to check everything is working.

- \$ cd examples
- \$ ipython
- \$ run example-01-hello-world.py

7. Run example Jupyter notebooks

- jupyter-notebook

To uninstall AMAT, use

- python setup.py develop -u

This will remove the AMAT installation from Python. You may simply delete the root folder where AMAT was installed to completely remove the files.

2.2 Option 2 : Install from pip (NOT recommended)

This allows you to download the package, but without most of the data files. You can run the program, but will need to visit the git repository later to download some of the data files and place them in an appropriate location. You will also need to change the location of data files in the example scripts if you use them.

Python Package Index limits the amount of additional data that can be packaged in the distribution, hence all data cannot be included in the built version.

- \$ pip install AMAT

2.3 Option 3 : Install in a virutalenv (for developers)

If you plan to test or develop the package, the recommended option is to to install it in a virtual environment. This allows you to discard changes and start afresh without having to do a system-wide installation.

1. Change directory to where you want the virtual environment to be created.

- \$ cd home/path

2. Create a virutal environment and activate it.

- \$ python3 -m venv env1
- \$ source env1/bin/activate

3. Change directory to env1

- \$ cd env1

4. Follow steps 1 through 6 in Option #1 : Install from source. pip will automatically fetch the required dependencies.
5. If you make changes to the source code, use
 - `python setup.py develop -u`to remove the previously installed version. Re-install using
 - `$ python setup.py install`
6. To create a distribution
 - `python3 setup.py sdist bdist_wheel`
7. To re-make docs if you made changes to the source code, you must have sphinx installed.
 - `cd ~root/docs`
 - `sphinx-apidoc -f -o source/ ../`
 - `make html`

If you added a new AMAT module, appropriate changes must be made to `docs/source/AMAT.rst`.

2.4 AMAT Usage

- `from AMAT.planet import Planet`
- `from AMAT.vehicle import Vehicle`
- `from AMAT.launcher import Launcher`

E. AMAT: EXAMPLE JUPYTER NOTEBOOKS

Refer to the next page for example Jupyter Notebooks illustrating the AMAT workflow. A more extensive set of examples is available online¹.

¹↑<https://amat.readthedocs.io>

CHAPTER 4

Example Jupyter Notebooks

4.1 Example - 01 - Hello World!

In this ‘hello world’ program, you will learn to use AMAT to create a planet object.

First let us import the Planet class from AMAT

```
[1]: from AMAT.planet import Planet
```

Now let us create a planet object which represents Venus.

```
[2]: planet = Planet("VENUS")
```

Let us look at the an attribute of the created object. For example let us, print the radius of the planet. A full list of attributes and functions can be obtained using help(planet).

```
[3]: print(planet.RP)
```

```
6051800.0
```

Congratulations! You have now created a planet object using AMAT. In the next example, we will add an atmosphere model to this planet object.

4.2 Example - 02 - Atmosphere

In this example, you will learn to use add an atmosphere model to planets.

Let us re-use the code from example-01 to create a planet object for Venus.

```
[1]: from AMAT.planet import Planet  
planet = Planet("VENUS")
```

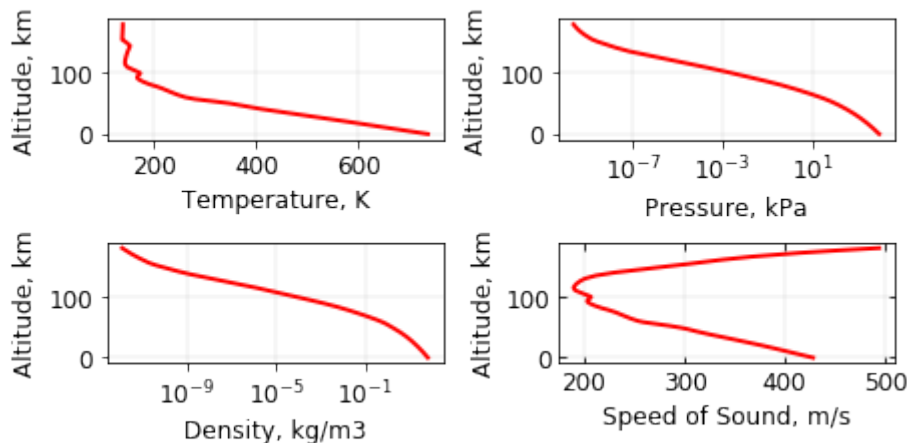
We are now ready to add an atmosphere model to the planet object.

AMAT stores atmospheric data in the form of look up tables located in ~root/atmdata. Typically, data is stored in the following format.

#Z(m)	Temp(K)	Pres (Nm2)	rho(kgm3)	a (m/s)
0	735.30	9.209E+06	6.479E+01	428.03
1000	727.70	8.645E+06	6.156E+01	425.46
2000	720.20	8.109E+06	5.845E+01	422.88
3000	712.40	7.601E+06	5.547E+01	420.27
4000	704.60	7.120E+06	5.262E+01	417.63
5000	696.80	6.666E+06	4.987E+01	415.09

```
[2]: # the atmosphere model provided in atmdata/Venus/venus-gram-avg.dat.
# The columns for height, Temp, pressure, density are 0, 1, 2, 3
planet.loadAtmosphereModel('..../atmdata/Venus/venus-gram-avg.dat', 0 , 1 ,2, 3)
```

```
[3]: # Let us now use the checkAtmProfiles function to inspect the atmospheric profiles.
planet.checkAtmProfiles()
```



```
[4]: # Compute the scale height at the Venusian surface for illustration.
# planet.density_int is the interpolation function created by planet object
# when atmosphere model is loaded.
planet.scaleHeight(0, planet.density_int)
```

```
[4]: 16127.792366356383
```

Congratulations! Your planet now has an atmosphere model. In the next example, we will compute aerocapture trajectories for a vehicle flying in the Venusian atmosphere.

4.3 Example - 03 - Venus Aerocapture: Part 1

In this example, you will learn to create a vehicle object in AMAT and simulate its aerocapture trajectory in the Venusian atmosphere.

For reference, we will re-create a few results from the paper “Craig and Lyne, Parametric Study of Aerocapture for Missions to Venus, Journal of Spacecraft and Rockets, Vol. 42, No. 6., 2005. DOI:10.2514/1.2589

Let us re-use the code from example-01, 02 to create a planet object for Venus and add an atmosphere model. In addition to Planet, import the Vehicle class from AMAT for this example.

```
[1]: from AMAT.planet import Planet
from AMAT.vehicle import Vehicle

# Create a planet object
planet=Planet("VENUS")

# Load an nominal atmospheric profile with height, temp, pressure, density data
planet.loadAtmosphereModel('../atmdata/Venus/venus-gram-avg.dat', 0 , 1 ,2, 3)
```

```
[2]: # Create a vehicle object flying in the target planet atmosphere.
# with params m = 300 kg, beta = 78.0, L/D = 0.35, A = 3.1416, AoA = 0, RN = 1.54

# These values are taken from the reference article mentioned above.
vehicle=Vehicle('Apollo', 300.0, 78.0, 0.35, 3.1416, 0.0, 1.54, planet)
```

Set initial conditions for the vehicle at atmospheric entry interface.

```
[3]: # h0 = 180 km, LON = 0 deg, LAT = 0 deg
# v0 = 12 km/s, HDG = 0 deg, FPA = 0 deg
# DOWNRANGE0 = 0 deg, HEATLOAD0 = 0.

# See help(vehicle) for more details.
vehicle.setInitialState(180.0,0.0,0.0,12.0,0.0,-4.5,0.0,0.0)

# Set solver tolerance = 1E-6 (recommended value)
# Setting this too low can result in long execution times.
vehicle.setSolverParams(1E-6)
```

```
[4]: # Compute the overshoot and undershoot limit EFPA

# Set max. propogation time = 2400.0 secs.
# Set max. time step = 0.1 sec.
# Set low value for guess = -80.0 deg
# Set high value for guess = -4.0 deg
# Set EFPA tolerance = 1E-10 (recommended)
# Set target apoapsis = 407 km

# This calculation migt take a couple of minutes. Hang on!
overShootLimit, exitflag_os  = vehicle.findOverShootLimit (2400.0,0.1,-80.0,-4.0,1E-
                                                               -10,407.0)
underShootLimit,exitflag_us  = vehicle.findUnderShootLimit(2400.0,0.1,-80.0,-4.0,1E-
                                                               -10,407.0)
```

```
[5]: # exitflag_os and exitflag_us will be set to 1 if a solution was found. Otherwise, it
# will be 0.
print(exitflag_os)
print(exitflag_us)

1.0
1.0
```

```
[6]: # print the overshoot and undershoot limits we just computed.
print("Overshoot limit : "+str('{:.4f}'.format(overShootLimit))+ " deg")
print("Undershoot limit : "+str('{:.4f}'.format(underShootLimit))+ " deg")
```

```
Overshoot limit : -7.0519 deg
Undershoot limit : -9.4396 deg
```

These are the limiting flight path angles for our vehicle at Venus. Let us now calculate these trajectories, and their associated deceleration and heating profiles.

```
[7]: import matplotlib.pyplot as plt
from matplotlib import rcParams

# Reset initial conditions and propagate overshoot trajectory
vehicle.setInitialState(180.0,0.0,0.0,12.0,0.0,overShootLimit,0.0,0.0)
vehicle.propogateEntry (2400.0,0.1,180.0)

# Extract and save variables to plot
t_min_os      = vehicle.t_minc
h_km_os       = vehicle.h_kmc
acc_net_g_os  = vehicle.acc_net_g
q_stag_con_os = vehicle.q_stag_con
q_stag_rad_os = vehicle.q_stag_rad

# Reset initial conditions and propagate undershoot trajectory
vehicle.setInitialState(180.0,0.0,0.0,12.0,0.0,underShootLimit,0.0,0.0)
vehicle.propogateEntry (2400.0,0.1,0.0)

# Extract and save variable to plot
t_min_us      = vehicle.t_minc
h_km_us       = vehicle.h_kmc
acc_net_g_us  = vehicle.acc_net_g
q_stag_con_us = vehicle.q_stag_con
q_stag_rad_us = vehicle.q_stag_rad

'''

Create fig #1 - altitude history of aerocapture maneuver
'''


fig = plt.figure()
fig.set_size_inches([3.25,3.25])
plt.rc('font',family='Times New Roman')
params = {'mathtext.default': 'regular' }
plt.rcParams.update(params)
plt.plot(t_min_os , h_km_os, linestyle='solid' , color='xkcd:blue', linewidth=2.0, ↴label='Overshoot')
plt.plot(t_min_us , h_km_us, linestyle='solid' , color='xkcd:green', linewidth=2.0, ↴label='Undershoot')

plt.xlabel('Time, min', fontsize=10)
plt.ylabel("Altitude, km", fontsize=10)

ax = plt.gca()
ax.tick_params(direction='in')
ax.yaxis.set_ticks_position('both')
ax.xaxis.set_ticks_position('both')
plt.tick_params(direction='in')
plt.tick_params(axis='x', labelsize=10)
plt.tick_params(axis='y', labelsize=10)

plt.legend(loc='lower right', fontsize=8)
```

(continues on next page)

(continued from previous page)

```

plt.savefig('../plots/craig-lyne-altitude.png',bbox_inches='tight')
plt.savefig('../plots/craig-lyne-altitude.pdf', dpi=300,bbox_inches='tight')
plt.savefig('../plots/craig-lyne-altitude.eps', dpi=300,bbox_inches='tight')

plt.show()

fig = plt.figure()
fig.set_size_inches([3.25,3.25])
plt.rc('font',family='Times New Roman')
plt.plot(t_min_os , acc_net_g_os, linestyle='solid' , color='xkcd:blue', linewidth=1.0,
         label='Overshoot')
plt.plot(t_min_us , acc_net_g_us, linestyle='solid' , color='xkcd:green', linewidth=1.0,
         label='Undershoot')

plt.xlabel('Time, min', fontsize=10)
plt.ylabel("Deceleration, Earth g", fontsize=10)

ax = plt.gca()
ax.tick_params(direction='in')
ax.yaxis.set_ticks_position('both')
ax.xaxis.set_ticks_position('both')
plt.tick_params(direction='in')
plt.tick_params(axis='x', labelsize=10)
plt.tick_params(axis='y', labelsize=10)

plt.legend(loc='upper right', fontsize=8)

plt.savefig('../plots/craig-lyne-deceleration.png',bbox_inches='tight')
plt.savefig('../plots/craig-lyne-deceleration.pdf', dpi=300,bbox_inches='tight')
plt.savefig('../plots/craig-lyne-deceleration.eps', dpi=300,bbox_inches='tight')

plt.show()

fig = plt.figure()
fig.set_size_inches([3.25,3.25])
plt.rc('font',family='Times New Roman')
plt.plot(t_min_os , q_stag_con_os, linestyle='solid' , color='xkcd:blue', linewidth=1.0,
         label='Overshoot convective')
plt.plot(t_min_os , q_stag_rad_os, linestyle='solid' , color='xkcd:red', linewidth=1.0,
         label='Overshoot radiative')
plt.plot(t_min_us , q_stag_con_us, linestyle='solid' , color='xkcd:magenta',
         linewidth=1.0, label='Undershoot convective')
plt.plot(t_min_us , q_stag_rad_us, linestyle='solid' , color='xkcd:green', linewidth=1.0,
         label='Undershoot radiative')

plt.xlabel('Time, min', fontsize=10)
plt.ylabel("Stagnation-point heat rate, "+r'$W/cm^2$', fontsize=10)

ax = plt.gca()
ax.tick_params(direction='in')
ax.yaxis.set_ticks_position('both')
ax.xaxis.set_ticks_position('both')
plt.tick_params(direction='in')
plt.tick_params(axis='x', labelsize=10)

```

(continues on next page)

(continued from previous page)

```
plt.tick_params(axis='y', labelsize=10)

plt.legend(loc='upper right', fontsize=8)

plt.savefig('../plots/craig-lyne-heating.png', bbox_inches='tight')
plt.savefig('../plots/craig-lyne-heating.pdf', dpi=300, bbox_inches='tight')
plt.savefig('../plots/craig-lyne-heating.eps', dpi=300, bbox_inches='tight')

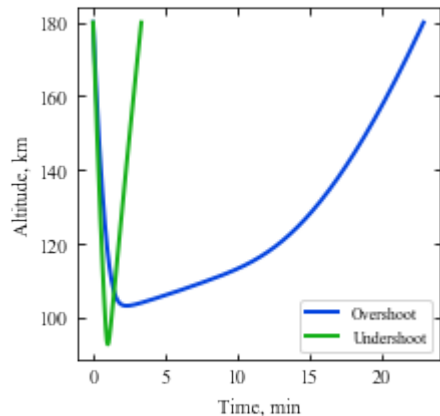
plt.show()
```

The PostScript backend does not support transparency; partially transparent artists
will be rendered opaque.

The PostScript backend does not support transparency; partially transparent artists
will be rendered opaque.

The PostScript backend does not support transparency; partially transparent artists
will be rendered opaque.

The PostScript backend does not support transparency; partially transparent artists
will be rendered opaque.

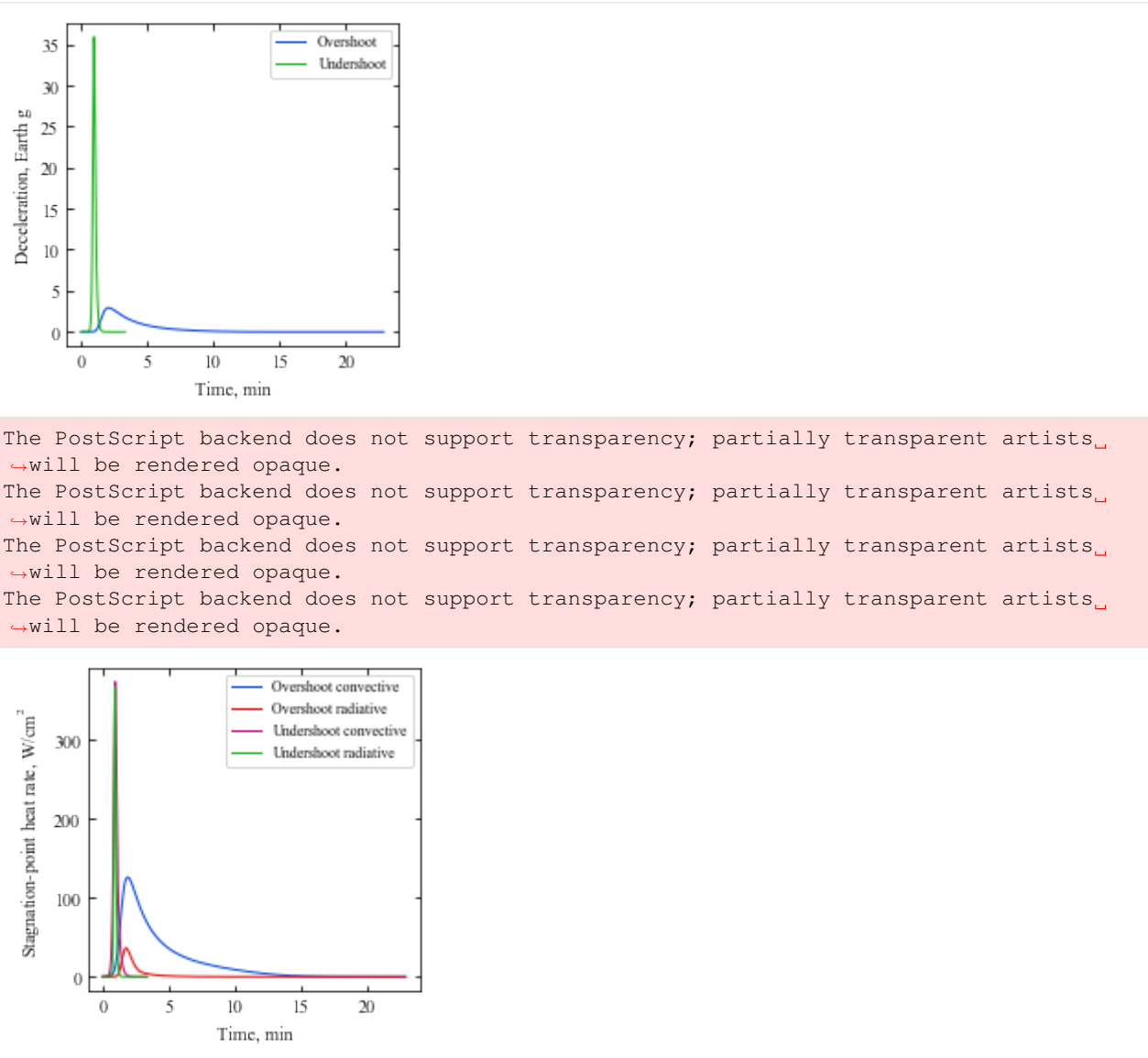


The PostScript backend does not support transparency; partially transparent artists
will be rendered opaque.

The PostScript backend does not support transparency; partially transparent artists
will be rendered opaque.

The PostScript backend does not support transparency; partially transparent artists
will be rendered opaque.

The PostScript backend does not support transparency; partially transparent artists
will be rendered opaque.



The PostScript backend does not support transparency; partially transparent artists
will be rendered opaque.
The PostScript backend does not support transparency; partially transparent artists
will be rendered opaque.
The PostScript backend does not support transparency; partially transparent artists
will be rendered opaque.
The PostScript backend does not support transparency; partially transparent artists
will be rendered opaque.

The plots are now saved in plots/craig-lyne-* and should match with the results from the paper.

Congratulations! You have simulated an aerocapture vehicle flying in the Venusian atmosphere. In the next tutorial, we will compute the corridor widths for drag modulation aerocapture at Venus.

4.4 Example - 04 - Venus Aerocapture: Part 2

In this example, you will learn to create a drag modulation vehicle object and compute the theoretical corridor width available for drag modulation aerocapture at Venus.

For reference, we will re-create a figure from the paper “Putnam and Braun, Drag-Modulation Flight-Control System Options for Planetary Aerocapture, Journal of Spacecraft and Rockets, Vol. 51, No. 1, 2014. DOI: 10.2514/1.A32589

Import AMAT and required libraries

```
[2]: from AMAT.planet import Planet
from AMAT.vehicle import Vehicle

import numpy as np
import matplotlib.pyplot as plt
from matplotlib import rcParams
import os
```



```
[3]: # Create a planet object
planet=Planet("VENUS")

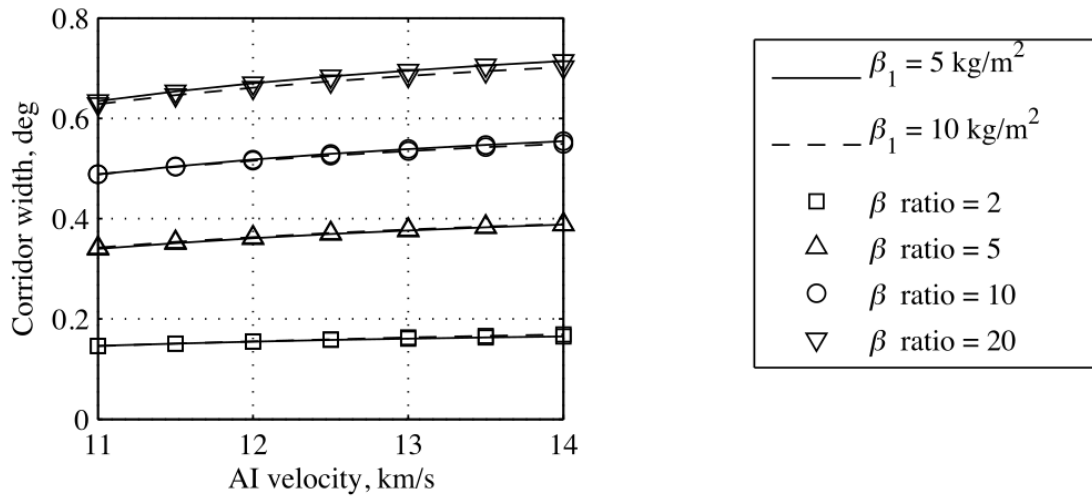
# Load an nominal atmospheric profile with height, temp, pressure, density data
planet.loadAtmosphereModel('../atmdata/Venus/venus-gram-avg.dat', 0 , 1 ,2, 3)

# The reference paper uses 150 km as entry interface altitude (vs 180 km as pre-
# defined in AMAT).
# Hence reset planet.h_skip to 150 km
planet.h_skip = 150000.0
# Create a vehicle object flying in the target planet atmosphere
vehicle=Vehicle('DMVehicle', 1500.0, 50.0, 0.0, 3.1416, 0.0, 0.10, planet)

# Set vehicle conditions at entry interface
# Note that the EFPA initial value is arbitrary. It will be computed and reset later.
vehicle.setInitialState(150.0,0.0,0.0,11.0,0.0,-4.5,0.0,0.0)
vehicle.setSolverParams(1E-6)
```

```
[4]: from IPython.display import Image
Image(filename='../plots/putnam-2014-reference.png')
```

[4]:



This is the figure that we want to reproduce using AMAT. Let us start setting up the simulation parameters.

```
[7]: # Define the AI velocity and ballistic ratio range
VAI_array = np.linspace(11,14,7)
BR_array = np.array([2.0,5.0,10.0,20.0])

# NOTE: You will get a FileExistsError if you run this as such. Re-name the directory
# to something else.
```

(continues on next page)

(continued from previous page)

```
# Create a directory in ../data/ to store the data
os.makedirs('../data/putnamBraun2013')

# Store the speed range and ballistic coefficient range
np.savetxt('../data/putnamBraun2013/VAI_array.txt', VAI_array)
np.savetxt('../data/putnamBraun2013/BR_array.txt', BR_array)

# Create two empty matrices to store the TCW values
TCW_array1 = np.zeros((len(VAI_array), len(BR_array)))
TCW_array2 = np.zeros((len(VAI_array), len(BR_array)))

# Define the two values for beta_1 used in the paper.
beta11 = 5.0
beta12 = 10.0
```

```
[8]: # Compute the corridor width values to create the figure.
# NOTE: This calculation will take several minutes.
print('Running beta1=5.0')

for i in range(0, len(VAI_array)):
    for j in range(0, len(BR_array)):
        vehicle.setInitialState(150.0, 0.0, 0.0, VAI_array[i], 0.0, -4.5, 0.0, 0.0)
        vehicle.setDragModulationVehicleParams(beta11, BR_array[j])
        TCW_array1[i, j] = vehicle.computeTCWD(2400.0, 0.1, -80.0, -4.0, 1E-10, 400.0)
        print('VAI: '+str(VAI_array[i])+' km/s, BETA RATIO: '+str(BR_array[j])+' TCW: '
              +'+str(TCW_array1[i, j])+' deg.')

np.savetxt('../data/putnamBraun2013/TCW_array1.txt', TCW_array1)

print('Running beta1=10.0')
for i in range(0, len(VAI_array)):
    for j in range(0, len(BR_array)):
        vehicle.setInitialState(150.0, 0.0, 0.0, VAI_array[i], 0.0, -4.5, 0.0, 0.0)
        vehicle.setDragModulationVehicleParams(beta12, BR_array[j])
        TCW_array2[i, j] = vehicle.computeTCWD(2400.0, 0.1, -80.0, -4.0, 1E-10, 400.0)
        print('VAI: '+str(VAI_array[i])+' km/s, BETA RATIO: '+str(BR_array[j])+' TCW: '
              +'+str(TCW_array2[i, j])+' deg.')

np.savetxt('../data/putnamBraun2013/TCW_array2.txt', TCW_array2)
print('Done!')
```

```
Running beta1=5.0
VAI: 11.0 km/s, BETA RATIO: 20.0 TCW: 0.6330942395761667 deg.
VAI: 14.0 km/s, BETA RATIO: 20.0 TCW: 0.7133574859435612 deg.
Running beta1=10.0
VAI: 11.0 km/s, BETA RATIO: 20.0 TCW: 0.6273882169480203 deg.
VAI: 14.0 km/s, BETA RATIO: 20.0 TCW: 0.7018732332253421 deg.
Done!
```

Load the data and make the plot.

```
[9]: VAI_array = np.loadtxt('../data/putnamBraun2013/VAI_array.txt')
BR_array = np.loadtxt('../data/putnamBraun2013/BR_array.txt')
TCW_array1 = np.loadtxt('../data/putnamBraun2013/TCW_array1.txt')
```

(continues on next page)

(continued from previous page)

```

TCW_array2 = np.loadtxt('../data/putnamBraun2013/TCW_array2.txt')

fig = plt.figure()
fig.set_size_inches([3.25,3.25])
plt.rc('font',family='Times New Roman')
params = {'mathtext.default': 'regular' }
plt.rcParams.update(params)

plt.plot(VAI_array, TCW_array1[:,0], linestyle='-', linewidth=0.75, marker='s',ms=6,_
markerfacecolor="None", markeredgecolor='black', markeredgewidth=0.75, color='black'
_, clip_on=False)
plt.plot(VAI_array, TCW_array1[:,1], linestyle='-', linewidth=0.75, marker='^',ms=6,_
markerfacecolor="None", markeredgecolor='black', markeredgewidth=0.75, color='black'
_, clip_on=False)
plt.plot(VAI_array, TCW_array1[:,2], linestyle='-', linewidth=0.75, marker='o',ms=6,_
markerfacecolor="None", markeredgecolor='black', markeredgewidth=0.75, color='black'
_, clip_on=False)
plt.plot(VAI_array, TCW_array1[:,3], linestyle='-', linewidth=0.75, marker='v',ms=6,_
markerfacecolor="None", markeredgecolor='black', markeredgewidth=0.75, color='black'
_, clip_on=False)

plt.plot(VAI_array, TCW_array2[:,0], linestyle='--', linewidth=0.75, marker='s',ms=6,_
markerfacecolor="None", markeredgecolor='black', markeredgewidth=0.75, color='black'
_, clip_on=False)
plt.plot(VAI_array, TCW_array2[:,1], linestyle='--', linewidth=0.75, marker='^',ms=6,_
markerfacecolor="None", markeredgecolor='black', markeredgewidth=0.75, color='black'
_, clip_on=False)
plt.plot(VAI_array, TCW_array2[:,2], linestyle='--', linewidth=0.75, marker='o',ms=6,_
markerfacecolor="None", markeredgecolor='black', markeredgewidth=0.75, color='black'
_, clip_on=False)
plt.plot(VAI_array, TCW_array2[:,3], linestyle='--', linewidth=0.75, marker='v',ms=6,_
markerfacecolor="None", markeredgecolor='black', markeredgewidth=0.75, color='black'
_, clip_on=False)

plt.xlabel('Entry velocity, km/s', fontsize=10)
plt.ylabel('Corridor width, deg', fontsize=10)
plt.yticks(np.arange(0, 0.9, step=0.2))
plt.xticks(np.arange(11.0, 14.5, step=1.0))

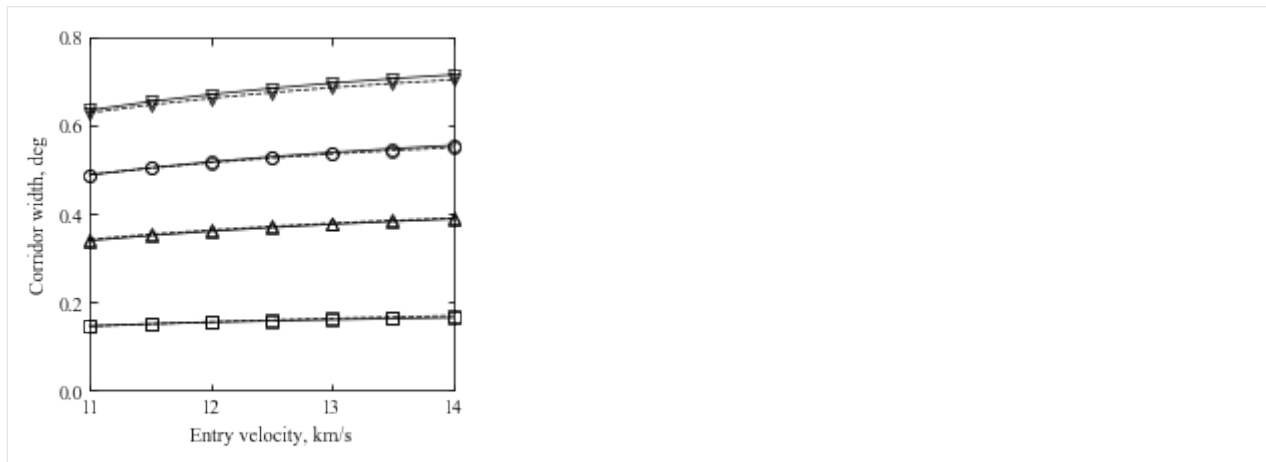
plt.xlim([11.0,14.0])
plt.ylim([0.0, 0.8])

ax = plt.gca()
ax.tick_params(direction='in')
ax.yaxis.set_ticks_position('both')
ax.xaxis.set_ticks_position('both')
plt.tick_params(direction='in')
plt.tick_params(axis='x',labelsize=10)
plt.tick_params(axis='y',labelsize=10)

plt.savefig('../plots/putnam-braun-2013.png',bbox_inches='tight')
plt.savefig('../plots/putnam-braun-2013.pdf', dpi=300,bbox_inches='tight')
plt.savefig('../plots/putnam-braun-2013.eps', dpi=300,bbox_inches='tight')

plt.show()

```



The plots are now saved in plots/putnam-braun-* and should match with the results from the paper.

Congratulations! You have now computed the corridor widths for a drag modulation aerocapture vehicle at Venus. In the next example, we will create an aerocapture feasibility chart for Titan.

[]:

4.5 Example - 05 - Titan Aerocapture: Part 1

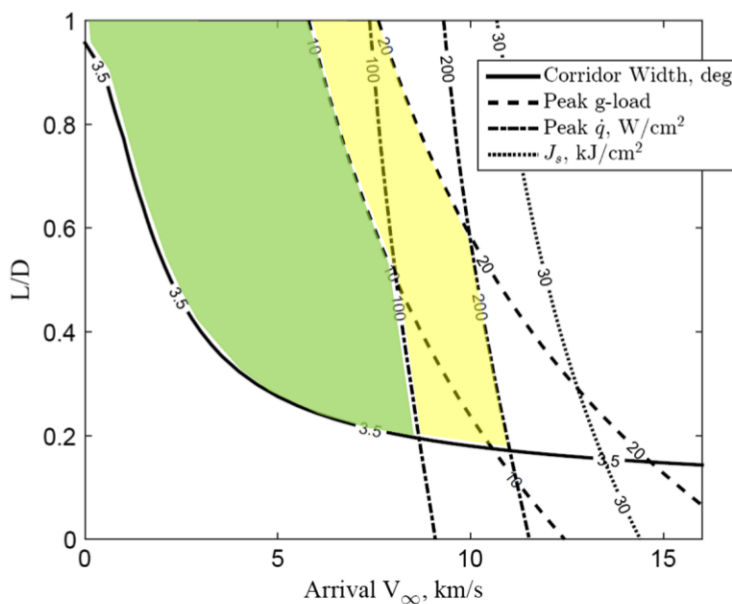
In this example, you will learn to create an aerocapture feasibility chart for Titan.

For reference, we will re-create a figure from the paper “Lu and Saikia, Feasibility Assessment of Aerocapture for Future Titan Orbiter Missions, Journal of Spacecraft and Rockets, Vol. 55, No. 5, 2018”. DOI: 10.2514/1.A34121

[3]:

```
from IPython.display import Image
Image(filename='../plots/lu-saikia-reference-a.png', width=400)
```

[3]:

Fig. 16 Aerocapture applicable regions for β of 90 kg/m^2 .

We will use AMAT to recreate this figure.

```
[4]: from AMAT.planet import Planet
from AMAT.vehicle import Vehicle

import numpy as np
from scipy import interpolate
import pandas as pd

import matplotlib.pyplot as plt
from matplotlib import rcParams
from matplotlib.patches import Polygon
import os
```

```
[6]: # Create a planet object for Titan
planet=Planet("TITAN")

# Load an nominal atmospheric profile with height, temp, pressure, density data
planet.loadAtmosphereModel('../atmdata/Titan/titan-gram-avg.dat', 0 , 1 , 2, 3)

# Define the range for arrival Vinf and vehicle L/D
vinf_kms_array = np.linspace( 0.0, 16.0, 17)
LD_array       = np.linspace( 0.0, 1.0 , 11)

#vinf_kms_array = np.linspace( 0.0, 16.0, 2)
#LD_array       = np.linspace( 0.0, 1.0 , 2)
```

```
[7]: # Create a directory to store the data.
# NOTE: You will get an error if the file already exists,
# Rename the folder to something else.

os.makedirs('../data/luSaikia2018a')
```

(continues on next page)

(continued from previous page)

```
# Use a runID to prefix the files for easy access for post-processing.
runID = 'BC90RAP1700'

num_total      = len(vinf_kms_array)*len(LD_array)
count = 1

# Compute the inertial entry speed from the hyperbolic excess speed.
v0_kms_array    = np.zeros(len(vinf_kms_array))
v0_kms_array[:] = np.sqrt(1.0*(vinf_kms_array[:]*1E3)**2.0 + \
                         2*np.ones(len(vinf_kms_array))*\
                         planet.GM/(planet.RP+1000.0*1.0E3))/1.0E3

# Initialize matrices to store data.
overShootLimit_array = np.zeros((len(v0_kms_array),len(LD_array)))
underShootLimit_array = np.zeros((len(v0_kms_array),len(LD_array)))
exitflag_os_array    = np.zeros((len(v0_kms_array),len(LD_array)))
exitflag_us_array    = np.zeros((len(v0_kms_array),len(LD_array)))
TCW_array            = np.zeros((len(v0_kms_array),len(LD_array)))
```

```
[8]: # Compute the corridor width over the defined Vinf and L/D matrix.
# Note this will take maybe about an hour.
# If you simply want to create the plot, you can load the existing data
# in the ../data/luSaikia2018a folder as done below this cell.

for i in range(0,len(v0_kms_array)):
    for j in range(0,len(LD_array)):
        vehicle=Vehicle('Kraken', 1000.0, 90.0, LD_array[j], 3.1416, 0.0, 1.00,_
        ↪planet)
        vehicle.setInitialState(1000.0,0.0,0.0,v0_kms_array[i],0.0,-4.5,0.0,0.0)
        vehicle.setSolverParams(1E-5)
        overShootLimit_array[i,j], exitflag_os_array[i,j] = \
        vehicle.findOverShootLimit (6000.0, 1.0 , -88.0, -2.0, 1E-10, 1700.0)
        underShootLimit_array[i,j], exitflag_us_array[i,j] = \
        vehicle.findUnderShootLimit(6000.0, 1.0 , -88.0, -2.0, 1E-10, 1700.0)

        TCW_array[i,j] = overShootLimit_array[i,j] - underShootLimit_array[i,j]

        print("Run #"+str(count)+" of "+ str(num_total)+\
              ": Arrival V_infty: "+str(vinf_kms_array[i])+\
              " km/s+", " L/D:"+str(LD_array[j]) +\
              " OSL: "+str(overShootLimit_array[i,j])+\
              " USL: "+str(underShootLimit_array[i,j])+\
              ", TCW: "+str(TCW_array[i,j])+\
              " EFOS: "+str(exitflag_os_array[i,j])+\
              " EFUS: "+str(exitflag_us_array[i,j]))

        count = count +1

np.savetxt('../data/luSaikia2018a/'+runID+'vinf_kms_array.txt',vinf_kms_array)
np.savetxt('../data/luSaikia2018a/'+runID+'v0_kms_array.txt',v0_kms_array)
np.savetxt('../data/luSaikia2018a/'+runID+'LD_array.txt',LD_array)
np.savetxt('../data/luSaikia2018a/'+runID+'overShootLimit_array.txt',overShootLimit_\
array)
np.savetxt('../data/luSaikia2018a/'+runID+'exitflag_os_array.txt',exitflag_os_array)
```

(continues on next page)

(continued from previous page)

```

np.savetxt('..../data/luSaikia2018a/' + runID + 'undershootLimit_array.txt', underShootLimit_
array)
np.savetxt('..../data/luSaikia2018a/' + runID + 'exitflag_us_array.txt', exitflag_us_array)
np.savetxt('..../data/luSaikia2018a/' + runID + 'TCW_array.txt', TCW_array)

Run #1 of 4: Arrival V_infty: 0.0 km/s, L/D:0.0 OSL: -24.635471317420524 USL: -24.
→ 635471317420524, TCW: 0.0 EFOS: 1.0 EFUS: 1.0
Run #2 of 4: Arrival V_infty: 0.0 km/s, L/D:1.0 OSL: -23.422944245403414 USL: -27.
→ 0515137471466, TCW: 3.6285695017431863 EFOS: 1.0 EFUS: 1.0
Run #3 of 4: Arrival V_infty: 16.0 km/s, L/D:0.0 OSL: -37.36673820708165 USL: -37.
→ 36673820708165, TCW: 0.0 EFOS: 1.0 EFUS: 1.0
Run #4 of 4: Arrival V_infty: 16.0 km/s, L/D:1.0 OSL: -33.47214682791673 USL: -73.
→ 89901192915568, TCW: 40.426865101238945 EFOS: 1.0 EFUS: 1.0

```

Compute the deceleration and heating loads.

```

[9]: acc_net_g_max_array      = np.zeros((len(v0_kms_array), len(LD_array)))
stag_pres_atm_max_array    = np.zeros((len(v0_kms_array), len(LD_array)))
q_stag_total_max_array     = np.zeros((len(v0_kms_array), len(LD_array)))
heatload_max_array         = np.zeros((len(v0_kms_array), len(LD_array)))

for i in range(0, len(v0_kms_array)):
    for j in range(0, len(LD_array)):
        vehicle=Vehicle('Kraken', 1000.0, 90.0, LD_array[j], 3.1416, 0.0, 1.00,_
→planet)
        vehicle.setInitialState(1000.0, 0.0, 0.0, v0_kms_array[i], 0.0, overShootLimit_
→array[i,j], 0.0, 0.0)
        vehicle.setSolverParams(1E-5)

        vehicle.propogateEntry(6000.0, 1.0, 180.0)

        # Extract and save variables to plot
        t_min_os      = vehicle.t_minc
        h_km_os       = vehicle.h_kmc
        acc_net_g_os  = vehicle.acc_net_g
        q_stag_con_os = vehicle.q_stag_con
        q_stag_rad_os = vehicle.q_stag_rad
        rc_os          = vehicle.rc
        vc_os          = vehicle.vc
        stag_pres_atm_os = vehicle.computeStagPres(rc_os, vc_os) / (1.01325E5)
        heatload_os    = vehicle.heatload

        vehicle=Vehicle('Kraken', 1000.0, 90.0, LD_array[j], 3.1416, 0.0, 1.00,_
→planet)
        vehicle.setInitialState(1000.0, 0.0, 0.0, v0_kms_array[i], 0.0, underShootLimit_
→array[i,j], 0.0, 0.0)
        vehicle.setSolverParams(1E-5)

        vehicle.propogateEntry(6000.0, 1.0, 0.0)

        # Extract and save variable to plot
        t_min_us      = vehicle.t_minc
        h_km_us       = vehicle.h_kmc
        acc_net_g_us  = vehicle.acc_net_g
        q_stag_con_us = vehicle.q_stag_con
        q_stag_rad_us = vehicle.q_stag_rad
        rc_us          = vehicle.rc

```

(continues on next page)

(continued from previous page)

```

vc_us           = vehicle.vc
stag_pres_atm_us = vehicle.computeStagPres(rc_us, vc_us) / (1.01325E5)
heatload_us     = vehicle.heatload

q_stag_total_os   = q_stag_con_os + q_stag_rad_os
q_stag_total_us   = q_stag_con_us + q_stag_rad_us

acc_net_g_max_array[i,j]      = max(max(acc_net_g_os),max(acc_net_g_us))
stag_pres_atm_max_array[i,j]   = max(max(stag_pres_atm_os),max(stag_pres_atm_
os))
q_stag_total_max_array[i,j]   = max(max(q_stag_total_os),max(q_stag_total_us))
heatload_max_array[i,j]       = max(max(heatload_os),max(heatload_us))

print("V_infty: "+str(vinf_kms_array[i])+" km/s+", L/D: "+str(LD_array[j])+"_
G_MAX: "+str(acc_net_g_max_array[i,j])+" QDOT_MAX: "+str(q_stag_total_max_array[i,
j])+" J_MAX: "+str(heatload_max_array[i,j])+" STAG. PRES: "+str(stag_pres_atm_max_
array[i,j])))

np.savetxt('..../data/luSaikia2018a/' + runID + 'acc_net_g_max_array.txt', acc_net_g_max_
array)
np.savetxt('..../data/luSaikia2018a/' + runID + 'stag_pres_atm_max_array.txt', stag_pres_atm_
max_array)
np.savetxt('..../data/luSaikia2018a/' + runID + 'q_stag_total_max_array.txt', q_stag_total_
max_array)
np.savetxt('..../data/luSaikia2018a/' + runID + 'heatload_max_array.txt', heatload_max_array)

V_infty: 0.0 km/s, L/D: 0.0 G_MAX: 0.0810485245607735 QDOT_MAX: 1.0607636054752763 J_
MAX: 1020.003796275038 STAG. PRES: 0.000720422444467468
V_infty: 0.0 km/s, L/D: 1.0 G_MAX: 0.20202892551813917 QDOT_MAX: 1.3893301148573975 J_
MAX: 1252.170615904772 STAG. PRES: 0.0004253391968484517
V_infty: 16.0 km/s, L/D: 0.0 G_MAX: 17.704051243426182 QDOT_MAX: 536.4530046363565 J_
MAX: 35907.65472341787 STAG. PRES: 0.15433527803169042
V_infty: 16.0 km/s, L/D: 1.0 G_MAX: 125.7389398961218 QDOT_MAX: 1065.8317771270392 J_
MAX: 63948.52565398295 STAG. PRES: 0.044601211536270044

```

We are now ready to create the plot!

```
[17]: x = np.loadtxt('..../data/luSaikia2018a/' + runID + 'vinf_kms_array.txt')
y = np.loadtxt('..../data/luSaikia2018a/' + runID + 'LD_array.txt')

Z1 = np.loadtxt('..../data/luSaikia2018a/' + runID + 'TCW_array.txt')
G1 = np.loadtxt('..../data/luSaikia2018a/' + runID + 'acc_net_g_max_array.txt')
Q1 = np.loadtxt('..../data/luSaikia2018a/' + runID + 'q_stag_total_max_array.txt')
H1 = np.loadtxt('..../data/luSaikia2018a/' + runID + 'heatload_max_array.txt')

f1 = interpolate.interp2d(x, y, np.transpose(Z1), kind='cubic')
g1 = interpolate.interp2d(x, y, np.transpose(G1), kind='cubic')
q1 = interpolate.interp2d(x, y, np.transpose(Q1), kind='cubic')
h1 = interpolate.interp2d(x, y, np.transpose(H1), kind='cubic')

x_new = np.linspace(0.0, 16, 170)
y_new = np.linspace(0.0, 1.0, 110)
z_new = np.zeros((len(x_new), len(y_new)))

z1_new = np.zeros((len(x_new), len(y_new)))
```

(continues on next page)

(continued from previous page)

```
g1_new = np.zeros((len(x_new), len(y_new)))
q1_new = np.zeros((len(x_new), len(y_new)))
h1_new = np.zeros((len(x_new), len(y_new)))

for i in range(0, len(x_new)):
    for j in range(0, len(y_new)):

        z1_new[i,j] = f1(x_new[i],y_new[j])
        g1_new[i,j] = g1(x_new[i],y_new[j])
        q1_new[i,j] = q1(x_new[i],y_new[j])
        h1_new[i,j] = h1(x_new[i],y_new[j])

Z1 = z1_new
G1 = g1_new
Q1 = q1_new
H1 = h1_new/1000.0

X, Y = np.meshgrid(x_new, y_new)

Zlevels = np.array([2.5,3.5])
Glevels = np.array([10.0, 20.0])
Qlevels = np.array([100.0, 200.0])
Hlevels = np.array([30.0])

fig = plt.figure()
fig.set_size_inches([3.25,3.25])
plt.ion()
plt.rc('font',family='Times New Roman')
params = {'mathtext.default': 'regular' }
plt.rcParams.update(params)

ZCS1 = plt.contour(X, Y, np.transpose(Z1), levels=Zlevels, colors='black')
plt.clabel(ZCS1, inline=1, fontsize=10, colors='black',fmt='%.1f',inline_spacing=1)
ZCS1.collections[0].set_linewidths(1.50)
ZCS1.collections[1].set_linewidths(1.50)
ZCS1.collections[0].set_label(r'$TCW, deg.$')

GCS1 = plt.contour(X, Y, np.transpose(G1), levels=Glevels, colors='blue',linestyles=
    'dashed')
plt.clabel(GCS1, inline=1, fontsize=10, colors='blue',fmt='%.d',inline_spacing=0)
GCS1.collections[0].set_linewidths(1.50)
GCS1.collections[1].set_linewidths(1.50)
GCS1.collections[0].set_label(r'$g$'+r'-load')

QCS1 = plt.contour(X, Y, np.transpose(Q1), levels=Qlevels, colors='red',linestyles=
    'dotted',zorder=11)
plt.clabel(QCS1, inline=1, fontsize=10, colors='red',fmt='%.d',inline_spacing=0)
QCS1.collections[0].set_linewidths(1.50)
QCS1.collections[1].set_linewidths(1.50)
QCS1.collections[0].set_label(r'$\dot{q}$'+', '+r'$W/cm^2$')

HCS1 = plt.contour(X, Y, np.transpose(H1), levels=Hlevels, colors='xkcd:brown',
    linestyles='dashdot')
plt.clabel(HCS1, inline=1, fontsize=10, colors='xkcd:brown',fmt='%.d',inline_spacing=0)
HCS1.collections[0].set_linewidths(1.75)
```

(continues on next page)

(continued from previous page)

```

HCS1.collections[0].set_label(r'$Q$+', ' +r'$kJ/cm^2$')

plt.xlabel("Arrival "+r'$V_{\infty}$'+r', km/s' , fontsize=10)
plt.ylabel("L/D", fontsize=10)
plt.xticks(fontsize=10)
plt.yticks(fontsize=10)
ax = plt.gca()
ax.tick_params(direction='in')
ax.yaxis.set_ticks_position('both')
ax.xaxis.set_ticks_position('both')
plt.legend(loc='upper right', fontsize=8)

dat0 = ZCS1.allsegs[1][0]
x1,y1=dat0[:,0],dat0[:,1]
F1 = interpolate.interp1d(x1, y1, kind='linear', fill_value='extrapolate', bounds_-
                           ↵error=False)

dat1 = GCS1.allsegs[0][0]
x2,y2=dat1[:,0],dat1[:,1]
F2 = interpolate.interp1d(x2, y2, kind='linear', fill_value='extrapolate', bounds_-
                           ↵error=False)

dat2 = QCS1.allsegs[0][0]
x3,y3= dat2[:,0],dat2[:,1]
F3 = interpolate.interp1d(x3, y3, kind='linear', fill_value='extrapolate', bounds_-
                           ↵error=False)

x4 = np.linspace(0,30,301)
y4 = F1(x4)
y5 = F2(x4)
y6 = F3(x4)

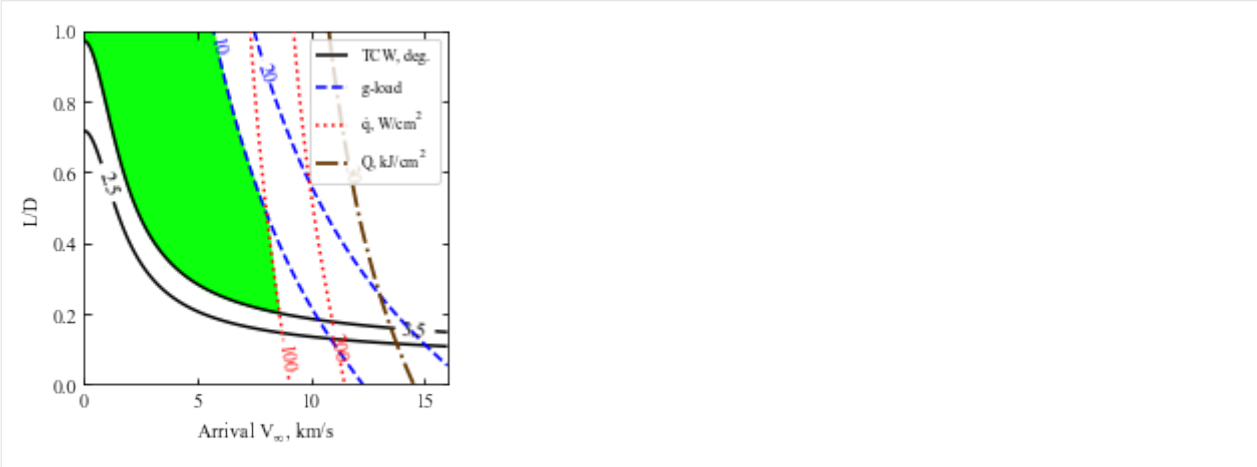
y7 = np.minimum(y5,y6)

plt.fill_between(x4, y4, y7, where=y4<=y7, color='xkcd:neon green')
plt.xlim([0.0,16.0])
plt.ylim([0.0,1.0])

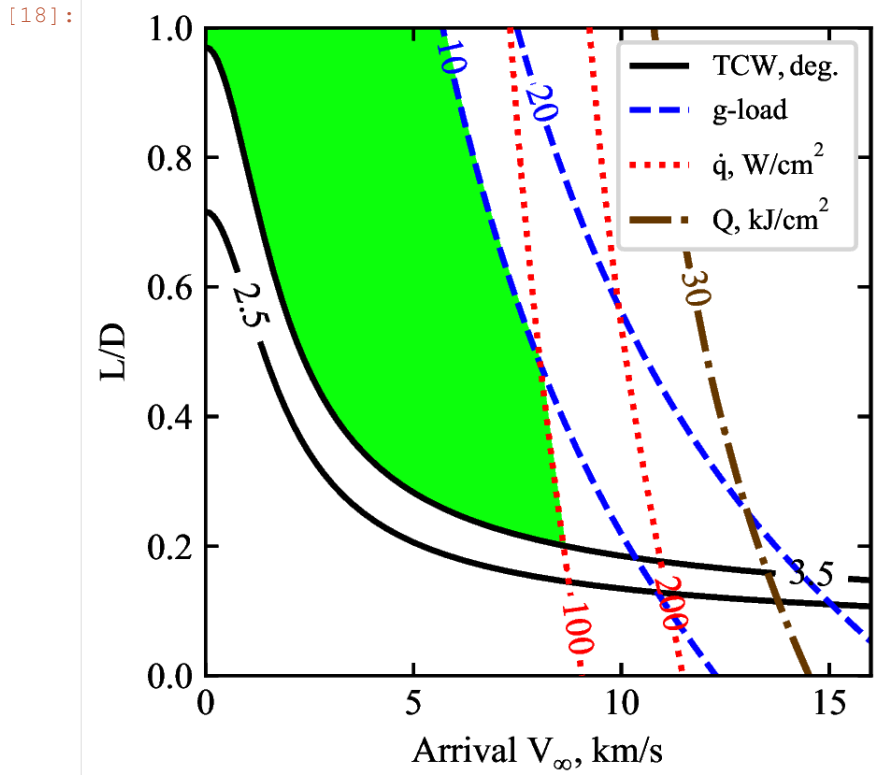
plt.savefig('../plots/LuSaikia2018a-fig16.png',bbox_inches='tight')
plt.savefig('../plots/LuSaikia2018a-fig16.pdf', dpi=300,bbox_inches='tight')
plt.savefig('../plots/LuSaikia2018a-fig16.eps', dpi=300,bbox_inches='tight')

```

The PostScript backend does not support transparency; partially transparent artists ↵ will be rendered opaque.
The PostScript backend does not support transparency; partially transparent artists ↵ will be rendered opaque.
The PostScript backend does not support transparency; partially transparent artists ↵ will be rendered opaque.
The PostScript backend does not support transparency; partially transparent artists ↵ will be rendered opaque.



```
[18]: from IPython.display import Image
Image(filename='../plots/LuSaikia2018a-fig16-higher-res.png', width=400)
```



The plots are now saved in plots/LuSaikia2018a and should match with the results from the paper.

Congratulations! You have created an aerocapture feasibility chart for Titan. In the next example, you will recreate the same chart for a different vehicle ballistic coefficient.

4.6 Example - 06 - Titan Aerocapture: Part 2

In this example, you will learn to create an aerocapture feasibility chart for Titan.

F. AMAT EXAMPLE: VENUS SMALLSAT

AEROCAPTURE: PART 1

Refer to the next page for illustration of how AMAT is used to generate the feasibility charts for comprehensive trade space exploration before selecting a baseline design. The Jupyter notebook is available online¹ at the project documentation website.

¹[↑https://amat.readthedocs.io/en/master/examples/example-08-venus-aerocapture-4.html](https://amat.readthedocs.io/en/master/examples/example-08-venus-aerocapture-4.html)

[1]:

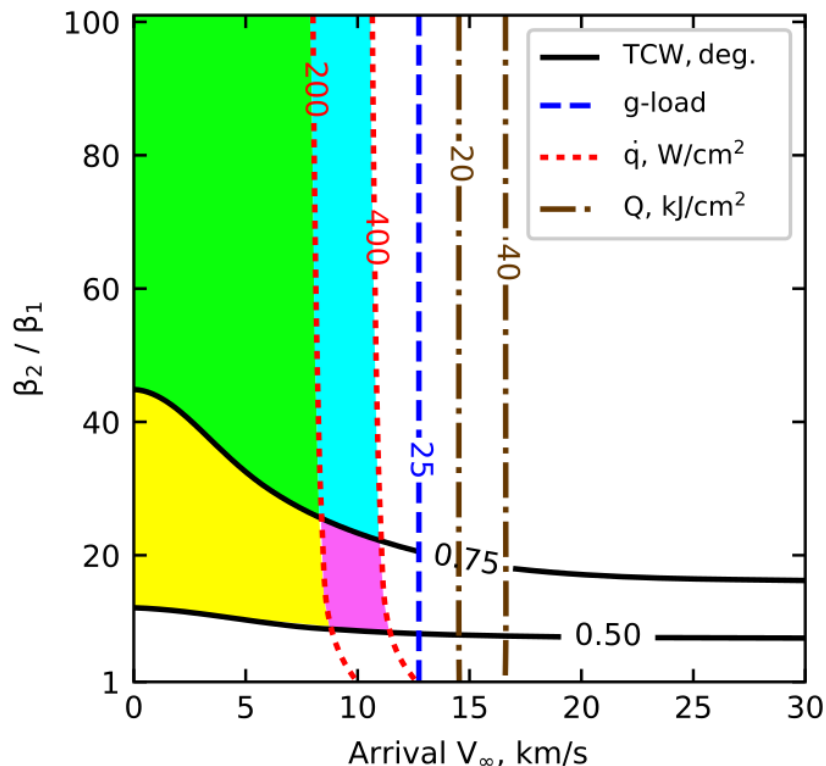


Fig. 16 Feasible design space for drag modulation aerocapture with $\beta_1 = 5 \text{ kg/m}^2$.

```
[2]: from AMAT.planet import Planet
from AMAT.vehicle import Vehicle

import numpy as np
from scipy import interpolate

import matplotlib.pyplot as plt
from matplotlib import rcParams
from matplotlib.patches import Polygon
import os
```

```
[3]: # Create a planet object
planet=Planet("VENUS")
planet.h_skip = 150000.0

# Load an nominal atmospheric profile with height, temp, pressure, density data
planet.loadAtmosphereModel('../atmdata/Venus/venus-gram-avg.dat', 0 , 1 ,2, 3)

vinf_kms_array = np.linspace( 0.0, 30.0, 11)
betaRatio_array = np.linspace( 1.0, 101.0 , 11)

#vinf_kms_array = np.linspace( 0.0, 30.0, 2)
#betaRatio_array = np.linspace( 1.0, 101.0 , 2)
```

```
[4]: beta1 = 5.0

os.makedirs('../data/girijaYe2019c')
runID = 'DMBC5RAP400EI150'

[5]: v0_kms_array      = np.zeros(len(vinf_kms_array))
v0_kms_array[:] = np.sqrt(1.0*(vinf_kms_array[:]*1E3)**2.0 + 2*np.ones(len(vinf_kms_
array))*planet.GM/(planet.RP+150.0*1.0E3))/1.0E3

overShootLimit_array = np.zeros((len(v0_kms_array),len(betaRatio_array)))
underShootLimit_array = np.zeros((len(v0_kms_array),len(betaRatio_array)))
exitflag_os_array    = np.zeros((len(v0_kms_array),len(betaRatio_array)))
exitflag_us_array    = np.zeros((len(v0_kms_array),len(betaRatio_array)))
TCW_array            = np.zeros((len(v0_kms_array),len(betaRatio_array)))

[6]: for i in range(0,len(v0_kms_array)):
    for j in range(0,len(betaRatio_array)):
        vehicle=Vehicle('DMVehicle', 1500.0, beta1, 0.0, 3.1416, 0.0, 0.10, planet)
        vehicle.setInitialState(150.0,0.0,0.0,v0_kms_array[i],0.0,-4.5,0.0,0.0)
        vehicle.setSolverParams(1E-6)
        vehicle.setDragModulationVehicleParams(beta1,betaRatio_array[j])

        underShootLimit_array[i,j], exitflag_us_array[i,j] = vehicle.
        ↪findUnderShootLimitD(2400.0, 0.1, -80.0,-4.0,1E-10,400.0)
        overShootLimit_array[i,j] , exitflag_os_array[i,j] = vehicle.
        ↪findOverShootLimitD (2400.0, 0.1, -80.0,-4.0,1E-10,400.0)

        TCW_array[i,j]      = overShootLimit_array[i,j] - underShootLimit_array[i,j]

        print('VINF: '+str(vinf_kms_array[i])+' km/s, BETA RATIO: '+str(betaRatio_
        ↪array[j])+' TCW: '+str(TCW_array[i,j])+' deg.')

np.savetxttxt('../data/girijaYe2019c/'+runID+'vinf_kms_array.txt',vinf_kms_array)
np.savetxttxt('../data/girijaYe2019c/'+runID+'v0_kms_array.txt',v0_kms_array)
np.savetxttxt('../data/girijaYe2019c/'+runID+'betaRatio_array.txt',betaRatio_array)
np.savetxttxt('../data/girijaYe2019c/'+runID+'overShootLimit_array.txt',overShootLimit_
array)
np.savetxttxt('../data/girijaYe2019c/'+runID+'exitflag_os_array.txt',exitflag_os_array)
np.savetxttxt('../data/girijaYe2019c/'+runID+'underShootLimit_array.txt',underShootLimit_
array)
np.savetxttxt('../data/girijaYe2019c/'+runID+'exitflag_us_array.txt',exitflag_us_array)
np.savetxttxt('../data/girijaYe2019c/'+runID+'TCW_array.txt',TCW_array)

VINF: 0.0 km/s, BETA RATIO: 1.0 TCW: 0.0 deg.
VINF: 0.0 km/s, BETA RATIO: 101.0 TCW: 0.8981981236029242 deg.
VINF: 30.0 km/s, BETA RATIO: 1.0 TCW: 0.0 deg.
VINF: 30.0 km/s, BETA RATIO: 101.0 TCW: 1.192248803385155 deg.

[8]: acc_net_g_max_array      = np.zeros((len(v0_kms_array),len(betaRatio_array)))
stag_pres_atm_max_array    = np.zeros((len(v0_kms_array),len(betaRatio_array)))
q_stag_total_max_array     = np.zeros((len(v0_kms_array),len(betaRatio_array)))
heatload_max_array          = np.zeros((len(v0_kms_array),len(betaRatio_array)))

for i in range(0,len(v0_kms_array)):
```

(continues on next page)

(continued from previous page)

```

for j in range(0, len(betaRatio_array)):
    vehicle=Vehicle('DMVehicle', 1500.0, beta1, 0.0, 3.1416, 0.0, 0.10, planet)
    vehicle.setInitialState(150.0,0.0,0.0,v0_kms_array[i],0.0,overShootLimit_
    ↪array[i,j],0.0,0.0)
    vehicle.setSolverParams(1E-6)

    vehicle.propogateEntry (2400.0, 0.1, 0.0)

    # Extract and save variables to plot
    t_min_os      = vehicle.t_minc
    h_km_os       = vehicle.h_kmc
    acc_net_g_os  = vehicle.acc_net_g
    q_stag_con_os = vehicle.q_stag_con
    q_stag_rad_os = vehicle.q_stag_rad
    rc_os          = vehicle.rc
    vc_os          = vehicle.vc
    stag_pres_atm_os = vehicle.computeStagPres(rc_os,vc_os) / (1.01325E5)
    heatload_os   = vehicle.heatload

    vehicle=Vehicle('DMVehicle', 1500.0, beta1*betaRatio_array[j], 0.0, 3.1416, 0.
    ↪0, 0.10, planet)
    vehicle.setInitialState(150.0,0.0,0.0,v0_kms_array[i],0.0,underShootLimit_
    ↪array[i,j],0.0,0.0)
    vehicle.setSolverParams( 1E-6)

    vehicle.propogateEntry (2400.0, 0.1, 0.0)

    # Extract and save variable to plot
    t_min_us      = vehicle.t_minc
    h_km_us       = vehicle.h_kmc
    acc_net_g_us  = vehicle.acc_net_g
    q_stag_con_us = vehicle.q_stag_con
    q_stag_rad_us = vehicle.q_stag_rad
    rc_us          = vehicle.rc
    vc_us          = vehicle.vc
    stag_pres_atm_us = vehicle.computeStagPres(rc_us,vc_us) / (1.01325E5)
    heatload_us   = vehicle.heatload

    q_stag_total_os  = q_stag_con_os + q_stag_rad_os
    q_stag_total_us  = q_stag_con_us + q_stag_rad_us

    acc_net_g_max_array[i,j]      = max(max(acc_net_g_os),max(acc_net_g_us))
    stag_pres_atm_max_array[i,j]   = max(max(stag_pres_atm_os),max(stag_pres_atm_
    ↪os))
    q_stag_total_max_array[i,j]   = max(max(q_stag_total_os),max(q_stag_total_us))
    heatload_max_array[i,j]       = max(max(heatload_os),max(heatload_us))

    print("V_infty: "+str(vinf_kms_array[i])+" km/s", BR: "+str(betaRatio_
    ↪array[j])+" G_MAX: "+str(acc_net_g_max_array[i,j])+" QDOT_MAX: "+str(q_stag_total_
    ↪max_array[i,j])+" J_MAX: "+str(heatload_max_array[i,j])+" STAG. PRES: "+str(stag_
    ↪pres_atm_max_array[i,j]))

np.savetxt('..../data/girijaYe2019c/' + runID + 'acc_net_g_max_array.txt', acc_net_g_max_
↪array)
np.savetxt('..../data/girijaYe2019c/' + runID + 'stag_pres_atm_max_array.txt', stag_pres_atm_
↪max_array)

```

(continues on next page)

(continued from previous page)

```

np.savetxt('..../data/girijaYe2019c/' + runID + 'q_stag_total_max_array.txt', q_stag_total_
           _max_array)
np.savetxt('..../data/girijaYe2019c/' + runID + 'heatload_max_array.txt', heatload_max_array)

V_infty: 0.0 km/s, BR: 1.0 G_MAX: 4.2619678756684065 QDOT_MAX: 107.04783114721339 J_
           _MAX: 9963.95886102549 STAG. PRES: 0.00206384918146089
V_infty: 0.0 km/s, BR: 101.0 G_MAX: 4.2619678756684065 QDOT_MAX: 1069.8045659113661 J_
           _MAX: 105153.41622997135 STAG. PRES: 0.00206384918146089
V_infty: 30.0 km/s, BR: 1.0 G_MAX: 143.43437041606074 QDOT_MAX: 763604.549664235 J_
           _MAX: 4964898.795992032 STAG. PRES: 0.06941820444237855
V_infty: 30.0 km/s, BR: 101.0 G_MAX: 143.43437041606074 QDOT_MAX: 182872814.4356986 J_
           _MAX: 1231040818.2242763 STAG. PRES: 0.06941820444237855

```

```

[9]: x = np.loadtxt('..../data/girijaYe2019c/' + runID + 'vinf_kms_array.txt')
y = np.loadtxt('..../data/girijaYe2019c/' + runID + 'betaRatio_array.txt')

Z1 = np.loadtxt('..../data/girijaYe2019c/' + runID + 'TCW_array.txt')
G1 = np.loadtxt('..../data/girijaYe2019c/' + runID + 'acc_net_g_max_array.txt')
Q1 = np.loadtxt('..../data/girijaYe2019c/' + runID + 'q_stag_total_max_array.txt')
H1 = np.loadtxt('..../data/girijaYe2019c/' + runID + 'heatload_max_array.txt')
S1 = np.loadtxt('..../data/girijaYe2019c/' + runID + 'stag_pres_atm_max_array.txt')

f1 = interpolate.interp2d(x, y, np.transpose(Z1), kind='cubic')
g1 = interpolate.interp2d(x, y, np.transpose(G1), kind='cubic')
q1 = interpolate.interp2d(x, y, np.transpose(Q1), kind='cubic')
h1 = interpolate.interp2d(x, y, np.transpose(H1), kind='cubic')
s1 = interpolate.interp2d(x, y, np.transpose(S1), kind='cubic')

x_new = np.linspace(0.0, 30, 110)
y_new = np.linspace(0.0, 101, 110)

z1_new = np.zeros((len(x_new), len(y_new)))
g1_new = np.zeros((len(x_new), len(y_new)))
q1_new = np.zeros((len(x_new), len(y_new)))
h1_new = np.zeros((len(x_new), len(y_new)))
s1_new = np.zeros((len(x_new), len(y_new)))

for i in range(0, len(x_new)):
    for j in range(0, len(y_new)):

        z1_new[i, j] = f1(x_new[i], y_new[j])
        g1_new[i, j] = g1(x_new[i], y_new[j])
        q1_new[i, j] = q1(x_new[i], y_new[j])
        h1_new[i, j] = h1(x_new[i], y_new[j])
        s1_new[i, j] = s1(x_new[i], y_new[j])

Z1 = z1_new
G1 = g1_new
Q1 = q1_new
S1 = s1_new
H1 = h1_new / 1000.0

X, Y = np.meshgrid(x_new, y_new)

```

(continues on next page)

(continued from previous page)

```

Zlevels = np.array([0.5,0.75])
Glevels = np.array([25.0])
Qlevels = np.array([200.0, 400.0])
Hlevels = np.array([20.0,40.0])

fig = plt.figure()
fig.set_size_inches([3.25,3.25])
plt.ion()
plt.rc('font',family='Times New Roman')
params = {'mathtext.default': 'regular' }
plt.rcParams.update(params)

ZCS1 = plt.contour(X, Y, np.transpose(Z1), levels=Zlevels, colors='black')
plt.clabel(ZCS1, inline=1, fontsize=10, colors='black',fmt='%.2f',inline_spacing=1)
ZCS1.collections[0].set_linewidths(1.50)
ZCS1.collections[1].set_linewidths(1.50)
ZCS1.collections[0].set_label(r'$TCW, deg.$')

GCS1 = plt.contour(X, Y, np.transpose(G1), levels=Glevels, colors='blue',linestyles=
    ↪'dashed')
Glabels=plt.clabel(GCS1, inline=1, fontsize=10, colors='blue',fmt='%d',inline_
    ↪spacing=0)
GCS1.collections[0].set_linewidths(1.50)

GCS1.collections[0].set_label(r'$g$'+r'-load')

QCS1 = plt.contour(X, Y, np.transpose(Q1), levels=Qlevels, colors='red',linestyles=
    ↪'dotted',zorder=11)
plt.clabel(QCS1, inline=1, fontsize=10, colors='red',fmt='%d',inline_spacing=0)
QCS1.collections[0].set_linewidths(1.50)
QCS1.collections[1].set_linewidths(1.50)
QCS1.collections[0].set_label(r'$\dot{q}$+', '+r'$W/cm^2$')

HCS1 = plt.contour(X, Y, np.transpose(H1), levels=Hlevels, colors='xkcd:brown',
    ↪linestyles='dashdot')
Hlabels=plt.clabel(HCS1, inline=1, fontsize=10, colors='xkcd:brown',fmt='%d',inline_
    ↪spacing=0)
HCS1.collections[0].set_linewidths(1.75)
HCS1.collections[1].set_linewidths(1.75)
HCS1.collections[0].set_label(r'$Q$+', '+r'$kJ/cm^2$')

for l in Hlabels:
    l.set_rotation(-90)
for l in Glabels:
    l.set_rotation(-90)

#SCS1 = plt.contour(X, Y, transpose(S1), levels=Slevels, colors='cyan')
#plt.clabel(SCS1, inline=1, fontsize=10, colors='xkcd:neon green',fmt='%.1f',inline_
    ↪spacing=1)
#SCS1.collections[0].set_linewidths(1.75)
#SCS1.collections[0].set_label(r'$Peak$'+r' '+'r'$stag. pressure,atm$')

plt.xlabel("Arrival "+r'$V_\infty$'+r', km/s' ,fontsize=10)
plt.ylabel(r'$\beta_2$'+r' / '+r'$\beta_1 $' ,fontsize=10)

```

(continues on next page)

(continued from previous page)

```

plt.xticks(fontsize=10)
plt.yticks(np.array([ 1, 20, 40, 60, 80, 100]), fontsize=10)
ax = plt.gca()
ax.tick_params(direction='in')
ax.yaxis.set_ticks_position('both')
ax.xaxis.set_ticks_position('both')
plt.legend(loc='upper right', fontsize=8)

dat0 = ZCS1.allsegs[1][0]
x1,y1=dat0[:,0],dat0[:,1]
F1 = interpolate.interp1d(x1, y1, kind='linear', fill_value='extrapolate', bounds_
↪error=False)

dat1 = QCS1.allsegs[0][0]
x2,y2=dat1[:,0],dat1[:,1]
F2 = interpolate.interp1d(x2, y2, kind='linear', fill_value='extrapolate', bounds_
↪error=False)

dat0a = ZCS1.allsegs[0][0]
xla,yla=dat0a[:,0],dat0a[:,1]
Fla = interpolate.interp1d(xla, yla, kind='linear', fill_value='extrapolate', bounds_
↪error=False)

x3 = np.linspace(0,30,301)
y3 = F1(x3)
y4 = F2(x3)
y4a = Fla(x3)

y8 = np.minimum(y3,y4)

plt.fill_between(x3, y3, y4, where=y3<=y4, color='xkcd:neon green')
plt.fill_between(x3, y4a, y8, where=y4a<=y8, color='xkcd:bright yellow')

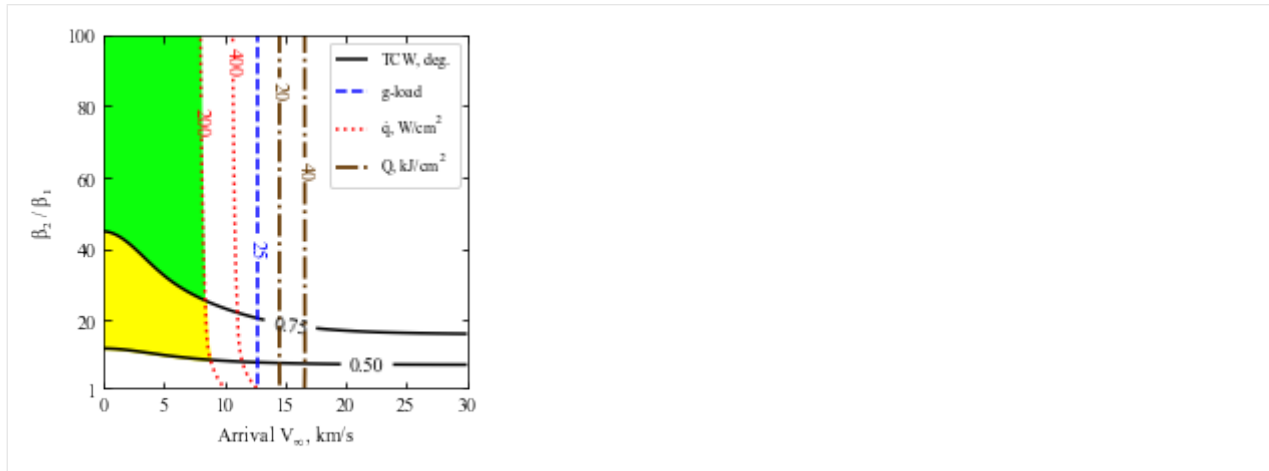
plt.xlim([0.0,30.0])
plt.ylim([1.0,100])

plt.savefig('../plots/giriJaYe2019c-fig16.png',bbox_inches='tight')
plt.savefig('../plots/giriJaYe2019c-fig16.pdf', dpi=300,bbox_inches='tight')
plt.savefig('../plots/giriJaYe2019c-fig16.eps', dpi=300,bbox_inches='tight')

plt.show()

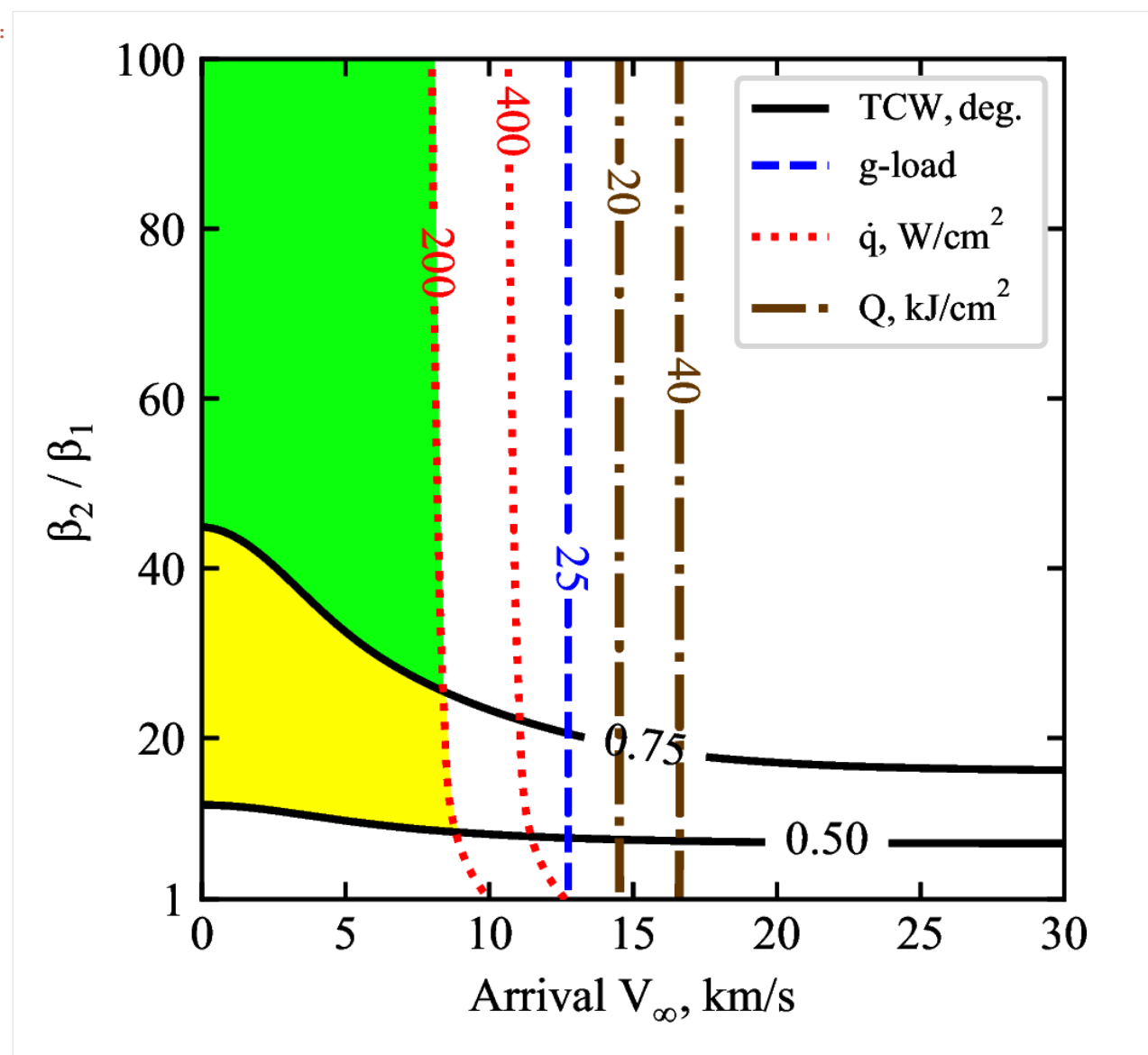
/home/athul/anaconda3/lib/python3.7/site-packages/scipy/interpolate/interp1d.py:
↪609: RuntimeWarning: divide by zero encountered in true_divide
    slope = (y_hi - y_lo) / (x_hi - x_lo)[:, None]
The PostScript backend does not support transparency; partially transparent artists_
↪will be rendered opaque.
The PostScript backend does not support transparency; partially transparent artists_
↪will be rendered opaque.
The PostScript backend does not support transparency; partially transparent artists_
↪will be rendered opaque.
The PostScript backend does not support transparency; partially transparent artists_
↪will be rendered opaque.

```



```
[10]: from IPython.display import Image
Image(filename='../plots/girijaYe2020c-higher-res.png', width=600)
```

[10]:



The plots are now saved in plots/girijaYe2019c.

Congratulations! You could now create the results for referenced journal article in less than a day. It took nearly a year for the authors to put everything together to create these results!

4.9 Example - 09 - Uranus Aerocapture

In this example, we will create combined interplanetary and aerocapture feasibility charts for Uranus.

```
[1]: from AMAT.planet import Planet
from AMAT.vehicle import Vehicle

import numpy as np
from scipy import interpolate
import pandas as pd
```

(continues on next page)

G. AMAT EXAMPLE: VENUS SMALLSAT AEROCAPTURE: PART 2

Refer to the next page for illustration of how AMAT is used for performance assessment of the baseline design using Monte Carlo simulations. The Jupyter notebook is available online¹ at the project documentation website.

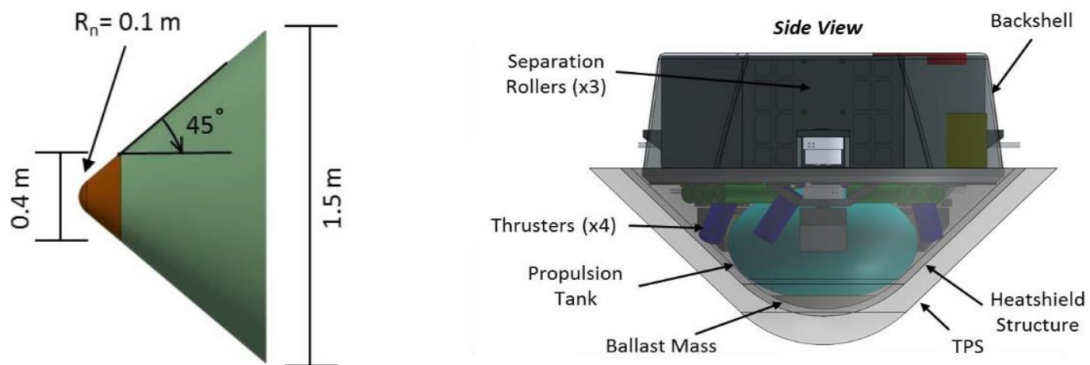
¹[↑https://amat.readthedocs.io/en/master/examples/example-13-venus-aerocapture-5a.html](https://amat.readthedocs.io/en/master/examples/example-13-venus-aerocapture-5a.html)

We analyze the design proposed by “Austin et al. SmallSat Aerocapture to Enable a New Paradigm of Planetary Missions, IEEE Aerospace Conference, 2019, Big Sky, MT. DOI: 10.1109/AERO.2019.8742220

Shown below is the aerocapture vehicle design for Venus SmallSat proposed by Austin et al. The design consists of a drag skirt (shown in green), which is jettisoned. The vehicle parameters are $m = 68.1 \text{ kg}$, $\beta_1 = 38.1 \text{ kg/m}^2$, $\beta_2/\beta_1 = 7.5$. The objective is to insert the small satellite (shown in brown) into a 2,000 km x 200 km orbit around Venus. We will use AMAT to perform Monte Carlo analysis to assess aerocapture performance.

```
[3]: from IPython.display import Image
Image(filename='../plots/drag-modulation-vehicle.png', width=800)
```

[3]:



```
[1]: from AMAT.planet import Planet
from AMAT.vehicle import Vehicle
```

```
[2]: import numpy as np
from scipy import interpolate
import pandas as pd

import matplotlib.pyplot as plt
from matplotlib import rcParams
from matplotlib.patches import Polygon
```

```
[3]: # Set up the planet and atmosphere model.
planet=Planet("VENUS")
planet.loadAtmosphereModel('../atmdata/Venus/venus-gram-avg.dat', 0 , 1 ,2, 3)
planet.h_skip = 150000.0

# Set up the drag modulation vehicle.
vehicle=Vehicle('DMVehicle', 68.2, 38.1, 0.0, 3.1416, 0.0, 0.10, planet)
vehicle.setInitialState(150.0,0.0,0.0,11.0,0.0,-5.50,0.0,0.0)
vehicle.setSolverParams(1E-6)
vehicle.setDragModulationVehicleParams(38.1,7.5)

# Set up the drag modulation entry phase guidance parameters.
vehicle.setDragEntryPhaseParams(6.0, 80.0, 101, -300.0)

# Set the target orbit parameters.
vehicle.setTargetOrbitParams(200.0, 2000.0, 50.0)

# Define the path to atmospheric files to be used for the Monte Carlo simulations.
atmfiles = ['../atmdata/Venus/LAT80S.txt',
            '../atmdata/Venus/LAT60S.txt',
            '../atmdata/Venus/LAT40S.txt',
```

(continues on next page)

(continued from previous page)

```

'../atmdata/Venus/LAT20S.txt',
'../atmdata/Venus/LAT10S.txt',
'../atmdata/Venus/LAT80N.txt',
'../atmdata/Venus/LAT60N.txt',
'../atmdata/Venus/LAT40N.txt',
'../atmdata/Venus/LAT20N.txt',
'../atmdata/Venus/LAT10N.txt',
]

# Set up the Monte Carlo simulation for drag modulation.
# NPOS = 151, NMONTE = 200
# Target EFPA = -5.40 deg
# EFPA 1-sigma error = +/- 0.033 deg
# Nominal beta_1 = 38.1 kg/m2
# beta_1 1-sigma = 0.0
# guidance time step for entry = 0.1s (Freq. = 10 Hz)
# guidance time step after jettison = 1.0 s
# max. solver time step = 0.1 s
# max. time used by solver = 1200 s

vehicle.setupMonteCarloSimulationD(151, 200, atmfiles, 0, 1, 2, 3, 4, True,
                                   -5.40, 0.033, 38.1, 0.0,
                                   0.1, 1.0, 0.1, 1200.0)

```

[4]: # N = 10 shown here, run for a few thousand to be realistic. This will take several hours.

```

vehicle.runMonteCarloD(10, '../data/austin2019/MCB1')

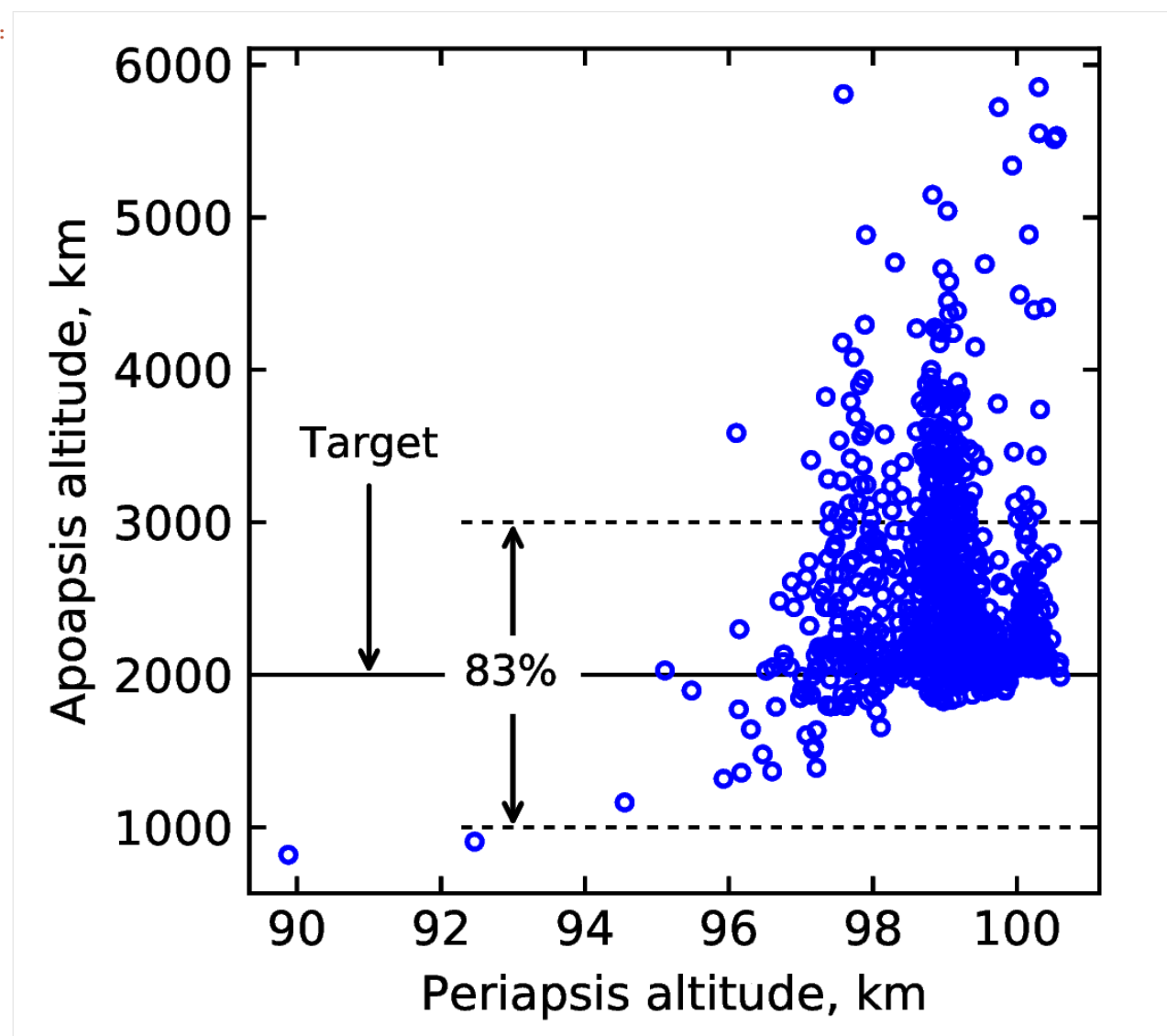
BATCH :../data/austin2019/MCX1, RUN #: 1, PROF: ../atmdata/Venus/LAT10N.txt, SAMPLE #:
→ 51, EFPA: -5.43, SIGMA: -1.67, APO : 2881.64
BATCH :../data/austin2019/MCX1, RUN #: 2, PROF: ../atmdata/Venus/LAT40S.txt, SAMPLE #:
→ 77, EFPA: -5.41, SIGMA: 0.10, APO : 2290.41
BATCH :../data/austin2019/MCX1, RUN #: 3, PROF: ../atmdata/Venus/LAT80N.txt, SAMPLE #:
→ 108, EFPA: -5.43, SIGMA: 2.31, APO : 4615.14
BATCH :../data/austin2019/MCX1, RUN #: 4, PROF: ../atmdata/Venus/LAT60S.txt, SAMPLE #:
→ 195, EFPA: -5.41, SIGMA: 1.61, APO : 2753.68
BATCH :../data/austin2019/MCX1, RUN #: 5, PROF: ../atmdata/Venus/LAT40S.txt, SAMPLE #:
→ 194, EFPA: -5.40, SIGMA: 0.26, APO : 2283.65
BATCH :../data/austin2019/MCX1, RUN #: 6, PROF: ../atmdata/Venus/LAT80N.txt, SAMPLE #:
→ 61, EFPA: -5.37, SIGMA: -1.13, APO : 2059.74
BATCH :../data/austin2019/MCX1, RUN #: 7, PROF: ../atmdata/Venus/LAT20N.txt, SAMPLE #:
→ 126, EFPA: -5.38, SIGMA: -0.53, APO : 2918.58
BATCH :../data/austin2019/MCX1, RUN #: 8, PROF: ../atmdata/Venus/LAT80N.txt, SAMPLE #:
→ 188, EFPA: -5.42, SIGMA: 2.00, APO : 2318.39
BATCH :../data/austin2019/MCX1, RUN #: 9, PROF: ../atmdata/Venus/LAT40N.txt, SAMPLE #:
→ 8, EFPA: -5.40, SIGMA: 1.06, APO : 2264.39
BATCH :../data/austin2019/MCX1, RUN #: 10, PROF: ../atmdata/Venus/LAT80N.txt, SAMPLE #:
→ 183, EFPA: -5.42, SIGMA: 0.05, APO : 2667.25

```

Shown below is the apoapsis dispersion for 1000 runs.

[5]: `from IPython.display import Image`
`Image(filename='../plots/austin-drag-modulation-N1000.png', width=600)`

[5]:

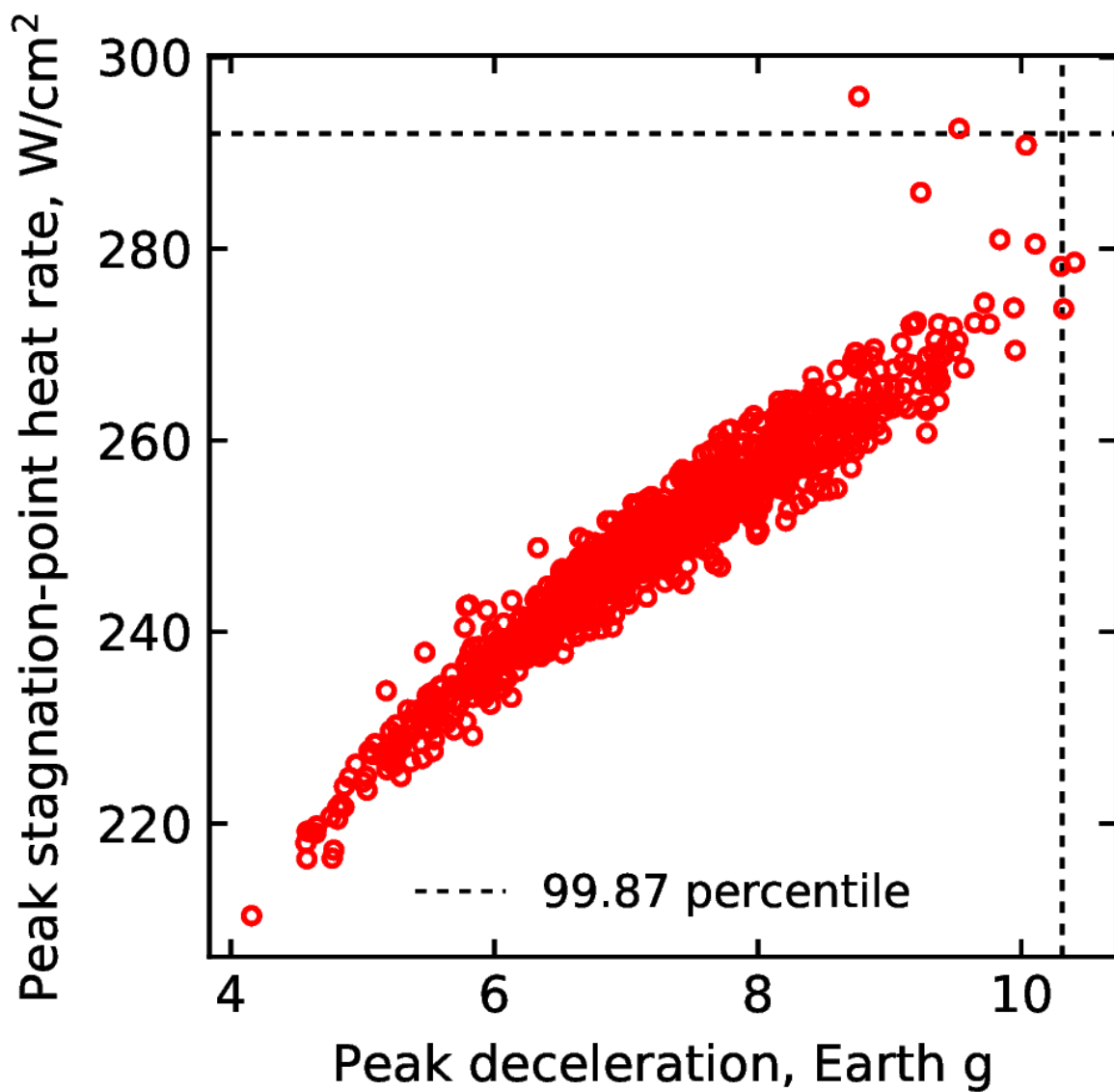


No cases resulted in escape or crashing into the planet. 3 of 1000 cases resulted in apoapsis exceeding 6000 km.

Shown below is the heating rate and g-load dispersion.

```
[6]: from IPython.display import Image
Image(filename='../plots/austin-drag-modulation-heat.png', width=600)
```

[6]:



H. AMAT EXAMPLE: NEPTUNE AEROCAPTURE: PART 1

Refer to the next page for illustration of how AMAT is used to generate the feasibility charts for comprehensive trade space exploration before selecting a baseline design. The Jupyter notebook is available online¹ at the project documentation website.

¹[↑https://amat.readthedocs.io/en/master/examples/example-10-neptune-aerocapture-part-1.html](https://amat.readthedocs.io/en/master/examples/example-10-neptune-aerocapture-part-1.html)

```
[3]: from AMAT.planet import Planet
from AMAT.vehicle import Vehicle

import numpy as np
from scipy import interpolate
import pandas as pd

import matplotlib.pyplot as plt
from matplotlib import rcParams
from matplotlib.patches import Polygon
import os

[4]: # Create a planet object
planet=Planet("NEPTUNE")

# Load an nominal atmospheric profile with height, temp, pressure, density data
planet.loadAtmosphereModel('../atmdata/Neptune/neptune-gram-avg.dat', 0 , 7 , 6 , 5 , \
                           heightInKmFlag=True)

vinf_kms_array = np.linspace( 0.0,      30.0,    11)
LD_array       = np.linspace( 0.0,      1.0 ,    11)

#vinf_kms_array = np.linspace( 0.0,      30.0,    2)
#LD_array       = np.linspace( 0.0,      1.0 ,    2)

[5]: os.makedirs('../data/girijaSaikia2019b')
runID = '20DAY'

num_total      = len(vinf_kms_array)*len(LD_array)
count = 1

v0_kms_array   = np.zeros(len(vinf_kms_array))
v0_kms_array[:] = np.sqrt(1.0*(vinf_kms_array[:]*1E3)**2.0 + \
                          2*np.ones(len(vinf_kms_array))*\
                          planet.GM/(planet.RP+1000.0*1.0E3))/1.0E3

overShootLimit_array = np.zeros((len(v0_kms_array),len(LD_array)))
underShootLimit_array = np.zeros((len(v0_kms_array),len(LD_array)))
exitflag_os_array   = np.zeros((len(v0_kms_array),len(LD_array)))
exitflag_us_array   = np.zeros((len(v0_kms_array),len(LD_array)))
TCW_array          = np.zeros((len(v0_kms_array),len(LD_array)))

[6]: for i in range(0,len(v0_kms_array)):
    for j in range(0,len(LD_array)):
        vehicle=Vehicle('Trident', 1000.0, 200.0, LD_array[j], 3.1416, 0.0, 1.00, \
                         planet)
        vehicle.setInitialState(1000.0,0.0,0.0,v0_kms_array[i],0.0,-4.5,0.0,0.0)
        vehicle.setSolverParams(1E-6)
        overShootLimit_array[i,j], exitflag_os_array[i,j] = vehicle.
        ↪findOverShootLimit (2400.0, 0.1, -80.0, -4.0, 1E-10, 1553575.10)
        underShootLimit_array[i,j], exitflag_us_array[i,j] = vehicle.
        ↪findUnderShootLimit(2400.0, 0.1, -80.0, -4.0, 1E-10, 1553575.10)

        TCW_array[i,j] = overShootLimit_array[i,j] - underShootLimit_array[i,j]

        print("Run #"+str(count)+" of "+ str(num_total)+": Arrival V_infty:
        ↪"+str(vinf_kms_array[i])+" km/s", " L/D:"+str(LD_array[j]) + " OSL:
        ↪"+str(overShootLimit_array[i,j])+" USL: "+str(underShootLimit_array[i,j])+", TCW:
        ↪"+str(TCW_array[i,j])+" EFOS: "+str(exitflag_os_array[i,j])+" EFUS: "+str(exitflag_
```

(continued from previous page)

```

count = count +1

np.savetxt('..../data/girijaSaikia2019b/' +runID+'vinf_kms_array.txt',vinf_kms_array)
np.savetxt('..../data/girijaSaikia2019b/' +runID+'v0_kms_array.txt',v0_kms_array)
np.savetxt('..../data/girijaSaikia2019b/' +runID+'LD_array.txt',LD_array)
np.savetxt('..../data/girijaSaikia2019b/' +runID+'overShootLimit_array.txt',
           ↵overShootLimit_array)
np.savetxt('..../data/girijaSaikia2019b/' +runID+'exitflag_os_array.txt',exitflag_os_
           ↵array)
np.savetxt('..../data/girijaSaikia2019b/' +runID+'undershootLimit_array.txt',
           ↵underShootLimit_array)
np.savetxt('..../data/girijaSaikia2019b/' +runID+'exitflag_us_array.txt',exitflag_us_
           ↵array)
np.savetxt('..../data/girijaSaikia2019b/' +runID+'TCW_array.txt',TCW_array)

Run #1 of 4: Arrival V_infny: 0.0 km/s, L/D:0.0 OSL: -10.88548090497352 USL: -10.
           ↵88548090497352, TCW: 0.0 EFOS: 1.0 EFUS: 1.0
Run #2 of 4: Arrival V_infny: 0.0 km/s, L/D:1.0 OSL: -10.83489821571493 USL: -10.
           ↵93779864834869, TCW: 0.10290043263375992 EFOS: 1.0 EFUS: 1.0
Run #3 of 4: Arrival V_infny: 30.0 km/s, L/D:0.0 OSL: -14.18370732049516 USL: -14.
           ↵18370732049516, TCW: 0.0 EFOS: 1.0 EFUS: 1.0
Run #4 of 4: Arrival V_infny: 30.0 km/s, L/D:1.0 OSL: -13.15751718847605 USL: -20.
           ↵524218087299232, TCW: 7.366700898823183 EFOS: 1.0 EFUS: 1.0

```

```

[7]: acc_net_g_max_array      = np.zeros((len(v0_kms_array),len(LD_array)))
stag_pres_atm_max_array    = np.zeros((len(v0_kms_array),len(LD_array)))
q_stag_total_max_array    = np.zeros((len(v0_kms_array),len(LD_array)))
heatload_max_array         = np.zeros((len(v0_kms_array),len(LD_array)))

for i in range(0,len(v0_kms_array)):
    for j in range(0,len(LD_array)):
        vehicle=Vehicle('Trident', 1000.0, 200.0, LD_array[j], 3.1416, 0.0, 1.00,
                         ↵planet)
        vehicle.setInitialState(1000.0,0.0,0.0,v0_kms_array[i],0.0,overShootLimit_
        ↵array[i,j],0.0,0.0)
        vehicle.setSolverParams(1E-6)

        vehicle.propogateEntry(2400.0, 0.1, 180.0)

        # Extract and save variables to plot
        t_min_os          = vehicle.t_minc
        h_km_os           = vehicle.h_kmc
        acc_net_g_os      = vehicle.acc_net_g
        q_stag_con_os     = vehicle.q_stag_con
        q_stag_rad_os     = vehicle.q_stag_rad
        rc_os              = vehicle.rc
        vc_os              = vehicle.vc
        stag_pres_atm_os  = vehicle.computeStagPres(rc_os,vc_os) / (1.01325E5)
        heatload_os        = vehicle.heatload

        vehicle=Vehicle('Trident', 1000.0, 200.0, LD_array[j], 3.1416, 0.0, 1.00,
                         ↵planet)
        vehicle.setInitialState(1000.0,0.0,0.0,v0_kms_array[i],0.0,underShootLimit_
        ↵array[i,j],0.0,0.0)
        vehicle.setSolverParams(1E-6)

        vehicle.propogateEntry(2400.0, 0.1, 0.0)

```

(continues on next page)

(continued from previous page)

```

# Extract and save variable to plot
t_min_us      = vehicle.t_minc
h_km_us       = vehicle.h_kmc
acc_net_g_us  = vehicle.acc_net_g
q_stag_con_us = vehicle.q_stag_con
q_stag_rad_us = vehicle.q_stag_rad
rc_us          = vehicle.rc
vc_us          = vehicle.vc
stag_pres_atm_us = vehicle.computeStagPres(rc_us, vc_us) / (1.01325E5)
heatload_us    = vehicle.heatload

q_stag_total_os  = q_stag_con_os + q_stag_rad_os
q_stag_total_us  = q_stag_con_us + q_stag_rad_us

acc_net_g_max_array[i,j]      = max(max(acc_net_g_os),max(acc_net_g_us))
stag_pres_atm_max_array[i,j]   = max(max(stag_pres_atm_os),max(stag_pres_atm_
os))
q_stag_total_max_array[i,j]   = max(max(q_stag_total_os),max(q_stag_total_us))
heatload_max_array[i,j]        = max(max(heatload_os),max(heatload_us))

print("V_infty: "+str(vinf_kms_array[i])+" km/s", L/D: "+str(LD_array[j])+"_
G_MAX: "+str(acc_net_g_max_array[i,j])+" QDOT_MAX: "+str(q_stag_total_max_array[i,
j])+" J_MAX: "+str(heatload_max_array[i,j])+" STAG. PRES: "+str(stag_pres_atm_max_
array[i,j])))

np.savetxt('..../data/girijaSaikia2019b/' + runID + 'acc_net_g_max_array.txt', acc_net_g_max_
array)
np.savetxt('..../data/girijaSaikia2019b/' + runID + 'stag_pres_atm_max_array.txt', stag_pres_
atm_max_array)
np.savetxt('..../data/girijaSaikia2019b/' + runID + 'q_stag_total_max_array.txt', q_stag_
total_max_array)
np.savetxt('..../data/girijaSaikia2019b/' + runID + 'heatload_max_array.txt', heatload_max_
array)

V_infty: 0.0 km/s, L/D: 0.0 G_MAX: 0.1330431053594133 QDOT_MAX: 140.91155406501474 J_
MAX: 29874.621801169895 STAG. PRES: 0.002580414807141991
V_infty: 0.0 km/s, L/D: 1.0 G_MAX: 0.19458771430807223 QDOT_MAX: 143.0988625244372 J_
MAX: 30285.689932384335 STAG. PRES: 0.0024914483287594756
V_infty: 30.0 km/s, L/D: 0.0 G_MAX: 17.53516238321169 QDOT_MAX: 50974.88161005046 J_
MAX: 3359148.4906504373 STAG. PRES: 0.3397375503761374
V_infty: 30.0 km/s, L/D: 1.0 G_MAX: 120.73071641252108 QDOT_MAX: 93546.94104353685 J_
MAX: 5072351.332692758 STAG. PRES: 0.08214636492111621

```

```

[8]: N1 = pd.read_excel('..../interplanetary-data/Neptune/N1.xlsx', sheet_name='Sheet1')
N2 = pd.read_excel('..../interplanetary-data/Neptune/N2.xlsx', sheet_name='Sheet1')
N3 = pd.read_excel('..../interplanetary-data/Neptune/N3.xlsx', sheet_name='Sheet1')
N4 = pd.read_excel('..../interplanetary-data/Neptune/N4.xlsx', sheet_name='Sheet1')
N5 = pd.read_excel('..../interplanetary-data/Neptune/Neptune.xlsx', sheet_name='Neptune
')

TOF1 = N1['Atof'].values
TOF2 = N2['Atof'].values
TOF3 = N3['Atof'].values
TOF4 = N4['Atof'].values
TOF5 = N5['TOF'].values*365.0

```

(continues on next page)

(continued from previous page)

```
VINF1 = N1['Avinf'].values
VINF2 = N2['Avinf'].values
VINF3 = N3['Avinf'].values
VINF4 = N4['Avinf'].values
VINF5 = N5['ArrVinf_mag'].values

LC31 = N1['LC3'].values
LC32 = N2['LC3'].values
LC33 = N3['LC3'].values
LC34 = N4['LC3'].values
LC35 = N5['C3'].values

TOF = np.concatenate((TOF1, TOF2, TOF3, TOF4), axis=0)
TOF_y = TOF / 365.0

VINF_kms = np.concatenate((VINF1, VINF2, VINF3, VINF4), axis=0)

LC3 = np.concatenate((LC31, LC32, LC33, LC34), axis=0)

# plt.axhline(y=13.5, linewidth=1, linestyle='dotted', color='black', zorder=0)
# plt.axvline(x=13.0, linewidth=1, linestyle='dotted', color='black', zorder=0)

fig, axes = plt.subplots(1, 2, figsize = (6.5, 3.5))
fig.tight_layout()
plt.subplots_adjust(wspace=0.30)
plt.rc('font', family='Times New Roman')
params = {'mathtext.default': 'regular' }
plt.rcParams.update(params)

a0 = axes[0].scatter(TOF5 / 365.0, VINF5, c=LC35, cmap='jet', vmin=0, vmax=LC35.max(), zorder=10, s=5.0)
a1 = axes[0].scatter(TOF_y, VINF_kms, c=LC3, cmap='jet', vmin=0, vmax=LC35.max(), zorder=11, s=5.0)
cbar = fig.colorbar(a0, ax=axes[0])
cbar.ax.tick_params(labelsize=10)
cbar.set_label(r'$C_3, km^2/s^2$', labelpad=-27, y=1.10, rotation=0, fontsize=10)
cbar.ax.tick_params(axis='y', direction='in')

axes[0].tick_params(direction='in')
axes[0].yaxis.set_ticks_position('both')
axes[0].xaxis.set_ticks_position('both')

axes[0].set_xlabel("Time of flight (TOF), years", fontsize=10)
axes[0].set_ylabel("Arrival "+r'$V_{\infty}$', fontsize=10)

axes[0].set_yticks(np.arange(5, 26, step=5))
axes[0].set_xticks(np.arange(6, 13, step=2))

axes[0].tick_params(axis='x', labelsize=10)
axes[0].tick_params(axis='y', labelsize=10)

x = np.loadtxt('../data/girijaSaikia2019b/' + runID + 'vinf_kms_array.txt')
y = np.loadtxt('../data/girijaSaikia2019b/' + runID + 'LD_array.txt')
```

(continues on next page)

(continued from previous page)

```

Z1 = np.loadtxt('../data/girijaSaikia2019b/' + runID + 'TCW_array.txt')
G1 = np.loadtxt('../data/girijaSaikia2019b/' + runID + 'acc_net_g_max_array.txt')
Q1 = np.loadtxt('../data/girijaSaikia2019b/' + runID + 'q_stag_total_max_array.txt')
H1 = np.loadtxt('../data/girijaSaikia2019b/' + runID + 'heatload_max_array.txt')
S1 = np.loadtxt('../data/girijaSaikia2019b/' + runID + 'stag_pres_atm_max_array.txt')

f1 = interpolate.interp2d(x, y, np.transpose(Z1), kind='cubic')
g1 = interpolate.interp2d(x, y, np.transpose(G1), kind='cubic')
q1 = interpolate.interp2d(x, y, np.transpose(Q1), kind='cubic')
h1 = interpolate.interp2d(x, y, np.transpose(H1), kind='cubic')
s1 = interpolate.interp2d(x, y, np.transpose(S1), kind='cubic')

x_new = np.linspace(0.0, 30, 110)
y_new = np.linspace(0.0, 1.0, 110)
z_new = np.zeros((len(x_new), len(y_new)))

z1_new = np.zeros((len(x_new), len(y_new)))
g1_new = np.zeros((len(x_new), len(y_new)))
q1_new = np.zeros((len(x_new), len(y_new)))
h1_new = np.zeros((len(x_new), len(y_new)))
s1_new = np.zeros((len(x_new), len(y_new)))

for i in range(0, len(x_new)):
    for j in range(0, len(y_new)):

        z1_new[i, j] = f1(x_new[i], y_new[j])
        g1_new[i, j] = g1(x_new[i], y_new[j])
        q1_new[i, j] = q1(x_new[i], y_new[j])
        h1_new[i, j] = h1(x_new[i], y_new[j])
        s1_new[i, j] = s1(x_new[i], y_new[j])

Z1 = z1_new
G1 = g1_new
Q1 = q1_new
S1 = s1_new
H1 = h1_new/1000.0

X, Y = np.meshgrid(x_new, y_new)

Zlevels = np.array([0.75, 1.25, 2.0])
Glevels = np.array([30.0])
Qlevels = np.array([8000.0])
Hlevels = np.array([600.0])
Slevels = np.array([1.0])

ZCS1 = axes[1].contour(X, Y, np.transpose(Z1), levels=Zlevels, colors='black')

plt.clabel(ZCS1, inline=1, fontsize=9, colors='black', fmt='%.2f', inline_spacing=1)
ZCS1.collections[0].set_linewidths(1.0)
ZCS1.collections[1].set_linewidths(1.0)
ZCS1.collections[2].set_linewidths(1.0)

```

(continues on next page)

(continued from previous page)

```
ZCS1.collections[0].set_label(r'$TCW, deg$')

GCS1 = axes[1].contour(X, Y, np.transpose(G1), levels=Glevels, colors='blue',  
    linestyles='dashed')

plt.clabel(GCS1, inline=1, fontsize=9, colors='blue', fmt='%d')
GCS1.collections[0].set_linewidths(1.0)
GCS1.collections[0].set_label(r'$Peak$'+ r' '+r'$g$'+r'$-load$')

QCS1 = axes[1].contour(X, Y, np.transpose(Q1), levels=Qlevels, colors='red',  
    linestyles='dotted')

plt.clabel(QCS1, inline=1, fontsize=9, colors='red', fmt='%d')
QCS1.collections[0].set_linewidths(1.0)
QCS1.collections[0].set_label(r'$Peak$'+r' '+r'$\dot{q}$'+', '+r'$W/cm^2$')

HCS1 = axes[1].contour(X, Y, np.transpose(H1), levels=Hlevels, colors='magenta',  
    linestyles='dashdot')
plt.xlim([0.0,30.0])
plt.clabel(HCS1, inline=1, fontsize=9, colors='magenta', fmt='%d', inline_spacing=1)
HCS1.collections[0].set_linewidths(1.0)
HCS1.collections[0].set_label(r'$Heat$'+ ' '+r'$ load, kJ/cm^2$')

SCS1 = axes[1].contour(X, Y, np.transpose(S1), levels=Slevels, colors='xkcd:emerald',  
    green, linestyles='dashed')
plt.xlim([0.0,30.0])
plt.clabel(SCS1, inline=1, fontsize=9, colors='xkcd:emerald green', fmt='%.1f', inline_  
    spacing=1)
SCS1.collections[0].set_linewidths(1.0)
SCS1.collections[0].set_label(r'$Peak$'+r' '+'stag. pres., bar')

for c in SCS1.collections:  
    c.set_dashes([(0.5, (7.0, 2.0))])

axes[1].tick_params(direction='in')
axes[1].yaxis.set_ticks_position('both')
axes[1].xaxis.set_ticks_position('both')

#axes[1].set_xlabel("Exam score-1", ylabel="Exam score-2")

axes[1].set_xlabel("Arrival "+r'$V_{\infty}$'+r', km/s', fontsize=10)
axes[1].set_ylabel("L/D", fontsize=10)

axes[1].tick_params(axis='x', labelsize=10)
axes[1].tick_params(axis='y', labelsize=10)

legend1 = axes[1].legend(loc='lower left', fontsize=8, frameon=False)

plt.scatter(19.96, 0.40, s=40, c='k', marker='o', zorder=25)
```

(continues on next page)

(continued from previous page)

```

dat0 = ZCS1.allsegs[2][0]
x1,y1=dat0[:,0],dat0[:,1]
F1 = interpolate.interp1d(x1, y1, kind='linear', fill_value='extrapolate', bounds_
↪error=False)

dat1 = GCS1.allsegs[0][0]
x2,y2=dat1[:,0],dat1[:,1]
F2 = interpolate.interp1d(x2, y2, kind='linear', fill_value='extrapolate', bounds_
↪error=False)

dat2 = HCS1.allsegs[0][0]
x3,y3= dat2[:,0],dat2[:,1]
F3 = interpolate.interp1d(x3, y3, kind='linear', fill_value='extrapolate', bounds_
↪error=False)

x4 = np.linspace(0,30,301)
y4 = F1(x4)
y5 = F2(x4)
y6 = F3(x4)

y7 = np.minimum(y5,y6)

plt.fill_between(x4, y4, y7, where=y4<=y7,color='xkcd:neon green')

dat0 = ZCS1.allsegs[1][0]
x1,y1=dat0[:,0],dat0[:,1]
F1 = interpolate.interp1d(x1, y1, kind='linear', fill_value='extrapolate', bounds_
↪error=False)

dat1 = ZCS1.allsegs[2][0]
x2,y2=dat1[:,0],dat1[:,1]
F2 = interpolate.interp1d(x2, y2, kind='linear', fill_value='extrapolate', bounds_
↪error=False)

dat2 = HCS1.allsegs[0][0]
x3,y3= dat2[:,0],dat2[:,1]
F3 = interpolate.interp1d(x3, y3, kind='linear', fill_value='extrapolate', bounds_
↪error=False)

x4 = np.linspace(0,30,301)
y4 = F1(x4)
y5 = F2(x4)
y6 = F3(x4)

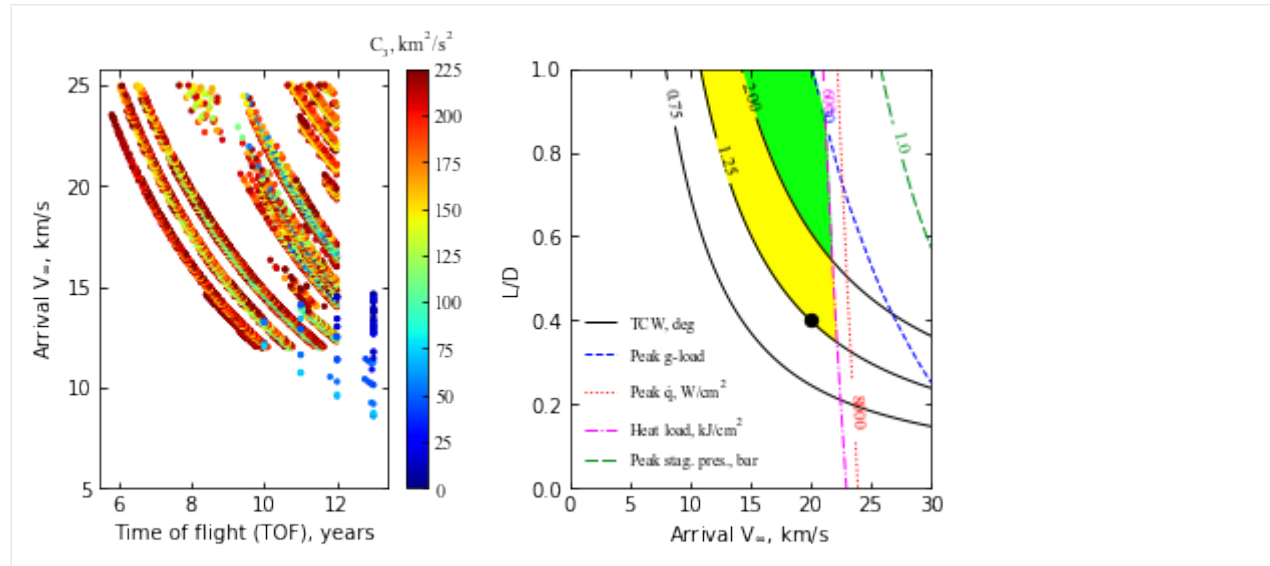
y7 = np.minimum(y5,y6)

plt.fill_between(x4, y4, y7, where=y4<=y7,color='xkcd:bright yellow')
plt.xlim([0.0,30.0])
plt.ylim([0.0,1.0])

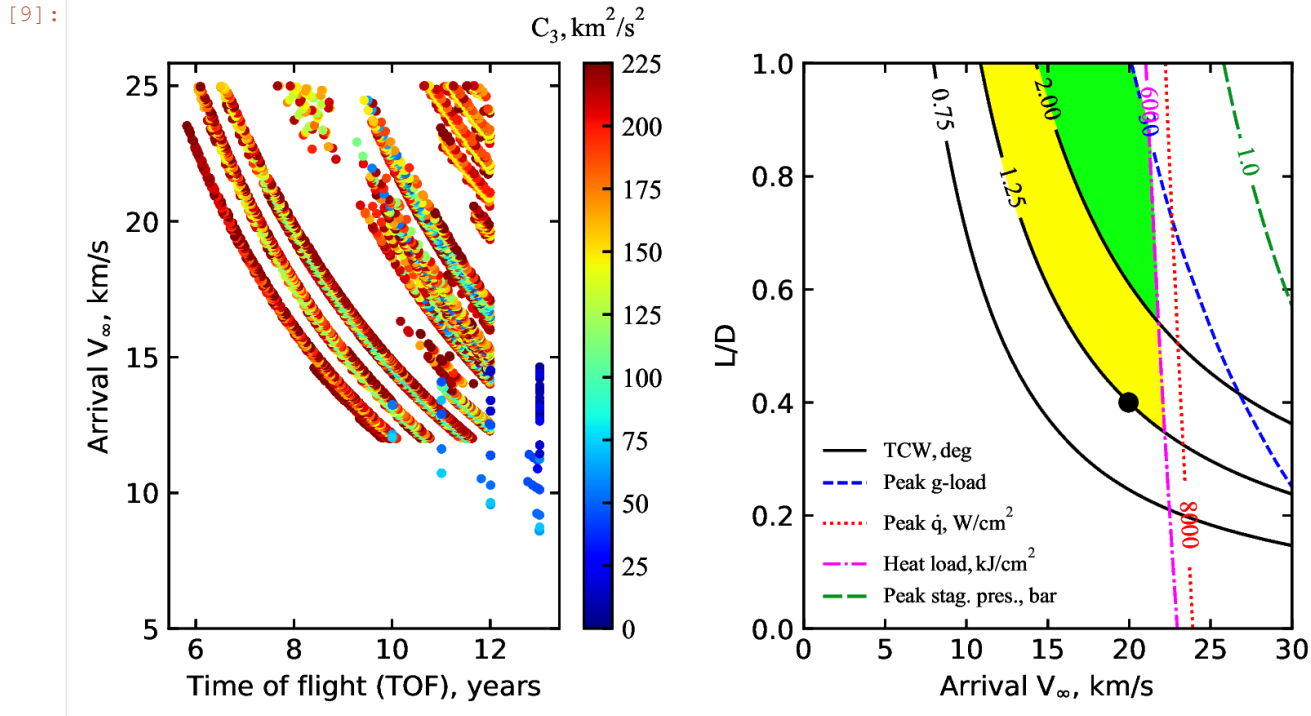
plt.savefig('../plots/girijaSaikia2019b.png',bbox_inches='tight')
plt.savefig('../plots/girijaSaikia2019b.pdf', dpi=300,bbox_inches='tight')
plt.savefig('../plots/girijaSaikia2019b.eps', dpi=300,bbox_inches='tight')

plt.show()

```



```
[9]: from IPython.display import Image
Image(filename='../plots/girijaSaikia2019b-high-res.png', width=800)
```



The plots are now saved in plots/girijaSaikia2019b

Congratulations! You have created the aerocapture feasibility chart for Neptune. The black dot indicates a baseline reference design selected for Monte Carlo analysis in the next example.

I. AMAT EXAMPLE: NEPTUNE AEROCAPTURE: PART 2

Refer to the next page for illustration of how AMAT is used for performance assessment of the baseline design incorporating the effect of delivery, atmospheric, and aerodynamics uncertainties. The Jupyter notebooks are available online^{1,2} at the project documentation website.

¹↑<https://amat.readthedocs.io/en/master/examples/example-11-neptune-aerocapture-part-2a.html>

²↑<https://amat.readthedocs.io/en/master/examples/example-11-neptune-aerocapture-part-2b.html>

4.11 Example - 11 - Neptune Aerocapture - Part 2a: Monte Carlo Simulations

In this example, we will use AMAT to perform Monte Carlo simulations to assess aerocapture vehicle performance.

We reproduce the example Monte Carlo results from “Girija, Saikia, Longuski et al. Feasibility and Performance Analysis of Neptune Aerocapture Using Heritage Blunt-Body Aeroshells, Journal of Spacecraft and Rockets, June, 2020, In press. DOI: 10.2514/1.A34719. Refer Section VIII A: Results for **prograde** entry with maximum range of FMINMAX.

```
[1]: from AMAT.planet import Planet
from AMAT.vehicle import Vehicle

import numpy as np
from scipy import interpolate
import pandas as pd

import matplotlib.pyplot as plt
from matplotlib import rcParams
from matplotlib.patches import Polygon
```

```
[2]: # Create a planet object
planet=Planet("NEPTUNE")

# Load an nominal atmospheric profile with height, temp, pressure, density data
planet.loadAtmosphereModel('../atmdata/Neptune/neptune-gram-avg.dat', 0 , 7 , 6 , 5 ,
                           \\
                           heightInKmFlag=True)

# Create a vehicle object
vehicle=Vehicle('Trident', 1000.0, 200.0, 0.40, 3.1416, 0.0, 1.00, planet)

# Set vehicle conditions at entry interface
# The EFPA selection process is described in Sec. VII in the reference article.
vehicle.setInitialState(1000.0, 0.0, 0.0, 28.00, 0.0,-13.85, 0.0, 0.0)
vehicle.setSolverParams(1E-6)
```

```
[3]: # Set the guidance parameters described in the paper.
# See the function description for parameter details.

# Set max roll rate constraint to 30 deg/s
vehicle.setMaxRollRate(30.0)

# Set Ghdot = 75
# Set Gq = 3.0
# Set v_switch_kms = 18.9
# Set low_Alt_km = 120
# Set numPoints_lowAlt = 101
# Set hdot_threshold = -500 m/s
vehicle.setEquilibriumGlideParams(75.0, 3.0, 18.9, 120.0, 101, -500.0)

# Set target orbit parameters
# periapsis = 4000.0 km
# apoapsis = 400,000 km
# apoapsis tolerance = 10 km
vehicle.setTargetOrbitParams(4000.0, 400.0E3, 10.0E3)
```

```
[4]: # Set path to atmfiles with randomly perturbed atmosphere files.
```

```
atmfiles = ['../atmdata/Neptune/FMINMAX-10L.txt',
            '../atmdata/Neptune/FMINMAX-08L.txt',
            '../atmdata/Neptune/FMINMAX-06L.txt',
            '../atmdata/Neptune/FMINMAX-04L.txt',
            '../atmdata/Neptune/FMINMAX-02L.txt',
            '../atmdata/Neptune/FMINMAX+00L.txt',
            '../atmdata/Neptune/FMINMAX+02L.txt',
            '../atmdata/Neptune/FMINMAX+04L.txt',
            '../atmdata/Neptune/FMINMAX+06L.txt',
            '../atmdata/Neptune/FMINMAX+08L.txt',
            '../atmdata/Neptune/FMINMAX+10L.txt']
```

```
[5]: # Set up Monte Carlo simulation parameters
```

```
# See function description for details.

# NPOS = 1086
# NMONTE = 200

vehicle.setupMonteCarloSimulation(1086, 200, atmfiles, 0, 1, 2, 3, 4, True, \
                                  -13.85, 0.11, 0.40, 0.013, 0.5, 0.1, 2400.0)
```

```
[6]: # Run the Monte Carlo simulation.
```

```
# N = 10 shown here, run for a few thousand to be realistic. This will take several ↴ hours.

vehicle.runMonteCarlo(10, '../data/girijaSaikia2020a/MCB1')

BATCH :../data/girijaSaikia2020a/MCBX, RUN #: 1, PROF: ../atmdata/Neptune/FMINMAX-04L.
↪txt, SAMPLE #: 22, EFPA: -13.97, SIGMA: -1.04, LD: 0.41, APO : 379646.10
BATCH :../data/girijaSaikia2020a/MCBX, RUN #: 2, PROF: ../atmdata/Neptune/FMINMAX+10L.
↪txt, SAMPLE #: 194, EFPA: -13.86, SIGMA: 1.66, LD: 0.39, APO : 397722.98
BATCH :../data/girijaSaikia2020a/MCBX, RUN #: 3, PROF: ../atmdata/Neptune/FMINMAX+04L.
↪txt, SAMPLE #: 188, EFPA: -13.89, SIGMA: -0.71, LD: 0.39, APO : 367641.10
BATCH :../data/girijaSaikia2020a/MCBX, RUN #: 4, PROF: ../atmdata/Neptune/FMINMAX+10L.
↪txt, SAMPLE #: 125, EFPA: -13.79, SIGMA: -1.81, LD: 0.41, APO : 360589.69
BATCH :../data/girijaSaikia2020a/MCBX, RUN #: 5, PROF: ../atmdata/Neptune/FMINMAX-02L.
↪txt, SAMPLE #: 172, EFPA: -13.83, SIGMA: 1.24, LD: 0.40, APO : 383384.65
BATCH :../data/girijaSaikia2020a/MCBX, RUN #: 6, PROF: ../atmdata/Neptune/FMINMAX+02L.
↪txt, SAMPLE #: 29, EFPA: -13.77, SIGMA: -0.44, LD: 0.39, APO : 372647.16
BATCH :../data/girijaSaikia2020a/MCBX, RUN #: 7, PROF: ../atmdata/Neptune/FMINMAX-04L.
↪txt, SAMPLE #: 63, EFPA: -13.71, SIGMA: 0.76, LD: 0.39, APO : 376441.97
BATCH :../data/girijaSaikia2020a/MCBX, RUN #: 8, PROF: ../atmdata/Neptune/FMINMAX+00L.
↪txt, SAMPLE #: 162, EFPA: -13.67, SIGMA: -2.19, LD: 0.41, APO : 380977.85
BATCH :../data/girijaSaikia2020a/MCBX, RUN #: 9, PROF: ../atmdata/Neptune/FMINMAX+06L.
↪txt, SAMPLE #: 60, EFPA: -13.73, SIGMA: 0.86, LD: 0.40, APO : 382393.74
BATCH :../data/girijaSaikia2020a/MCBX, RUN #: 10, PROF: ../atmdata/Neptune/
↪FMINMAX+00L.txt, SAMPLE #: 161, EFPA: -13.77, SIGMA: 0.79, LD: 0.40, APO : 368610.27
```

```
[7]: # Post process Monte Carlo simulation data.
```

```
peri = np.loadtxt('../data/girijaSaikia2020a/MCB1/terminal_periapsis_arr.txt')
apoa = np.loadtxt('../data/girijaSaikia2020a/MCB1/terminal_apoapsis_arr.txt')
```

(continues on next page)

(continued from previous page)

```

peri_dv = np.loadtxt('../data/girijaSaikia2020a/MCB1/periapsis_raise_DV_arr.txt')

del_index1 = np.where(apoa < 0)
del_index2 = np.where(apoa>800.0E3)

del_index = np.concatenate((del_index1, del_index2), axis=1)

print('Simulation statistics')
print('-----')
print("No. of cases escaped :" +str(len(del_index1[0])))
print("No. of cases with apo. alt > 800.0E3 km :" +str(len(del_index2[0])))

Simulation statistics
-----
No. of cases escaped :3
No. of cases with apo. alt > 800.0E3 km :0

```

```
[8]: # Remove escaped cases before plotting
peri_new = np.delete(peri, del_index)
apoa_new = np.delete(apoa, del_index)
peri_dv_new = np.delete(peri_dv, del_index)
```

```
[9]: # Create apoapsis dispersion plot.

fig = plt.figure()
fig.set_size_inches([3.25,3.25])
plt.rc('font',family='Times New Roman')
params = {'mathtext.default': 'regular' }
plt.rcParams.update(params)

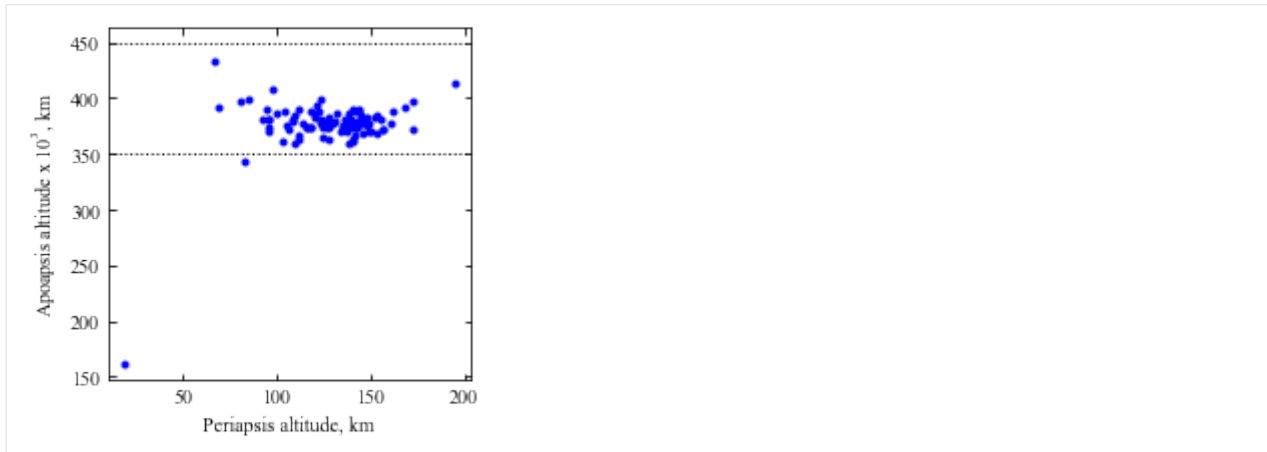
plt.plot(peri_new, apoa_new/1000.0, 'bo', markersize=3)

plt.xlabel('Periapsis altitude, km', fontsize=10)
plt.ylabel('Apoapsis altitude x '+r'$10^3$', km, fontsize=10)

plt.axhline(y=350.0, linewidth=1, color='k', linestyle='dotted')
plt.axhline(y=450.0, linewidth=1, color='k', linestyle='dotted')

ax=plt.gca()
ax.tick_params(direction='in')
ax.yaxis.set_ticks_position('both')
ax.xaxis.set_ticks_position('both')
ax.tick_params(axis='x',labelsize=10)
ax.tick_params(axis='y',labelsize=10)

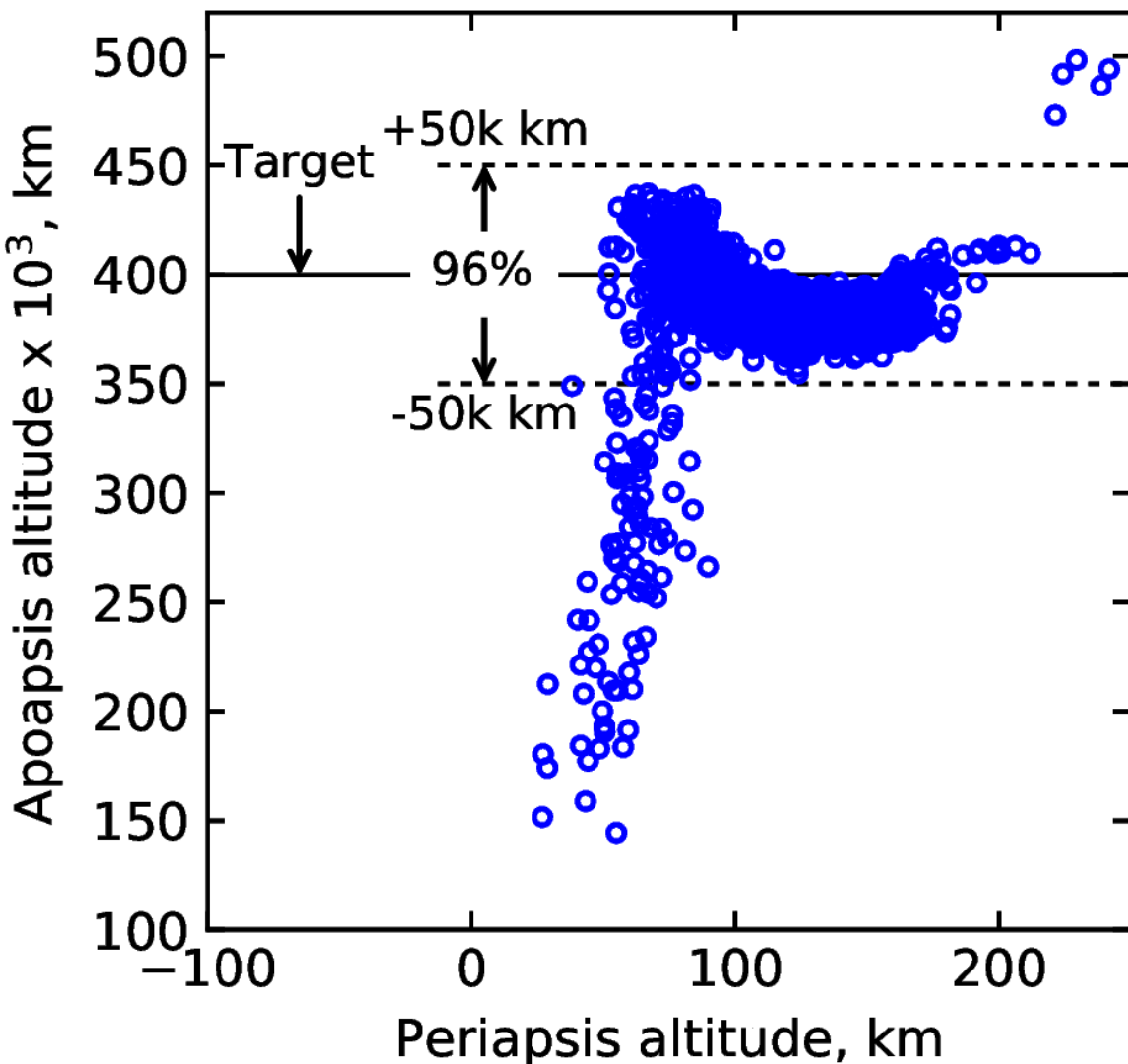
plt.savefig('../plots/girijaSaikia2020a-fig-15-N100.png',bbox_inches='tight')
plt.savefig('../plots/girijaSaikia2020a-fig-15-N100.pdf', dpi=300,bbox_inches='tight')
plt.savefig('../plots/girijaSaikia2020a-fig-15-N100.eps', dpi=300,bbox_inches='tight')
```



This plot only has 100 trajectories. Below is a similar plot with 5000 trajectories

```
[15]: from IPython.display import Image  
Image(filename='../plots/prograde-higher-res.png', width=600)
```

[15]:



[13]: # Create histogram of periapse raise manuever DV

```

fig = plt.figure()
fig.set_size_inches([3.25,3.25])
plt.rc('font',family='Times New Roman')
params = {'mathtext.default': 'regular' }
plt.rcParams.update(params)

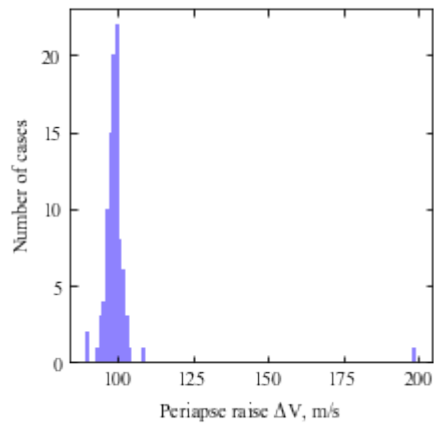
plt.hist(peri_dv_new, bins=100, color='xkcd:periwinkle')
plt.xlabel('Periapse raise '+r'$\Delta V$+', m/s', fontsize=10)
plt.ylabel('Number of cases', fontsize=10)
ax=plt.gca()
ax.tick_params(direction='in')
ax.yaxis.set_ticks_position('both')
ax.xaxis.set_ticks_position('both')
ax.tick_params(axis='x', labelsize=10)
ax.tick_params(axis='y', labelsize=10)

```

(continues on next page)

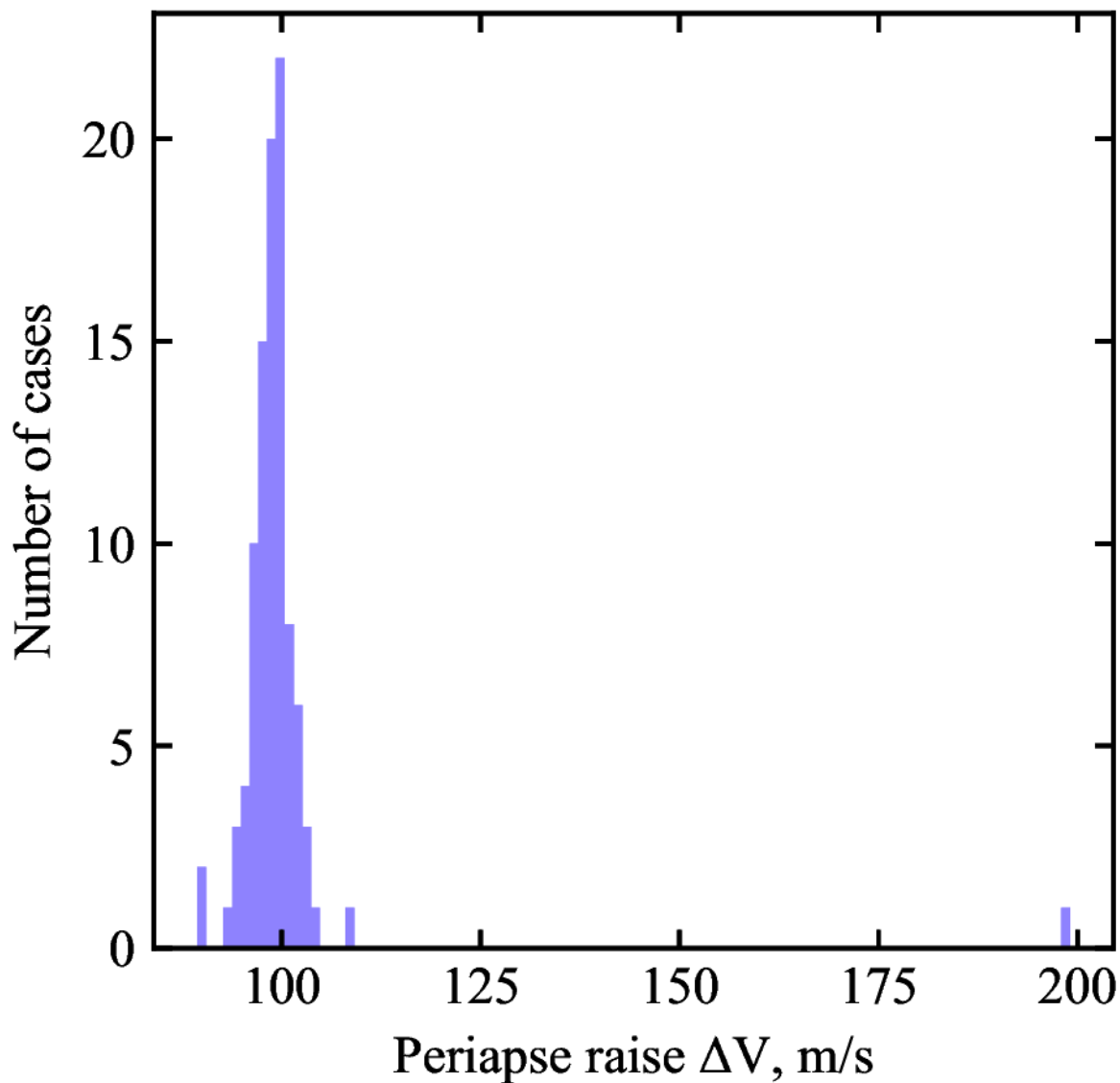
(continued from previous page)

```
plt.savefig('../plots/girijaSaikia2020a-prm-histogram.png',bbox_inches='tight')
plt.savefig('../plots/girijaSaikia2020a-prm-histogram.pdf', dpi=300,bbox_inches='tight
')
plt.savefig('../plots/girijaSaikia2020a-prm-histogram.eps', dpi=300,bbox_inches='tight
')
plt.show()
```



```
[14]: from IPython.display import Image
Image(filename='../plots/girijaSaikia2020a-PRM-higher-res.png', width=600)
```

[14] :



4.12 Example - 12 - Neptune Aerocapture - Part 2b: Monte Carlo Simulations

In this example, we will demonstrate the another published result for aerocapture at Neptune.

We reproduce the example Monte Carlo results from “Girija, Saikia, Longuski et al. Feasibility and Performance Analysis of Neptune Aerocapture Using Heritage Blunt-Body Aeroshells, Journal of Spacecraft and Rockets, June, 2020, In press. DOI: 10.2514/1.A34719. Refer Section VIII A: Results for **retrograde** entry with maximum range of FMINMAX.

```
[1]: from AMAT.planet import Planet
      from AMAT.vehicle import Vehicle
```

(continues on next page)

(continued from previous page)

```
import numpy as np
from scipy import interpolate
import pandas as pd

import matplotlib.pyplot as plt
from matplotlib import rcParams
from matplotlib.patches import Polygon
```

```
[2]: # Create a planet object
planet=Planet("NEPTUNE")

# Load an nominal atmospheric profile with height, temp, pressure, density data
planet.loadAtmosphereModel('../atmdata/Neptune/neptune-gram-avg.dat', 0 , 7 , 6 , 5 , \
                           \heightInKmFlag=True)

# Create a vehicle object
vehicle=Vehicle('Trident', 1000.0, 200.0, 0.40, 3.1416, 0.0, 1.00, planet)

# Set vehicle conditions at entry interface
# Note these conditions are for retrograde equatorial entry
# The EFPA selection process is described in Sec. VII in the reference article.
vehicle.setInitialState(1000.0, 0.0, 0.0, 33.00, 180.0,-11.43, 0.0, 0.0)
vehicle.setSolverParams(1E-6)
```

```
[3]: vehicle.setMaxRollRate(30.0)
vehicle.setEquilibriumGlideParams(75.0, 3.0, 18.9, 120.0, 101, -500.0)
vehicle.setTargetOrbitParams(4000.0, 400.0E3, 10.0E3)
```

```
[4]: atmfiles = ['../atmdata/Neptune/FMINMAX-10L.txt',
               '../atmdata/Neptune/FMINMAX-08L.txt',
               '../atmdata/Neptune/FMINMAX-06L.txt',
               '../atmdata/Neptune/FMINMAX-04L.txt',
               '../atmdata/Neptune/FMINMAX-02L.txt',
               '../atmdata/Neptune/FMINMAX+00L.txt',
               '../atmdata/Neptune/FMINMAX+02L.txt',
               '../atmdata/Neptune/FMINMAX+04L.txt',
               '../atmdata/Neptune/FMINMAX+06L.txt',
               '../atmdata/Neptune/FMINMAX+08L.txt',
               '../atmdata/Neptune/FMINMAX+10L.txt']
```

```
[5]: vehicle.setupMonteCarloSimulation(1086, 200, atmfiles, 0, 1, 2, 3, 4, True, \
                                         -11.43, 0.11, 0.40, 0.013, 0.5, 0.1, 2400.0)
```

```
[6]: # N = 10 shown here, run for a few thousand to be realistic. This will take several \
hours.
```

```
vehicle.runMonteCarlo(100, '../data/girijaSaikia2020b/MCB1')
```

```
BATCH ../data/girijaSaikia2020b/MCBX, RUN #: 1, PROF: ../atmdata/Neptune/FMINMAX+06L. \
txt, SAMPLE #: 42, EFPA: -11.53, SIGMA: 1.86, LD: 0.41, APO : 210233.74
BATCH ../data/girijaSaikia2020b/MCBX, RUN #: 2, PROF: ../atmdata/Neptune/FMINMAX+00L. \
txt, SAMPLE #: 82, EFPA: -11.47, SIGMA: 0.65, LD: 0.42, APO : 404021.05
BATCH ../data/girijaSaikia2020b/MCBX, RUN #: 3, PROF: ../atmdata/Neptune/FMINMAX-08L. \
txt, SAMPLE #: 197, EFPA: -11.39, SIGMA: -0.66, LD: 0.39, APO : 389028.95
```

(continues on next page)

(continued from previous page)

```
BATCH :./data/girijaSaikia2020b/MCBX, RUN #: 4, PROF: ./atmdata/Neptune/FMINMAX+06L.
→txt, SAMPLE #: 172, EFPA: -11.34, SIGMA: 0.10, LD: 0.40, APO : 374039.92
BATCH :./data/girijaSaikia2020b/MCBX, RUN #: 5, PROF: ./atmdata/Neptune/FMINMAX+08L.
→txt, SAMPLE #: 160, EFPA: -11.48, SIGMA: -0.25, LD: 0.41, APO : 294339.22
BATCH :./data/girijaSaikia2020b/MCBX, RUN #: 6, PROF: ./atmdata/Neptune/FMINMAX+04L.
→txt, SAMPLE #: 196, EFPA: -11.46, SIGMA: 0.90, LD: 0.40, APO : 404630.18
BATCH :./data/girijaSaikia2020b/MCBX, RUN #: 7, PROF: ./atmdata/Neptune/FMINMAX-10L.
→txt, SAMPLE #: 167, EFPA: -11.44, SIGMA: 1.80, LD: 0.38, APO : 386631.37
BATCH :./data/girijaSaikia2020b/MCBX, RUN #: 8, PROF: ./atmdata/Neptune/FMINMAX+08L.
→txt, SAMPLE #: 78, EFPA: -11.53, SIGMA: -0.14, LD: 0.42, APO : 209689.06
BATCH :./data/girijaSaikia2020b/MCBX, RUN #: 9, PROF: ./atmdata/Neptune/FMINMAX+08L.
→txt, SAMPLE #: 135, EFPA: -11.46, SIGMA: 0.30, LD: 0.40, APO : 245398.87
BATCH :./data/girijaSaikia2020b/MCBX, RUN #: 10, PROF: ./atmdata/Neptune/
→FMINMAX+10L.txt, SAMPLE #: 45, EFPA: -11.34, SIGMA: 0.40, LD: 0.40, APO : 410500.72
```

```
[7]: peri = np.loadtxt('.../data/girijaSaikia2020b/MCB1/terminal_periapsis_arr.txt')
apoa = np.loadtxt('.../data/girijaSaikia2020b/MCB1/terminal_apoapsis_arr.txt')

peri_dv = np.loadtxt('.../data/girijaSaikia2020b/MCB1/periapsis_raise_DV_arr.txt')

del_index1 = np.where(apoa < 0)
del_index2 = np.where(apoa>800.0E3)

del_index = np.concatenate((del_index1, del_index2), axis=1)

print('Simulation statistics')
print('-----')
print("No. of cases escaped :" +str(len(del_index1[0])))
print("No. of cases with apo. alt > 800.0E3 km :" +str(len(del_index2[0])))

Simulation statistics
-----
No. of cases escaped :0
No. of cases with apo. alt > 800.0E3 km :0
```

```
[8]: peri_new = np.delete(peri, del_index)
apoa_new = np.delete(apoa, del_index)
peri_dv_new = np.delete(peri_dv, del_index)
```

```
[9]: fig = plt.figure()
fig.set_size_inches([3.25,3.25])
plt.rc('font',family='Times New Roman')
params = {'mathtext.default': 'regular' }
plt.rcParams.update(params)

plt.plot(peri_new, apoa_new/1000.0, 'bo', markersize=3)

plt.xlabel('Periapsis altitude, km', fontsize=10)
plt.ylabel('Apoapsis altitude x '+r'$10^3$+', km', fontsize=10)

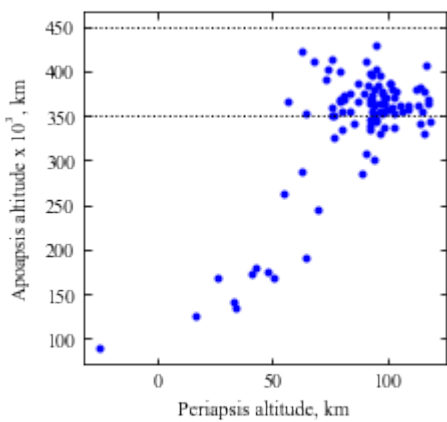
plt.axhline(y=350.0, linewidth=1, color='k', linestyle='dotted')
plt.axhline(y=450.0, linewidth=1, color='k', linestyle='dotted')
```

(continues on next page)

(continued from previous page)

```
ax=plt.gca()
ax.tick_params(direction='in')
ax.yaxis.set_ticks_position('both')
ax.xaxis.set_ticks_position('both')
ax.tick_params(axis='x',labelsize=10)
ax.tick_params(axis='y',labelsize=10)

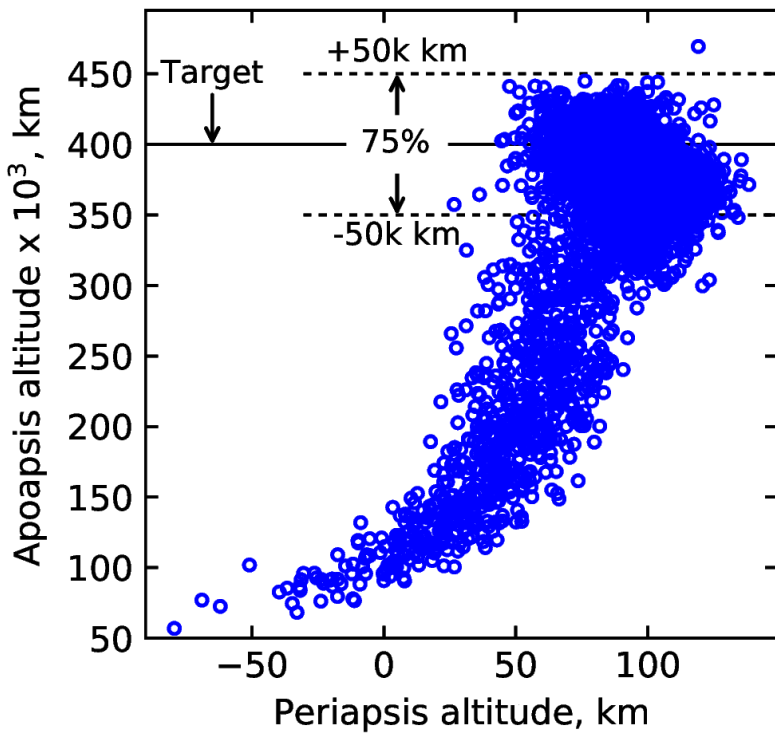
plt.savefig('../plots/girijaSaikia2020b-fig-13-N100.png',bbox_inches='tight')
plt.savefig('../plots/girijaSaikia2020b-fig-13-N100.pdf', dpi=300,bbox_inches='tight')
plt.savefig('../plots/girijaSaikia2020b-fig-13-N100.eps', dpi=300,bbox_inches='tight')
```



This plot only has 100 trajectories. Below is a similar plot with 5000 trajectories

```
[11]: from IPython.display import Image
Image(filename='../plots/retrograde-higher-res.png', width=400)
```

[11]:



[12]:

```

fig = plt.figure()
fig.set_size_inches([3.25,3.25])
plt.rc('font',family='Times New Roman')
params = {'mathtext.default': 'regular' }
plt.rcParams.update(params)

plt.hist(apoa_new/1000.0, bins=50, color='xkcd:periwinkle')
plt.xlabel('Apoapsis altitude x '+r'$10^3$'+', km', fontsize=10)
plt.ylabel('Number of cases', fontsize=10)
ax=plt.gca()
ax.tick_params(direction='in')
ax.yaxis.set_ticks_position('both')
ax.xaxis.set_ticks_position('both')
ax.tick_params(axis='x',labelsize=10)
ax.tick_params(axis='y',labelsize=10)

plt.savefig('../plots/girijaSaikia2020b-apo-histogram-N100.png',bbox_inches='tight')
plt.savefig('../plots/girijaSaikia2020b-apo-histogram-N100.pdf', dpi=300,bbox_inches=
    ↪'tight')
plt.savefig('../plots/girijaSaikia2020b-apo-histogram-N100.eps', dpi=300,bbox_inches=
    ↪'tight')

plt.show()

```

VITA

Athul Pradeepkumar Girija earned his Dual Degree (B.Tech + M.Tech) in Aerospace Engineering with Honors from the Indian Institute of Technology (IIT), Madras in July 2016. He was awarded the Mayan prize and the silver medal for the best academic record (aerospace engineering) in the Class of 2016. During his study at IIT Madras, Athul worked at the National Center for Combustion Research and Development (NCCRD) under Prof. S. R. Chakravarthy on low-NOX lean premixed gas turbine combustors. In the Fall of 2016, Athul began his working in the Advanced Astrodynamics Concepts (AAC) Lab under the supervision of Prof. Sarag Saikia and Prof. James Longuski. During his Ph.D. studies he worked as a Graduate Research Assistant for the JPL-funded Outer Planet Aerocapture Studies and the NASA-funded Ocean Worlds Single Wheel Test Rig project. He also worked as a Graduate Teaching Assistant in the School of Aeronautics and Astronautics for dynamics, signal analysis, and senior design classes. He was awarded the IPPW Student Travel Scholarship in 2017, 2018, and 2019; and the VEXAG Student Travel Grant in 2017 and 2018. Athul was a participant of the 30th NASA Planetary Science Summer Seminar (PSSS) at the Jet Propulsion Laboratory in Pasadena, CA where he led the mission design and the magnetosphere science team for a New Frontiers class Uranus mission concept study. In the 2020 IPPW Webinar Series, Athul was one of the eight invited student speakers selected to present their work to the planetary science and engineering community. During the final year of his Ph.D., he worked as an intern at Pioneer Astronautics in Lakewood, CO under the supervision of Dr. Rubert Zubrin on magnetic sails for spacecraft deorbit and ilmenite enrichment from lunar regolith to produce steel and oxygen in support of NASA's Artmeis program. Athul's interests lie in the general areas of planetary science, mission systems engineering, concept formulation, scientific programming, and software development.

PUBLICATIONS

Peer-reviewed journal articles from this dissertation (published)

A. P. Girija, S. J. Saikia, J. M. Longuski, S. Bhaskaran, M. S. Smith, and J. A. Cutts, Feasibility and Performance Analysis of Neptune Aerocapture Using Heritage Blunt-Body Aeroshells, *Journal of Spacecraft and Rockets*, Vol. 57, No. 6, November 2020. DOI: [10.2514/1.A34719](https://doi.org/10.2514/1.A34719).

A. P. Girija, Y. Lu, and S. J. Saikia, Feasibility and Mass-Benefit Analysis of Aerocapture for Missions to Venus, *Journal of Spacecraft and Rockets*, Vol. 57, No. 1, January 2020. DOI: [10.2514/1.A34529](https://doi.org/10.2514/1.A34529).

Peer-reviewed journal articles from this dissertation (under review)

A. P. Girija, S. J. Saikia, Y. Lu, J. M. Longuski, and J. A. Cutts, Quantitative Assessment of Aerocapture for Solar System Exploration, submitted to *Journal of Spacecraft and Rockets*, June 2021.

A. P. Girija, S. J. Saikia, and J. M. Longuski, Aerocapture Mission Analysis Tool (AMAT), March 2019. [\[GitHub\]](#) [\[Docs\]](#) (Pending submission to *SoftwareX*)

Other peer-reviewed journal articles (published)

S. Jarmak, E. Leonard, A. Akins, E. Dahl, D. R. Cremons, S. Cofield, A. Curtis, C. Dong, E. T. Dunham, B. Journaux, D. Murakami, W. Ng, M. Piquette, **A. P. Girija**, K. Rink, L. Schurmeier, N. Stein, N. Tallarida, M. Telus, L. Lowes, C. Budney, K. L. Mitchell, QUEST: A New Frontiers Uranus Orbiter Mission Concept Study, *Acta Astronautica*, Vol. 170, May 2020. DOI: [10.1016/j.actaastro.2020.01.030](https://doi.org/10.1016/j.actaastro.2020.01.030).

A. Austin, .., **A. P. Girija**, .., + 57 co-authors, Enabling and Enhancing Science Exploration Across the Solar System: Aerocapture Technology for SmallSat to Flagship Missions, *Bulletin of the AAS*, Vol. 53, Issue 4, March 2021. DOI: [10.3847/25c2cfab.4b23741d](https://doi.org/10.3847/25c2cfab.4b23741d)

S. Dutta, Miguel Perez-Ayucar, .., **A. P. Girija**, .., + 59 co-authors, Aerocapture as an Enhancing Option for Ice Giants Missions, *Bulletin of the AAS*, Vol. 53, Issue 4, March 2021. DOI: [10.3847/25c2cfab.e8e49d0e](https://doi.org/10.3847/25c2cfab.e8e49d0e).

S. Limaye, .., **A. P. Girija**, .., + 30 co-authors, Venus Observing System, *Bulletin of the AAS*, Vol. 53, Issue 4, March 2021. DOI: [10.3847/25c2cfab.7e1b0bf9](https://doi.org/10.3847/25c2cfab.7e1b0bf9).

Full-length conference papers

A. P. Girija, S. J. Saikia, J. A. Cutts, and J. M. Longuski, A Unified Framework for Aerocapture Systems Analysis, AAS 19-811, *AAS/AIAA Astrodynamics Specialist Conference*, Portland, ME, August 2019. DOI: [10.31224/osf.io/xtacw](https://doi.org/10.31224/osf.io/xtacw)

A. P. Girija, S. J. Saikia, J. M. Longuski, S. Bhaskaran, M. Smith, and J. A. Cutts, Aerocapture Performance Analysis for a Neptune Mission using Blunt-Body Aeroshell, AAS 19-815, *AAS/AIAA Astrodynamics Specialist Conference*, Portland, ME, August 11–15, 2019. DOI: [10.31224/osf.io/bf3du](https://doi.org/10.31224/osf.io/bf3du)

Conference presentations and extended abstracts

A. P. Girija, S. J. Saikia, J. M. Longuski, S. Bhaskaran, M. Smith, and J. A. Cutts, Ice Giant Aerocapture Using Low-L/D Aeroshells: Uncertainty Quantification and Risk Assessment, *16th International Planetary Probe Workshop (IPPW)*, Oxford University, Oxford, United Kingdom, July 8–12, 2019. [\[PDF\]](#)

A. P. Girija, Y. Lu, S. J. Saikia, J. M. Longuski, and J. A. Cutts, Feasibility and Mass-Benefit Analysis of Aerocapture for SmallSat Missions to Venus, *16th NASA Venus Exploration Group (VEXAG) Meeting*, Johns Hopkins University Applied Physics Lab, Laurel, MD, November 5–8, 2018. [\[PDF\]](#)

Y. Lu, **A. P. Girija**, S. J. Saikia, and J. A. Cutts, Venus Aerocapture Assessment, *15th NASA Venus Exploration Group Meeting*, Johns Hopkins University Applied Physics Lab, Laurel, MD, November 14–16, 2017. [\[PDF\]](#)